Photolibération de NO et absorption à deux photons remarquable dans des complexes dipolaires et quadripolaires de ruthénium à ligand nitrosyle : synthèses et mécanismes

Yael Juarez Martinez

Université Fédérale
Toulouse Midi-Pyrénées

THÈSE

En vue de l'obtention du
DOCTORAT DE L'UNIVERSITÉ DE TOULOUSE
Délivré par l'Université Toulouse 3 - Paul Sabatier

Présentée et soutenue par

YAEL JUAREZ MARTINEZ

Le 9 novembre 2023

Dipolar and quadripolar ruthenium nitrosyl complexes with enhanced two-photon absorption for nitric oxide delivery: syntheses and mechanism

---

Ecole doctorale : **SDM - SCIENCES DE LA MATIERE - Toulouse**

Spécialité : **Chimie Organométallique et de Coordination**

Unité de recherche :
LCC - Laboratoire de Chimie de Coordination

Thèse dirigée par
Isabelle MALFANT et Pascal LACROIX

Jury

Mme. Patricia VICENDO, Présidente
M. Guy ROYAL, Rapporteur
M. Jean-François NIERENGARTEN, Rapporteur
M. Gabriel RAMOS ORTIZ, Membre Invité
Mme Isabelle MALFANT, Directrice de thèse
M. Pascal LACROIX, Co-directeur de thèse

Table of Contents

Contents

Abbreviations and symbols

ACh: Acetylcholine

ASL: Arginosuccinate Lyase

ASS: Argininosuccinate Synthetase

CcO: Cytochrome c Oxidase

COSY: Correlation Spectroscopy

CPS-I: Carbamoyl Phosphate Synthetase I

DFT: Density Functional Theory

DHFR: Dihydrofolate Reductase

EDRF: Endothelium-Derived Relaxing Factor

eNOS: Endothelial NOS

EOKE: Optical Kerr Effect

EOPE: Optoelectronic Pockels Effect

EPR: Electron Paramagnetic Resonance

HMBC: Heteronuclear Multiple Bond Correlation Spectroscopy

HOMO: Highest Occupied Molecular Orbital

HpD: Hematoporphyrin Derivative

HRMS: High Resolution Mass Spectrometry

HSQC: Heteronuclear Single Quantum Coherence Spectroscopy

INOS: Inducible NOS

LUMO: Lowest Unoccupied Molecular Orbital

NMR: Nuclear Magnetic Resonance

nNOS: Neuronal NOS

NOESY: Nuclear Overhauser Effect Spectroscopy

NOS: Nitric Oxyde Synthase

OCT: Ornithine Carbamoyltransferase

OR: Optical Rectification

PACT: Photoactivated chemotherapy

PDT: Photodynamic Therapy

PS: Photosensitizer

ROS: Reactive Oxygen Species

sGC: Guanylate Cyclase

SHG: Second Harmonic

THG: Third Harmonic Generation

TPA: Two-photon absorption

TPEF: Two-photon excitation fluorescence

ε: Molar extinction coefficient

σ_{TPA}: Two-photon Absorption Cross Section

Φ_{NO}: Quantum yield of NO•

INTRODUCTION

Introduction

Nitric oxide (NO•) has attracted significant attention in the research domain over the last three decades. It has been gradually recognized for its numerous physiological roles and various biological functions. Given its antioxidant and antibacterial properties, it clearly holds significant importance. Indeed, the potential of using NO• as a therapeutic agent is immensely promising. Yet, the deployment of this agent presents a major challenge. The currently available drugs release NO• spontaneously and without control, raising concerns about their precision of action to avoid undesirable effect on untargeted cells.

Control the local concentration of NO• is vital since its role in many biological processes is closely tied to this concentration. In this context, it is imperative to design molecules capable of releasing NO• in a controlled manner, triggered by an external stimulus. Among the different methods considered, the use of light proves particularly attractive. Along this line, ruthenium nitrosyl complexes (**RuNO**) appear particularly promising in relation to their capability to release NO• under irradiation in the λ=300–500 nm domain, exclusively, taking advantage of the non-invasive and highly controllable characteristics of light.

However, many of the **RuNO** compounds, ideal for such an application, absorb light in the ultraviolet (UV), which risks damaging tissues. The primary objective of this study is to design and synthesize **RuNO** complexes that can release nitric oxide (NO•) through Two-Photon Absorption (**TPA**) within the therapeutic window of λ = 600–1300 nm. ***Chapter I*** reviews NO• history, its biomedical significance, and its potential in Photodynamic Therapy (PDT) and Photoactivated Chemotherapy (PACT) against diseases like cancer. The chapter also touches on nonlinear optics and their role in TPA.

The core of the ***Chapter II*** focuses on the design, development, and characterization of compounds capable of reach this demand. We proposed a series of **RuNO** complexes (**Figure 1**) where two primary molecular architectures were examined: the dipolar (**Donor**-**Acceptor**) structure in **RuNO-1** and **RuNO-2**, and the quadrupolar (**Acceptor**-**Donor**-**Acceptor**) in the **RuNO-3** to **RuNO-5**.

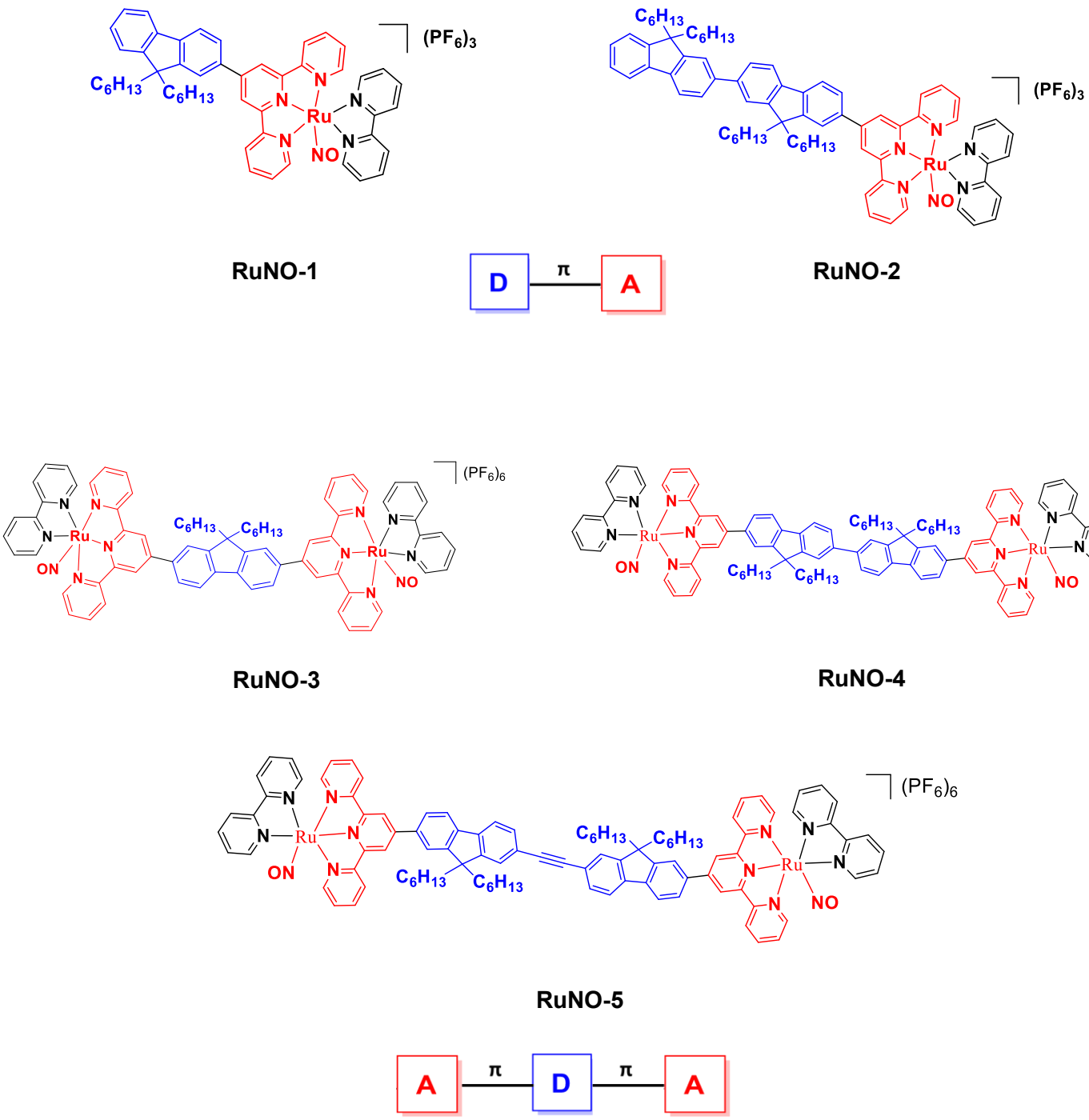

Figure 1. Structure of the dipolar (**Donor**-**Acceptor**, **D**-**A**) complexes for **RuNO-1** and **RuNO-2**, and quadrupolar complexes (**Acceptor**-**Donor**-**Acceptor**, **A**-**D**-**A**) for **RuNO-3** to **RuNO-5**.

The **RuNO** complexes were characterized by UV-vis, Infrared, ^{1}H-NMR, ^{13}C-NMR, High Resolution Mass Spectrometry (HRMS) and for some of them the X-ray structure is presented. Special attention is paid to the role of the hexyl chains in **RuNO$_2$-2**, as X-ray analyses revealed intriguing structural information.

The utility of the Z-Scan technique, particularly in the assessment of TPA properties, is underscored, especially given the low photoluminescence (PL) of these **RuNO** complexes. The experiments were done under irradiation wavelengths of 700 nm, 800 nm, 850 nm, 900 nm, 950 nm, and 1000 nm to have a complete study inside the therapeutic window.

This exploration has not only provided clarity regarding TPA processes but has also illuminated the intrinsic link between these processes and transition selection rules. The experiment results on this chapter shows how the TPA efficiency exhibited by quadrupolar chromophores are higher compared to their dipolar counterparts, having values cross-sections (σ_{TPA}) greater than 1500 GM.

The central topic of ***Chapter III*** is about the study of **RuNO** complexes and their capacity to deliver NO• upon irradiation, the understanding of NO• release mechanism and the photokinetic studies. In this investigation, the formation of NO• during photolysis was primarily confirmed through Griess test and electron paramagnetic resonance (EPR).

After starting with irradiation experiments at 490 nm, it was noticed for **RuNO-3**, a bimetallic complex, the loss of the isosbestic point implied that $\boldsymbol{A \rightarrow C}$ photokinetic model might not be suitable. Instead, they might follow $\boldsymbol{A \rightarrow B \rightarrow C}$ reaction as indicated by reactions (**1**) and (**2**), in which "**A**" denotes the starting **RuNO** complexes, "**B**" the intermediate product which exchange only one NO• ligand with acetonitrile, and finally the final product "**C**" with two acetonitrile as ligands.

$$\underset{\mathbf{A}}{[Ru(NO)Ru(NO)]} + CH_3CN \xrightarrow{h\nu} \underset{\mathbf{B}}{[Ru(NO)Ru(CH_3CN)]} + NO\bullet \quad (1)$$

$$\underset{\mathbf{B}}{[Ru(NO)Ru(CH_3CN)]} + CH_3CN \xrightarrow{h\nu} \underset{\mathbf{C}}{[Ru(CH_3CN)Ru(CH_3CN)]} + NO\bullet \quad (2)$$

To have a better understanding and determined the quantum yield of nitric oxide (Φ_{NO}) for the different complexes at varying wavelengths, the synthesis of the final products "**C**" (**Scheme 1**) and the synthesis of intermediate "**B**" for **RuNO-5** (**Fig. 2**) were done.

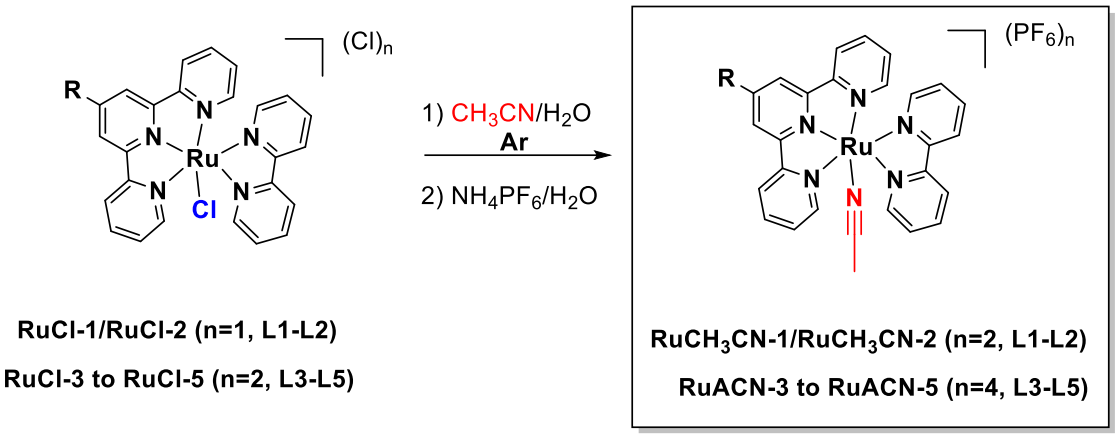

Scheme 1. Synthesis of products **RuCH$_3$CN-1** to **5** from **RuCl-1** to **5**.

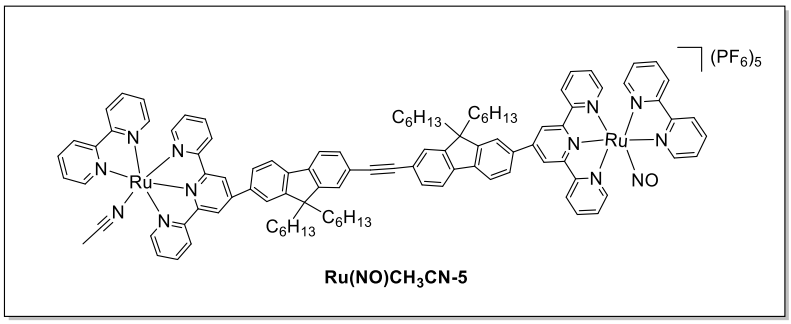

Figure 2. Intermediate **Ru(NO)CH$_3$CN-5**.

In this chapter the quantum yield Φ_{NO} is determined for **RuNO** complexes at different wavelengths by a computer program developed. Among all complexes, **RuNO-5** stood out for its potential applications, given its high quantum yields and versatility with irradiation wavelength.

Finally in ***Chapter IV*** some results with the **RuNO-3** complexes highlight the need for modifications in the bipyridine ligand, in order to conduct *in vitro* tests. Due to the fact that ruthenium nitrosyl complexes can convert the nitrosyl ligand into nitrite in

an aqueous environment and might be toxic to cells, the synthesis of the **trans, trans-Ru(NO)Cl(OH)-3** is proposed as a promising alternative.

The results of this work provide a comprehensive analysis of **RuNO** complexes, emphasizing their potential in PACT, particularly given the profound biological implications of NO•. This work lays the foundation for future research in optimizing these complexes, especially **RuNO-3** and **RuNO-5**, and further explores their potential applications in real-world therapeutic scenarios.

CHAPTER I

State of Art

I-1. Historical Perspective

Nitric oxide (NO•) was initially described in 1772 in "Experiments and Observations on Different Kinds of Air". It was during these early explorations that NO• was first identified and termed as "nitrous air".[1] J. Piestley was the first to describe the reaction of NO• with iron. This discovery marked the beginning of understanding the characteristics and potential applications of NO•, despite the scientific community long-standing belief that NO• had a little significant purpose.

In 1977, F. Murad and his research team discovered that nitric oxide, either in pure form or in combination with other nitrogen compounds such as sodium azide, sodium nitrite, hydroxylamine, or sodium nitroprusside, can stimulate guanylate cyclase activity which generates an enzymatic activity that leads into vascular relaxation.[2] However, the mechanism underlying this discovery remained unclear at this time.

In 1980, R. F. Furchgott made a significant discovery. He found that acetylcholine (ACh) has a strong vasodilatory effect *in vitro*, but it could only cause blood vessels to relax if endothelial cells were present. This means that ACh acts on some receptors of these cells and triggers the release of one or more substances that cause vascular smooth muscle relaxation.[3] This substance was named endothelium-derived relaxing factor (EDRF),[4] and the race to identify it began.

A few years later, in 1986, L. J. Ignarro determined the identity of the elusive EDRF.[5,6] He discovered, that both, NO• and EDRF demonstrate identical properties in their interactions with oxyhemoglobin, oxymyoglobin, and superoxide.[7] The conclusion was thus that EDRF possesses “chemical properties identical to NO• radical”.

For their groundbreaking work in identifying and understanding the role of NO•, R. F. Furchgott, F. Murad and L. J. Ignarro received the Nobel Prize in Medicine or Physiology in 1998. Since then, NO• has become one of the most studied molecules, playing diverse roles in neurotransmission,[8] immunology,[9,10] regulation of local blood flow and platelet function,[11] vasodilatation[12,13] and angiogenesis.[14] Surprisingly, there are not many gases known to play such a crucial biological role in cells.

I-2. Physicochemical Properties of Nitric Oxide

To fully understand the reactivity of NO•, it is important to know its main characteristics and properties. Nitric oxide is a colorless gas at room temperature with a solubility in water (at 25 °C) of about 1.94 mM, similar to oxygen.[15] Also noteworthy is the low polarity of the molecule, which allows diffusion through membranes.

What distinguishes NO• from other molecules is its paramagnetic property, indicating that it is a free radical, Lewis structure of the molecule is shown in **Scheme I-1**. Formal convention indicates that free radicals such as nitric oxide should be written as 'NO•' to clearly indicate the presence of the single unpaired electron.[16] Interestingly, NO• shows no tendency to dimerize under normal pressure,[17] a property that is important for its reactivity in biological media.

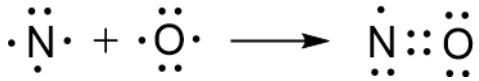

Scheme I-1. Lewis structure for nitric oxide.

Figure I-1 shows the molecular orbital diagram for NO•.[17] It can be noted that the unpaired electron is located in an antibonding orbital π^* and the calculated bond order for NO• is 2.5. The bond length of this molecule is 1.15 Å, a value that falls between the bond lengths of N_2 (1.06 Å) and O_2 (1.18 Å)[18] as shown in **Table I-1.**

Table I-1. Bond order and bond length values of N_2, O_2 and NO•.

Molecule	Bond order	Bond Length (Å)
Nitrogen (N≡N)	3	1.06
Oxygen (O=O)	2	1.18
Nitric oxide (˙N=O)	2.5	1.15

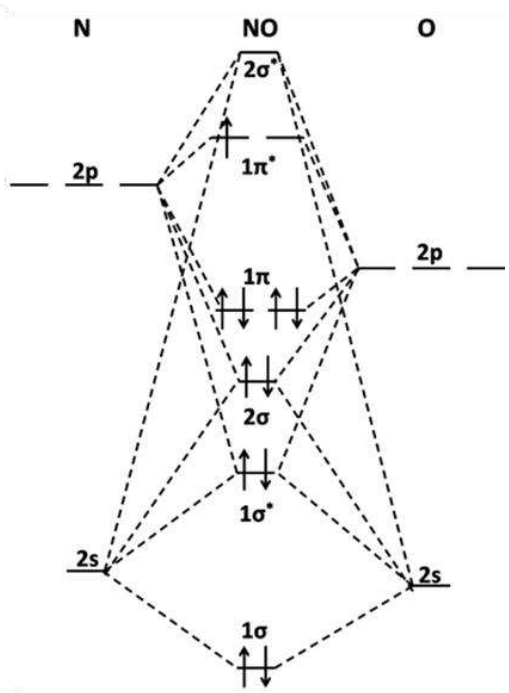

Figure I-1. Qualitative energy level and molecular orbitals diagram of NO•.[17]

The high reactivity of NO• is due to the fact that it contains an unpaired electron, and it has a half-life of 2–30 s.[19] Some basic reactions with a biological importance are going to be introduced.

When exposed to oxygen, nitric oxide converts into nitrogen dioxide[20] (**Equation I-1**):

$$2\ NO\bullet + O_2 \rightarrow 2\ NO_2 \qquad \text{(I-1)}$$

NO• and NO_2• (another paramagnetic species) can combine to give dinitrogen trioxide (N_2O_3) (**Equation I-2**), this reaction can occur in the human body, and it contributes to the regulation of many proteins.[21]

$$NO_2\bullet + NO\bullet \leftrightharpoons N_2O_3 \qquad \text{(I-2)}$$

The role of N_2O_3 in biological reactions is crucial for the regulation of many protein functions. One example is the reaction of coupling a nitroso group to thiols (**Equation I-3**).

$$N_2O_3 + RSH \rightarrow RS{-}NO + NO_2^- + H^+ \qquad \text{(I-3)}$$

Some other representative reactions are presented in **Figure I-2**. Some examples are the reaction of NO• with superoxide ($O_2^{\bullet -}$) that generates peroxynitrite ($ONOO^-$); with strong one-electron reductants, NO• generates nitroxyl (HNO) and with thiyl radical (RS•), it produces S-nitrosothiol (RSNO).[22] Many of these species are reactive and can yield further products.

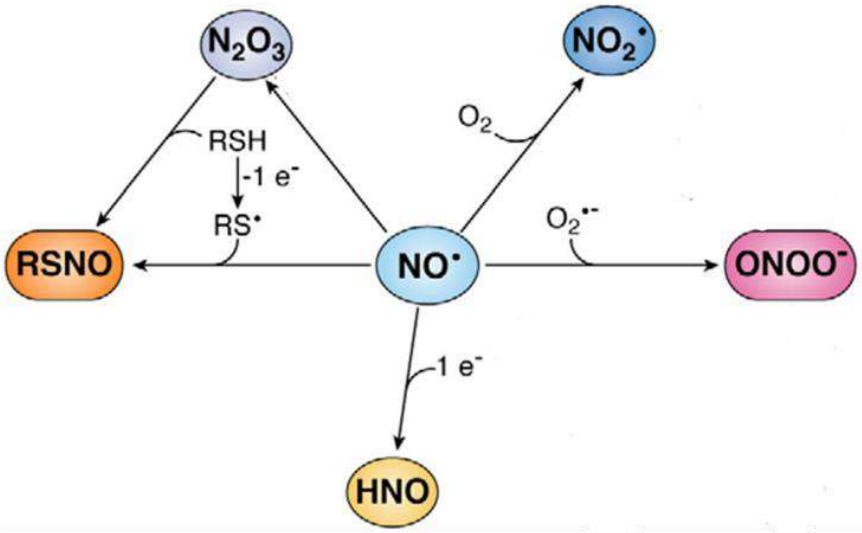

Figure I-2. Some relevant reactions of nitric oxide.[22]

NO• can also react with transition metals to give complexes called "metal nitrosyls". The general reaction can be expressed as in the **Equation I-4**.

$$M + NO^{\bullet} \rightarrow [M{-}NO] \qquad (I\text{-}4)$$

The atoms in nitric oxide can exhibit different hybridization and oxidation states, implying that two possible geometries exist (**Figure I-3**) in which the NO• can be coordinated to the metal center.[23] When the ligand is in the form of nitrosonium cation (NO^+), the angle between M−N-O is about 180°. The second form is a coordination as anion nitroxide form (NO^-), that have a bond angle M-N-O of about 120°.

To determine the electronic structure, various spectroscopic techniques must be employed, with infrared (IR) spectroscopy being the primary method. This is due to the pronounced differences observed among NO^+ (1828-1957 cm^{-1}) and NO• (1584-1630 cm^{-1})[24] in the coordinated form. These values differed between the ones from the

isolated form of NO• (1850-1900 cm^{-1})[25] and from the nitrosonium in the salt $NOBF_4$ (990 cm^{-1}).[26]

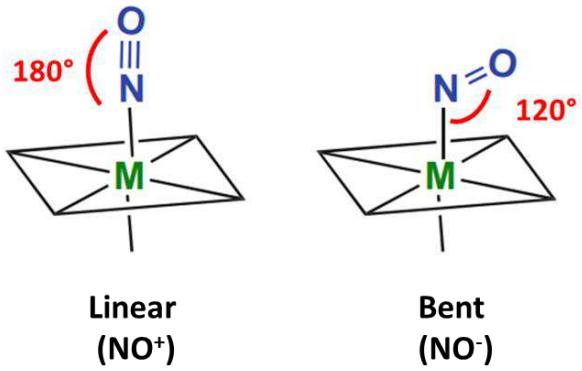

Figure I-3. Geometries of coordination bond between metal center (M) and NO. Linear geometry forming a 180° (left) and bent geometry with 120° angle (right).[27]

In linear metal-nitrosyl complexes the NO^+ serves as a two-electron donor through *σ* donation to the metal. Simultaneously, it accepts electrons from the metal via back-bonding[28] (**Figure I-4**). This back-bonding is facilitated through the orbital overlap between the *d* orbital of the metal center and the *π** orbital of the nitrosyl, adding electron density to this antibonding molecular orbital, strengthening the M- NO• bond while weakening the N-O bond. Consequently, this process of back-bonding can facilitate the release of NO• from the complex with the use of a source of energy such as light.

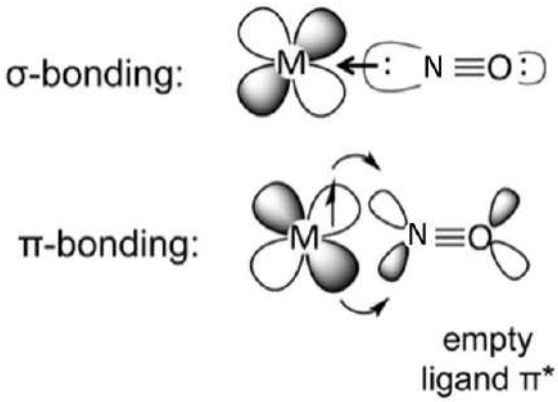

Figure I-4. Components in a coordination bond between a metal center and nitric oxide.

I-3. Photodynamic Therapy (PDT)

Photodynamic Therapy (PDT) is a promising medical treatment based on light and photosensitizing agents to selectively target and destroy abnormal cells.[29] Some of the most successful photosensitizing agents are porfimer sodium, known as Photofrin®[30] and 5-aminovulinic acid, known as ALA-Levulan®[31]. This innovative approach has gained significant attention in recent years due to its non-invasive nature and potential applications in various medical fields, including oncology,[32] dermatology,[33] and ophthalmology.[34] In PDT, the photosensitizer is activated by specific wavelengths of light, leading to the production of reactive oxygen species that induce cell death through oxidative damage (**Figure I-5**).

The history of PDT started back to the early 20th century when, in 1903, the Danish physician N. Finsen was awarded with the Nobel Prize in Medicine for his work on phototherapy in skin tuberculosis,[35] a disease also known as lupus vulgaris. N. Finsen had the idea that light could be harnessed therapeutically, setting the stage for the development of PDT.

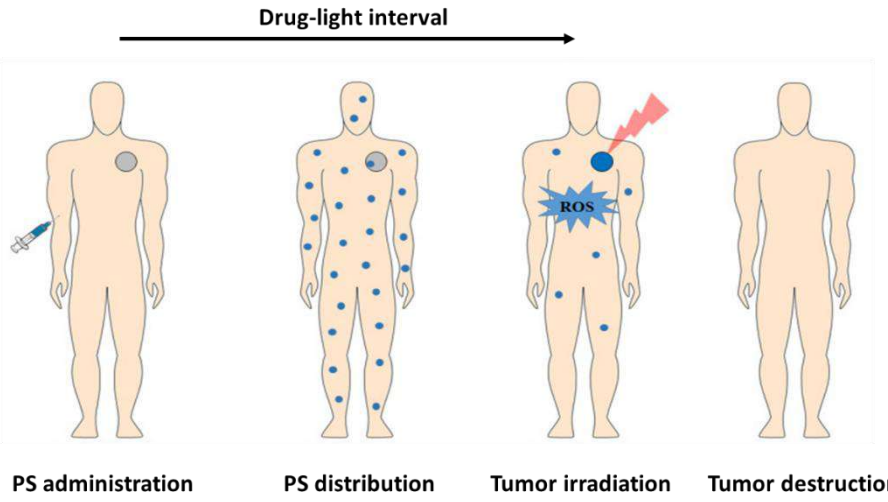

Figure I-5. Representation of the clinical application of PDT protocol for the treatment of a solid and localized tumor.[36]

A significant advance in PDT research happened in the mid-20th century when R. L. Lipson and S. Schwartz, working at the Mayo Clinic, developed a technique to detect and localize malignant tumors in the bladder using a hematoporphyrin,[36] a

compound that selectively accumulates in cancerous cells and fluoresces upon light exposure.

After T. Dougherty and colleagues, through their research at Roswell Park Memorial Institute, found the way for clinical acceptance of PDT. In their landmark 1978 study, "Photoradiation therapy for the treatment of malignant tumors"[37] published in Cancer Research, they demonstrated the therapeutic potential of PDT in treating malignancies. They used a hematoporphyrin derivative (HpD), later named as Photofrin®[38] (**Figure I-6**), and light to treat a variety of malignancies, leading to remarkable tumor regressions. The results demonstrated not only the effectiveness of PDT in treating cancer but also its comparative safety, as it caused minimal damage to healthy tissue.

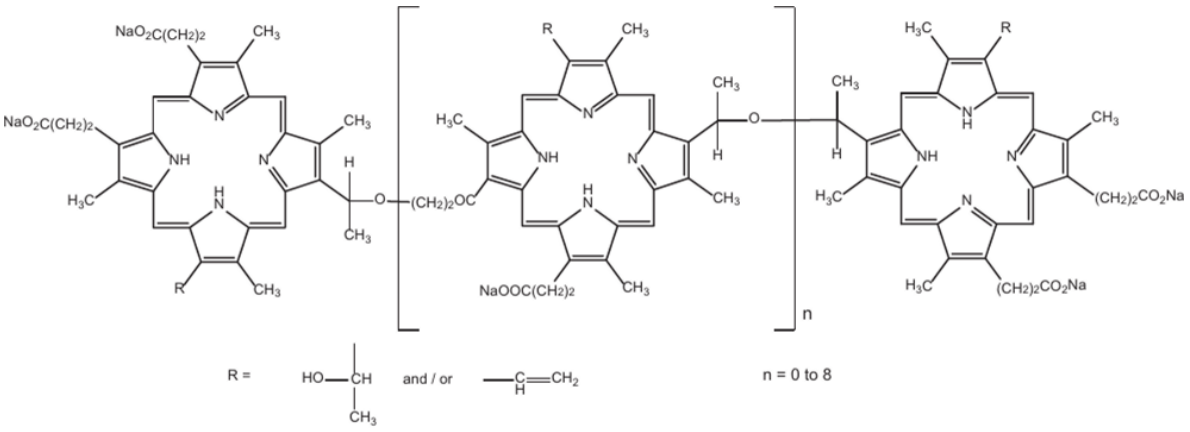

Figure I-6. Structure of porfimer sodium Photofrin®.[38]

The research and clinical results from these studies marked significant milestones in the evolution of PDT and formed the foundation for the wide range of applications of PDT that we see today, from cancer treatment to antimicrobial therapies. Also, the mechanism is known, PDT basically depends on three elements: a photosensitizer (PS), light of a specific wavelength, and molecular oxygen.[39]

Upon exposure to specific light wavelengths, PS triggers a series of photochemical reactions that produce reactive oxygen species (ROS)[40] (**Figure I-7**). After light absorption, the PS transitions from its normal state (singlet state) to an excited singlet state. This state, though unstable, can change to a more stable, excited

state (triplet state) via intersystem crossing. This state can then transfer energy to molecular oxygen (O_2), resulting in the formation of highly reactive singlet oxygen ($^1O_2$) and causing oxidative damage that can lead to cell death, this is known as a type II reaction. Alternatively, the excited PS can directly react with substrates such as cell membranes, resulting in free radicals and radical ions that interact with molecular oxygen to produce ROS, a process known as a type I reaction. These ROS can cause oxidative damage leading to cellular lesions. In simpler terms, PDT is a process in which light and a PS work together in the presence of oxygen to generate harmful reactive species that damage cells.

The specificity of PDT lies in the preferential accumulation of the photosensitizer in target tissues, making it a selective and precise therapeutic option.

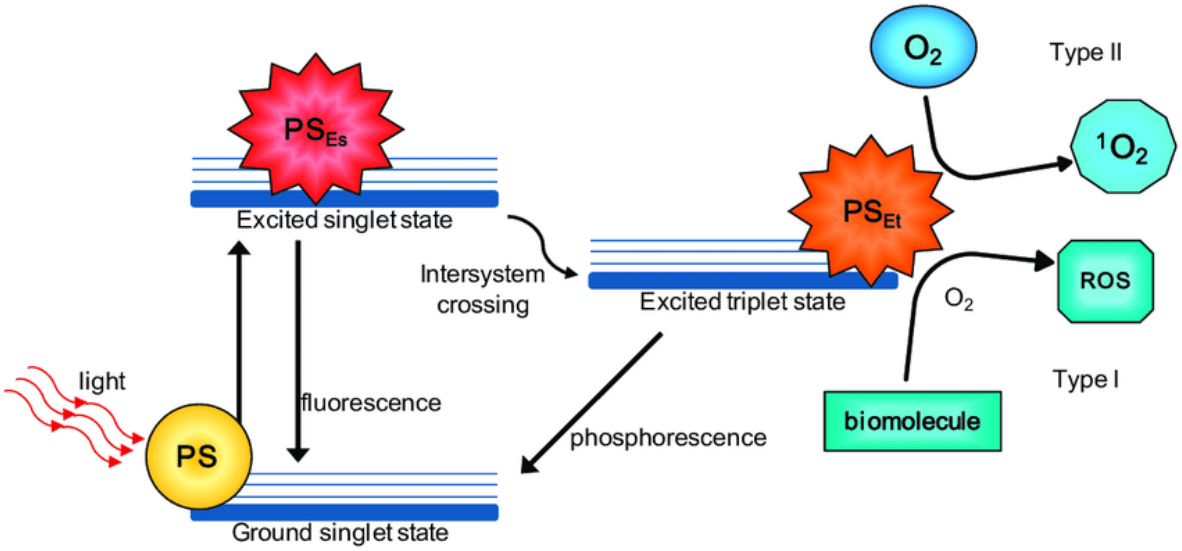

Figure I-7. Mechanisms of Type I and Type II Reactions in Photodynamic Therapy (PDT). An illustrative Jablonski's diagram shows how PDT operates. Here, PS denotes photosensitizer; PS_{Es} stands for PS excited singlet state; PS_{Et} indicates PS excited triplet state; ROS refers to reactive oxygen species, and O_2 represents singlet oxygen.[39]

However, PDT effectiveness is dependent on appropriate tissue oxygenation,[41] and the depth of light penetration can be limiting in some cases so developing of new photosensitizing agents with a high response in the biomedical window (650–1000 nm) is needed.

I-4. Photoactivated Chemotherapy (PACT)

Cancer treatment strategies have evolved significantly over time, with growing interest in therapies that precisely target neoplastic cells, thereby reducing systemic toxicity and improving treatment efficacy. Two of these promising strategies are photodynamic therapy (PDT), which was discussed in the previous section, and photoactivated chemotherapy (PACT).

PACT uses photoactive chemotherapeutic agents that remain inactive and nontoxic until irradiated with light of a specific wavelength.[42] Upon irradiation, these agents undergo chemical transformation through a bond dissociation, like small bioactive molecules such as NO•[43] and CO[44] producing this highly reactive species capable of interacting directly with cellular components such as DNA. This reaction is not necessarily dependent on the presence of oxygen, making PACT potentially more effective under hypoxic conditions,[45] which are common in solid tumors.

Recently, in 2018, a compound for PACT that does not require metallic center, called phototrexate, was synthetized by P. Gorostiza group[46] (**Fig. I-8**). It is considering the first photoswitchable inhibitor of the human dihydrofolate reductase (DHFR), a photochromic analogue of methotrexate, that is a drug to treat cancer and psoriasis.

Different compounds with metal center have been investigated, such as Rh^{III}, Pt^{IV}, Fe^{III}, Ir^{III}, V^{V} and Ru^{II}.[47] Photoactivated metal-based drugs bring a unique set of desirable traits for combating cancer. These features extend beyond typical drug considerations such as water solubility, stability in biological settings, and cellular absorption.

Examples of active PACT compounds (**Figure I-8**) are oxovanadium(IV) complexes,[48] which are extensively studied. These complexes can attach to a type of DNA (from a calf thymus gland) and break it apart when exposed to UV light and red light. This process occurs through a pathway involving $^1O_2$. Other examples are tris-chelated Ir^{III} complexes[49] (**Figure I-8**) that also generate destructive $^1O_2$ efficiently, even under relatively hypoxic conditions.

A notable aspect of these drugs is their capability to differentiate their toxicity levels with and without exposure to light. This feature can limit unwanted side effects

and potentially enhance drug efficacy. Ideally, the activation wavelength of these drugs should fall within the phototherapeutic window of 620–850 nm for maximum tissue penetration.[42]

Finally, ruthenium-based complexes (**Figure I-8**) have become an important class of photoactive agents for PACT due to their unique photophysical properties such as high photostability, long-lived excited triplet states, and the ability to undergo photoinduced ligand exchange reactions.[50] In their inactive state, ruthenium complexes are generally non-toxic. However, exposure to light can convert them into highly reactive species[51] capable of forming covalent bonds with biological targets, often leading to local cell death.

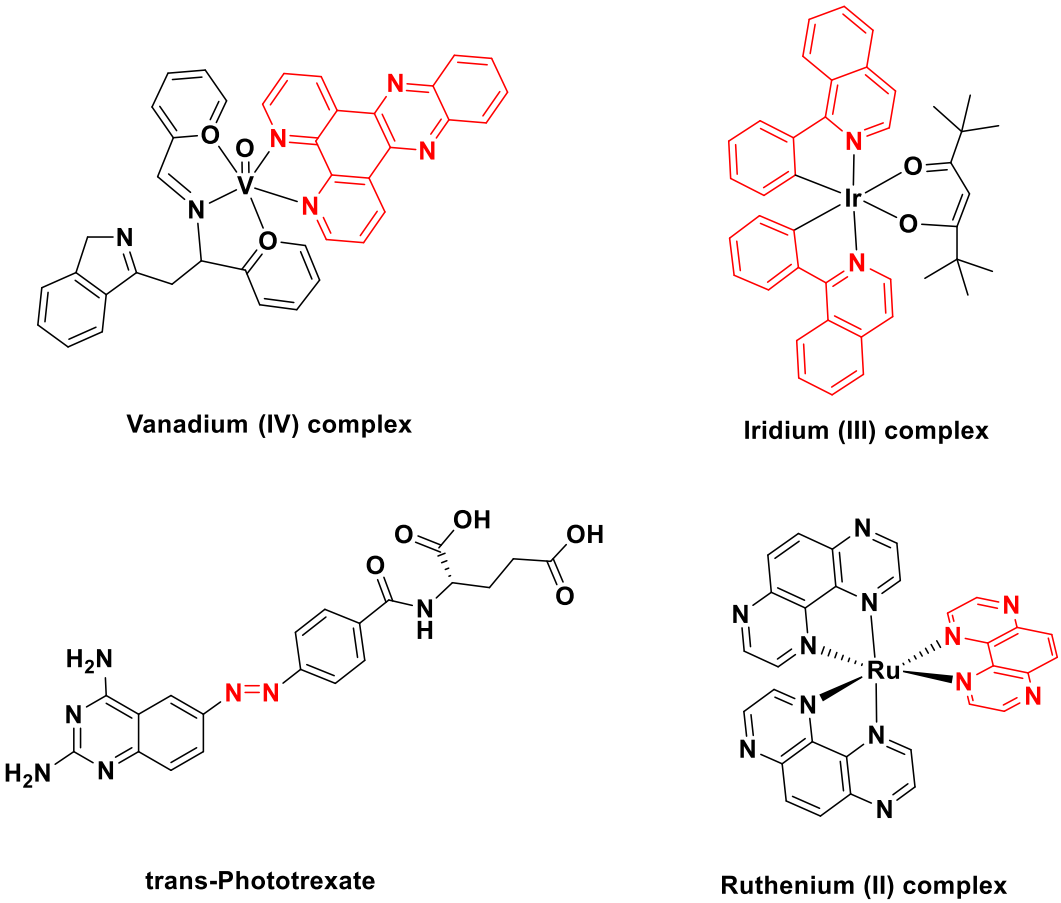

Figure I-8. Examples of molecules for PACT. The active part is drawn in red.

While most ruthenium complexes absorb light in the ultraviolet or visible (UV-vis) range, limiting their ability to penetrate tissue, complexes capable of absorbing in the near-infrared (NIR) range have recently been developed,[50] improving tissue penetration and expanding the treatment area.

With recent advancements in PACT, a new paradigm for the development of therapeutic agents is emerging. Specifically, on creating complexes that, upon exposure to light, can release NO• in a controlled manner. NO• is a potent biological messenger that can induce a multitude of physiological responses, including vasodilation, immune response modulation, and neurotransmission.[53]

I-5. Nitric Oxide Donors

Nitric oxide donors are compounds capable of generating NO•, it has been the focus of considerable attention across different fields, especially within biomedical research due to their therapeutic potential. The most significant applications of these compounds are their utilization in cancer therapy.[54] The concentration of NO• can significantly influence the development of this disease (**Figure I-9**), thereby highlighting the importance of compounds that can release NO• in a controlled manner. At low concentrations (50-100 nM), NO• can promote angiogenesis and cellular proliferation, while at higher concentrations (> 300 nM), it can induce cell death, primarily through apoptosis.[55] For this reason, NO• is regarded as a powerful anticancer agent and holds significant therapeutic potential.

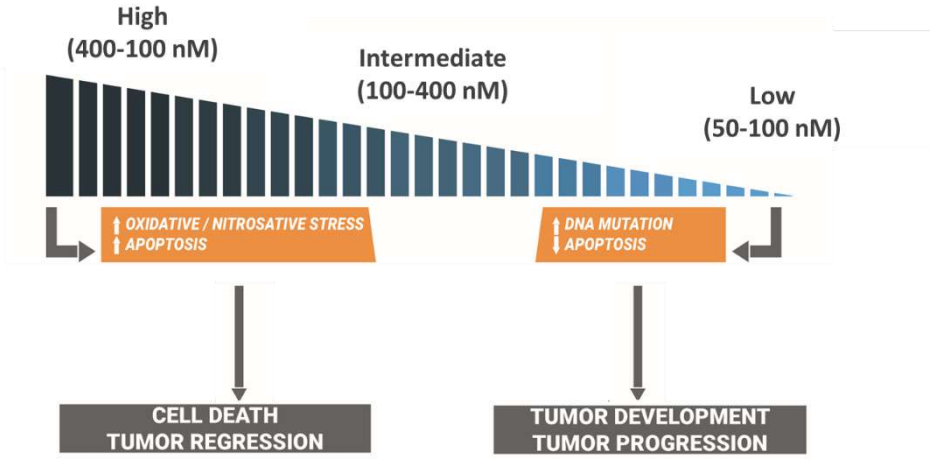

Figure I-9. Biological effects of NO• at different concentration.[55]

Some of the most important NO• donor compounds belong into different categories as organic compounds or coordination. Each category has its unique characteristics and applications, contributing to the broad range of nitric oxide therapeutic potential.

a) Endogenous source of NO•

The formation of NO• in the human body involves the amino acid L-arginine (**Fig. I-10**), This amino acid serves as the primary substrate in a reaction facilitated by enzymes known as nitric oxide synthases (NOS). When L-arginine encounters NOS, it gets converted into N-hydroxyl-L-arginine by oxidation of reduced nicotinamide adenine dinucleotide phosphate (NADPH) to $NADP^+$, the process is repeated to form L-citrulline, which serves as a crucial precursor for the synthesis of proteins and other important molecules such as polyamines, proline, glutamate, dimethylarginine, and urea [56-58] In essence, NO• is released as a byproduct.

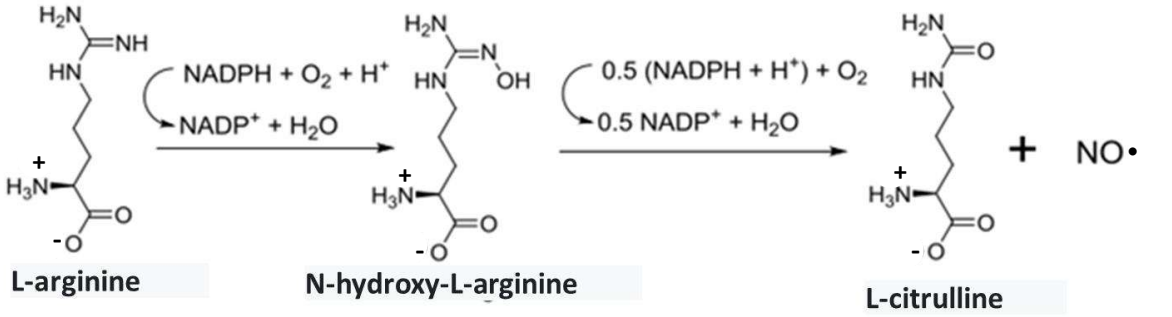

Figure I-10. NO• synthesis through L-arginine.

The synthesis of arginine depends on the presence of enzymes such as ornithine carbamoyltransferase (OCT) and carbamoyl phosphate synthetase I (CPS-I),[59] which are located in the mitochondrial matrix. Most of the citrulline is taken up by the liver, converted to arginine, and then released into the blood. This process is effectuated by argininosuccinate synthetase (ASS) and arginosuccinate lyase (ASL). Moreover, arginine appears to be the only physiological substrate for nitric oxide formation in eukaryotic cell.[60]

There are a few types of NOS enzymes,[61] but three major isoforms play significant roles in different tissues:

- Endothelial NOS (eNOS): Found in the endothelium, which is the inner lining of blood vessels. The NO• produced by eNOS plays a pivotal role in vasodilation,

which is the relaxation of blood vessels, helping in blood pressure regulation and promoting blood flow.

- Neuronal NOS (nNOS): Located in nerve cells, this form of NOS helps produce NO• that functions as a neurotransmitter, playing roles in neuronal communication, memory, and learning.

- Inducible NOS (iNOS): Found in various cells, especially immune cells. Its production is usually triggered by certain immune stimuli, like infections. The NO• produced here can have antimicrobial effects, assisting the immune system in fighting off pathogens.

The metabolism of arginine is complex and involves several enzymes. Among them, the urea cycle is involved, it was one of the first cycles discovered. Its main role is to eliminate excess nitrogen from the body and remove it from the nervous system,[62] acting as a detoxification pathway for ammonia.

b) Organic NO• donor compounds

Organic NO• donor compounds have emerged as a significant class of therapeutic agents. This class of drugs includes notable compounds such as amyl nitrite, a vasodilator that is use in angina treatment. It releases NO• to cause smooth muscle relaxation within blood vessels.[63] Glycerin trinitrate and isosorbide mononitrate are used for the same purpose as well[64] (**Fig. I-11**).

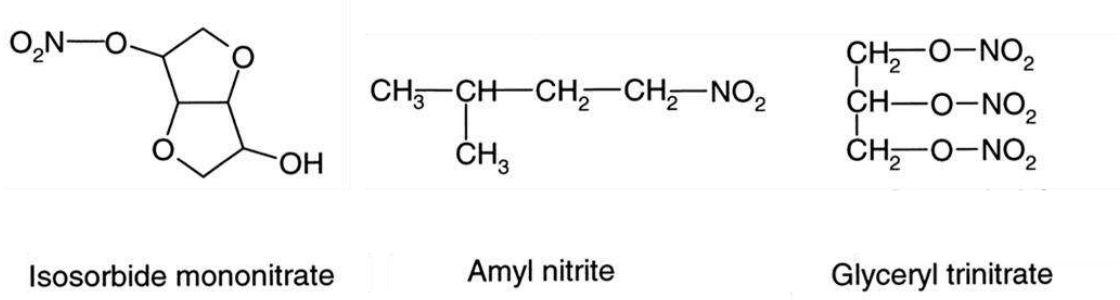

Figure I-11. Main non-steroidal drugs for the release of NO•.

However, this type of compounds come with their own set of challenges.[65,66] One major limitation is the development of tolerance, particularly in glycerin trinitrate. With chronic use, patients might require progressively higher doses to achieve the same therapeutic effect, which could diminish the long-term efficacy of the drug. Additionally, although many NO• donors are designed for controlled release, there are instances where they release NO• unpredictably in certain physiological environments. This unpredictability can lead to suboptimal therapeutic effects or even adverse reactions.

Storage and stability are yet another concern. Some NO• donors are particularly sensitive to external conditions such as light, heat, or moisture, making necessary a special storage conditions to prevent premature NO• release or degradation of the compound.[67] Beyond these, the widespread role of NO• in various physiological processes means that there is potential for NO• donors to exhibit off-target effects. Although some NO• donors can be tailored to target specific tissues or cells, many lack this specificity, leading to systemic effects that may not always be desired.

In conclusion, while the therapeutic potential of organic NO• donors is vast, it is crucial to address their inherent challenges to maximize their clinical utility. However, despite their widespread use, these drugs have significant drawbacks, most notably the lack of control over their release NO•. This uncontrolled release can lead to undesirable side effects and limit their therapeutic efficacy.[68]

c) Coordination NO• donor compounds, iron, and ruthenium

Iron is the most abundant metal in the human body, no independent life forms on earth can survive without iron.[69] This is one of the principal reasons why iron-based transition metal complexes have attracted considerable interest from researchers, their biological applications, and photochemical properties.[70-72]

The first known nitric oxide complex (NO•) was introduced by Playfair in 1849; it was sodium nitroprusside (SNP),[73] that has the chemical formula $Na_2[Fe(CN)_5(NO)]$ (**Figure I-12**). This compound has been utilized as a vasodilator and for angina treatment since 1928. However, its potential to release toxic cyanide ligands (CN^-)[74] and its sensitivity to light, heat, and moisture render it a less-than-ideal option.

After, Roussin's pioneering work laid the foundation for the discovery of key polynuclear cluster compounds of nitric oxide, notably Roussin's Black Salt (RBS) and Roussin's Red Salt (RRS)[75] (**Figure I-12**). Recent studies demonstrate the RBS act has a potential antibacterial agent in the treatment of animal infectious disease where drug resistance is present.[76]

Another family of compound that serve with the same NO• donating capability are dinitrosyl iron complexes (DNICs), they have garnered significant interest in recent years. These complexes are considered potential storage and transport agents for NO•,[77] contributing to the controlled and effective delivery of this important molecule. S.-C. Wu et al. recently investigated a compound from this family,[78] a compound that we will call DNIC-2 (**Figure I-12**), it was synthesized to serve as a NO•-donor species, this water-soluble compound may serve as a promising drug for cancer therapy, but even though its good activity, is air sensitive in aqueous solution.

One of the advantages of these nitrosyl iron complexes with sulfur-containing ligands is that they can release NO• at physiological pH without the need for an external stimulus.[79] However, this also brings with it a drawback: the release of NO• cannot be controlled.

Another remarkable example is the $[(PaPy_3)Fe(NO)](ClO_4)_2$ complex ($PaPy_3H$: N,N-bis(2-pyridylmethyl)amine-N-ethyl-2-pyridine-2-carboxamide), as illustrated in **Figure I-12**. While this type of complex can readily release NO• under physiological conditions in the presence of water,[80] their lack of controlled release mechanisms poses significant challenges. The unregulated release of NO•, given its dual role in cancer progression or inhibition depending on concentration, is not ideal for therapeutic purposes.

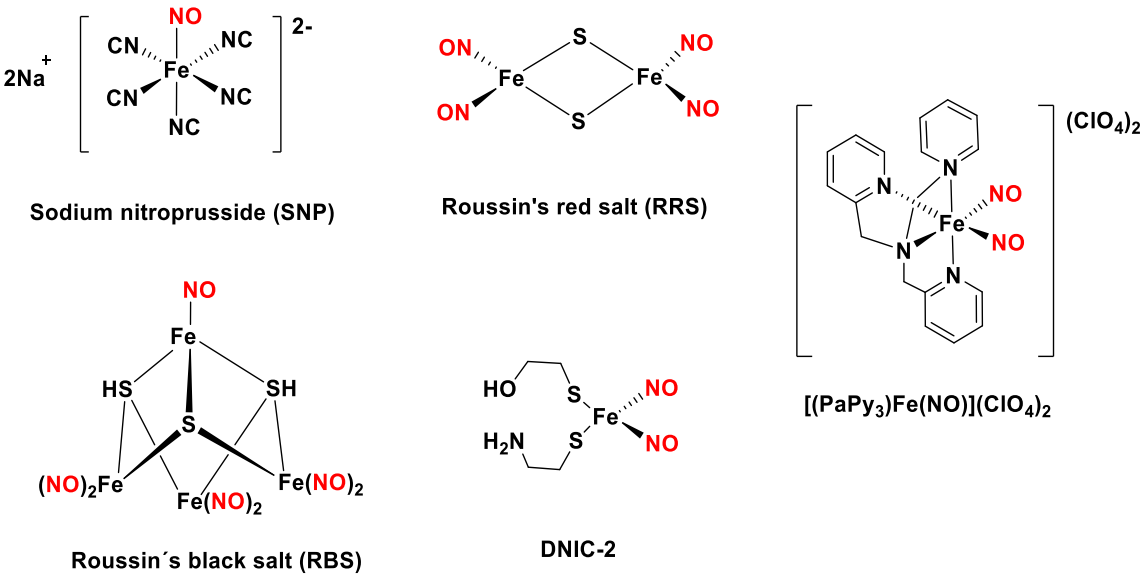

Figure I-12. Examples of iron complexes for NO• delivering capabilities.

Having established the limitations of iron complexes, it is crucial to explore other potential candidates for NO• delivery. One such promising element is ruthenium. Ruthenium complexes have gained significant attention in the field of NO• donors due to a unique set of properties that potentially overcome the challenges posed by iron complexes. In the forthcoming sections, we will explain the advantages of ruthenium complexes and explain why they may present a more viable alternative for controlled NO• delivery in therapeutic applications. Ruthenium complexes exhibit enhanced stability, especially in aqueous environments common in biological systems.[81] This stability is critical for drug delivery, as premature decomposition or reaction can undermine therapeutic efficacy or cause undesirable side effects.

In the case of ruthenium-nitrosyl complexes, the NO• release during photolysis follows the reaction outlined in **Equation I-5**[82] This process involves an exchange in which a solvent molecule replaces the NO• group. This reaction is often associated with a redox process in which the ruthenium changes from a Ru^{II} to a Ru^{III} state.

$$[Ru^{II}(L)\text{-}NO]^{x+} + \text{Solvent} \xrightarrow{h\nu} [Ru^{III}(L)\text{-}\text{Solvent}]^{z+} + NO\bullet \qquad \text{(I-5)}$$

The earliest accounts of photoactive ruthenium nitrosyls indicate the photosensitivity of the $K_2[Ru(NO)(Cl)_5]$, In 1971,[83] L. Cox and G. Wallace observed that an acidic aqueous solution of $K_2[Ru(NO)(Cl)_5]$ turned brown over a period of hours when exposed to light due to the formation of $K_2[Ru(H_2O)(Cl)_5]$ (**Fig. I-13**). In 1983, S. Sinitsyn and co-workers investigated the nature of that product following UV irradiation of $K_2[Ru(NO)(Cl)_5]$ in aqueous solution by EPR spectroscopy and they confirmed the generation of the Ru^{III} specie and NO•.[84]

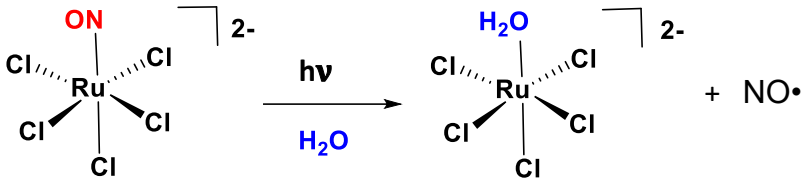

Figure I-13. One of the first NO• photoliberation reactions.

The P. K. Mascharak group has systematically developed an extensive series of ruthenium nitrosyls with polypyridyl ligands containing carboxyamide moieties[85] (**Fig. I-14**). The primary set of complexes, derived from pentadentate polypyridines like $Ru(PaPy_3)(NO)$, showed a promising capacity for NO• delivery to biologically significant proteins such as cytochrome c oxidase (CcO) and soluble guanylate cyclase (sGC). The extension of the ligand conjugation in $Ru(PaPy_2Q)(NO)$ resulted in a beneficial rise in NO• release efficiency and a desired shift of the photoband to longer wavelengths.[86]

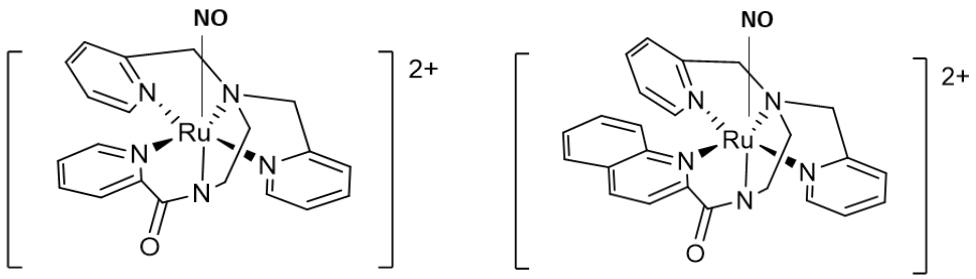

Figure I-14. Chemical structures of $[Ru(PaPy_3)(NO)]^{2+}$ (left) and $[Ru(PaPy_2Q)(NO)]^{2+}$(right).

The group further devised a second series of complexes using tetradentate ligands, incorporating two carboxamide groups that coordinate the Ru center in the equatorial plane (**Figure I-15**).[86] By adjusting the donor-acceptor properties of the equatorial binding groups and modifying the periphery of the tetradentate ligands, a bathochromic shift of the photoband in the resulting complexes was achieved.

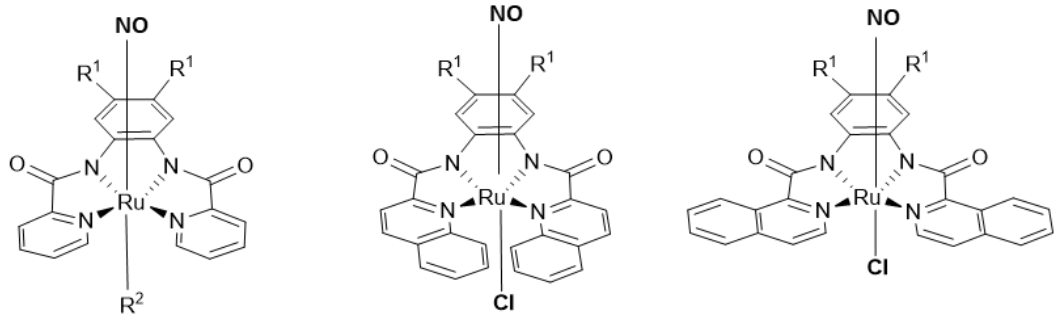

Figure I-15. Chemical structures of different ruthenium complexes containing different tetradentate ligands.

To date, [Ru(terpy-bipy)(Ligand)NO]$^{3+}$(**Fig. I-16**), are the most extensively described ruthenium-based NO• releasing molecule in the literature.[87] Many of this ruthenium complexes have been examined for their potential therapeutic properties, as they release NO• under specific irradiation wavelengths which further underscores their potential in therapeutic applications.

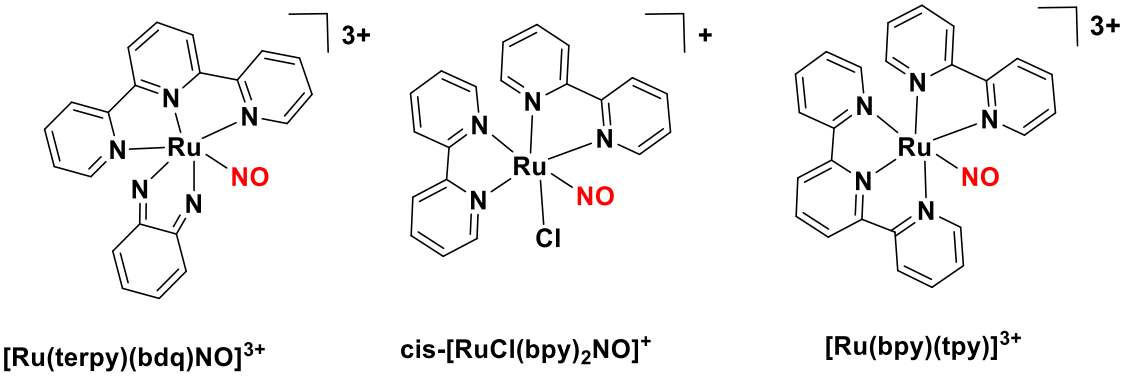

Figure 1-16. Examples of ruthenium complexes containing terpyridine and/or bipyridine in their structure.

In the past two decades, researchers have increasingly focused on metal-nitrosyl complexes, specifically those that release NO• via photoactivation, as promising therapeutic applications. In 2014,[88] Malfant and colleagues reported the synthesis of two ruthenium nitrosyl complexes, derived from the 4'-(2-fluorenyl)-2.2':2'',6''-terpyridine ligand, namely the cis-(Cl,Cl) and trans-(Cl,Cl) isomers (**Fig. I-17**), positioning these as potential candidates for photodynamic therapy. Subsequent studies in 2016[89] demonstrated the photocytotoxicity of the trans-(Cl,Cl) isomer against HCT-116 colon cancer cells, with promising results.

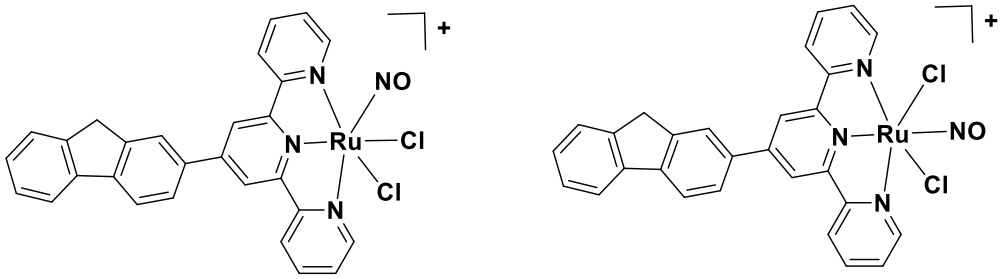

cis-(Cl, Cl)-[Ru(flutpy)]$^+$ **trans-(Cl, Cl)-[Ru(flutpy)]$^+$**

Figure I-17. Cis and trans ruthenium isomers derived from 4'-(2-fluorenyl)-2.2':2'',6''-terpyridine ligand.

The field continues to evolve and research into the potential applications of these complexes in medicine is increasing. These compounds promise to play an increasingly important role in the future of medicine.

In general, most ruthenium complexes absorb light in the ultraviolet-visible (UV-vis) range, which limits their ability to absorb optical radiation at different depths of the biological tissue (**Fig I-18**), Due to inherent limitations of implementing PACT with photosensitizer with absorption bands in the UV-vis range, novel complexes capable of absorbing in the near-infrared (NIR) range through nonlinear optical effects have recently been developed,[90-92] improving the tissue depth at which PACT can be implemented and expanding the treatment area. The nonlinear effect of TPA allow to generate photoexcitation ruthenium complexes in the IR wavelength range, this not only increases tissue penetration of the phototherapy, but also allows precise spatial localization of the treatment, minimizing potential damage to healthy tissue.

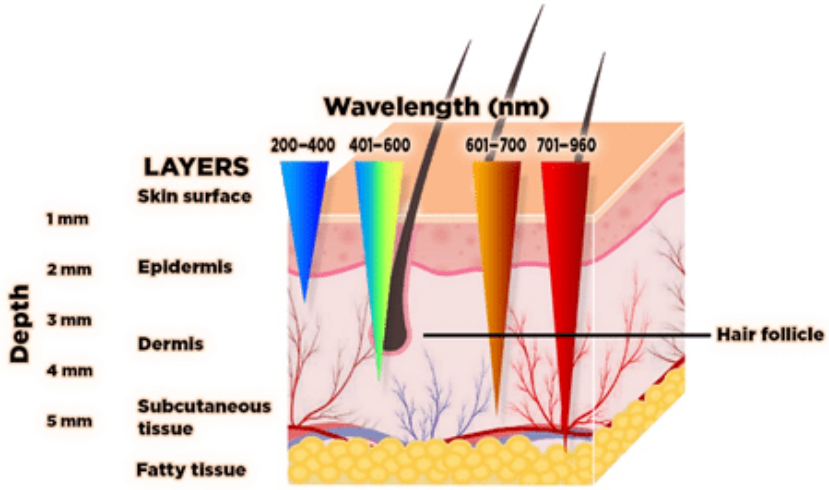

Figure I-18. Light skin penetration under different wavelengths of irradiation.[93]

Ruthenium complexes suitable for TPA offer a new horizon for PACT. They allow the use optical radiation of lower-energy, deeper light penetration for photoactivation, expanding the range of treatable diseases as skin cancer[94] and the depth at which effective treatment can be delivered. While further research is needed to optimize these complexes for clinical use, preliminary results suggest a promising future for ruthenium-based PACT with TPA in cancer treatment.

I-6. Nonlinear Optics

Nonlinear optics involves the study of phenomena in which the interaction between light and matter deviates from the predictions of classical linear optics.[95] These interactions lead to phenomena such as frequency conversion,[96] optical harmonic generation,[97] modulation of linear refractive index[98] and TPA processes,[99] to name a few.

One of the fundamental elements that plays an important role in nonlinear optics is the dipole moment. An electric dipole essentially consists of two charges of equal magnitude but opposite sign, located in close proximity to each other[100] (**Fig. I-19**). The interaction of an electromagnetic wave with a material result in the induction of a polarization in that material, causing a redistribution or realignment of the charges. This

in turn leads to the generation of an induced dipole moment ($\vec{\mu}$), which aligns itself in the opposite direction to the applied field.[101]

The dipole moment ($\vec{p}$) can be defined as the product of the magnitude of the charge and the separation ($\vec{r}$) between the centers of the positive and negative charges on a molecule.[102] This relationship is expressed in **Equation (I-6)** as follows:

$$\vec{p} = q\vec{x} \tag{I-6}$$

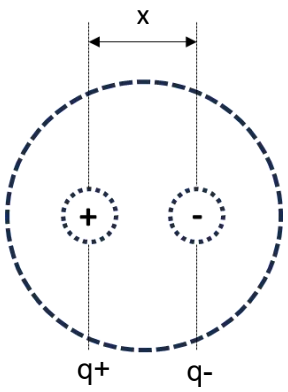

Figure I-19. Separation of center of masses of charges due to electric field.

In the other hand, polarizability is the tendency of matter to acquire an electric dipole moment proportional to the applied electric field.[103] While polarizability occurs in a molecular level, a collection of electric dipole moments leads to polarization. Both terms, the dipole moment and polarization are related by the **Equation I-7**:

$$\vec{P} = \vec{p}N \tag{I-7}$$

Where *N* is the number of dipoles per unit volume.

Under conditions where a low intensity electric field is present, the polarization of the sample is characterized by a linear relationship with the intensity of the applied field.[104] If the field oscillates at a certain optical frequency, the polarization will also oscillate at the same frequency and phase. The polarization vector ($\vec{P}$) is directly proportional to the electric field ($\vec{E}$) interacting with the medium, as shown by **Equations (I-8)** and **(I-9)**.

$$\vec{P} \propto \vec{E} \tag{I-8}$$

$$\vec{P} = \chi^{(1)} \varepsilon_0 \vec{E} \tag{I-9}$$

Here ε_0 represents the permittivity of the vacuum and $\chi^{(1)}$ the lineal electric susceptibility constant.

For conventional optics, this linear approximation is suitable. However, with the advent of laser technologies that enable the production of high-intensity light sources, new phenomena have been observed that are referred to as nonlinear optical effects. In such cases, polarization must be expressed by a series expansion, as shown in **Equation (1-10)**.

$$\vec{P} = \vec{P}^{(1)} + \vec{P}^{(2)} + \vec{P}^{(3)} + \cdots = \chi^{(1)}\vec{E} + \chi^{(2)}\vec{E}^2 + \chi^{(3)}\vec{E}^3 + \cdots \tag{I-10}$$

where $\chi^{(1)}$ corresponds to the linear behavior of susceptibility, giving rise to linear phenomena, $\chi^{(2)}$ represents the quadratic behavior of susceptibility, leading to second-order nonlinear phenomena, $\chi^{(3)}$ is the cubic behavior of the susceptibility[105] and it gives rise to third order non-linear phenomena. Higher-order terms beyond $\chi^{(3)}$ may also contribute to non-linear effects.

The emergence of nonlinear optics is commonly associated with the groundbreaking experiment on second harmonic generation conducted by Franken and his colleagues in 1961.[106] Second-order effects include the generation of second harmonic (SHG), phenomena of optical rectification (OR), and the electro-optical effect, also known as the Pockels effect (EOPE). Among the third-order effects are the generation of third harmonic (THG), optical Kerr effect (EOKE), and the TPA process.[107] To study the parameters involved in nonlinear optical processes, the wave **Equation (I-11)** needs to be solved.[108]

$$\nabla^2 \vec{E} - \frac{\epsilon^{(1)}}{c^2} \frac{\partial^2 \vec{E}}{\partial t^2} = \mu_0 \frac{\partial^2 \overrightarrow{P^{NL}}}{\partial t^2} \tag{I-11}$$

The solution of the wave **Equation (I-11)** allows for the description of both; linear processes, such as classical absorption of OPA, and nonlinear processes, such as two-photon absorption.

The simplest way to make approximations of linear susceptibility is using the classical approach, such as the Drude-Lorentz model. The Lorentz electrons model considers that the valence is most affected by the external field. When an electric field is applied, the distance between the electron and the nucleus changes, inducing a

change in polarization[109] (**Fig. I-20**). This change is modeled as a harmonic oscillator in the **Equation I-12**, where the electromagnetic force $q\vec{E}(t)$ is the damping force, and a restoring force constant *k* that is the interaction with the nucleus acts on the electron, *x* represents the position.

$$q\vec{E}(t) = \vec{F}(t) = -xk \tag{I-12}$$

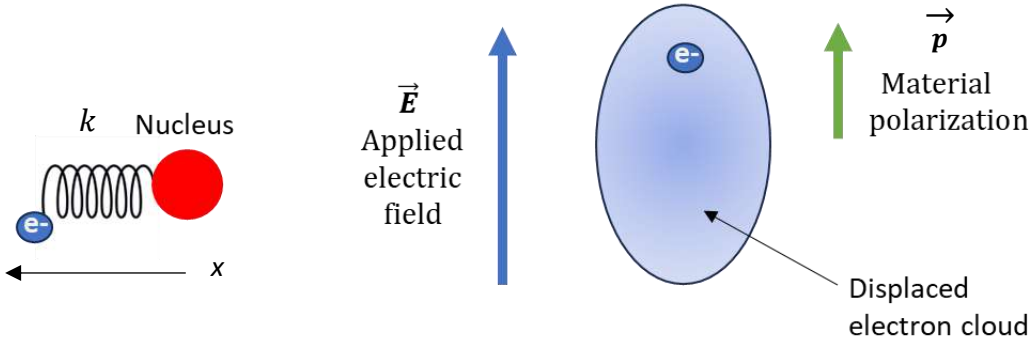

Figure I-20. Lorentz oscillator modeling an electron as a driven damped harmonic oscillator.

The driving oscillating electric field is E = E_0cos(-ωt). The damping force is velocity-dependent, described by damping coefficient γ.

$$F_{net} = m\ddot{x} \tag{I-13}$$

$$F_{driving} + F_{spring} + F_{damping} = m\ddot{x} \tag{I-14}$$

In this model the electron is connected to the nucleus via a hypothetical spring with spring constant *k*. The driving force is the oscillating electric field. The source of the damping is present so that the oscillations do not go infinite.

$$\mathrm{E} = E_0\cos(-\omega t) - \mathrm{k}x - \gamma m\dot{x} - m\ddot{x} \tag{I-14}$$

$$\ddot{x} + \gamma + \frac{k}{m}x = \frac{qE_0}{m}\cos(-\omega t), \quad \omega_0 = \sqrt{\frac{k}{m}} \tag{I-15}$$

$$x + \gamma\dot{x} \ddot{+} \omega^2 x = \frac{qE_0}{m}\cos(-\omega t) \tag{I-16}$$

Equation I-16 is the equation of motion that needs to be solve, after finding the solution and its derivatives we obtained the complex amplitude of electron motion:

$$\widetilde{x_0} = \frac{qE_0}{m} \frac{1}{\omega_0^2 - \omega^2 - i\omega\gamma} \quad \text{(I-17)}$$

The fact that **Equation I-17** is complex means it exist a time delay between the driving electric field and the response of the electron motion. With the time dependence added back in, we obtain:

$$\vec{x} = \frac{qE_0}{m} \frac{1}{\omega_0^2 - \omega^2 - i\omega\gamma} e^{-i\omega t} \quad \text{(I-18)}$$

Replacing the **Equation I-18** in the **Equation I-6**, we obtained the complex dipole moment.

$$\vec{p} = \frac{q^2 E_0}{m} \frac{1}{\omega_0^2 - \omega^2 - i\omega\gamma} e^{-i\omega t} \quad \text{(I-19)}$$

By replacing **Equation I-19** in the **Equation I-7** it is possible to get the complex polarization, The complex nature of the proportionality constant means that there is a phase shift between $\vec{P}$ and $\vec{E}$.

$$\vec{P} = \frac{Nq^2}{m} \frac{1}{\omega_0^2 - \omega^2 - i\omega\gamma} \vec{E} \quad \text{(I-20)}$$

Finally, by replacing the **Equation I-20** in the **Equation I-9**, we obtained the first order susceptibility:

$$\chi^{(1)} = \frac{Nq^2}{m} \frac{1}{\omega_0^2 - \omega^2 - i\omega\gamma} \quad \text{(I-21)}$$

The solution of the equation of a damped harmonic oscillator[110] (**Eq. I-16**) provides the description of the linear first-order susceptibility as it was just demonstrated, but this model can be extended to take into account the non-linear third-order susceptibility (**Eq. I-22**):

$$\chi^{(3)_{ijkl}}(3\omega, \omega, \omega, \omega) = \frac{Nbe^4 \delta_{jk} \delta_{il}}{\epsilon_0 m^3 (\omega_0^2 - \omega^2 - 2i\omega\gamma)^3 (\omega_0^2 - (3\omega)^2 - 2i(3\omega)\gamma)} \quad \text{(I-22)}$$

in which it can be noticed that third-order susceptibility depends on the natural frequency of the material ω_0. *N* represents the number density of particles in the material, *b* represents oscillator strength between the light and the medium, ϵ_0 is the permittivity of free space with a value of 8.854×10^{-12} F/m, *m* represents the mass of an electron, ω is the angular frequency of the applied field, ω_0 represents the resonance

frequency of the system and γ is the damping or dephasing rate. It describes how quickly the system loses energy to its surroundings.

In the quantum approximation, the properties of an atomic system can be described using the wave function $\psi(\vec{r},t)$ of the system, which satisfies the Schrodinger **Equation (I-23)**:

$$i\hbar\frac{\partial\psi}{\partial t} = \left(\hat{H}_0 + \hat{V}(t)\right)\psi \tag{I-23}$$

where $\hat{H}_0$ is the Hamiltonian of the free particle and the interaction of the particle with the electromagnetic field is described by $\hat{V}(t)$, equal to the potential $-\hat{\mu}\cdot\vec{E}(t)$ as show in the **Equation (I-24)**, where $\hat{\mu}$ represents the dipole moment.

$$\hat{V}(t) = -\hat{\mu}\cdot\vec{E}(t) \tag{I-24}$$

The solution of the **Equation (I-23)** provides an expression **(I-25)** for the third-order susceptibility:[111]

$$\chi^{(3)_{ijkl}}(3\omega,\omega,\omega,\omega) = \frac{N}{\in_0\hbar^3}\sum_i \frac{\mu_{gi}^2\mu_{if}^2}{(\omega_i-\omega_g-3\omega)(\frac{E_f-E_g}{\hbar}-\frac{i\Gamma_f}{2}-2\omega)(\omega_i-\omega_g-\omega)} \tag{I-25}$$

In these processes, the susceptibility is determined by the decay of the excited state to the ground state as real intermediate states are not involved. The Two-Photon absorption process depends on the square of the product $\mu_{gi}^2\mu_{if}^2$ and the symmetry of the molecule, where μ_{gi}^2 and μ_{if}^2 are the induced dipoles by the electric field of photons that generates excitations between real states |g⟩ and |f⟩ and the intermediate state |i⟩.

I-7. Two Photon Absorption Process (TPA)

Two-Photon absorption (TPA) is the process through which a material absorbs a pair of photons, with the sum of their energy matching the transition energy. This phenomenon happens when a molecule is exposed to light of a specific photon energy (or a combination of photon energies), and it depends on intrinsic characteristics of the material and its surrounding environment.[112] Understanding the underlying mechanisms of TPA is essential for accurately quantifying the nonlinear optical response of materials and exploring their potential applications in different fields. The TPA *cross section* (σ_{TPA}) serves as a key parameter for evaluating the magnitude of the third-order nonlinear optical process at molecular level.

As previously mentioned, TPA involves the absorption of two photons by an atom or molecule, causing it to transition from its ground state (g) to an excited state (e). In this process, energy conservation within the atom-radiation system requires that the energy difference between the excited state (E_e) and ground state (E_g) equals the sum of the photon energies ($\hbar\omega_x$) as shown in the **Equation (I-26)**:

$$E_e - E_g = \hbar\omega_1 + \hbar\omega_2 \quad \text{(I-26)}$$

It is important to distinguish TPA from the more common process of sequential absorption of two photons (**Fig. I-21**). In the latter process, two independent OPA transitions occur: the first transition promotes the atom to an intermediate excited state (i), while the second corresponds to the transition between states (i) and (e).[113]

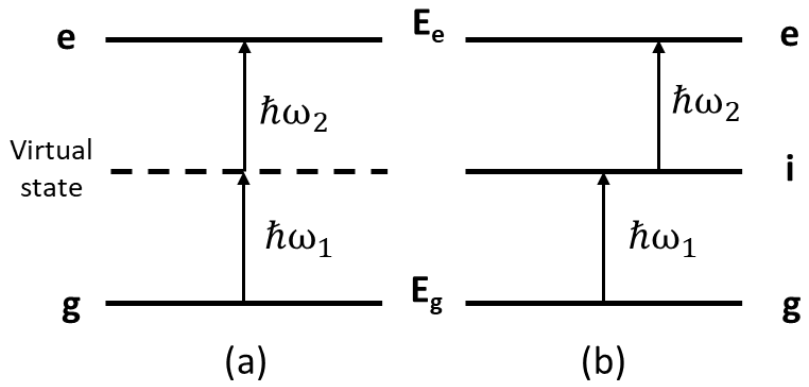

Figure I-21. (a) TPA process. (b) Excited state absorption.

The energy-level configurations of the electronic states involved in TPA can be divided into degenerate and non-degenerate types.[114] In degenerate TPA, the system is simultaneously activated from its ground state to an excited state by two identical photons of the same energy, increasing the absorption efficiency. In non-degenerate cases the system is excited by two photons of different energies (**Fig. I-22**).

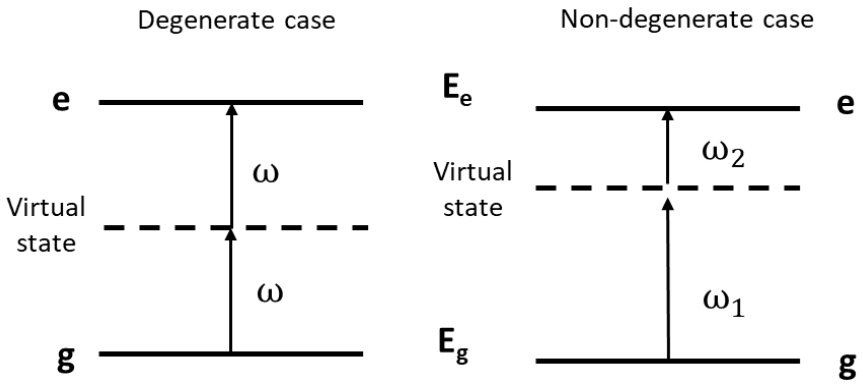

Figure I-22. Energy diagram showing degenerate case (left) and non- degenerate case (right), where E_g represents the ground state and E_e the excited state.

I-8. TPA *cross section* (σ_{TPA})

The TPA *cross section* (σ_{TPA}) is a parameter to characterize the probability of a material undergoing two-photon excitation when it is exposed to light. To calculated it is necessary start with the **Equation 1-27**, in which the rate of change of intensity with respect to propagation of light in direction *z* is determined by a macroscopic parameter of the material denoted as β, called nonlinear absorption coefficient (**Fig. I-23**). It establishes that the probability of the sample to absorb two photons, is directly proportional to the square of the intensity of the incident light.[115] It is important to notice that **Equation I-27** does not consider the lineal absorption contribution.

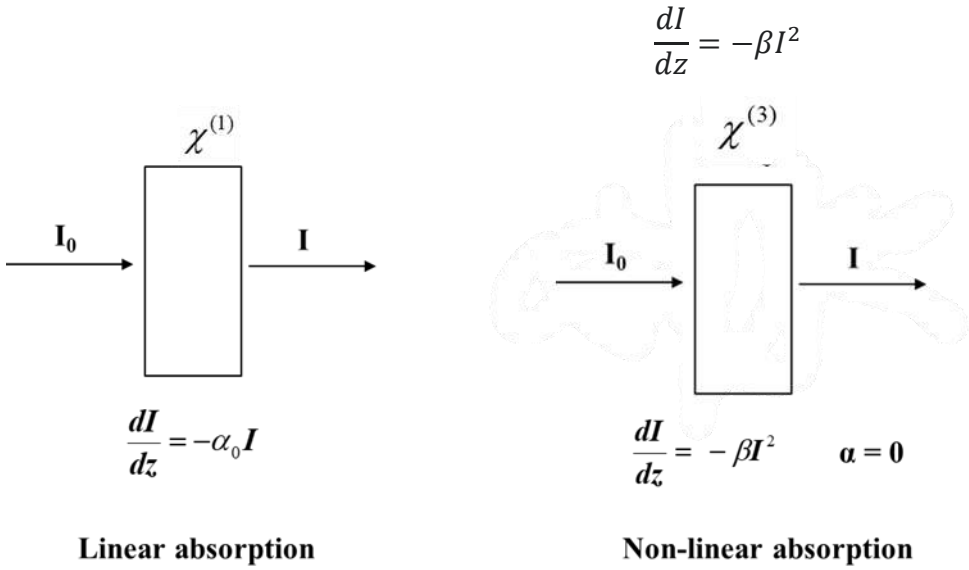

Figure I-23. Linear and non-linear absorption examples whit its expressions.

Solving the differential **Equation (1-27)**, the intensity of the transmitted light beam upon for two photons is denoted by:

$$I(z,\lambda) = \frac{I_0(\lambda)}{1+\beta(\lambda)I_0(\lambda)z} \qquad \text{(I-28)}$$

where I_0 is the intensity of the incident light beam, *z* is the propagation length in the medium, and $\beta(\lambda)$ is the nonlinear absorption coefficient that depends on the medium and the wavelength used. The **Equation (I-28**) is the Beer-Lambert Law for the nonlinear regime, particularly for TPA and it measured the intensity of the light in function of the position. $\beta(\lambda)$ can be expressed using macroscopic parameters[116] and the molecular parameter $\sigma_2(\lambda)$ as shown in **Equation (I-29)**:

$$\beta(\lambda) = \sigma_2(\lambda) N_A C_0 \quad \text{(I-29)}$$

where $\sigma_2(\lambda)$ is the molecular cross-section, where N_a is Avogadro's constant, and C_0 is the molar concentration of absorbing molecules.

Also, a parameter called transmittance can be introduced, which is given by **Equation I-30**:

$$\mathrm{T(z)} = \frac{I(z)}{I_0} = \frac{1}{1+\beta_0(\lambda)\mathrm{z}} \quad \text{(I-30)}$$

The previous analysis elucidates the physics behind the absorption process and highlights measurable experimental parameters. Moreover, it emphasizes that nonlinear phenomena, in this case nonlinear absorption, are intensity dependent.

The interaction of light with matter depends on the spatial inversion symmetries of molecular orbitals, categorized as gerade (g) (remaining the same under spatial inversion) and ungerade (u) (reflected under spatial inversion). Light absorption by a molecule requires a change in symmetry, but TPA processes preserve the molecule symmetry, as they involve two dipole steps. The orientation of electric dipoles within the molecule plays a vital role in TPA. The absorption cross section of two photons incorporates a dipole term (**D**) and an absorption term (**T**) representing transitions through virtual states.[117] For centrosymmetric molecules, the dipole term becomes zero.

$$\sigma \propto \underbrace{\left(\frac{\Delta\mu_{gf}\mu_{gf}}{h\nu}\right)^2}_{\mathbf{D}} + \sum_{i\neq g,f} \underbrace{\frac{\mu_{gi}^2\mu_{if}^2}{(E_{gi}-h\nu)^2}}_{\mathbf{T}} \quad \text{(I-31)}$$

I-9. Two-Photon Excitation Fluorescence (TPEF)

Two-Photon excitation fluorescence (TPEF) is a technique grounded on the principle of fluorescence induction in a sample due to the absorption of two photons.[118] This implies that the sample must inherently possess fluorescence properties. It can be understood that, in scenarios where there is no stimulated emission or self-quenching, the number of photons emitted are proportional to the photons absorbed through TPA. Consequently, the fluorescence quantum yield becomes a significant parameter.

When excited states are formed through Two-Photon excitation, the number of photons emitted correlates directly with the σ_{TPA}. The pulse duration of excitation is a critical aspect in this process. If the pulse is overly extended (larger than ps), it favors multi-photon excited states. Hence, it is generally perceived that a pulse within the femtosecond range ensures an accurate σ_{TPA} value.

Commonly, the Two-Photon excited fluorescence (TPEF) technique is employed to measure σ_{TPA} is a given sample; in this technique a reference or standard sample with a known σ_{TPA} value is used. Through the **Equation I-32**:

$$\sigma_S = \sigma_R \frac{F_S P_R^2 C_R \varphi_R \eta_R}{F_R P_S^2 C_S \varphi_S \eta_S} \qquad \text{I-32}$$

Where, *F* represents the emission band area, *C* is the molar concentration, ϕ is the fluorescence quantum yield, *n* stands for the refractive index, and *P* indicates the laser excitation power. The subscript *R* pertains to the reference, while S denotes the sample in question. In this approach both the TPEF from sample and the standard are detected under the same experimental conditions.

One notable advantage of TPEF is its incredible sensitivity, attributed to the inherent fluorescence. It demands a concentration ranging from 10^{-5} M to 10^{-4} M. Regardless of the excitation state of the molecule, fluorescence emission invariably originates from its lowest energy excited state according to Kasha´s rule. This unique property amplifies the technique's applicability in various research domains.[119]

I-10. Z-scan Technique

By Using the Z-scan method is possible to learn about the nonlinear optical properties of the material by scanning the sample under test through a focused laser beam in z-axis (**Fig. I-24**), resulting in a change in intensity transmitted with respect to z. It should be noted that when a nonlinear sample characterized by $\chi^{(3)}$ not only exhibit nonlinear absorption, but it can also show nonlinear refractive index. The technique of Z-scan is the best option to measure both the nonlinear absorption and nonlinear refractive effects. To specifically discern the nonlinear refractive index, n_2, a closed aperture in Z-scan is employed; if one aims to observe purely the absorption part, an open aperture is used, resulting in nonlinear absorption (β) within the sample.[120,121a]

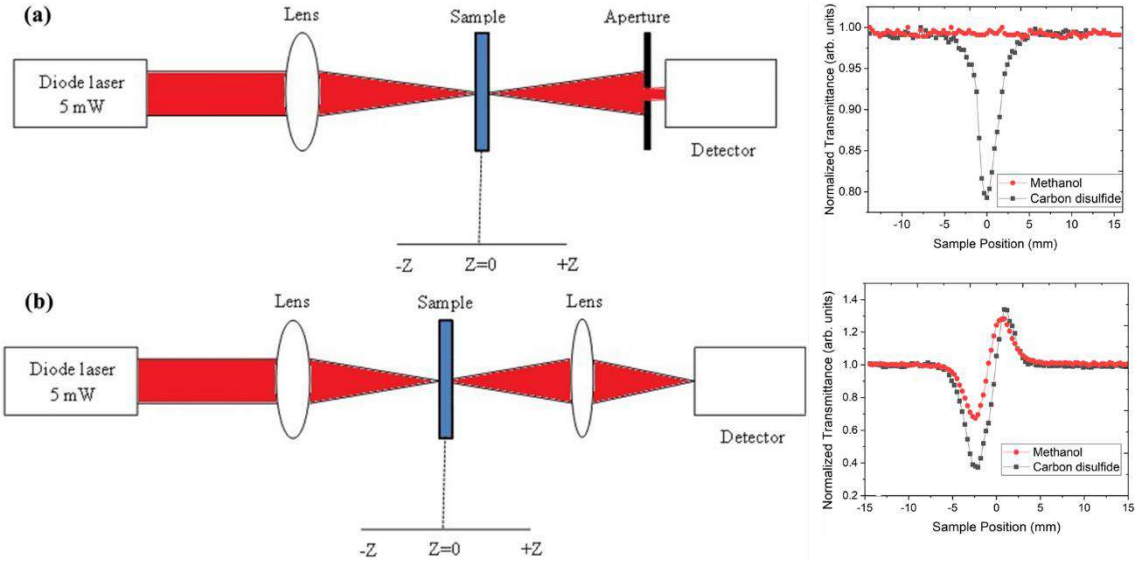

Figure I-24. Schematic of (a) closed and (b) open aperture Z–scan method.[121b]

Z-scan (**Fig. I-25**) is becoming standard technique for determining optical nonlinearities, particularly nonlinear refraction, and absorption.[122-124] A significant advantage of Z-scan is its ability to immediately determine the sign and type of nonlinearity (refractive or absorptive) in the sample. This method has many uses, including the investigation of substances with potential for all-optical switching[125] and photonic devices[126] to mentioned some. Z-scan experiments are a vital tool in the study of nonlinear optics because they reveal important information about how materials behave when exposed to intense laser light.

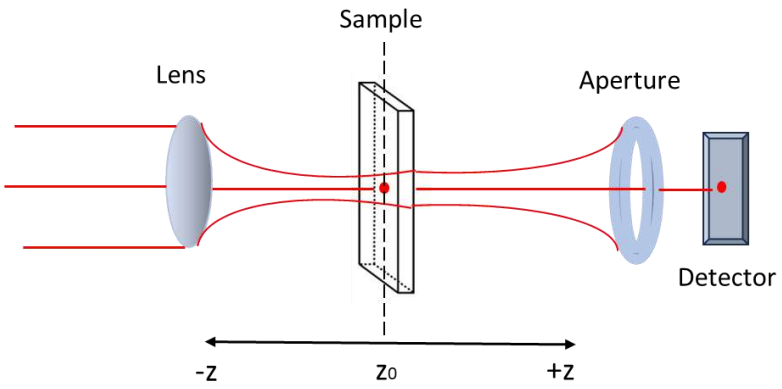

Figure I-25. In the Z-scan technique, the energy of a train of pulses remains constant, while changes in intensity are attained by moving the sample along the Z direction.

In commercial laser the delivered beam has a transversal profile of intensity typically Gaussian (**Fig. I-26**). Gaussian beams are often preferred as laser sources due to their simplicity and predictable behavior because the central region of the beam is more intense than its edges. The amplitude function of a Gaussian beam can be derived from the optical cavity's boundary conditions, determining the type of emission obtained based on the geometric characteristics of the cavity.[127]

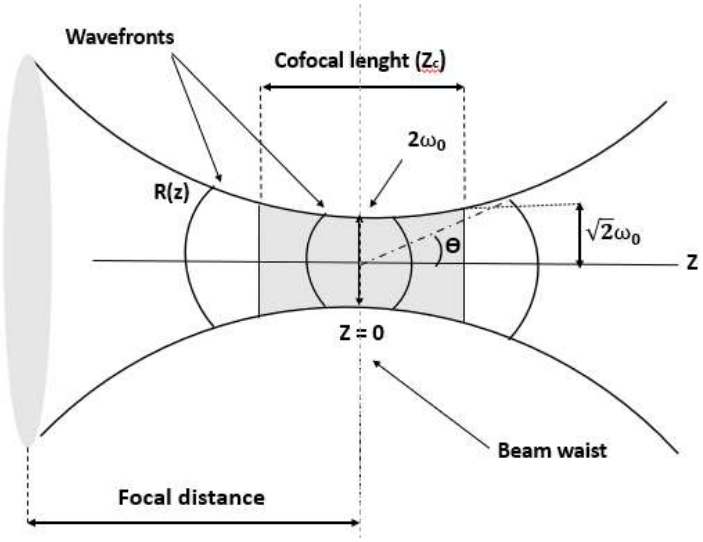

Figure I-26. Propagation of a Gaussian beam.

As the laser beam propagates in a nonlinear sample under test along the z-axis, it undergoes intensity variations that induce a lensing effect known as self-focusing.[128]

Samples typically exhibit a nonlinear refractive index phenomenon, n_2. To measure n_2, T is taken in a closed aperture configuration. However, it's essential to distinguish between different effects. In practice, a sample might show a non-zero value for n_2 with β=0. Conversely, another sample could have a non-zero value for β, while n_2 remains at zero.

In the context of the Z-scan technique, the measurement results are expressed using the normalized transmittance T(z), which is defined as the ratio of the intensity at position ***z,*** that is $I(z)$ to the transmitted intensity with the sample far from the focus $I(z >> z_c)$, where nonlinear effects are negligible (**Eq. I-33**).

$$T(z) = \frac{P(z)}{P(z >> z_c)} \quad \text{(I-33)}$$

Figure I-27 depicts a typical Z-scan signal in the close aperture regime for a sample with either negative or positive n_2 (nonlinear refractive index). For simplicity of analysis, the $T(z)$ signal is normalized. This normalization removes from the data any linear contribution leaving only in the plot changes in the transmission due to nonlinear effects. Briefly, the transmission of the sample in the configuration of close aperture regime is as follows: As the sample moves from –z to the focal plane (position z=0 in Figure I-23) the intensity $I(z)$ increases since the optical power is confined in a beam of a smaller cross section; this induces a chance in the nonlinear refractive index and, consequently, the beam divergence change. Under these considerations, when the sample is far from the focus, T(z) approaches one, indicating negligible nonlinear refraction. The nonlinearity can be evaluated by considering the difference in normalized transmittance, known as ΔT. It must be noted that the total refractive index of a sample comprises the linear and nonlinear contribution:

$$n = n_0 + n_2 I(z) \quad \text{(I-34)}$$

Where n_0 is the linear contribution. The nonlinear refractive index n_2 can be positive or negative depending on the material. **Figure I-26** shows the trends of transmission depending on the sign of n_2.[129]

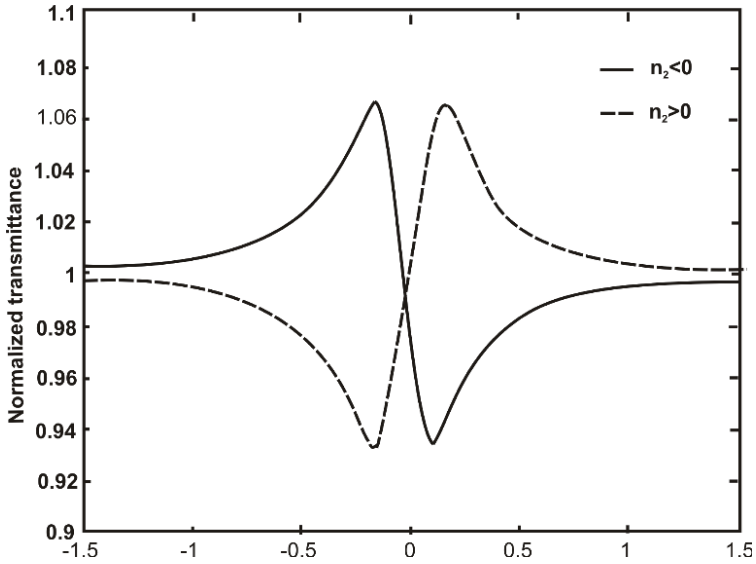

Figure I-27. Theoretical Z-scan curves of the transmittance as a function of z.[129b]

There is an empirical relationship to extract n_2 by fitting the experimental transmittance curve. The lensing effect generated by the nonlinear medium on the propagating beam leads to a phase change $\Delta\Phi_0$ in the wavefront. This phase change is related in a straightforward manner to the transmission change $\Delta T = T_P - T_V$ between the peak transmittance, T_P, and the valley transmittance, T_V (**Fig. I-28**). The expression relating these parameters to the nonlinear refractive index n_2 is given by **Equation (I-34)**:

$$\Delta T_{pv} \cong 0.406(1-S)^{0.27}|\Delta\Phi_0| \tag{I-34}$$

where:

$$\Delta\Phi_0 = \frac{2\pi}{\lambda} n_2 I_0 L_{eff} \tag{I-35}$$

and L_{eff} represents the effective thickness of the sample. In the close aperture regime, the parameter S denotes the transmission of the aperture without the sample, often set to 40% (S = 0.4) for an optimized signal-to-noise ratio. In a standard z-scan system employing a Gaussian beam with a waist ω_0[130,131]

$$|\Delta Z_{PV}| = 1.7 Z_0 \tag{I-36}$$

where Z_0 represents the Rayleigh distance of the beam, defined as

$$Z_0 = \pi\omega_0^2/\lambda \tag{I-37}$$

In the case of close aperture regimen, the normalized transmittance is determined using the relation:

$$T(z) = 1 - \Delta\Phi_0 \frac{4(Z/Z_0)}{((Z/Z_0)^2+1)((Z/Z_0)^2+9)} \quad \text{(I-38)}$$

For purposes of measuring the nonlinear absorption in the sample, the Z-scan configuration to be utilized is the known as open aperture regime. In this configuration, the S is set to 1. Thus, the transmittance is given by:

$$\Delta T(z) = -\frac{\beta I_0 L_{eff}}{2\sqrt{2}} \frac{1}{[1+\frac{Z^2}{Z_0^2}]} \quad \text{(I-39)}$$

Formula that allows us to get the σ_{TPA} from the analyzed material, and finally it is obtained from the following **Equation I-40**:

$$\sigma_{TPA} = \frac{\hbar\omega}{N} \beta \quad \text{(I-40)}$$

Were *N* being the molecular density and ω is the optical frequency, β is the nonlinear absorption coefficient. This parameter is usually expressed in Goppert-Mayer units (1 GM = 10^{-50} cm^4.s/photon).

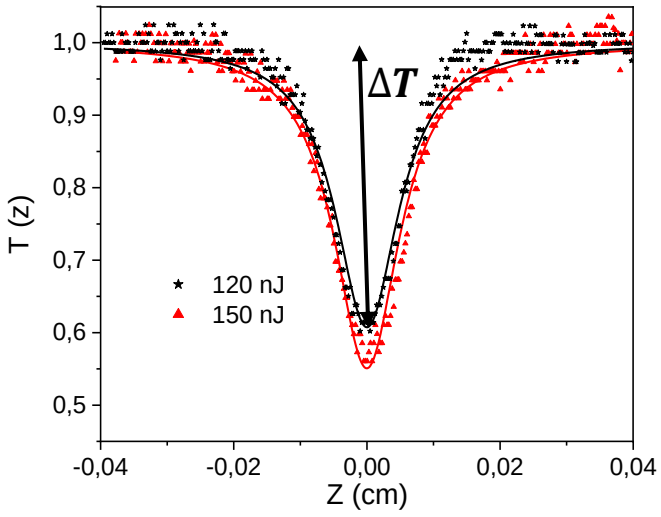

Figure I-28. Typical Z-scan result, showing the graphic representation of ΔT.

From an experimental perspective, the measurement of σ_{TPA} for a given samples implies four basic requirements to obtain good signal to noise ratio and preclude artifacts leading to the overestimation or such nonlinear parameter: i) insignificant

linear absorption in the required spectral range of excitation; ii) molecular solutions of the sample at high enough concentration to produce significant values of β at the lowest possible optical excitation; iii) solvents of negligible nonlinear response at the range of energies in which the samples is tested; iv) sufficient physicochemical stability, and durability under high-intensity laser irradiation.

The Z-scan technique used for this project is depicted in **Figure I-29**. It can be observed that it is composed of a laser source, a Zaber platform for sample displacement, an iris diaphragm, an acquisition device (oscilloscope), and an intensity detector, using short laser pulses of 80 fs at 1 kHz of repetition rate. The characterization at 800 nm is performed by the train of pulses delivered by a Ti:Sa amplifier (Libra HE from Coherent). For other wavelengths, the Z-scan method was implemented with an optical parametric amplifier (TOPAs, from Light Conversion).

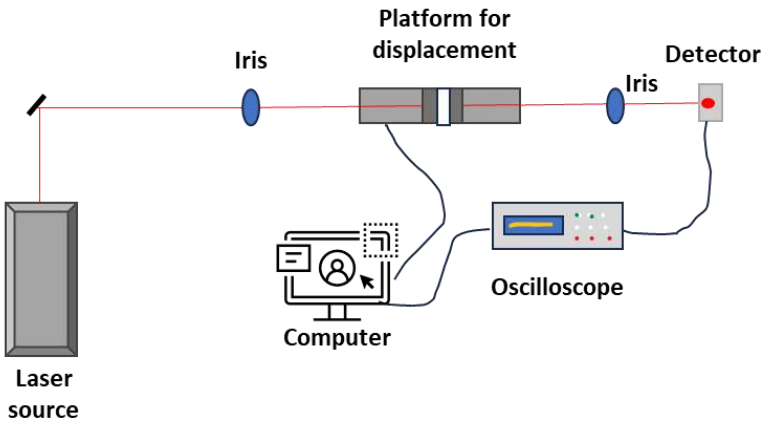

Figure I-29. Experimental Z-scan set up.

I-11. Dipolar structures

In the context of IUPAC, conjugation occurs when molecules exhibit alternate single and multiple (double or triple) bonds. This interaction involves pairing one atomic type p_π-orbital with another p_π-orbital across a single (σ) bond or with an electron lone-pair.[132] This π-conjugation system allows electrons to be shared among multiple nuclei, rather than being confined to a single nucleus or covalent bond.

Conjugation and donor-acceptor structures play a crucial role in the realm of TPA processes. Conjugation can be understood using Lewis's model, which involves a chain of carbon or hetero atoms with alternating single and double or triple bonds,

creating free valences[133] (**Fig. I-30**). This arrangement promotes electron delocalization, significantly increasing the likelihood of electronic transitions between energy levels, thus facilitating the polarization, and generating TPA optics.

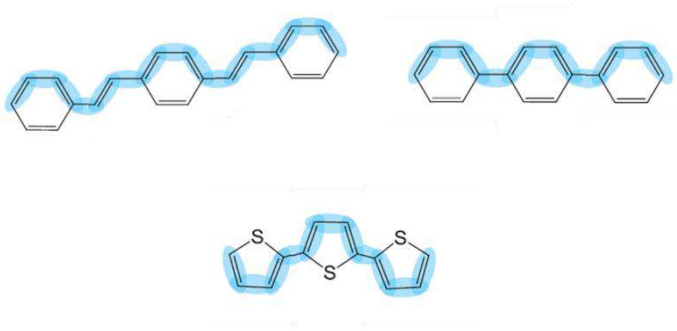

Figure I-30. Example of conjugated molecules. The conjugation path is marked in blue.

There are two ways to efficiently generate conjugation in molecules. The first method involves extending π-conjugation with a well-optimized planarity and orbital overlap between adjacent local π-orbitals. This extension leads to an increased delocalization of electrons and results in a smaller energy gap between the highest occupied and lowest unoccupied orbitals[134] (**Fig. I-31**).

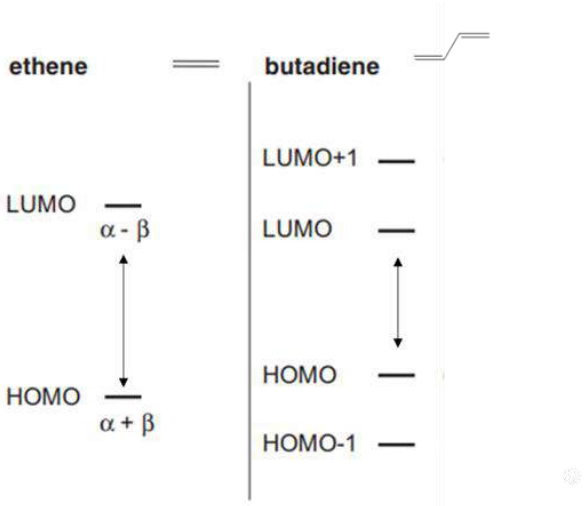

Figure I-31. A schematic representation of increased conjugation in an oligoene and its impact on the HOMO-LUMO energy gap. Long conjugated compounds exhibit a smaller HOMO-LUMO gap compared to compounds with a shorter conjugated path.

The second approach involves introducing a donor-acceptor (DA) system. These structures have a D-π-A architecture, with π representing a conjugated bridge. In D-π-A systems, common frontier molecular orbitals (MOs) are formed; however, despite through-conjugation in the system, the HOMO will be more localized on the donor unit, and the LUMO will be more localized on the acceptor unit[135] (**Fig. I-32**) By employing these two methods, it is possible to design molecules with enhanced conjugation, which significantly influences the electronic and optical properties of the materials.

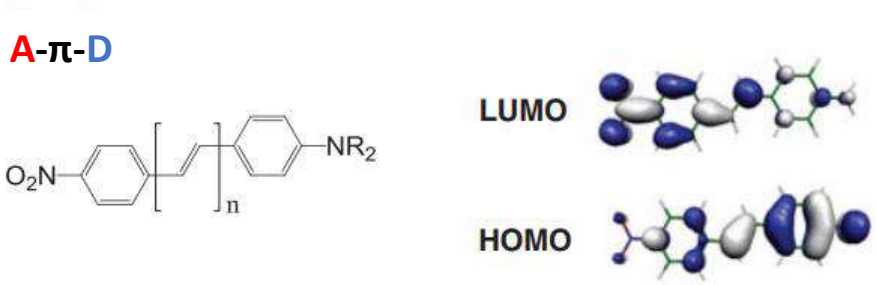

Figure I-32. Representative example for donor–acceptor substituted conjugated molecules and their frontier MO topologies.[135]

These materials, also known as "push-pull" compounds (**Fig. I-33**), consist of a donor (D) fragment that can donate electron density and an acceptor (A) fragment that can accept this electron density. The system is linked by covalent bonds through a π delocalized electron system. The donor-acceptor structures are normally not centrosymmetric,[136] meaning they lack a center of inversion symmetry. Additionally, a significant difference between the dipole moments in the fundamental state (Ug) and the excited state (Ue) is essential to enhance the TPA response. By satisfying these conditions, the compound exhibits efficient TPA and can be tailored to suit specific applications in nonlinear optics and related fields.

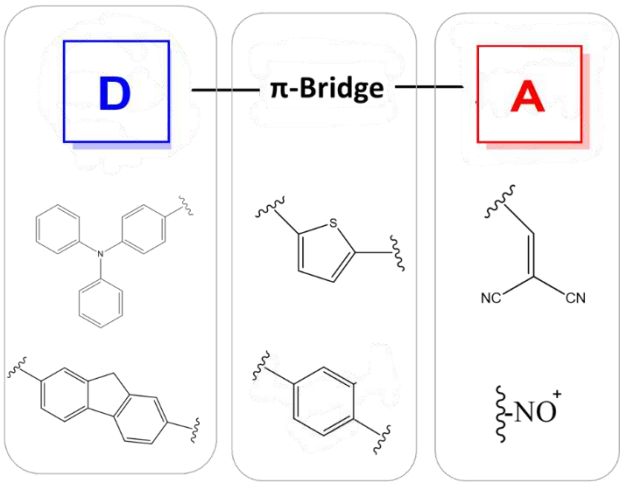

Figure I-33. Dipolar molecule's structure ("push-pull" molecules) with some examples of electron donor, π-bridge, and acceptor groups.[137]

The electron donor and acceptor strengths are crucial factors in determining properties of these dipolar chromophores. The presence of efficient charge transfer within the molecule, driven by the D-π-A architecture, enhances the response, making these materials appealing for various applications in nonlinear optics and photonics.

To determine σ_{TPA} for dipolar structures we use **Equation (I-41)**,[138] in which σ_{TPA} is directly proportional to the square of the difference in dipole moments between the excited and ground states $(\mu_{ee} - \mu_{gg})^2$ which highlights the importance of a strong charge transfer character, and the square of the transition dipole moment μ_{ge}^2. It is worth noting that the inverse proportionality to the square of Planck's constant ($\hbar^2$), to the square of the speed of light in vacuum (c^2), and to the line broadening parameter (Γ) illustrates the crucial role that these physical constants play in mediating the TPA cross section.

$$\sigma_{TPA} \approx \frac{16\pi^2 \mu_{ge}^2 (\mu_{ee}-\mu_{gg})^2}{5\hbar^2 c^2 \Gamma} \qquad \text{(I-41)}$$

The line broadening parameter Γ accounts for various homogeneous and inhomogeneous broadening mechanisms. In most cases, it is approximated as a constant value, typically 0.1 eV, to simplify calculations.

In summary, the TPA cross section for dipolar systems is closely related to molecular structure and environment, both of which determine the intrinsic charge

transfer type of the material. Therefore, a thorough understanding of these parameters is crucial for the development and optimization of materials for nonlinear optical applications.

I-12. Quadrupolar Structures

Quadrupolar structures, as shown in **Figure I-34**, represent a molecular architecture endowed with nonlinear optics properties. One configuration example consists of two electron-donating (D) units connected by a conjugated π-bridge and two electron-accepting (A) units anchored at the ends of the molecule.[139] The careful arrangement of both the electron-donating and electron-accepting groups allows efficient charge transfer leading to the induction of a quadrupole moment in the molecule.

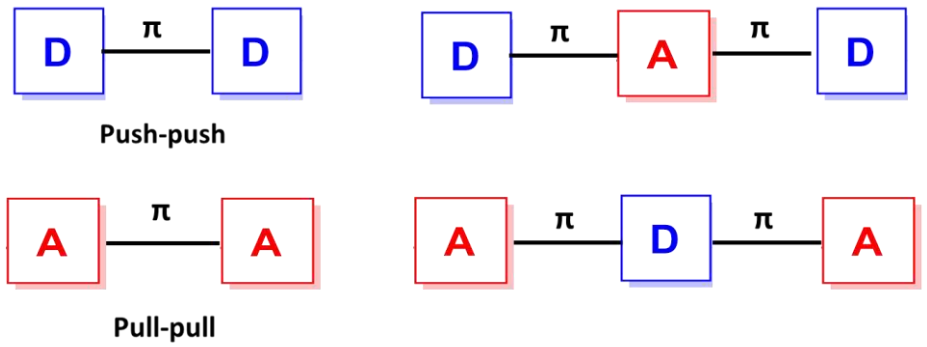

Figure I-34. Example of quadrupolar architectures.

On closer inspection, quadrupolar centrosymmetric systems typically contain two dipolar push-pull subunits. In the simplest case (**Eq. I-42**), three states (g, e, e') come into play, paving the way for the TPA process to the second excited state (e'). The attractiveness of quadrupolar TPA chromophores stems from their potential for significant enhancement of the effective cross section. This enhancement is evident when the denominator nearly vanishes as the g → e transition energy ($\hbar\omega_{ge}$) approaches the energy of the incident laser beam ($\frac{\hbar\omega_{ge'}}{2}$).[138]

$$\sigma_{TPA} \approx \frac{4\pi^2\omega_{ge'}^2}{5\hbar^2c^2} \frac{\mu_{ge}^2\mu_{ee'}^2}{(\omega_{ge}^2-\frac{\omega_{ge'}}{2})^2\Gamma_{e'}} \quad \text{(I-42)}$$

I-13. Comparison of Dipolar and Quadrupolar Structures

Comparative analysis of compounds constructed using "push-pull" or dipolar structures reveals startling revelations. For example, examination of structures (a) and (b)[140] reveals that the introduction of a parent electron-attracting ligand such as NO_2^- can effectively double the sigma TPA value $\sigma_{TPA} = 630$ GM for (a) and $\sigma_{TPA} = 1300$ GM for (b).

Further studies also show that quadrupolar structures outperform their dipolar counterparts in terms of efficiency (**Fig. I-35**).[141] To illustrate, a molecule (d) designed with quadrupolar architecture has a $\sigma_{TPA} = 1253$ GM, a value about five times higher than the corresponding dipolar structure (c), which has the same donor and acceptor, where $\sigma_{TPA} = 266$ GM.

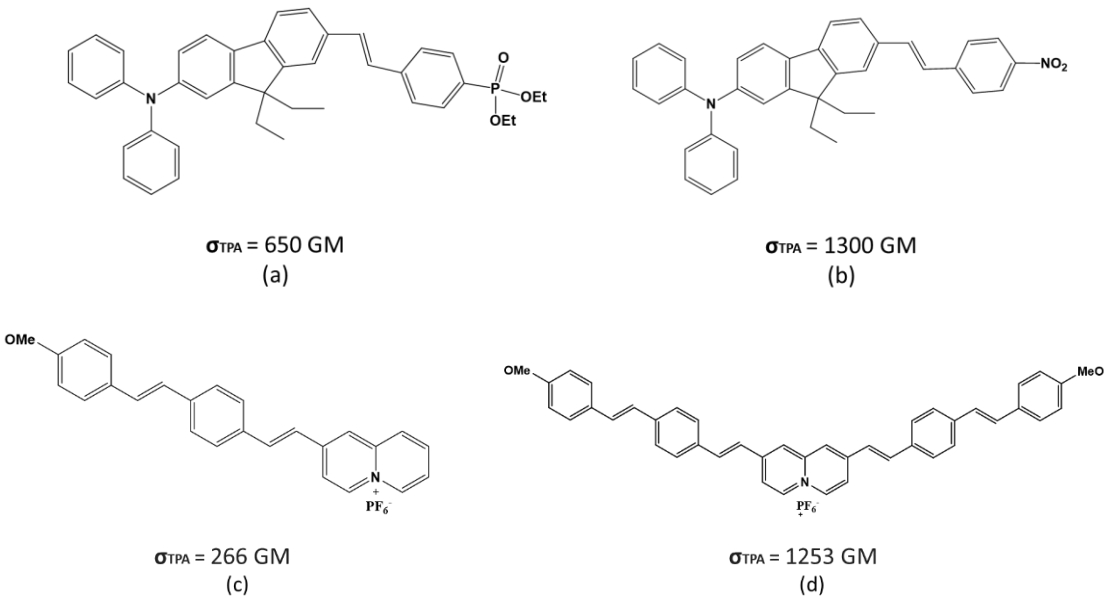

Figure I-35. (a), (b) and (c) Efficient TPA chromophores with dipolar approach. (d) TPA chromophores designed with quadrupolar approach based on the structure of (c).

These analyses highlight the central role of molecular architecture in enhancing the TPA response, thus highlighting the potential of this approach in developing nonlinear optical materials with higher efficiency for advanced applications.

TPA has various applications in different fields, mainly due to its unique characteristics and advantages. Some of the notable applications of TPA include

Biomedical Imaging,[142] Three-Dimensional Microfabrication,[143] Optical Limiting,[144] Nonlinear Optical Switching[145] and PDT as it was discussed in Section **1.3**.

Overcoming these hurdles requires innovative approaches, such as the technique of TPA. The focus of our research group is to pioneer the development of nitrosyl ruthenium complexes. These complexes show promise for use in PACT, primarily due to their ability to release nitric oxide by TPA. Our efforts are aimed at advancing the field of chemotherapy by exploiting these unique light-responsive properties.

TPA facilitates the required transition by absorbing two photons at twice the wavelength (600-1000 nm). Under TPA conditions, the release of NO• from RuNO complexes can be precisely controlled. This advantage of TPA, combined with its ability to confine to a specific irradiation focus, allows precise targeting of individual cells, minimizing collateral damage to healthy tissue.

By using TPA with RuNO complexes, we offer an advanced approach to more targeted and effective therapies that enable efficient NO• release under controlled conditions and reduce damage to healthy tissue. The ability of most ruthenium complexes to release NO• under UV irradiation raises concerns regarding their applicability for medical purposes, as UV light can potentially harm the surrounding tissue. To address this issue, irradiation within the therapeutic window using a TPA process becomes essential (**Fig. I-36**). By using TPA, the excitation of the ruthenium complexes can occur with lower-energy photons, thereby minimizing the risk of tissue damage and maximizing their potential for medical applications.

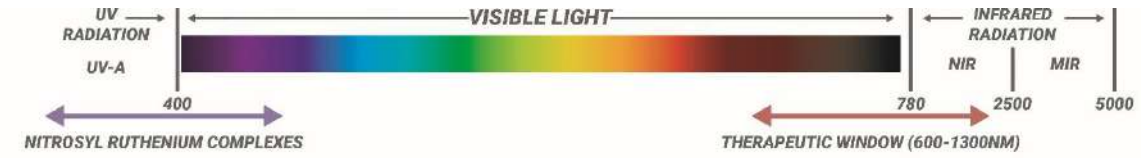

Figure I-36. Electromagnetic spectrum diagram highlighting the visible light spectra, UV region, and IR region.

In an effort to develop efficient ruthenium-nitrosyl complexes (RuNO) for Two-Photon induced NO• release, our research team has investigated various strategic modifications to these complex structures[146,147] (**Fig. I-37**). Key to these strategies is the insertion of double and triple carbon-carbon bonds within a family of "push-pull" species. In these species, the nitrosyl ligand acts as an electron acceptor, while fluorenyl units act as electron donors. This approach has led to the development of two RuNO complexes that can successfully release NO•.

These findings serve as an important foundation for our current project, which focuses on quadrupolar architectures and their potential in this area of research.

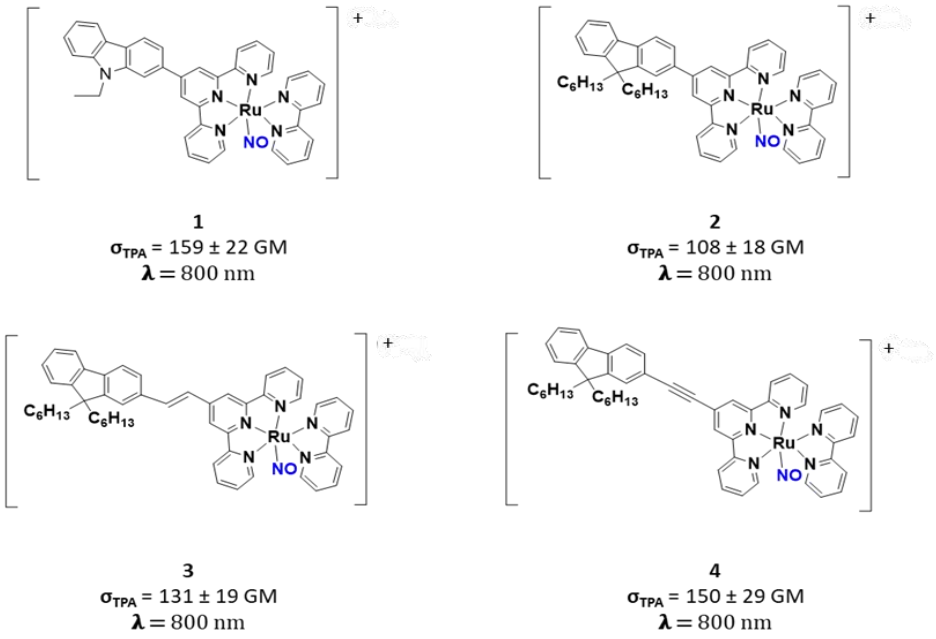

Figure I-37. Structures and σ_{TPA} values of ruthenium nitrosyl complexes investigated by our research team.[146, 147]

CHAPTER II

Syntheses and characterization of ruthenium nitrosyl complexes and determination of the Two-Photon absorption response

II-1. Method.

The primary objective of this study is to design and synthesize ruthenium nitrosyl (RuNO) complexes that can release nitric oxide (NO•) through Two-Photon absorption (TPA) within the therapeutic window of λ = 600–1300 nm. This research is driven by the need to overcome the limitation of NO• release imposed by the one-photon excitation of ruthenium nitrosyl (RuNO) complexes limited to the λ = 300–500 nm range, and to achieve a non-invasive and controllable NO• release within the biologically transparent window. By modifying the ligands of the RuNO complexes, we aim to enhance their TPA response and optimize their PACT potential. The utilization of TPA offers several advantages, including improved spatial resolution, enhanced tissue penetration, and reduced side effects compared to traditional one-photon absorption methods.

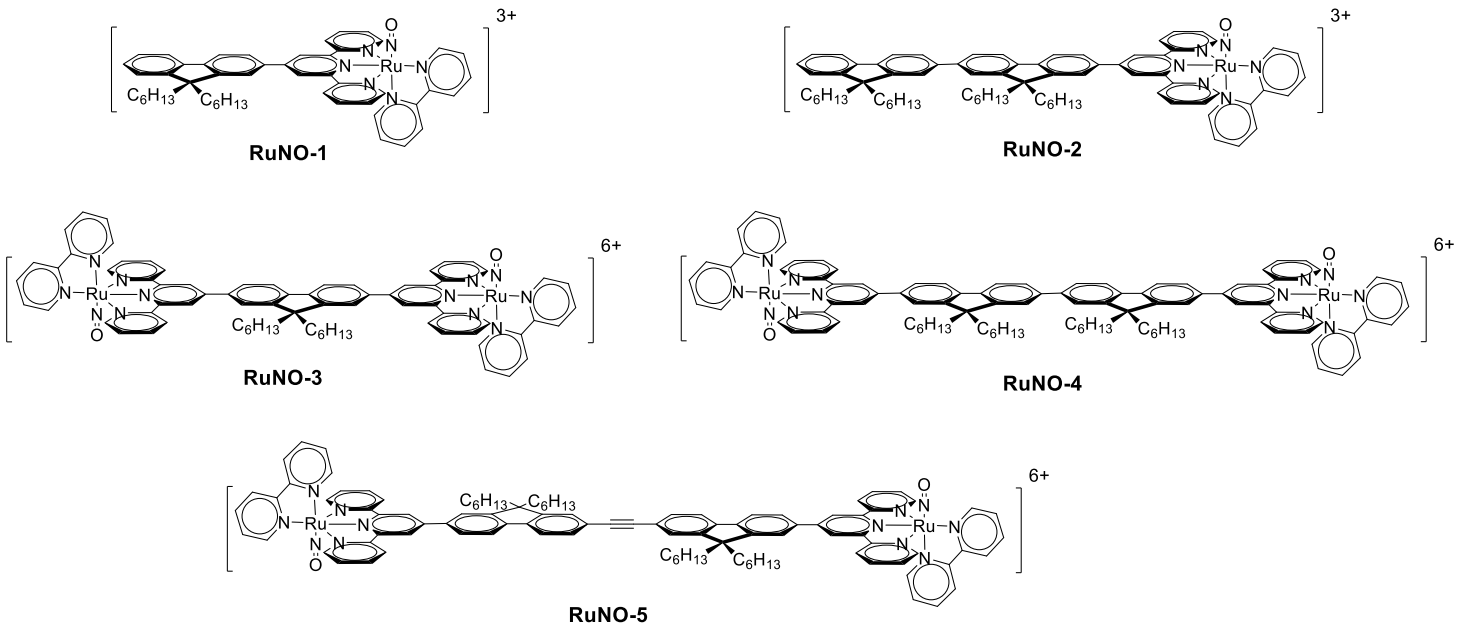

Figure II-1. Serie of ruthenium nitric oxide complexes synthetized for this project. For this chapter if the anion is not written it should be understood as PF_6^-. In any other case it will be indicated.

II-2. Synthesis of the Building Block 4'-(9,9-Dihexyl-7-Iodo-Fluoren-2-Yl)-2,2':6',2''-Terpyridine, and its Crystal Structure.

In the synthesis of the target complexes, the process started by synthesizing the main building block compound, 4'-(9,9-dihexyl-7-iodo-fluoren-2-yl)-2,2':6',2''-terpyridine (**3**), as illustrated in **Scheme II-1**. All ligands in the complexes contain two alkylated hexyl chains at the C-9 position of the fluorene moiety to avoid any further reaction of the acid protons in that position in the fluorene, also this modification was intended to enhance the solubility of the final complexes. It is worth noting that compound **3** was specifically chosen to have an iodine atom at position C7 on the fluorene moiety instead of other possible halogens. This choice was based on the known reactivity of palladium (0) oxidative addition to carbon-halogen bonds generally follows the order Ar-I>Ar-Br>>Ar-Cl.[148]

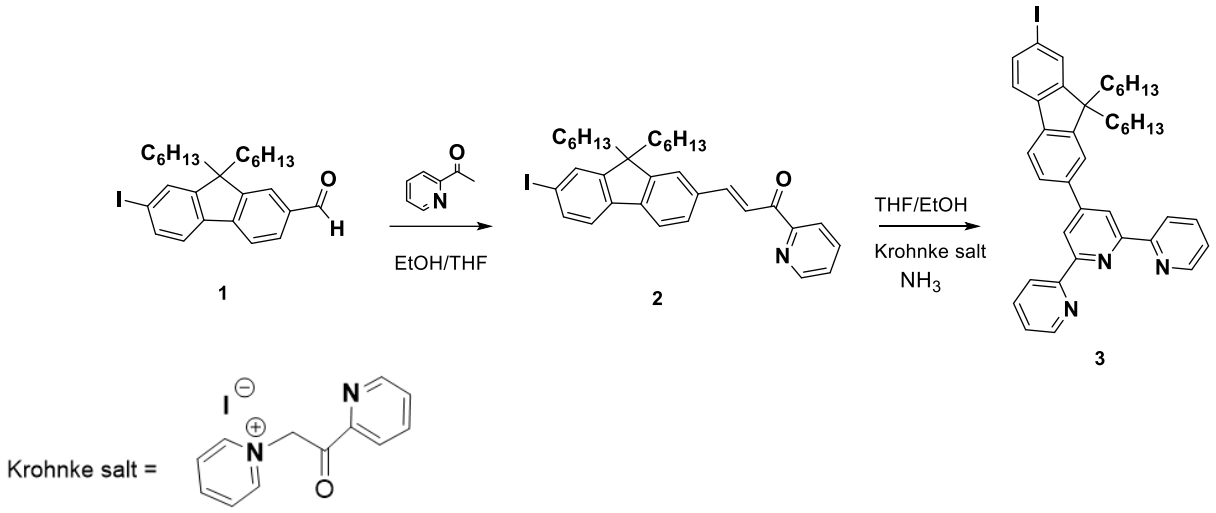

Scheme II-1. Synthesis of compound **3** that serves for further formation of Ligands **L1** to **L5**.

The synthesis began with an aldol condensation reaction between 9,9-dihexyl-7-iodo-fluorene-2-carbaldehyde **1** and 2-acetylpyridine, exclusively yielding (E)-3-(9,9-dihexyl-7-iodo-fluoren-2-yl)-1-(pyridin-2-yl)prop-2-en-1-one **2**. The confirmation of the structure of this compound was achieved by ^{1}H-NMR analysis, in which the characteristic “J” value of 16 Hz for both hydrogens (**H**-**H**) involved in the double bond was founded (**Fig. II-2**). Isomer *Z* was not formed due to steric hindrance caused by the substituents.

Subsequently, compound **2** underwent a Michael addition reaction with the enolate of Krönhke salt. This resulted in a non-isolated 1,5-dicarbonyl intermediate that cyclized in situ in the presence of ammonia, yielding the desired 4'-(9,9-dihexyl-7-iodo-fluoren-2-yl)-2,2':6',2''-terpyridine **3**. It is noteworthy that exceeding the reflux temperature was necessary to increase the yield of this step.

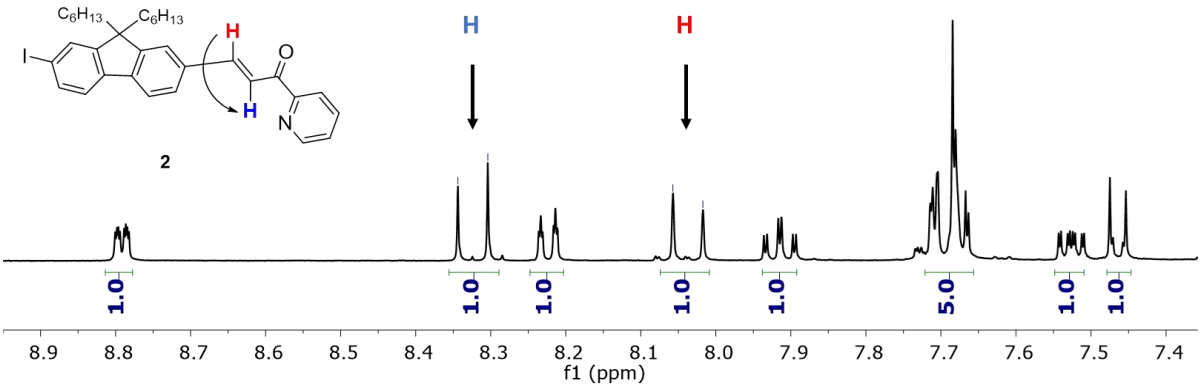

Figure II-2. ^{1}H-NMR spectra (CD_3Cl, 400 MHz) with zoom in the aromatic region for compound **2** showing the two signals corresponding to the protons of the double bond in the *enone*.

X-ray diffraction analysis was performed on single crystal of compound **3**, which was obtained by the slow evaporation of a solution in acetone. The crystal structure was confirmed (**Fig. II-3**). The molecule crystallizes in the triclinic space group P-1. The asymmetric unit contains two molecules of and two disordered acetone molecules.

In the crystal structure, the fluorene unit is planar, with a torsion angle (C7-C8-C16-C28) of 14.23° between the fluorene moiety and the terpyridine moiety. Notably, the positions between N1-N2 and N2-N3 adopt a *cisoid* conformation to prevent interaction with the free electron pair on each nitrogen atom.

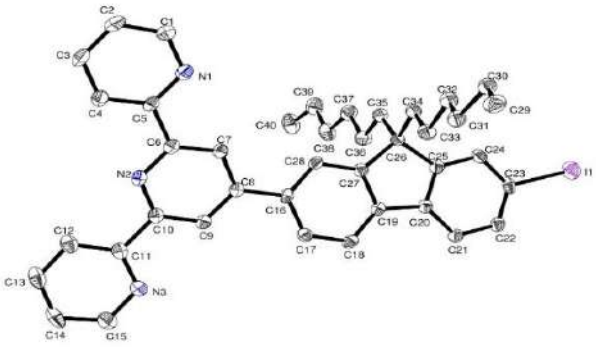

Figure II-3. Structure for the compound **3**.

A notable observation is the presence of interactions between the hexyl chains of each molecule within the unit cell. These hexyl chains are oriented perpendicular to the axis of the fluorene-terpyridine moieties. The interaction occurs at a 3.899-3.951 Å, range between adjacent carbon-carbon pairs in their vicinity. This type of Van der Waals interactions between carbon-carbon has a value <3.40 Å.[149] (**Fig. II-4**).

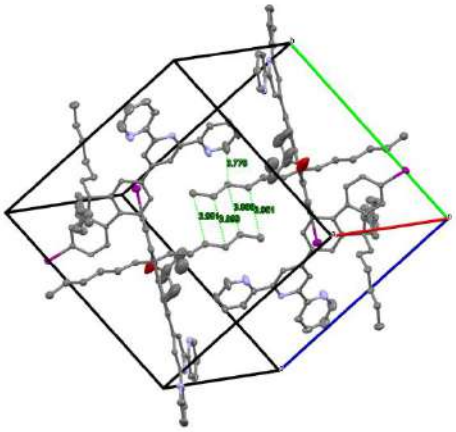

Figure II-4. Intermolecular interactions in compound **3**.

This interaction between the hexyl chains is of interest as prior studies have indicated that the inclusion of aliphatic chains within molecular structures can have a substantial impact on conformational dynamics and the packing arrangements within crystals.[150] The presence of these interactions can influence the overall molecular arrangement and potentially affect the physical properties of the material.

II-3. Synthesis of Ligand 1

The synthesis of **Ligand 1** has been previously reported by our team, where it was obtained through a Kröhnke condensation reaction between 1-(2-oxo-2-pyridin-2-ylethyl)pyridinium iodide in the presence of ammonium acetate. However, from **3**, an alternative methodology was followed in this study. It involved the reduction of 4'-(9,9-Dihexyl-7-iodo-fluoren-2-yl)-2,2':6',2''-terpyridine (**3**) by forming an organometallic complex with a lithium cation, followed by protonation with an acid to yield the final product, 4'-(9,9-Dihexylfluoren-2-yl)-2,2':6',2''-terpyridine **Ligand 1** (**L1**) (**Scheme II-2**).

To achieve the dehalogenation step using organolithium compounds, very low reaction temperature (-78°C) was required to avoid any risk of explosion. By employing this methodology, **Ligand 1** (**L1**) was successfully synthesized, with a yield near to 100%, due to the high reactivity of organolithium compounds with water.

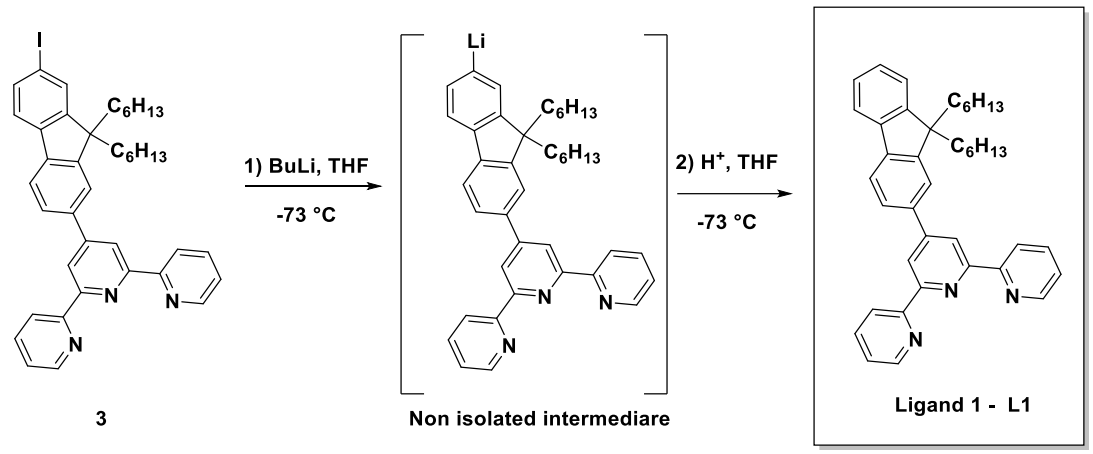

Scheme II-2. Synthesis of **Ligand 1** by lithiation reaction following by acid treatment, the non-insolated unstable intermediate generated in-situ is shown at the middle of the scheme.

II-4. Synthesis of Ligand 2

Ligand 2 (**L2**) was synthesized by a Suzuki-Miyaura cross-coupling reaction with 9,9-dihexylfluorene-2-boronic acid (**4**) as the starting material (**Scheme II-3**). Although the exact mechanism of this reaction is still not fully understood, some advancements have been made in this area. The use of boronic acid in the reaction provides stabilization for the transmetalation intermediate and generates a strong Pd-O interaction, which is more pronounced compared to other reagents such as boropinacolate commonly used in similar reactions,[151] making a stronger bond. Consequently, higher reaction temperatures were required.

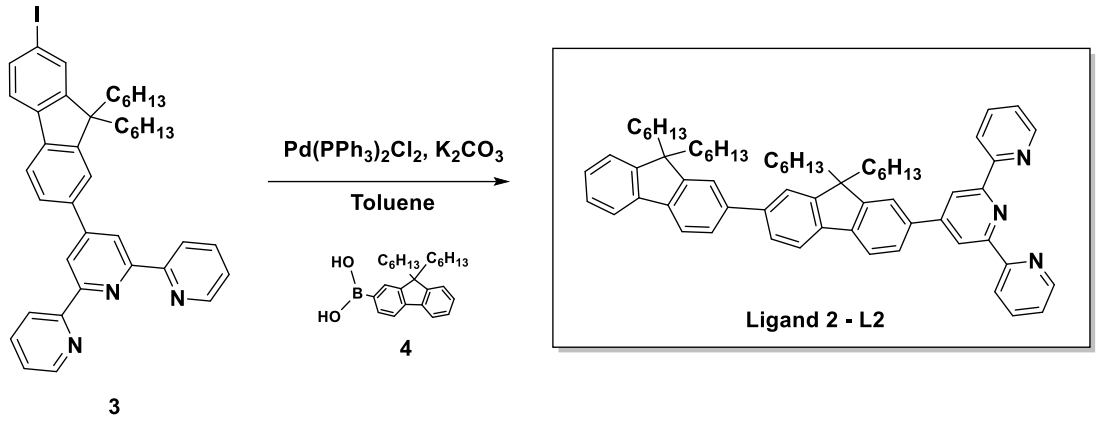

Scheme II-3. Synthesis of **Ligand 2** by Suzuki-Miyara reaction using boronic acid **4** in basic media.

Furthermore, an excess of the boronic acid reagent was employed due to its tendency to undergo dehydration and form triply zwitterionic mesomers (**Scheme II-4**). This was confirmed by the absence of the proton signal corresponding to the boronic acid in the ^{1}H-NMR spectra **(Fig. II-5**). It is worth noting that in the Suzuki-Miyaura coupling reaction, the reactivities of both boronic acids and boroxines are similar, and the presence of water, which is used to dissolve K_2CO_3, can lead to the hydrolysis of boroxines back into the corresponding acids. Therefore, achieving the correct stoichiometry in the reaction was not a trivial task. For future syntheses, it is highly recommended to convert the boronic acid into the catechol species. Nonetheless, despite the challenges, the reaction exhibited a good yield of 66%.

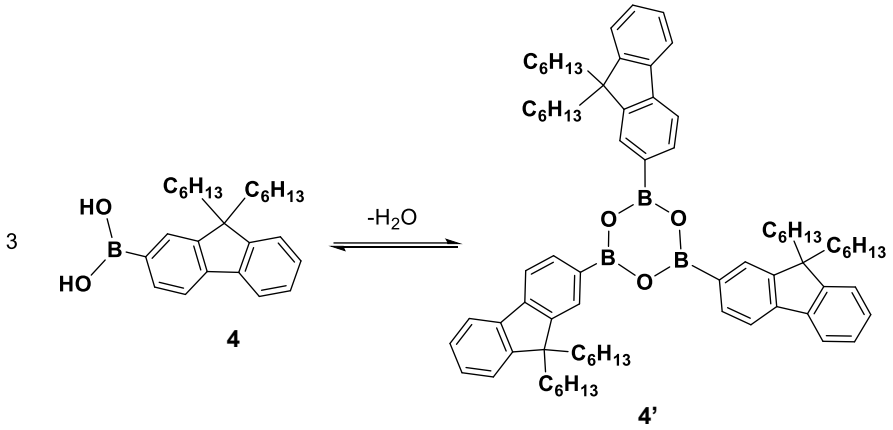

Scheme II-4. Entropically favorable dehydration of boronic acid **4** to form partially aromatic boroxine **4'**.

The ^{1}H-NMR shows the absence of signal belonging to the proton connected to the boronic acid, located at 7.994 ppm in the case of phenylboric acid.[152]This means the formation of the boroxine **4'** is favorized.

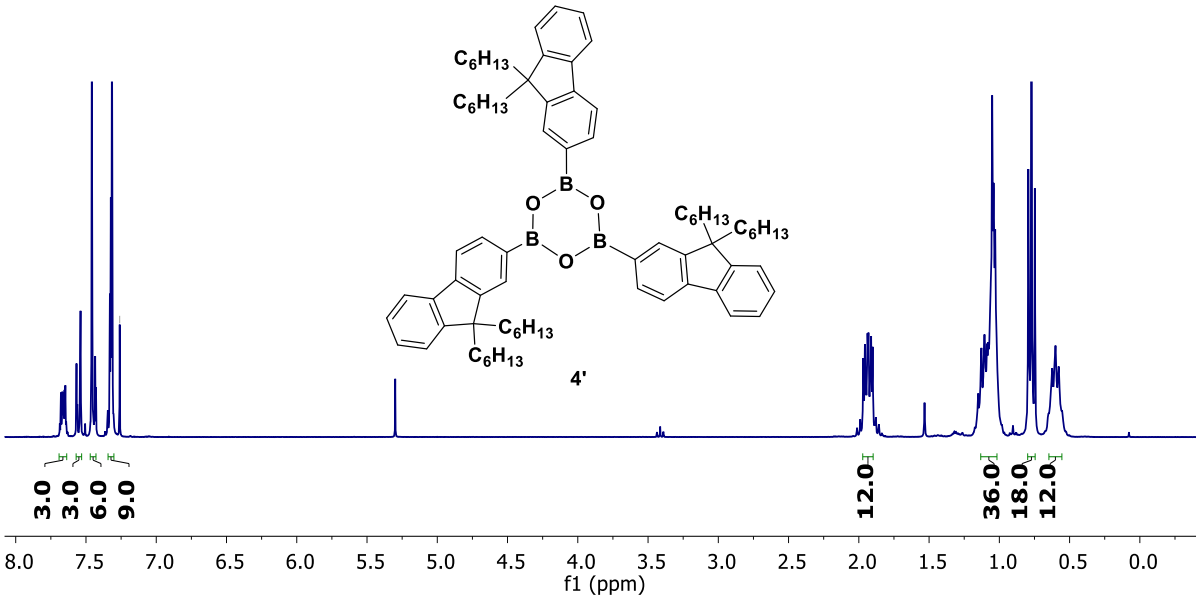

Fig. II-5. ^{1}H-NMR spectra (CD_3Cl, 400 MHz) for the compound **4**.

II-5. Synthesis and Characterization of Ligand 3

The synthesis of Bis-terpyridyl **Ligand 3** (**L3**) was carried out using an alternative synthetic route (**Scheme II-5**) as compared to the previously described method. The previous approach required the use of 4'-bromo-2,2':6',2''-terpyridine reagents as coupling partners,[153] which involved complex and time-consuming synthetic procedures. In our approach, synthesis began with the aldol condensation between compound **3** and 2-acetylpyridine taking place simultaneously at both sides of the fluorene backbone to yield *enone* **6**, which was efficiently transformed through Kröhnke synthesis reaction into **Ligand 3**.

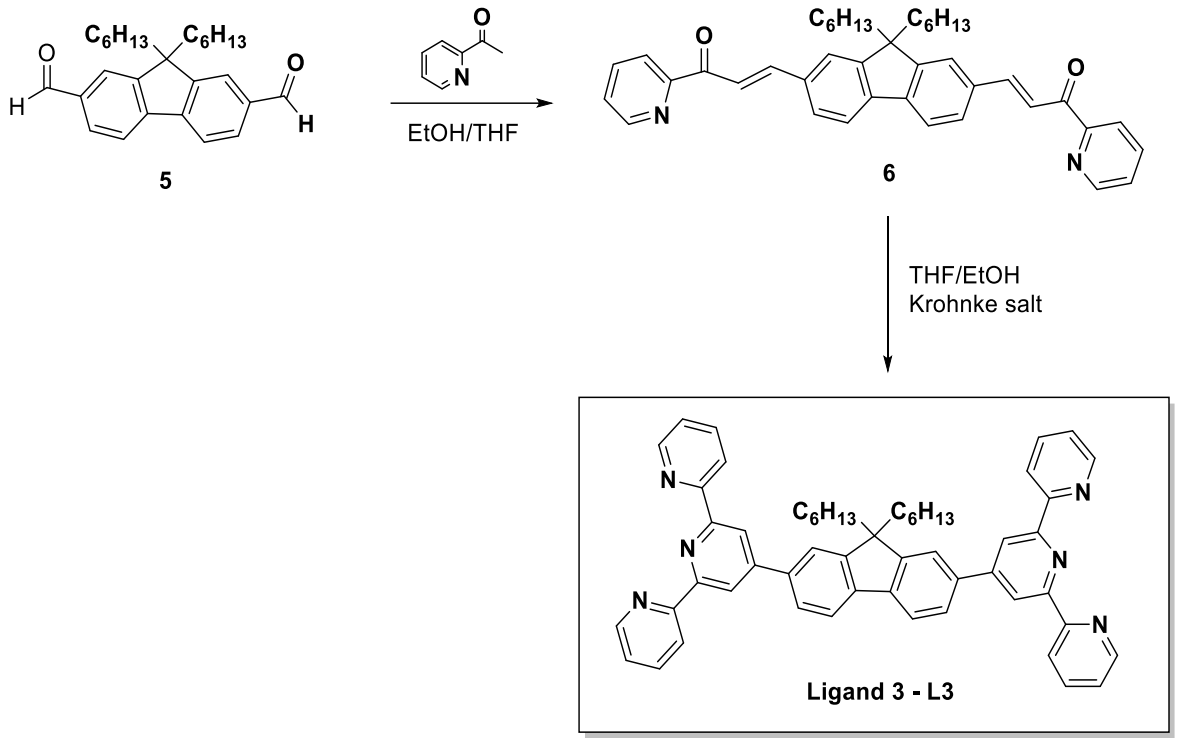

Scheme II-5. Synthesis of **Ligand 3** through Kröhnke terpyridine synthesis.

^{1}H-NMR, ^{13}C-NMR, NOESY, COSY, HMBC and HMQC analyses were used to determine the structure of the **Ligand 3** (**Fig. II-6**).

Upon analysis, it was observed that all protons associated with the fluorene moiety from **L3** appeared in the aromatic region in the range δ = 7.96-7.86 ppm. In comparison to the isolated fluorene molecule, which exhibited proton resonances in the range of δ = 7.35-7.61 ppm, it can be noted that the terpyridine moiety has an

influence on the electron density of the fluorene moiety, causing the chemical shifts to increase.

On the other hand, the protons in the terpyridine moiety from **L3** (*H-9* = 8.81, *H-15* = 8.77, *H-12* = 8.69, *H-13* = 7.96-7.86, *H-14* = 7.36) exhibited similar chemical shifts to those of the isolated terpyridine molecule (*H-9* = 8.45, *H-15* = 8.68, *H-12* = 8.61, *H-13* = 7.83, *H-14* = 7.30 for the terpyridine).[154] Comparing these values, it is evident that the only affected protons are the located in position H9, which is *ortho* to the fluorene moiety and connected through C4-C8 position. This implies that the fluorene moiety does not exert a strong influence on the terpyridine rings.

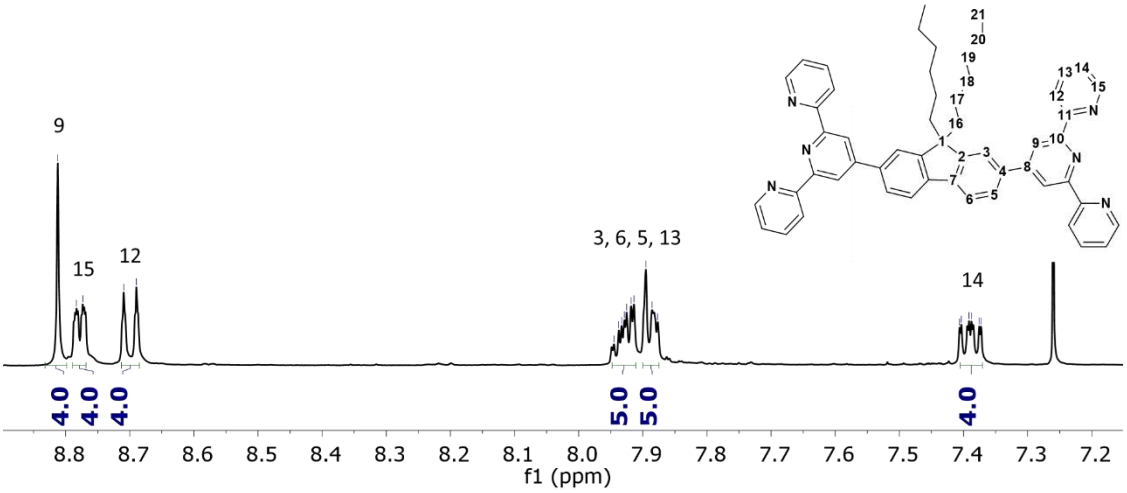

Figure II-6. ^{1}H-NMR spectra (CD_3Cl, 400 MHz) for the Ligand **3** showing the assignation of the protons in the aromatic region.

II-6. Synthesis and Characterization of Ligand 4

For **Ligand 4** (**L4**), we adopted the strategy of simultaneously synthesizing the terpyridine units on both sides of the molecule (**Scheme II-6**), similar to the successful approach used for synthesis of **L3**. Initially, the synthesis proceeded as planned, resulting in the formation of the desired *double enone* intermediate (**b**).

However, it was encountered that this double *enone* intermediate exhibited poor solubility in most solvents. Consequently, the final step of the synthesis, which aimed to obtain **L4**, was not possible to be obtained.

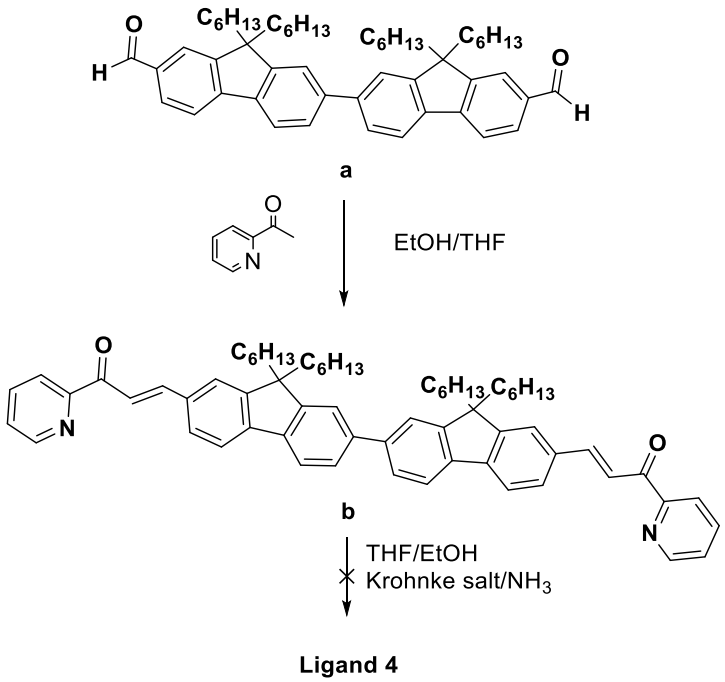

Scheme II-6. First trial for synthesis of **Ligand 4** through double Kröhnke terpyridine synthesis.

Therefore, taking into consideration the challenges encountered in the first trial for synthesis of **L4** through the simultaneous synthesis of terpyridine units, an alternative approach using a convergent synthetic route was deemed more appropriate (**Scheme II-7**). Convergent methods have been shown to offer enhanced overall efficiency when synthesizing large organic molecules, as opposed to divergent approaches. Previous studies have demonstrated the successful application of convergent strategies for the synthesis of related polyfluorene bis-terpyridyl ligands.[155]

In this particular synthesis, the starting point was the iodinated terpyridine (**3**). The key final steps involved the Suzuki-Miyaura reaction, employing pinacolboryl terpyridine (**7**) as the coupling partner. By adopting this approach, **L4** was efficiently

prepared, thereby circumventing the previous challenges associated with the use of boronic acids.

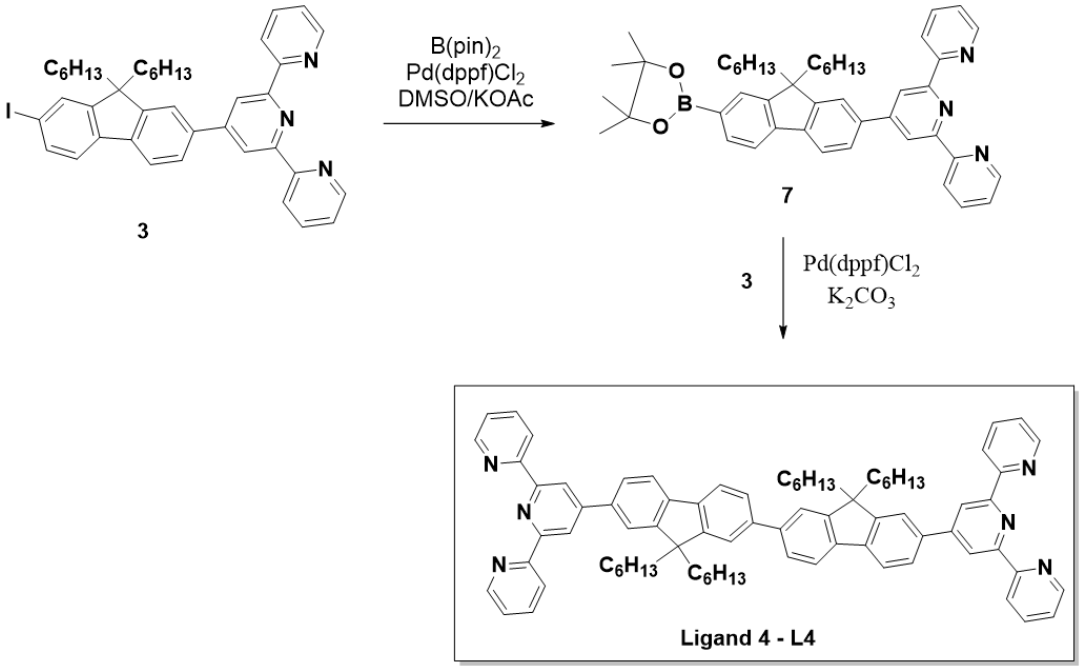

Scheme II-7. Synthesis of **Ligand 4** through Suzuki-Miyaura reaction.

The structure of **L4** was elucidated through the analysis of its ^{1}H-NMR spectra (**Fig. II-7**) and ^{13}C-NMR, NOESY, COSY, HMBC and HMQC analyses, following a similar approach to that employed for **L3**. In the obtained spectra, all the protons belonging to the fluorene moiety were successfully identified. The proton assignments exhibited a resemblance to those observed in **L3**.

Particular attention was drawn to the behavior of the protons located at positions *2* and *12* that appear in the region located at δ = 7.74-7.64 ppm. These protons exhibited a distinct characteristic by appearing outside the multiplet region at δ = 7.97-7.83 ppm, value similar to the multiplet found for the protons belonging to fluorene moiety in **L3** (δ = 7.96-7.86 ppm). This observation suggests that protons *2* and *12* experienced minimal influence from the neighboring terpyridine groups. However, it is important to note that their chemical shifts were slightly affected due to the presence of the linked fluorene moiety at position C1.

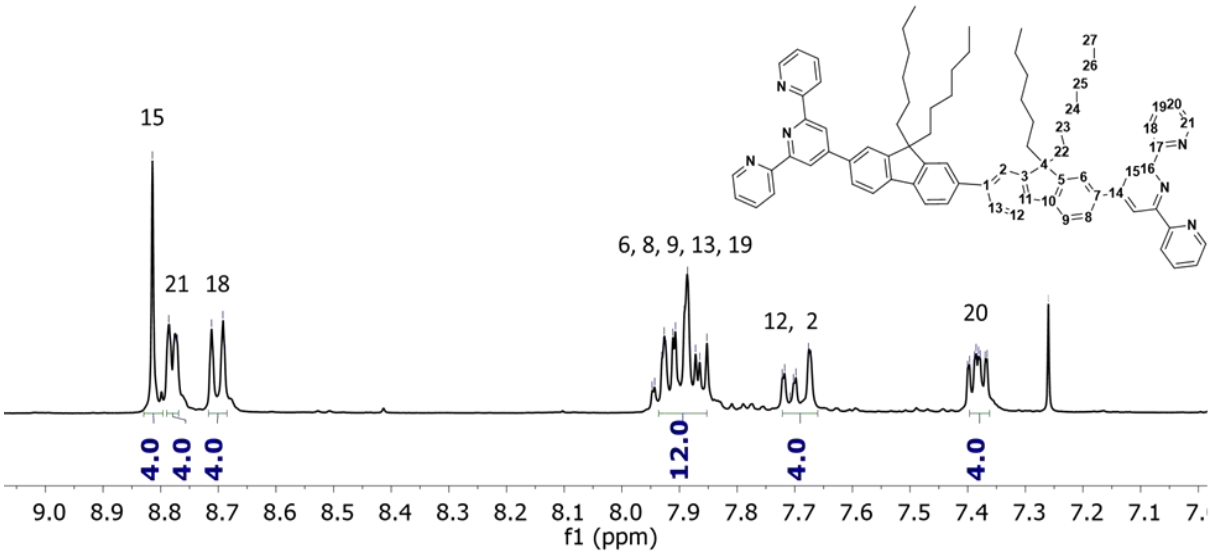

Figure II-7. ^{1}H-NMR spectra (CD_3Cl, 400 MHz) for the **L4** in the aromatic region.

II-7. Synthesis of Ligand 5

The synthesis of **Ligand 5** (**L5**) (**Scheme II-8**) followed a similar approach to that employed for **L4**, using a convergent route via the Sonogashira reaction. This reaction methodology offers an excellent means of incorporating unsaturation under very mild conditions.

The synthetic sequence started with (E)-3-(7-ethynyl-9,9-dihexyl-fluoren-2-yl)-1-(pyridin-2-yl)prop-2-en-1-one (**8**), which underwent a Michael addition to form the enone intermediate (**9**). Subsequently, compound (**9**) underwent a Kröhnke terpyridine synthesis, similar to previous ligands, leading to the formation of compound (**10**). Finally, **L5** was obtained through the Sonogashira reaction. Interestingly, it was observed that proton in terminal alkyne remained unaffected by the strong basic conditions of the reaction media, with a pH of approximately 12-13. This was verified by locating the terminal proton by ^{1}H-NMR spectrum, located at δ = 3.17 ppm (s, 1H), which exhibited the same chemical shift value as that of compound (**10**) for the corresponding proton.

During the purification process, it was crucial to employ a short column, as terpyridine exhibits a strong affinity for silica. Failure to consider this factor can significantly impact the yield of the desired ligand.

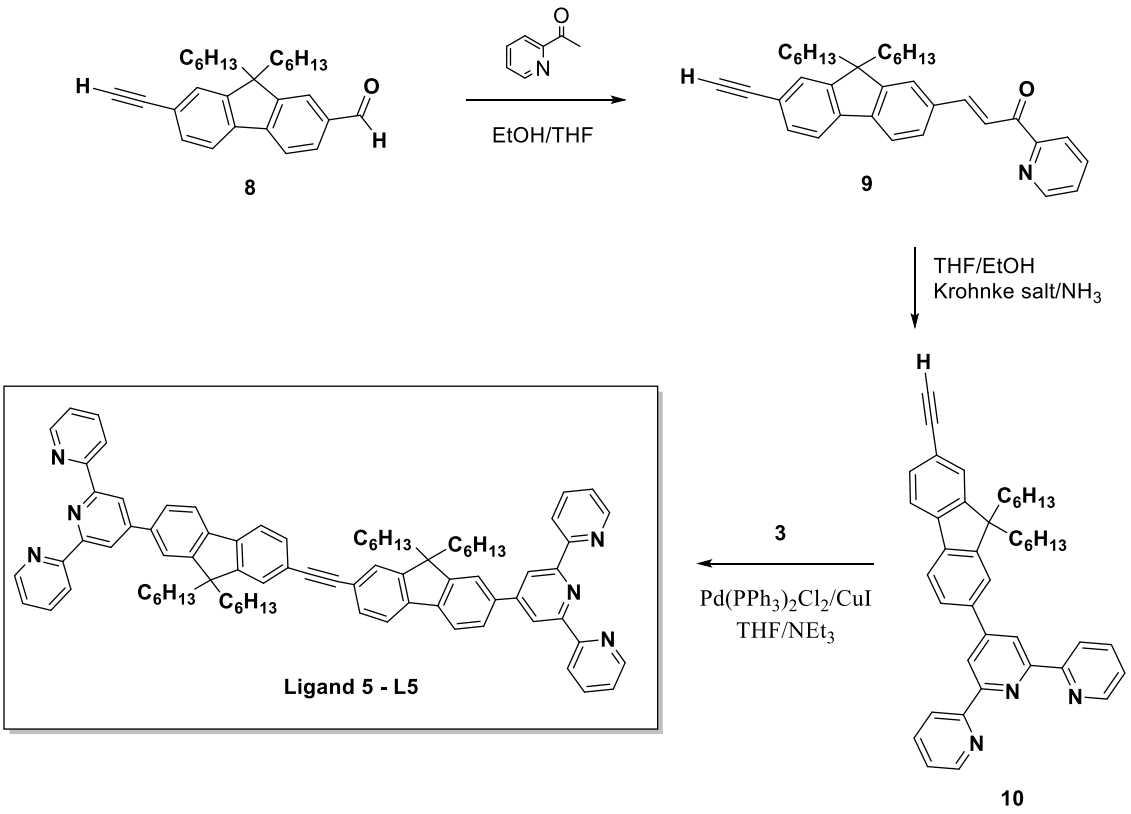

Scheme II-8. Synthesis of **L5** through Sonogashira reaction.

II- 8. Synthesis of Ligand 4’ and 2’ and Crystal Structure

In order to obtain crystal structures, homologues of **L2** and **L4** were synthesized by incorporating methyl chains instead of hexyl chains. They were chosen as they have demonstrated a higher propensity for generating crystals compared to compounds having hexyl chains, which are typically used to enhance solubility. The inclusion of short, alkylated moieties helps to minimize disorder within the crystal lattice, leading to the formation of more organized and precisely defined structures. Bromo compounds were selected for the synthesis to take advantage of the abundance of the starting material.

Ligand 2' (**L2'**) was synthesized (**Scheme II-9**) following a similar approach as for **L2**, starting from 7-bromo-9,9-dimethyl-9H-fluorene (**11**). The synthesis involved a Suzuki-Miyaura cross-coupling reaction between compound (**11**) and compound (**12**) to form the desired compound **L2'**.

The synthesis of **L4'** (**Scheme II-10**) started with the aldol condensation between aldehyde (**13**) and 2-acetylpyridine, resulting in the formation of the *enone* (**14**). Compound (**14**) then underwent a Kröhnke terpyridine synthesis, leading to the production of compound (**15**), which contained the brominated terpyridine moiety. The subsequent step involved Suzuki-Miyaura cross-coupling reactions, with pinacolboryl terpyridine (**12**) serving as the coupling partner. In this final synthetic step, the addition of dichloromethane was necessary due to the low solubility of the compound in the toluene/ethanol mixture. However, the yield achieved in this step was 25%, which is relatively low compared to the yield obtained for **L4**, which was almost the double, 56%.

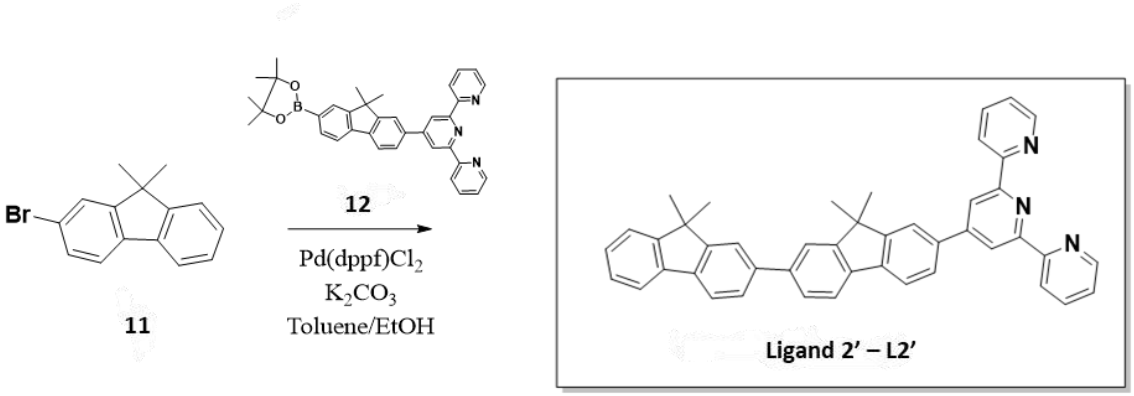

Scheme II-9. Synthesis of **Ligand 2'** through Suzuki-Miyaura reaction.

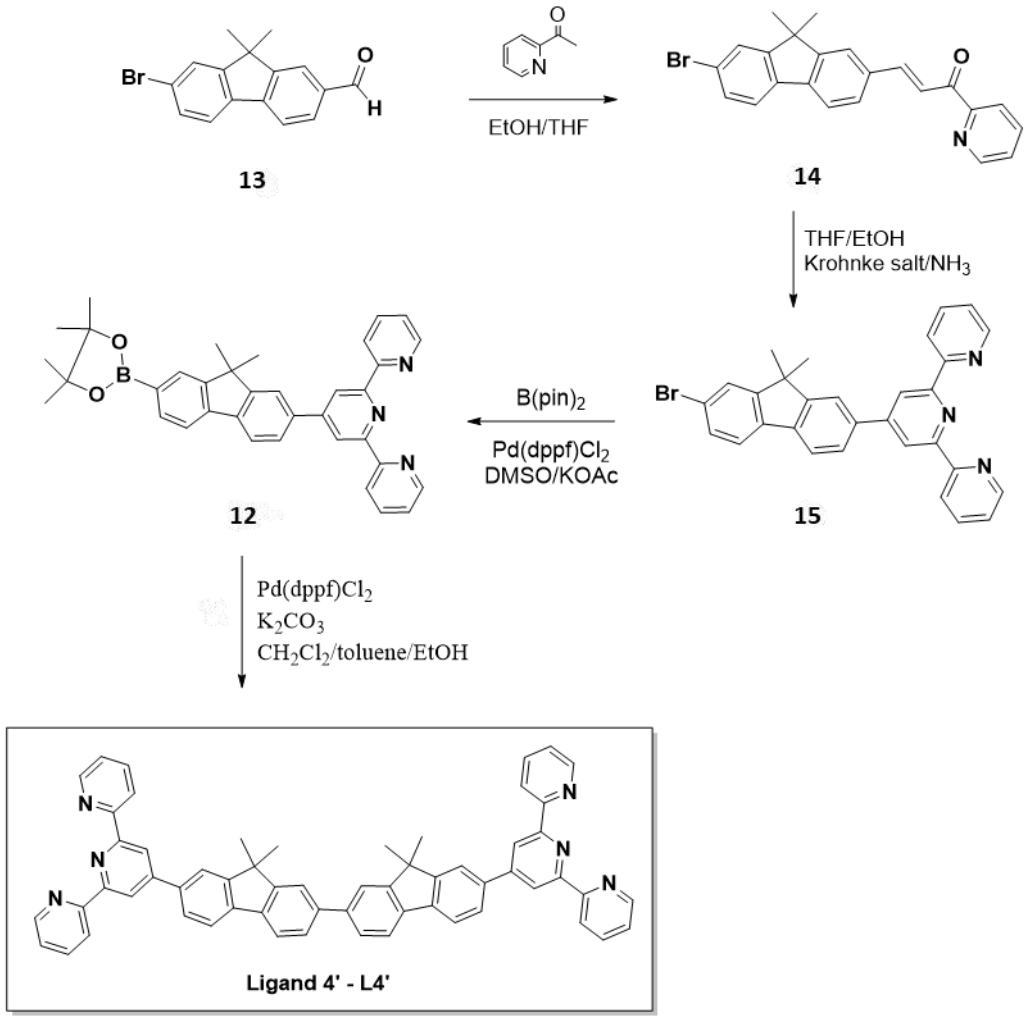

Scheme II-10. Synthesis of **Ligand 4'** through Suzuki-Miyaura reaction.

X-ray diffraction analysis was conducted on the single crystals of **L2'** and **L4'** obtained through the slow evaporation of a dichloromethane solution (**Fig. II-8**). Both ligands crystallize in the triclinic P-1 space group, in which two molecular units refer to one-another by an inversion center.

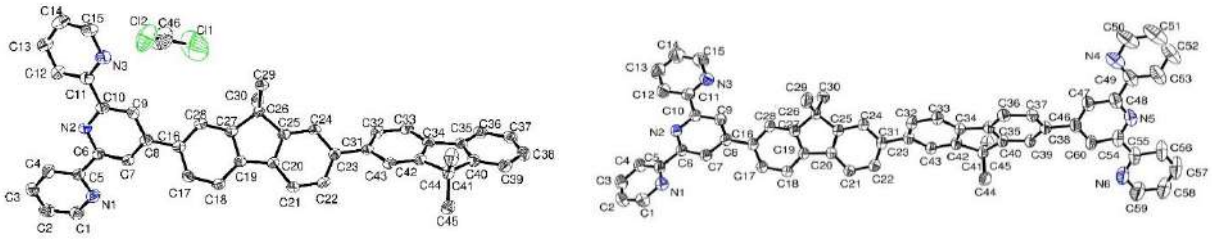

Figure II-8. Structure for **L2'** (left) and **L4'** (right), hydrogen atoms are omitted for clarity.

For **L2'**, a molecule of dichloromethane is present in the asymmetric unit. The terpyridine fragment consisting of 18 atoms, is nearly planar. The torsion angles between the terpyridine and the planar adjacent fluorene, which has 13 heavy atoms, is 39.78°, while the torsion angle between the two fluorenes is 44.05 Å. The structure shows 23 close interactions with nearby molecules, shorter than the sum of their Van der Waals radii between H-H.[156] The shortest intermolecular contact is equal to 2.373 Å (H13···H39).

In the case of **L4'**, the molecular structure is not symmetric. Specifically, while one terpyridine segment (C46–C59) appears almost flat, the other (C1–C15) shows noticeable distortion with the most prominent deviation from the mean plane being 0.427 Å at N1. The torsion angle between terpyridine fragments (18 atoms) and fluorene fragments (13 atoms) are as follows: 27.05° between terpyridine C1–C15 and fluorene C16–C26; 33.46° between terpyridine C46–C59 and fluorene C31–C41. The torsion angle between the two fluorenes is equal to 49.09°, which indicates a slight overlap between the π-electron cores of each fluorene.

II-9. Synthesis of Ruthenium Complexes With L1-L5

Once the ligands **L1**-**L5** were synthesized, it was possible to continue with the synthesis of target RuNO complexes through a general 4-step synthetic route, as illustrated in (**Scheme II-11**). The first step involved metalation using $RuCl_3 \cdot xH_2O$, resulting in the formation of neutral Ru^{III} complexes **[Ru(L1-L2)Cl$_3$]** and **[Cl$_3$Ru(L3-L5)RuCl$_3$]** with high yields.

In the second step, two chlorido ligands were replaced by a 2,2'-bipyridine ligand, accompanied by the reduction of Ru^{III} to Ru^{II}. This transformation yielded complexes **RuCl-1** to **RuCl-5** in satisfactory yields. These complexes served as crucial intermediates for the subsequent steps. The third step involved an efficient ligand exchange reaction, where the chlorido ligands of **RuCl-1** to **RuCl-5** were replaced by $NaNO_2$, to give the formation of **RuNO$_2$-1** to **RuNO$_2$-5** complexes. This ligand exchange reaction was essential for introducing the nitrosyl ligand (NO^+) into the complexes.

In the final step, the **RuNO$_2$-1** to **RuNO$_2$-5** complexes were treated with concentrated hydrochloric acid, followed by metathesis with aqueous NH_4PF_6. This series of reactions yielded the desired **RuNO-1** to **RuNO-5** complexes in high yields.

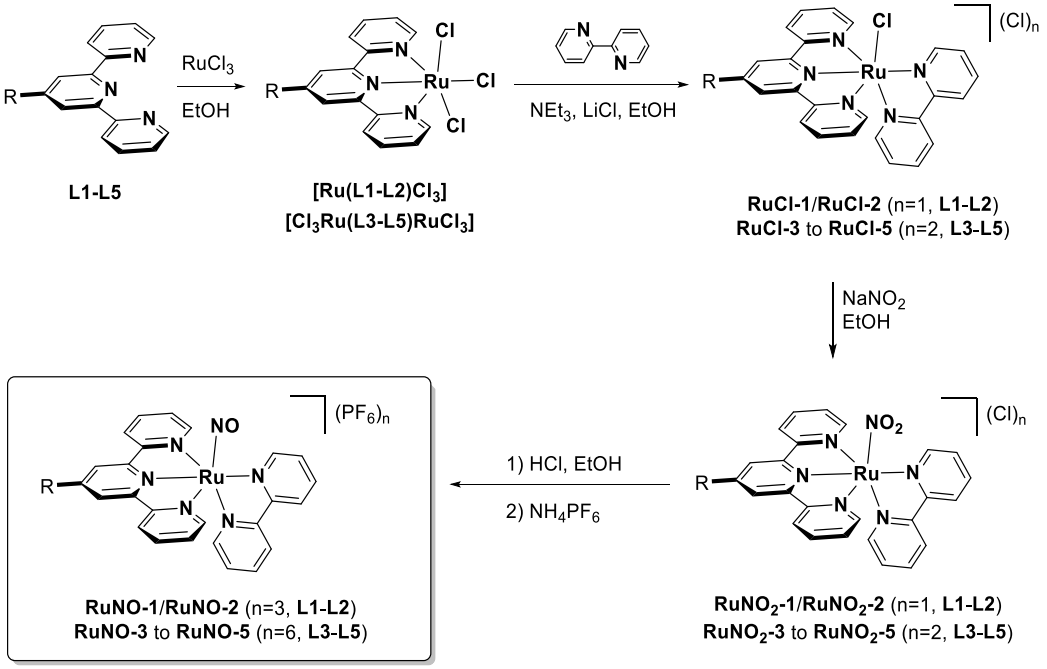

Scheme II-11. Synthesis of complexes **RuNO-1** to **RuNO-5.**

II-10. ^{1}H-NMR and HRMS Analyses of Representative Signals in RuNO-n Complexes

The identity of all the diamagnetic Ru^{II} complexes were confirmed through ^{1}H-NMR and ^{13}C-NMR analyses, which provided a convenient method to assess the completeness of the transformations. As shown in **Figure II-9**, characteristic changes in chemical shifts were observed for the hydrogen atoms ortho to the annular nitrogen of the equatorial rings of the bipyridine ligands. These changes in chemical shift were attributed to the spatial proximity of these hydrogen atoms to the varying monodentate ligands.

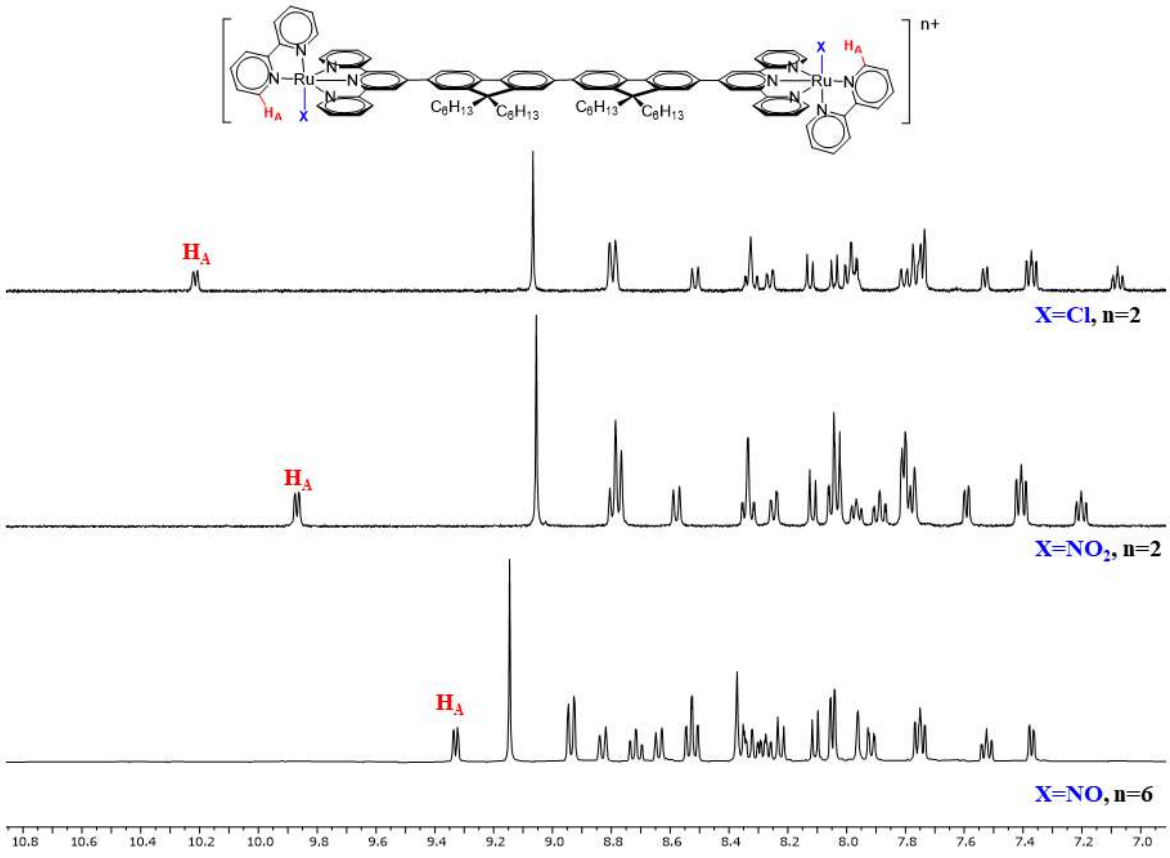

Figure II-9. Representative example of the changes in the ^{1}H-NMR spectra (298 K, 400 MHz) associated with the Ru-Cl→$RuNO_2$→RuNO transformations.

Furthermore, the identity of these complexes was also supported by HRMS/MS analyses. The spectra for **RuCl-1** to **RuCl-5** and **$RuNO_2$-1** to **$RuNO_2$-5** complexes exhibited dominant peaks corresponding to the unaltered cations. However, the spectra for the final **RuNO-1** to **RuNO-5** series were more complex. In the case of **RuNO-2**, **RuNO-4**, and **RuNO-5**, the Ru-NO^+ moieties were reduced to Ru-NO• during the experiment. In the case of **RuNO-3** (**Fig. II-10**), partial transformation to **Ru-NO_2** occurred due to the presence of traces of water during the measurement. It should be noted that these complexes are overly sensitive to water.

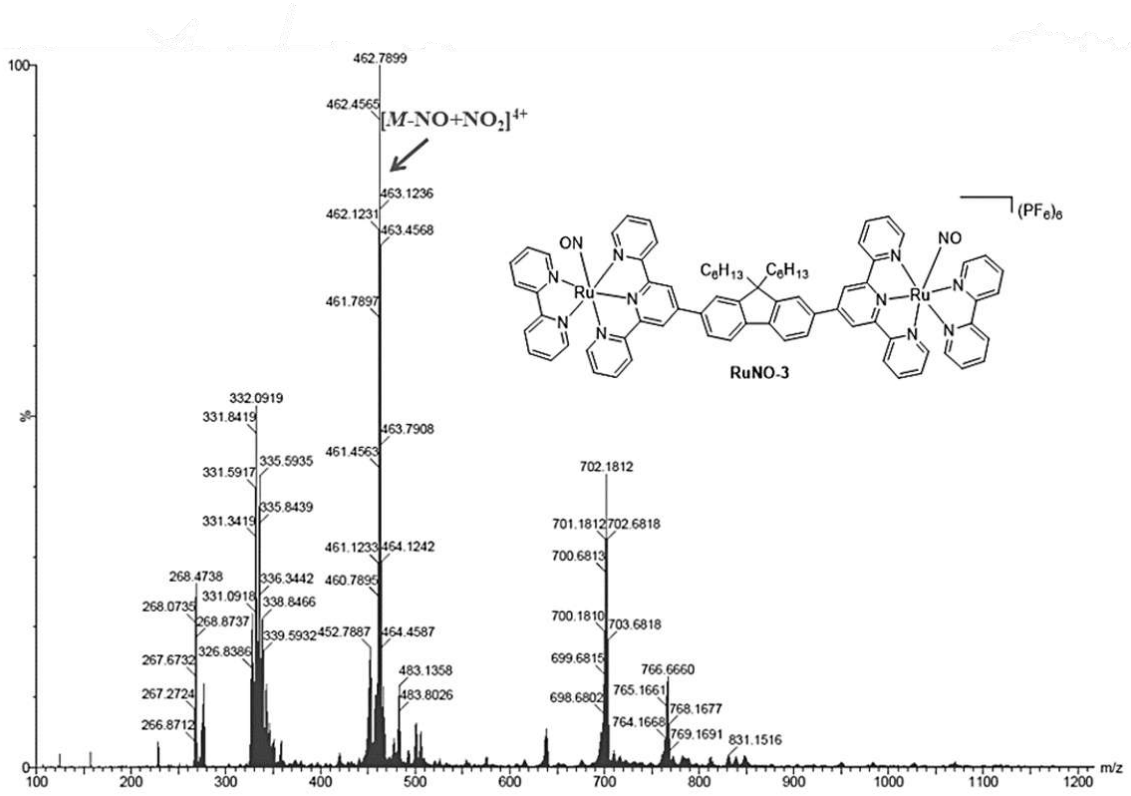

Figure II-10. HRMS (ESI-TOF+) for the complex **RuNO-3** in which the base pic corresponds to the partial transformation of NO^+ to NO_2^- ligand.

II-11. Side Reactions During Complexation of Ligand 4' and NMR Analyses

For the synthesis of complexes containing **Ligand 4'** (**L4'**), the same synthetic route as depicted in **Scheme II-11** was followed. However, a modification was made during the metalation step. Due to the poor solubility of **L4'** in various solvents, a different approach was required. It was found that adding dichloromethane in a 1:1 proportion to ethanol provided the best solvent ratio for the reaction. This solvent combination enabled the successful metalation step, and after purification, the desired complex was obtained. This methodology contrasted with the synthesis using **L1**-**L5**, that were completely soluble in the media.

During the addition of the bipyridine ligand, the same protocol was followed. However, during the purification process, several fractions were separated, leading to the collection of multiple complexes. Among these fractions, an oligomer was identified that contained two units of **L4'** and three ruthenium metal centers (**Scheme II-12**). This observation suggested that the solubility issue encountered in the initial step influenced the formation of the *homoleptic* complex, but, due to the presence of a terpyridine ending in the ligand, it was capable of undergoing further reactions which further reacted with the ruthenium present in the reaction mixture, resulting in the formation of several oligomers.

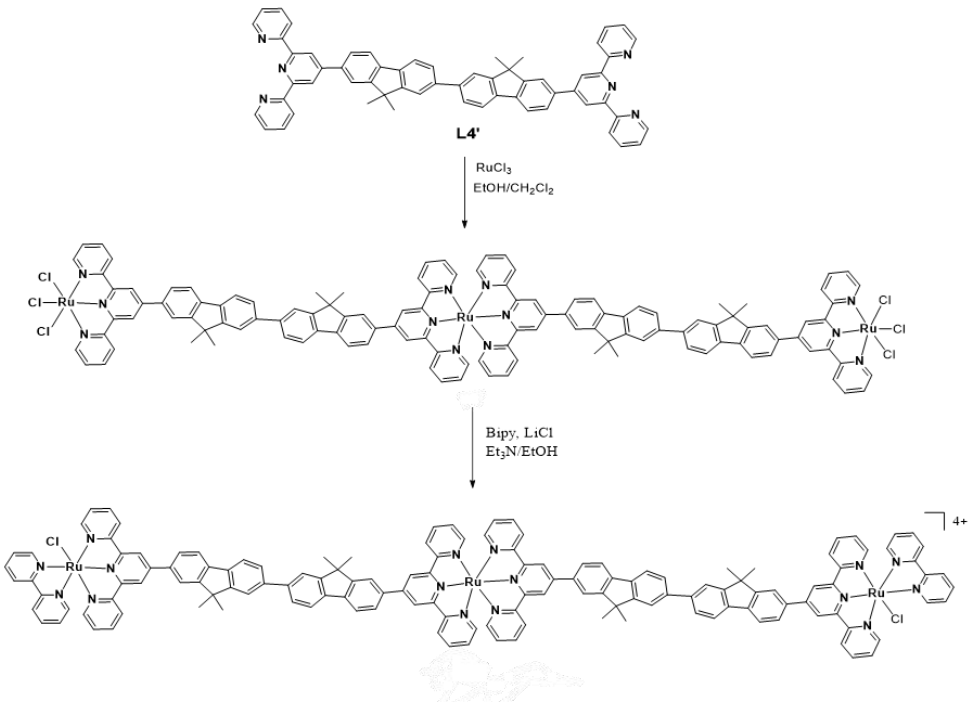

Scheme II-12. Proposed reaction for **RuCl-L4'$_2$**.

Unfortunately, the remaining isolated oligomers exhibited extremely poor solubility in any solvents, making complicated any further analysis.

By analyzing the ^{1}H-NMR spectrum, it was possible to assign the protons belonging to the bipyridine ligands, that remains the same quantity as for the regular bimetallic complexes, indicating that the maximum possible quantity of bipyridines that can be present is two molecules, one at each end (16 protons). In the aromatic region, numerous signals corresponding to the fluorene and terpyridine moieties are observed. Additionally, in the aliphatic region, 24 protons are detected, which are divided into two singlets at δ = 1.81 and 1.85 ppm (**Fig. II-11**). One singlet corresponds to the methyl group near the center of the structure, while the other singlet corresponds to the methyl groups near the extremes.

It is important to note that the ^{1}H-NMR spectrum contains some impurities, as indicated by the blue stars. However, the spectrum still allows for the identification of 79 out of the total 80 protons present in the structure.

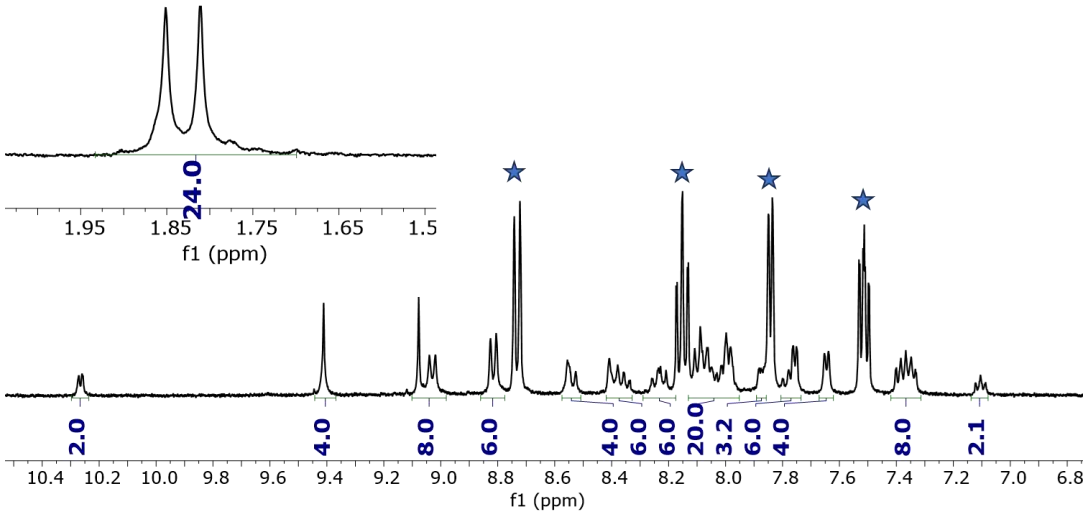

Figure II-11. ^{1}H-NMR spectra (CD_2Cl_2, 400 MHz) for the complex **RuCl-L4'$_2$**. The blue stars marked impurity. In zoom the aliphatic region shows the protons of methyl chain.

After the separation of different components using column chromatography with alumina and a CH_2Cl_2/MeOH eluent, complex **RuCl-4'** was isolated. Eventually, the final **RuNO-4'** complex was successfully obtained. Hydrogen (H_A) close to the ligand (**X**), which change at each step of the reaction, were analyze by ^{1}H-NMR in CD_3CN as a solvent (**Fig. II-12**). The experiments exhibited a similar pattern to its homologues, and almost the same results as the RuX-4 complexes.

Unfortunately, it was not possible to obtain high-quality crystals for any of the complex structures due to their low solubility. Additionally, the complex **RuNO-4'** readily decomposed into **$RuNO_2$-4'**. These challenges were not encountered in the synthesis of complexes containing **Ligand 2'**. However, since crystallization attempts with the bimetallic complexes **L4'** were unsuccessful, the synthesis was halted after **RuCl-2'**.

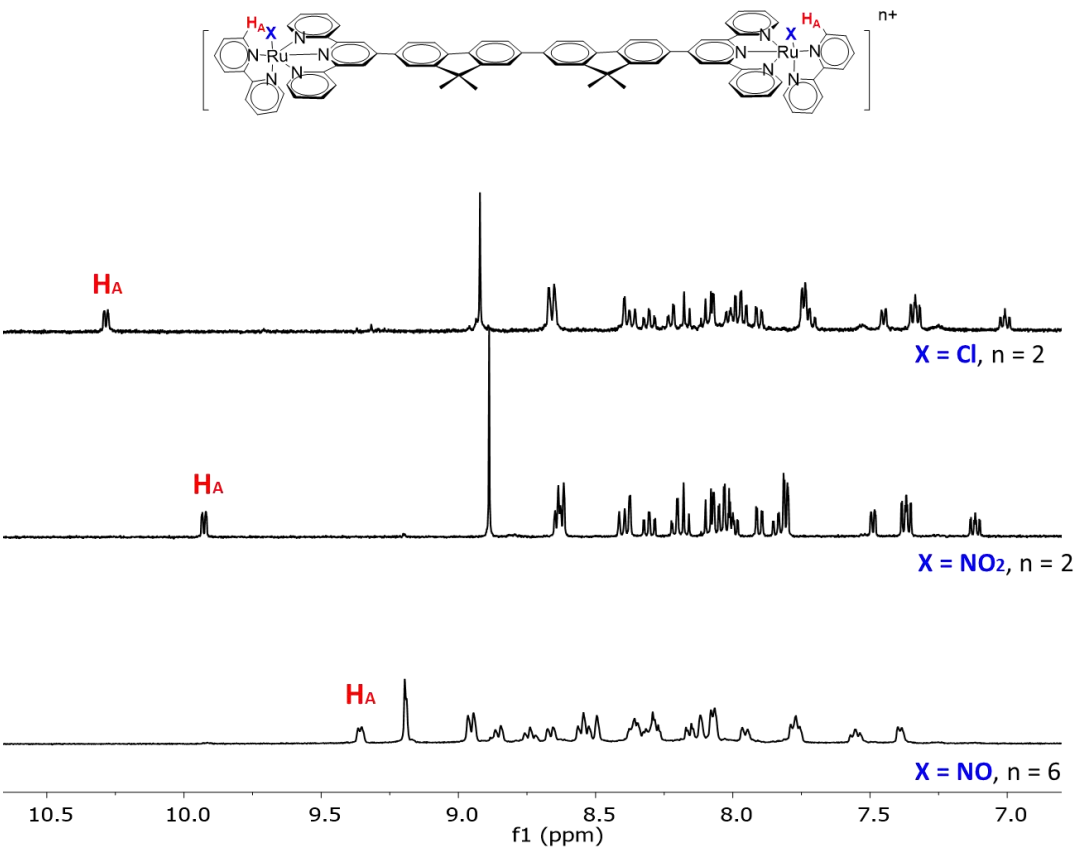

Figure II-12. NMR spectra (298 K, 400 MHz) associated with the Ru-Cl→$RuNO_2$→RuNO transformations as observed.

II-12. ^{1}H-NMR Pic Assignment for $RuNO_2$-5 and RuNO-5

To gain a better understanding of how the exchange of ligand from NO_2 to NO affects the chemical environment of molecules, the structures **$RuNO_2$-5** and **RuNO-5** were investigated as representative examples using various NMR techniques, including ^{1}H-NMR, ^{13}C-NMR, HMQC, HMBC, COESY, and NOESY.

As it can be observed in the ^{1}H-NMR of **$RuNO_2$-5** (**Fig. II-13**), within the bipyridine moiety, all eight protons can be identified. However, there is an overlap in the signals of *H22* and *H1* (7.83-7.78 ppm), which is a singlet from the fluorene moiety. *H23* (7.25 ppm) and *H-24* (7.98-7.92 ppm) exhibit similar values to their counterparts in the free terpyridine (*H'23* = 7.32 ppm and *H'24* = 7.83 ppm). *H25* (8.68 ppm) displays a doublet of doublets (dd) signal. The most significantly affected region (comparing the values to the one from free bipyridine) is the cycle closer to the NO_2 ligand, where *H-28* (8.90 ppm) shows a doublet of doublets (dd) signal and *H29* (8.46-8.39 ppm) exhibits a triplet of doublets (td) signal. *H30* (8.15-8.08 ppm) overlaps with another signal originating from the fluorene moiety. The pronounced downfield shift of the *H31* (10.06 ppm) resonance is attributed to the proximity of the NO_2^- ligand as it was discussed.

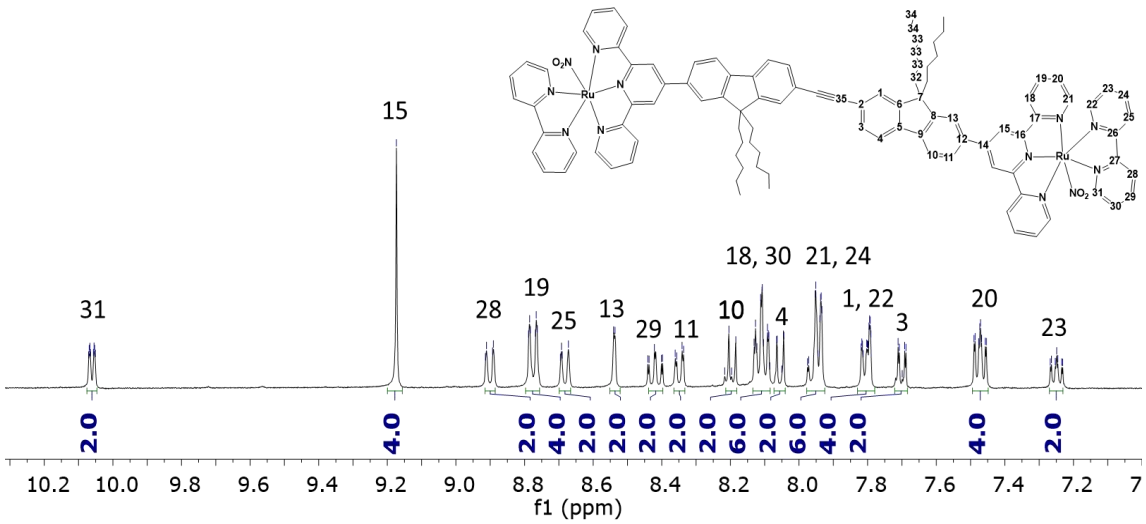

Figure II-13. ^{1}H-NMR spectra (298 K, 400 MHz) in CD_3CN.

A similar analysis can be conducted for **RuNO-5** (**Fig. II-14**), wherein the protons of the bipyridine moiety are predominantly influenced by the ligand exchange. In general, all the protons in positions *H22* to *H30* experience an upfield shift, due to the increased electronic density attraction resulting from the presence of nitric oxide. However, the proton in position *H31*, in close proximity to the NO^+ ligand, exhibits a downfield shift, indicating a decrease in its chemical shift value, which can be attributed to direct interaction effects.

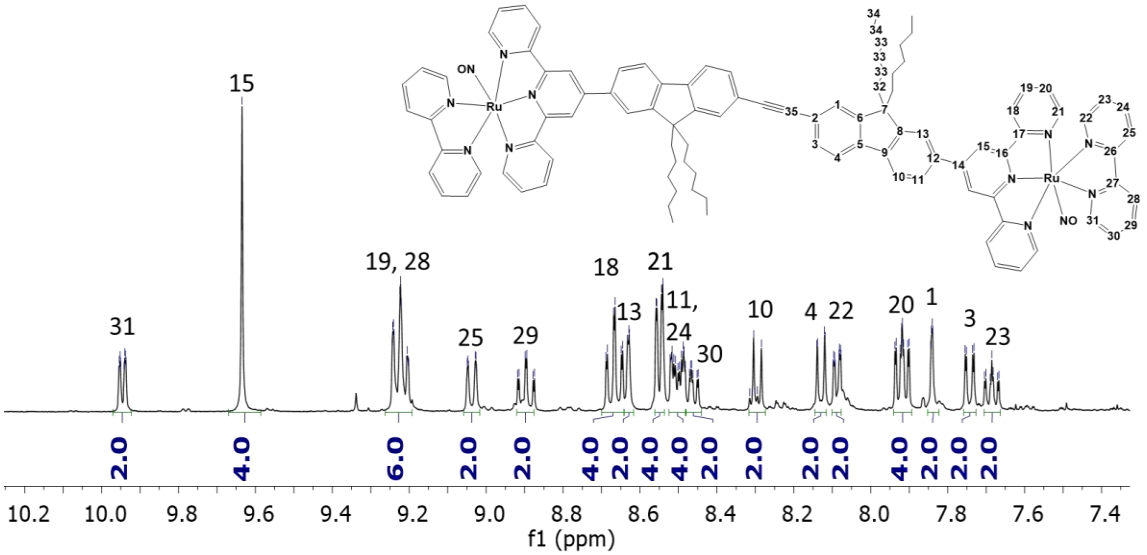

Figure II-14. ^{1}H-NMR spectra (298 K, 400 MHz) in CD_3CN with proton assignation.

When comparing the fluorenyl moieties of each complex, **$RuNO_2$-5,** and **RuNO-5**, it is evident that the chemical environment is not significantly affected by exchanging the ligand -NO_2 for -NO, as indicated in **Table II-1**. The maximum difference is observed for the proton in position *H11*, which is in closer proximity to the coordination sphere, with a Δδ of 0.15 ppm.

Table II-1. Comparison of chemical shift values from protons in the fluorene moiety between **$RuNO_2$-5** and **RuNO-5.**

Position	δ (ppm) Fluorene in $RuNO_2$-5	δ (ppm) Fluorene in RuNO-5
1	7.83-7.78	7.84
3	7.70	7.74
4	8.05	8.13
10	8.20	8.29
11	8.35	8.52-8.48
13	8.54	8.64-8.61

Nevertheless, when conducting a thorough comparison of the protons at position *H15* in the terpyridine moiety and the proton at position *H31* in the bipyridine moiety (**Table II-2**), which are the most representative ones, it becomes evident that the chemical shift is solely dependent on the nature of the substituent in the ruthenium core (Cl, NO_2, NO).

Table II-2. Comparison of chemical shift values for protons H-15 in the terpyridine moiety and H-31 in the fluorene moiety between different complexes.

Complex	δ (ppm) H-15 (tpy)	δ (ppm) H-31 (bpy)
RuCl-2	8.87	10.28-10.23
RuCl-3	8.86	10.27-10.22
RuCl-4	8.86	10.24.-10.20
RuCl-5	8.87	10.28-10.22
$RuNO_2$-2	8.83	9.92-9.89
$RuNO_2$-3	8.85	9.89-9.83
$RuNO_2$-4	8.84	9.88
$RuNO_2$-5	8.97	9.92-9.85
RuNO-2	9.14	9.36-9.28
RuNO-3	9.19	9.35-9.32
RuNO-4	9.15	9.35-9.31
RuNO-5	9.14	9.33

II-13. Studies on Hexyl Chains in Runo$_2$-2 by X-Ray and NMR Analyses

The structure of **RuNO$_2$-2** is shown in **Figure II-15**, which contained an impurity of **RuCl-2.** The crystal structure was determined to be triclinic, with the space group P-1. The fact to investigate crystals of ruthenium nitrite ($RuNO_2$) complex is related to the difficulties encountered in the crystal growth of any crystal containing hexyl chains, which encouraged us to multiply the attempts on any sample available. In the present structure, a Ru^{II} is evidenced from the presence of one PF_6^- and one NO_2^-. The torsion angle between the mean planes of terpyridine and fluorene is equal to 31.16°, and 24.44° between the two fluorene units.

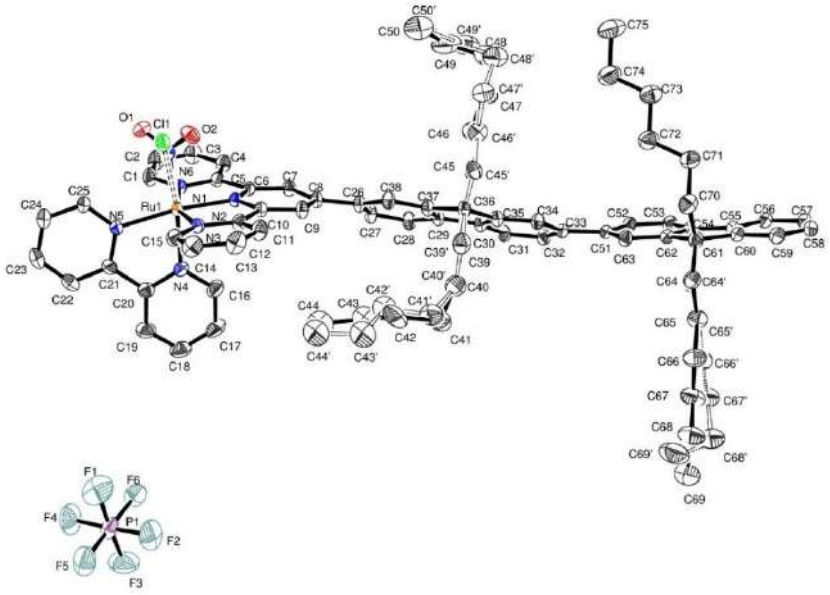

Figure II-15. Structure for **RuNO$_2$-2·RuCl-2**.

In the structures, the hexyl chains were found to be oriented in the same direction, adopting a *cisoid* conformation. This orientation is opposite to that observed in crystal structures for **L2'** and **L4'** (**Section II-8**), which contain methyl chains in *transoid* conformation. This observation can potentially be explained by the interaction between the two hexyl chains in the fluorene moieties, which serves to stabilize the structure. Despite the steric hindrance that two large chains might occur, the interaction between the hexyl chains could contribute to the overall stability of the crystal structure.

However, the effect of these chains on the cisoid/transoid configuration in bis-fluorene species warrants further exploration due to potential interactions between the chains. To delve into this, computational studies made by Dr. P. Lacroix were conducted on bis-fluorene molecules with tetra-alkylated chains of varying lengths, ranging from i = 1 (methyl) to i = 6 (hexyl), using density functional theory (DFT). The difference in Gibbs free energy ($\Delta G = G_{transoid} - G_{cisoid}$) is presented in **Figure II-16**. In all instances, ΔG is positive, pointing to the cisoid as the favored conformation in solution. Intriguingly, the longer the chain, the more pronounced this preference becomes, indicating that chain interactions play a crucial role in stabilizing the cisoid form. Still, due to a modest energy difference (ΔG = 0.6 kcal/mol for tetra-hexylated species), the cisoid/transoid ratio stands at 73/27, meaning both conformations coexist in solution.

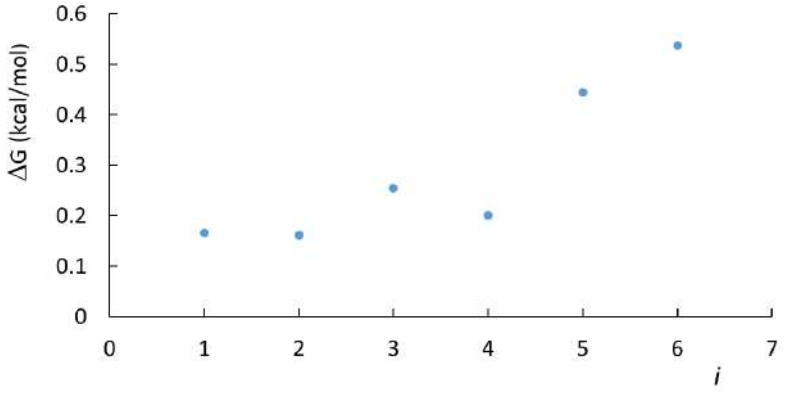

Figure II-16. Stabilization of the cisoid form ($\Delta G = G_{transoid} - G_{cisoid}$) in bis-fluorenes tetra substituted by alkyl chains of various lengths (i= number of carbon atoms in the chains).

To experimentally investigate this interaction between hexyl chains, ^{1}H-NMR (**Fig. II-17**) and NOESY-NMR (**Fig. II-18**) analyses for complex **RuCl-2** were performed in CD_3CN at a temperature of 233 K. The results revealed some insights into the nature of these interactions. Specifically, it was observed that the protons belonging to the fluorene moiety in closer proximity to the terpyridine ruthenium moiety exhibited a displacement towards higher values of ppm (blue chain), compared to its counterpart (red chain).

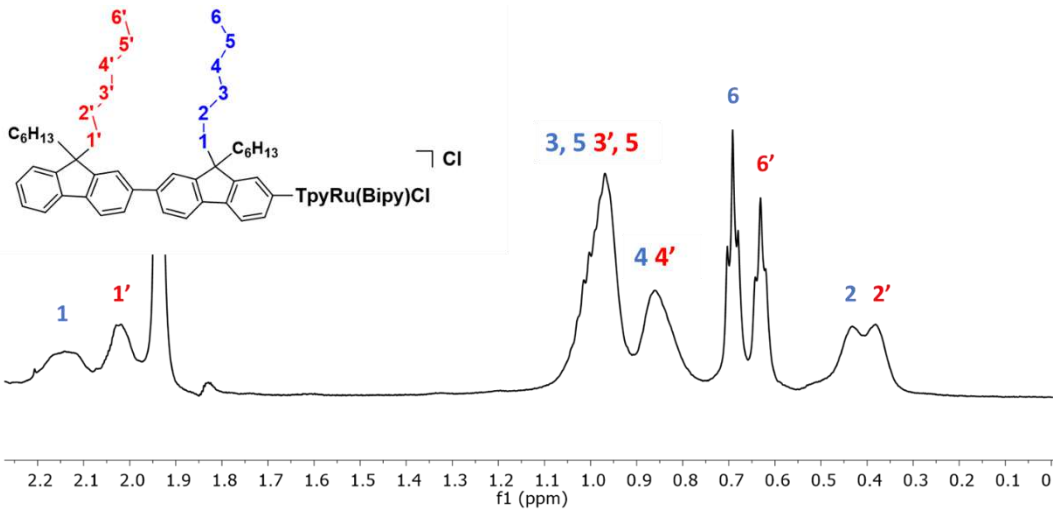

Figure II-17. ^{1}H-NMR spectrum in the aliphatic region for **RuCl-2** (CD_3CN, 600 MHz) .

NOESY-NMR experiment can reveal significant interactions occurring at approximately 5 Å.[157] These interactions can be further explored by adjusting the temperature during the experiment. The results obtained from NOESY-NMR spectra indicate a notable interaction between protons in position *1-4' and 1'-4*, protons in this position seems to be far from each other, making think that hexyl chain is twisted. This also would explain the asymmetric signal for the protons in position ***H1-H1'*** and ***H6-H6'*** due to interaction of protons in alkylated chain with the π system. Further analyses may be needed for a conclusive result.

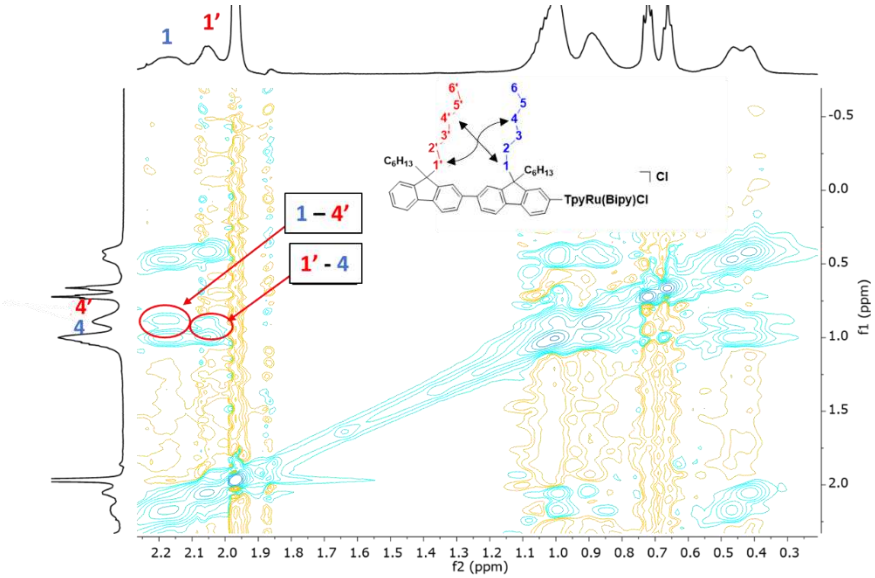

Figure II-18. NOESY-NMR spectrum for **RuCl-2** (CD_3CN, 600 MHz, 233 K).

II-14. Crystal Structure of $RuNO_2$-3 and RuNO-3

X-ray crystal structures were successfully obtained for **RuNO-3** and **$RuNO_2$-3**. Notably, these crystal structures represent the first reported instances of bimetallic complexes based on the [Ru(tpy)(NO_2)] and [Ru(tpy)(NO)] cores. A comprehensive survey conducted in the Cambridge Crystallographic Data Centre (CCDC) revealed no existing entries for either [Ru(tpy)(NO)] or [Ru(tpy)(NO_2)] bimetallic species.

$RuNO_2$-3 (**Fig. II-19**) crystallizes in the monoclinic space group P2 1/c. The asymmetric unit contains a single bis $RuNO_2$-3 cationic species, two disordered PF_6^- anions, and one molecule of DMF. Consequently, the complex carries a charge of 2+, with the ruthenium atoms assumed to be Ru^{II}. The overall conformation of the π-conjugated subunit approximately aligns with Cs symmetry.

Taking apart the disordered hexyl chains and the two anionic NO_2^- ligands, the remaining molecular structure exhibits Cs, indicating that the two coordination spheres around the ruthenium centers are roughly equivalent. Distance between the ruthenium and the nitrogen atoms in terpyridine have a value around 2.08 Å, value inside the range for this type of ruthenium complexes 2.01 Å –2.24 Å. The fluorene unit remains planar, with torsion angles between the fluorene (13 atoms) and terpyridine (18 atoms) measuring 27.77° and 32.57°, respectively.

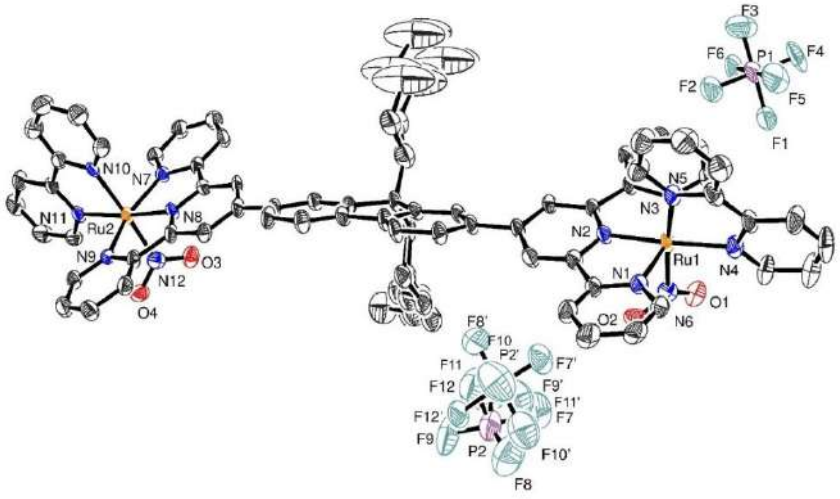

Figure II-19. Structure for **$RuNO_2$-3**.

RuNO-3 (**Fig. II-20**) crystallizes in the orthorhombic space group Pbcn. The asymmetric unit consists of one bis Ru-NO cation and six PF_6^- anions. The complex

carries a charge of 6+, and the RuNO fragments exhibit linear geometries with Ru-NO+ angles of 176.15° and 177.56°. Accordingly, the electronic configuration corresponds to $Ru^{II}(NO^{+})$. Unlike the previously described **$RuNO_2$-3** compound, this complex lack of symmetry. Interestingly, the torsion angles between the fluorene and the two terpyridines exhibit significant differences, with values of 45.21° and 24.24°.

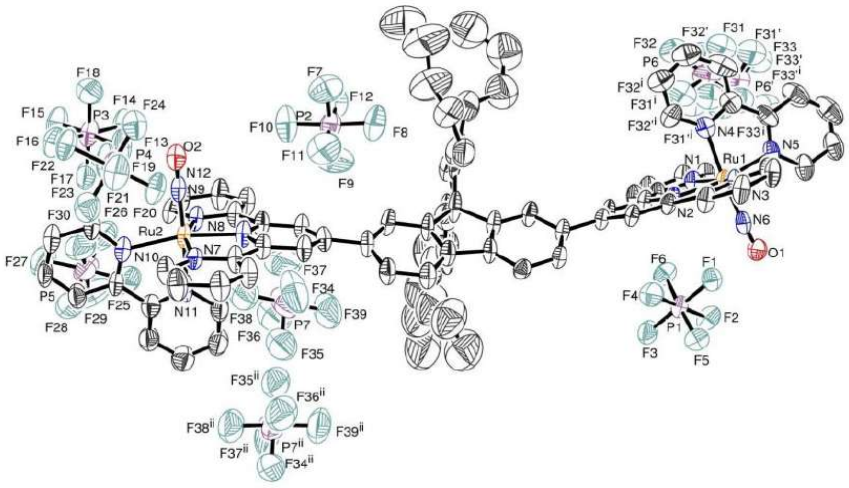

Figure II-20. Structure for **RuNO-3** in which $6PF_6^-$ can be observed.

The crystal structures reveal an interesting interaction between the oxygen atom in the N-O and one of the fluoride ions (F^-) in the PF_6^- counterion. Since the N-O is linked to the complex as NO^+, the oxygen atom carries a positive charge, preventing a direct face-to-face interaction with another oxygen atom. As a result, an interaction between the cation and the anion is favored in which the PF^{6-} anion plays an important role in the crystallization process (**Fig. II-21**). This interaction acts as a bridge between two molecules, with a distance of 2.697 Å and 2.764 Å and an angle of 137.84° (N-O···F···O-N).

Table II-3 presents the most significant distances and angles in the crystal structures. Notably, the Ru-O-N angle is close to 180°, which is expected considering the coordination of N-O as NO^+. In the case of **$RuNO_2$-3**, the Ru-N-O angles are close to 120°, indicating a trigonal planar structure. Furthermore, it is observed that the distance between the ruthenium and the nitrogen atom in NO_2^- is longer compared to the one for NO^+, reflecting the stronger interaction of NO^+ with the metallic center due to its ability to attract electron density.

Table II-3. Characteristic distances (Å) and bond angles (°) for **RuNO-3** and **$RuNO_2$-3**.

	RuNO-3	**$RuNO_2$-3**
N(1)-Ru(1)	2.102(5)	2.071(6)
N(2)-Ru(1)	1.988(5)	1.973(5)
N(3)-Ru(1)	2.087(5)	2.084(6)
N(4)-Ru(1)	2.074(7)	2.087(5)
N(5)-Ru(1)	2.095(6)	2.076(6)
N(6)-O(1)	1.147(8)	1.238(8)
N(6)-Ru(1)	1.739(7)	2.048(7)
N(7)-Ru(2)	2.067(7)	2.068(5)
N(8)-Ru(2)	2.002(6)	1.968(5)
N(9)-Ru(2)	2.091(6)	2.082(5)
N(10)-Ru(2)	2.116(6)	2.074(6)
N(11)-Ru(2)	2.023(8)	2.092(5)
N(12)-O(2)	1.141(9)	1.264(8)
N(12)-Ru(2)	1.761(8)	2.035(6)

	RuNO-3		**$RuNO_2$-3**
O(2)-N(12)-Ru(2)	177.5(6)	**O(3)-N(12)-Ru(2)**	121.9(5)
O(1)-N(6)-Ru(1)	176.1(5)	**O(4)-N(12)-Ru(2)**	120.4(5)
		O(1)-N(6)-Ru(1)	122.6(5)
		O(2)-N(6)-Ru(1)	118.5(5)

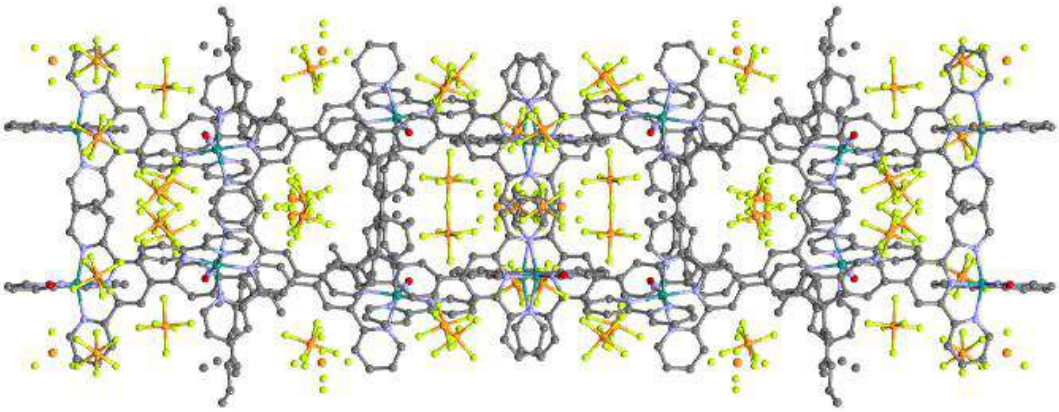

Figure II-21. Packing arrangement along *c* axis for **RuNO-3**, the PF_6^- anions are drawn in yellow (F) and orange (P).

II-15. UV-vis Spectra for RuCl, $RuNO_2$ and RuNO Series

The UV-vis spectra for the series of complexes **RuCl** and **$RuNO_2$** were recorded qualitatively in CH_3CN, both of the graphics shown in **Figure II-22** can be divided in three groups of bands: a low-lying band (a) in a wavelength range λ=450–600 nm in the case of **RuCl** series and λ=400–550 nm in the case of **$RuNO_2$** series. A multicomponent band (b) in the λ =250–400 nm range, and a very intense band (c) around 200 nm for both series.

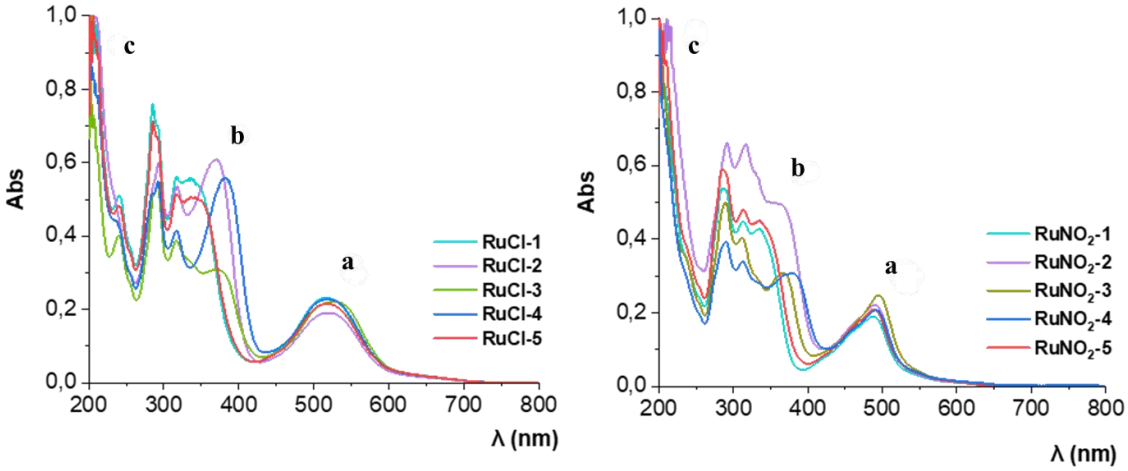

Figure II-22. UV-visible absorption spectra for **RuCl** complexes (left) and **$RuNO_2$** complexes (right).

The UV-visible spectra of the five **RuNO** complexes recorded in CH_3CN are shown in **Figure II-23**. The spectra reveal the presence of numerous transitions, which can be roughly classified in three groups as follows: a low-lying band (a) in a wavelength range λ=400–550 nm, a multicomponent band (b) in the λ =250–400 nm range, and a very intense band (c) around 200 nm. In any case, the low-energy bands (a) arise from single HOMO→LUMO based transitions from Ru→NO.

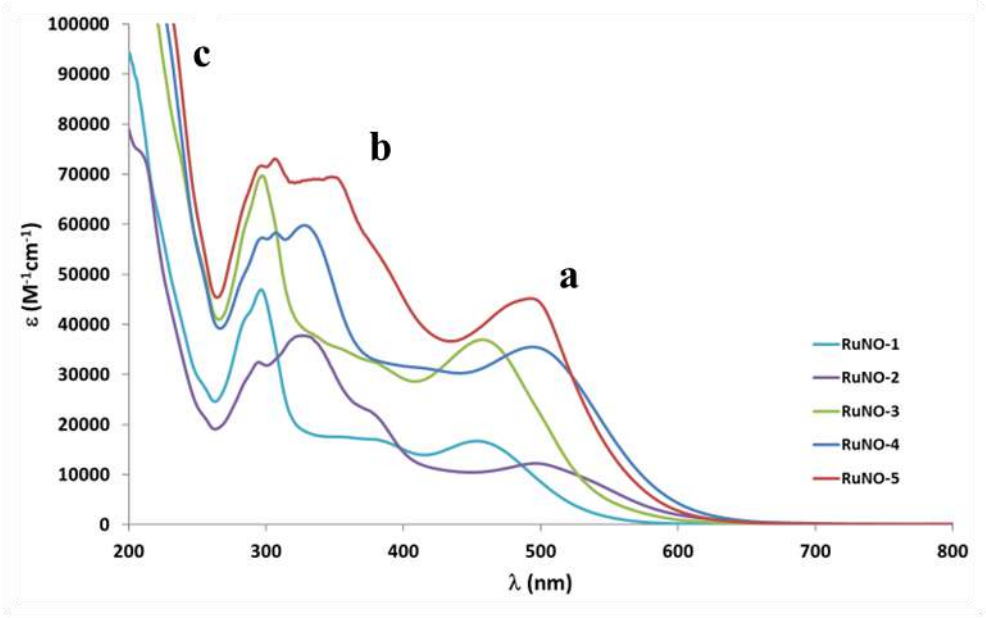

Figure II-23. UV-visible absorption spectra for **RuNO-1** to **RuNO-5**, in acetonitrile.

More intense bands observed at higher energy appear to be a general trend along the series. Concerning band (a), two tendencies are clearly observed: the complexes containing two fluorenyl units (**RuNO-2**, **RuNO-4**, and **RuNO-5**) are shifted to lower absorption maxima (λ_{Max}) values (from 450–460 nm to 490–500 nm) and the bimetallic complexes (**RuNO-3**, **RuNO-4**, and **RuNO-5**) exhibit intensities (extinction coefficient ε) at least twice as large as those of the monometallic species (ε=35 000 to 45 000 versus 12 000 to 17 000 $M^{-1}cm^{-1}$). This λ_{Max} values are resumed in the **Table II-4**.

Table II-4. Maximum absorption wavelengths and molar extinction coefficients for the different ruthenium complexes.

Compound	λ Max (nm)	Ɛ ($M^{-1}cm^{-1}$)
RuNO-1	453	16700
RuNO-2	497	12200
RuNO-3	457	37000
RuNO-4	494	35500
RuNO-5	493	45100

II-16. Infrared (IR) Spectra for RuNO Series.

As it was mentioned before in the **Section I-2**, IR spectra can be used to determine the type of ruthenium nitrosyl complex, due to the characteristic stretching band for each type of N-O form. But also, it can detect the energy transfer from the metal to the nitrosyl due to retro donation effect in Ru^{II}->π*(NO). As this electronic transfer is going to an antibonding orbital, the bond order between oxygen and nitrogen is reduced, meaning that frequencies of ν(NO) decreased as well.

The values of the IR bands ν(NO) are 1942 cm^{-1} for **RuNO-1,** 1938 cm^{-1} for **RuNO-2**, 1940 cm^{-1} for **RuNO-3**, 1937 cm^{-1} for **RuNO-4** and 1934 cm^{-1} for **RuNO-5** (**Table II-5**).This result show that **Ligand 5** acts as the best electron donating group as it was expected.

Table II-5. Experimental values of stretching frequency ν(NO).

Compound	ν(NO) (cm^{-1})
RuNO-1	1942
RuNO-2	1938
RuNO-3	1940
RuNO-4	1937
RuNO-5	1934

II-17. Designed Dipolar and Quadrupolar Molecules for TPA.

To achieve an increased TPA response, complexes **RuNO-1** and **RuNO-2** were synthesized with a dipolar architecture (**Acceptor**-**Donor**) (**Figure II-24**), while complexes **RuNO-3** to **RuNO-5** were designed with a quadrupolar architecture (**Acceptor**-**Donor**-**Acceptor**) (**Fig. II-25.1 and II-25.2**), effectively increasing the π-system of the molecules. As it was mentioned in **Section I-12**, it is noteworthy that the quadrupolar architectures generally demonstrate a superior TPA response compared to dipolar architectures.

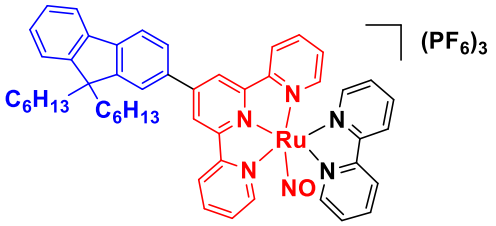

RuNO-1

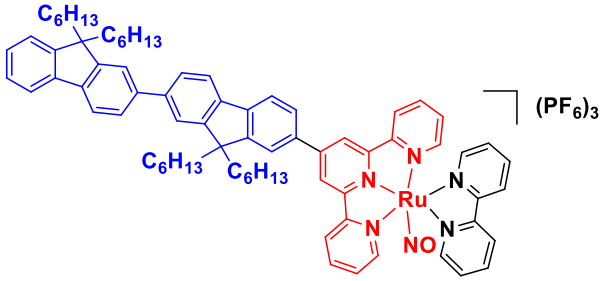

RuNO-2

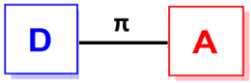

Figure II-24. Structure of the dipolar (**Donor**-**Acceptor**, **D**-**A**) complexes for **RuNO-1** and **RuNO-2**.

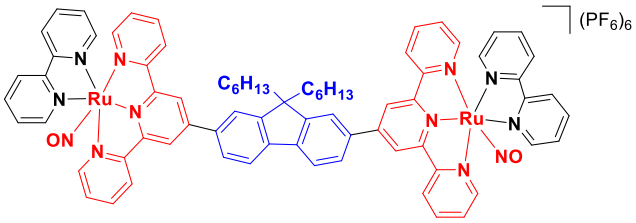

RuNO-3

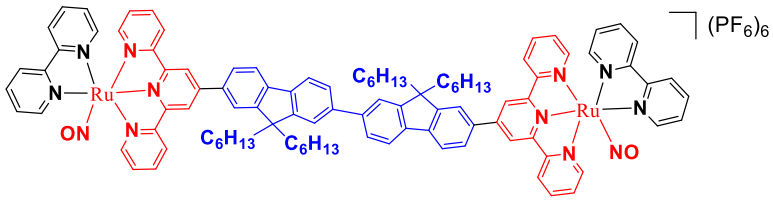

RuNO-4

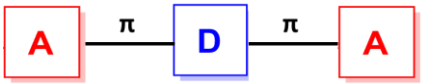

Scheme II-25. Structure of quadrupolar complexes (**Acceptor**-**Donor**-**Acceptor**, **A**-**D**-**A**) for **RuNO-3** and **RuNO-4**.

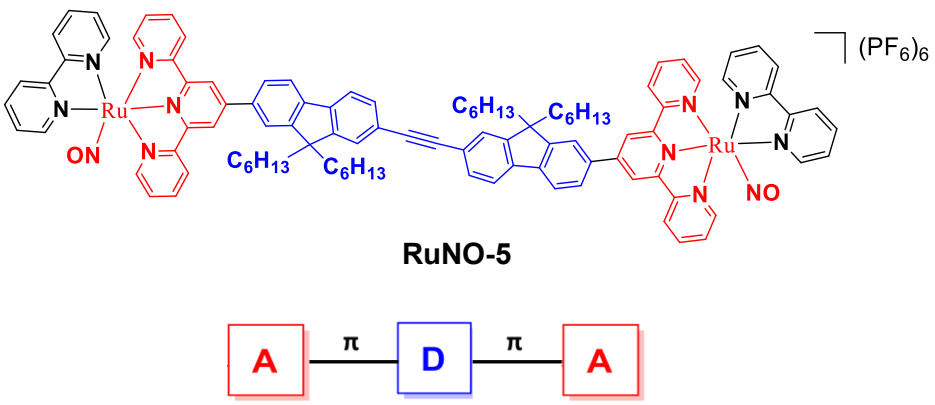

RuNO-5

Scheme II-25.5. Structure of quadrupolar complexes (**Acceptor**-**Donor**-**Acceptor**, **A**-**D**-**A**) for **RuNO-5**.

II-18. Attempt to Use TPEF to Measure TPA response

To evaluate the TPA properties of the different molecules, the Z-Scan technique was employed. This technique was chosen due to the weak photoluminescence exhibited by the RuNO complexes upon excitation of either one-photon (in the Uv-Vis range) or two photons in the infrared range (around 800 nm), rendering other techniques such as two-photon excited fluorescence impractical (**Fig. II-26**).

The PL signal detected for these complexes was found to be very weak, with peaks of maximum emission in the infrared wavelengths. These complexes are very sensitive to illumination, even under room illumination conditions they are transformed into products. To see this effect, **Figure II-26** shows as example the emission measured from a fresh sample of **RuNO-3**. In this case special care was taken in the fresh sample to avoid exposition to light. In these conditions, the peak of emission is at *ca* 785 nm. To provide a comparative reference, this figure also includes the emission spectrum of **L2** and the product of **RuNO-2,** with maxima of emission at 415 and 590 nm, respectively. Notably, when the fresh samples of any of the complexes are exposed to light, their corresponding emission spectra are blue shifted. **Figure II-26** presents the emission spectra for the of **RuNO-2,3,4,5** after they were exposed few minutes to light in normal room conditions. As it can be seen, the PL spectrum of these compounds exposed to light displayed clear differences from that of a sample of **RuNO** complex not exposed to light. These results suggest that the response of **RuNO-2,3,4,5** to light can be monitored directly from their photoluminescence. Although the

small quantum yield of PL for these samples makes difficult to performs this kind of emission spectroscopy, it is clear that such emission deserves further investigations in order to get more insight about their photophysics.

Even though some PL signal can be detected from **RuNO** complexes upon one-photon excitation, the small quantum yield of PL precludes obtaining significant TPEF signals. Further, the PL emission of the **RuNO** complexes is within the Two-Photon excitation wavelength range of used in this work, precluding then TPEF as technique to measured TPA activity. For this reason, the nonlinear absorption at infrared wavelengths was determined with Z-scan technique.

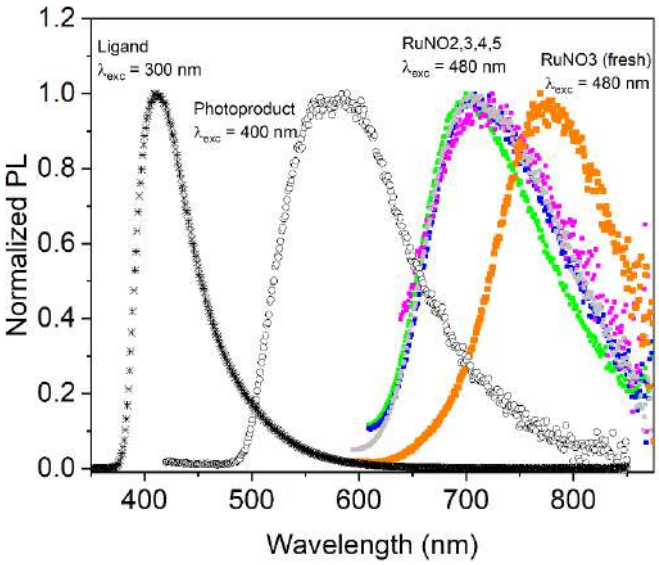

Figure II-26. Results of photoluminescence (PL) measurements conducted on the RuNO complexes (**RuNO-2**, **RuNO-3**, **RuNO-4**, and **RuNO-5**).

II-19. Z-scan Experiments

It is known that several factors can influence the TPA process, including solvent effects, solubility, variations found in the synthesized molecule batches, and sample concentration. To address the good performance of the Z-scan apparatus, a reference substance was employed. For this purpose, the laser dye rhodamine B (RhB) in methanol at a concentration of $2x10^{-2}$ M was used. RhB has no electronic transitions

above 600 nm, ensuring that the infrared excitation light does not induce one-photon absorption transitions. Additionally, the TPA cross-section of RhB has been extensively documented in the literature,[158] making it suitable for verifying the sensitivity and accuracy obtained in the determination of Two-Photon absorption cross sections with the experimental setup. **Figure II-27** presents a typical Z-scan trace obtained from the sample of RhB; this trace was obtained with pulses of 60 nJ and 80 fs of temporal pulse-width. As it can be seen, a good signal to noise ratio is obtained in this trace. Considering the characteristic parameters of the laser beam and the corresponding peak intensity of excitation, the resulting nonlinearity from this trace resulted 120 GM. This value is in good agreements with literature. This means that under these experimental conditions, we can stablish that the level of sensitivity of our Z-scan apparatus is such that it is able to measure TPA cross sections similar or larger than that of RhB.

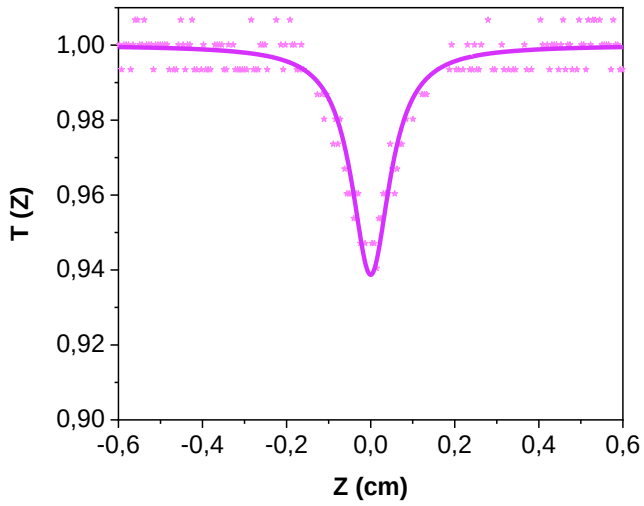

Figure II-27. Representative example for a Z-scan measurements of a reference RhB at open aperture, at 800 nm irradiation with an energy of laser beam equal to 60 nJ.

To ensure accuracy in the measurements on Z-scan and avoid saturation of the photodetector used to register the nonlinear transmission of the sample under tests of the photodetector, a series of optical density filters were strategically placed in front of the photodetector. These filters not only avoided saturation of the detector, but also allowed to operate the system linearly within an acceptable dynamic range. Similarly, to control de intensity of excitation of samples, filters of neutral density were employed

at the input of the Z-scan apparatus. Additionally, due to limited sample quantities and the required high concentration (Z-Scan technique typically requires samples with concentration in the range $1x10^{-3}$ - $1x10^{-2}$ M depending on the nonlinearities), the thickness of the quartz cell was increased from 1 mm to 2 mm. This adjustment allowed for working concentrations of approximately $5x10^{-3}$ M in acetonitrile while ensuring reliable Z-Scan measurements.

The TPA process exhibits a quadratic intensity dependence, indicating that excitation within a focused beam is not constant and becomes stronger at the beam's waist (ω_0). The TPA process can only be observed when the sample is positioned within the Rayleigh range (a distance ranging from ω_0 to $\sqrt{2}\omega_0$). To determine this range where TPA occurs, a widely recognized standard material, carbon disulfide (CS_2),[159] was used. CS_2 was irradiated with the same energy and wavelength as the samples. By analyzing the results obtained from CS_2, it was possible to locate the beam's waist, which is situated between the peak and the valley of the beam profile (**Fig. II-28**). This approach not only facilitated the determination of the beam waist but also ensured the stability of the laser source throughout the measurements.

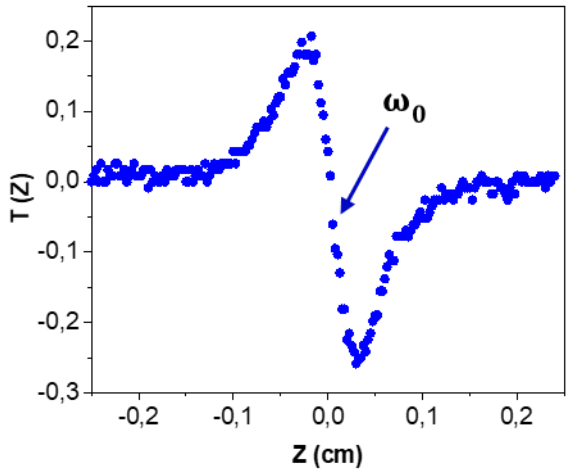

Figure II-28. Representative example of Z-scan measurements performed on a reference material, carbon disulfide (CS_2), with a close aperture configuration. λ_{irr}= 800 nm irradiation and a laser beam energy of 36 nJ.

For preciseness in the measurements, multiple repetitions were performed. At least three separate experiments were conducted for each sample along the scan section. The distance traversed by the sample ranged from 6-8 cm, depending on the

specific experiment, with each measurement taking approximately 5-6 minutes. A total of 800-1000 data points were collected for analysis, with an average of three measurements per point.

II-20. Cross-section (σ_{TPA}) Values for the RuNO Series

Table II-6 compiles the σ_{TPA} values obtained from the Z-scan experiments. Initially. The TPA measurements were recorded at various incident wavelengths within the therapeutic window, included an incident wavelength of 800 nm, a widely adopted choice in biophotonics applications owing to the availability of Ti-sapphire laser technology operating at this wavelength.

Table II-6. Two-Photon absorption (TPA) cross-sections (σ_{TPA} in GM) for different ruthenium nitrosyl complexes.

	700 nm	800 nm	850 nm	900 nm	950 nm	1000 nm
RuNO-1	279 ± 39	115 ± 20	233 ± 50	62 ± 14	18 ± 4	34 ± 0.2
RuNO-2	662 ± 140	152 ± 13	421 ± 14	68 ± 19	34 ± 12	109 ± 18
RuNO-3	1182 ± 180	401 ± 40	452 ± 63	82 ± 24	37 ± 11	80 ± 14
RuNO-4	838 ± 250	185 ± 19	435 ± 70	87 ± 19	49 ± 18	200 ± 43
RuNO-5	1523 ± 98	309 ± 35	510 ± 63	103 ± 19	63 ± 25	229 ± 46

The symmetry of the molecules plays an important role in their optical properties. The complexes **RuNO-1** and **RuNO-2** exhibit only the identity operator (E), indicating that they do not possess any symmetry elements other than the trivial symmetry. On the other hand, the complexes **RuNO-3** and **RuNO-4** have the C_2 symmetry, which means they possess a twofold rotational symmetry axis. This symmetry allows for certain optical transitions in the OPA process but limits the intensity of these transitions in the TPA process.

RuNO-5 is the only molecule among the complexes that exhibits centrosymmetry, represented by the C_i symmetry. This special case has unique characteristics, as any forbidden transition in OPA becomes active in TPA, while any allowed transition in OPA becomes silent in TPA. Although **RuNO-4** possesses the C_2 symmetry, it can be regarded as pseudo-centrosymmetric, which implies that the

intense OPA transitions are allowed but necessarily weak in the TPA process. The same analysis can be transposed to **RuNO-3**, however to a far less extent, as this complex moves away from the strict centrosymmetry.

It should be noted that the TPA spectra of the RuNO complexes cannot be accurately predicted solely based on their corresponding OPA spectra. The two-photon electronic spectra can exhibit significant differences from the one-photon spectra. To overcome these challenges, a range of incident wavelengths, from λ = 700 nm to 1000 nm, was selected for the final TPA investigations. This selection allows for a comprehensive exploration of the therapeutic window, covering a wide wavelength domain. The TPA spectra for the five **RuNO** complexes are plotted in **Figure II-29.**

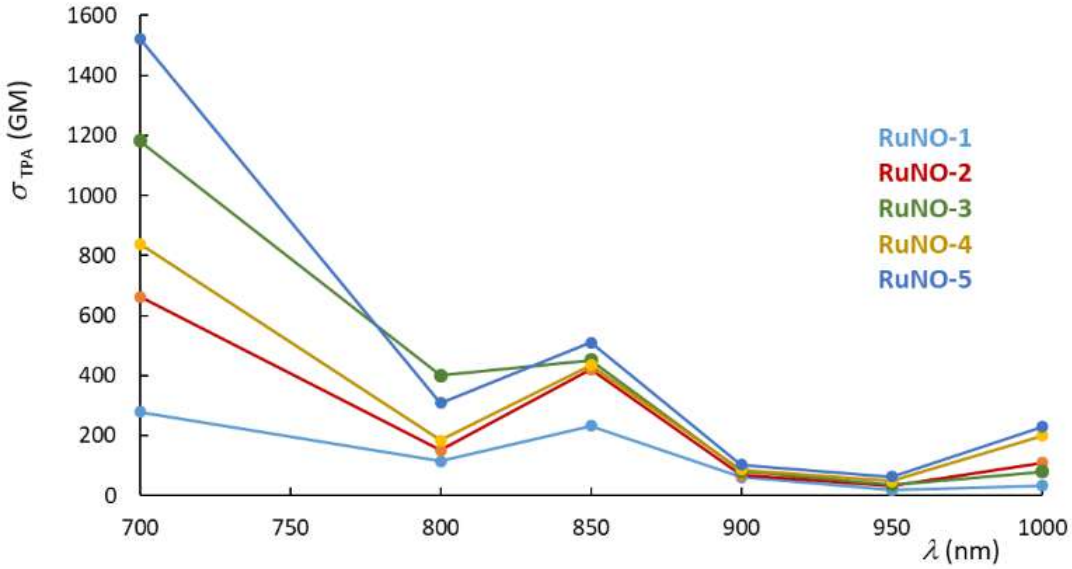

Figure II-29. TPA spectra for the five **RuNO** complexes recorded in acetonitrile at various incident wavelengths.

The Z-scan traces obtained for each irradiation wavelength show symmetrical behavior around the Z=0 position, indicating good optical alignment. The decrease in transmission with increasing excitation intensity follows a linear trend, suggesting that the measured nonlinearity is attributed only to TPA (**Fig. II-30**).

Different remarks will be discussed for the different measurements made at each irradiation wavelengths for the Z-scan experiments.

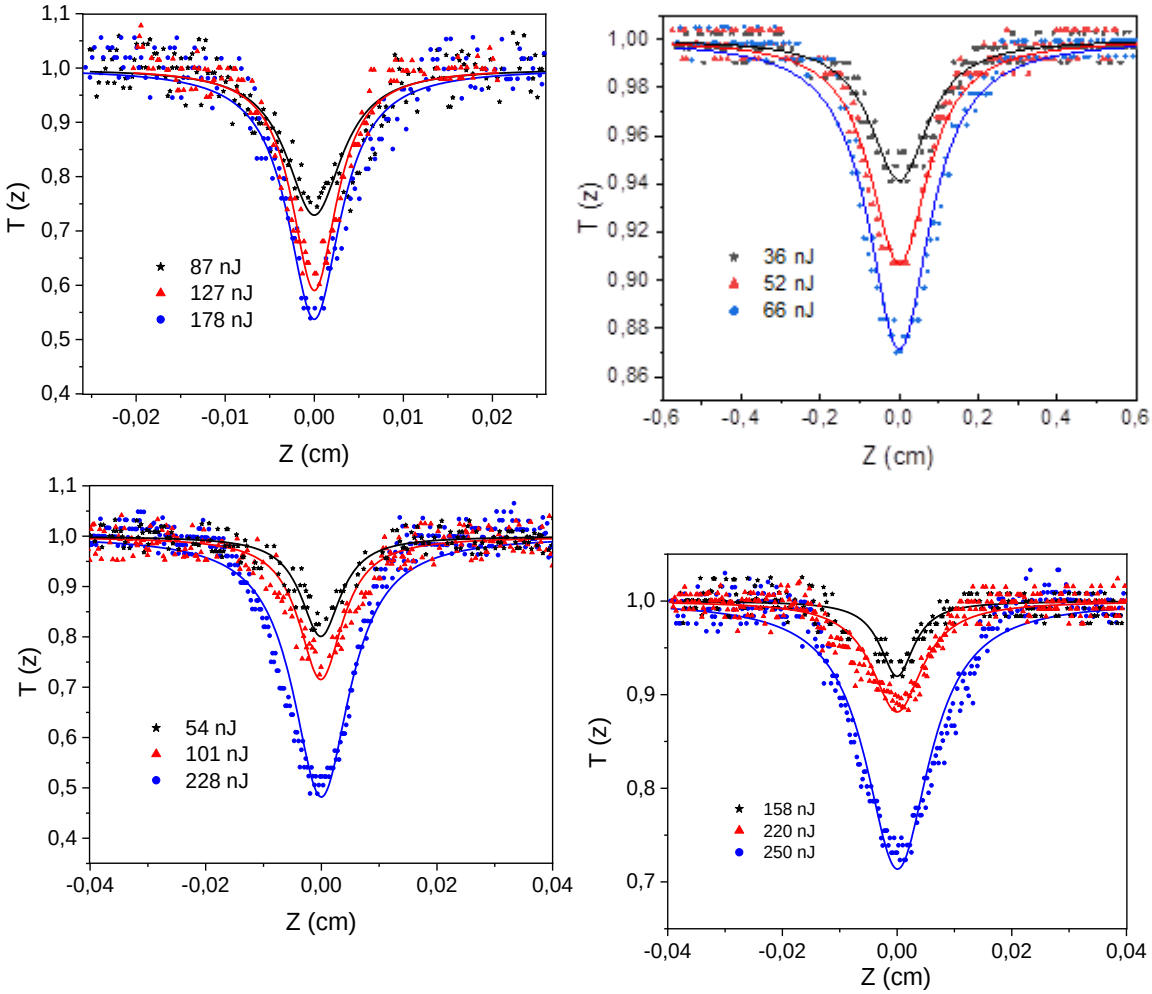

Figure II-30. Normalized transmission T(Z) in Z-scan experiment at various laser pulse energies for **RuNO-2** at λ = 700 nm. C = 1 x 10^{-3} mol.L^{-1} (left, top). **RuNO-5** at λ = 800 nm. C = 5 x 10^{-3} mol.L^{-1} (right, top). **RuNO-3** at λ = 900 nm. C = 5 x 10^{-3} mol.L^{-1} (left, bottom) and **RuNO-1** at λ = 950 nm. C = 4 x 10^{-3} mol.L^{-1} (right, bottom) all in CH_3CN.

II-21. Measurements at λ_{irr} = 1000 nm

The analysis of the TPA spectra for the **RuNO** complexes within the therapeutic window reveals interesting findings. At λ = 1000 nm, it can be observed an enhancement in the TPA spectra. This enhancement can be attributed to the coincidence of the energy of a pair of infrared photons ($2\hbar\omega$) with the low-lying band (a) observed in the OPA spectra (**Fig. II-22, Section II-15**). Notably, the complexes with two fluorene moieties (**RuNO-**

2, **RuNO-4**, and **RuNO-5**) where the maximum ε value is located around 500 nm in the OPA spectra show higher σ_{TPA} values at 1000 nm compared to the complexes with a single fluorene moiety (**RuNO-1** and **RuNO-3**), where the maximum ε value is located around 450 nm in the OPA spectra. This observation suggests that the introduction of an extra fluorenyl moiety in the system in the molecular structure results in increased σ_{TPA}. That could explain why a compound with a dipolar structure (**RuNO-1** and **RuNO-2**) shows a higher value than a quadrupolar one (**RuNO-3**) at this specific wavelength.

II-22. Measurements at λ_{irr} = 950 and 900 nm

In the range of 950-900 nm, a clear tendency is observed, the quadrupolar structure containing the larger π backbone system (**RuNO-5**) exhibit the highest σ_{TPA} values compared to the dipolar structure (**RuNO-1**) with the shortest π backbone system. This trend is evident in **Figure II-31**, showing the order of σ_{TPA} values as follow **RuNO-1** < **RuNO-2** < **RuNO-3** < **RuNO-4** < **RuNO-5**.

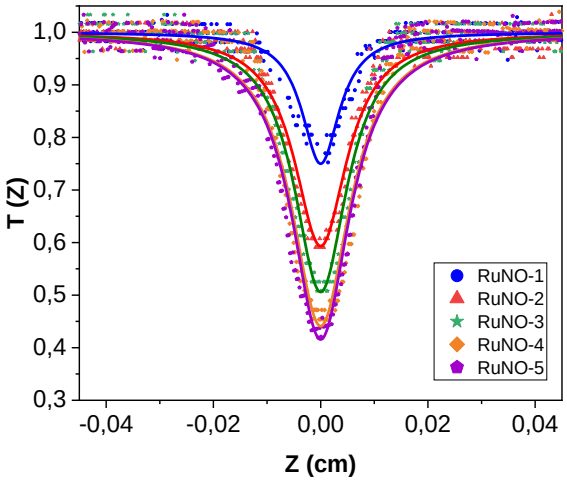

Figure II-31. Normalized transmission T(Z) in Z-scan experiment at 228 nJ for all the **RuNO** complexes series at C = 2.5 x 10^{-3} mol.L^{-1} at λ = 900 nm.

II-23. Measurements at λ_{irr} = 850 and 800 nm

The TPA spectra exhibit another enhancement at λ = 850 nm, coinciding with the low-lying band (a) observed in the OPA spectra (**Fig. II-22, Section II-15**) within the 400-550 nm range. At 850 nm, the quadrupolar complexes **RuNO-3**, **RuNO-4**, and **RuNO-**

5 exhibit maximum σ_{TPA} values in the range of 435 - 510 GM, which are approximately twice the value measured for the push-pull complex **RuNO-1** (233 GM). As well, complex **RuNO-2** (421 GM) shows higher σ_{TPA} than **RuNO-1**. This indicates that the addition of a second fluorene moiety significantly enhances the nonlinearities in the push-pull complexes. Similarly, the extension of π-conjugation from **RuNO-4** to **RuNO-5** by inserting a triple bond further enhances the nonlinearities.

It should be noted that the behavior of the bimetallic complexes (**RuNO-3**, **RuNO-4**, and **RuNO-5**) differs from the trend observed in the dipolar complexes. In some cases, **RuNO-3** exhibits higher σ_{TPA} values than **RuNO-4** in the range from 850 to 700 nm.

II-24. Measurements at λ_{irr} = 700 nm and General Results

The highest enhancement in the σ_{TPA} spectra is observed at 700 nm (**Fig. II-32**). The presence of one-photon resonance effects near the onset of linear absorption suggests the possibility of significant cross-section enhancement in the TPA process due to two-step process, where a real intermediate excited state could be involved. Nevertheless, the high σ_{TPA} values recorded at 700 nm (e.g., 1523 GM for **RuNO-5**) hold promise and are compatible with the therapeutic window.

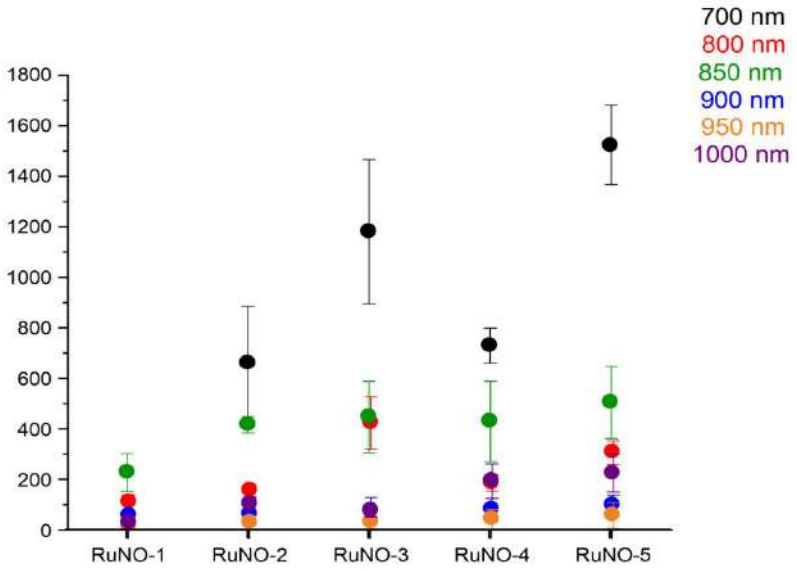

Figure II-32. TPA spectra for the five **RuNO** complexes recorded in acetonitrile at various incident wavelengths showing the standard deviation.

The investigation of pseudo-symmetric ruthenium complexes in our study has shed light on TPA process and its connection to transition selection rules. The monotonic increase in σ_{TPA} values shown in **Figure II-33** for wavelengths below 800 nm can be attributed to a combination of one-photon resonance and a stepwise process. Notably, the most intriguing quadrupolar species (**RuNO-3**, **RuNO-4**, and **RuNO-5**) can be described by a simplified three-state (g, e, e') model, where the TPA process occurs from the ground state (g) to the second excited state (e'). As discussed in the **Section I-12** the presence of a strong g → e OPA transition, with a large transition moment (μ_{ge}) and an energy ($\hbar\omega_{ge}$) close to that of the incident laser beam ($^{\hbar\omega_{ge'}}/_{2}$), can lead to significant cross-section enhancement due to a nearly vanishing denominator in the TPA expression (Eq. I-42). Hence, quadrupolar chromophores tend to exhibit higher TPA efficiency compared to their parent dipolar species.

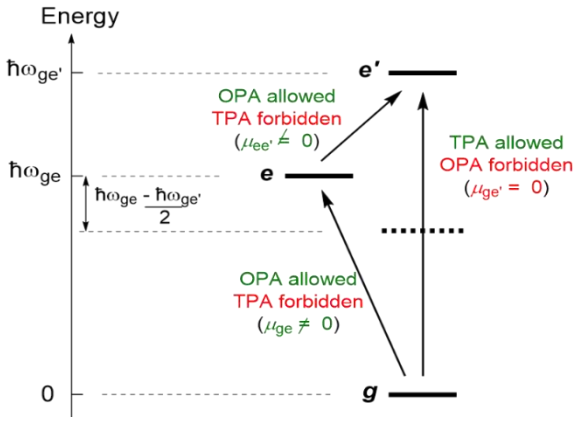

Figure II-33. OPA and TPA allowed and forbidden transitions in centrosymmetric molecules.

The measurement of σ_{TPA} values, such as 1523 GM (**RuNO-5**) at 700 nm (or 309 GM at 800 nm), raises questions about the maximum achievable σ_{TPA} value in RuNO complexes. It is well-known that nonlinear optical phenomena are related to intramolecular charge transfers, highlighting the desirability of increasing the size of the π-delocalized skeleton to enhance the molecular TPA response.[160] However, it is crucial to consider that the challenge in molecular devices lies not only in optimizing the molecular properties but also in incorporating as many chromophores as possible

into the device. This context shifts the focus to the molecular property expressed per mass unit (σ_{TPA}/MW) as a relevant factor of merit.

To date, the highest reported σ_{TPA}/MW value for ruthenium-based TPA chromophores stands at 1.46 GM.mol.g^{-1}, as observed by Humphrey et al. in a dendrimer structure comprising 9 bis(diphosphine)ruthenium units and 25 phenyl rings.[161] Notably, in the case of the **[RuNO-5]$^{6+}$** cation, the σ_{TPA}/MW at 700 nm reaches 0.88 GM.mol.g^{-1}. It is worth mentioning that if we exclude the hexyl chains, which serve solely for solubility and have no direct impact on charge transfer properties, the σ_{TPA}/MW value rises to 1.10 GM.mol.g^{-1}, approximately three-quarters of the record value reported by Humphrey et al.

These findings substantiate the exceptional TPA properties exhibited by the investigated bimetallic species in the realm of ruthenium-based materials. However, it is essential to underscore that the primary objective of our research program is centered around the initiation of NO• release through Two-Photon processes. In this regard, the present compounds demonstrate great promise, offering exciting possibilities for future advancements.

II-25. Measurements at λ_{irr} = 600 nm

Attempts to extend the TPA spectra to a wavelength of 600 nm were unsuccessful due to the saturation of absorption caused by OPA processes in some of the molecules (**Fig. II-34**). This can be observed in the Z-scan traces of compounds **RuNO-2** and **RuNO-4**, where there is a clear competition between the OPA and TPA processes. However, in the wavelength range of 700-1000 nm, this competition is not observed, providing more confidence in the TPA results obtained in that range. It is important to note that only **RuNO-3** (orange) and **RuNO-5** (green) exhibit favorable behavior at this wavelength. Unfortunately, there are some uncertainties about the estimation of these values since at such wavelength the TPA cross section of RhB has not been reported, thus it could not be used to corroborate the calibration of the Z-scan apparatus.

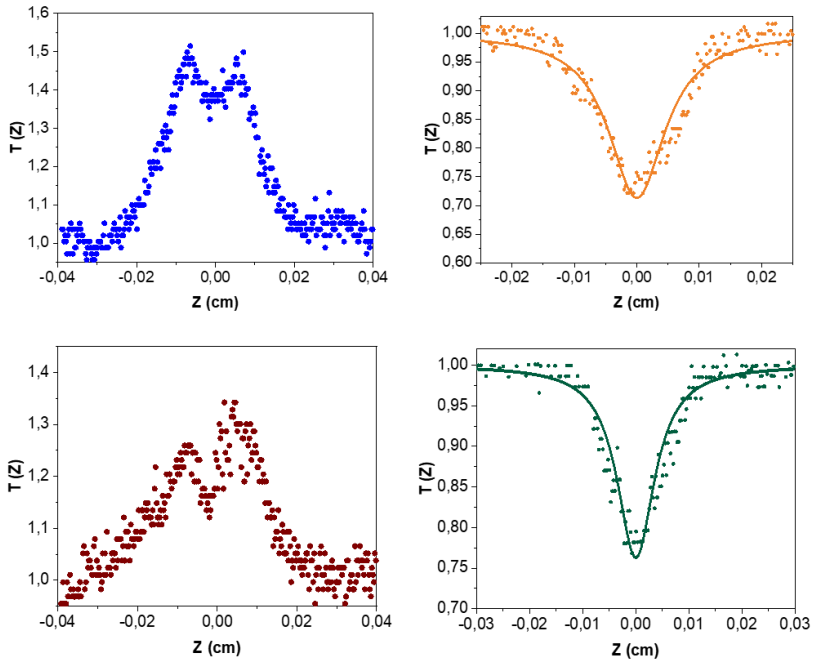

Figure II-34. Normalized transmission T(Z) in Z-scan experiment at 180 nJ for **RuNO-2** at C = 1 x 10^{-3} mol.L^{-1} (left, top). **RuNO-3** C = 5 x 10^{-3} mol.L^{-1} (right, top). **RuNO-4** C = 5 x 10^{-3} mol.L^{-1} (left, bottom) and **RuNO-5** C = 4 x 10^{-3} mol.L^{-1} (right, bottom) all in CH_3CN, λ = 600 nm.

II-26. σ_{TPA} Values for the $RuNO_2$-2 and $RuCH_3CN$-2

$RuNO_2$-2 was subjected to measurements at 800 nm (**Fig. II-32**) to investigate the effect of ligand exchange. The Z-scan results demonstrated a decrease in transmission with increasing excitation intensity, following a linear trend. The calculated σ_{TPA} value for **$RuNO_2$-2** was determined to be 127 ± 40 GM. Additionally, the product of irradiation of **RuNO-2**, denoted as **$RuCH_3CN$-2**, was also examined. However, due to the presence of fluorescence in these compounds, the Two-Photon Excited Fluorescence (TPEF) technique was employed to assess their nonlinear properties.

The fluorescence quantum yield of the product compound was 0.112%. A comparative analysis was conducted between the TPEF signal detected for the product compound at 800 nm, using a 100 fs laser with an 800 MHz repetition rate, and RhB as the standard. The resulting TPA cross-section value for the product compound was determined to be σ = 120.4 GM. The results are shown in the **Table II-8**.

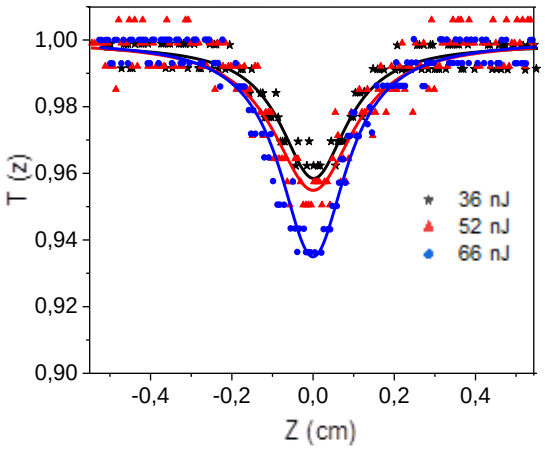

Figure II-35. Normalized transmission T(Z) in Z-scan experiment at different energies for **$RuNO_2$ -2** at C = 1 x 10^{-2} mol.L^{-1}, λ = 800 nm (left).

Considering that acetonitrile and NO_2^- are not strong electron acceptors, the push-pull effect within the system is affected, resulting in a decrease in the σ_{TPA} values compared to compounds with NO^+ as a ligand. This observation was evident after measuring the complexes, with the trend observed as **RuNO-2** > **$RuNO_2$-2** ~ **$RuCH_3CN$-2**.

Table 7. TPA cross-sections (σ_{TPA} in GM) for **RuNO-2**, **$RuNO_2$-2** and **$RuCH_3CN$-2** recorded at 800 nm.

	RuNO-2	**$RuNO_2$-2**	**$RuCH_3CN$-2**
σ_{TPA}	152 ± 13	127 ± 40	120.4

II-27. Conclusions

The search for **RuNO** capable of releasing NO• under illumination has been a central focus of the research team. Initially, focused on monometallic species with σ_{TPA} values around 100 GM, but the exploration of bimetallic species has yielded a significant breakthrough, with σ_{TPA} values exceeding 1500 GM. These substantial TPA responses compare favorably with the most efficient TPA materials reported to date. They are well suited for applications in the therapeutic window of biological tissues and represent a possibility for the use of these complexes as NO• donors in biological media.

This work provides compelling evidence for the efficacy of terpyridine-based ligands in developing bimetallic **RuNO** complexes with improved TPA efficiency and remarkable NO• release capabilities. These results have significant implications for the advancement of photodynamic therapy.

Future research could explore the optimization of these complexes for specific therapeutic applications as well as the development of novel bimetallic complexes that could further enhance TPA efficiency. A potential challenge remains the practical implementation of these complexes in a biological context. Nevertheless, the results obtained in this study represent a significant advance in the development of effective tools for photodynamic therapy and other biomedical applications.

CHAPTER III

Mechanism based on one- or two-step photokinetic model involved in nitric oxide photorelease process

III-1. NO• release in RuNO series

For this chapter it is important to remind that ruthenium-nitrosyl complexes release NO• release during photolysis following the general equation:

$$[Ru^{II}(L)\text{-}NO]^{x+} + Solvent \xrightarrow{h\nu} [Ru^{III}(L)\text{-}Solvent]^{z+} + NO\bullet \qquad (III\text{-}0)$$

In these cases, we have always observed the release of NO as a neutral NO• thus leading to a subsequent $Ru^{II} \rightarrow Ru^{III}$ conversion during the release process. Also, the UV-visible spectra of the five RuNO complexes recorded in acetonitrile are shown again in the **Figure III-0**. The spectra reveal a low-lying band (a) in a wavelength range λ=400–550 nm, a multicomponent band (b) in the λ =250– 400 nm range, and a very intense band (c) around 200 nm.

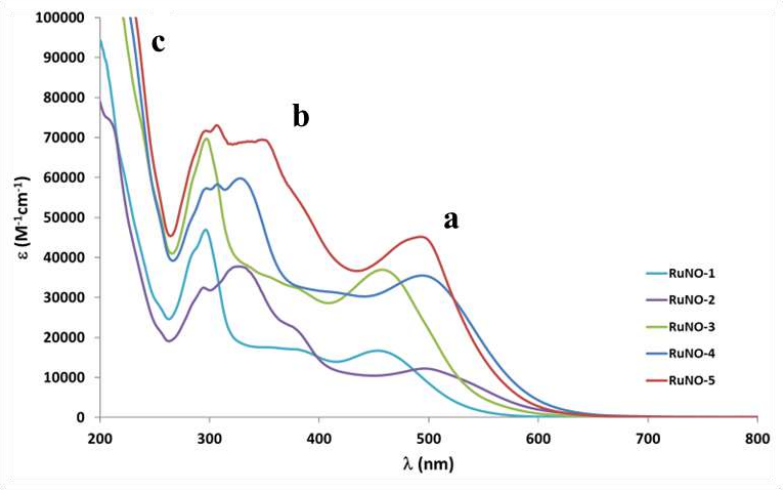

Figure III-0. UV-visible absorption spectra for **RuNO-1** to **RuNO-5**, in acetonitrile.

Knowing that the band (a) involve arise from single Ru→NO based transitions, the initial experiment was conducted with the objective of confirming the photodissociation of the Ru-NO upon irradiation at 490 nm. This wavelength was chosen as the band of interest is around 400–550 nm as it is related to the dominant contribution of the single HOMO-LUMO excitation involving fluorene – Ru(NO) charge transfer. The experiment was carried out for the five complexes (**RuNO-1**, **RuNO-2**, **RuNO-3**, **RuNO-4**, and **RuNO-5**) that were previously detailed in **Chapter II.** The

proposed photodissociation reaction can be represented as follows in the reaction (**III-1**) :

$$[Ru(NO)_x] + xCH_3CN \xrightarrow{h\nu} [Ru(CH_3CN)_x] + xNO\bullet \qquad \text{(III-1)}$$

In this equation, 'x' stands for the number of -NO groups bound to the ruthenium center, 'x' equals 1 for the monometallic species (**RuNO-1** and **RuNO-2**), and 'x' equals 2 for the bimetallic species (**RuNO-3**, **RuNO-4**, and **RuNO-5**). It is important to note that all experiments were conducted in CH_3CN, which leads to the formation of a complex with acetonitrile coordinated to the ruthenium center after photodissociation.

III-2. Irradiation of Monometallic RuNO Complexes Under 490 nm Wavelength

Figure III-1 illustrates the absorption spectra recorded using UV-visible spectroscopy for the complexes, **RuNO-1**, and **RuNO-2**. The spectrum recorded before the irradiation is indicated in blue, while the red spectrum shows the fully converted product after irradiation. The key absorption band of interest lies within the 400–550 nm range. This absorption band is significant due to its association with the predominant HOMO-LUMO excitation event, which primarily involves charge transfer from the fluorene moiety to the Ru(NO) unit.[162] In each experiment the time was different due to the change of concentration on each one, this means that we cannot directly compared the speed of the reaction just considering this factor.

For complex **RuNO-1**, we observe a decrease in the absorption bands at 390 nm and 453 nm, while a new band emerges at 470 nm. This suggests a blue shift. Three isosbestic points appear at 376 nm, 420 nm, and 498 nm, indicating a straightforward conversion[163] from the $Ru^{II}(NO^+)$ complexes to the corresponding photolyzed species without any observable back-reaction upon discontinuation of irradiation.

Upon irradiating complex **RuNO-2**, it can be noting the appearance of absorption bands at 310 nm, 376 nm, and 474 nm. Contrary to **RuNO-1**, **RuNO-2**

exhibits a red shift. An isosbestic point is clearly visible at 487 nm, close to the irradiation wavelength.

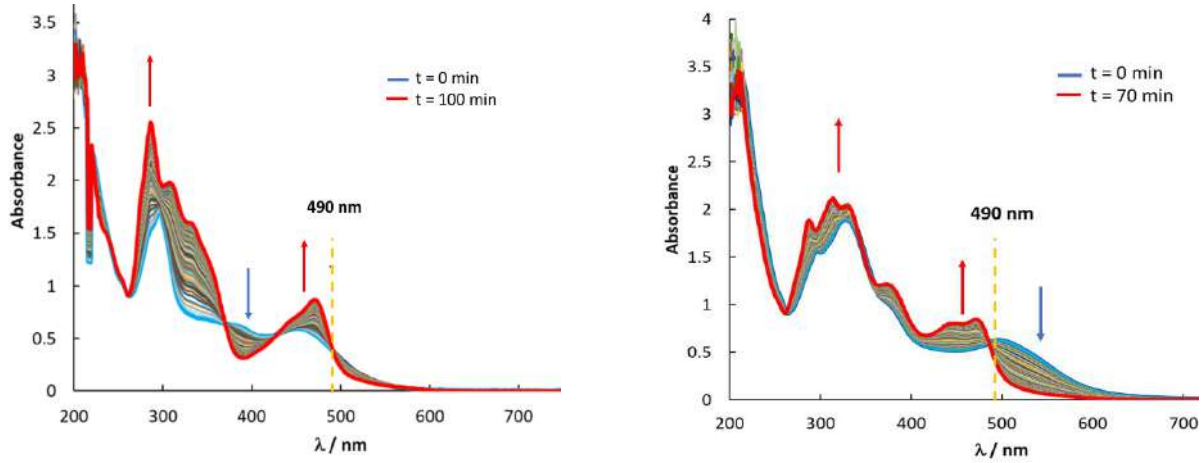

Figure III-1. Evolution in the absorption spectra of **RuNO-1** (left) and **RuNO-2** (right) in acetonitrile under irradiation at λ=490 nm (see yellow line). The red arrows indicate the increase of the red graph and blue arrows indicates the decreasing of the blue graph. Blue line: before irradiation; red line: after completeness of the photo-chemical process.

III-3. Irradiation of Bimetallic RuNO Complexes Under 490 nm Wavelength

We extended these experiments to bimetallic complexes, starting with **RuNO-3**. **Figure III-2** shows the reaction progress, where we observe a blue shift similar to **RuNO-1**. However, a closer inspection of the absorption spectra (**Figure III-3**), (i), (ii) and (iii) reveals the loss of isosbestic points at 266 nm, 384 nm, and 496 nm, implying that a simple $A \rightarrow C$ model might not be suitable for these bimetallic complexes. Instead, they might follow a two-step reaction as indicated by reactions (**III-2**) and (**III-3**), in which "**A**" denotes the starting **RuNO** complexes, "**B**" the intermediate product which exchange only one NO^+ ligand with acetonitrile, and finally the final product "**C**" with two acetonitrile as ligands.

$$\underset{\mathbf{A}}{[Ru(NO)Ru(NO)]} + CH_3CN \xrightarrow{h\nu} \underset{\mathbf{B}}{[Ru(NO)Ru(CH_3CN)]} + NO\bullet \qquad \text{(III-2)}$$

$$\underset{\mathbf{B}}{[Ru(NO)Ru(CH_3CN)]} + CH_3CN \xrightarrow{h\nu} \underset{\mathbf{C}}{[Ru(CH_3CN)Ru(CH_3CN)]} + NO\bullet \qquad \text{(III-3)}$$

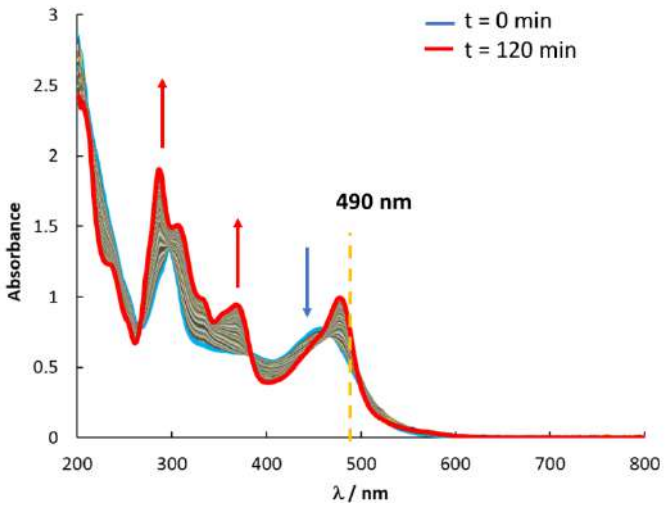

Figure III-2. Evolution in the absorption spectra of **RuNO-3** in acetonitrile under irradiation at λ=490 nm (see yellow line).

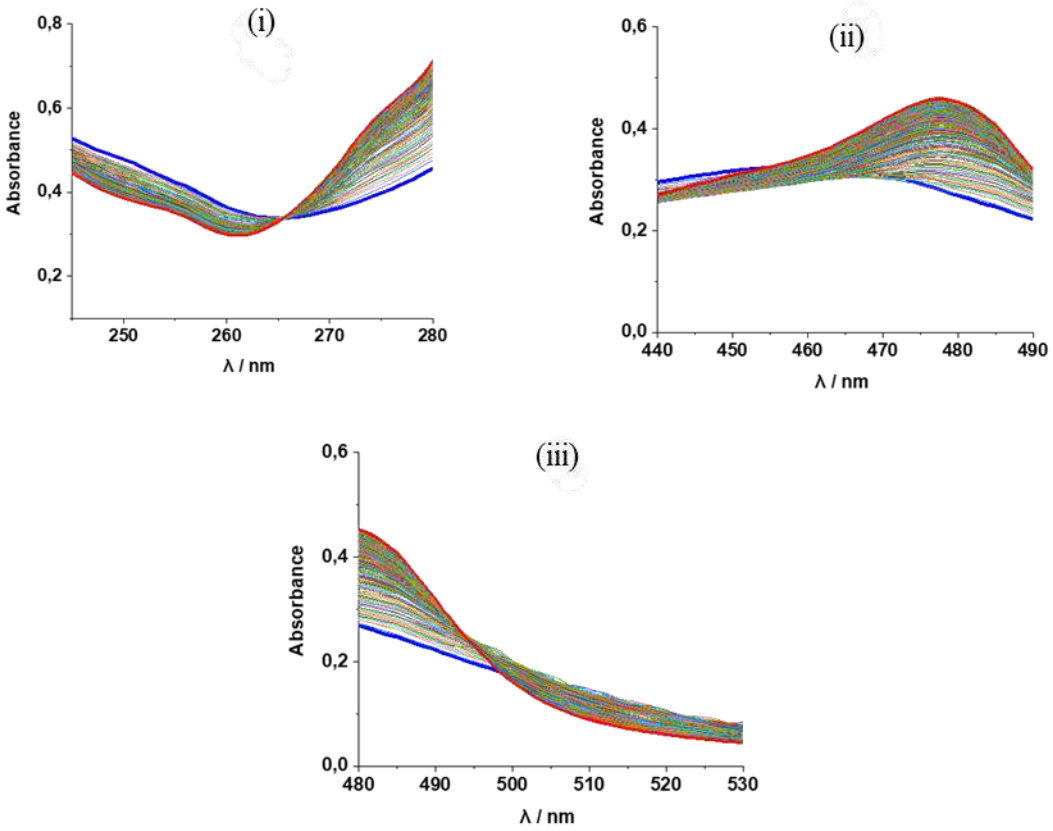

Figure III-3. a), b) and c) zooms for evolution in the absorption spectra of **RuNO-3** highlighting the behavior at the crossover points at 266, 384 and 496 nm respectively.

Interestingly, irradiation of **RuNO-4** and **RuNO-5** does not result in any detectable loss of isosbestic points (**Figure III-4**). However, this does not confirm the one-step photochemical process. It is possible that a pseudo-isosbestic point is involved. To further clarify this aspect, the synthesis and characterization of possible intermediates **B** and final products **C** is essential to verify the completion of each irradiation experiment. Also, it is important to probe the formation of NO• in each experiment.

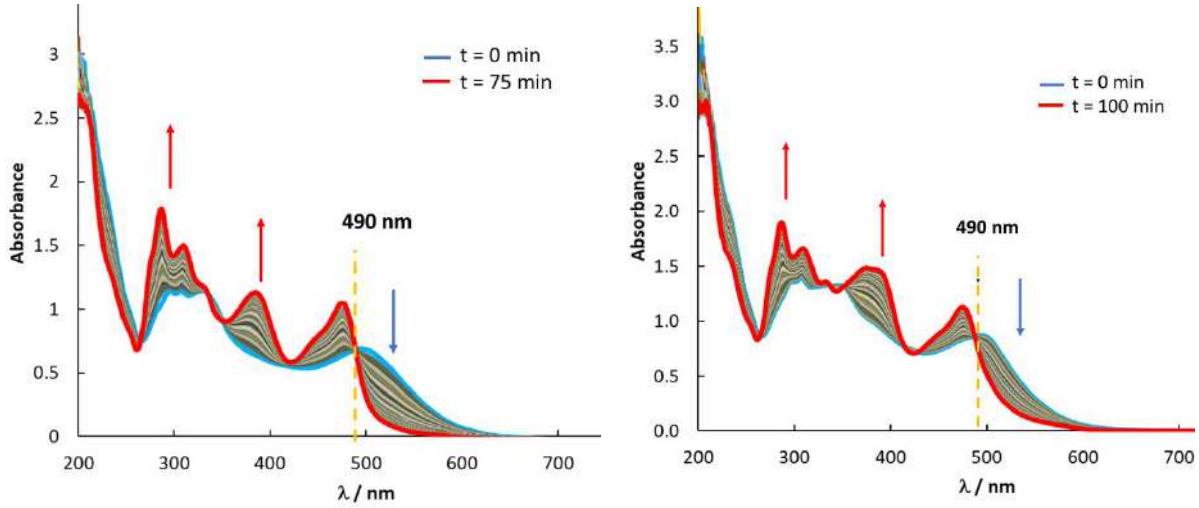

Figure III-4. Evolution in the absorption spectra of **RuNO-4** (left) and **RuNO-5** (right) in acetonitrile under irradiation at λ=490 nm (see yellow line).

III-4. NO• Release Capabilities by Griess Test

The release of NO• is evidenced qualitatively by the use of the Griess test, which involves observing an azo dye with intense absorption at λ= 548 nm,[164] produced by the reaction between NO_2^- ions generated in situ (as the oxidized form of NO•) and sulfanilic acid. This shows the formation of the azo dye in a mixture of equal volumes of the compound solution (10^{-5} M in CH_3CN) and the Griess reagent (0.04 g/mL in water), under irradiation at λ= 490 nm. This experiment was done for all the **RuNO** series, in the **Figure III-5** is shown a representative example for **RuNO-3**.

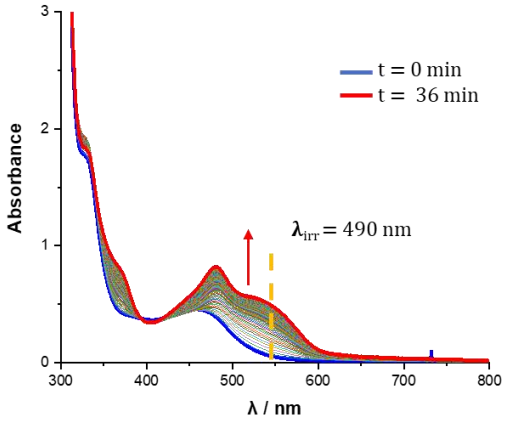

Figure III-5. The evolution of the electronic spectrum of **RuNO-3** shows the formation of the azo dye in a mixture under irradiation at λ= 490 nm.

III-5. NO• Release Capabilities by Electron Paramagnetic Resonance (EPR).

To confirm the formation of NO• during the photolysis, as a direct and quantitively method, EPR experiment was performed for the five **RuNO** complexes in CH_3CN. As NO• is a free radical with a relatively short lifetime in solution, a spin trap using N-methyl-D-glucamine dithiocarbamate (MGD) and reduced iron (Fe^{2+}) was employed to form a stable water-soluble complex, [$(MGD)_2$-Fe^{2+}-NO] (**Scheme III-1**). This complex produces a distinct three-line EPR spectrum, allowing for its detection.

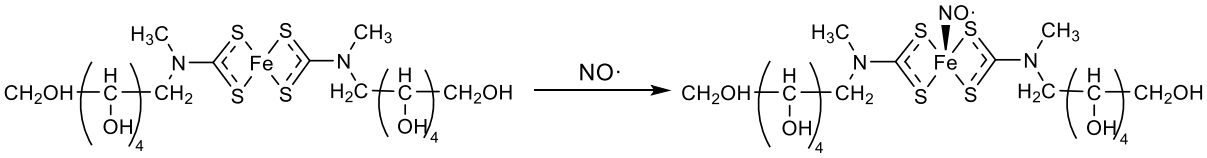

Scheme III-1. Formation reaction of [$(MGD)_2$-Fe^{2+}-NO] by the spin trap and NO• radical.

The mixture solution of **RuNO-3** complex and Fe-MGD were subjected to photolysis for 10 minutes, and the resulting EPR spectrum is shown in **Figure III-6**. The EPR spectrum displays a triplet signal with a hyperfine splitting constant (a_N) value of 1.2×10^{-3} cm^{-1} and a g-factor of 2.040, consistent with the formation of the [$(MGD)_2$-Fe^{2+}-NO] complex.[165] In contrast, when the same solution is kept in the dark, no presence of NO• is detected, confirming the light-triggered nature of NO• generation.

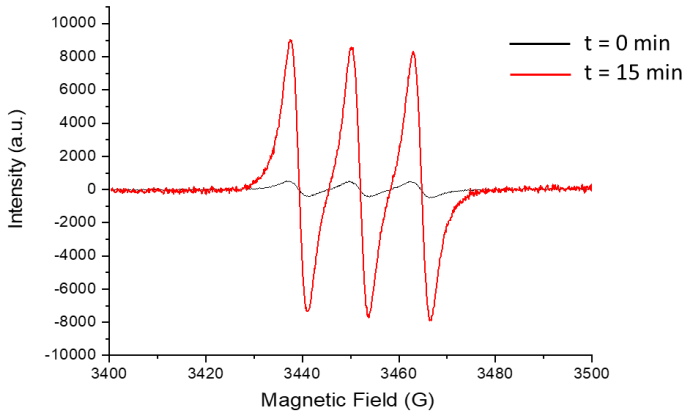

Figure III-6. Triplet EPR signals from NO• trapped by [$Fe(MGD)_2$] for **RuNO-3.**

III-6. Synthesis of Final Complex "C

The synthesis of **C** plays a central role in our research and highlights the ability of the **RuNO** complexes presented in **Chapter II** to release NO•. Following this process, we expect the formation of a ligand exchange complex to form the final products. Since this irradiation process is carried out in acetonitrile, this solvent is the corresponding ligand for the formation of the product.

Our initial approach to synthesizing the product was to use acetonitrile and ascorbic acid.[166] The latter served as a reducing agent to prevent possible oxidation of the central metal atom from Ru^{II} to Ru^{III}. The first experimental approach began with the **RuCl-2** complex, with the goal of synthesizing the **$RuCH_3CN$-2**. This attempt resulted in a complete conversion of the starting material to the desired product, as shown in **Scheme III-2.**

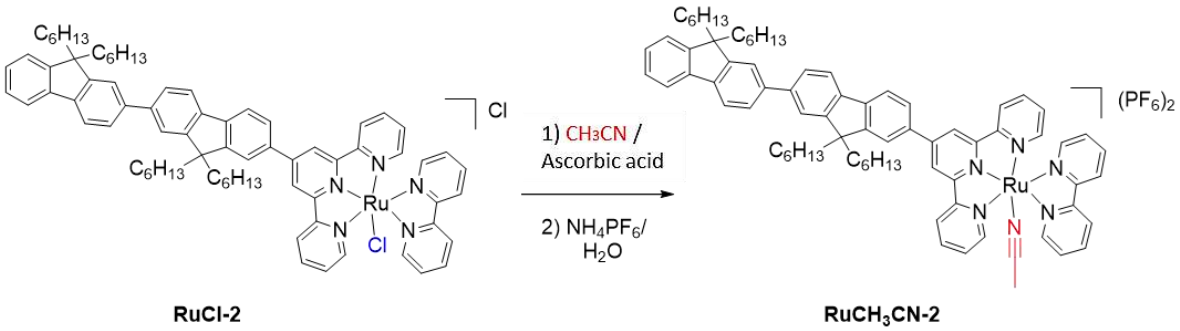

Scheme III-2. Ligand exchange reaction: the synthesis of the product **$RuCH_3CN$-2** from **RuCl-2**.

The method applied for monometallic complexes was used for bimetallic complexes. However, the first attempts with the **RuCl-3** complex were unsuccessful. Despite all efforts, the reaction always produced a mixture of products that was difficult to separate by alumina column chromatography. This highlighted the need for change synthesis protocol.

The **RuCl-1** complex was chosen for testing this new protocol, using a 1:1 mixture of water and acetonitrile as the solvent system[167] under argon atmosphere. This strategic adaptation led to excellent results, culminating in the successful synthesis of the desired product. In this reaction argon avoid any oxidation reaction and avoid the use of any other reagent that can contaminated the final product, as it was the case of the reaction with ascorbic acid.

This improved protocol was then extended to the synthesis of the bimetallic products **C**, leading to satisfactory results. The generalized reaction scheme for the synthesis of the compound using this revised method is shown in **Scheme III-3**.

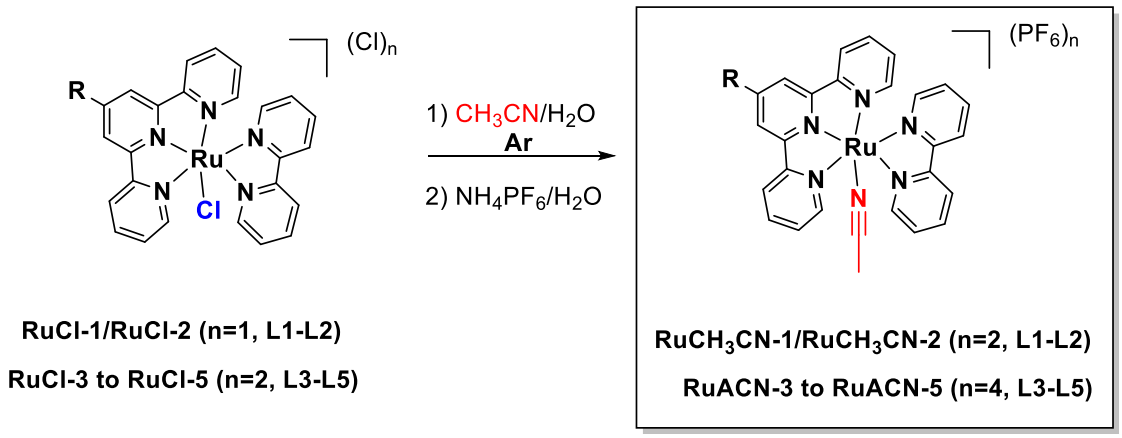

Scheme III-3. Synthesis of products **RuCH$_3$CN-1** to **5** from **RuCl-1** to **5**.

All the final products had been synthesized, which allowed for the determination of additional parameters, such as the epsilon values. During the synthesis of **C**, no evidence of any intermediate **B** was observed. Regardless, attempts were made to synthesize them, as obtaining their parameters was crucial.

III-7.1 Synthesis of Intermediate "B" RuNO-3.

The first attempt to synthesize one of the potential intermediates began with the intermediate **Ru(NO)CH$_3$CN-3** (**Scheme III-4**). There were two main reasons for this choice: First, the **L3** is more readily available, which simplifies the initial conditions;

second, the irradiation experiments at 490 nm showed a significant loss of isosbestic points for this compound in particular, indicating a possible transition to an intermediate state.

The synthesis started with the compound **Ru(NO)CH$_3$CN-3** using half an equivalent of $NaNO_2$ expecting to achieve a ligand exchange on one side of the molecule. However, subsequent ^{1}H-NMR analysis revealed a reaction mixture that contained not only the starting compound but also the symmetric complex **RuNO$_2$-3**. This result suggested that the reaction favored the formation of the symmetric product over the intended asymmetric one. This observation was also confirmed by HRMS, which showed the basic peak of the mentioned complexes (702.1815 for **RuNO$_2$-3** and 437.6696 for **RuCH$_3$CN-3**) but no traces of the desired complex **Ru(NO$_2$)CH$_3$CN-3.** In view of these results, it became clear that a different strategy was required, leading us to consider a convergent synthetic route.

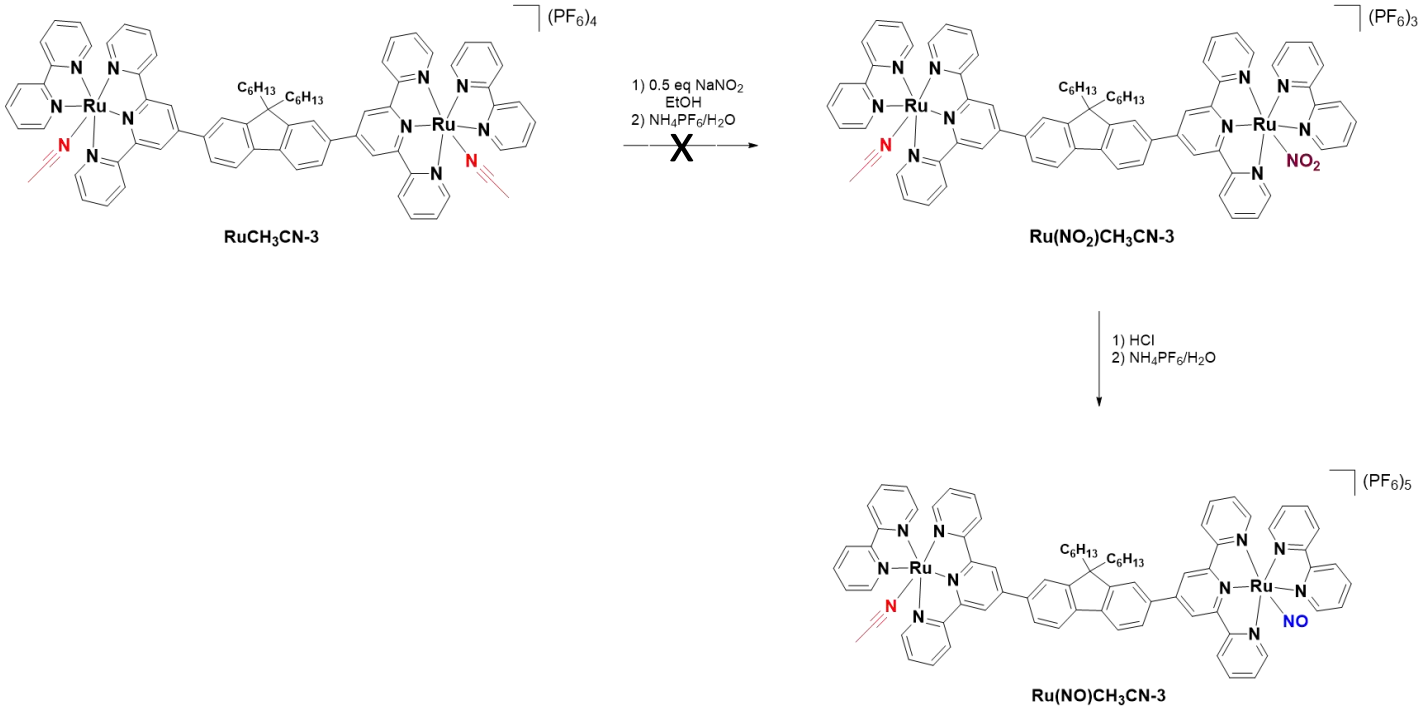

Scheme III-4. Unsuccessful synthesis proposal to obtain intermediate **Ru(NO)CH$_3$CN-3**.

III-7.2 Synthesis of Intermediate "B" RuNO-5.

Continue with the idea of synthesizing an intermediate **B**, a more nuanced approach was considered necessary based on the observations from the previous experiment. As mentioned earlier, we had difficulty obtaining the asymmetric product **Ru(NO)CH_3CN-3**. We decided to use a strategic method that involved the stepwise formation of the final asymmetric complex by synthesizing each component separately.

Sonogashira cross-coupling reaction, known for its ability to form carbon-carbon bonds between terminal alkynes and aryl or vinyl halides,[168] offers two potential separation pathways, as shown in **Scheme III-5**. Each pathway has its own advantages and challenges, so careful consideration was required to select the most viable option.

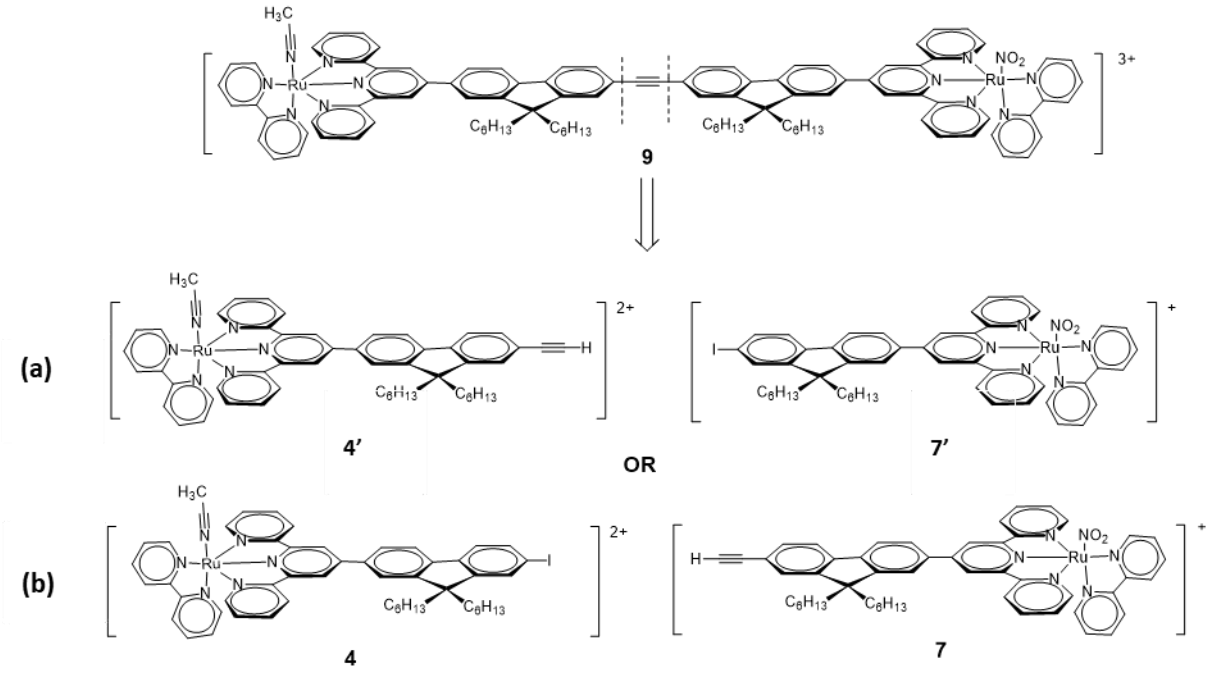

Scheme III-5. Retrosynthetic analysis for the preparation of **Ru(NO_2)CH_3CN-5.**

The pathway (**a**) involved the synthesis of complex **4'** that has the acetonitrile ligand linked to the ruthenium and it has the terminal alkyne on its structure, while the compound **7'** has the NO_2 ligand linked to the ruthenium, and it has the iodide on its structure. The second route (**b**) exchange the place of the ligands, in this case compound **7** has the NO_2 ligand bonded to the ruthenium and the terminal alkyne on its structure.

Given the unique requirements and peculiarities of our target molecule, we opted for the second route (**b**) using the relatively electron deficient halogenated-I-$RuCH_3CN$ complex **4**. This decision was based on a thorough evaluation of both the reactivity and electronic properties of the complexes involved.

Electron deficient complexes, such as halogenated-$RuCH_3CN$ complex **4**, generally exhibit higher reactivity in cross-coupling reactions.[169] By choosing this route, we therefore aimed to increase the yield to obtain the final target complex.

As it was discussed, the synthetic route was to employ a multistep reaction sequence to synthesize our target complex **Ru(NO)CH_3CN-5**, as shown in **Scheme III-6.1** and **III-6.2.** This new strategy was chosen, instead of doing the intermediate **4**, because in this case, a Suzuki-Miyaura reaction is needed. Its conditions required higher temperatures than in Sonogashira reaction and can affect the product stability.

The chosen synthetic route started with the metalation of iodinated terpyridine **1** using $RuCl_3 \cdot xH_2O$, yielding the neutral Ru^{III} complex **2** with high yield. The subsequent step was the replacement of two chloride ligands with 2,2'-bipyridine, which concurrently reduced Ru^{III} to Ru^{II} and led to the formation of complex **3**. To finally obtain the first half, **RuCH$_3$CN** complex **4**, of our desired intermediate **Ru(NO)CH_3CN-5**, we employed an efficient ligand exchange reaction with CH_3CN on complex **3** under an argon atmosphere. This step was followed by a metathesis reaction with aqueous NH_4PF_6, culminating in the formation of complex **4**.

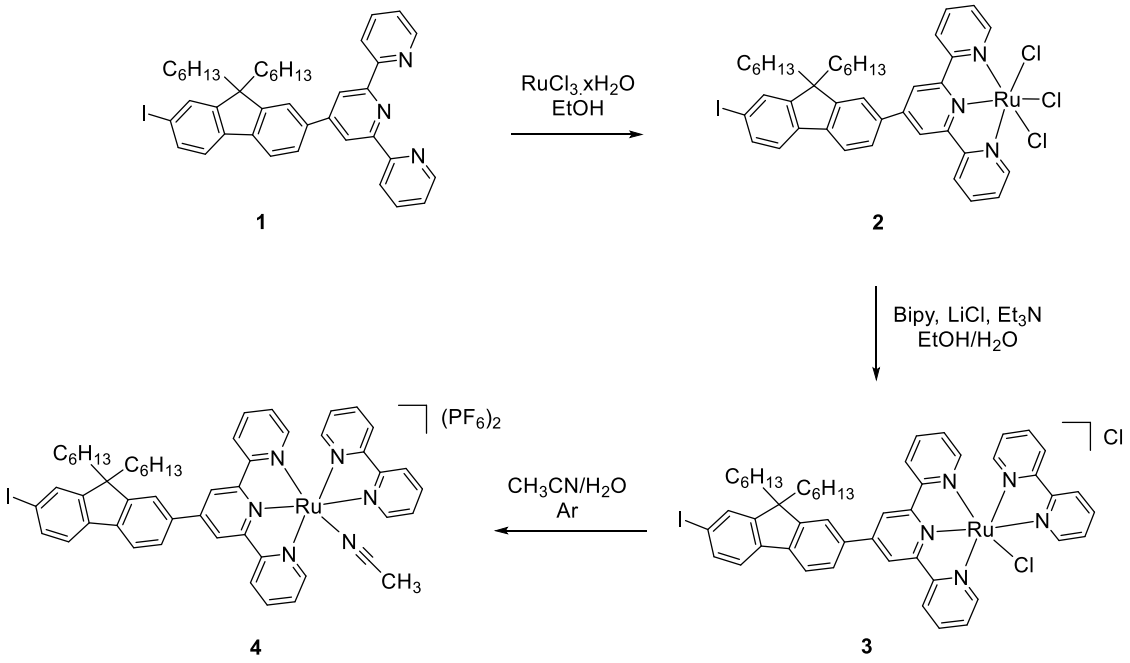

Scheme III-6.1. Synthesis of complex **4**, the first half of the desired intermediate **Ru(NO)CH_3CN-5**.

The subsequent synthetic pathway (**Scheme III-6.2**) was designed to maximize efficiency and circumvent potential risk associated with oxidative side reactions. Compound **5** was synthesized by a Sonogashira cross-coupling reaction starting from the iodinated fluorene terpyridine 1. Significantly, the trimethylsilane moiety was deliberately retained at this stage and served as a protecting group to mitigate undesirable oxidative side reactions that could arise from the interaction between the ruthenium salt and the terminal hydrogen.[170]

The subsequent complexation of compound **5** resembled the earlier reaction from **1** to **2** and led to the formation of complex **6**. This step was followed by a ligand replacement reaction, in which two chloride ligands were replaced by 2,2'-bipyridine. Simultaneously, the trimethylsilane group was eliminated by adding K_2CO_3 into the reaction mixture, leading to the successful synthesis of complex **7** in satisfactory yield.

The next step was an effective ligand exchange reaction with $NaNO_2$ followed by a metathesis reaction with aqueous NH_4PF_6. This led to the preparation of complex **8**. It is noteworthy that complexes **4** and **8** contained the same counterion (PF_6^-), a strategic decision to avoid possible solubility problems in subsequent reactions.

The Sonogashira cross-coupling reaction was used to synthesize the C-C coupled Ru^{II} fluorene-terpyridine complex **9**. This versatile reaction methodology is an exceptional tool for the covalent linkage of two large molecules. In addition, it exhibits excellent compatibility with a wide range of functional groups, eliminating the risk of introducing unwanted reactive metal centers or substituents into our target complex.

After the successful purification of the asymmetric complex **9**, **Ru(NO_2)MeCN-5**, we proceeded to its further transformation by treatment of the complex with concentrated hydrochloric acid, followed by a metathesis reaction with aqueous NH_4PF_6, led to the preparation of the desired **Ru(NO)MeCN-5** complex. This elaborate synthetic sequence reflects our continuous efforts to optimize the synthesis process while maintaining a careful balance between chemical practicality, yield optimization, and strategic planning to achieve our target complex.

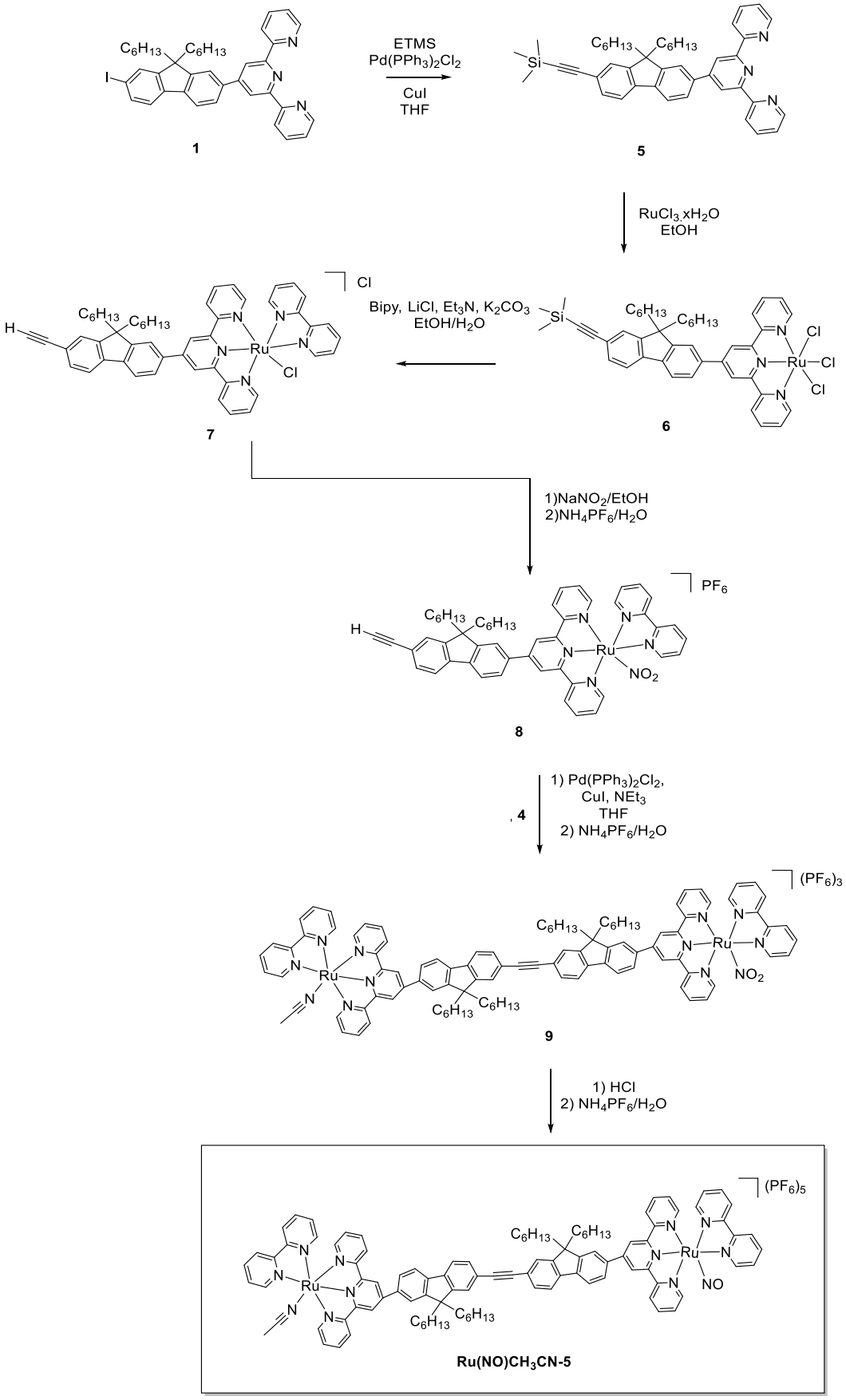

Scheme III-6.2. Second part of synthesis of the desired intermediate **Ru(NO)CH$_3$CN-5** (**B**).

III-8. ^{1}H-NMR Comparisons of Intermediate B and Proton Assignment for RuCH$_3$CN-5 (C).

The ^{1}H-NMR, NOESY, COSY, HMBC and HMQC spectrums of the compound **RuCH$_3$CN-5** were obtained in acetone-d6 at a frequency of 400 MHz, whit this it was possible to properly assigned the protons and carbons in the molecule, ^{1}H-NMR is shown in **Figure III-7**. The most characteristic signals as for the other complexes presented in the *chapter I*, are for *H-15*, which has a chemical displacement of 9.35 ppm and integrates for 2 protons giving a *singlet* as there is no neighbor hydrogens. The other important signal is for the *H-31* to the proximity of the CH_3CN ligand with a chemical displacement of 9.96 ppm giving a *ddd* and integrating for 2 protons.

The fluorene moiety displays a multitude of chemical shifts ranging from 8.42 (*H-11*, *dd*, 2H) to 7.73 ppm (*H-4*, *dd*, 2H). In the case of the bipyridine another signal that can be easily identify is the one for *H-23* that is the signal with the lowest valued of chemical sift in the aromatic region, it integrated for 2 protons and generates a *ddd*,

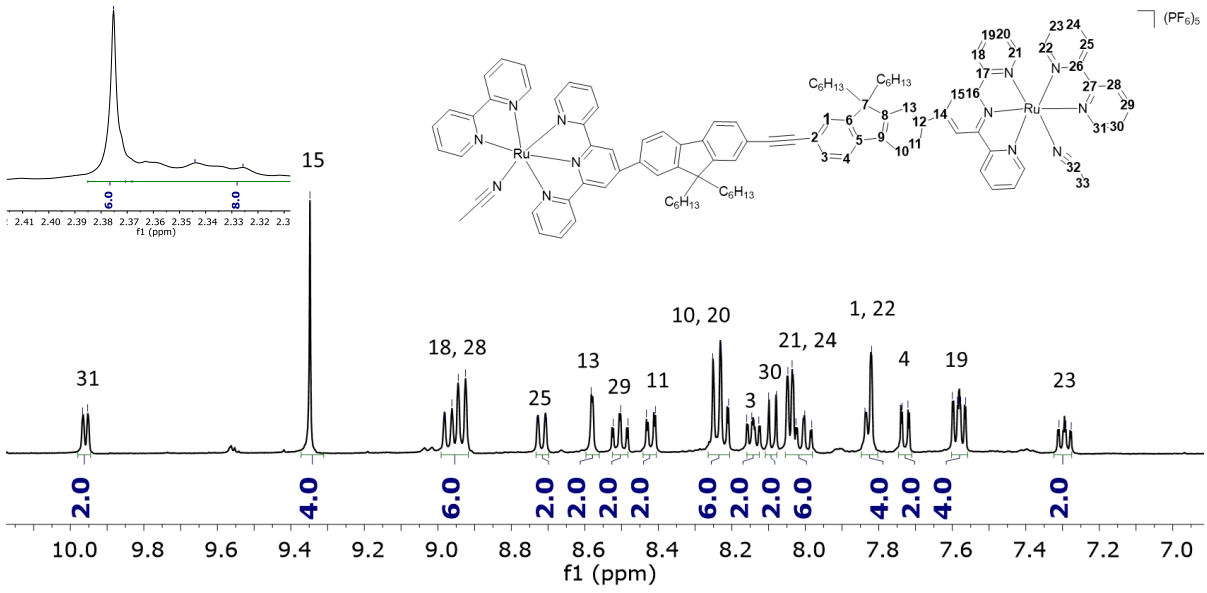

Figure III-7. ^{1}H-NMR spectrum for **RuMeCN-5** ($(CD_3)_2CO$, 400 MHz). Zoom on the aliphatic region showing the corresponding signal that integrates for 6 protons belonging to the CH_3CN linked to the ruthenium metallic center.

Lastly, the resonance at 2.38 ppm (*H-33*, s, 6H) belongs to the acetonitrile ligand coordinated to the ruthenium center. This signal, represented as a singlet, is consistent with the three equivalent protons in the methyl group of the acetonitrile molecule.

Proving the successful synthesis of complexes at each stage was critical to our approach, and NMR analyzes played a crucial role. We observed changes in the ^{1}H-NMR spectra that were consistent with our expectations based on the structure of our target complex **Ru(NO)CH$_3$CN-5** and the symmetric analogs **RuNO$_2$-5** and **RuCH$_3$CN-5**.

An important observation from ^{1}H-NMR analysis was the shift of hydrogen atoms ortho to the annular nitrogen of the equatorial rings of the *bpy* ligands (noted as *H-31*,). These shifts can be attributed to the spatial proximity of these hydrogen atoms to the various monodentate ligands (**X**, **Y**). In the ^{1}H-NMR spectrum (**Fig. III-8**) of the target complex **Ru(NO$_2$)CH$_3$CN-5**, the chemical shifts at *H-31* and *H-69* were 9.94 and 10.04 ppm, respectively. Interestingly, this ^{1}H-NMR spectrum can be interpreted as a superposition of the spectra of the symmetric molecules **RuNO$_2$-5** and **RuCH$_3$CN-5**, with the chemical shifts at *H-31* being 10.06 ppm and 9.96 ppm, respectively.

Nearly identical values for the chemical shift between the symmetric complexes and the target asymmetric complex were observed for all protons and carbons. This observation supports our understanding of the independent behavior of the two sides of the **Ru(NO$_2$)CH$_3$CN-5**complex. That is, changes in one side of the complex do not cause corresponding changes in the other side, underscoring the distinct and autonomous nature of each side of the complex. These results provided important insight into the structural and chemical integrity of the complexes we synthesized and gave us the confidence to proceed with subsequent phases of our research.

The intriguing behavior of the distinct but combined features of the symmetric counterparts in our target complex **Ru(NO)MeCN-5** was further demonstrated in the final stages of our synthesis. A similar pattern was observed in the final complex, with the ^{1}H-NMR spectrum (**Fig. III-9**) showing distinct signals for H31 and H69.

In this analysis, these signals combined and integrated for 4 protons, exhibiting a chemical shift value of 9.96 ppm. Of particular interest is the matching of this value

with the chemical shift of *H-31* in the **RuCH$_3$CN-5** complex, which was observed at 9.96 ppm. Furthermore, a strikingly similar chemical shift was noted for the *H31* proton in the complex **RuNO-5**, which had a value of 9.95 ppm.

These spectral similarities provide further evidence for understanding the composite nature of the asymmetric complex **Ru(NO)CH$_3$CN -5**, suggesting that this complex, although asymmetric, exhibits properties derived from its two symmetric counterparts. This underscores the success of our synthetic strategy and the unique nature of our target complex, further supporting its potential for our studies.

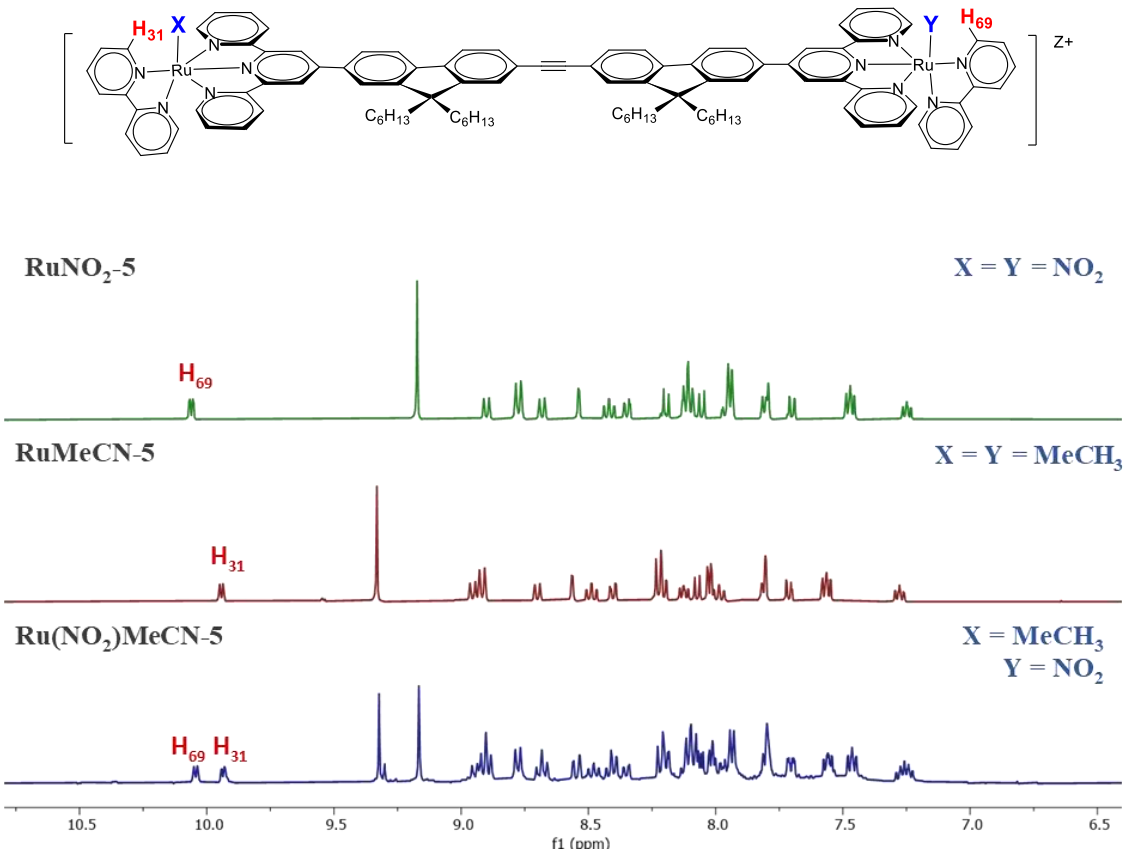

Figure III-8. Aromatic region of the ^{1}H-NMR spectrum for (top) **RuNO$_2$-5**, (X = Y, H_{31} = H_{69}, Z =2+), (middle) **RuCH$_3$CN-5**, (X = Y, H_{31} = H_{69}, Z = 4+), (bottom) **Ru(NO$_2$)MeCN-5**, (Z =3+), ($(CD_3)_2CO$, 600 MHz).

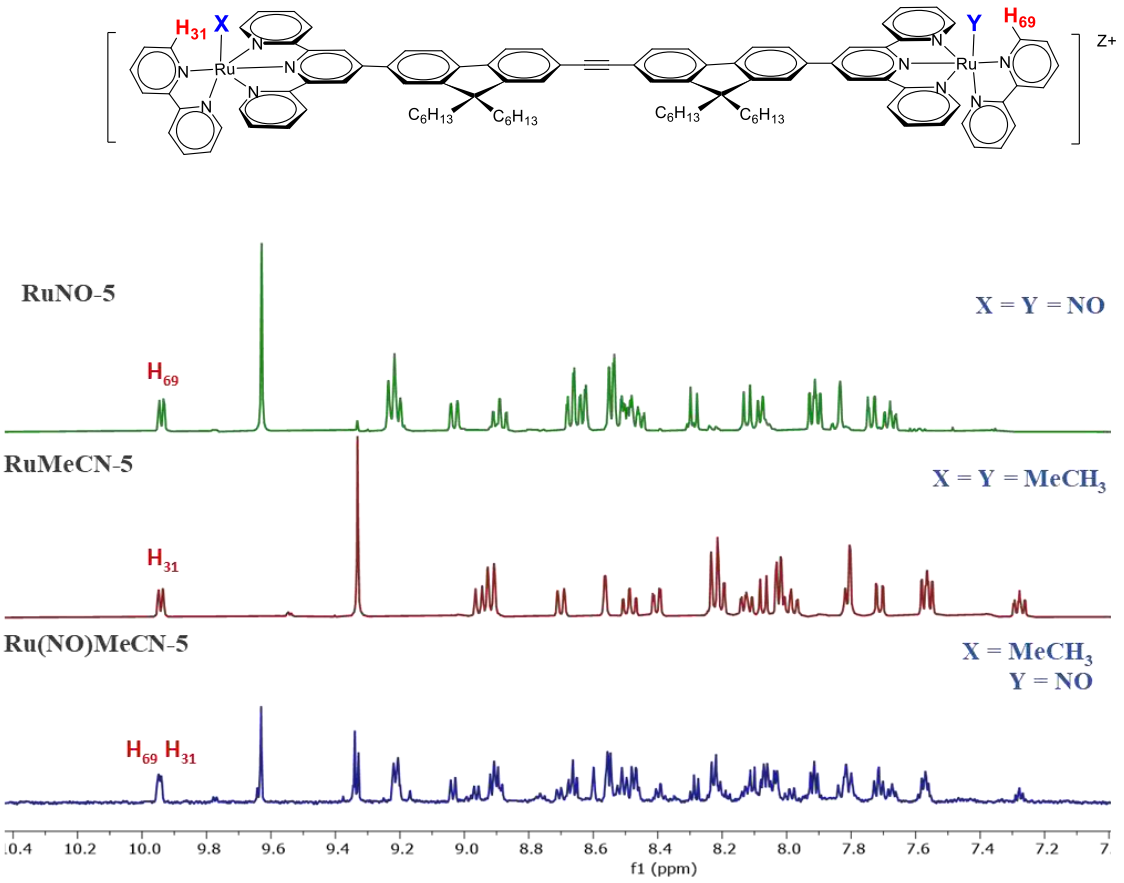

Figure III-9. b) Aromatic region of the ^{1}H-NMR spectrum for (top) **RuNO-5**, (X = Y, H_{31} = H_{69}, Z = 6+), (middle) **RuCH$_3$CN-5**, (X = Y, H_{31} = H_{69}, Z = 4+), (bottom) **Ru(NO$_2$)MeCN-5**, (Z =5+), ($(CD_3)_2CO$, 600 MHz).

III-9. ^{1}H-NMR Following for Irradiation at 490 nm of Bimetallic Complexes.

Further analysis of the ^{1}H-NMR spectra for **Ru(NO)CH$_3$CN-5** provided deeper insights into our proposed reaction pathway. While the ^{1}H-NMR spectra of **Ru(NO)CH$_3$CN-5** can essentially be seen as the sum of the spectra for **RuNO-5** and **RuCH3CN-5**, the chemical shifts of the signals are not identical.

To identify the formation of this elusive intermediate **B**, we employed ^{1}H-NMR to monitor the irradiation of **RuNO-5** over time (as shown in **Fig III-10**). Initially, at t=0 min, only **RuNO-5** was present in the solution. Its decrease was evident by the diminishing signal at 9.32 ppm, which disappeared entirely after 72 hours of irradiation.

Conversely, the final product **C** manifested an increasing signal at 9.64 ppm, culminating at its peak after the same 72-hour irradiation period. As for intermediate **B**, a subtle signal emerged at 8.90 ppm following an hour of irradiation that finally decreased at the end of the experiment.

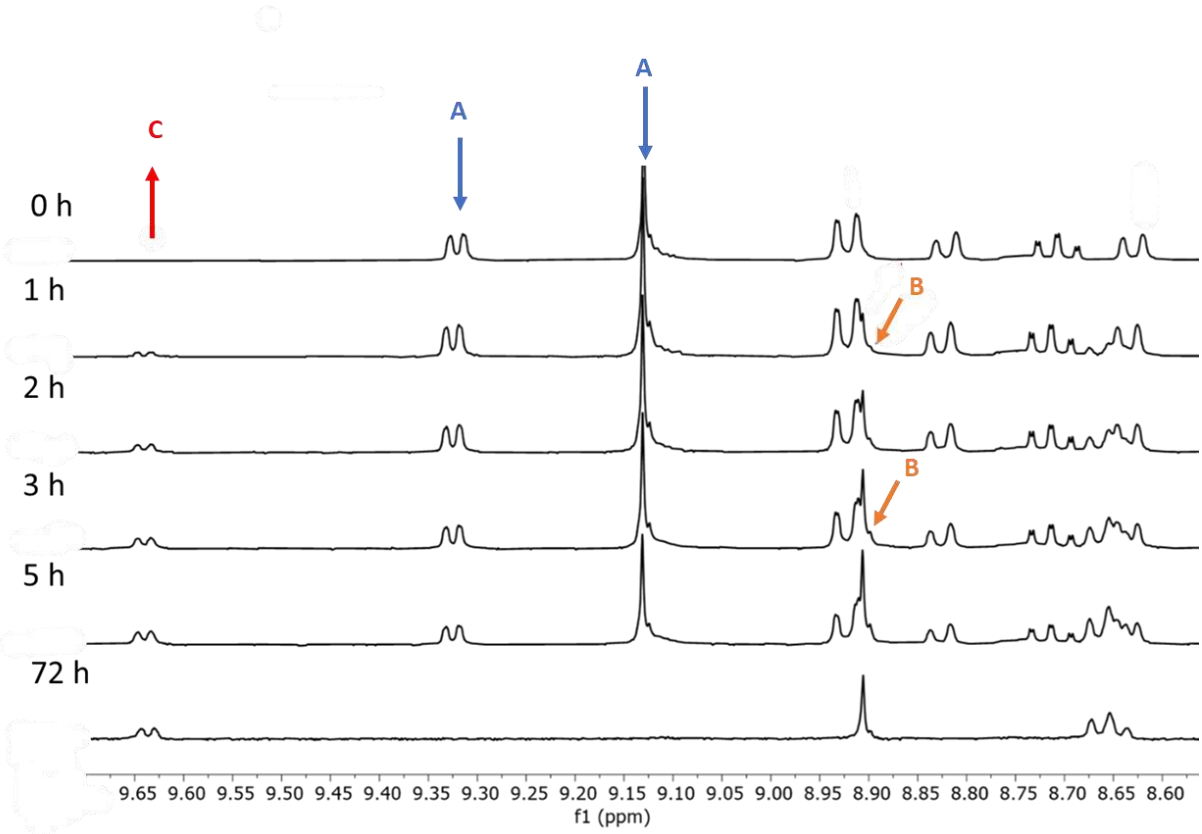

Figure III-10. Aromatic region of the ^{1}H-NMR spectrum for irradiation of **RuNO-5** as a function of time.

Our investigations also extended to **RuNO-3**, where we wanted to identify any potential signals corresponding to the intermediate in our experimental setup. However, despite rigorous analysis, we could not discern any signals indicative of the intermediate **B**. It is important to note that, given our understanding at this point, the intermediate **B** would most likely emerge at the initiation of the irradiation experiment. As it stands, we cannot definitively ascertain whether the intermediate **B** is unstable or not.

In **Figure III-11**, the emergence of signals relating to the ultimate product, **RuCH$_3$CN-3**, is evident. Concurrently, we observe the disappearance of signals

associated with the original complex, **RuNO-3**. The complete transformation from **A** to **C** took approximately three days.

Interestingly, the beginning of the transformation process appears to be rapid. After approximately 40 minutes of irradiation, the emergence of some signal growth is evident, at 9.70, 7.85-7.90 and 7.12-7.18 ppm as examples. These signals growth becomes even more pronounced after 160 minutes of irradiation. While it is challenging to definitively judge the velocity rate from these experiments, the almost instantaneous appearance of a signals after following 40 minutes of irradiation might suggest the formation of one or both of these species (either **B** or **C**).

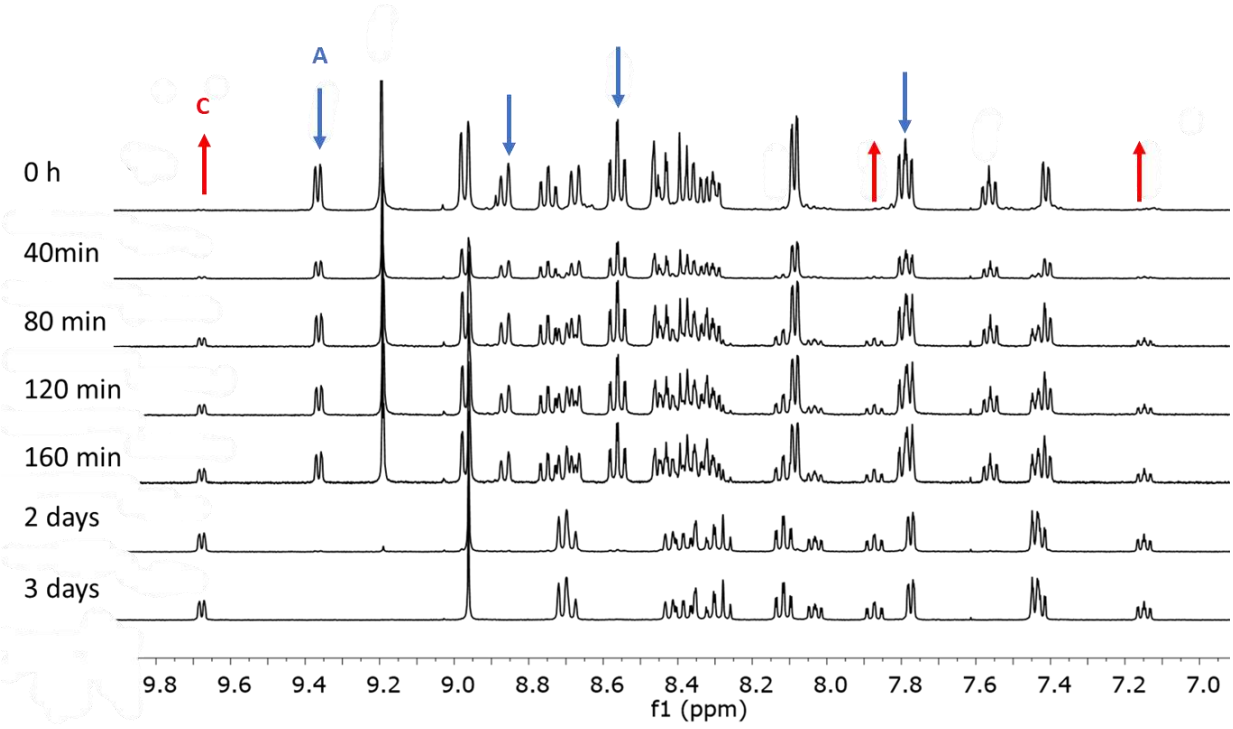

Figure III-11. Aromatic region of the ^{1}H-NMR spectrum of irradiation experiment for **RuNO-3** under 490 nm as a function of time.

Finally, we did the experiments for the complex **RuNO-4** using same irradiation wavelength at 490 nm (**Fig. III-12**). The results consistently indicated a reduction in the signal from the initial complex **A**. For example, the signals with a chemical shift value of 9.35, 9.15, 8.55-8.58 and 7.54-7.58 ppm. The emergence of some signals associated with the final product **C** can be located at a chemical shift value of 9.38, 7.75, 7.50-7.55 and 7.10-7.15 ppm.

Notably, after four hours of irradiation, a signal appearing between 7.60-7.64 ppm (highlighted with an orange arrow) was observed. Interestingly, this signal disappeared after four days of irradiation, which might be suggestive of the transient formation of **B** as many of these unexpected pics disappear at the end of the experiment.

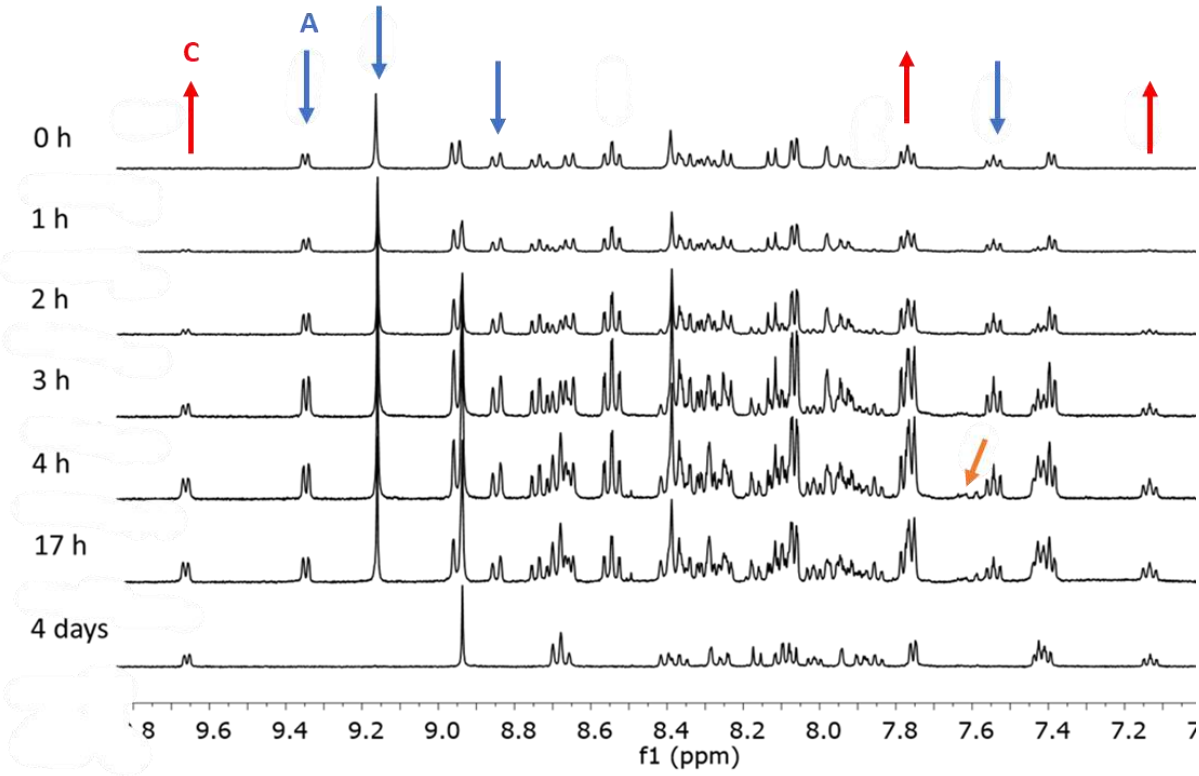

Figure III-12. Aromatic region of the ^{1}H-NMR spectrum of irradiation experiment for **RuNO-4** under 490 nm as a function of time.

III-10. HRMS Analyses for Ru(NO)CH_3CN-5 and C Complexes

The identity of the final products **C** and the intermediate **B** was further corroborated by HRMS/MS analyses. The spectra obtained for **RuCH_3CN-1** to **RuCH_3CN-5** and **Ru(NO_2)MeCN-5** predominantly exhibited the unaltered cations, confirming their structural integrity.

However, the spectrum of the final product **Ru(NO)CH_3CN-5** showed more complexity (**Fig. III-13**). In this case, partial transformation of the Ru-NO^+ moiety to $RuNO_2$ was observed, likely due to the presence of traces of water during the measurement. It should be noted that this complex is highly sensitive to the presence of water, thus explaining the observed alteration in the spectra.

These HRMS/MS analyses provide compelling evidence for the identities of the synthesized complexes. At the same time, they underscore the necessity of meticulous handling and strict moisture control during the analysis of water-sensitive complexes like **Ru(NO)CH_3CN-5**.

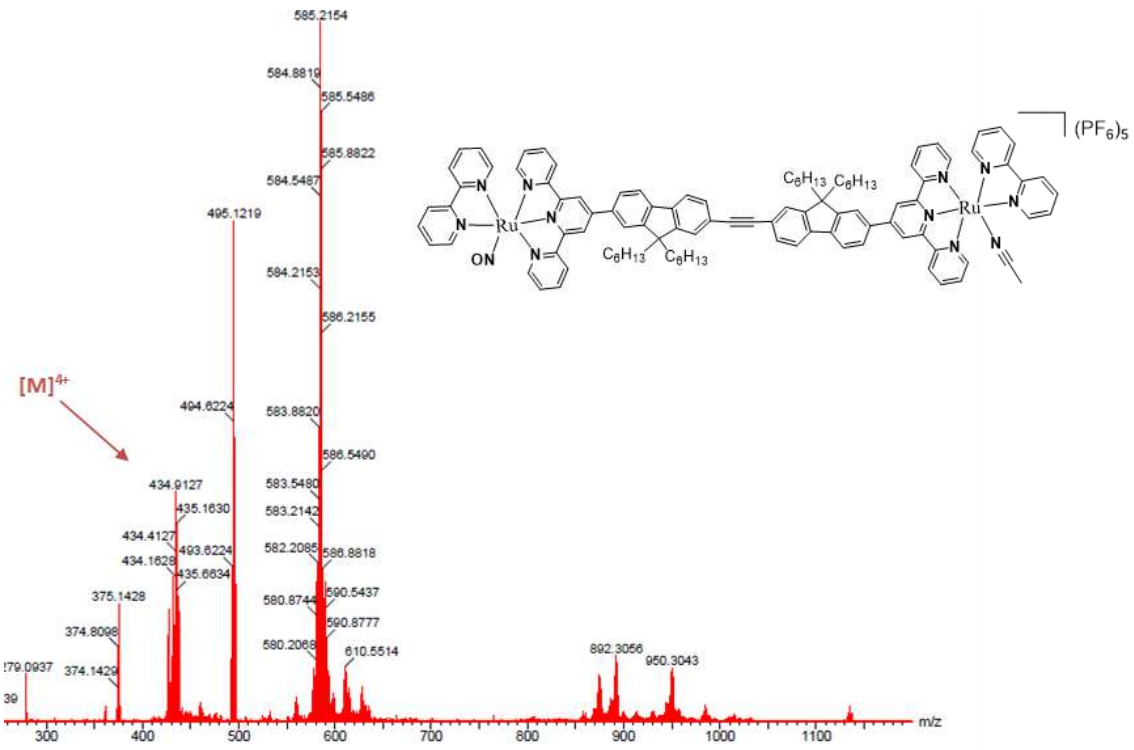

Figure III-13. HRMS (ESI-TOF+) spectrum for **Ru(NO)CH_3CN-5** showing the base pic at 434.9127.

III-11. UV-vis Spectra of Complexes C.

The UV-Vis spectra of the complexes (**Fig. III-14**) exhibit three notable bands, referred to as Bands (a), (b), and (c). For **RuCH$_3$CN-1** and **2** band (b) is less intense, having a reduction on the epsilon value compared to the other bimetallic complexes. Band (c) are the band exhibiting maximum absorption, it has similar values for all complexes, with wavelengths ranging from 471 to 478 nm.

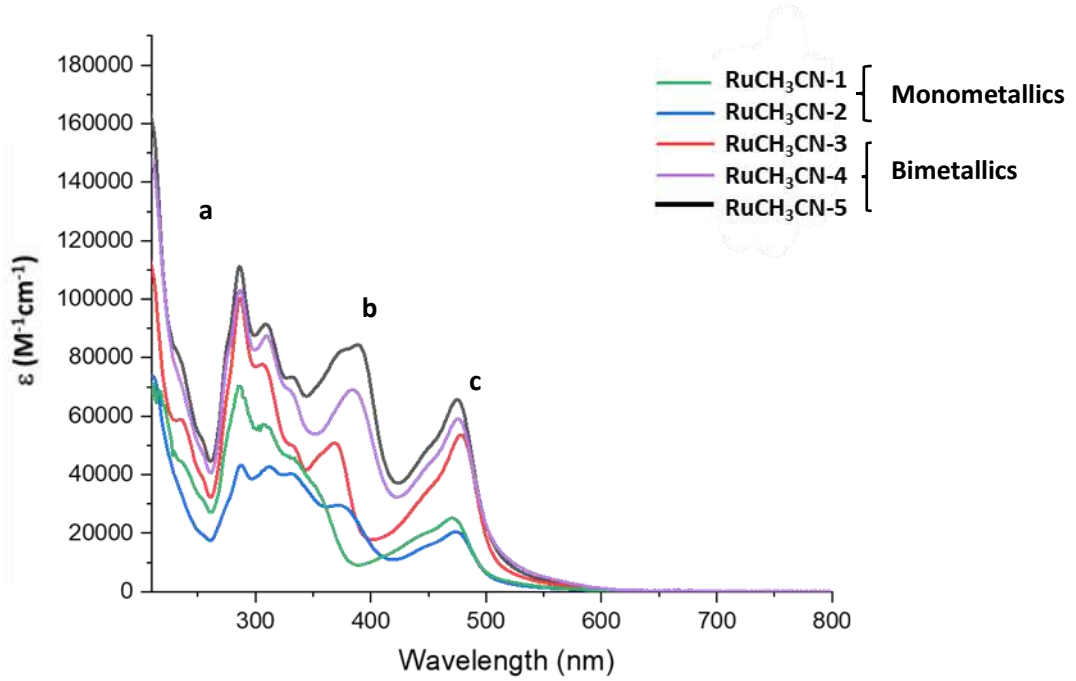

Figure III-14. UV-vis spectra for the different synthetized products **C** from **RuCH$_3$CN-1** to **RuCH$_3$CN-5**.

When examining the molar extinction coefficients in the **Table III-1**, it appears that the quantity of fluorenes does not significantly influence these values in this series of compounds as for the **RuNO** series (**Section II-15**). The monometallic complexes in this set display lower extinction coefficients. **RuNO-1** has the smallest value of 20300 $M^{-1}cm^{-1}$, whereas the bimetallic complexes exhibit values approximately double those of their monometallic counterparts. Among these, **RuNO-3** shows the lowest value of 53300 $M^{-1}cm^{-1}$, and **RuNO-5** possesses the highest, with a value of 65100 $M^{-1}cm^{-1}$.

Table III-1.1. Values of Ɛ ($M^{-1}.cm^{-1}$) and λ_{Max} (nm) for the final complex **C** series from **$RuCH_3CN$-1** to **$RuCH_3CN$-5** measured in CH_3CN.

	Complex	λ_{Max} in nm	Ɛ in $M^{-1}.cm^{-1}$
Monometallic	**$RuCH_3CN$-1**	471	20300
	$RuCH_3CN$-2	474	25100
Bimetallic	**$RuCH_3CN$-3**	478	53300
	$RuCH_3CN$-4	475	58700
	$RuCH_3CN$-5	475	65700

Table III-1.2 Values of Ɛ ($M^{-1}.cm^{-1}$) and λ_{Max} (nm) for the final **RuNO** series measured in CH_3CN.

	Complex	λ_{Max} in nm	Ɛ in $M^{-1}.cm^{-1}$
Monometallic	**RuNO-1**	453	16700
	RuNO-2	497	12200
Bimetallic	**RuNO-3**	457	37000
	RuNO-4	494	35500
	RuNO-5	493	45100

The data obtained from these analyses lead to the study of the efficiency of NO· delivery. We used a photokinetic model based on UV-vis spectra. In the next section we present two different models depending on the presence of intermediates **B**.

III-12. Photochemical Processes in Ruthenium Nitrosyl Complexes

In photochemical reactions, the reactant molecules absorb photons, promoting them to higher energy states and enabling various transformations, one of which is the liberation of nitric oxide from ruthenium nitrosyl complexes.

The basic photochemical process involved in the liberation of NO· as a radical can be represented as follows in reaction (**III-4**):

$$[Ru(NO)(Ligand)] \xrightarrow{h\nu} [Ru(NO)(Ligand)]^* \rightarrow [Ru(Ligand)] + NO\cdot \quad \text{(III-4)}$$

In this process, a **RuNO** absorbs a photon (h**ν**), which promotes an electron from a ground state to an excited state (RuNO*), leading to a change in the electronic configuration of the complex Then, this excited state complex undergoes internal conversion to a lower-energy excited state, which facilitates the breaking of the Ru-NO bond and thus releases the stored NO· radical molecule.

The efficiency of this photochemical reaction, also referred to as the quantum yield, is calculated using the following **Equation** (**III-5**):

$$\Phi_{NO} = \frac{\text{number of moles of NO released}}{\text{number of moles of photons absorbed}} \quad \text{(III-5)}$$

It represents the number of events (here, the release of NO· molecules) that occur per photon absorbed. A deep understanding of these factors is crucial for optimizing the use of these complexes as light-controlled NO· donors and finding their potential applications in biomedical fields.

In the case of bimetallic complexes two cases can be envisioned; the first one, in which the NO· is releasing in one single step, following a reaction of the type **A**→**C**, or in two steps in which one NO· is liberated first and then, the second one, following a reaction **A**→**B**, and then **B**→**C**.

III-13. Photokinetic of A $\overset{\Phi_A}{\rightarrow}$ C Type Reaction

Photochemically excited molecules can not only undergo physical processes, such as relaxation or intersystem crossing, but also initiate chemical changes. For instance, the transformation into the product *C* can start from a high-energy electronic or vibrational state. By light irradiation, there are different processes that a molecule can undergo, but for chemical reactions, three significant steps are considered:

- Light Absorption (Photon excitation): The molecule **A** absorbs a photon (hv) and is promoted to an excited state (**A***), as shown in reaction (**III-6**).

$$A \xrightarrow{h\nu} A^* \ (I_a^A, \text{ in mol.} L^{-1}.s^{-1}) \quad \text{(III-6)}$$

In this step, the rate of the reaction is proportional to the light intensity absorbed by **A** (I_a^A).

- Non-reactive Deactivation: The excited molecule **A*** can deactivate and return to the ground state, as in reaction (**III-7**).

$$A^* \xrightarrow{h\nu} A \ (k_d, \text{ in } s^{-1}) \quad \text{(III-7)}$$

Here, k_d is the deactivation constant.

- Reactive Deactivation (Photochemical Reaction): Alternatively, the excited molecule **A*** can undergo a photochemical reaction to form the photoproduct **C**, as shown in reaction (**III-8**).

$$A^* \xrightarrow{h\nu} C \ (k_r, \text{ in } s^{-1}) \quad \text{(III-8)}$$

In this case, k_r is the reaction constant.

Following these steps, the reactions can be modeled by differential equations (**III-9** to **III-11**):

$$\frac{d[A]}{dt} = -I_a^A + k_d[A^*] \quad \text{(III-9)}$$

$$\frac{d[A^*]}{dt} = I_a^A - (k_d + k_r)[A^*] \quad \text{(III-10)}$$

$$\frac{d[C]}{dt} = k_r[A^*] \quad \text{(III-11)}$$

The light intensity absorbed by **A** (I_a^A) can be related to the absorbance of **A** (Abs_A^λ), the total absorbance (Abs_{Tot}^λ), and the incident light intensity (I_0) through the photochemical factor (F), as given in equations (**III-12** and **III-13**):

$$I_a^A = Abs_A^\lambda I_0 F \tag{III-12}$$

$$F = \frac{1-10^{-Abs_{Tot}^\lambda}}{Abs_{Tot}^\lambda} \tag{III-13}$$

due to the short-lived nature of the excited state **A***, the steady-state approximation can be used to simplify equation (**III-10**):

$$0 = \frac{d[A^*]}{dt} = I_a^A - (k_d + k_r)[A^*] \tag{III-14}$$

then equation (**III-14**), $[A^*]$ can be given as:

$$[A^*] = \frac{I_a^A}{(k_d+k_r)} \tag{III-15}$$

substituting equation (**III-15**) into (**III-11**) provides:

$$\frac{d[C]}{dt} = -\frac{d[A]}{dt} = I_a^A \frac{k_r}{k_d+k_r} = \Phi_A I_a^A \tag{III-16}$$

meaning that $\frac{k_r}{k_d+k_r} = \Phi_A$.

For equation (**III-16**), the quantum yield (Φ_A) is defined as the rate at which **A** is consumed. By substituting equation (**III-12**) into (**III-16**), the differential equation (**III-17**) is obtained with one unknown (Φ_A), and the rest of the values can be experimentally determined. Solving equation (**III-17**) provides the value of the quantum yield for the reaction:

$$\frac{d[A]}{dt} = -\Phi_A Abs_a^\lambda I_0 F \tag{III-17}$$

light intensities (I_0) were determined before each photolysis experiments by measuring the power of the LED at the beginning of each experiment and then following the equation (**III-18**):

$$I_0 = \frac{P\lambda}{VNhc} \qquad \text{(III-18)}$$

where "P" is the power of the LED in W, "λ" is the wavelength of irradiation, "V" is the volume in mL, N the Avogadro's number, h the Planck constant in J. s and c the speed of light in $m.s^{-1}$.

The equation can be fitted with the experimental data Abs_{Tot}^{λ} = f(t) and 2 parameters Φ_{NO} and ε_C (where ε_C is the molar extinction coefficient of the final product) at two wavelengths (λ_{irr} and λ_{obs}).

III-14. Photokinetic of A $\overset{\Phi_A}{\longrightarrow}$ B $\overset{\Phi_B}{\longrightarrow}$ C Type Reaction

Our study builds upon the foundational model to account for a two-step photochemical reaction sequence, A to B to C, as shown in the following sequence of reactions:

$$A \xrightarrow{h\nu} A^* \qquad (I_a^A, \text{in mol}.L^{-1}.s^{-1}) \qquad \text{(III-19)}$$

$$A^* \xrightarrow{h\nu} A \qquad (k_d, \text{ in } s^{-1}) \qquad \text{(III-20)}$$

$$A^* \xrightarrow{h\nu} B \qquad (k_{r1}, \text{ in } s^{-1}) \qquad \text{(III-21)}$$

$$B \xrightarrow{h\nu} B^* \qquad (I_a^B, \text{ in mol}.L^{-1}.s^{-1}) \qquad \text{(III-22)}$$

$$B^* \xrightarrow{h\nu} C \qquad (k_{r2}, \text{in } s^{-1}) \qquad \text{(III-23)}$$

In this sequence, A represents a compound, B is the intermediate product generated during the irradiation process, and C is the final product. B* represents the excited state of B which reacts to form C.

The concentration of A* is given by equation (**III-24**):

$$[A^*] = \frac{I_a^A}{k_d + k_{r1}} \quad \text{(III-24)}$$

and similarly, the concentration of B* can be represented as:

$$[B^*] = \frac{I_a^B}{k + k_{r2}} \quad \text{(III-25)}$$

the rate of appearance and disappearance of B is given by equation (**III-26**):

$$\frac{d[B]}{dt} = (k_{r1}[A^*] + k_{r2}[B^*]) \quad \text{(III-26)}$$

substituting equation (**III-25**) into equation (**III-26**), we get:

$$\frac{d[B]}{dt} = k\left(\frac{I_a^A}{k_d + k_{r1}}\right) - k_{r2}[B^*] \quad \text{(III-27)}$$

The rate of formation of C, the end product, is given by:

$$\frac{d[C]}{dt} = k[B^*] \quad \text{(III-28)}$$

Finally, the differential equations giving the evolution of A, B and C are given by:

$$\frac{d[A]}{dt} = -\Phi_A I_a^A \quad \text{(III-29)}$$

$$\frac{d[B]}{dt} = -\Phi_B I_a^B + \Phi_A I_a^A \quad \text{(III-30)}$$

$$\frac{d[C]}{dt} = \Phi_B I_a^B \quad \text{(III-31)}$$

We encounter three interdependent differential equations that rely on the ε values of A, B, and C. To solve the differential equations and obtained a fitting that ensured consistency and reliable results, a simultaneous fitting model was proposed by Pr. V. Pimienta in IMRCP at Toulouse, which can reproduce a large experimental

base. The data set consists of four experiments performed at 4 irradiation wavelengths, for which the kinetics at 4 wavelengths can be reproduced.

One of the main objectives in synthesizing the final products **C** was to obtain its ε. For the first time in our team, it is possible to integrate these ε values directly into the photokinetic model, significantly enhancing the precision of our calculations. This enables us to determine the Φ_{NO} with a higher degree of accuracy, further refining our understanding of the photochemical reactions involved.

III-15. Determination of Nitric Oxide Quantum Yield $(\boldsymbol{\Phi_{NO}})$ for Monometallic Complexes at Different Wavelengths by One-Photon Absorption

Having established the necessary information and characterizations for all final products **C** and one of the intermediates **B**, we can proceed with the relevant studies to calculate the efficiency of Φ_{NO}. Our investigation will start with the monometallic species, **RuNO-1,** and **RuNO-2**, which follows the **A** $\xrightarrow{\Phi_A}$ **C** one-step model.

All samples were studied in pure acetonitrile and subjected to irradiation at wavelengths of 490, 455, 400, and 365 nm. We have already introduced the data for irradiation at 490 nm in the **Section III-2**, in the following sections, we will focus on detailing the outcomes from the other wavelengths: 455 nm, 400 nm, and 365 nm. Generally, all photokinetic graphs are similar and can be described in the same way. It is only upon calculation of the quantum yield that the differences in reaction rates become noticeable. These observations will further elucidate how the irradiation wavelength impacts the velocity and efficiency of the photochemical transformation in these ruthenium-based complexes.

Figure III-15 shows how the electronic absorption spectrum evolutes for **RuNO-1** upon exposure to light at different wavelengths in acetonitrile. Isosbestic points visible at λ=376, 420, and 498 nm suggest a straightforward conversion from the **$Ru^{II}NO$** complex to the associated photolyzed specie **$Ru^{II}CH_3CN$**. No back-reaction

occurs as the sample was analyzed by HRMS, showing only the pic corresponding to the **RuCH$_3$CN-1** complex with a value of 432.1733.

In the spectrum of **B** (red curve), new absorption bands emerge at λ=310, 334, and 470 nm. As it was mentioned, the spectral profile of the final product is indicative of a Ru^{II} complex, marked by the absence of a band at λ=600 nm, typically characteristic of Ru^{III} species.[171] This suggests that the product may undergo an immediate reduction post-photoreaction, resulting in the **Ru^{II}CH$_3$CN-1** complex as the last observable product. Despite this, the isosbestic points are evident, implying that the second stage of the process, likely the reduction, proceeds really fast.

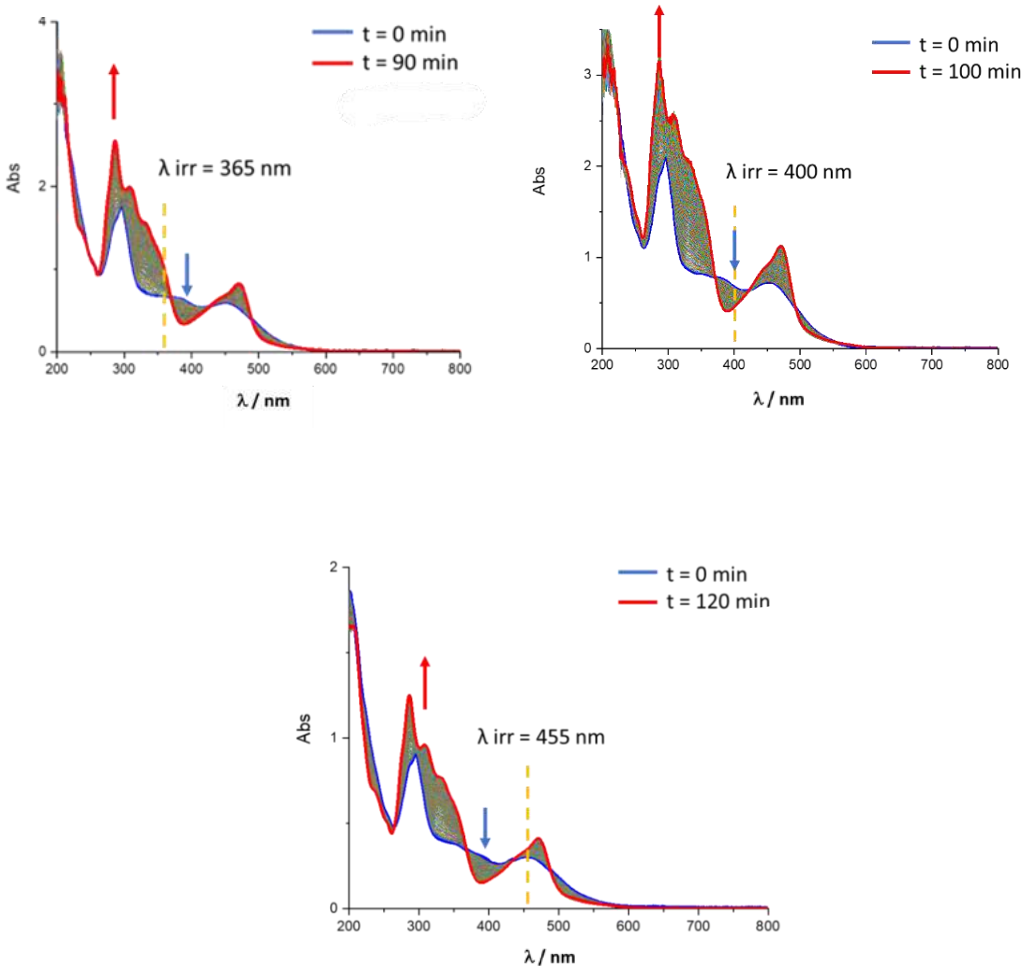

Figure III-15. Evolution of absorption spectra for **RuNO-1** at λ_{irr} = 365 nm (left, top), 400 nm (right top) and 455 nm (bottom middle) in CH_3CN (λ_{irr} is indicated by yellow line).

As previously discussed in **Section III-9**, the photokinetic model for the reaction **A** $\xrightarrow{\Phi_A}$ **C** results in a differential equation. With the information obtained from the irradiation experiments and the support of a computational program, Sa3.3 (Adjustment Simulation), developed by Prof. Véronique Pimienta and Dr. Lavabre, we are able to analyze the evolution of absorbance. This method enables to calibrate the system accurately and track the evolution of the reaction precisely, ultimately offering us a means to determine the quantum yield and overall efficiency of our photochemical reaction. For this experiments the initial concentration, molar extinction coefficients, and the photon flux are constants, whereas the quantum yield is a parameter.

Figure III-16 show a representative example of the experimental data, for the complex **RuNO-1** that follows the established model. The specific experimental conditions can be found in Table 5.1 on the Appendix 5. This synchronicity between theoretical modeling and experimental data provides compelling evidence of our photokinetic accuracy of the model in predicting the photoreaction dynamics.

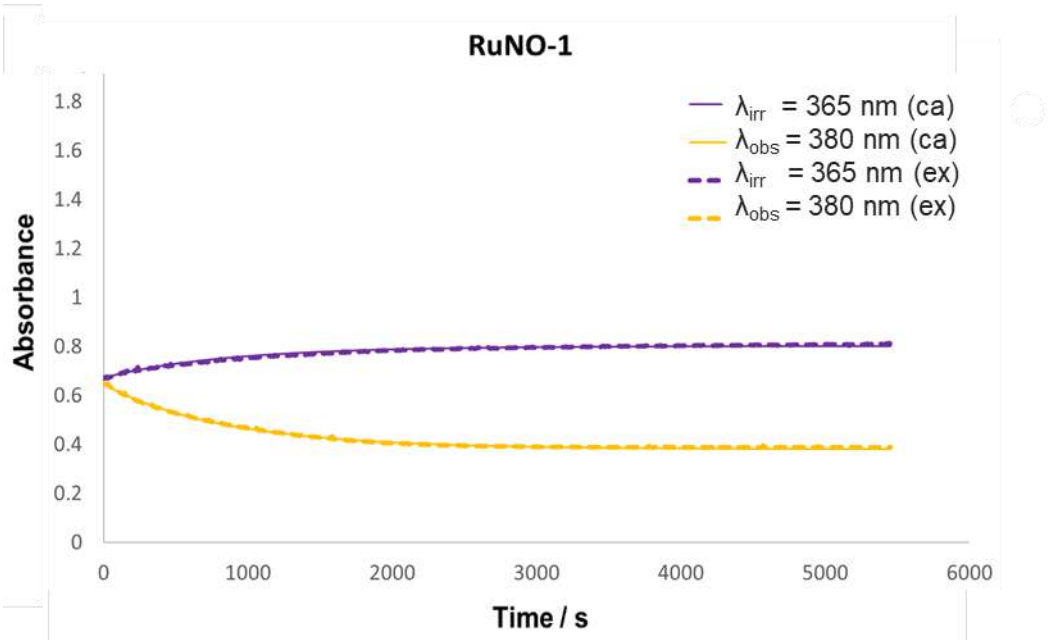

Figure III-16. Experimental (ex) and calculated (ca) evolution of absorbance during irradiation (λ_{irr} = 365 nm for **RuNO-1**.

It can be observed in **Figure III-17**, that all the experiments have a clear isosbestic point, suggesting a similar photochemical transformation pathway. The behavior and implications of these observations align with the explanations provided for the **RuNO-1** complex, validating the reliability of the applied methods and models for monometallic species.

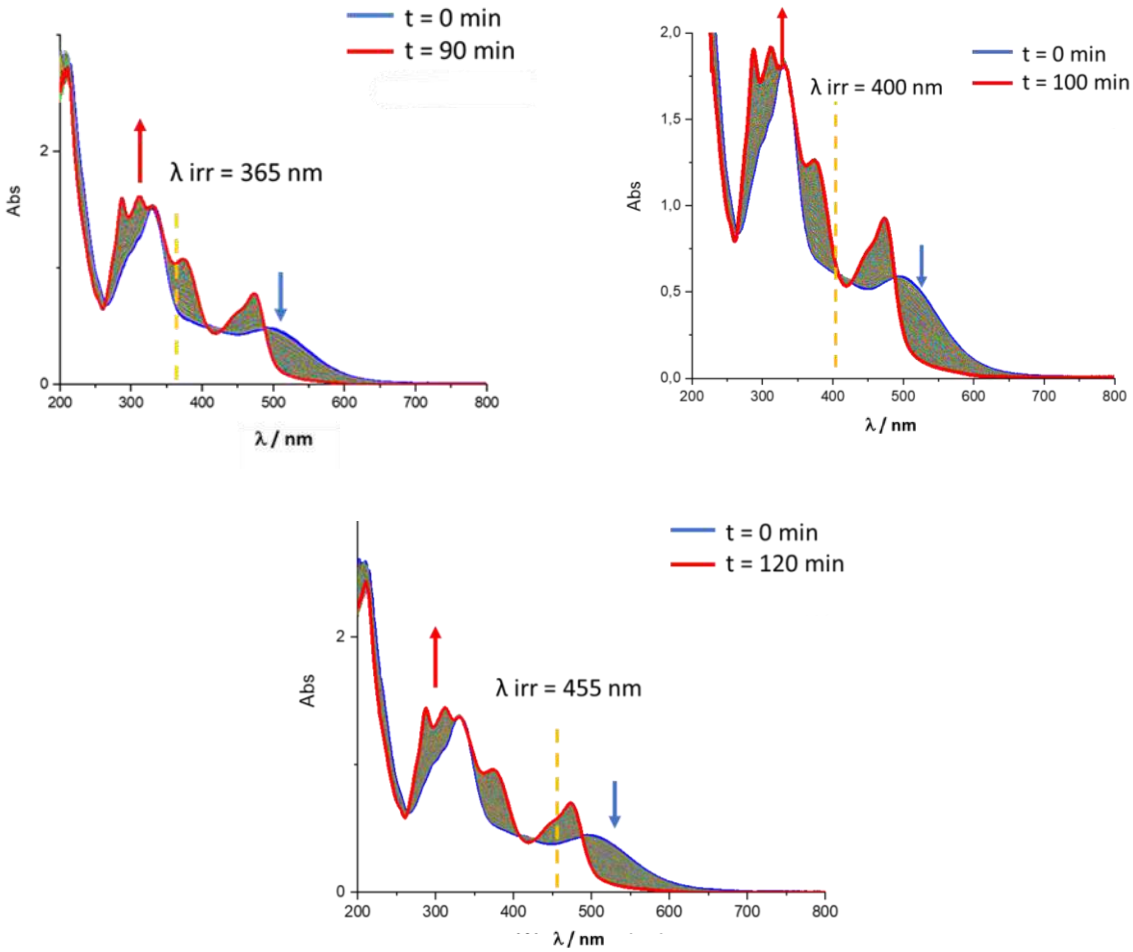

Figure III-17. Evolution of absorption spectra for **RuNO-2** at 365 nm (left, top), 400 nm (right top) and 455 nm (bottom middle) in CH_3CN (λ_{irr} is indicated by yellow line).

The **Figure III-18** illustrates the evolution of the reaction for the **RuNO-2** complex, it can be observed that follows the same tendency as for **RuNO-1**. In the first case, a red shift is observed while it is a blue shift in the second case.

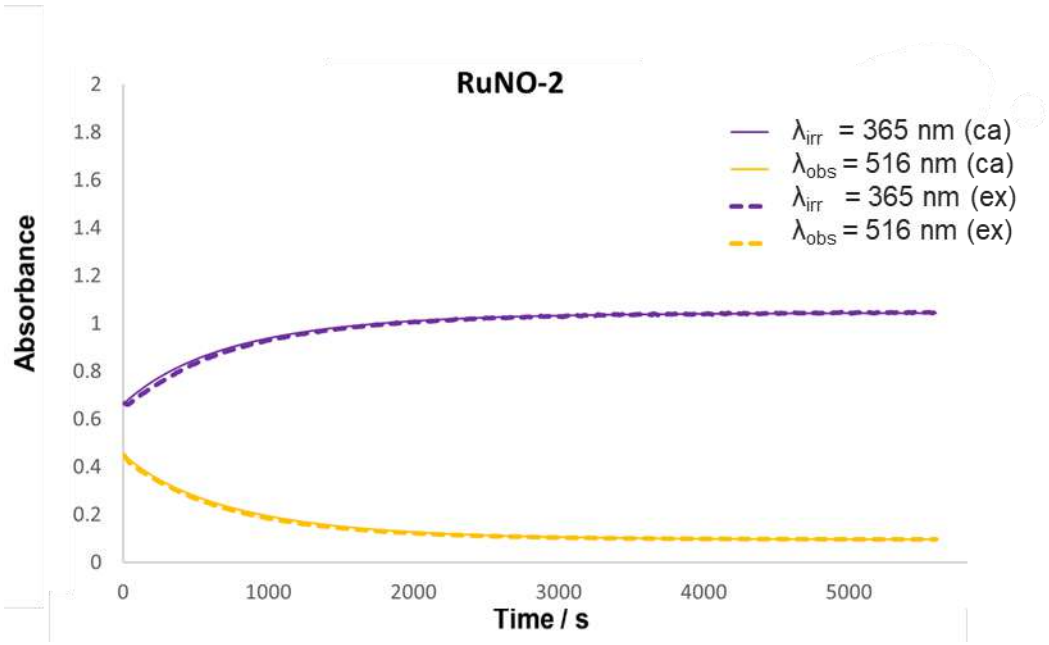

Figure III-18. Experimental (ex) and calculated (ca) evolution of absorbance during irradiation (λ = 365 nm on the left, λ = 400 nm on the right, λ = 455 nm on the bottom) at observation wavelengths as a function of time for **RuNO-2**.

The products **C** obtained from the irradiation of **A** were compared to the synthetized one to confirm that the end point of the transformation was reached. It can be seen in **Figure III-19**, that all the irradiation wavelengths successfully reach the complete conversion of **A** into **C**. The Φ_{NO} for the **RuNO-1** and **RuNO-2** at the different wavelengths are presented in the **Table III-2**.

Table III-2. Quantum yield of NO· for **RuNO-1** and **RuNO-2** at different irradiation wavelengths.

	Φ_{NO}^{365}	Φ_{NO}^{400}	Φ_{NO}^{455}	Φ_{NO}^{490}
RuNO-1	*0.0084*	*0.0062*	*0.0024*	*0.0024*
RuNO-2	*0.0120*	*0.0085*	*0.0068*	*0.0024*

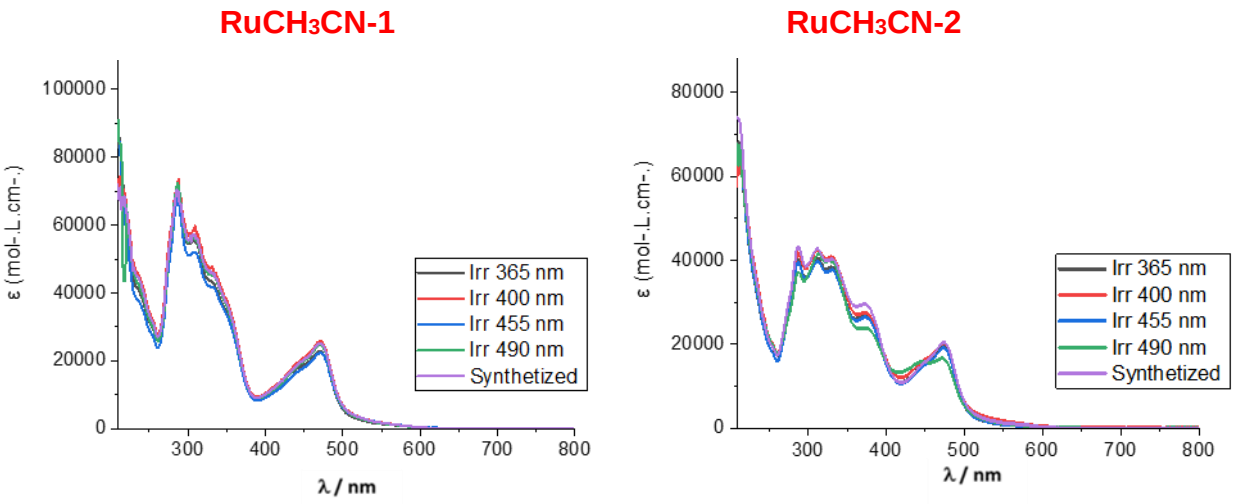

Figure III-19. UV-visible absorption spectra for **RuCH₃CN-1** (left) and **RuCH₃CN-2** (right) in acetonitrile obtained by irradiation of **RuNO-1** and **RuNO-2** at the end of the experiment for different wavelengths (365, 400, 455 and 490 nm) and synthetized one.

For the four irradiation wavelengths the higher quantum yield was obtained for the complex **RuNO-2**, at least at **λ** = 365 and 400 nm the value of Φ_{NO}^{λ} is 1.4 times higher than the one for **RuNO-1**, at **λ** = 455 nm the value of Φ_{NO}^{455} shows the biggest difference as the value for **RuNO-2** is 2.8 times higher than from the one for **RuNO-1**, finally at **λ** = 490 nm both complexes shows the same value.

The main distinguishing feature between **RuNO-1** and **RuNO-2** is the extra fluorene present in **RuNO-2**. As discussed previously, the quantum yield reflects the efficiency of NO· release. It means that the number of photons absorb by the complex is directly related to its molar extinction coefficient at a given irradiation wavelength. Therefore, a larger molar extinction coefficient increases the likelihood of the complex absorbing the required number of photons for nitric oxide liberation. Then, the product of the molar extinction coefficient and the quantum yield ($\varepsilon\Phi_{NO}$) can serve as a valuable metric for comparing the efficiency of nitric oxide liberation between different complexes.

Table III-3. Quantum yield of NO· multiplied by the correspondent epsilon values for **RuNO-1** and **RuNO-2** at different irradiation wavelengths.

	$\varepsilon^{365}\Phi_{NO}^{365}$	$\varepsilon^{400}\Phi_{NO}^{400}$	$\varepsilon^{455}\Phi_{NO}^{455}$	$\varepsilon^{490}\Phi_{NO}^{490}$
RuNO-1	*192*	*63*	*51*	*29*
RuNO-2	*350*	*135*	*112*	*29*

For both complexes, the product $\varepsilon^{\lambda}\,\Phi_{NO}^{\lambda}$ evolves in a similar way to Φ_{NO}^{λ} itself. Typically, a higher product value is observed where Φ_{NO}^{λ} is higher in the case of 490 nm product. As seen in **Table II-4**, Φ_{NO}^{λ} increases with the energy of the incident photons. There are a couple of hypotheses to explain this general observation. Firstly, at an irradiation wavelength of 365 nm, the energy generates an excitation to a state ($S_{n\text{-}365}$) that is higher in energy compared to when it is irradiated at 490 nm ($S_{n\text{-}490}$). The transition S_0->S_{365} could be implicated in the NO· liberation process since it involves a charge transfer to the **Ru-NO** complex.

A second hypothesis is that after the complex reaches the higher energy excited state ($S_{n\text{-}365}$) via irradiation at 365 nm, it experiences vibrational relaxations that lower the complex to the excited state $S_{n\text{-}490}$. The energy released from this relaxation could be involved in the NO· liberation process, leading to an efficacy of liberation that is higher than what is observed when the complex absorbs a photon of weaker energy.

III-16. Determination of Nitric Oxide Quantum Yield $(\boldsymbol{\Phi_{NO}})$ for Bimetallic Complexes at Different Wavelengths by One-Photon Absorption

As for the previous experiments, the experimental basis of the kinetic study for the compound **RuNO-3** consists of the spectral evolutions recorded under continuous irradiation during four experiments carried out at four irradiation wavelengths 365, 400, 455 and 490 nm, are shown in the **Figure III-20**. The evolution obtained by irradiations at all wavelengths show qualitatively similar evolutions. As for **RuNO-1** that also contains one fluorene in its structure, a blue shift is observed.

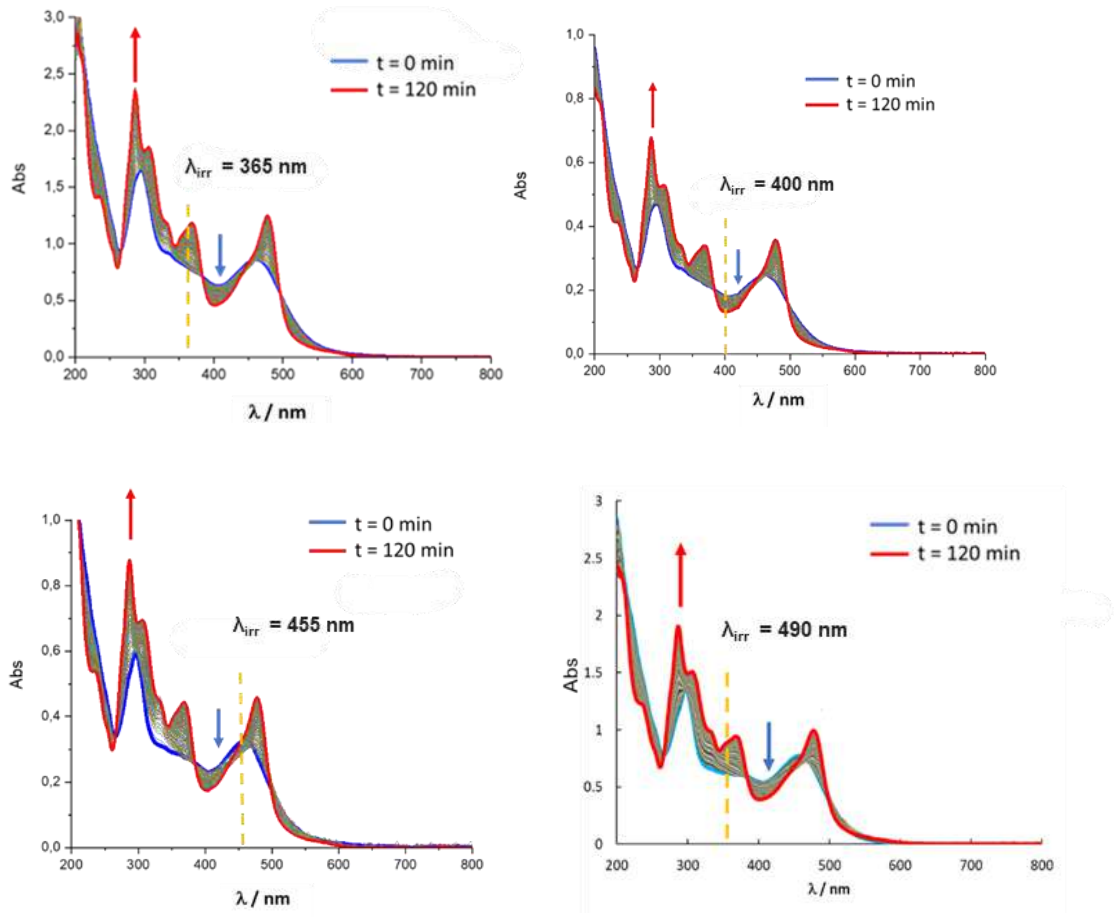

Figure III-20. Evolution of absorption spectra for **RuNO-3** at λ_{irr} = 365 (left, top), 400 (right top), 455 (left, bottom) and 490 nm (right, bottom) in acetonitrile.

The final spectrum in the irradiation experiments in different wavelengths corresponds to the spectrum obtained by synthesis of the product (**Fig. III-21**). For each irradiation, the recordings were made until the absorbance no longer varies, indicating total transformation of the reactant into the final product, this can been also probe by superposing the UV-vis spectra for the synthetized **RuCH$_3$CN-3**.

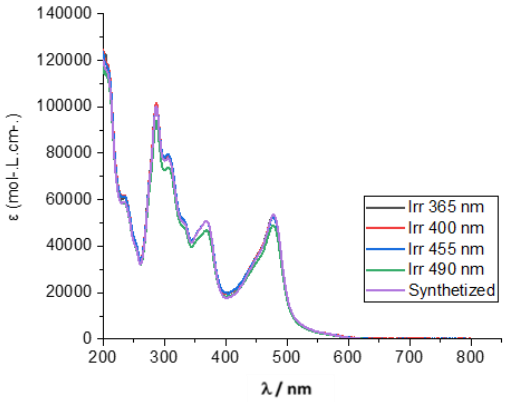

Figure III-21. UV-visible absorption spectrum for **RuCH$_3$CN-3** in acetonitrile obtained by irradiation of **RuNO-3** at the end of the experiment for different wavelengths (365, 400, 455 and 490 nm) and synthetized one.

The crossover points denote the back reaction. They are called isosbestic points when it results in a constant absorption, and they indicated a conversion from one species (reactant) directly to another (product) without observable intermediates.

In the case of **RuNO-3**, the crossover points are identified at wavelengths of 266, 384, 452, and 496 nm. If any of these crossover points deviate from being isosbestic, it would suggest the formation of an intermediate species in the transformation process. On **Figure III-22**, it can be observed that the point at 452 nm is not constant, neither at 384 nor 496 nm, only the absorbance at 266 nm remains perfectly invariant during irradiation.

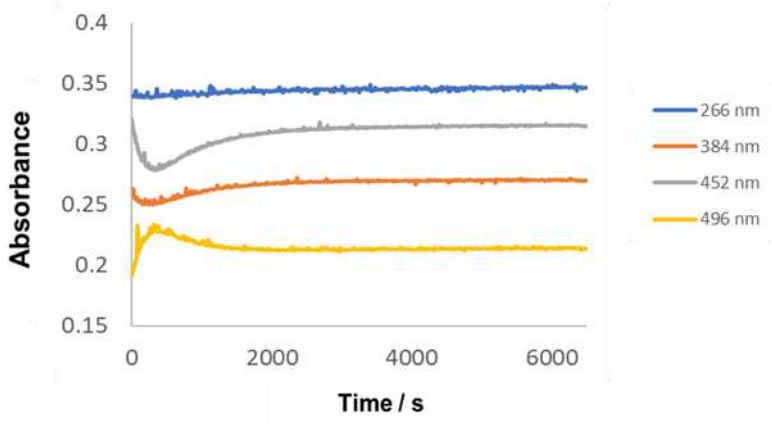

Figure III-22. Kinetics recorded at the crossover points 266, 384, 452 and 496 nm for **RuNO-3** at λ_{irr} = 455 nm.

During the photochemical process, the first step leads to the formation of **B** (**Eq III-32**) **Ru(NO)CH$_3$CN-3**, which then undergoes a further reaction to release the second NO molecule and form **C** (**Eq. III-33**) **RuCH$_3$CN-3**. The specific pattern of the kinetics shows insights into the relative values of the absorption coefficients for the three compounds involved in the process.

$$\underset{\mathbf{A}}{\mathbf{RuNO\text{-}3}} + CH_3CN \xrightarrow{h\nu} \underset{\mathbf{B}}{\mathbf{Ru(NO)CH_3CN\text{-}3}} + NO\bullet \qquad \text{(III-32)}$$

$$\underset{\mathbf{B}}{\mathbf{Ru(NO)CH_3CN\text{-}3}} + CH_3CN \xrightarrow{h\nu} \underset{\mathbf{C}}{\mathbf{RuCH_3CN\text{-}3}} + NO\bullet \qquad \text{(III-33)}$$

Even though the intermediate compound **Ru(NO)CH$_3$CN-3** could not be synthesized (see **Section III-4**), its presence during the irradiation process is clearly observable in the spectral data.

In order to fully describe the photoreaction process, two quantum yields (Φ_A^λ and Φ_B^λ) at the four different irradiation wavelengths, as well as the spectrum of the intermediate (Φ_B^λ), are necessary to get. The solution of the differential equation for a model **A** $\xrightarrow{\Phi_A}$ **B** $\xrightarrow{\Phi_B}$ **C** allowed us to extract this data. Detailed experimental conditions under which these investigations were performed are shown in the **Table III-4**.

Table III-4. Experimental data for the determination of Φ_{NOirr} for the **RuNO-3** in CH_3CN under different irradiation wavelength (λ_{irr}) equal to 490, 455, 400 and 365 nm. The wavelengths of observation (λ_{obs}) are equal to λ_{irr}.

RuNO-3 / (λ_{irr})	**490 nm**	**455 nm**	**400 nm**	**365 nm**
$\Phi_{1\,NO}^{irr}$	0.060	0.0019	0.0019	0.0029
$\Phi_{2\,NO}^{irr}$	0.050	0.040	0.070	0.018
I_0 (mol.L^{-1}.s^{-1}.)	8.68x10^{-6}	6,85x10^{-6}	6,02x10^{-6}	6,35x10^{-6}
[A]$_{initial}$ (mol.L^{-1})	2.05x10^{-5}	3,64x10^{-5}	4,85x10^{-5}	3,98x10^{-5}
[B]$_{initial}$ (mol.L^{-1})	2.05x10^{-5}	3,64x10^{-5}	4,85x10^{-5}	3,98x10^{-5}
ε_A^{irr} (mol.L^{-1}.cm^{-1}.)	25530	36918	27218	33411
$\varepsilon_A^{obs\,1}$ (mol.L^{-1}.cm^{-1}.)	30781	32137	33370	27436
$\varepsilon_A^{obs\,2}$ (mol.L^{-1}.cm^{-1}.)	26782	26713	36827	36840
$\varepsilon_A^{obs\,3}$ (mol.L^{-1}.cm^{-1}.)	36954	25378	27298	27169
ε_C^{irr} (mol.L^{-1}.cm^{-1}.)	34280	37120	19611	49983
$\varepsilon_C^{obs\,1}$ (mol.L^{-1}.cm^{-1}.)	48008	49997	50078	19686
$\varepsilon_C^{obs\,2}$ (mol.L^{-1}.cm^{-1}.)	19627	19924	37511	37744
$\varepsilon_C^{obs\,3}$ (mol.L^{-1}.cm^{-1}.)	35744	36462	36759	36290

The graphics in **Figure III-23** shows that the model curves perfectly fit the experimental data. The parameters are presented in **Table III-5**. These values are coherent with prior observations where the quantum yield consistently decrease as the irradiation wavelength increases for both the reactant and the intermediate. The standard deviation values obtained for ε_B, which were needed to achieve the optimal fit, remain within an acceptable range (roughly 3%) comparable to the experimental variations observed for ε_A and ε_C.

It is observed that at 490 nm, both ϕ_A^λ and ϕ_B^λ display approximately similar values. However, at the wavelengths of 400 nm and 455 nm, ϕ_A^λ remains constant, exhibiting a value of 1.9×10^{-2}. In the case of ϕ_B^λ goes from 0.4×10^{-2} at a wavelength of 455 nm to 0.7×10^{-2} at a wavelength of 400 nm. Finally for irradiation wavelength of 490 nm, the value of ϕ_B^λ is 1.6 times higher than that of ϕ_A^λ. In all these instances $\phi_A^\lambda > \phi_B^\lambda$.

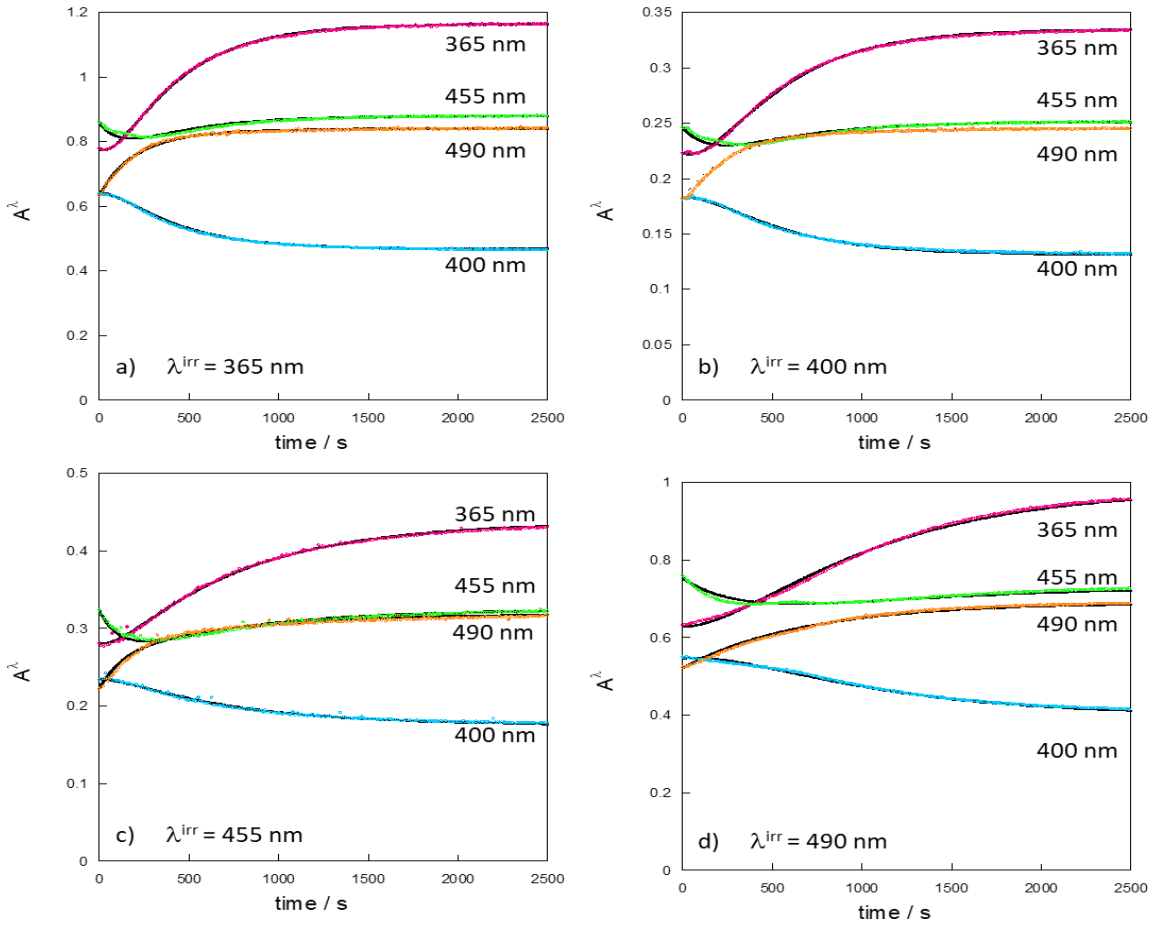

Figure III-23. Kinetic evolution under continuous irradiation at a) λ_{irr} = 365 nm; b) λ_{irr} = 400 nm; c) λ_{irr} = 455 nm; d) λ_{irr} = 490 nm of **RuNO-3**. The coloured symbols represent experimental points at the four wavelengths, whereas the continuous line is derived from the model.

Table III-5. Quantum yields (Φ_A^λ and Φ_B^λ) and absorption coefficient (ε_B^λ) obtained through modeling. Standard deviations were derived from the parameter $\Delta\varepsilon_j^\lambda$ within the model. Experimentally obtained absorption coefficients (ε_A and ε_C) are also included, with provided standard experimental deviations.

λ / nm	ϕ_A^λ	ϕ_B^λ	ε_A/L.mol^{-1}.cm^{-1}	ε_B/L.mol^{-1}.cm^{-1}	ε_C/L.mol^{-1}.cm^{-1}
365 nm	2.9x10^{-2}	1.8x10^{-2}	32400 ± 990	31300 ± 200	49500 ± 800
400 nm	1.9x10^{-2}	0.7x10^{-2}	27000 ± 300	28600 ± 600	37030 ± 300
455 nm	1.9x10^{-2}	0.4x10^{-2}	36900 ± 300	31000± 1000	37030 ± 600
490 nm	6.0x10^{-3}	5.0x10^{-3}	26300 ± 900	32800 ± 1100	35900 ± 800

The model also provides real-time concentrations for the components **A**, **B**, and **C**, which enables us to ascertain the spectrum of B across all wavelengths. In addition, the model helps in determining the concentration of NO•, calculated by the equation [NO•] = $[A]_0$ - [A] + [C]. Notably, the proportion of intermediate B formed during the reaction is substantial in every case.

Relative to the initial concentration of **A**, the peak concentration of **B** increases across the first three irradiation wavelengths, incrementally rising from 46% at 365 nm (**Fig. III-24**). The concentration of NO• produced by the reaction initially surges quickly, then continues to increase during the formation of **C**.

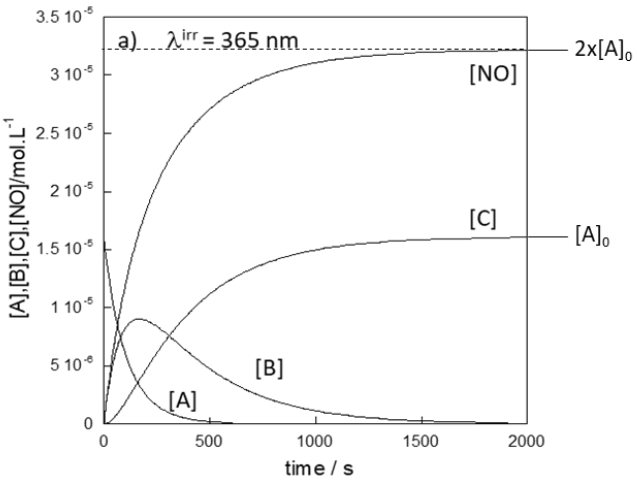

Figure III-24. Real-time evolution of the concentrations of species **A**, **B**, and **C** under λ_{irr} = 365 nm for **RuNO-3**.

III-17. Determination of Nitric Oxide Quantum Yield (Φ_{NO}) for RuNO-4 at Different Wavelengths.

In the experiments conducted at 365, 400, and 455 nm, a single crossover point was found at 494 nm. Analyzing the kinetic data, specifically for irradiation at 400 nm (**Fig. III-25**) , reveals a slight deviation in absorbance. This deviation indicates the presence of an intermediate with $\varepsilon_B^{400} < \varepsilon_A^{400} \approx \varepsilon_C^{\lambda}$. The subtle changes in kinetic curves, primarily observed around the intersection point, might seem insufficient to confirm the intermediate presence. Such dynamics are inconsistent with a simple **A** → **C** process.

Similar to **RuNO-3**, **RuNO-4** requires determining two quantum yields (Φ_A^{λ} and Φ_B^{λ}) and the spectrum of the intermediate. Due to a discrepancy observed at 490 nm, the analyses were focused on the three experiments conducted at 365, 400, and 455 nm.

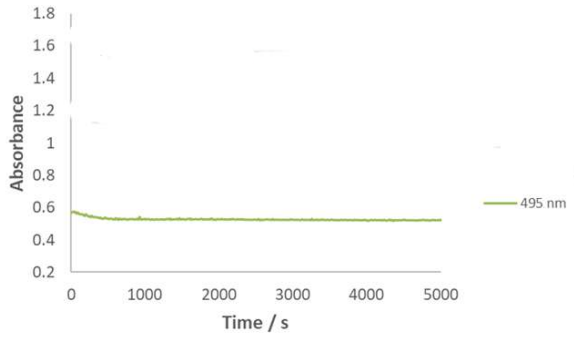

Figure III-25. Kinetics recorded at the crossover point for the irradiation experiment at **λ** = 400 nm for **RuNO-4**.

As for **RuNO-3**, the parameters to be determined are the two quantum yields Φ_A^{λ} and Φ_B^{λ} and the spectrum of the intermediate. For this compound it was possible to only use the three experiments recorded under irradiation at 365, 400 and 455 nm. Indeed, as mentioned before, the crossover point observed at 494 nm for these three experiments is displaced to 488 nm for the irradiation at 490 nm. At that point, it is unknow the origin of such discrepancy, but it clearly appeared that coherent parameters could not be extracted by including this experiment in our set. The origin of this difference is beyond the scope of this study, we have hence only analyzed the experiments performed with the three first irradiation wavelengths. The kinetic

evolution under irradiation at 365, 400 and 455 nm are shown in Figure **III-26** for **RuNO-4**.

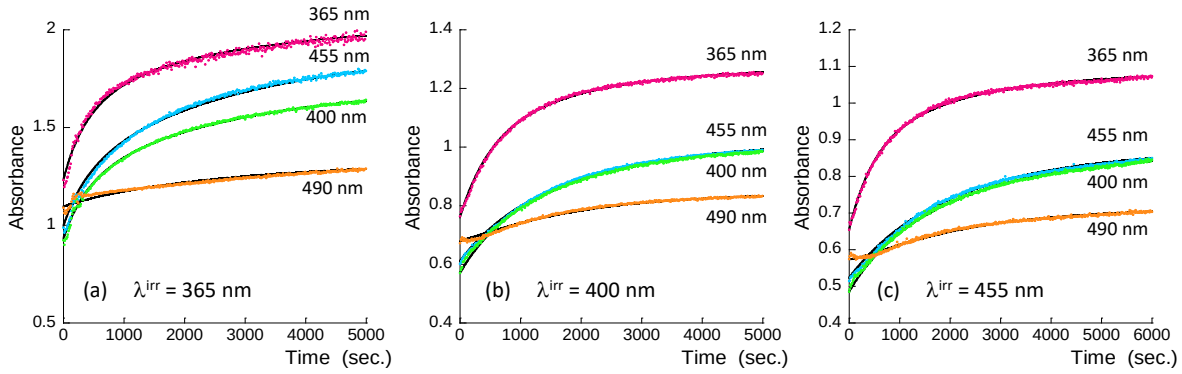

Figure III-26. Kinetic evolution under continuous irradiation at a) λ_{irr} = 365 nm; b) λ_{irr} = 400 nm; c) λ_{irr} = 455 nm; d) λ_{irr} = 490 nm. Dotted lines: **A** $\xrightarrow{h\nu}$ **C** model, solid lines: **A** $\xrightarrow{h\nu}$ **B** $\xrightarrow{h\nu}$ **C.**

The experimental curves align well with the two-step model, and the obtained parameters are detailed in **Table III-6**. Quantum yields decrease with increasing irradiation wavelength for both reactant and intermediate, and $\Phi_A^\lambda > \Phi_B^\lambda$. The standard deviation values for ε_B^λ (approximately 7%) remain consistent with the experimental ones for ε_C^λ.

Table III-6. Quantum yields (Φ_A^λ and Φ_B^λ) and absorption coefficient (ε_B^λ) obtained through modelling.

λ / nm	ϕ_A^λ	ϕ_B^λ	ε_A/L.mol^{-1}.cm^{-1}	ε_B/L.mol^{-1}.cm^{-1}	ε_C/L.mol^{-1}.cm^{-1}
365 nm	1.5×10^{-2}	0.2×10^{-2}	40620 ± 300	57560 ± 2000	67350 ± 800
400 nm	0.8×10^{-2}	0.2×10^{-2}	32550 ± 200	40900 ± 2800	59000 ± 4500
455 nm	0.6×10^{-2}	0.1×10^{-2}	30660 ± 400	40100± 2600	55000 ± 1600

The quantum yields for **RuNO-4** are lower than those for **RuNO-3**, reflecting an extended photoreaction duration. The slow release of NO· lasts about three times longer in this case due to the lower overall reactivity of the compound.

III-18. Determination of Nitric Oxide Quantum Yield (Φ_{NO}) for Ru(NO)CH$_3$CN-5 at Different Wavelengths.

As intermediate **B** for the complex **RuNO-5** was synthetized, it was possible to extract the data experimentally for this intermediate step. As the complex contains only one NO ligand it can be use the simple model **B** $\xrightarrow{\Phi_B}$ **C** as show in the reaction **III-34**. In the **Figure III-27** shows a representative example of the evolution absorption spectra at absorption wavelength of 455 nm, it can be observed a clear isosbestic points at 264, 340, 355, and 486 nm. The **Figure III-28** shows the experimental data and the fitting obtained by the program. Experimental and calculated data are matching perfectly, indicating the accuracy of applying the model **B** $\xrightarrow{\Phi_B}$ **C** to describe the evolution of the reaction under irradiation for intermediate **B**.

$$\text{Ru(NO)CH}_3\text{CN-}\mathit{5} + \text{CH}_3\text{CN} \xrightarrow{h\nu} \text{RuCH}_3\text{CN-5} + \text{NO}\bullet \qquad \text{(III-34)}$$

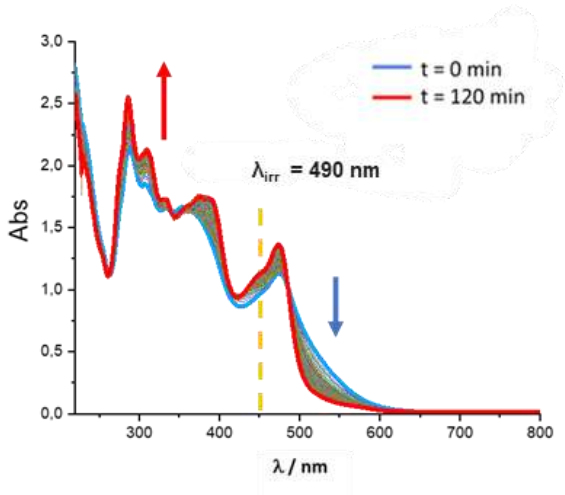

Figure III-27. Evolution of absorption spectra for Ru(NO)CH$_3$CN-5 at λ_{irr} = 455 nm.

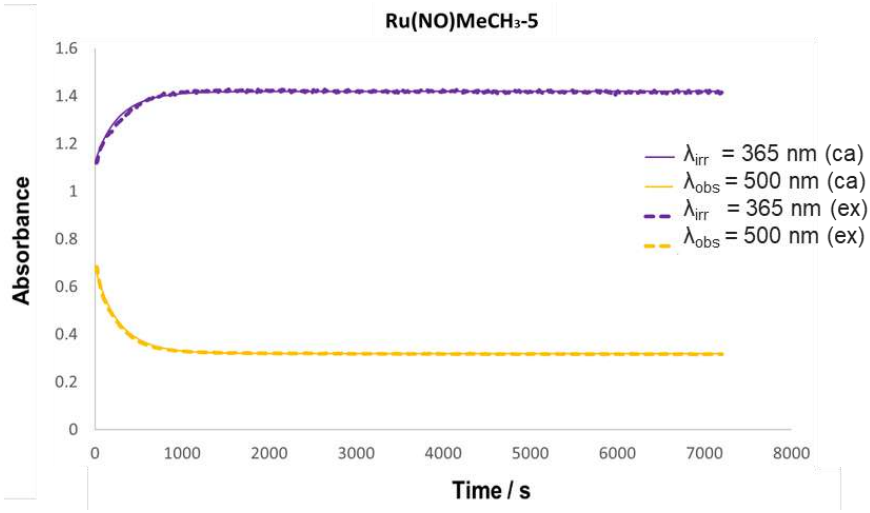

Figure III-28. Experimental (ex) and calculated (ca) evolution of absorbance during irradiation (λ_{irr} = 455 nm) for **Ru(NO)CH₃CN-5**.

The Φ_{NO}^{λ} values are presented at the **Table II-7**. The model shows almost the same tendency that for Φ_{B}^{λ} obtained by calculations for **Ru(NO)CH₃CN-3**, values at 490 and 455 nm are similar or equal, while increasing the energy of the irradiation wavelength the quantum yield increase as well. This data will be useful to determine the missing parameters for the calculation of Φ_{NO}^{λ} for **RuNO-5**.

Table III-7. Quantum yield of NO· for **Ru(NO)CH₃CN-5** at different irradiation wavelengths.

	Φ_{NO}^{365}	Φ_{NO}^{400}	Φ_{NO}^{455}	Φ_{NO}^{490}
Ru(NO)CH₃CN-1	*0.09*	*0.08*	*0.05*	*0.05*

The final spectrum in the irradiation experiments in different wavelengths corresponds to the spectrum obtained by synthesis of the final product C have been probe by superposing the UV-vis spectra for the synthetized **RuCH₃CN-5** as it is show in **Figure III-29.**

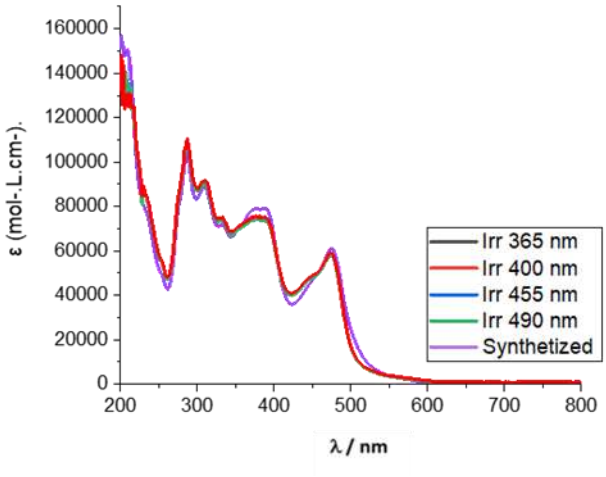

Figure III-29. UV-visible absorption spectra for **RuCH$_3$CN-5** in acetonitrile obtained by irradiation of **Ru(NO)CH$_3$CN-5** at the end of the experiment for different wavelengths (365, 400, 455 and 490 nm) and synthetized one.

III-19. Determination of Nitric Oxide Quantum Yield (Φ_{NO}) for RuNO-5 at Different Wavelengths.

The spectral evolutions for **RuNO-5** were obtained under continuous irradiation during the four distinct experiments conducted at the four irradiation wavelengths as for the other experiments (**Fig. III-30)**.

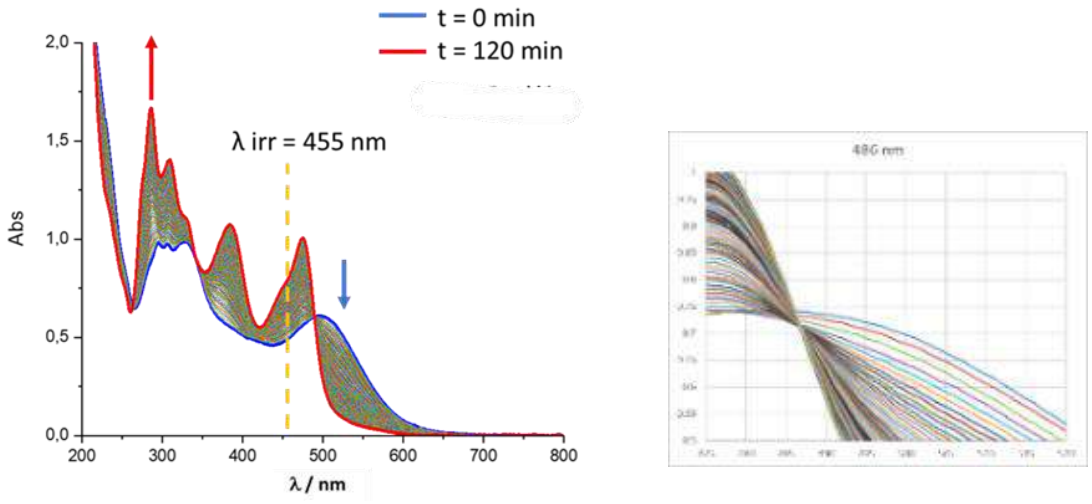

Figure III-30. (a) Evolution of absorption spectra for **RuNO-5** at 455 nm and zooms highlighting the behavior of crossover point at 496 nm.

Applying the same methodology for the **RuNO-5** complex than for **RuNO-3**, the crossover points between the spectra of the reactant and the final product are identified at 264, 338, 352, 414, 430, and 486 nm. When analyzing the kinetics at these wavelengths, we observe nearly horizontal absorbance at 264, 338, and 414 nm. In contrast, 352, 430, and 486 nm show slight deviations (**Fig III-31**). This means that pseudo-isosbestic points could be present, meaning that the intermediate should behave as a mixture of A and C.

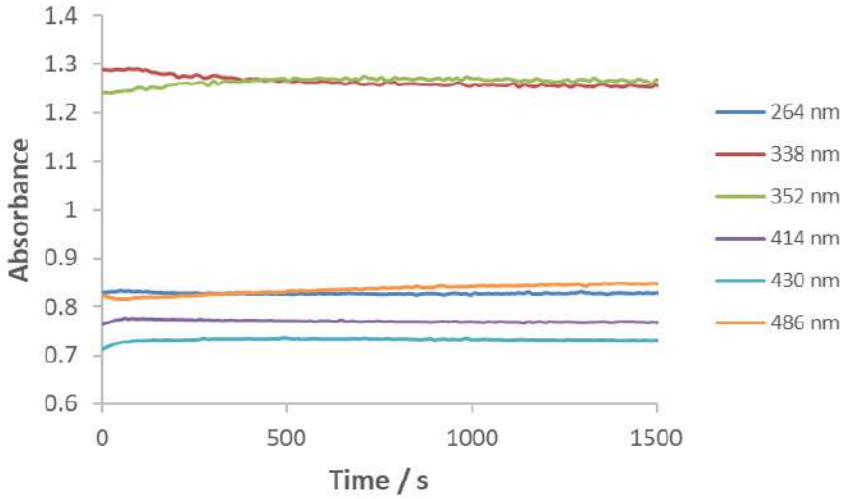

Figure III-31. Kinetics recorded at the crossover point for the irradiation experiment at **λ** = 455 nm for **RuNO-5**.

In the case of **RuNO-3**, the emergence of the intermediate is evident and can be readily discerned in the kinetic shifts observed in **Figure III-22**. For **RuNO-5**, these deviations are less pronounced and become non longer visible once we move further from the crossover points. This apparent isobestic point is due the fact that UV-vis absoprtion spectrum of intermeidate **B** is roghly the average value of the one from **A** and **C** (**Fig. III-32**)

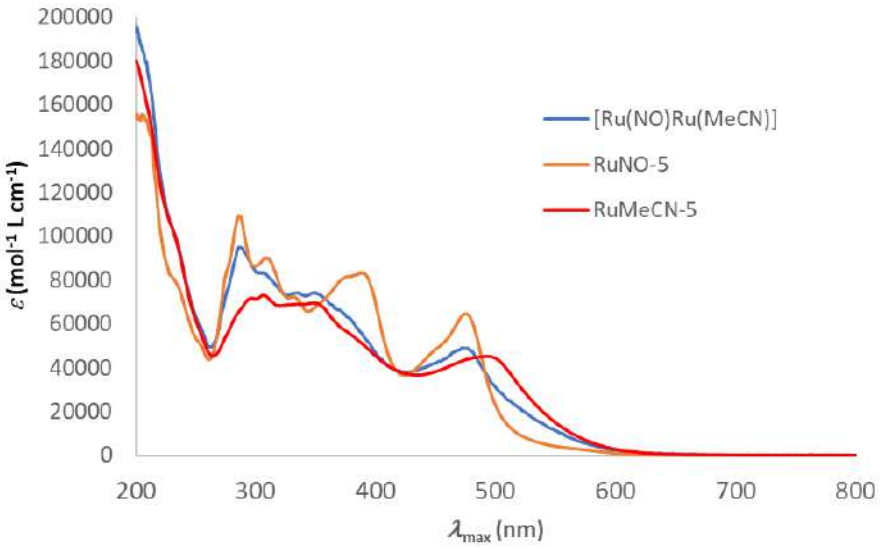

Figure III-32. Comparison of UV-vis spectra for **A**, **B** and **C**.

This analysis probes this bimetallic specie **RuNO-5** is not following a reaction on one step of type **A** $\xrightarrow{h\nu}$ **C**. This does not necessarily indicate a one-step mechanism but the possibility of a very small accumulation of the intermediate for which the quasi-stationary state approximation would then be applicable.

In the context of a mechanism represented by **C**, the only adjustable parameter is Φ_A^λ, with the values of ε_A^λ and ε_C^λ being fixed by the experimental data. Here, the four experiments conducted at different irradiation wavelengths are independent, but the model have to reproduce the absorbances at all four wavelengths using the same Φ_A^λ value. The best fits are shown in **Figure III-33**, the coloured symbols represent experimental points at the four wavelengths; dotted line corresponds to **A** $\xrightarrow{h\nu}$ **C** model that is not matching, whereas the continuous line is derived from the model **A** $\xrightarrow{h\nu}$ **B** $\xrightarrow{h\nu}$ **C.**

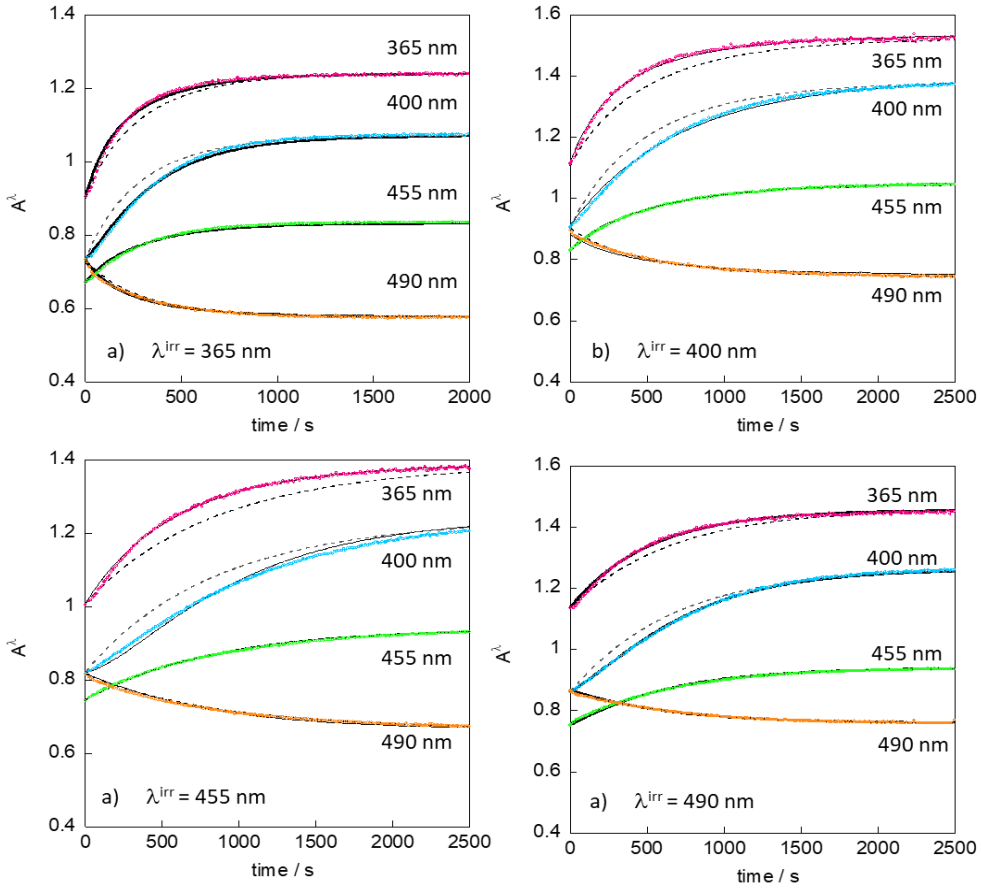

Figure III-33. Kinetic evolution under continuous irradiation at a) λ_{irr} = 365 nm; b) λ_{irr} = 400 nm; c) λ_{irr} = 455 nm; d) λ_{irr} = 490 nm. Dotted lines: **A** $\xrightarrow{h\nu}$ **C** model, solid lines: **A** $\xrightarrow{h\nu}$ **B** $\xrightarrow{h\nu}$ **C.**

It is worth noting that the kinetics at 455 and 490 nm are model really good. However, the kinetics at 365 and 400 nm exhibit notable deviations from the experimental points. The model, therefore, encounters challenges when subjected to multi-wavelength analysis. In order to accurately reproduce the curves, the formation of the intermediate must be taken into consideration.

Applying a fitting procedure to **RuNO-5** like that used for **RuNO-3**, one which could deliver all three parameters, Φ_A^λ, Φ_B^λ, and ε_B^λ, proves challenging given the limited information that can be extracted by the kinetic curves. Preliminary attempts in this direction have resulted in incompatible solutions and ε_B^λ values that significantly deviate from experimental ones. Without additional information, it would be precarious to assert parameter values in this scenario.

Fortunately, a separate examination of the intermediate compound provides two supplementary parameters, Φ_B^λ and ε_B^λ, leaving Φ_A^λ as the only adjustable parameter.

By setting Φ_B^λ and ε_B^λ to previously obtained values, we achieved an excellent fit across all wavelengths and for all four experiments (as represented by the solid line in **Figure III-33**), with results given in **Table III-8**.

The ε_B^λ values reported in **Table III-8** are an average of the results garnered from the fit. The values obtained in the independent study conducted on the intermediate compound fall within the margin of error, which remains within acceptable limits (< 6.8%) across all cases.

Table III-8. Quantum yields (Φ_A^λ and Φ_B^λ) and absorption coefficient (ε_B^λ) obtained through modelling.

λ / nm	ϕ_A^λ	ϕ_B^λ	ε_A/L.mol^{-1}.cm^{-1}	ε_B/L.mol^{-1}.cm^{-1}	ε_C/L.mol^{-1}.cm^{-1}
365 nm	2.8x10^{-2}	0.9x10^{-2}	56800 ± 1100	69 300 ± 1500	76800 ± 600
400 nm	2.2x10^{-2}	0.8x10^{-2}	45400 ± 400	50000 ± 3400	67800 ± 2000
455 nm	0.9x10^{-2}	0.5x10^{-2}	41050 ± 1000	45500 ± 2400	51500 ± 1400
490 nm	0.8x10^{-2}	0.5x10^{-2}	45500 ± 300	41400 ± 2800	37500 ± 1000

III-20. Global Results

In the **Table III-9** is shown the values of Φ_{NO} obtained until now, in the case of the monometallic complexes only one model can be applied, in the case bimetallic complexes values applying the **A→C** were obtained as well at λ_{irr} = 490 nm, as the concentration of **B** has the lowest value among the different wavelength of irradiation, in any case the Φ_{NO} value that should be considered for any further analysis are the one obtained by **A→B→C**. The highest value obtained is for RuNO-5 for ϕ_B^{365} = 0.090 and for the same complex ϕ_A^{455} having the same value. In the first case as $\phi_B^{365} > \phi_A^{365}$ complex B is being consumed to generated **C**, while in the second case there is an accumulation of B as $\phi_A^{455} > \phi_B^{455}$. This behaviour could be interesting for applications in PACT as the velocity rate of NO• liberation can be controlled depending on the irradiation wavelength.

Table III-9. Φ_{NO} in GM under different wavelengths of irradiation in CH_3CN for **RuNO-1-5** complexes.

Complex	Model	365 nm		400 nm		455 nm		490 nm	
RuNO-1	**A→C**	0.0084		0.0062		0.0024		0.0024	
RuNO-2	**A→C**	0.0120		0.0085		0.0068		0.0024	
RuNO-3	**A→C**	-		-		-		0.0039	
	A→B→C	0.029	0.018	0.019	0.070	0.019	0.040	0.006	0.005
RuNO-4	**A→C**	-		-		-		0.0030	
	A→B→C	0.015	0.020	0.080	0.020	0.060	0.10	-	-
RuNO-5	**A→C**	-		-		-		0.0038	
	A→B→C	0.028	0.090	0.022	0.080	0.090	0.050	0.080	0.050

III-21. Conclusions

Throughout this investigative journey, we have deeply explored the photochemistry of **RuNO** complexes. The synthesis of products **$RuCH_3CN$** demonstrates the complete transformation of reactants into final products by irradiation. The presence of isosbestic points highlights the direct conversion from reactant to product, without the formation of observable intermediates. Meaning, **RuNO-1** and **RuNO-2**, fitting with a **A→C** model.

In the case of bimetallic species, fa two-step reaction model, **A→B→C** is more appropriated. The emergence of the intermediate **$Ru(NO)CH_3CN$-3**, though not synthesized, becomes undeniably evident during the irradiation process of **RuNO-3**, further supported by the spectral data. The use of two models enriched our understanding of the photoreaction processes, and allowed for the extraction of quantum yields at varied irradiation wavelengths.

In the case of **RuNO-5**, contrary to **RuNO-4**, it was possible to apply the two steps model thanks to the synthesized **$Ru(NO)CH_3CN$-5**. Its synthesis was a considerable challenge, yet it was tackled effectively through varied strategies. The adoption of the Sonogashira reaction by a multi-step reaction sequence, was both innovative and pragmatic, ensuring the stability of the final product.

CHAPTER IV

Studies of ruthenium nitrosyl complexes in water - Perspectives for in vitro investigations

IV-1. Synthesis of Ruthenium Nitrosyl Complexes for Enhanced *In Vitro* Efficiency

Following the promising outcomes observed with the **RuNO-3** and **RuNO-5** complexes, modifications are necessary for effective *in vitro* testing. Specifically, the bipyridine ligand needs to be substituted. While the incorporation 2,2'-bipyridine, may seem enticing due to its introduction of extra charge transfer pathways in the compound, it is crucial to note a limitation. This type of ruthenium nitrosyl complexes exhibits an undesirable behavior in aqueous environments: the nitrosyl ligand transforms into nitrite, also we may consider that bipyridine derivative compounds are toxic for the cells.[172] Such chemical instability poses significant constraints on the therapeutic potential of these systems. For this reason, the synthesis of **trans,trans-(NO,OH)-Ru(NO)Cl(OH)-3** (called as **trans-Ru(NO)Cl(OH)-3** for this work) is proposed as an alternative (**Fig IV-1**).

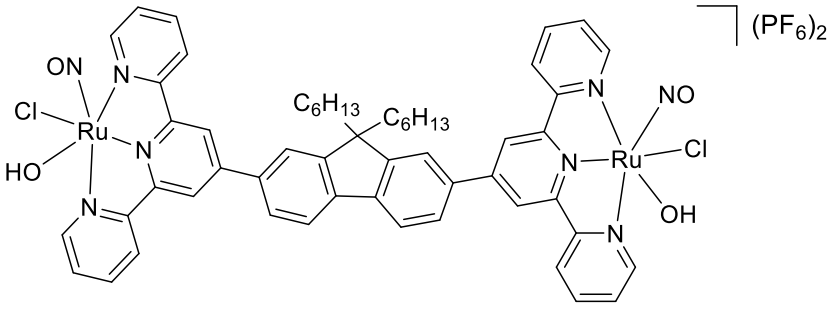

Figure IV-1. Structure of **trans-Ru(NO)Cl(OH)-3.**

The synthesis of **trans-Ru(NO)Cl(OH)-3 (Scheme IV-1)** started by the **[Cl_3Ru(L3)RuCl_3]** complex previously obtained. From this complex, the reaction led to the three geometrical isomers: *cis/cis, trans/trans* and *cis/trans*; the trans/trans being the most favorable. In monometallic complexes is known by our group that the ratio between the *cis* and *trans* isomers are 1/3 and 2/3 respectively. In bimetallic complexes the ratio in which the isomers are obtained are *trans/trans* (4/9), *trans/cis* (4/9) and *cis/cis* (1/9).

The complexes were obtained by bubbling NO gas, obtained through a control reaction of concentrated nitric acid and cupper. The reaction was done on a solution of

N,N-dimethylformamide (DMF). After the evaporation of the solvent, they were separated by alumina column using CH_2Cl_2 and MeOH 95:5 as an eluent. Furthermore, only the **trans, trans-RuCl$_2$NO-3** complex was possible to be isolated.

For the obtention of **trans-Ru(NO)Cl(OH)-3**, the mixture of isomers **RuCl$_2$NO-3** was dissolved in boiling water under argon atmosphere for two days avoiding light exposure, as a second step NH_4PF_6 was added to precipitate the final product. The reaction mixture showed the formation of only one isomer. This corresponds to the **trans-Ru(NO)Cl(OH)-3** complex.

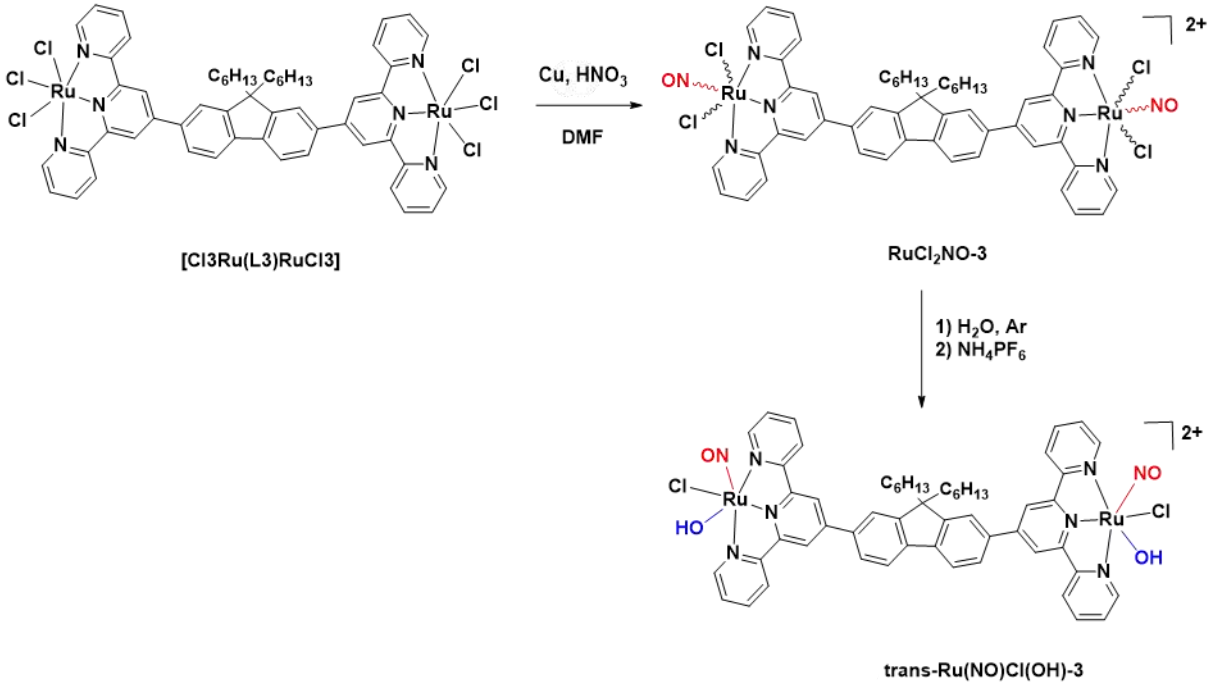

Scheme IV-1. Synthesis route of **trans-Ru(NO)Cl(OH)-3.**

The frequencies of the **ν**(NO) stretching vibration in this type of complexes (1955 and 1924 cm^{-1}) indicate that the degree of the positive charge residue on the coordinated NO is high. Such high values reflect the electrophilic reactivity of the NO group.[173]

IV-2. Characterization of trans,trans-$RuCl_2NO$-3

The identity and purity of the compounds were confirmed using ^{1}H and ^{13}C-NMR, and HRMS with satisfactory results obtained. The ^{1}H-NMR for **trans, trans-$RuCl_2NO$-3** (**Fig. IV-2**) shows 26 protons corresponding to the aromatic region and 26 protons from the aliphatic hexyl chains. The pic located at 9.36-9.38 ppm correspond to the protons near to the chloride ligand in each terpyridine moieties.

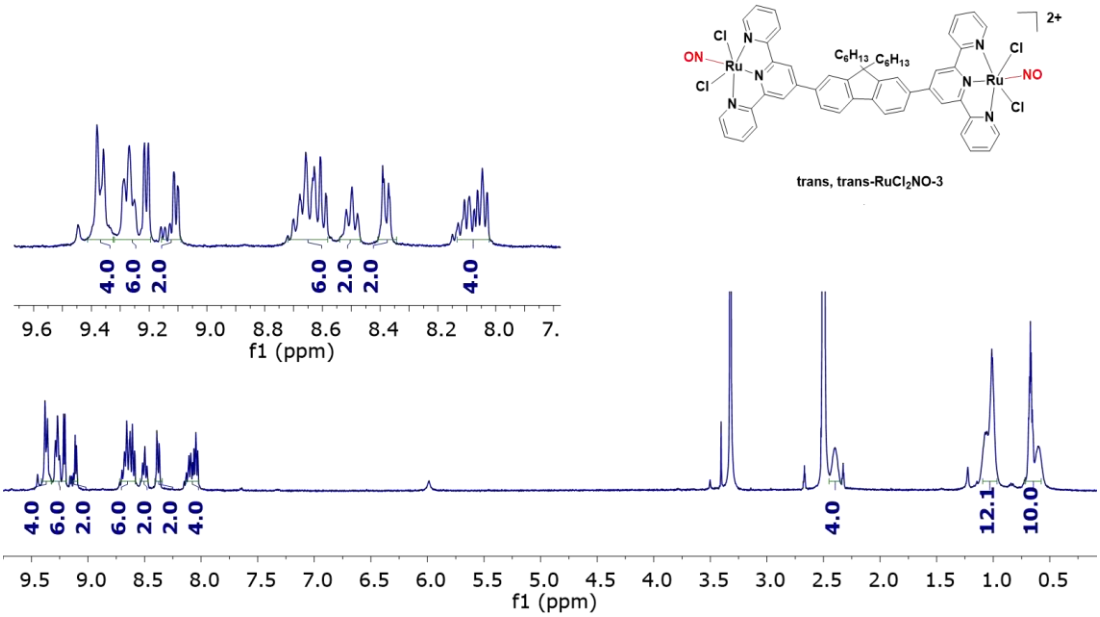

Figure IV-2. ^{1}H-NMR for the **trans, trans-$RuCl_2NO$-3.**

Mass spectrometry displays a single peak with a value of 601.17 corresponding to half the molecular weight of the complex (1200.11), confirming its identity.

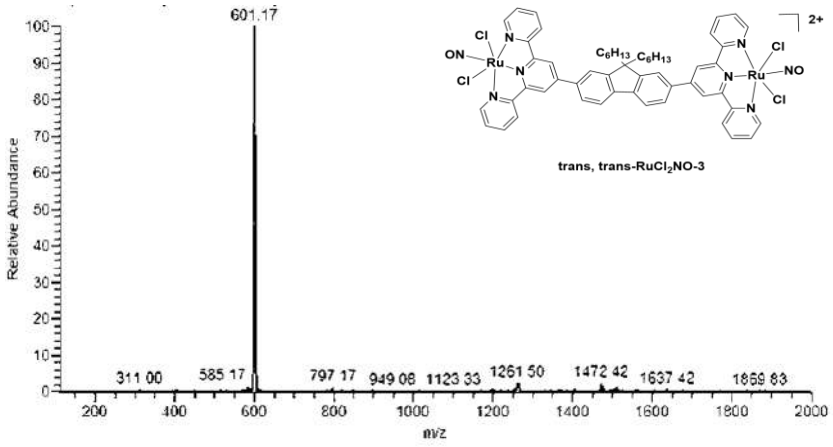

Figure IV-3. MS for **trans, trans-$RuCl_2NO$-3.**

IV-3. Characterization of trans-Ru(NO)Cl(OH)-3

The ^{1}H-NMR for **trans-Ru(NO)Cl(OH)-3** (**Fig. IV-4**) shows 26 protons corresponding to the aromatic region, 2 protons that corresponds to the 2 protons form the ligand -OH, and 26 protons from the aliphatic hexyl chains. HRMS also confirms the identity of the final complex, in which it can be observed the main pic at 582.088 that corresponds to half of the total mass.

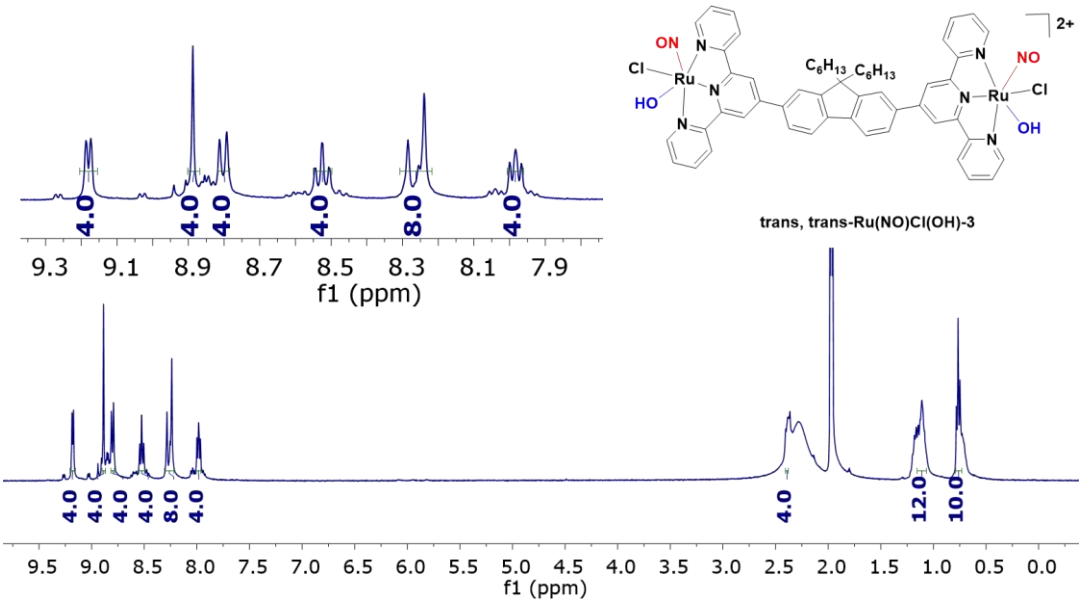

Figure IV-4. ^{1}H-NMR for the **trans-Ru(NO)Cl(OH)-3.**

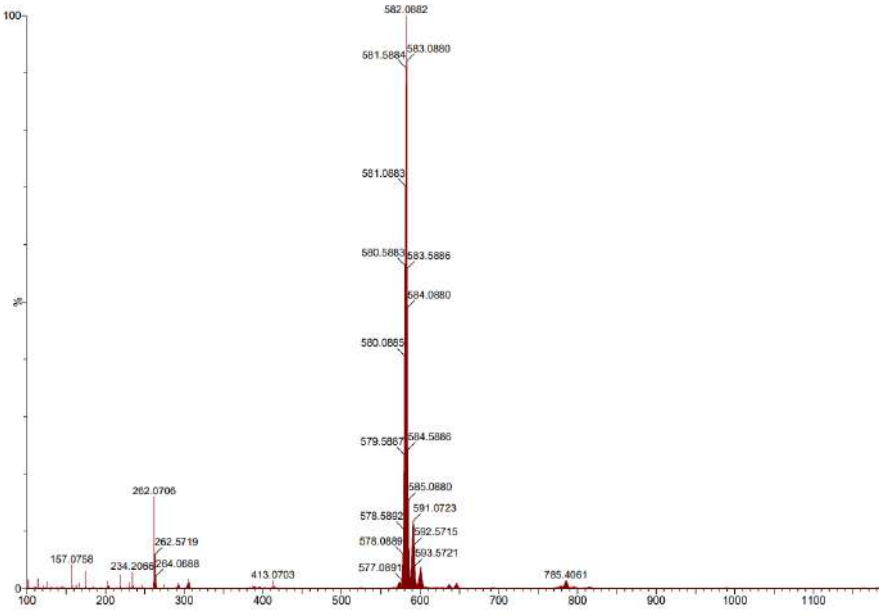

Figure IV-5. HRMS for the **trans-Ru(NO)Cl(OH)-3.**

IV-4. Study of trans, trans-$RuCl_2NO$-3 in the Presence of Water/DMSO (0.5%) by UV-vis

The UV-Vis absorbance monitoring either the complex **trans, trans-$RuCl_2NO$-3,** or **mixture-$RuCl_2NO$-3** in CH_3CN revealed that these solutions remain stable when protected from light for at least 48 hours. A solution of the complex in a 95/5 water/DMSO (0.5%), this quantity of DMSO was chosen as it helps to solubilize the complex and also it is the maximum percentage of DMSO in which is possible to make biological studies.

The experiment had the purpose to study the stability of the complex in the presence of water. The concentration of the solution was not controlled for this experiment since the primary goal is simply to determine whether the complex remains stable under these conditions. The time-dependent UV-Vis absorbance spectra, taken in the absence of light exposure, are shown in **Figure IV-6.**

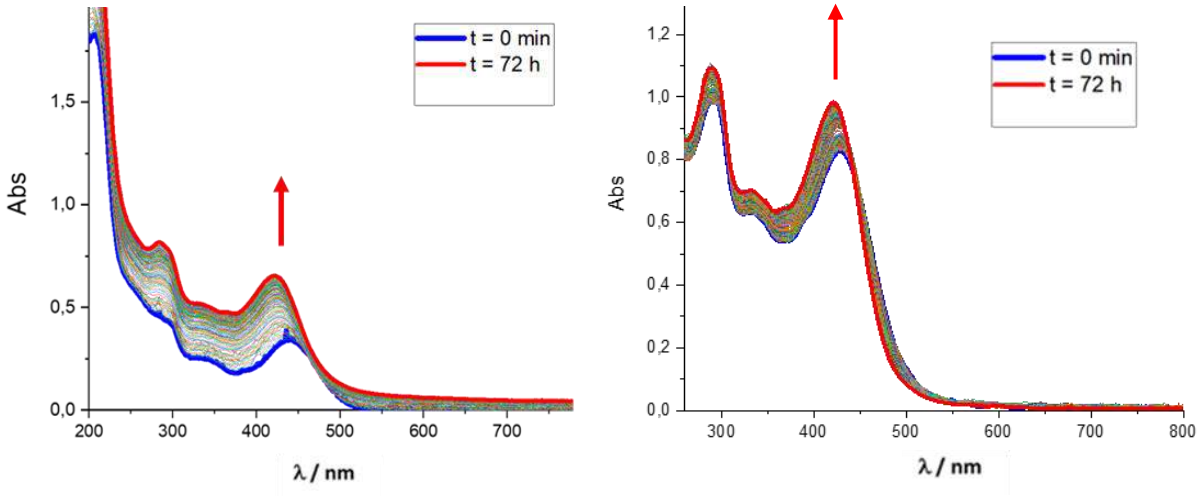

Figure IV-6. Evolution of **mixture-$RuCl_2NO$-3** spectrum (left) and evolution of **trans, trans-$RuCl_2NO$-3** spectrum (right) on water/DMSO solution.

The **Figure IV-6** shows that the complex changes when it is in the presence of water. The maximum absorption at t=0 minutes is located at 430 nm, and the overall shape of the curve varies significantly between 0 and 120 minutes, with the maximum absorption being at 422 nm at the end of the experiment.

As shown in **Figure IV-7,** starting from the **$RuCl_2NO$-3** mixture and the isolated **trans, trans-$RuCl_2NO$-3** it is possible to arrive at the same final product. This was achieved by monitoring the spectral evolution of the samples in water/DMSO. The fact that both samples arrive to the same spectra aligning perfectly, strongly suggests a clean transition to a single isomer (**Scheme IV-2**).

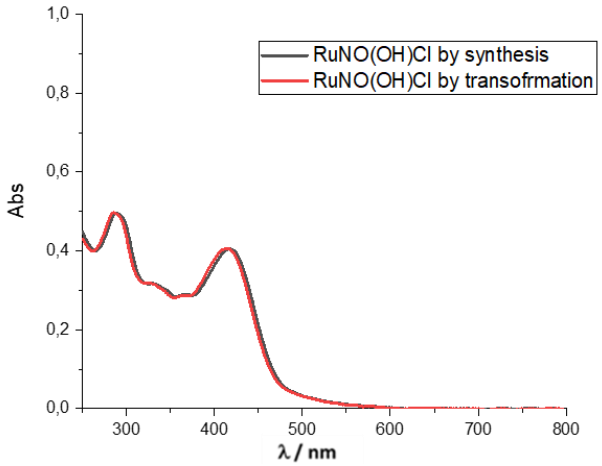

Figure IV-7. UV-visible absorption spectra for **trans-Ru(NO)Cl(OH)-3** in water obtained by transformation of **trans, trans-$RuCl_2NO$-3** and synthetized **trans-Ru(NO)Cl(OH)-3**.

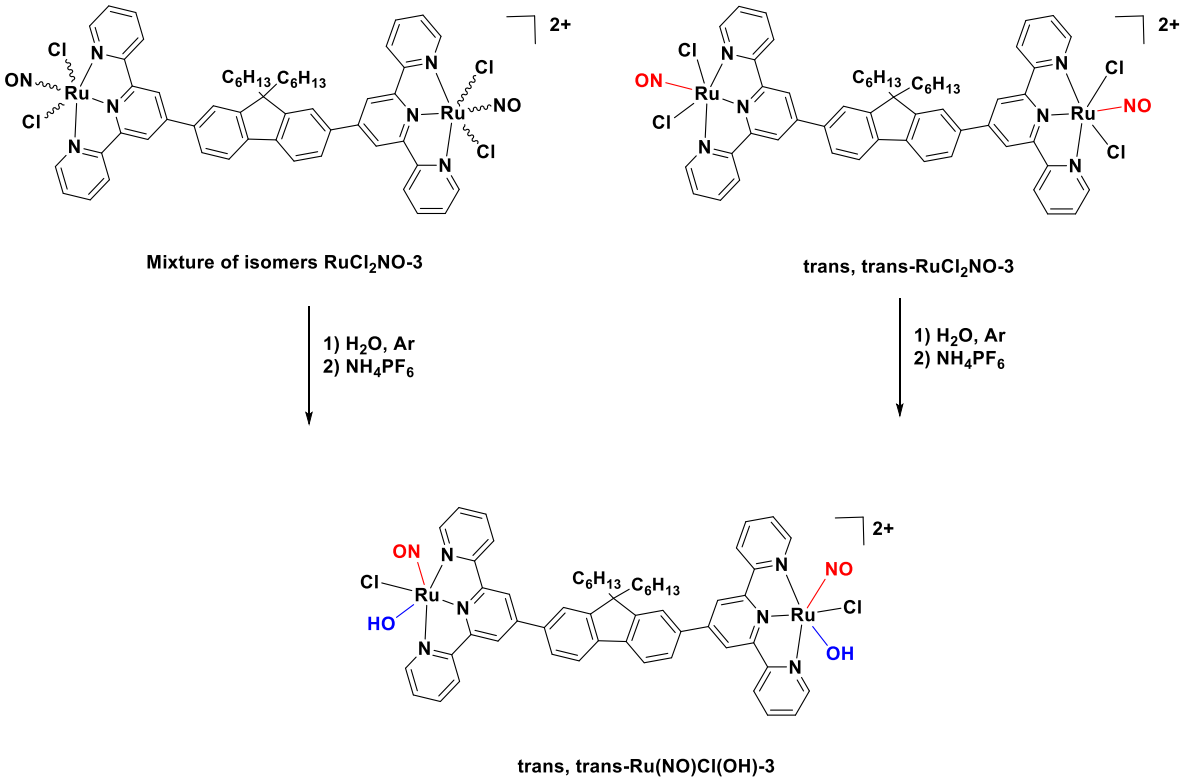

Scheme IV-2. Proposed reactions for the Cl^- to OH^- ligand exchange starting from **mixture-$RuCl_2NO$-3** and from **trans, trans-$RuCl_2NO$-3**.

IV-5. Z-scan Analysis for trans, trans-$RuCl_2NO$-3 and trans-Ru(NO)Cl(OH)-3

To determine the TPA of the ruthenium nitrosyl complexes, the Z-scan technique was used. Since they neither exhibit fluorescence, it was impossible to use the TPEF technique. The methodology employed is the same as the one used in ***Chapter II***.

For this analysis, only the wavelength of 800 nm was used. Although this does not correspond to the maximum observed for a photon in the ruthenium complexes, the maximum absorption wavelength of the band of interest has a value of 440 nm in the case of **trans, trans-$RuCl_2NO$-3,** and 420 nm for **trans-Ru(NO)Cl(OH)-3**. This wavelength is one of the most commonly used in biophotonics applications and is the most frequently used in our research group, allowing for comparisons with other molecules.

The measurements were conducted in acetonitrile, and in water, at a concentration of 10^{-2} M. From this, the value of the nonlinear absorption coefficient and the corresponding value of σ_{TPA} were obtained. The Z-scan results for different energies (36, 51 and 65 nJ) exhibit symmetry around the Z=0 point. As the excitation intensity rises, there is a consistent reduction in transmission, pointing to the presence of a TPA process (**Fig. IV-8**).

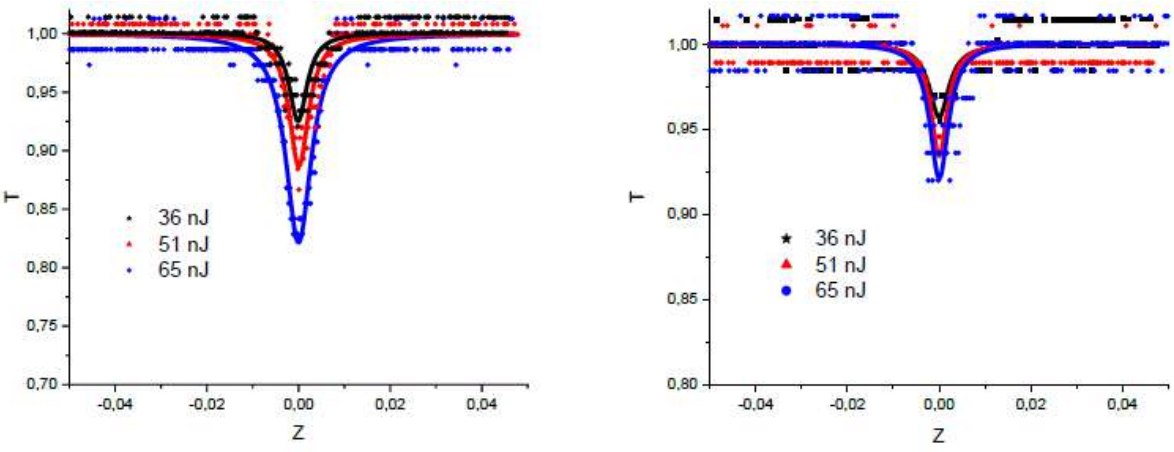

Figure IV-8. Normalized transmission T(Z) in Z-scan experiment at various laser pulse energies for **trans, trans-$RuCl_2NO$-3** (left). **trans, trans- Ru(NO)Cl(OH)-3** (right) at λ_{irr} = 800 nm, C = 1 x 10^{-2} mol.L^{-1}.

As observed in **Table IV-1**, the fluorene-derived compounds have σ_{TPA} values around 169-331 GM, which fall within the range of other compounds already studied. Due to the uncertainty values, it can be concluded that both molecules fall within the same magnitude range, and the exchange of a chloride ligand for a hydroxyl does not really affect the σ_{TPA} value. In terms of the solvent, it can be seen that the σ_{TPA} value relatively decreases in water, with the factor dropping by 1.8 in both cases. It is evident that in all cases, the value is less than that for the compound with bipyridine (**RuNO-3**, **Fig. IV-6**), but is still important.

Table IV-1. σ_{TPA} in GM for **trans, trans-$RuCl_2NO$-3** and **trans, trans- Ru(NO)Cl(OH)-3** recorded at 800 nm.

Solvent	**H_2O**		**CH_3CN**	
Complex	**$RuCl_2NO$-3**	**Ru(NO)Cl(OH)-3**	**$RuCl_2NO$-3**	**Ru(NO)Cl(OH)-3**
σ_{TPA}	169 ± 44	188 ± 54	301 ± 66	331 ± 63

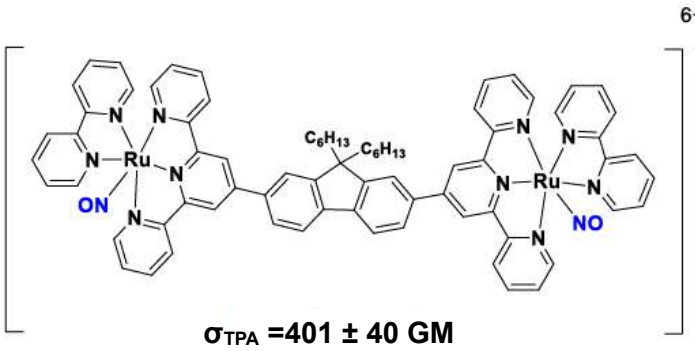

σ_{TPA} =401 ± 40 GM

Figure IV-6. RuNO-3 whit its respective σ_{TPA} value.

IV-6. NO• Release Capabilities of trans-Ru(NO)Cl(OH)-3

For **trans-Ru(NO)Cl(OH)-3** and **trans,trans-RuCl$_2$NO-3** the release of NO• is confirmed through the Griess test. This test identifies the formation of an azo dye, which exhibits a pronounced absorption at λ= 548 nm. This dye forms when NO_2^- (the oxidized form of NO•) reacts in situ with sulfanilic acid. The **Figure IV-9** shows a clean conversion.

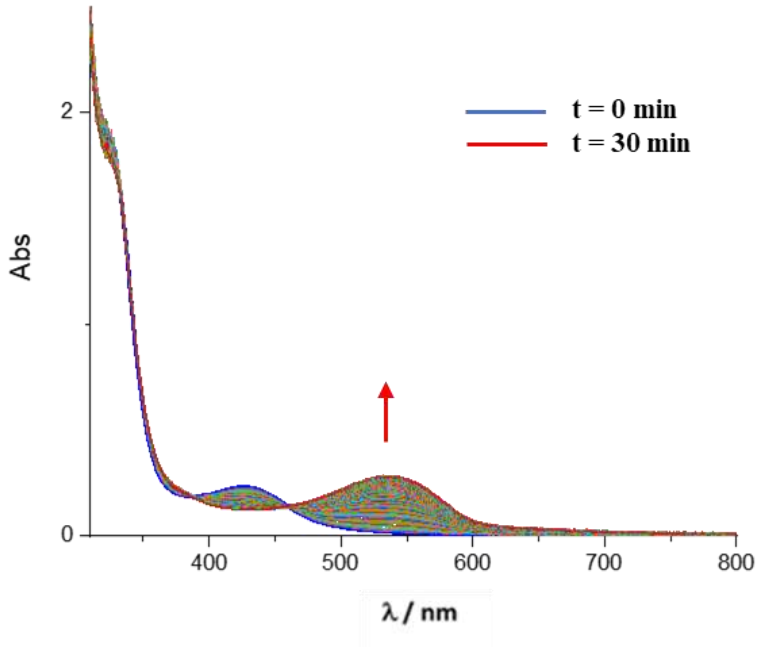

Figure IV-9. The evolution of the electronic spectrum of **trans-Ru(NO)Cl(OH)-3** shows the formation of the azo dye in a mixture under irradiation at λ= 365 nm.

IV-7. Irradiation at 365 nm of mixture-$RuCl_2NO$-3 in CH_3CN

As previously highlighted, **$RuCl_2NO$-3** demonstrates stability in CH_3CN. To examine the complex behavior under irradiation, a sample solution was exposed to 365 nm light. The results reveal a pseudo-isosbestic point, suggesting the formation of a singular end product (**Fig. IV-10**). This may indicate the creation of the **trans-Ru(OH)Cl(CH_3CN)-3** as a final product. After fitting the experimental values with the one obtained by the logiciel program, it can be observed that the model **A**→**C** model can partially fit (Φ_{NO} = 0.012), meaning that the formation of **B** is negligeable.

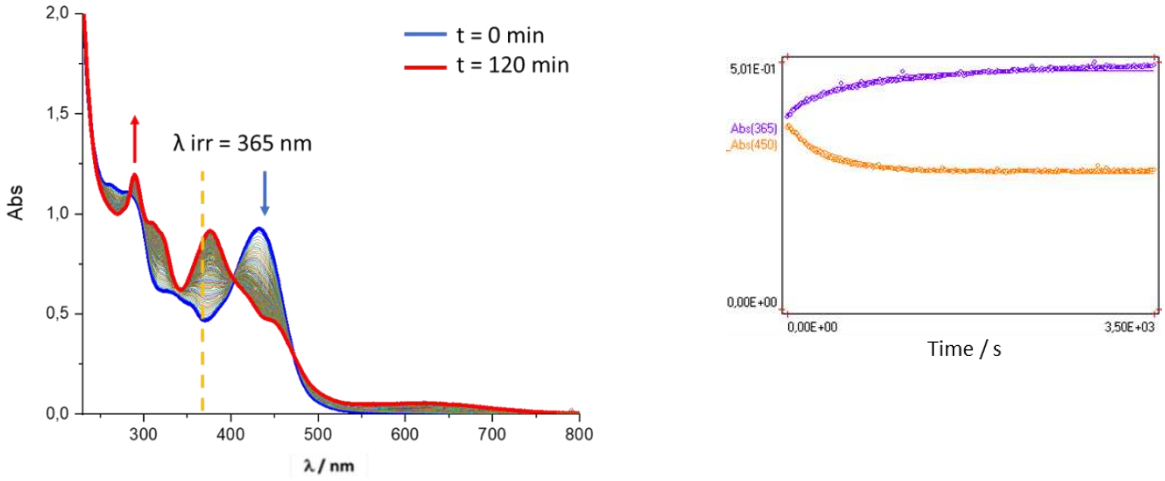

Figure IV-10. Evolution of **mixture-$RuCl_2NO$-3** in CH_3CN under λ_{irr} = 365 nm (left). Experimental and calculated evolution of absorbance during irradiation (right).

The proposal reaction during irradiation is show in the **Scheme IV-3** in which the two NO• were liberated and exchanged for two acetonitrile, for this moment the intermediate state remains unclear and requires further investigation.

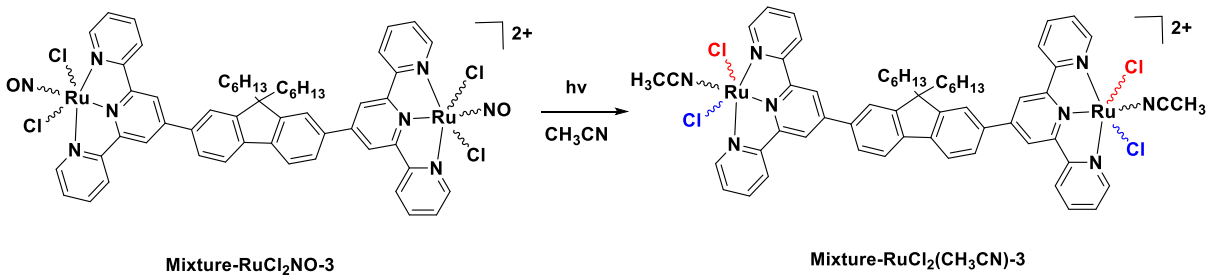

Scheme IV-3. Proposed reaction for ligand exchange after irradiation at 365 nm of **mixture-$RuCl_2$(NO)-3**.

IV-8. Photokinetic of trans-Ru(NO)Cl(OH)-3 under 365 nm irradiation in CH_3CN

The results from water irradiation aligned well with the **A→C** model. Given that CH_3CN is one of the solvents used in the Z-scan experiments, we decided to conduct the same irradiation in this solvent. In this context, the curves intersect at five distinct points: 249, 282, 300, 386, and 447 nm (**Fig. IV-11**). When analyzing the kinetics at these wavelengths (**Fig. IV-12**), we observe only one horizontal absorbance at 249 nm. In contrast, the rest show important deviations. This suggests that the **A→C** model may not be applicable here, leaving open the possibility of the presence of an intermediate.

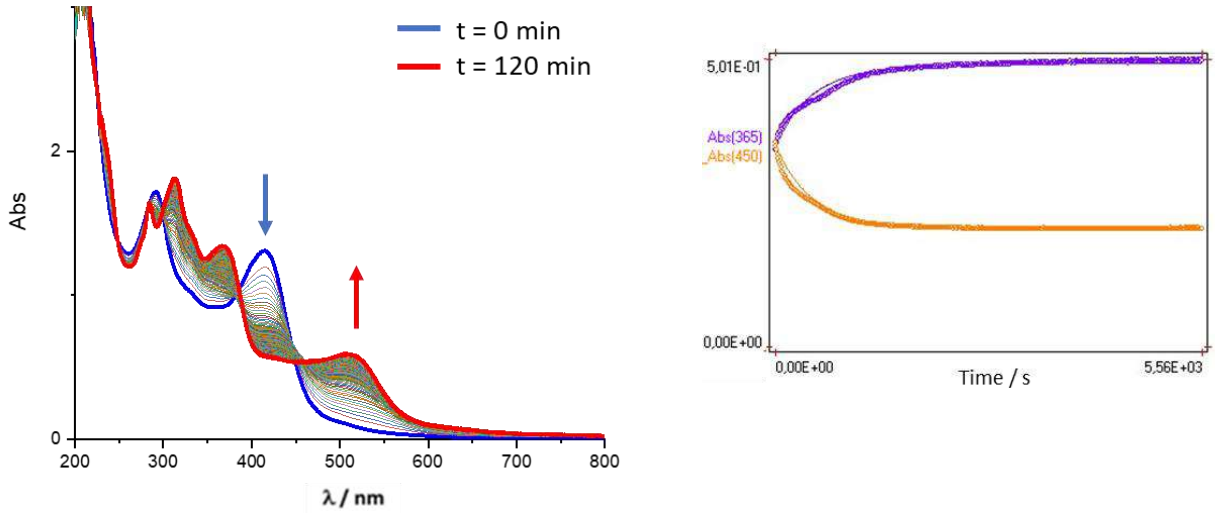

Figure IV-11. Evolution of **trans-Ru(NO)Cl(OH)-3** in CH_3CN under λ_{irr} = 365 nm (left). Experimental and calculated evolution of absorbance during irradiation (λ_{irr} = 365 nm) (right).

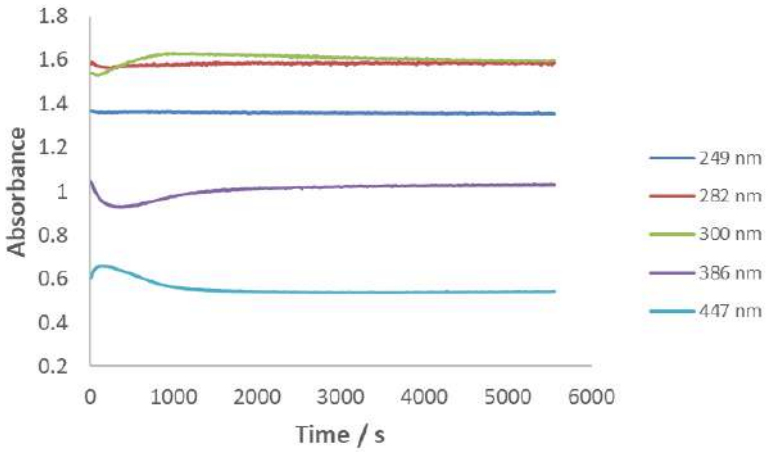

Figure IV-12. Kinetics recorded at the crossover point for the irradiation experiment at **λ** = 365 nm for **trans-Ru(NO)Cl(OH)-3** in CH_3CN.

IV-9. Photokinetic of trans-Ru(NO)Cl(OH)-3 under 365 nm irradiation in H_2O/DMSO (0.5%)

After irradiation of the sample at 365 nm, it can be observed the curves intersect at three isosbestic points, at 286 nm, 377 and 451 nm, representing the equilibrium between the complex trans **trans-Ru(NO)Cl(OH)-3** and its product. The band at 422 nm disappears, and a new band emerges at 444 nm, as depicted in **Figure IV-13**.

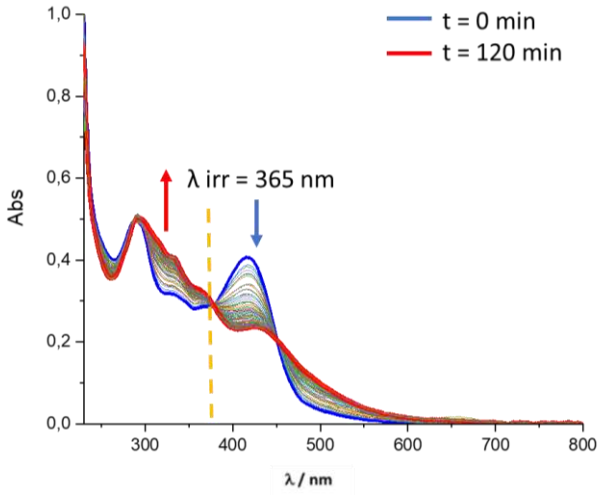

Figure IV-13. Evolution of **trans-Ru(NO)Cl(OH)-3** spectrum on water/DMSO solution.

Another experiment was tested, as for the previous one, a sample of **mixture-$RuCl_2NO$-3** was left for three days to assure the entire transformation into **trans, trans-$RuCl_2NO$-3**, after that the sample was irradiated at 365 nm wavelength, the **Figure IV-14** shows the evolution. Both experiments show the same final UV-vis spectra.

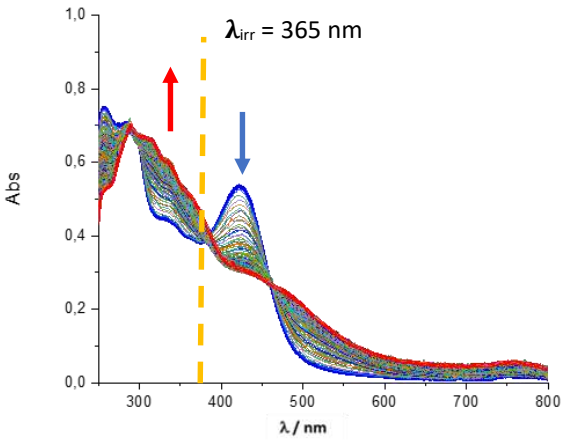

Figure IV-14. Evolution of **mixture-$RuCl_2NO$-3** in water after 3 days and subsequent irradiation at λ_{irr} = 365 nm.

Assuming that a model **A**→**C** fits the reaction mechanism then the proposal looks as follow in the **Scheme IV-4**:

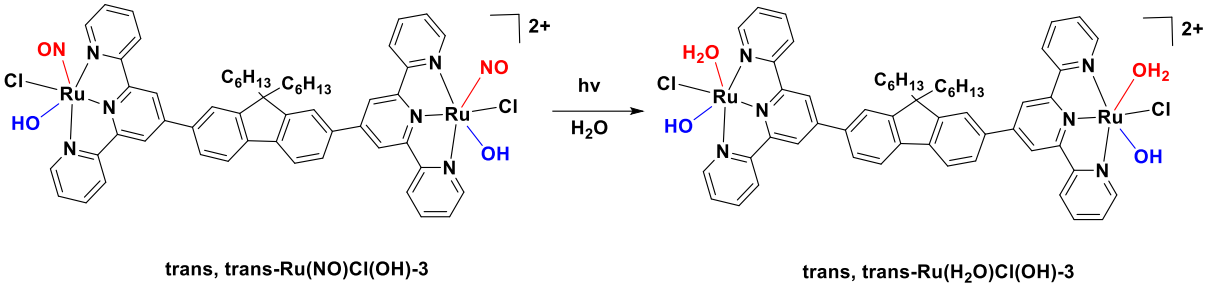

Scheme IV-4. Proposed reaction for ligand exchange after irradiation at 365 nm of **trans, trans-Ru(NO)Cl(OH)-3** in H_2O. .

The quantum yield, Φ_{NO}, can be obtained from the progression of absorbance at the irradiation wavelength and a second observation wavelength, just as it was explained in the **Chapter III**. In **Figure IV-15**, the experimental curves are drawn with dashed lines, and the curves resulting from solving the differential equation that relates the evolution of concentration in **A** to the quantum yield are drawn with solid lines, for both irradiation wavelengths. The obtained Φ_{NO} = 0.022.

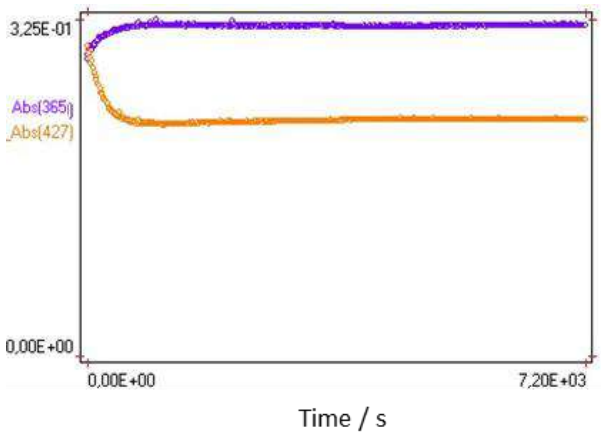

Figure IV-15. Experimental and calculated evolution of absorbance during irradiation (λ_{irr} = 365 nm) for **trans-Ru(NO)Cl(OH)-3**.

IV-10. Conclusions

The results observed with the **RuNO-3** and **RuNO-5** complexes underscore the need for modifications in the bipyridine ligand in order to conduct in vitro tests. Despite the appeal of the charge transfer pathways of 2,2'-bipyridine, these ruthenium nitrosyl complexes can convert the nitrosyl ligand into nitrite in aqueous environments and may be toxic to cells. Therefore, the synthesis of the **trans-Ru(NO)Cl(OH)-n** series appears to be a promising alternative as **trans-Ru(NO)Cl(OH)-3** shows high σ_{TPA} values and high Φ_{NO} values as well.

FINAL CONCLUSION AND PERSPECTIVE

Final Conclusion

This study focused into the exploration of chemical strategies to enhance the effectiveness of a promising modern cancer therapy: photoactivated chemotherapy via nitric oxide (NO•) release (PACT). Born out of the need to provide more selective cancer treatments that can reduce collateral damage to healthy tissues, a common drawback of conventional chemotherapies and radiotherapies, PACT is emerging as a promising approach.

The potential of the photoinduced release of NO• in PACT to induce tumor cell death is notable, particularly given the inherent sensitivity of human cells to this radical. However, its practical application often confronts challenges associated with release efficiency. To overpass this cause, this work centered on designing and synthesizing Ru^{II} nitrosyl complexes (**RuNO**) with fluorene-substituted ligands. With the precise control of NO• release using light, these compounds stand as strong candidates for future therapeutic applications in the realm of PACT.

Lastly, in the pursuit of heightened TPA responses, certain **RuNO** complexes were designed with either a dipolar (monometallic) or quadrupolar (bimetallic) architecture. The Z-Scan technique, adopted in the absence of strong photoluminescence signals from **RuNO** complexes, indicated varying two-photon absorption cross-section values across the series, depending on the complex and incident wavelength.

While our initial endeavors revolved around monometallic species that exhibited σ_{TPA} values in the ballpark of 100 GM, the shift towards bimetallic species ushered in a transformative phase, culminating in remarkable σ_{TPA} values surpassing 1500 GM. To contextualize, such TPA responses is one of the most effective TPA materials known to date. Crucially, they align with the therapeutic window of transparency, opening doors to potential applications as NO• donors in biological contexts.

However, the extensive investigation into **RuNO** complexes, undertaken in this research, sought to illuminate their potential in PACT. The presence of NO• during photolysis was confirmed using electron paramagnetic resonance (RPE), with a discernible generation of NO• only under irradiation for specific RuNO complexes. The

Griess test, which capitalized on the formation of an azo dye, further evidenced the production and subsequent oxidation of NO• in the solution.

A pivotal wavelength of 490 nm was identified for the photodissociation of these complexes, based on its significant absorption. Monometallic complexes showcased straightforward photolysis, aligning with the A →C photokinetic model, while the bimetallic counterparts exhibited a more intricate A→B→C photodissociation. The successful synthesis of final products, especially for the **Ru(NO)CH_3CN-5** complex, using a multi-step reaction sequence underlined the nuanced approach to the creation of these molecules.

By leveraging a computational method, the quantum yield of nitric oxide (ΦNO) across these complexes was determined. The quantum yields varied, reinforcing the idea of different dissociation pathways for mono and bimetallic complexes, with distinct absorption spectra changes before and after irradiation.

Besides, the complex **trans-Ru(NO)Cl(OH)-3** offers a possibility to be tested for its potential microbicidal activity on *Staphylococcus aureus* Gram(+) or *Pseudomonas aeruginosa* Gram (-) bacteria, work are in progress (collaboration).

In sum, this study offers a profound insight into the behavior and potential of ruthenium nitrosyl complexes, marking a significant stride towards their utilization in photoactivated therapeutic applications. Future work may delve deeper into optimizing the properties of these complexes and evaluating their potential in medical applications.

Perspectives.

Throughout this research, we have searched deeply into the understatement and intricacies of ligand design, specifically focusing on dipolar and quadripolar architectures. The exchange of bipyridine to a chlorido and a hydroxyl moiety not only represents an innovative approach, but it can also reach in a series of promising implications for future biological applications. One cannot overstate the significance of this modification: the introduction of the hydroxyl group can enhance water solubility and the potential for bioconjugation and bring stability to the complexes.

Yet, while venturing into these modifications, the preservation of the original ligand structure remains paramount. By maintaining this structural backbone, we have witnessed an enhancement in the TPA response for structures as **RuNO-3** and **RuNO-5**. This improved TPA response, combined with the ligands modified functionality, can open the doors to advanced applications, such as PACT, and other areas where TPA properties are sought after. In any case, the synthesis and analyses of the whole series can arise to an interesting investigation (**Fig. P.1** and **P.2**)

As of now, the analyses presented in this thesis represent our current understanding and progress in TPA and photokinetic. However, it is important to note that this research is an ongoing endeavor. We anticipate further investigations and deeper insights in the future, building upon the foundation laid here.

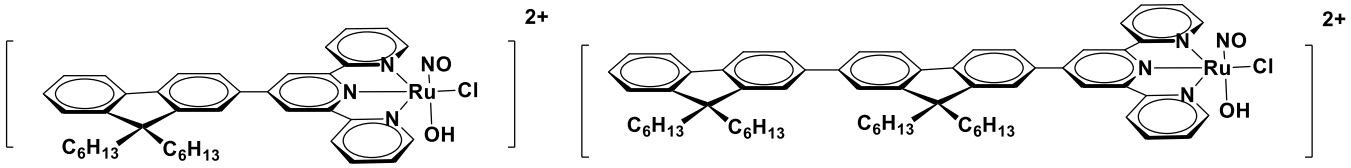

trans-Ru(NO)OH-1

trans-Ru(NO)OH-2

Figures P.1. Structure of monometallic complexes for further investigation on biological media.

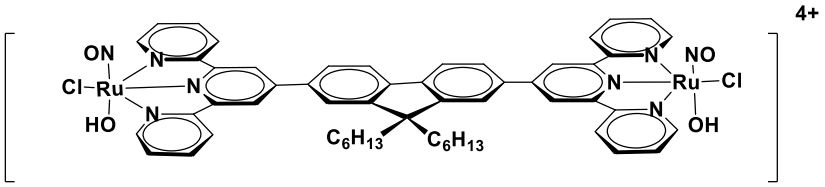

trans, trans-Ru(NO)OH-3

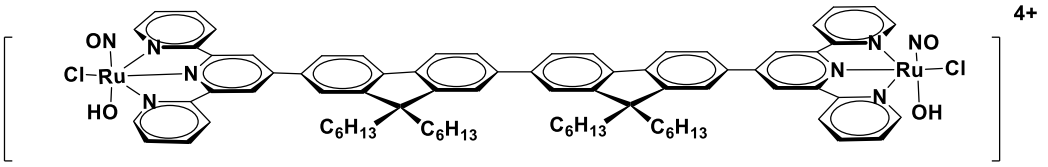

trans, trans-Ru(NO)OH-4

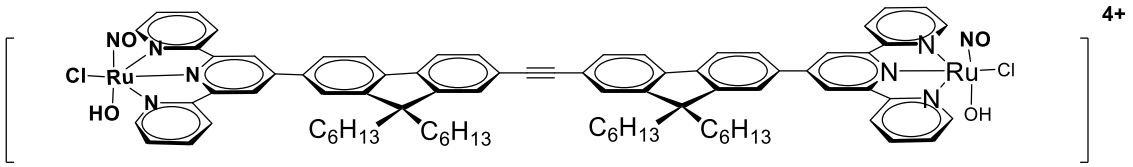

trans, trans-Ru(NO)OH-5

Fig. P.2. Structure of bimetallic complexes for further investigation on biological media.

Appendix

Appendix 1:

Chemical products and equipment

List of reactants and solvents:

[1,1′-Bis(diphenylphosphino)ferrocene]dichloropalladium(II), complex with dichloromethane, $C_{35}H_{30}Cl_4FeP_2Pd$, Sigma-Aldrich, CAS: 95464-05-4

1-Bromohexane, $CH_3(CH_2)_5Br$, Alfa-Aesar, CAS: 111-25-1

2,7-Dibromofluorene, $C_{13}H_8Br_2$, Sigma-Aldrich, CAS: 16433-88-8

2,2'-bipyridine, $C_{10}H_8N_2$, Alfa-Aesar, CAS: 366-18-7

2-acetylpyridine, C_7H_7NO, Alfa-Aesar, CAS: 1122-62-9

Absolute ethanol, C_2H_6O, VWR Chemicals, CAS: 64-17-5

Acetone, CH_3COCH_3, Carlo Alba Reagents, CAS: 67-64-1

Acetonitrile, C_2H_3N, Carlo Alba Reagents, CAS: 75-05-8

Acid acetic glacial, CH_3COOH, Carlo Alba Reagents, CAS: 64-19-7

Ammonium acetate, $C_2H_7NO_2$, Sigma-Aldrich, CAS: 631-61-8

Ammonium hexaflurophosphate, NH_4PF_6, Thermo Scientific, CAS: 16941-11-0

Bis(triphenylphosphine)palladium(II) dichloride, $[(C_6H_5)_3P]_2PdCl_2$, Sigma-Aldrich, CAS: 13965-03-2

Bis(pinacolato)diboron, $C_{12}H_{24}B_2O_4$, Sigma-Aldrich, CAS: 73183-34-3

Chlorhydric acid (37 %), HCl, VWR Chemicals, CAS: 7647-01-0

Cupper, Cu, Sigma-Aldrich, CAS: 7440-50-8

Copper(I) iodide, CuI, Thermo Scientific, CAS: 7681-65-4

Deuterated acetonitrile, CD_3CN, Eurisotop, CAS: 2206-26-0

Deuterated chloroform, $CDCl_3$, Eurisotop, CAS: 865-49-6

Deuterated dimethylformamide, CD_3CNOCD_3, Eurisotop, CAS: 4472-47-7

Deuterated dimethylsulfoxide, C_2D_6OS, Eurisotop, CAS: 2206-27-1

Deuterated methanol, CD_3OD, Eurisotop, CAS: 811-98-3

Deuterated methylene chloride, CD_2Cl_2, Eurisotop, CAS: 1665-00-5

Dichloromethane, CH_2Cl_2, VWR Chemicals, CAS: 75-09-2

Diethyl ether, $C_4H_{10}O$, VWR Chemicals, CAS: 60-29-7

Diiodo, I_2, Thermo Scientific, CAS: 7553-56-2

Dimethylsulfoxide, C_2H_7NO, Carlo Alba Reagents, CAS: 67-68-5

Ethanol (96%), C_2H_6O, VWR Chemicals, CAS: 64-17-5

Ethyl acetate, $C_4H_8O_2$, VWR Chemicals, CAS: 141-78-6

Fluorene, $C_{13}H_{10}$, Alfa-Aesar, CAS: 1133-80-8

Hexane, C_6H_{14}, VWR Chemicals, CAS: 110-54-3

Iodomethane, CH_3I, Sigma-Aldrich, CAS: 74-88-4

L (+) ascorbic acid, $C_6H_8O_6$, Merck, CAS: 50-81-7

Lithium cloride, LiCl, Thermo Scientific, CAS: 7447-41-8

Methanol, CH_4O, VWR Chemicals, CAS: 67-56-1

N, N-Dimethylformamide, C_3H_7NO, Carlo Alba Reagents, CAS: 68-12-2

N-butyllithium solution (2.5 M in hexanes), C_4H_9Li, Sigma-Aldrich, CAS: 109-72-8

Nitric acid (65 %), HNO_3, Carlo Alba Reagents, CAS: 7697-37-2

Pentane, C_5H_{12}, VWR Chemicals, CAS: 109-66-0

Periodic acid, H_5IO_6, Sigma-Aldrich, CAS: 10450-60-9

Potassium acetate, CH_3CO_2K, Alfa-Aesar, CAS: 127-08-2

Potassium carbonate, K_2CO_3, Sigma-Aldrich, CAS: 584-08-7

Potassium hydroxide, KOH, Sigma-Aldrich, CAS: 1310-58-3

Pyridine, C_5H_5N, Prolabo, CAS: 110-86-1

Ruthenium chloride, $RuCl_3.xH_2O$, Strem Chemicals, CAS: 14898-67-0

Sodium Bicarbonate, $NaHCO_3$, Prolabo, CAS: 144-55-8

Sodium hydroxide, NaOH, Sigma-Aldrich, CAS: 1310-73-2

Sodium nitrite, $NaNO_2$, Fluka, CAS: 7632-00-0

Sulfuric acid (98%), H_2SO_4, Carlo Alba Reagents, CAS: 7664-93-9

Tetrabutylammonium bromide, $C_{16}H_{36}BrN$, Sigma-Aldrich, CAS: 1643-19-2

Tetraethylammonium bromide, $(C_2H_5)_4N(Br)$, Sigma-Aldrich, CAS: 71-91-0

Tetrahydrofurane, C_4H_8O, VWR Chemicals, CAS: 109-99-9

Trimethylsilylacetylene, $(CH_3)_3SiC{\equiv}CH$, Sigma-Aldrich, CAS: 1066-54-2

Trimethylborate, $C_3H_9BO_3$, Sigma-Aldrich, CAS: 121-43-7

Toluene, C_7H_8, Sigma-Aldrich, CAS: 108-88-3

Triethylamine (99 %), $C_6H_{15}N$, Sigma-Aldrich, CAS: 121-44-8

All the solvents and chemical products were used without any extra purification.

Equipment:

Nuclear Magnetic Resonance.

NMR spectra were recorded with a Bruker Avance III 300/400/600 (300 MHz/400 MHz/600 MHz) at 298 K at LCC using deuterated solvents: CD_3CN, $CDCl_3$, CD_3CNOCD_3, C_2D_6OS, CD_3OD and CD_2Cl_2; the chemical shifts, δ, for ^1H and ^{13}C NMR are expressed in ppm and data are related to the residual nondeuterated solvent signal, fixed at δ= 1.940 (CD_3CN), δ= 7.26 ($CDCl_3$), δ= 2.84 (CD_3CNOCD_3), δ= 3.33 (C_2D_6OS), δ= 3.310 ppm (MeOD), and δ= 5.32 (CD_2Cl_2) for ^1H-NMR and δ=77.00 ($CDCl_3$), δ=1.320 (CD_3CN) ppm for ^{13}C-NMR. ^{11}B-NMR spectra were recorded using $BF_3{\cdot}OEt_2$ as an external reference. The Coupling constants (J) values are given in Hertz (Hz). Abbreviations have been used to indicate the multiplicity of the signals: s-singlet, d-doublet, t-triplet, dd-double doublet, td-double triplet, m-multiplet.

Elemental analyses.

Elemental analyses were performed at LCC, using a Perkin Elmer 2400 series II Instrument.

Infrared spectra.

Infrared analysis was recorded on a Perkin Elmer FT-IR Frontier MIR/FIR spectrometer, using a diamond ATR (Attenuated Total Reflection).

UV-visible spectra.

The ultraviolet (UV) absorption spectra were obtained on a Cary 60 UV-Visible spectrometer from Agilent Instruments.

High Resolution Mass Spectrometry.

HRMS were acquired using an Xevo G2 Q TOF (Waters) UPLC spectrometer, the analysis was recorded by Nathalie Martins-Froment. For clarity “M” refers to the molecular ion in the case of organic molecules and neutral complexes or to the cation in the case of ionic coordination compounds.

X-ray diffraction.

The X-ray diffraction analysis were collected on a Bruker Kappa Apex II diffractometer equipped with a 30 W air-cooled microfocus source using MoKα radiation (λ=0.71073 Å) and on a Rigaku XtaLAB Synergy Dualflex diffractometer using a PhotonJet X-ray source (Cu, λ=1.54184 Å). Oxford Cryosystems Cryostream cooling devices were used to collect the data at low temperature (100(2) K). Measurements were at LCC. The structures were solved with the SHELXS-97 program.

Electron paramagnetic resonance (EPR).

The EPR analysis were done from the magnetic measurements service at LCC. Data was acquired using a Bruker elexsys E500 on X band with a high sensitivity cave 4122SHQE.

One Photon Irradiation.

One photon irradiation was performed from a chassis wheeled wavelength switchable LED source from Mightex Company.

Two Photon Irradiation.

The Two-photon irradiation was performed in the CIO, Mexico, using short laser pulses of 80 fs at 1 kHz of repetition rate for the 700-1000 nm range experiments. The characterization at 800 nm was performed by the train of pulses delivered by a Ti: Sa amplifier (Libra HE from Coherent). For the other wavelengths, the method was implemented with an optical parametric amplifier (TOPAs, from Light Conversion). The Griess test under two photon absorption was performed in the IS2M, Mulhousse.

Photokinetic measurements

The Photokinetic studies on the photolysis reactions allow to measure the quantum yields of NO liberation and they were carried out at LCC with a Cary 60 UV-Visible spectrophotometer equipped with a cooling water regulator. The temperature was maintained at 25°C during the experiments. Irradiation was performed from a chassis wheeled wavelength switchable LED source from Mightex Company.

Appendix 2.

Synthesis and characterization of ruthenium nitrosyl complexes.

1. Synthesis of ligands.

II-2. (E)-3-(9,9-dihexyl-7-iodo-fluoren-2-yl)-1-(pyridin-2-yl)prop-2-en-1-one

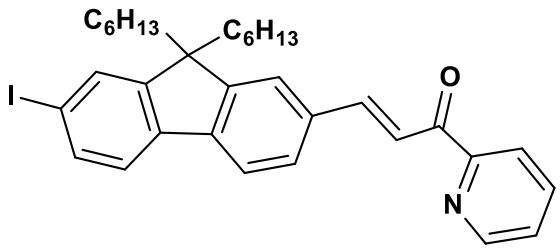

A round-bottom flask containing 9,9-dihexyl-7-iodofluorene-2-carboxaldehyde (3.0 g, 6.14 mmol), tetrahydrofuran (1 mL) and 2-acetylpyridine (0.69 mL, 6.14 mmol) was charged with 60 mL of ethanol. Aqueous NaOH solution (6.2 mL, 1M) was then added slowly to the mixture. The reaction was allowed to stir for 7 hours at room temperature. After completion, the solid was collected by filtration, washed with ethanol, and recrystallized from ethanol to yield 3.1709 g (5.36 mmol, 87 %) of 1a as a yellow solid.

^{1}H-NMR (300 MHz, CDCl3) δ 8.79 – 8.76 (m, 1H), 8.32 (d, J = 16.0 Hz, 1H), 8.21 (d, J = 7.8 Hz, 1H), 8.04 (d, J = 16.0 Hz, 1H), 7.88 (td, J = 7.7, 1.7 Hz, 1H), 7.72 – 7.65 (m, 4H), 7.52 – 7.44 (m, 2H), 1.98 (q, J = 7.8 Hz, 4H), 1.16 – 1.00 (m, 12H), 0.76 (t, J = 6.9 Hz, 6H), 0.60 (q, J = 7.7, 7.2 Hz, 4H).

^{13}C-NMR (75 MHz, CDCl3) δ 189.36, 154.39, 153.75, 150.75, 148.78, 145.43, 142.84, 139.88, 137.05, 136.03, 134.56, 132.15, 128.69, 126.83, 122.97, 122.83, 121.82, 120.14, 120.06, 93.59, 55.40, 40.19, 31.42, 29.54, 23.65, 22.51, 13.95.

HRMS (ESI-TOF+) m/z anal. calcd. for $C_{33}H_{39}INO$ $[M+H]^+$: 592.2076. Found: 592.2077. Error: 0.2 ppm.

II-3. 4'-(9,9-dihexyl-7-iodo-fluoren-2-yl)-2,2':6',2''-terpyridine

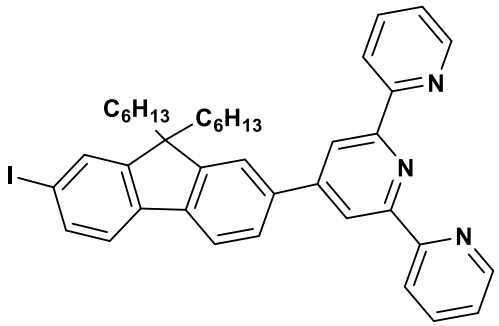

In a round-bottom flask, E-3-(7-iodo-9,9-dihexyl-fluoren-2-yl)-1-(1-pyridin-2-yl)-prop-2-en-1-one (2.810 g, 4.75 mmol), 1-[2-oxo-2-(2-pyridyl)ethyl]pyridinium iodide (1.5492 g, 4.75 mmol), and NH_4OAc (4.8 g, 62 mmol) were disolved in a mixture of ethanol (28 mL) and tetrahydrofuran (10 mL). The resulting mixture was stirred overnight. The crude product was purified by column chromatography using an ethyl acetate/hexane mixture (15:85) as eluent to yield 1.9147 g (2.77 mmol, 58 %) of a pale purple microcrystalline solid.

^{1}H-NMR (300 MHz, $CDCl_3$) δ 8.82 – 8.73 (m, 4H), 8.69 (dt, *J* = 8.0, 1.1 Hz, 2H), 7.94 – 7.85 (m, 3H), 7.83 – 7.76 (m, 2H), 7.73 – 7.66 (m, 2H), 7.50 (d, *J* = 8.4 Hz, 1H), 7.38 (ddd, *J* = 7.5, 4.8, 1.2 Hz, 2H), 2.13 – 1.92 (m, 4H), 1.18 – 1.02 (m, 12H), 0.77 (t, *J* = 6.9 Hz, 6H), 0.69 – 0.58 (m, 4H).

^{13}C-NMR (75 MHz, $CDCl_3$) δ 156.39, 155.99, 153.59, 151.00, 150.80, 149.13, 141.09, 140.17, 138.08, 136.93, 135.94, 132.11, 126.65, 123.84, 121.70, 121.49, 120.26, 119.00, 93.03, 55.70, 40.27, 31.45, 29.58, 23.69, 22.56, 13.98.

HRMS (ESI-TOF$^+$) *m/z* anal. calcd. for $C_{40}H_{43}IN_3$ [*M*+H]$^+$: 692.2502. Found: 692.2498. Error: -0.6 ppm.

II-4. 9,9-dihexylfluorene-2-boronic acid

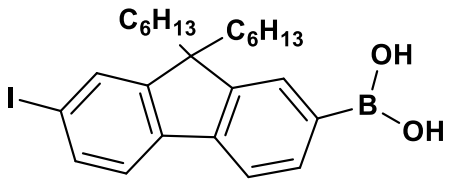

9,9-dihexyl-2-bromofluorene (7.8080 g, 18.9 mmol) was dissolved in THF (60 mL) in a Schlenk flask. The mixture was sparged with argon for 15 min and cooled down to -78 °C. A solution of n-BuLi (14.0 mL, 1.6 M) was added dropwise to the flask, and the resulting mixture was stirred for one hour at -78°C. $B(OCH_3)_3$ (2.2027 g, 21.2 mmol) was then added to the solution, and the reaction was stirred for an additional hour at -78 °C. The mixture was slowly warmed up to room temperature overnight. The reaction was then poured into 50 mL of HCl 2 M, and the resulting mixture was extracted with ethyl acetate and dried over Na_2SO_4. The crude product was purified by column chromatography using a hexane/ethyl acetate mixture as eluent to yield 3.8833 g (10.3 mmol, 55%) of a white powder.

^{1}H-NMR (300 MHz, $CDCl_3$, 298 K): δ(ppm) 8.79 (s, 2H), 8.77 –8.75 (m, 2H), 8.69 (d, J= 7.9 Hz, 2H), 7.92 –7.83 (m, 6H), 7.80 –7.75 (m, 2H), 7.39 –7.34 (m, 2H), 2.12 –2.06 (m, 4H), 1.35 –1.22 (m, 9H), 1.15 –0.99 (m, 14H), 0.75 (t, J= 7.0 Hz, 7H), 0.68 –0.57 (m, 4H).

II-L2. Ligand 2

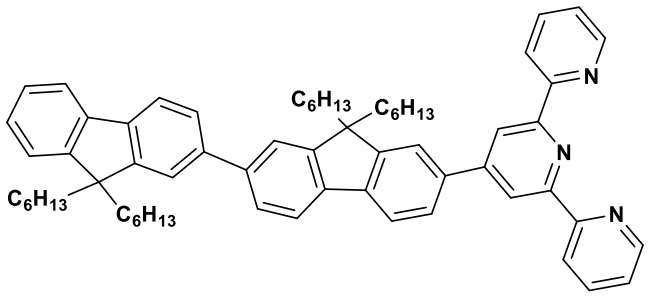

In a Schlenk flask, 4'-(7-iodo-9,9-dihexyl-fluoren-2-yl)-2,2':6',2''-terpyridine (0.5390 g, 0.78 mmol) and 9,9-dihexylfluorene-2-boronic acid (0.3205 g, 0.85 mmol) were added to K_2CO_3 (0.1230 g, 0.89 mmol) and $Pd(PPh_3)_2Cl_2$ (0.0287 g, 0.041 mmol) under an argon atmosphere. A 10 mL mixture of toluene/methanol (1:1) was added and the reaction mixture was stirred at reflux temperature overnight. The mixture was then cooled to room temperature, filtered, and the solvent was removed under reduced pressure. The resulting residue was purified by column chromatography using silica gel and a dichloromethane/ethyl acetate mixture (9:1) as an eluent to yield 0.5023 g (0.56 mmol, 66%) of L2 as a pale-yellow solid.

^{1}H-NMR (300 MHz, $CDCl_3$, 298 K): δ (ppm) 8.89 – 8.77 (m, 4H), 8.72 (d, *J* = 8.0 Hz, 2H), 7.98 – 7.61 (m, 12H), 7.46 – 7.30 (m, 5H), 2.21 – 1.97 (m, 8H), 1.17 – 1.04 (m, 24H), 0.81 – 0.71 (m, 20H).

^{13}C-NMR (100 MHz, $CDCl_3$) δ 156.64, 156.13, 152.12, 152.04, 151.64, 151.18, 149.30, 142.04, 141.15, 140.93, 140.57, 140.55, 139.84, 137.50, 137.08, 127.15, 126.93, 126.72, 126.35, 126.22, 123.98, 123.08, 121.70, 121.66, 121.61, 120.40, 120.32, 120.04, 119.88, 119.17, 55.72, 55.32, 40.55, 40.51, 31.62, 29.84, 29.79, 23.93, 22.71, 14.15.

HRMS (ESI-TOF$^+$) *m/z* anal. calcd. for $C_{65}H_{76}N_3$ [*M*+H]$^+$: 898.6039. Found: 898.6019. Error: -2.2 ppm.

II-6. (2E,2'E)-3,3'-(9,9-dihexyl-fluorene-2,7-diyl)bis(1-(pyridin-2-yl)prop-2-en-1-one)

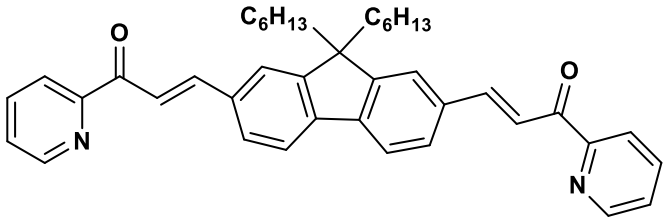

9,9-Dihexyl-fluoreno-2,7-dicarboxaldehyde (1.8864 g, 4.83 mmol) was suspended in 80 mL of ethanol, 2-acetylpyridine (1.08 mL, 9.66 mmol) was added in a single step; 10 mL of an aqueous solution of sodium hydroxide (400 mg, 10 mmol) was added dropwise and allowed to stir at room temperature overnight, obtaining a yellow solid. The reaction was poured into 100 mL of ice and water, filtered under vacuum, and washed with water and cold ethanol, to yield 2.2799 g (3.82 mmol, 90 %) of the desired product as a yellow solid.

^{1}H-NMR (400 MHz, $CDCl_3$) δ 8.79 (ddd, *J* = 4.8, 1.8, 0.9 Hz, 2H), 8.33 (d, *J* = 16.0 Hz, 2H), 8.22 (dt, *J* = 7.9, 1.1 Hz, 2H), 8.06 (d, *J* = 16.0 Hz, 2H), 7.90 (td, *J* = 7.7, 1.7 Hz, 2H), 7.78 – 7.70 (m, 6H), 7.52 (ddd, *J* = 7.5, 4.8, 1.3 Hz, 2H), 2.09 – 2.03 (m, 4H), 1.14 – 0.99 (m, 12H), 0.75 (t, *J* = 7.0 Hz, 6H), 0.66 – 0.56 (m, 4H).

^{13}C-NMR (100 MHz, $CDCl_3$) δ 189.42, 154.45, 152.11, 148.83, 145.49, 143.05, 137.10, 134.77, 128.75, 126.87, 123.02, 122.98, 120.59, 120.19, 55.33, 40.37, 31.49, 29.61, 23.75, 22.54, 13.96.

HRMS (ESI-TOF$^+$) *m/z* anal. calcd. for $C_{41}H_{45}N_2O_2$ [*M*+H]$^+$: 597.3481. Found: 597.3474. Error: -1.2 ppm.

II-L3. Ligand 3

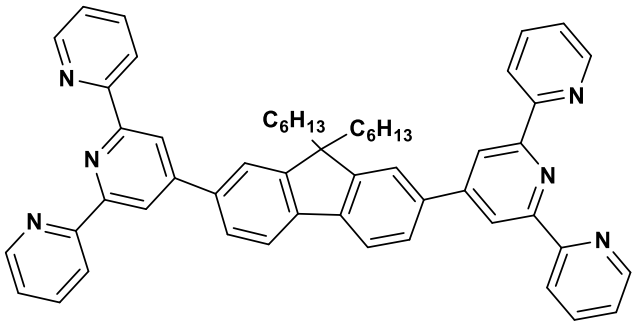

(2*E*,2'*E*)-3,3'-(9,9-Dihexyl-fluorene-2,7-diyl)bis(1-pyridin-2-yl-prop-2-en-1-one) (1.0981 g, 1.84 mmol), 1-(2-oxo-2-pyridin-2-yl-ethyl)pyridinium iodide (1.3991 g, 4.29 mmol) and ammonium acetate (4.1 g, 53 mmol), were added. They were suspended in 100 mL of ethanol, heated to reflux overnight to make the solution dark green; it was allowed to reach room temperature and evaporated to dryness, diluted with 70 mL of dichloromethane, and washed with water (3 x 30 mL), the organic phase was dried with anhydrous sodium sulfate and evaporated to dryness obtaining an oil of green-black color. It was purified on a silica gel column using hexane: ethyl acetate (7:3) as eluent, and the obtained solid was re-purified on silica gel using as eluent exclusively dichloromethane, to yield 0.6456 g (0.81 mmol, 44 %) of L3 as a pale-yellow solid.

^{1}H-NMR (300 MHz, $CDCl_3$) δ 8.81 (s, 4H), 8.77 (ddd, *J* = 4.8, 1.8, 0.9 Hz, 4H), 8.69 (dt, *J* = 8.0, 1.1 Hz, 4H), 7.96 – 7.86 (m, 10H), 7.36 (ddd, *J* = 7.5, 4.8, 1.2 Hz, 4H), 2.21 – 2.13 (m, 4H), 1.17 – 1.03 (m, 12H), 0.79 – 0.65 (m, 10H).

^{13}C-NMR (75 MHz, $CDCl_3$) δ 156.39, 155.95, 152.04, 150.86, 149.09, 141.53, 137.79, 136.86, 126.57, 123.77, 121.49, 121.44, 120.46, 118.99, 55.79, 40.41, 31.46, 29.58, 23.75, 22.53, 13.95.

HRMS (ESI-TOF$^+$) *m/z* anal. calcd. for $C_{55}H_{53}N_6$ [*M*+H]$^+$: 797.4332. Found: 797.4318. Error: -1.8 ppm.

II-7. 4'-(9,9-dihexyl-7-(4,4,5,5-tetramethyl-1,3,2-dioxaborolan-2-yl)-fluoren-2-yl)-2,2':6',2''-terpyridine

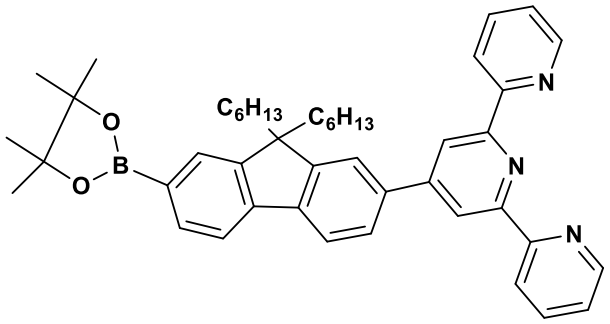

In a 5 mL Schlenk flask 4'-(7-iodo-9,9-dihexyl-fluoren-2-yl)-2,2':6',2''-terpyridine (0.1796 g, 0.26 mmol), borobipinacolate (0.1219 g, 4.8 mmol), potassium acetate (0.598 g, 0.61 mmol), and finally dimethylsulfoxide (2.0 mL) were added. The heterogeneous mixture was sparged with argon for 15 min, followed by the addition of Pd(dppf)Cl_2*DCM (0.0012 g, 0.0015 mmol). The mixture was heated at 110°C for 1 day. The mixture was filtered with the aid of sintered funnel No. 4, the compound was extracted from the filtrate using chloroform, and the organic layer was washed with brine and finally dried using Na_2SO_4. The remaining solvent was removed by distillation under reduced pressure and finally purified by column chromatography using silica gel and the pentane/ethyl acetate mixture as eluant to yield 0.1227 g (0.15 mmol, 56%) of compound **3a** as a pale-yellow solid.

^{1}H-NMR (300 MHz, $CDCl_3$) δ 8.79 – 8.74 (m, 4H), 8.68 (dt, J = 8.0, 1.1 Hz, 2H), 7.92 – 7.73 (m, 8H), 7.36 (ddd, J = 7.5, 4.8, 1.2 Hz, 2H), 2.12 – 2.03 (m, 4H), 1.39 (s, 12H), 1.14 – 1.00 (m, 12H), 0.74 (t, J = 6.9 Hz, 6H), 0.67 – 0.55 (m, 4H).

^{13}C-NMR (75 MHz, CDCl3) δ 156.39, 155.90, 152.15, 150.94, 150.32, 149.08, 143.45, 141.96, 137.80, 136.91, 133.77, 128.86, 126.40, 123.79, 121.52, 121.47, 120.53, 119.27, 119.02, 83.72, 55.47, 40.22, 31.43, 29.58, 24.91, 23.63, 22.52, 13.96.

^{11}B-NMR (96 MHz, CDCl3) δ 30.82 (s).

HRMS (ESI-TOF+) m/z anal. calcd. for $C_{46}H_{55}BN_3O_2$ $[M+H]^+$: 692.4387. Found: 692.4382. Error: -0.72 ppm.

II-L4. Ligand 4

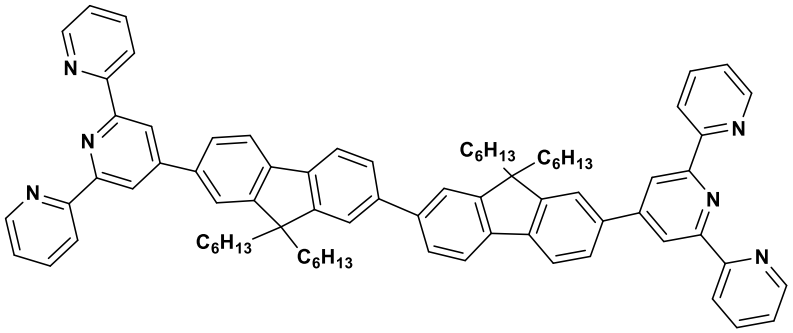

In a Schlenk flask, 4'-(9,9-dihexyl-7-(4,4,5,5-tetramethyl-1,3,2-dioxaborolan-2-yl)-fluoren-2-yl)-2,2':6',2''-terpyridine (0.1106 g, 0.16 mmol), compound 1b (0.0982 g, 0.12 mmol), potassium carbonate (0.0210 g, 0.15 mmol), tetra-n-butyl bromide ammonia (0.0032 g, 0.0099 mmol), and $Pd(dppf)_2Cl_2$ (0.0047 g, 0.0064 mmol) were mixed. The system was purged with argon, and 10/1 toluene/methanol mixture (20 mL) were added. The reaction mixture was stirred magnetically at reflux temperature for 24 hours. The product was cooled to room temperature, filtered, and purified by column chromatography on silica gel using dichloromethane/ethyl acetate (8/2) as eluent, yielding 0.0844 g (0.0747 mmol, 65 %) of L4 as a pale-yellow solid.

^{1}H-NMR (300 MHz, $CDCl_3$) δ 8.81 (s, 4H), 8.78 (ddd, *J* = 4.8, 1.8, 0.9 Hz, 4H), 8.70 (dt, *J* = 8.0, 1.1 Hz, 4H), 7.96 – 7.84 (m, 12H), 7.73 – 7.66 (m, 4H), 7.39 (ddd, *J* = 7.5, 4.8, 1.2 Hz, 4H), 2.19 – 2.11 (m, 8H), 1.20 – 1.04 (m, 24H), 0.81 – 0.72 (m, 20H).

^{13}C-NMR (100 MHz, $CDCl_3$) δ 156.48, 155.97, 152.00, 151.90, 151.01, 149.15, 141.86, 140.89, 139.79, 137.38, 136.93, 126.57, 126.24, 123.82, 121.55, 121.50, 120.28, 120.19, 119.02, 55.58, 40.40, 31.47, 29.63, 23.80, 22.56, 14.00.

HRMS (ESI-TOF$^+$) *m/z* anal. calcd. For $C_{80}H_{85}N_6$ $[M+H]^+$: 1129.6836. Found: 1129.6846. Error: 0.9 ppm.

II-14. (E)-3-(9,9-methyl-7-bromo-fluoren-2-yl)-1-(pyridin-2-yl)prop-2-en-1-one

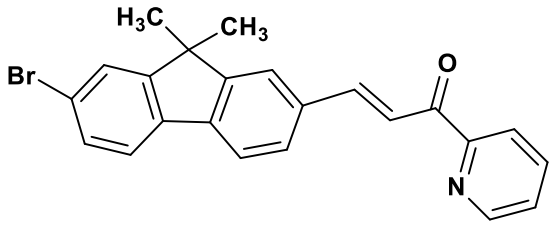

9,9-dimethyl-7-bromofluorene-2-carboxaldehyde (3.0010 g, 10.0 mmol) was dissolved in tetrahydrofuran (2.0 mL), and ethanol (60 mL), after a few minutes NaOH solution was added to the solution (10 mL, 0.1 M), finally 2-acetylpyridine (2.93 mL, 6.07 mmol) was added dropwise. The reaction was stopped after 7 hours under magnetic stirring at room temperature. The final crude was washed and recrystallized from ethanol to yield 2.6700 g (6.62 mmol, 66.2 %) of a yellow solid.

^{1}H-NMR. (300 MHz, CDCl3) δ (ppm) 8.80 (ddd, J= 4.8, 1.7, 1.1 Hz, 1H), 8.32 (d, J= 16.0 Hz, 1H), 8.23 (dt, J= 7.7, 1.1 Hz, 1H), 8.06 (d, J= 16.0 Hz, 1H), 7.91 (td, J= 7.7, 1.7 Hz, 1H), 7.77 –7.66 (m, 4H), 7.52 (ddd, J= 7.7, 4.8, 1.1 Hz, 1H), 7.39 –7.32 (m, 3H), 1.96-1.89 (m, 4H), 1.19-0.94 (m, 12H), 0.76 (t, J=7.0 Hz, 6H), 0.69-0.48 (m, 4H).

HRMS (ESI-TOF$^+$) *m/z* anal. calcd. For $C_{23}H_{18}BrNO$ [*M*+H]$^+$: 404.0644. Found: 404.0642. Error: 0.5 ppm.

II-15. 4'-(9,9-dimethyl-7-bromo-fluoren-2-yl)-2,2':6',2''-terpyridine.

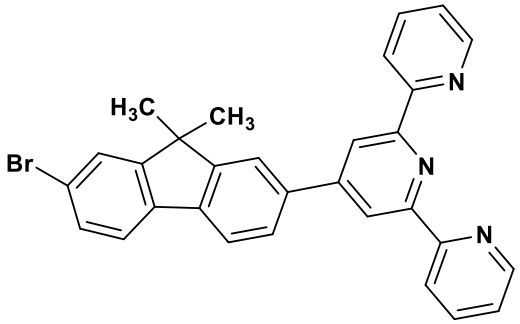

(E)-3-(9,9-methyl-7-bromo-fluoren-2-yl)-1-(pyridin-2-yl)prop-2-en-1-one (2.5000 g, 6.2 mmol) were mixed with 1-[2-oxo-2-(2- pyridyl)ethyl]pyridinium iodide (2.0350 g, 6.25 mmol) in 50 mL of ethanol and 25 mL of tetrahydrofuran, finally NH_4OAc (4.7750 g, 62.0 mmol) was added. The mixture was stirred magnetically overnight and purified by column chromatography using an ethyl acetate/hexane mixture at a 15:85 ratio as eluant to yield 1.7000 g (3.3790 mmol, 54.5 %) of a crystalline yellow solid.

^{1}H-NMR (400 MHz, Chloroform-d) δ 8.79 – 8.74 (m, 4H), 8.70 (dt, J = 8.0, 1.0 Hz, 2H), 7.95 – 7.87 (m, 4H), 7.84 – 7.78 (m, 1H), 7.67 – 7.57 (m, 2H), 7.50 (dd, J = 8.1, 1.8 Hz, 1H), 7.38 (ddd, J = 7.4, 4.8, 1.1 Hz, 2H), 1.57 (s, 6H).

HRMS (ESI-TOF$^+$) *m/z* anal. calcd. For $C_{30}H_{22}BrN_3$ [*M*+H]$^+$: 504.1075. Found: 504.1080. Error: 0.5 ppm.

II-12. 4'-(9,9-dimethyl-7-(4,4,5,5-tetramethyl-1,3,2-dioxaborolan-2-yl)-fluoren-2-yl)-2,2':6',2''-terpyridine

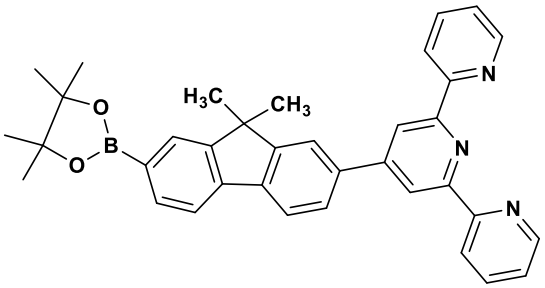

In a 5 mL Schlenk flask 4'-(9,9-dimethyl-7-bromo-fluoren-2-yl)-2,2':6',2''-terpyridine (2.200 g, 4.4 mmol), borobipinacolate (2.0501 g, 8.1 mmol), potassium acetate (2.3710 g, 24.1 mmol), and finally dimethylsulfoxide (40.0 mL) were added. The heterogeneous mixture was sparged with argon for 15 min, followed by addition of Pd(dppf)Cl_2*DCM (0.3001 g, 0.37 mmol). The mixture was heated at 110°C for 1 day. Then the mixture was filtered with the aid of sintered funnel No. 4, the compound was extracted from the filtrate using chloroform, and the organic layer was washed with brine and finally dried using Na_2SO_4. The remaining solvent was removed by distillation under reduced pressure and finally purified by column chromatography using silica gel and pentane/ethyl acetate mixture as eluant to yield 1.5 g (2.7 mmol, 61.8 %) of a white powder.

^{1}H-NMR (300 MHz, Chloroform-d) δ 8.80 (s, 2H), 8.76 (ddd, J = 4.8, 1.7, 0.8 Hz, 2H), 8.71 – 8.63 (m, 2H), 7.99 – 7.92 (m, 4H), 7.93 – 7.83 (m, 2H), 7.82 – 7.75 (m, 2H), 7.35 (ddd, J = 7.5, 4.8, 1.2 Hz, 2H), 1.40 (s, 6H), 1.14 – 1.01 (s, 12H).

LRMS (ESI-TOF$^+$) *m/z* anal. calcd. For $C_{36}H_{34}BN_3O_2$ [*M*+H]$^+$: 551.28. Found: 551.27. Error: 0.01 ppm.

II-L4'. Ligand 4'

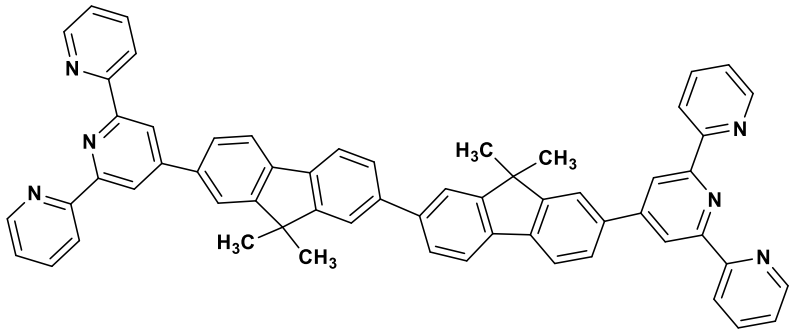

4'-(9,9-dimethyl-7-(4,4,5,5-tetramethyl-1,3,2-dioxaborolan-2-yl)-fluoren-2-yl)-2,2':6',2''-terpyridine (1.0001 g, 1.81 mmol) was mixed with 4'-(9,9-dimethyl-7-bromo-fluoren-2-yl)-2,2':6',2''-terpyridine (0.9200 g, 1.81 mmol), K_2CO_3 (0.08202 g, 5.97 mmol), tetra-n-butyl bromide ammonia (0.2470 g, 0.077 mmol), and $Pd(dppf)_2Cl_2$ (0.6270 g, 0.767 mmol). The system was placed under an argon atmosphere. After 12 mL of a 10:1 toluene/ethanol mixture was added, the reaction was placed under magnetic stirring and reflux for 24 hours. The product was filtered and purified by column chromatography using silica gel and a mixture of dichloromethane/ethyl acetate in a proportion of 8:2 as eluant, to yield 0.3803 g (0.45 mmol, 24.8 %) as a red solid.

^{1}H-NMR (300 MHz, Chloroform-d) δ 8.86 (s, 4H), 8.82 – 8.77 (m, 4H), 8.73 (d, J = 8.1 Hz, 4H), 8.04 (d, J = 1.2 Hz, 2H), 7.99 – 7.84 (m, 10H), 7.78 – 7.66 (m, 4H), 7.45 – 7.36 (m, 4H), 1.69 (s, 12H).

^{13}C-NMR (100 MHz, $CDCl_3$) δ 156.48, 155.97, 152.00, 151.90, 151.01, 149.15, 141.86, 140.89, 139.79, 137.38, 136.93, 126.57, 126.24, 123.82, 121.55, 121.50, 120.28, 120.19, 119.02, 55.58, 40.40, 31.47, 29.63, 23.80, 22.56, 14.00.

HRMS (ESI-TOF$^+$) *m/z* anal. calcd. For $C_{80}H_{85}N_6$ $[M+H]^+$: 1129.6836. Found: 1129.6846. Error: 0.9 ppm.

II-9. (*E*)-3-(7-ethynyl-9,9-dihexyl-fluoren-2-yl)-1-(pyridin-2-yl)prop-2-en-1-one.

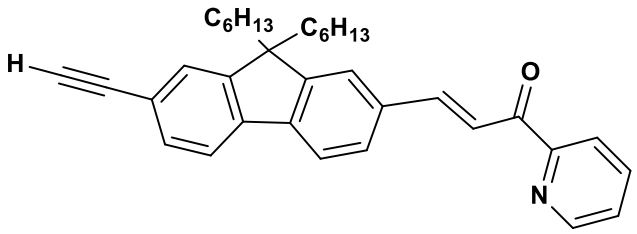

Synthesized as described above for **II-2** from 7-ethynyl-9,9-dihexyl-fluorene-2-carbaldehyde. Obtained as a yellow solid in 93 % yield.

^{1}H-NMR (300 MHz, $CDCl_3$) δ 8.77 (d, *J* = 4.3 Hz, 1H), 8.33 (d, *J* = 16.0 Hz, 1H), 8.21 (d, *J* = 7.8 Hz, 1H), 8.05 (d, *J* = 16.0 Hz, 1H), 7.87 (t, *J* = 7.5 Hz, 1H), 7.75 – 7.63 (m, 4H), 7.53 – 7.42 (m, 3H), 3.17 (s, 1H), 2.06 – 1.89 (m, 4H), 1.13 – 0.98 (m, 12H), 0.75 (t, *J* = 6.6 Hz, 6H), 0.65 – 0.53 (m, 4H).

^{13}C-NMR (75 MHz, $CDCl_3$) δ 189.33, 154.32, 151.65, 151.39, 148.75, 145.46, 143.00, 140.91, 137.03, 134.50, 131.24, 128.66, 126.81, 126.52, 122.95, 122.87, 121.03, 120.39, 120.07, 84.46, 77.51, 55.20, 40.23, 31.42, 29.56, 23.65, 22.49, 13.91.

HRMS (ESI-TOF^{+}) *m/z* anal. calcd. for $C_{35}H_{40}NO$ $[M+H]^{+}$: 490.3110. Found: 490.3107. Error: -0.6 ppm.

II-10. 4'-(7-ethynyl-9,9-dihexyl-fluoren-2-yl)-2,2':6',2''-terpyridine.

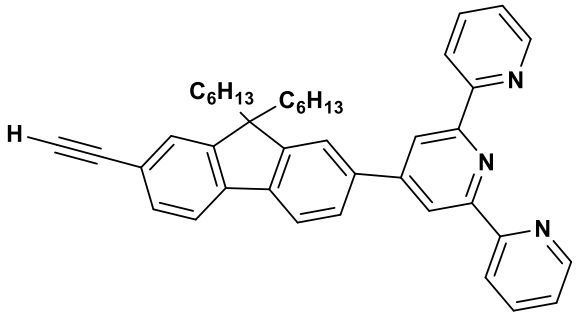

Synthesized as described above for **II-3** from compound **II-9** obtained as a pale orange solid in 68 % yield.

^{1}H-NMR (400 MHz, $CDCl_3$) δ 8.79 – 8.75 (m, 4H), 8.69 (dt, *J* = 8.0, 1.1 Hz, 2H), 7.93 – 7.88 (m, 3H), 7.84 – 7.79 (m, 2H), 7.71 (dd, *J* = 7.7, 0.8 Hz, 1H), 7.51 (dd, *J* = 9.1, 1.3 Hz, 2H), 7.38 (ddd, *J* = 7.5, 4.8, 1.2 Hz, 2H), 3.17 (s, 1H), 2.14 – 1.96 (m, 4H), 1.16 – 1.02 (m, 12H), 0.76 (t, *J* = 7.0 Hz, 6H), 0.62 (p, *J* = 7.3 Hz, 4H).

^{13}C-NMR (100 MHz, $CDCl_3$) δ 156.38, 155.97, 151.64, 151.19, 150.81, 149.11, 141.30, 141.25, 138.03, 136.95, 131.23, 126.64, 126.55, 123.85, 121.53, 121.50, 120.53, 119.92, 119.04, 84.69, 77.18, 55.52, 40.34, 31.49, 29.62, 23.71, 22.57, 13.97.

HRMS (ESI-TOF^{+}) *m/z* anal. calcd. for $C_{42}H_{44}N_3$ $[M+H]^{+}$: 590.3535. Found: 590.3528. Error: -1.2 ppm.

II-L5. Ligand 5

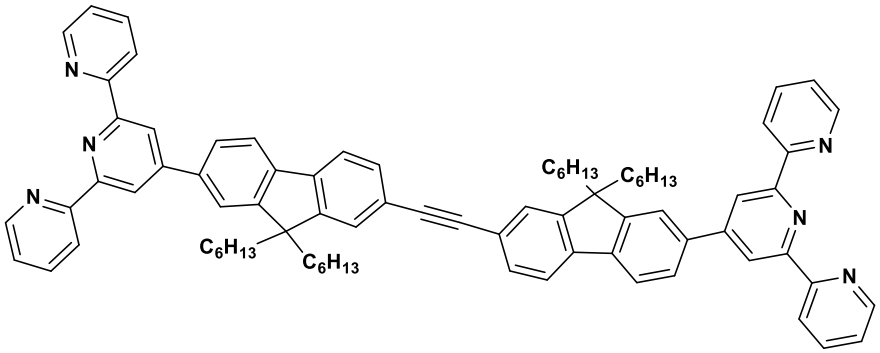

To a Schlenk flask containing 4'-(7-ethynyl-9,9-dihexyl-fluoren-2-yl)-2,2':6',2''-terpyridine (0.4012 g, 0.58 mmol), 1b (0.3421 g, 0.58 mmol), $Pd(PPh_3)_2Cl_2$ (0.0204 g, 5 mol %) and CuI (0.0110 g, 10 mol %) was added THF (14 mL) followed by the dropwise addition of Et_3N (14 mL) and stirring at reflux temperature under argon for 48 hrs. The reaction was evaporated to dryness under reduced pressure and purified by column chromatography on silica gel using hexane/ethyl acetate (8/2) as eluent to yield 0.4845 g (0.42 mmol, 72 %) of L5 as a yellow/orange solid.

^{1}H-NMR (300 MHz, $CDCl_3$) δ 8.80 – 8.76 (m, 8H), 8.70 (d, *J* = 7.9 Hz, 4H), 7.93 – 7.81 (m, 10H), 7.77 (d, *J* = 7.8 Hz, 2H), 7.61 (dd, *J* = 9.4, 1.8 Hz, 4H), 7.41 – 7.36 (m, 4H), 2.15 – 2.01 (m, 8H), 1.17 – 1.03 (m, 24H), 0.77 (t, *J* = 7.0 Hz, 12H), 0.66 (q, J = 6.5, 4.9 Hz, 8H).

^{13}C-NMR (100 MHz, $CDCl_3$) δ 156.43, 155.99, 151.91, 151.30, 150.86, 149.14, 141.50, 140.78, 137.87, 136.94, 130.75, 126.65, 125.96, 123.85, 121.99, 121.50, 120.45, 120.04, 119.03, 90.80, 55.57, 40.50, 31.56, 29.70, 23.78, 22.61, 14.00.

HRMS (ESI-TOF$^+$) *m/z* anal. calcd. for $C_{82}H_{85}N_6$ $[M+H]^+$: 1153.6836. Found: 1153.6830. Error: -0.15 ppm.

2. Synthesis of RuNO complexes

II-[Ru(L2)Cl_3]

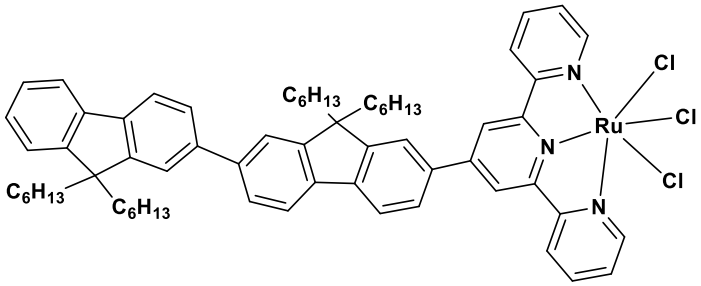

In this experiment, **L2** (0.3947 g, 0.44 mmol) and $RuCl_3xH_2O$ (0.2 g) were suspended in ethanol (5 mL) in a round-bottom flask. The mixture was stirred at reflux temperature for 4.5 hours, and subsequently allowed to cool down to room temperature. The precipitate obtained was then collected, washed with cold ethanol and ether, and dried under vacuum to obtain 0.4418 g (0.40 mmol, 90 %) of [**Ru(L2)Cl_3**] as a brown solid.

II-RuCl-2. [Ru(L2)(bpy)(Cl)](Cl)

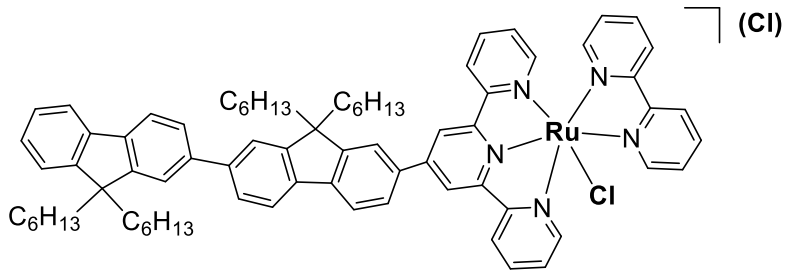

To a round-bottom flask were added **[Ru(L2)Cl$_3$]** (0.2209 g, 0.20 mmol), 2,2-bipyridine (0.0312 g, 0.20 mmol) and LiCl (0.0313 g, 0.74 mmol); the mixture was suspended in ethanol (4.2 mL) and deionized water (1.4 mL) and treated with Et_3N (20 µL). After stirring at reflux temperature for 3 hours, the mixture was evaporated to dryness under reduced pressure and purified by column chromatography on neutral alumina using dichloromethane/methanol (7/3) as eluent to yield 0.1512 g (0.12 mmol, 60 %) of **RuCl-2** as a purple solid.

^{1}H-NMR (400 MHz, CD_3CN) δ 10.28 – 10.23 (m, 1H), 8.87 (s, 2H), 8.64 (d, *J* = 7.8 Hz, 3H), 8.35 (d, *J* = 7.9 Hz, 1H), 8.29 – 8.24 (m, 2H), 8.20 (dd, *J* = 7.9, 1.7 Hz, 1H), 8.07 (d, *J* = 8.0 Hz, 1H), 8.01 – 7.94 (m, 2H), 7.93 – 7.86 (m, 3H), 7.85 – 7.77 (m, 4H), 7.74 (dd, *J* = 7.9, 1.7 Hz, 1H), 7.71 – 7.65 (m, 3H), 7.47 – 7.43 (m, 1H), 7.41 – 7.33 (m, 3H), 7.28 (ddd, *J* = 7.1, 5.6, 1.2 Hz, 2H), 6.95 (ddd, *J* = 7.3, 5.8, 1.3 Hz, 1H), 2.31 – 2.24 (m, 4H), 2.14 – 2.07 (m, 4H), 1.16 – 1.01 (m, 24H), 0.77 – 0.55 (m, 20H).

HRMS (ESI-TOF$^+$) *m/z* anal. calcd. For $C_{75}H_{83}ClN_5Ru$ [*M*]$^+$: 1190.53980. Found: 1190.5394. Error: -0.34 ppm.

I-($RuNO_2$-2). **[Ru(L2)(bpy)(NO_2)](Cl)**

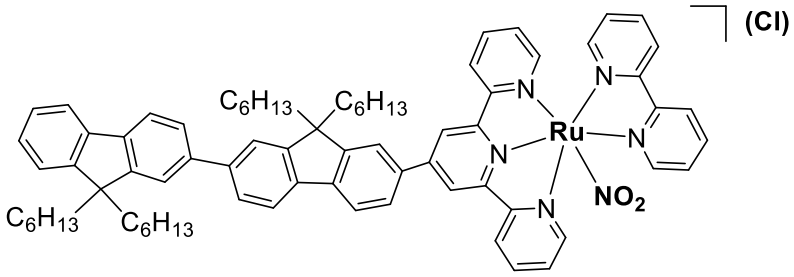

In a 10 mL ball flask **RuCl-2** was added (0.1512 g, 0.12 mmol), $NaNO_2$ (0.1380 g, 2 mmol), ethanol (3.6 mL) and deionized water (1.0 mL). The mixture was heated at reflux and under constant magnetic stirring for 3 hours. After this time ¾ parts of the solvent of the resulting mixture was evaporated by distillation under reduced pressure. The precipitate formed was collected, washed with water, cold ethanol and diethyl ether to yield 0.1398 g (0.11 mmol, 95 %) of **$RuNO_2$-2** as a reddish solid.

^{1}H-NMR (300 MHz, CD_3CN) δ 9.92 – 9.89 (m, 1H), 8.83 (s, 2H), 8.63 – 8.56 (m, 3H), 8.37 (d, *J* = 8.2 Hz, 1H), 8.30 – 8.22 (m, 2H), 8.18 (dd, *J* = 8.0, 1.7 Hz, 1H), 8.09 (d, *J* = 8.0 Hz, 1H), 8.03 – 7.94 (m, 4H), 7.90 – 7.74 (m, 9H), 7.48 – 7.44 (m, 2H), 7.40 – 7.30 (m, 4H), 7.08 (ddd, *J* = 7.3, 5.6, 1.2 Hz, 1H), 2.33 – 2.25 (m, 4H), 2.12 – 2.05 (m, 4H), 1.19 – 1.03 (m, 22H), 0.80 – 0.68 (m, 16H), 0.67 – 0.57 (m, 4H).

HRMS (ESI-TOF$^+$) *m/z* anal. calcd. for $C_{75}H_{83}N_6O_2Ru$ $[M]^+$: 1201.56420. Found: 1201.5667. Error: 2.08 ppm.

II-RuNO-2. [Ru(L2)(bpy)(NO)](PF$_6$)$_3$

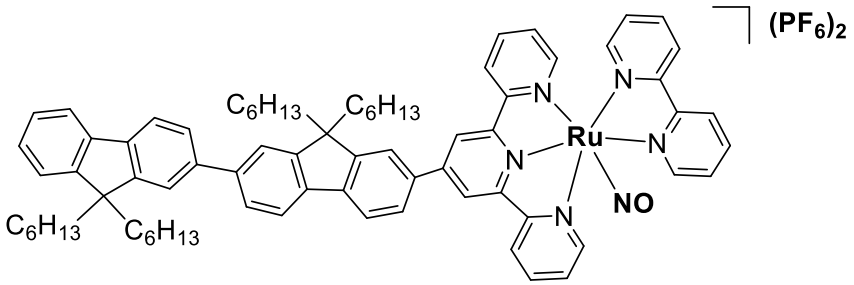

To a round-bottom flask containing **RuNO$_2$-2** (0.1398 g, 0.11 mmol) and ethanol (6.0 mL) was added HCl (38 %, 4.0 mL), the mixture was heated at 60°C for 3 hours under constant magnetic stirring. Once the reaction was finished, ¾ parts of the solvent were evaporated under reduced pressure, at this point NH_4PF_6 (0.0950 g, 0.56 mmol) dissolved in a small amount of water was added. The precipitate formed was collected, washed thoroughly with water, cold ethanol, and diethyl ether to yield 0.1620 g (0.10 mmol, 91 %) of **RuNO-2** as a dark purple/black solid.

^{1}H-NMR (400 MHz, CD_3CN) δ 9.36 – 9.28 (m, 1H), 9.14 (s, 2H), 8.93 (dd, *J* = 8.8, 1.3 Hz, 2H), 8.84 – 8.80 (m, 1H), 8.71 (td, *J* = 7.9, 1.4 Hz, 1H), 8.65 – 8.61 (m, 1H), 8.52 (td, *J* = 7.9, 1.4 Hz, 2H), 8.36 – 8.18 (m, 5H), 8.09 – 8.01 (m, 3H), 7.92 – 7.71 (m, 8H), 7.54 – 7.45 (m, 2H), 7.42 – 7.34 (m, 3H), 2.39 – 2.28 (m, 4H), 2.12 – 2.07 (m, 4H), 1.18 – 1.02 (m, 22H), 0.81 – 0.53 (m, 20H).

^{13}C-NMR (100 MHz, CD_3CN) δ 159.67, 157.78, 155.87, 155.39, 154.79, 154.46, 154.00, 153.74, 152.61, 151.98, 149.00, 146.99, 145.72, 145.33, 144.98, 143.25, 141.92, 141.67, 140.81, 139.80, 133.92, 131.68, 131.21, 131.17, 129.26, 128.63, 128.40, 128.07, 128.00, 127.60, 127.41, 127.17, 125.08, 124.08, 123.96, 122.80, 122.62, 122.49, 122.19, 121.12, 120.84, 57.04, 56.27, 40.83, 40.69, 32.23, 32.19, 30.21, 30.20, 24.78, 24.68, 23.21, 23.18, 14.29, 14.26.

HRMS (ESI-TOF$^+$) *m/z* anal. calcd. for $C_{75}H_{83}N_6ORu$ $[M]^{2+}$: 592.78460. Found: 592.7852. Error: 1.01 ppm.

FT-IR (ATR, cm^{-1}) 1938 (vNO).

UV-Vis λ_{max} in nm (Ɛ in M^{-1}cm^{-1}): 497 (12200).

II-[$Cl_3Ru(L3)RuCl_3$]

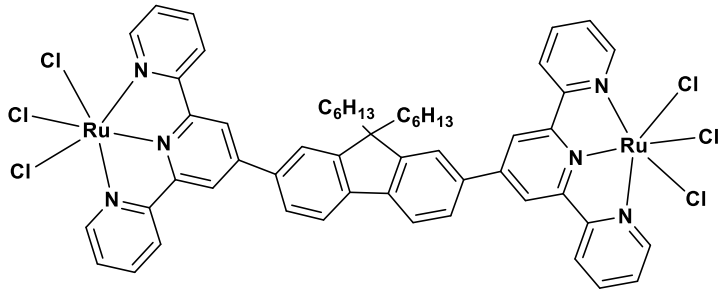

In a round-bottom flask, **L3** (0.5413 g, 0.68 mmol) and $RuCl_3$ x H_2O (2.8210 g) were suspended in 40 mL of ethanol, and the mixture was vigorously refluxed for 6 hours. After cooling to room temperature, the resulting precipitate was collected, washed with cold ethanol and ether, and dried under vacuum to obtain 0.7869 g (0.65 mmol, 96%) of **[$Cl_3Ru(L_3)RuCl_3$]** as a brown solid.

II-RuCl-3. [(Cl)(bpy)Ru(L3)Ru(bpy)(Cl)](Cl)$_2$

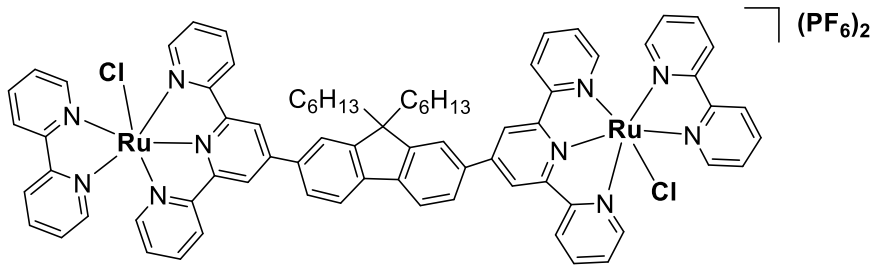

In a round-bottom flask, a mixture of **[Cl$_3$Ru(L3)RuCl$_3$]** (0.4964 g, 0.41 mmol), 2,2-bipyridine (0.1312 g, 0.84 mmol), and LiCl (0.0644 g, 1.52 mmol) was suspended in a solution of ethanol (30 mL) and deionized water (10 mL) and treated with Et3N (180 µL). The reaction mixture was then stirred at reflux temperature for 4 hours, followed by evaporation to dryness under reduced pressure. Purification by column chromatography on neutral alumina was carried out using dichloromethane/methanol (7/3) as eluent, resulting in a yield of 0.5372 g (0.37 mmol, 90%) of purple-colored **RuCl-3** as a solid.

^{1}H-NMR (300 MHz, MeOD) δ 10.27 – 10.22 (m, 2H), 9.08 (s, 4H), 8.84 – 8.78 (m, 6H), 8.52 (d, *J* = 8.1 Hz, 2H), 8.39 – 8.28 (m, 6H), 8.21 (d, *J* = 8.0 Hz, 2H), 8.06 – 7.96 (m, 6H), 7.80 – 7.70 (m, 6H), 7.55 – 7.50 (m, 2H), 7.37 (ddd, *J* = 7.5, 5.5, 1.3 Hz, 4H), 7.08 (ddd, *J* = 7.3, 5.8, 1.3 Hz, 2H), 2.50 – 2.41 (m, 4H), 1.26 – 1.09 (m, 12H), 0.82 – 0.74 (m, 10H).

HRMS (ESI-TOF$^+$) *m/z* anal. calcd. for $C_{75}H_{66}N_{10}Ru_2Cl_2$ $[M]^{2+}$: 691.15580. Found: 691.1568. Error: 1.45 ppm

II-RuNO$_2$-3. **[(NO$_2$)(bpy)Ru(L3)Ru(bpy)(NO$_2$)](Cl)$_2$**

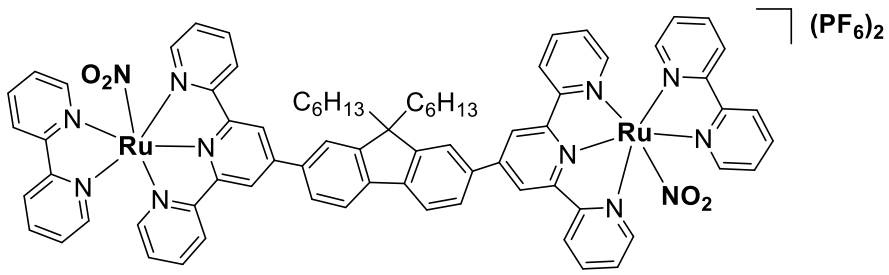

RuCl-3 (0.4936 g, 0.34 mmol), $NaNO_2$ (0.1656 g, 2.4 mmol), ethanol (30 mL), and deionized water (10 mL) were combined in a round-bottom flask, and the mixture was vigorously refluxed for 4 hours. The solution was then concentrated under reduced pressure to approximately 12 mL. The resulting precipitate was collected, washed with water, cold ethanol, and diethyl ether to yield 0.4569 g (0.31 mmol, 91%) of **RuNO$_2$-3** as a red solid.

^{1}H-NMR (300 MHz, CD_3CN) δ 9.92 – 9.88 (m, 2H), 8.88 (s, 4H), 8.62 (d, *J* = 8.1 Hz, 6H), 8.41 – 8.17 (m, 10H), 8.06 – 7.93 (m, 6H), 7.85 – 7.75 (m, 6H), 7.51 – 7.45 (m, 2H), 7.38 – 7.32 (m, 4H), 7.12 – 7.06 (m, 2H), 2.41 – 2.33 (m, 4H), 1.20 – 1.02 (m, 12H), 0.80 – 0.72 (m, 10H).

HRMS (ESI-TOF$^+$) *m/z* anal. calcd. for $C_{75}H_{68}N_{12}O_4Ru_2$ $[M]^{2+}$: 702.18040. Found: 702.1815. Error: 1.57 ppm.

II-RuNO-3. [(NO)(bpy)Ru(L3)Ru(bpy)(NO)](PF$_6$)$_6$

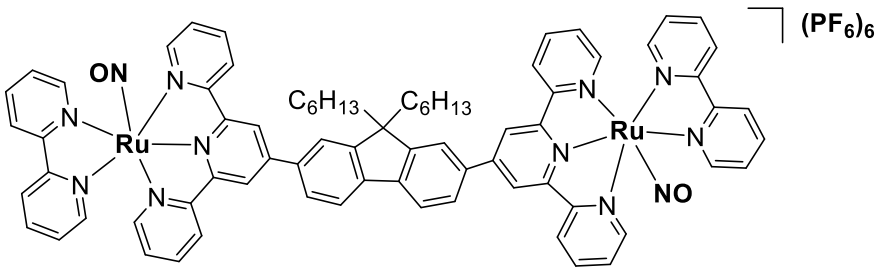

A mixture of 15 mL of ethanol and 4 mL of HCl (conc.) was added to **RuNO$_2$-3** (0.3980 g, 0.27 mmol) and heated at 60 °C for 1 h, allowed to cool to room temperature and then cooled in an ice bath, 3 mL of NH_4PF_6 (100.0 mg, 0.61 mmol) dissolved in distilled water was added in a single step. **RuNO-3** was filtered under vacuum and washed with water, ethanol, and diethyl ether, obtaining 0.4484 mg (0.20 mmol, 77%) of the desired product as red purple solid.

^{1}H-NMR (300 MHz, CD_3CN) δ 9.35 – 9.32 (m, 2H), 9.19 (s, 4H), 8.99 – 8.95 (m, 3H), 8.84 (d, J = 8.3 Hz, 2H), 8.72 (td, J = 8.1, 1.4 Hz, 2H), 8.65 (d, J = 8.2 Hz, 2H), 8.53 (td, J = 8.0, 1.4 Hz, 4H), 8.46 (s, 2H), 8.42 (dd, J = 8.3, 1.4 Hz, 2H), 8.37 – 8.26 (m, 7H), 8.07 – 8.04 (m, 4H), 7.76 (ddd, J = 7.3, 5.9, 1.2 Hz, 4H), 7.55 – 7.51 (m, 2H), 7.39 – 7.35 (m, 2H), 2.50 – 2.44 (m, 4H), 1.23 – 1.06 (m, 12H), 0.79 – 0.69 (m, 10H).

^{13}C-NMR (100 MHz, CD3CN) δ 159.42, 157.71, 155.91, 155.40, 154.93, 154.62, 154.47, 154.03, 148.99, 145.74, 145.34, 145.29, 145.00, 135.74, 131.69, 131.30, 131.20, 129.49, 128.72, 128.02, 127.45, 125.49, 124.33, 123.42, 57.65, 40.69, 32.37, 30.33, 24.95, 23.30, 14.30.

HRMS (ESI-TOF+) m/z anal. calcd. for $C_{75}H_{68}N_{12}O_3Ru_2$ $[M\text{-}NO\text{+}NO_2]^{4+}$: 462.7886. Found: 462.7899. Error: 2.81 ppm.

Elemental analysis found: C, 39.97; H, 3.11; N, 7.52. Required for $C_{75}H_{68}N_{12}O_2Ru_2P_6F_{36}$: C, 40.19; H, 3.06; N, 7.50.

FT-IR (ATR, cm^{-1}) 1940 (νNO).

UV-Vis λmax in nm (ε in M^{-1}cm^{-1}): 457 (37000).

II-[$Cl_3Ru(L4)RuCl_3$]

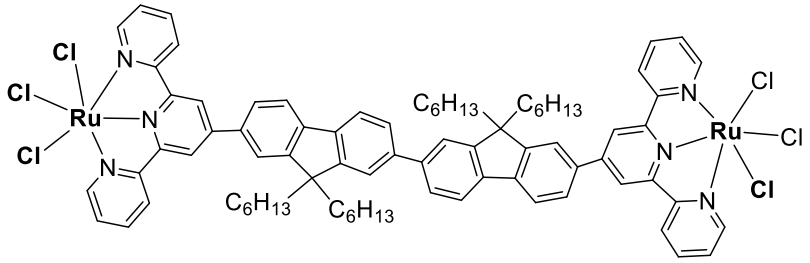

Prepared as described above **for [$Cl_3Ru(L3)RuCl_3$]** from **L4**. Yield : 92 % (Black solid).

II-RuCl-4. **[(Cl)(bpy)Ru(L4)Ru(bpy)(Cl)]$(Cl)_2$**

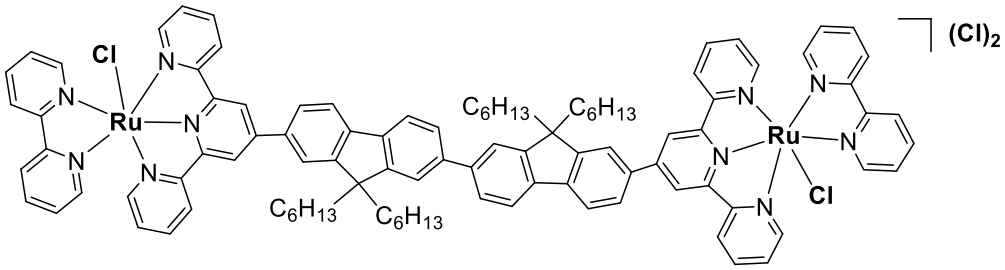

Prepared as described above for **RuCl-3** from **[$Cl_3Ru(L4)RuCl_3$].** Yield: 75 % (Purple/black solid).

^{1}H-NMR (400 MHz, MeOD) δ 10.23 – 10.20 (m, 2H), 9.07 (s, 4H), 8.81 – 8.78 (m, 6H), 8.52 (d, *J* = 8.1 Hz, 2H), 8.35 – 8.30 (m, 4H), 8.29 – 8.23 (m, 2H), 8.12 (d, *J* = 7.9 Hz, 2H), 8.04 (d, *J* = 7.8 Hz, 2H), 8.01 – 7.95 (m, 6H), 7.82 – 7.73 (m, 10H), 7.55 – 7.51 (m, 2H), 7.37 (ddd, *J* = 7.2, 5.7, 1.3 Hz, 4H), 7.08 (ddd, *J* = 7.3, 6.0, 1.3 Hz, 2H), 2.39 – 2.25 (m, 8H), 1.21 – 1.08 (m, 24H), 0.84 – 0.71 (m, 20H).

HRMS (ESI-TOF$^+$) *m/z* anal. calcd. for $C_{100}H_{100}Cl_2N_{10}Ru_2$ $[M]^{2+}$: 857.28140. Found: 857.2830. Error: 1.87 ppm.

II-RuNO$_2$-4. **[(NO$_2$)(bpy)Ru(L4)Ru(bpy)(NO$_2$)](Cl)$_2$**

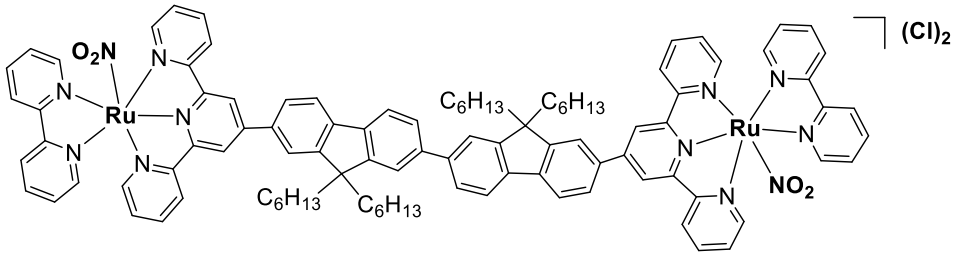

Prepared as described above for **RuNO$_2$-3** from **RuCl-4**. Yield: > 99 % (Dark red solid).

^{1}H-NMR (400 MHz, MeOD) δ 9.89 (d, *J* = 5.5 Hz, 2H), 9.07 (s, 4H), 8.80 (t, *J* = 7.8 Hz, 6H), 8.60 (d, *J* = 8.2 Hz, 2H), 8.38 – 8.33 (m, 4H), 8.26 (dd, *J* = 8.0, 1.7 Hz, 2H), 8.13 (d, *J* = 7.9 Hz, 2H), 8.09 – 8.03 (m, 6H), 8.01 – 7.96 (m, 2H), 7.90 (td, *J* = 7.9, 1.5 Hz, 2H), 7.84 – 7.77 (m, 8H), 7.61 (dd, *J* = 5.8, 0.8 Hz, 2H), 7.42 (ddd, *J* = 7.0, 5.5, 1.3 Hz, 4H), 7.22 (ddd, *J* = 7.2, 5.9, 1.2 Hz, 2H), 2.40 – 2.24 (m, 8H), 1.22 – 1.10 (m, 24H), 0.85 – 0.73 (m, 20H).

HRMS (ESI-TOF$^+$) *m/z* anal. calcd. for $C_{100}H_{100}N_{12}O_4Ru_2$ $[M]^{2+}$: 868.30600. Found: 868.3058. Error: -0.23 ppm.

II-RuNO-4. **[(NO)(bpy)Ru(L4)Ru(bpy)(NO)](PF$_6$)$_6$**

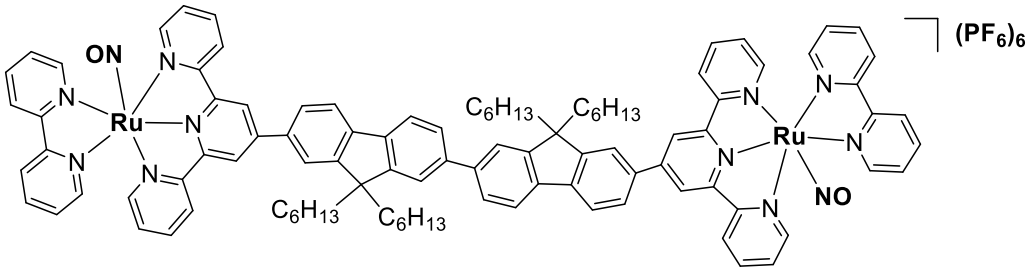

Prepared as described above for **RuNO-2** from **RuNO$_2$-4**. Yield: 89 % (Black solid).

^{1}H-NMR (400 MHz, CD_3CN) δ 9.35 – 9.31 (m, 2H), 9.15 (s, 4H), 8.96 – 8.92 (m, 4H), 8.83 (d, *J* = 8.1 Hz, 2H), 8.72 (td, *J* = 8.0, 1.4 Hz, 2H), 8.64 (d, *J* = 8.4 Hz, 2H), 8.53 (td, *J* = 7.9, 1.5 Hz, 4H), 8.38 – 8.20 (m, 10H), 8.11 (d, *J* = 7.9 Hz, 2H), 8.05 (dd, *J* = 5.8, 1.0 Hz, 4H), 7.97 – 7.95 (m, 2H), 7.92 (dd, *J* = 7.9, 1.6 Hz, 2H), 7.75 (ddd, *J* = 7.3, 5.7, 1.3 Hz, 4H), 7.52 (ddd, *J* = 7.5, 6.1, 1.3 Hz, 2H), 7.37 (dd, *J* = 6.1, 1.0 Hz, 2H), 2.41 – 2.32 (m, 8H), 1.22 – 1.06 (m, 24H), 0.82 – 0.67 (m, 20H).

^{13}C-NMR (100 MHz, CD_3CN) δ 159.61, 157.75, 155.87, 155.37, 154.79, 154.44, 153.99, 153.80, 148.99, 146.78, 145.70, 145.31, 144.96, 142.70, 140.27, 134.11, 131.65, 131.20, 129.28, 128.61, 127.98, 127.78, 127.40, 125.11, 124.00, 122.93, 122.57, 122.28, 57.08, 40.68, 32.23, 30.22, 24.78, 23.22, 14.30.

HRMS (ESI-TOF$^+$) *m/z* anal. calcd. for $C_{100}H_{100}F_{12}N_{12}O_2P_2Ru_2$ $[M+2xPF_6^-]^{2+}$: 997.27530. Found: 997.2747. Error: -0.60 ppm.

FT-IR (ATR, cm^{-1}) 1937 (νNO).

UV-Vis λmax in nm (ε in M^{-1}cm^{-1}): 494 (35500).

II-[$Cl_3Ru(L4)RuCl_3$].

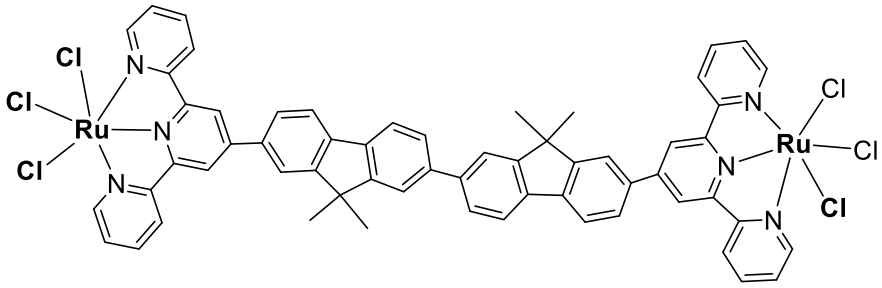

In a 10.0 mL ball flask, **L4'** (0.3870 g, 0.46 mmol) and $RuCl_{3x}H_2O$ (0.1040 g) in ethanol/dichloromethane 1:1 (80 mL) was added, the mixture was left under magnetic stirring and reflux for 4 hours, then it was cooled to room temperature. The black powder was collected, washed with cold ethanol and ether, and finally dried under vacuum to yield 0.3800 g (0.30 mmol, 65%) as a red dark solid.

II-RuCl-4'. **[(Cl)(bpy)Ru(L4')Ru(bpy)(Cl)](Cl)$_2$**.

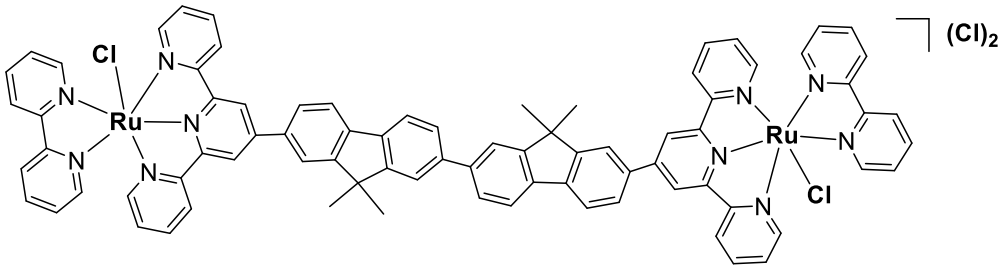

Prepared as described above for **RuCl-3** from **[Cl$_3$Ru(L'4)RuCl$_3$]**. Yield: 15 % (Purple/red solid).

^{1}H-NMR (400 MHz, Acetonitrile-d3) δ 10.24 – 10.19 (m, 2H), 8.85 (s, 4H), 8.59 (d, J = 8.1 Hz, 2H), 8.37 – 8.27 (m, 6H), 8.16 (dd, J = 8.0, 1.7 Hz, 2H), 8.10 (d, J = 8.0 Hz, 4H), 8.06 – 7.98 (m, 2H), 7.97 – 7.87 (m, 6H), 7.84 (dd, J = 7.9, 1.7 Hz, 10H), 7.71 – 7.64 (m, 2H), 7.38 (dd, J = 6.8, 1.0 Hz, 4H), 7.32 – 7.24 (m, 2H), 6.98 – 6.90 (m, 2H), 1.73 (s, 12H).

HRMS (ESI-TOF$^+$) *m/z* anal. calcd. for $C_{80}H_{60}Cl_2N_{10}Ru_2$ $[M]^{2+}$: 717.12460. Found: 717.1238. Error: 1.02 ppm.

II-RuNO$_2$-4'. **[(NO$_2$)(bpy)Ru(L4')Ru(bpy)(NO$_2$)](Cl)$_2$**

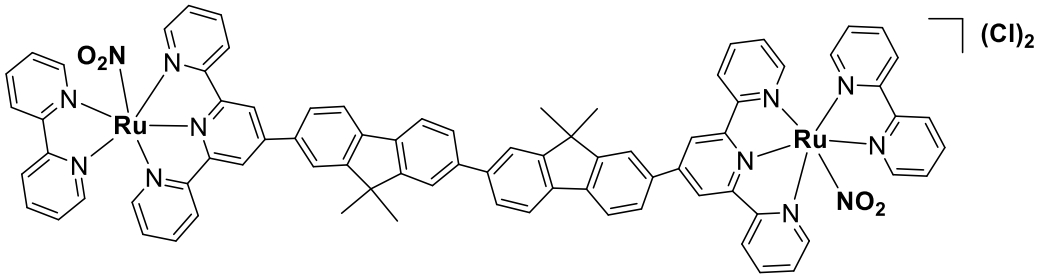

Prepared as described above for **RuNO$_2$-4** from **RuCl-4'**. Yield: > 99 % (Dark red solid).

^{1}H-NMR (300 MHz, Acetonitrile-d_3) δ 9.75 – 9.62 (m, 2H), 8.63 (s, 4H), 8.43 – 8.33 (m, 6H), 8.19 – 8.10 (m, 4H), 8.06 (td, *J* = 7.9, 1.5 Hz, 2H), 7.97 – 7.88 (m, 4H), 7.87 – 7.73 (m, 10H), 7.71 – 7.50 (m, 8H), 7.28 – 7.23 (m, 2H), 7.16 – 7.07 (m, 4H), 6.94 – 6.77 (m, 2H), 1.55 (s, 12H).

HRMS (ESI-TOF$^+$) *m/z* anal. calcd. for $C_{80}H_{60}N_{12}O_4Ru_2$ $[M]^{2+}$: 728.14920. Found: 728.1492. Error: 0.02 ppm.

II-RuNO-4'. [(NO)(bpy)Ru(L4')Ru(bpy)(NO)](PF$_6$)$_6$

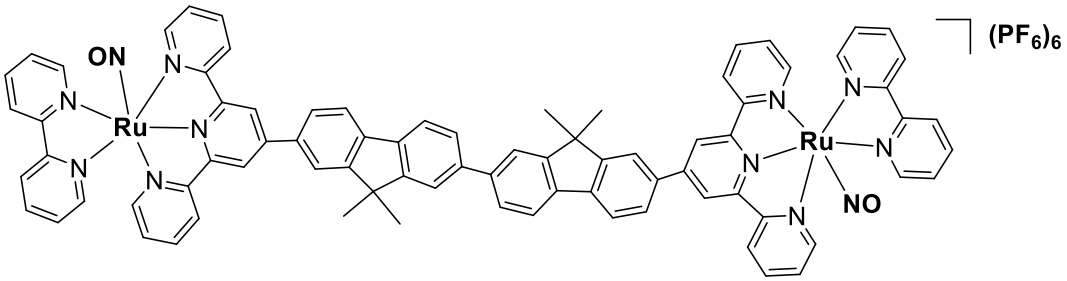

Prepared as described above for **RuNO-2** from **RuNO$_2$-4'**. Yield: 89 % (Purple solid).

^{1}H-NMR (400 MHz, Acetonitrile-d3) δ 9.40 – 9.31 (m, 2H), 9.19 (d, J = 2.9 Hz, 4H), 8.95 (dd, J = 9.4, 2.6 Hz, 4H), 8.86 (d, J = 7.9 Hz, 2H), 8.79 – 8.70 (m, 2H), 8.69 – 8.63 (m, 2H), 8.59 – 8.45 (m, 6H), 8.40 – 8.25 (m, 8H), 8.22 – 8.06 (m, 8H), 8.01 – 7.93 (m, 2H), 7.83 – 7.73 (m, 4H), 7.62 – 7.51 (m, 2H), 7.39 (d, J = 6.1 Hz, 2H), 1.82 (s, 12H).

HRMS (ESI-TOF$^+$) *m/z* anal. calcd. for $C_{80}H_{60}N_{12}O_2Ru_2$ $[M]^{3+}$: 475.10540. Found: 475.1048. Error: 1.46 ppm.

II-[$Cl_3Ru(L5)RuCl_3$]

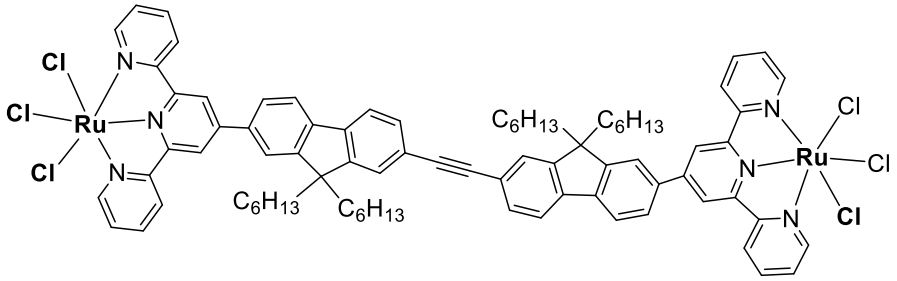

Prepared as described above for **[$Cl_3Ru(L3)RuCl_3$]** from ligand **L5**. Yield: 82 % (Dark orange solid).

II-RuCl-5. **[(Cl)(bpy)Ru(L4)Ru(bpy)(Cl)]$(Cl)_2$**

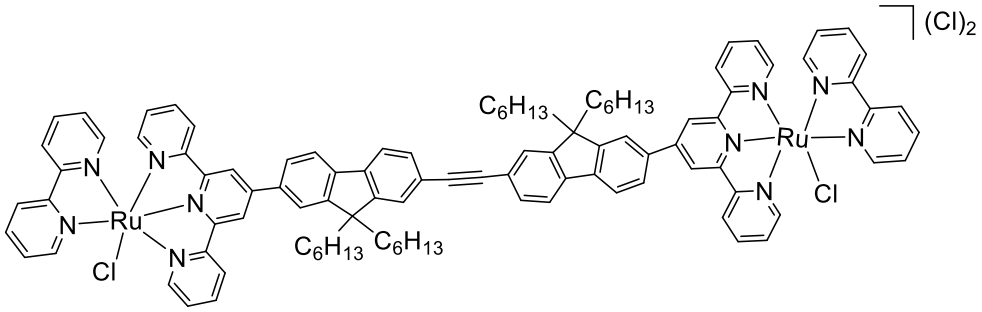

Prepared as described above for **RuCl-3** from **[$Cl_3Ru(L5)RuCl_3$]**. Yield: 53 % (Purple/black solid).

^{1}H-NMR (400 MHz, CD_3CN) δ 10.28 – 10.22 (m, 2H), 8.87 (s, 4H), 8.67 – 8.62 (m, 6H), 8.35 (d, *J* = 8.1 Hz, 2H), 8.32 – 8.23 (m, 4H), 8.22 – 8.19 (m, 2H), 8.09 (d, *J* = 7.9 Hz, 2H), 8.00 – 7.91 (m, 10H), 7.77 – 7.72 (m, 2H), 7.72 – 7.66 (m, 6H), 7.45 – 7.39 (m, 2H), 7.33 – 7.28 (m, 4H), 6.97 (ddd, *J* = 7.4, 6.3, 1.4 Hz, 2H), 2.28 – 2.20 (m, 8H), 1.19 – 1.08 (m, 24H), 0.78 (t, *J* = 6.9 Hz, 12H), 0.75 – 0.62 (m, 8H).

HRMS (ESI-TOF$^+$) *m/z* anal. calcd. for $C_{102}H_{100}Cl_2N_{10}Ru_2$ $[M]^{2+}$: 869.28140. Found: 869.2803. Error: -1,27 ppm.

II-[RuNO$_2$-5](Cl)$_2$ [(NO$_2$)(bpy)Ru(L5)Ru(bpy)(NO$_2$)](Cl)$_2$

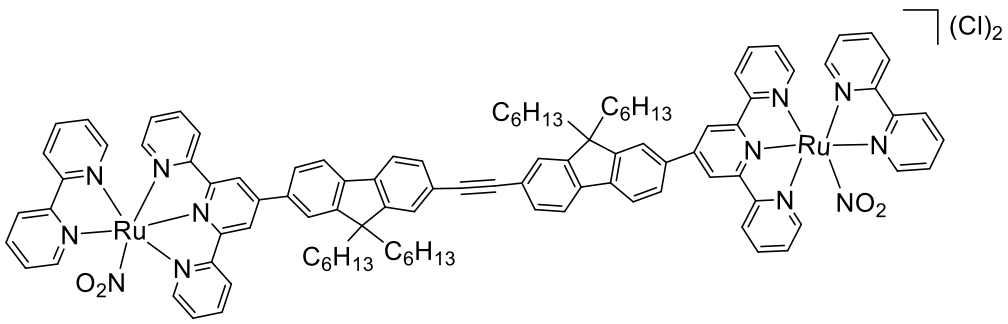

Prepared as described above for **RuNO$_2$-3** from **RuCl-5**. Yield: 96 % (Black solid).

^{1}H-NMR (400 MHz, MeOD) δ 9.92 – 9.85 (m, 2H), 8.97 (s, 4H), 8.81 – 8.69 (m, 6H), 8.56 (d, *J* = 8.2 Hz, 2H), 8.36 – 8.27 (m, 4H), 8.21 – 8.14 (m, 2H), 8.09 – 7.94 (m, 10H), 7.87 (td, *J* = 8.1, 1.4 Hz, 2H), 7.78 (dd, *J* = 5.8, 1.3 Hz, 4H), 7.72 (s, 2H), 7.66 (dd, *J* = 7.7, 1.4 Hz, 2H), 7.55 (d, *J* = 4.9 Hz, 2H), 7.38 (ddd, *J* = 6.9, 5.5, 1.2 Hz, 4H), 7.18 (ddd, *J* = 7.3, 5.9, 1.1 Hz, 2H), 2.33 – 2.15 (m, 8H), 1.21 – 1.05 (m, 24H), 0.83 – 0.68 (m, 20H).

HRMS (ESI-TOF$^+$) *m/z* anal. calcd. for $C_{102}H_{100}N_{12}O_4Ru_2$ $[M]^{2+}$: 876.30600. Found: 876.3052. Error: -0.91 ppm.

II-RuNO$_2$-5. [(NO$_2$)(bpy)Ru(L5)Ru(bpy)(NO$_2$)](PF$_6$)$_2$

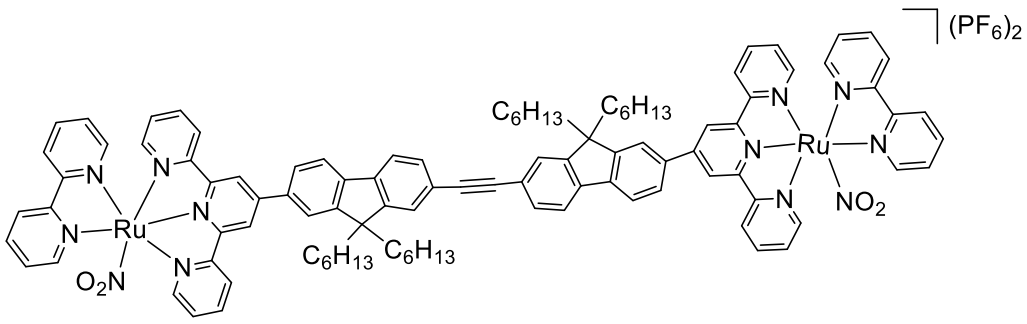

To a round-bottom flask containing **[RuNO$_2$-5](Cl)$_2$** (0.0200 g, 0.011 mmol) and acetonitrile (1.0 mL) was added a saturated aqueous solution of NH_4PF_6. The precipitate formed was collected, washed thoroughly with water and diethyl ether to yield 0.0214 g (0.010 mmol, 96 %) of **[RuNO$_2$-5](PF$_6$)$_2$** as a red solid.

^{1}H-NMR (400 MHz, Acetone) δ 10.06 (ddd, J = 5.6, 1.5, 0.7 Hz, 2H), 9.17 (s, 4H), 8.90 (dd, J = 8.2, 1.1 Hz, 2H), 8.78 (dt, J = 8.1, 1.2 Hz, 4H), 8.70 – 8.66 (m, 2H), 8.54 (d, J = 1.7 Hz, 2H), 8.46 – 8.39 (m, 2H), 8.35 (dd, J = 8.0, 1.8 Hz, 2H), 8.20 (dd, J = 8.0, 4.9 Hz, 2H), 8.15 – 8.08 (m, 6H), 8.05 (dd, J = 7.9, 0.7 Hz, 2H), 7.98 – 7.92 (m, 6H), 7.83 – 7.78 (m, 4H), 7.70 (dd, J = 7.8, 1.5 Hz, 2H), 7.47 (ddd, J = 7.6, 5.5, 1.3 Hz, 4H), 7.25 (ddd, J = 7.0, 5.8, 1.3 Hz, 2H), 2.30 (dq, J = 14.1, 7.5, 6.9 Hz, 8H), 1.23 – 1.05 (m, 24H), 0.82 – 0.70 (m, 20H).

^{13}C-NMR (100 MHz, Acetone) δ 159.91, 159.32, 157.99, 156.87, 154.15, 153.57, 153.42, 152.48, 152.29, 148.62, 143.61, 141.69, 138.53, 138.13, 137.93, 136.98, 131.91, 131.84, 130.59, 128.43, 128.00, 127.95, 127.92, 127.23, 126.98, 124.65, 124.13, 122.82, 121.98, 121.64, 121.16, 121.12, 92.49, 56.67, 40.92, 32.39, 24.78, 23.27, 14.29.

II-RuNO-5. **[(NO)(bpy)Ru(L5)Ru(bpy)(NO)](PF$_6$)$_6$**

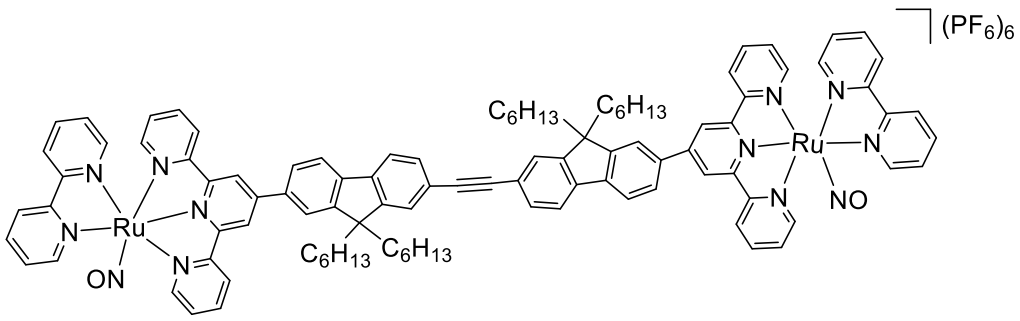

Prepared as described above for **RuNO-2** from **RuNO$_2$-5**. Yield: 84 % (Black solid).

^{1}H-NMR (400 MHz, CD_3CN) δ 9.33 (d, *J* = 5.0 Hz, 2H), 9.14 (s, 4H), 8.96 – 8.91 (m, 4H), 8.83 (d, *J* = 8.2 Hz, 2H), 8.71 (td, *J* = 8.0, 1.4 Hz, 2H), 8.64 (d, *J* = 8.2 Hz, 2H), 8.52 (td, *J* = 7.9, 1.4 Hz, 4H), 8.38 – 8.25 (m, 8H), 8.21 (d, *J* = 8.2 Hz, 2H), 8.08 – 8.00 (m, 6H), 7.81 (s, 2H), 7.78 – 7.70 (m, 6H), 7.52 (ddd, *J* = 7.5, 6.2, 1.3 Hz, 2H), 7.37 (dd, *J* = 6.0, 0.8 Hz, 2H), 2.38 – 2.22 (m, 8H), 1.20 – 1.05 (m, 24H), 0.79 (t, *J* = 7.0 Hz, 12H), 0.74 – 0.62 (m, 8H).

^{13}C-NMR (100MHz, CD_3CN) δ 159.52, 157.74, 155.88, 155.39, 154.84, 154.46, 154.01, 153.21, 148.99, 146.19, 145.72, 145.32, 144.98, 141.18, 134.59, 132.04, 131.68, 131.25, 131.18, 129.33, 128.67, 128.01, 127.39, 125.24, 124.25, 124.08, 122.58, 122.38, 92.05, 57.00, 40.71, 32.30, 30.29, 24.80, 23.27, 14.30.

MS (ESI-TOF$^+$) *m/z* anal. calcd. for $C_{102}H_{100}N_{12}O_2Ru_2$ $[M]^{4+}$: 431.9. Found: 431.9.

FT-IR (ATR, cm^{-1}) 1934 (νNO).

UV-Vis λ_{max} in nm (Ɛ in M^{-1}cm^{-1}): 493 (45100).

3. Synthesis intermediate [Ru(NO)MeCN-5](PF$_6$)$_5$.

III-2. Trichlorido(4'-(9,9-dihexyl-7-iodo-fluoren-2-yl)-2,2':6',2''-terpyridine-ruthenium (III).

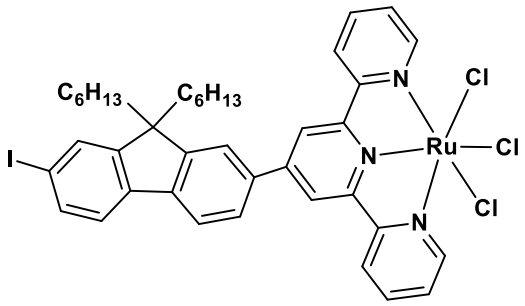

In a round-bottom flask, 4'-(9,9-dihexyl-7-iodo-fluoren-2-yl)-2,2':6',2''-terpyridine (0.4000 g, 0.58 mmol) and $RuCl_3xH_2O$ (0.130 g) were suspended in ethanol (40 mL). The mixture was stirred at reflux temperature for 7 hours, and then allowed to cool to room temperature. The resulting precipitate was collected by filtration, washed with cold ethanol and ether, and dried under vacuum to yield 0.4351 g (0.48 mmol, 84%) of complex **III-2** as a black solid.

HRMS (ESI-TOF+) *m/z* anal. calcd. for $C_{40}H_{46}Cl_3IN_4Ru$ $[M+NH_4]^+$: 916.08790. Found: 916.0865. Error: 1.66 ppm.

III-3. Chlorido(4'-(9,9-dihexyl-7-iodo-fluoren-2-yl)-2,2':6',2''-terpyridine)(2,2'-bipyridine) ruthenium(II) chloride

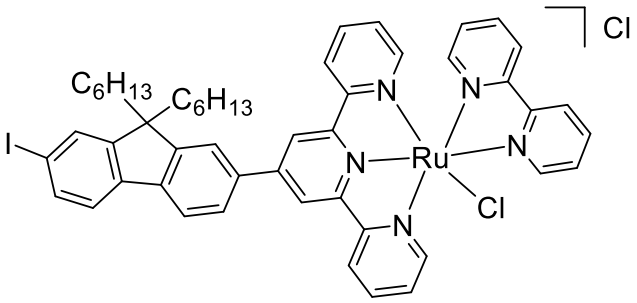

To a round-bottom flask were added **III-2** (0.4351 g, 0.48 mmol), 2,2-bipyridine (0.0756 g, 0.48 mmol) and LiCl (0.0814 g, 1.92 mmol). The mixture was suspended in 25.0 mL of ethanol and 8.0 mL of deionized water and treated with 60 µL of triethylamine. The resulting mixture was stirred at reflux temperature for 3 hours, and then evaporated to dryness under reduced pressure. The resulting residue was purified by column chromatography on neutral alumina using dichloromethane/methanol (9/1) as eluent, to yield 0.2837 g (0.28 mmol, 58%) of complex **III-3** as a purple solid.

^{1}H-NMR (300 MHz, CD_3CN) δ 10.24 (d, *J* = 5.1 Hz, 1H), 8.83 (s, 2H), 8.61 (dd, *J* = 7.9, 5.3 Hz, 3H), 8.36 – 8.23 (m, 2H), 8.21 – 8.13 (m, 2H), 8.04 (d, *J* = 8.1 Hz, 1H), 8.00 – 7.87 (m, 4H), 7.81 (dd, *J* = 8.1, 1.5 Hz, 1H), 7.73 – 7.63 (m, 4H), 7.42 – 7.37 (m, 1H), 7.28 (ddd, *J* = 7.0, 5.5, 1.2 Hz, 2H), 7.03 – 6.91 (m, 1H), 1.94 (p, *J* = 2.4 Hz, 4H), 1.17 – 1.02 (m, 12H), 0.81 – 0.72 (m, 6H), 0.70 – 0.56 (m, 4H).

^{13}C-NMR (100 MHz, CD_3CN) δ 207.89, 159.83, 159.77, 159.02, 157.19, 154.82, 153.46, 153.28, 152.97, 152.61, 147.03, 142.99, 141.06, 137.95, 137.48, 137.45, 137.39, 137.28, 136.51, 133.50, 128.21, 127.87, 127.03, 124.75, 124.46, 124.23, 123.18, 123.12, 121.80, 121.27, 121.24, 94.12, 56.88, 40.85, 40.62, 30.28, 30.19, 24.76, 24.68, 23.22, 14.29.

HRMS (ESI-TOF+) *m/z* anal. calcd. for $C_{50}H_{50}ClIN_5Ru$ $[M]^+$: 984.18530. Found: 984.1871. Error: 1.81 ppm.

III-4. Acetonitrile(4'-(9,9-dihexyl-7-iodo-fluoren-2-yl)-2,2':6',2''-terpyridine)(2,2'-bipyridine) ruthenium(II) hexafluorophosphate

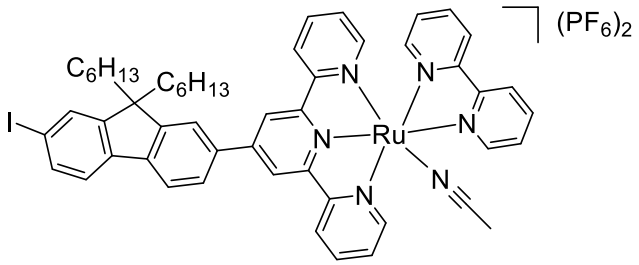

In a 5 mL Schlenk flask, compound **III-3** (0.2837 g, 0.28 mmol), distilled water (15.0 mL), and $MeCH_3$ (15.0 mL) were added. The mixture was sparged with argon for 15 minutes to remove any oxygen present. The reaction mixture was then heated to 100°C for 24 hours. After cooling to room temperature, the reaction mixture was concentrated under reduced pressure to approximately 5 mL, and then treated with a saturated aqueous solution of NH_4PF_6. The resulting precipitate was collected by filtration, washed thoroughly with water and diethyl ether, and then dried to yield 0.3225 g (0.25 mmol, 90%) of complex **III-4** as a dark red solid.

^{1}H-NMR (300 MHz, Acetone) δ 9.93 (d, *J* = 4.8 Hz, 1H), 9.30 (s, 2H), 8.91 (dd, *J* = 14.8, 8.0 Hz, 3H), 8.68 (d, *J* = 8.4 Hz, 1H), 8.53 – 8.43 (m, 2H), 8.36 (dd, *J* = 8.0, 1.8 Hz, 1H), 8.24 – 8.15 (m, 3H), 8.14 – 8.08 (m, 1H), 8.04 – 7.94 (m, 4H), 7.87 – 7.77 (m, 3H), 7.55 (ddd, *J* = 7.7, 5.5, 1.4 Hz, 2H), 7.26 (ddd, *J* = 7.3, 5.8, 1.4 Hz, 1H), 2.34 (s, 3H), 2.30 – 2.21 (m, 4H), 1.19 – 1.03 (m, 12H), 0.82 – 0.73 (m, 6H), 0.69 (m, 4H).

^{13}C-NMR (100 MHz, CD_3CN) δ 159.51, 158.70, 158.67, 156.95, 154.84, 154.26, 153.50, 152.75, 152.09, 150.13, 143.72, 140.89, 139.51, 138.67, 138.42, 137.38, 136.64, 133.57, 128.88, 128.57, 128.06, 127.68, 126.20, 125.45, 125.18, 124.57, 123.32, 123.03, 122.04, 121.98, 94.44, 56.96, 40.59, 32.22, 30.18, 24.68, 23.23, 14.29, 4.56.

HRMS (ESI-TOF+) *m/z* anal. calcd. for $C_{52}H_{53}IN_6Ru$ $[M]^{2+}$: 495.12170. Found: 495.1235. Error: 2.90 ppm.

III-5 4'-(9,9-dihexyl-7-(trimethylsilyl)fluoren-2-yl)-2,2':6',2''-terpyridine

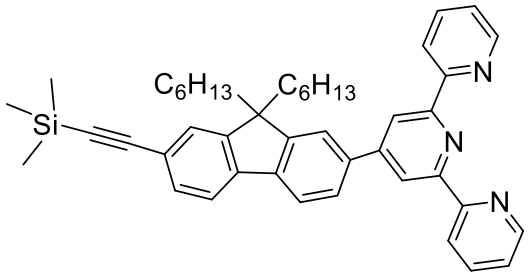

To a Schlenk flask containing 4'-(9,9-dihexyl-7-iodo-fluoren-2-yl)-2,2':6',2''-terpyridine (0.3000 g, 0.43 mmol), ethynyltrimethylsilane (0.3 mL, 2.15 mmol), $Pd(PPh_3)_2Cl_2$ (0.0090 g, 5 mol %) and CuI (0.0490 g, 10 mol %) were mixed, THF was added (15 mL) followed by the dropwise addition of Et_3N (15 mL) and stirring at room temperature under argon for 24 hrs. The reaction was evaporated to dryness under reduced pressure and purified by column chromatography on silica gel using hexane/ethyl acetate (9/1) as eluent to yield 0.1216 g (0.18 mmol, 43 %) of **III-5** as a yellow/orange solid.

^{1}H-NMR (300 MHz, $CDCl_3$) δ 8.80 – 8.73 (m, 4H), 8.68 (dt, *J* = 8.0, 1.1 Hz, 2H), 7.93 – 7.86 (m, 3H), 7.85 – 7.77 (m, 2H), 7.68 (dd, *J* = 7.8, 0.7 Hz, 1H), 7.53 – 7.46 (m, 2H), 7.37 (ddd, *J* = 7.5, 4.8, 1.2 Hz, 2H), 2.15 – 1.97 (m, 4H), 1.20 – 0.97 (m, 12H), 0.76 (t, *J* = 6.9 Hz, 6H), 0.67 – 0.55 (m, 4H), 0.30 (s, 9H).

^{13}C-NMR (150 MHz, $CDCl_3$) δ 156.32, 155.90, 152.10, 151.26, 151.07, 149.03, 141.62, 141.15, 137.87, 137.39, 131.38, 126.75, 126.41, 124.10, 121.81, 121.67, 120.66, 119.99, 119.37, 106.34, 94.30, 55.69, 40.54, 31.67, 29.79, 23.88, 22.83, 14.13, 0.39.

HRMS (ESI-TOF+) *m/z* anal. calcd. for $C_{45}H_{51}N_3Si$ $[M+H]^+$: 662.39230. Found: 662.3931. Error: 1.20 ppm.

III-6. Trichlorido(4'-(9,9-dihexyl-7-(trimethylsilyl)fluoren-2-yl)-2,2':6',2''-terpyridine)ruthenium (III)

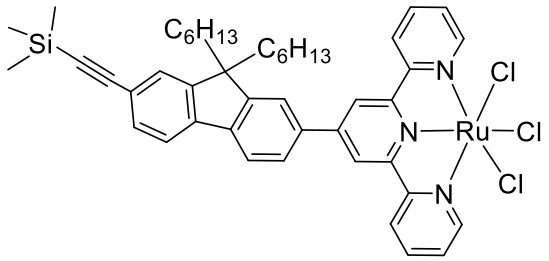

In a round-bottom flask, 4'-(9,9-dihexyl-7-(trimethylsilyl)fluoren-2-yl)-2,2':6',2''-terpyridine 3d (0.1200 g, 0.18 mmol) and $RuCl_3xH_2O$ (0.390 g) were suspended in ethanol (20 mL). The mixture was stirred at reflux temperature for 4 hours, and then allowed to cool to room temperature. The resulting precipitate was collected by filtration, washed with cold ethanol and ether, and dried under vacuum to yield 0.1450 g (0.17 mmol, 92%) of complex **III-6** as a black solid.

HRMS (ESI-TOF+) *m/z* anal. calcd. for $C_{45}H_{55}Cl_3N_4RuSi$ $[M+NH_4]^+$: 888.22980. Found: 888.2285. Error: 2.93 ppm.

III-7. Chlorido(4'-(9,9-dihexyl-7-(trimethylsilyl)fluoren-2-yl)-2,2':6',2''-terpyridine) (2,2'-bipyridine) ruthenium (II) chloride

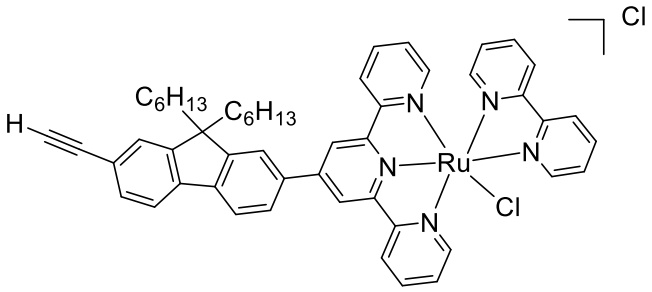

To a round-bottom flask were added **III-6** (0.1450 g, 0.17 mmol), 2,2-bipyridine (0.0281 g, 0.18 mmol) and LiCl (0.0288 g, 0.68 mmol). The mixture was suspended in 15.0 mL of ethanol and 5.0 mL of deionized water and treated with 40 µL of triethylamine. The resulting mixture was stirred at reflux temperature for 3 hours, then K_2CO_3 (0.0900 g, 0.65 mmol) were added and the solution was stirred overnight and then evaporated to dryness under reduced pressure The resulting residue was purified by column chromatography on neutral alumina using dichloromethane/methanol (9/1) as eluent to yield 99.7980 g (0.11 mmol, 64 %) of **III-7** as a dark purple solid.

^{1}H-NMR (300 MHz, CD_3CN) δ 10.27 (d, *J* = 6.0 Hz, 1H), 8.92 – 8.82 (m, 2H), 8.65 (d, *J* = 8.3 Hz, 3H), 8.36 (d, *J* = 7.9 Hz, 1H), 8.30 – 8.21 (m, 2H), 8.19 – 8.12 (m, 1H), 8.04 – 7.93 (m, 2H), 7.91 – 7.82 (m, 3H), 7.72 – 7.64 (m, 3H), 7.54 – 7.31 (m, 3H), 7.25 (ddd, *J* = 7.0, 5.6, 1.4 Hz, 2H), 6.94 (ddd, *J* = 7.2, 5.8, 1.3 Hz, 1H), 3.73 (s, 1H), 1.17 – 0.99 (m, 12H), 0.82 – 0.68 (m, 6H), 0.70 – 0.51 (m, 4H).

^{13}C-NMR (100 MHz, CD_3CN) δ 159.86, 159.02, 158.97, 157.20, 153.47, 153.28, 152.96, 137.93, 137.92, 137.47, 137.44, 136.50, 136.48, 132.28, 128.19, 127.87, 127.83, 127.72, 127.66, 127.02, 125.43, 124.70, 124.69, 124.46, 124.23, 123.19, 123.11, 121.44, 121.24, 121.19, 84.93, 79.39, 56.71, 56.49, 52.54, 41.69, 40.67, 32.24, 30.22, 24.70, 23.22, 14.26.

HRMS (ESI-TOF+) *m/z* anal. calcd. for $C_{52}H_{51}ClN_5Ru$ $[M]^+$: 882.2870. Found: 882.2876. Error: 0.70 ppm.

III-9. (4'-(9,9-dihexyl-7-(trimethylsilyl)ethynyl-fluoren-2-yl)-2,2':6',2''-terpyridine) (bipyridine)nitrito-ruthenium(II) hexafluorophosphate

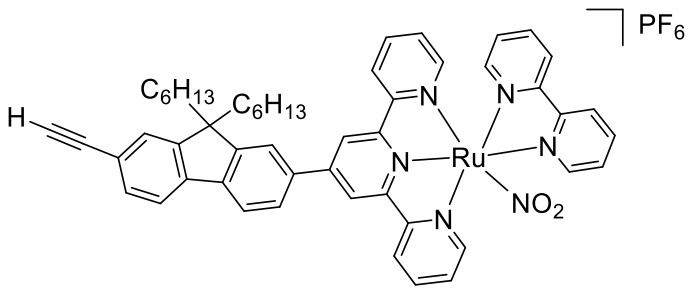

In a round-bottom flask, chlorido(4'-(9,9-dihexyl-7-(trimethylsilyl)fluoren-2-yl)-2,2':6',2''-terpyridine)(2,2'-bipyridine) ruthenium(II) chloride **III-7** (0.1000 g, 0.11 mmol), $NaNO_2$ (0.0759 g, 1.10 mmol), ethanol (5.0 mL), and deionized water (1.5 mL) were added. The resulting mixture was stirred at reflux temperature for 4 hours. Subsequently, the mixture was concentrated under reduced pressure to approximately 1.5 mL and then treated with a saturated aqueous solution of NH_4PF_6. The resulting precipitate was collected by filtration, washed with water and diethyl ether, and then dried to yield 0.1051 g (0.10 mmol, 92%) of **III-9** as a red solid.

^{1}H-NMR (300 MHz, CD_3CN) δ 9.92 (d, *J* = 5.3 Hz, 1H), 8.83 (d, *J* = 3.9 Hz, 2H), 8.61 (t, *J* = 8.8 Hz, 3H), 8.39 (d, *J* = 8.3 Hz, 1H), 8.29 (td, *J* = 8.0, 1.1 Hz, 1H), 8.23 – 8.14 (m, 2H), 8.13 – 8.02 (m, 1H), 8.05 – 7.94 (m, 'H), 7.91 – 7.75 (m, 'H), 7.52 – 7.43 (m, 2H), 7.39 – 7.29 (m, 2H), 7.10 (t, *J* = 6.6 Hz, 1H), 3.76 (s, 1H), 1.21 – 1.00 (m, 12H), 0.89 – 0.71 (m, 6H), 0.74 – 0.38 (m, 4H).

^{13}C-NMR (100 MHz, CD_3CN) δ 159.53, 158.93, 157.69, 156.70, 153.81, 153.54, 153.38, 152.46, 151.81, 148.83, 143.28, 141.86, 138.65, 138.11, 137.86, 136.91, 132.20, 128.32, 127.94, 127.82, 127.62, 127.01, 124.62, 123.99, 123.13, 123.04, 122.20, 121.95, 121.40, 121.34, 84.81, 79.37, 56.61, 40.57, 32.15, 30.11, 24.59, 23.12, 14.17.

HRMS (ESI-TOF+) *m/z* anal. calcd. for $C_{52}H_{51}N_{6O}2Ru$ $[M]^+$: 893.31340. Found: 893.3117. Error: 1.70 ppm.

3-Ru(NO_2)CH_3CN-5

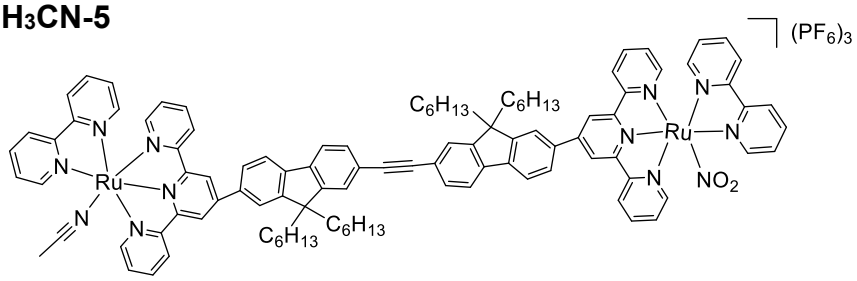

To a Schlenk flask were added complex **III-4** (0.1142 g, 0.11 mmol), complex 3g (0.1051 g, 0.10 mmol), CuI (0.0390 g, 10 mol %) and $Pd(PPh_3)_2Cl_2$ (0.0737 g, 5 mol %). After THF was added (25 mL) followed by the addition of Et_3N (25 mL). The reaction was stirred at reflux temperature overnight under argon. The mixture was chilled to room temperature, filtered, evaporated to dryness under reduced pressure and purified by column chromatography using silica gel and dichloromethane/ethyl acetate (9/1) as eluent, the pure complex was treated with a saturated aqueous solution of NH_4PF_6, the precipitate formed was collected, washed thoroughly with water and diethyl ether to yield yielding 0.0150 g, (0.007 mmol, 6.8 %) of **Ru(NO_2)CH_3CN-5** as a reddish solid.

^{1}H-NMR (400 MHz, Acetone) δ 10.04 (d, *J* = 5.6 Hz, 1H), 9.94 (d, *J* = 4.8 Hz, 1H), 9.31 (d, *J* = 9.0 Hz, 2H), 9.17 (s, 2H), 8.97 – 8.88 (m, 4H), 8.78 (dd, *J* = 8.5, 1.7 Hz, 2H), 8.71 – 8.65 (m, 2H), 8.58 – 8.52 (m, 2H), 8.51 – 8.42 (m, 2H), 8.42 – 8.38 (m, 2H), 8.35 (dd, *J* = 8.0, 1.7 Hz, 1H), 8.24 – 8.16 (m, 4H), 8.15 – 8.04 (m, 6H), 8.03 – 7.96 (m, 4H), 7.96 – 7.89 (m, 3H), 7.83 – 7.76 (m, 4H), 7.73 – 7.68 (m, 2H), 7.59 – 7.51 (m, 2H), 7.49 – 7.44 (m, 2H), 7.31 – 7.21 (m, 2H), 2.35 (s, 3H), 2.29 (m, 8H), 1.34 – 1.22 (m, 24H), 0.87 (t, *J* = 7.1 Hz, 20H).

^{13}C-NMR (150 MHz, Acetone) δ 206.32, 159.87, 159.61, 159.29, 158.83, 158.78, 157.93, 156.99, 156.86, 154.26, 154.06, 153.62, 153.54, 153.40, 152.52, 152.50, 152.31, 152.24, 152.09, 149.98, 148.65, 144.09, 143.58, 141.71, 141.53, 139.61, 138.81, 138.56, 138.52, 138.16, 137.96, 136.95, 136.45, 131.85, 131.82, 129.12, 128.80, 128.43, 128.08, 128.03, 127.97, 127.89, 127.86, 127.24, 126.97, 126.65, 125.55, 125.25, 124.67, 124.62, 124.11, 123.74, 122.81, 122.61, 122.10, 121.97, 121.78, 121.73, 121.63, 121.15, 121.11, 91.82, 91.67, 56.72, 56.66, 48.00, 41.24, 40.89, 32.62, 32.42, 32.37, 32.30, 30.39, 30.35, 24.79, 24.76, 23.25, 14.37, 14.28, 9.30, 3.93.

HRMS (ESI-TOF+) *m/z* anal. calcd. for $C_{104}H_{103}N_{12}O_2Ru_2$ $[M]^{3+}$: 585.21530. Found: 585.2148. Error: 1.16 ppm.

III-Ru(NO)CH_3CN-5

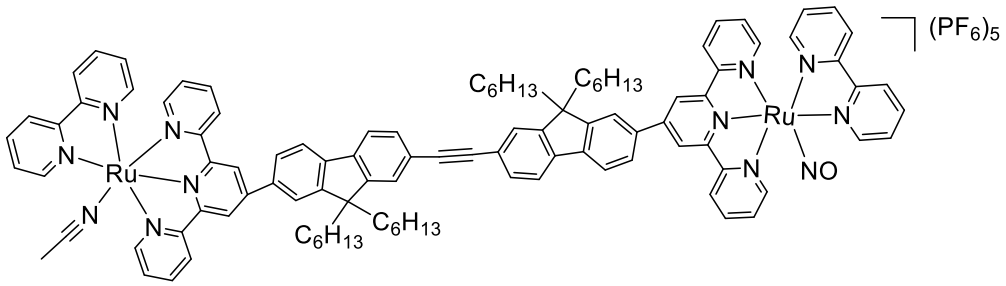

To a round-bottom flask containing **Ru(NO_2)CH_3CN-5** and ethanol (2.0 mL) was added HCl (38 %, 0.70 mL) and the mixture was stirred at 60°C for 60 minutes under protection from light. After chilling to room temperature, the reaction was concentrated under reduced pressure to ca. 2 mL, followed by treatment with a saturated aqueous solution of NH_4PF_6. The precipitate formed was collected, washed thoroughly with water and diethyl ether to yield 0.0155 g (0.006 mmol, 90 %) of **Ru(NO)CH_3CN-5**as a dark red/black solid.

^{1}H-NMR (400 MHz, Acetone) δ 9.96 (d, *J* = 5.7 Hz, 1H), 9.65 (d, *J* = 4.5 Hz, 1H), 9.34 (d, *J* = 4.5 Hz, 1H), 9.22 (d, *J* = 7.9 Hz, 2H), 9.08 – 9.01 (m, 1H), 9.01 – 8.94 (m, 2H), 9.02 – 8.86 (m, 3H), 8.74 – 8.64 (m, 1H), 8.62 (d, *J* = 1.4 Hz, 1H), 8.58 – 8.45 (m, 2H), 8.44 – 8.37 (m, 0H), 8.33 – 8.26 (m, 1H), 8.27 – 8.19 (m, 1H), 8.17 – 8.03 (m, 3H), 7.99 (d, *J* = 7.8 Hz, 1H), 7.96 – 7.88 (m, 1H), 7.87 – 7.79 (m, 1H), 7.71 (dd, *J* = 16.2, 7.0 Hz, 2H), 7.61 – 7.53 (m, 0H), 7.33 – 7.24 (m, -1H), 2.37 (s, 1H), 2.37 – 2.24 (m, 2H), 1.22 – 1.06 (m, 12H), 0.92 – 0.62 (m, 3H).

^{13}C-NMR (101 MHz, Acetone) δ 159.62, 159.16, 158.99, 158.78, 158.21, 156.99, 155.95, 155.77, 155.32, 154.49, 154.19, 153.61, 153.54, 152.52, 152.24, 149.99, 145.48, 145.16, 144.09, 141.70, 139.62, 138.53, 134.76, 131.65, 131.06, 129.12, 128.78, 128.08, 127.79, 127.01, 125.38, 124.83, 123.57, 122.76, 121.77, 92.27, 40.87, 32.41, 32.39, 24.79, 23.26, 23.24, 14.28, 3.95.

HRMS (ESI-TOF+) *m/z* anal. calcd. for $C_{104}H_{103}N_{12}ORu_2$ $[M]^{4+}$: 434.91270. Found: 434.9127. Error: 2.76 ppm.

4. Synthesis of products [RuMCH$_3$CN-x](PF$_6$)$_z$.

III-RuCH$_3$CN-1'

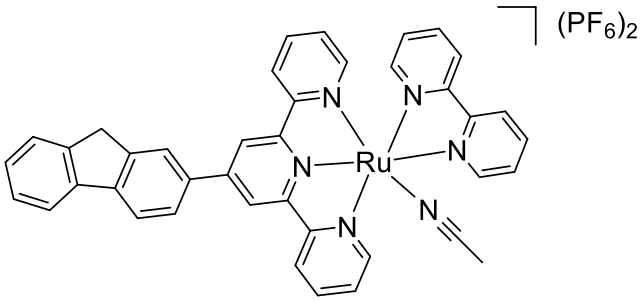

To a round-bottom flask containing **RuCl-1'** (0.0250 g, 0.026 mmol) and acetonitrile (10.0 mL) was added H_2O (10.0 mL). The mixture was sparged with argon for 15 minutes to remove any oxygen present. The reaction was stirred at reflux temperature overnight under argon. After chilling to room temperature, the reaction was concentrated under reduced pressure to ca. 2 mL, followed by treatment with a saturated aqueous solution of NH_4PF_6. The precipitate formed was collected, washed thoroughly with water and diethyl ether to yield 0.0244 g (0.025 mmol, 95 %) of **RuCH$_3$CN-1'** as an orange solid.

^{1}H-NMR (400 MHz, Acetone) δ 9.94 (ddd, *J* = 5.6, 1.5, 0.8 Hz, 1H), 9.31 (s, 2H), 9.00 (d, *J* = 7.6 Hz, 2H), 8.94 (dt, *J* = 8.3, 1.2 Hz, 1H), 8.69 (dt, *J* = 8.3, 1.3 Hz, 1H), 8.53 (dt, *J* = 1.9, 0.9 Hz, 1H), 8.48 (td, *J* = 7.9, 1.5 Hz, 1H), 8.33 (dd, *J* = 8.0, 2.0 Hz, 1H), 8.24 – 8.15 (m, 3H), 8.12 (ddd, *J* = 7.7, 5.6, 1.3 Hz, 1H), 8.05 (dt, *J* = 7.5, 1.2 Hz, 1H), 8.01 (ddd, *J* = 5.5, 1.5, 0.8 Hz, 2H), 7.97 (ddd, *J* = 8.2, 7.6, 1.5 Hz, 1H), 7.77 (ddd, *J* = 5.8, 1.5, 0.8 Hz, 1H), 7.70 (dt, *J* = 7.3, 1.0 Hz, 1H), 7.55 (ddd, *J* = 7.6, 5.5, 1.3 Hz, 2H), 7.49 (td, *J* = 7.5, 1.4 Hz, 1H), 7.44 (td, *J* = 7.4, 1.3 Hz, 1H), 7.26 (ddd, *J* = 7.5, 5.7, 1.4 Hz, 1H), 4.15 (s, 2H), 2.36 (s, 3H).

^{13}C-NMR (100 MHz, Acetone) δ 158.80, 157.95, 157.86, 156.13, 153.34, 152.72, 151.29, 149.70, 144.70, 144.17, 144.12, 140.61, 138.71, 137.89, 137.60, 134.75, 128.18, 127.89, 127.86, 127.15, 126.98, 126.77, 125.77, 125.37, 124.75, 124.46, 124.35, 123.71, 121.15, 120.81, 120.71, 36.73, 3.05.

HRMS (ESI-TOF+) *m/z* anal. calcd. for $C_{40}H_{30}N_6Ru$ $[M]^{2+}$: 348.07950. Found: 348.0796. Error: 0.54 ppm.

III-RuCH$_3$CN-1

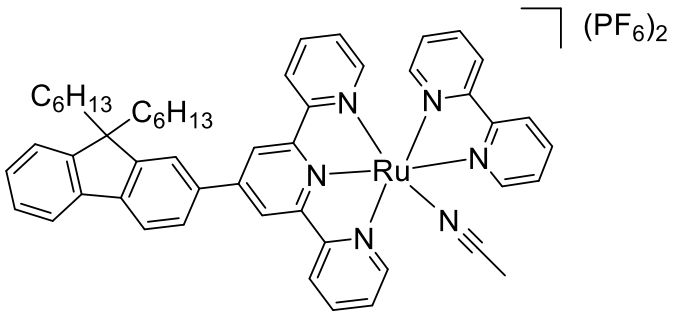

Prepared as described above for **RuCH$_3$CN-1'** from **RuCl-1** Yield: 92 % (Orange solid).

^{1}H-NMR (400 MHz, Acetone) δ 9.93 (ddd, *J* = 5.6, 1.5, 0.8 Hz, 1H), 9.31 (s, 2H), 8.94 (dt, *J* = 8.4, 1.3 Hz, 1H), 8.92 – 8.86 (m, 2H), 8.69 (dt, *J* = 8.3, 1.1 Hz, 1H), 8.52 – 8.44 (m, 2H), 8.35 (dd, *J* = 8.0, 1.8 Hz, 1H), 8.20 (td, *J* = 7.7, 1.5 Hz, 2H), 8.15 (dd, *J* = 8.0, 0.5 Hz, 1H), 8.12 (ddd, *J* = 7.7, 5.6, 1.4 Hz, 1H), 8.03 – 7.95 (m, 4H), 7.80 (ddd, *J* = 5.8, 1.5, 0.8 Hz, 1H), 7.56 (d, *J* = 7.8 Hz, 3H), 7.46 (d, *J* = 5.0 Hz, 2H), 7.27 (d, *J* = 13.3 Hz, 1H), 2.35 (s, 3H), 2.32 – 2.16 (m, 4H), 1.19 – 1.00 (m, 12H), 0.82 – 0.58 (m, 10H).

^{13}C-NMR (100 MHz, Acetone) δ 159.64, 158.85, 158.74, 157.02, 154.27, 153.63, 153.18, 152.26, 152.11, 150.20, 144.99, 141.05, 139.60, 138.80, 138.51, 135.68, 129.21, 129.10, 128.79, 128.15, 127.86, 127.83, 126.65, 125.51, 125.25, 124.61, 124.07, 122.48, 121.71, 121.62, 121.47, 56.49, 40.93, 32.35, 24.70, 23.20, 14.24, 3.94.

HRMS (ESI-TOF+) *m/z* anal. calcd. for $C_{52}H_{54}N_6Ru$ $[M]^{2+}$: 432.17340. Found: 432.1733. Error: 1.11 ppm.

III-RuCH$_3$CN-2

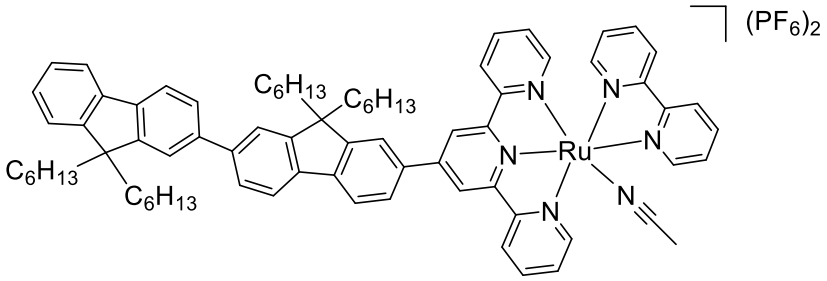

Prepared as described above for **RuCH$_3$CN-1'** from **RuCl-2**. Yield: 95 % (Orange solid).

^{1}H-NMR (400 MHz, Acetone) δ 9.96 – 9.93 (m, 1H), 9.34 (s, 2H), 8.99 – 8.84 (m, 3H), 8.70 (dt, *J* = 8.3, 1.3 Hz, 1H), 8.54 (d, *J* = 1.4 Hz, 1H), 8.49 (td, *J* = 7.9, 1.5 Hz, 1H), 8.38 (dd, *J* = 8.0, 1.8 Hz, 1H), 8.25 – 8.18 (m, 3H), 8.12 (ddd, *J* = 7.7, 5.6, 1.3 Hz, 1H), 8.08 (d, *J* = 7.9 Hz, 1H), 8.05 – 8.00 (m, 2H), 8.00 – 7.96 (m, 2H), 7.94 (d, *J* = 7.9 Hz, 1H), 7.91 (d, *J* = 1.2 Hz, 1H), 7.89 – 7.84 (m, 2H), 7.83 – 7.78 (m, 2H), 7.56 (ddd, *J* = 7.6, 5.5, 1.3 Hz, 2H), 7.52 – 7.49 (m, 1H), 7.42 – 7.34 (m, 2H), 7.28 (ddd, *J* = 7.2, 5.7, 1.3 Hz, 1H), 2.36 (s, 3H), 2.36 – 2.27 (m, 4H), 2.24 – 2.10 (m, 4H), 1.23 – 0.96 (m, 24H), 0.76 (td, *J* = 6.9, 3.7 Hz, 20H).

^{13}C-NMR (100 MHz, Acetone) δ 159.66, 158.86, 158.76, 157.04, 154.29, 153.63, 153.51, 153.00, 152.35, 152.27, 151.74, 150.18, 144.75, 142.52, 141.74, 141.70, 140.96, 140.25, 139.62, 138.81, 138.52, 135.62, 129.11, 128.79, 128.18, 127.92, 127.88, 127.30, 127.02, 126.67, 125.52, 125.26, 124.63, 123.86, 122.51, 122.44, 122.27, 121.90, 121.72, 121.69, 121.01, 120.73, 56.68, 56.06, 40.91, 40.85, 32.30, 32.22, 24.73, 24.59, 23.20, 23.15, 14.28, 14.25, 3.97.

HRMS (ESI-TOF+) *m/z* anal. calcd. for $C_{77}H_{86}N_6Ru$ $[M]^{2+}$: 598.29900. Found: 598.2992. Error: 0.40 ppm.

III-RuCH$_3$CN-3

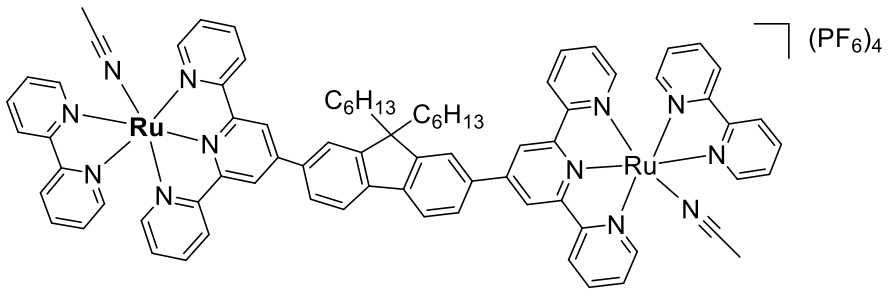

Prepared as described above for **RuCH$_3$CN-1'** from **RuCl-3**. Yield: 90 % (Red solid).

^{1}H-NMR (400 MHz, Acetone) δ 9.95 – 9.92 (m, 2H), 9.34 (s, 4H), 8.93 (ddd, *J* = 8.1, 7.1, 1.0 Hz, 6H), 8.72 – 8.67 (m, 2H), 8.62 (d, *J* = 1.8 Hz, 2H), 8.51 – 8.45 (m, 4H), 8.34 (d, *J* = 8.0 Hz, 2H), 8.21 (td, *J* = 7.7, 1.5 Hz, 4H), 8.12 (ddd, *J* = 7.7, 5.6, 1.3 Hz, 2H), 8.05 – 7.94 (m, 6H), 7.82 (ddd, *J* = 5.7, 1.5, 0.7 Hz, 2H), 7.56 (ddd, *J* = 7.6, 5.5, 1.3 Hz, 4H), 7.28 (ddd, *J* = 7.3, 5.8, 1.4 Hz, 2H), 2.47 (d, *J* = 16.3 Hz, 4H), 2.35 (s, 6H), 1.29 (s, 12H), 1.25 – 1.01 (m, 14H), 0.87 – 0.68 (m, 12H).

^{13}C-NMR (100 MHz, Acetone) δ 159.61, 158.83, 156.98, 154.25, 153.90, 153.65, 152.29, 149.86, 143.84, 139.62, 138.81, 138.51, 136.72, 129.13, 128.81, 128.16, 127.88, 126.67, 125.60, 125.25, 124.61, 122.70, 122.57, 121.76, 57.19, 40.84, 32.51, 24.93, 23.29, 14.30, 3.92.

HRMS (ESI-TOF+) *m/z* anal. calcd. for $C_{79}H_{74}N_{12}Ru_2$ $[M]^{4+}$: 348.60700. Found: 348.6063. Error: 2.71 ppm.

III-RuMeCN-4

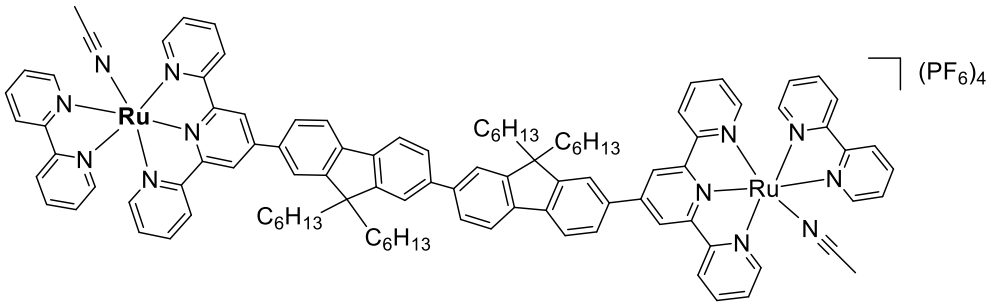

Prepared as described above for **RuCH$_3$CN-1'** from **RuCl-4**. Yield: 92 % (Red solid).

^{1}H-NMR (300 MHz, Acetone-d_6) δ 9.99 – 9.94 (m, 2H), 9.38 (s, 4H), 9.03 – 8.91 (m, 6H), 8.76 – 8.67 (m, 2H), 8.65 – 8.60 (m, 2H), 8.49 (td, *J* = 7.9, 1.5 Hz, 2H), 8.45 – 8.39 (m, 2H), 8.21 (ddd, *J* = 7.9, 5.8, 2.2 Hz, 6H), 8.17 – 8.09 (m, 4H), 8.06 – 7.90 (m, 12H), 7.88 – 7.80 (m, 2H), 7.61 – 7.50 (m, 4H), 7.32 – 7.23 (m, 2H), 2.46 – 2.32 (m, 14H), 1.24 – 1.08 (m, 24H), 0.78 (t, *J* = 6.7 Hz, 20H).

^{1}H-NMR (400 MHz, Acetonitrile-d3) δ 9.69 – 9.65 (m, 2H), 8.95 (s, 4H), 8.74 – 8.63 (m, 6H), 8.46 – 8.34 (m, 4H), 8.32 – 8.23 (m, 4H), 8.20 – 8.16 (m, 2H), 8.14 – 8.06 (m, 6H), 8.02 (ddd, J = 6.9, 6.1, 0.9 Hz, 2H), 7.98 – 7.93 (m, 2H), 7.92 – 7.83 (m, 4H), 7.81 – 7.73 (m, 4H), 7.46 – 7.39 (m, 6H), 7.18 – 7.10 (m, 2H), 2.15 (s, 6H), 2.42 – 2.33 (m, 8H), 1.26 – 1.06 (m, 24H), 0.80 (t, J = 6.7 Hz, 20H).

^{13}C NMR

HRMS (ESI-TOF+) *m/z* anal. calcd. for $C_{104}H_{106}N_{12}Ru_2$ $[M]^{4+}$: 438.42570. Found: 438.4236. Error: 3.18 ppm.

III-RuCH$_3$CN-5

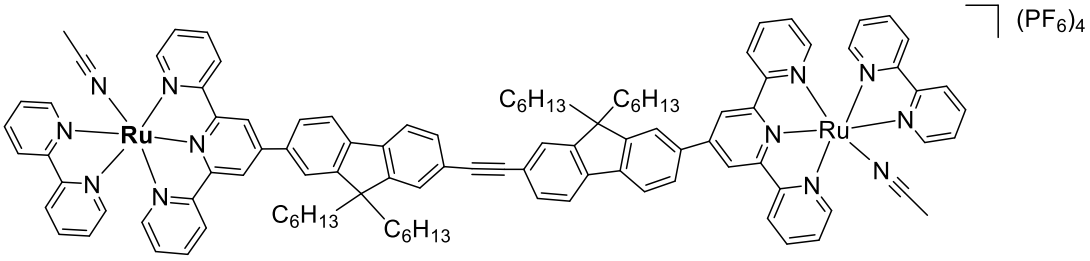

Prepared as described above for **RuCH$_3$CN-1'** from **RuCl-5**. Yield: 95 % (Red dark solid).

^{1}H-NMR (400 MHz, Acetone) δ 9.96 (ddd, *J* = 5.6, 1.5, 0.8 Hz, 2H), 9.35 (s, 4H), 8.97 (dt, *J* = 8.4, 1.2 Hz, 2H), 8.93 (dt, *J* = 8.1, 1.3 Hz, 4H), 8.72 (dt, *J* = 8.4, 1.1 Hz, 2H), 8.58 (d, *J* = 2.1 Hz, 2H), 8.50 (td, *J* = 7.9, 1.5 Hz, 2H), 8.42 (dd, *J* = 8.0, 1.8 Hz, 2H), 8.27 – 8.19 (m, 6H), 8.14 (ddd, *J* = 7.7, 5.6, 1.3 Hz, 2H), 8.09 (dd, *J* = 7.9, 0.7 Hz, 2H), 8.07 – 8.01 (m, 4H), 8.00 (td, *J* = 7.6, 1.5 Hz, 2H), 7.86 – 7.79 (m, 4H), 7.73 (dd, *J* = 7.8, 1.5 Hz, 2H), 7.58 (ddd, *J* = 7.7, 5.5, 1.3 Hz, 4H), 7.29 (ddd, *J* = 7.3, 5.8, 1.4 Hz, 2H), 2.38 (s, 6H), 2.36 – 2.29 (m, 8H), 1.23 – 1.08 (m, 24H), 0.80 (t, *J* = 7.0 Hz, 20H).

^{13}C-NMR (100 MHz, Acetone) δ 159.62, 158.84, 158.80, 157.02, 154.28, 153.62, 153.53, 152.53, 152.26, 149.98, 144.11, 141.56, 139.63, 138.83, 138.54, 136.31, 131.88, 129.13, 128.80, 128.08, 127.87, 126.98, 126.67, 125.56, 125.27, 124.63, 123.67, 122.61, 122.12, 121.78, 91.77, 56.73, 40.89, 32.42, 24.80, 23.27, 14.28, 3.96.

HRMS (ESI-TOF+) *m/z* anal. calcd. for $C_{106}H_{106}N_{12}Ru_2$ $[M]^{4+}$: 437.66990. Found: 437.6696. Error: 2.28 ppm.

IV-trans-RuNO(Cl)OH-3

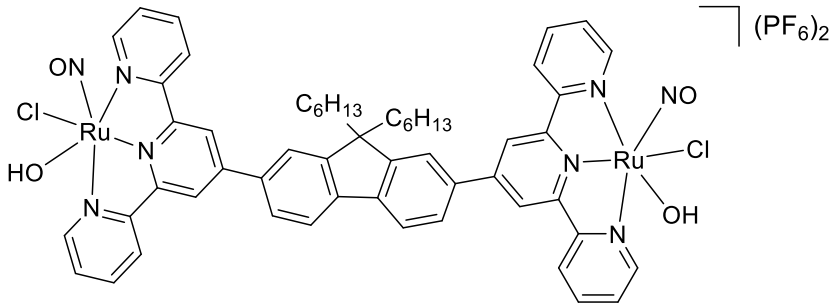

To a round-bottom flask containing **Ru(NO)Cl_2-3** (0.0500 g, 0.039 mmol) and H_2O (50.0 mL) w was sparged with argon for 15 minutes to remove any oxygen present. The reaction was stirred at reflux temperature for 2 days under argon. After chilling to room temperature, the reaction was treated with a saturated aqueous solution of NH_4PF_6. The precipitate formed was collected, washed thoroughly with water and diethyl ether to yield 0.0230 g (0.016 mmol, 40 %) of **trans-RuNO(Cl)OH-3** as dark red solid.

^{1}H-NMR (400 MHz, CD3CN) δ 9.20 – 9.14 (m, 4H), 8.86 (s, 4H), 8.77 (d, J = 7.5 Hz, 6H), 8.50 (td, J = 7.9, 1.7 Hz, 4H), 8.25 (s, 2H), 8.21 (s, 4H), 7.96 (ddd, J = 7.4, 5.6, 1.2 Hz, 4H), 2.39 – 2.31 (m, 4H), 1.21 – 1.01 (m, 12H), 0.80 – 0.65 (m, 10H).

^{13}C-NMR (100 MHz, CD3CN) δ 158.40, 157.84, 156.59, 154.86, 153.62, 143.33, 130.04, 129.74, 129.52, 128.72, 126.96, 124.02, 123.83, 123.49, 40.60, 32.19, 30.21, 24.72, 23.17, 14.20.

HRMS (ESI-TOF+) *m/z* anal. calcd. for $C_{55}H_{54}Cl_2N_8O_4Ru_2$ $[M]^{2+}$: 582.08740. Found: 582.0882. Error: 1.14 ppm.

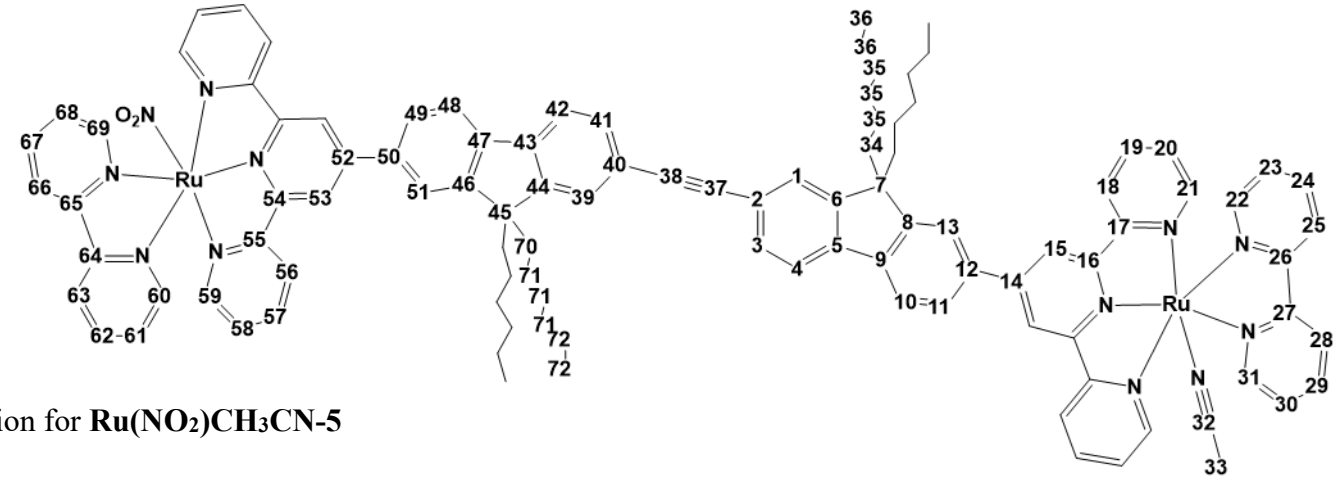

Table 1. Proton and carbon assignation for **Ru(NO$_2$)CH$_3$CN-5**

Position	^{13}C-NMR δ (Hz)	^{1}H-NMR δ (Hz)	Multiplet
1	126.97	7.83 - 7.76	m
2	125.55	-	-
3	121.73	8.15 - 8.04	m
4	131.85	7.73-7.68	m
5	152.52	-	-
6	141.53	-	-
7	56.66	-	-
8	144.09	-	-
9	153.54	-	-
10	122.10	8.24 - 8.16	m
11	128.08	8.42-8.38	dd
12	136.45	-	-
13	122.61	8.58 - 8.452	m
14	149.98	-	-
15	121.78	9.31	d
16	159.61	-	-
17	158.83	-	-
18	125.25	8.97 - 8.88	m
19	129.12	7.59 - 7.51	m
20	139.61	8.24 - 8.16	m

Position	^{13}C-NMR δ (Hz)	^{1}H-NMR δ (Hz)	Multiplet
21	154.26	8.15 - 8.04	m
22	152.24	7.83 - 7.76	m
23	127.86	7.31 - 7.21	m
24	138.52	7.96 - 7.89	m
25	123.74	8.71 - 8.65	m
26	158.78	-	-
27	156.99	-	-
28	124.67	8.97 - 8.88	m
29	138.81	8.51 - 8.42	m
30	128.80	8.15 - 8.04	m
31	153.62	9.94	d
32	126.72	-	-
33	3.93	2.35	s
34	40.89	2.36-2.29	m
35	32.42, 23.25	1.34 - 1.22	m
36	14.34	0.87	m
37	91.67	-	-
38	91.82	-	-
39	127.24	7.83-7.76	m
40	131.82	-	-

Position	^{13}C-NMR δ (Hz)	^{1}H-NMR δ (Hz)	Multiplet
41	131.36	7.73-7.68	m
42	121.15	8.15-8.04	m
43	138.16	-	-
44	143.58	-	-
45	56.66	-	-
46	141.71	-	-
47	135.68	-	-
48	121.97	8.16-8.24	m
49	128.03	8.35	dd
50	136.16	-	-
51	121.63	8.58-8.52	m
52	148.65	-	-
53	121.11	9.17	s
54	159.87	-	-
55	159.29	-	-
56	138.56	8.15-8.04	m
57	124.11	8.78	dd
58	128.43	7.49-7.44	m
59	153.40	7.96-7.89	m
60	152.09	7.83-7.76	m

Position	^{13}C-NMR δ (Hz)	^{1}H-NMR δ (Hz)	Multiplet
61	127.89	7.31-7.21	m
62	136.95	7.96-7.89	m
63	122.81	8.71-8.65	m
65	157.93	-	-
65	156.86	-	-
66	124.62	8.97-8.88	m
67	137.46	8.42-8.38	m
68	127.97	8.15-8.04	m
69	154.06	10.04	s
70	48.00	2.36-2.29	m
71	32.67, 24.76	1.34 – 1.22	m
72	14.37	0.87	m

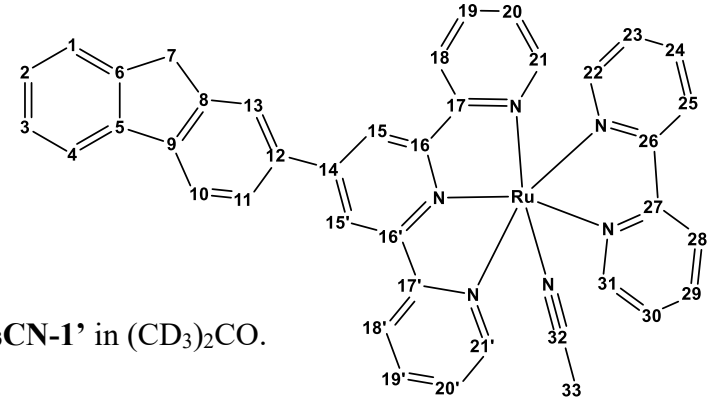

Table 2. Proton and carbon assignation for **RuCH$_3$CN-1'** in $(CD_3)_2CO$.

Position	^{13}C-NMR δ (Hz)	^{1}H-NMR δ (Hz)	Multiplet
1	125.37	7.70	dt
2	127.15	7.49	td
3	127.86	7.44	td
4	120.71	8.05	dt
5	144.12	-	-
6	140.61	-	-
7	36.73	4.15	s
8	144.70	-	-
9	144.17	-	-
10	120.81	8.24-8.15	m
11	126.77	8.33	dd
12	134.75	-	-
13	124.46	8.53	dt
14	149.70	-	-
15	121.15	9.31	s
16	158.80	-	-
17	157.86	-	-

Position	^{13}C-NMR δ (Hz)	^{1}H-NMR δ (Hz)	Multiplet
18	124.75	9.00	d
19	128.18	7.55	ddd
20	138.71	8.24-8.15	m
21	153.34	8.01	ddd
22	151.29	7.77	ddd
23	126.98	7.26	ddd
24	137.60	7.97	ddd
25	123.71	8.69	dt
26	157.95	-	-
27	156.13	-	-
28	124.35	8.94	dt
29	137.89	8.48	td
30	127.89	8.12	ddd
31	152.72	9.94	ddd
32	125.77	-	-
33	3.05	2.36	s

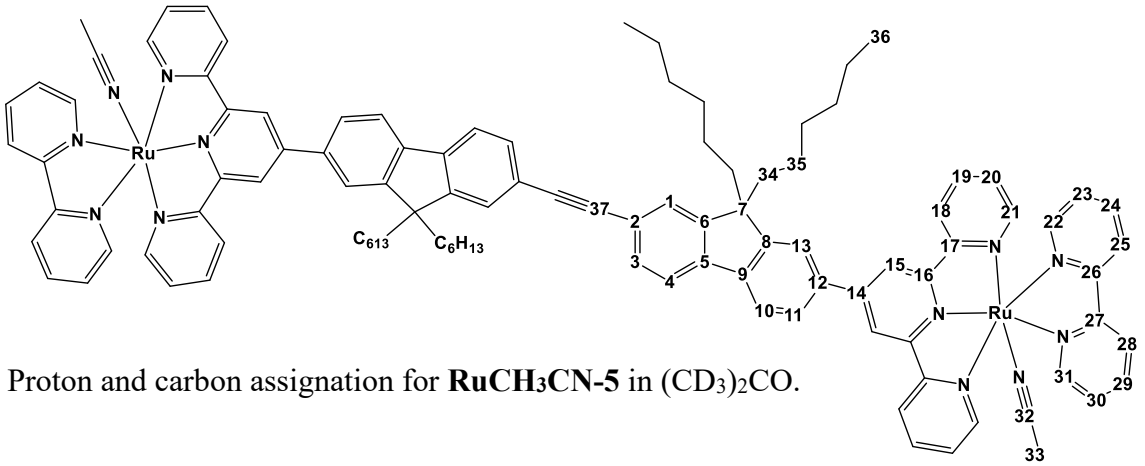

Table 3. Proton and carbon assignation for **RuCH$_3$CN-5** in $(CD_3)_2CO$.

Position	^{13}C-NMR δ (Hz)	^{1}H-NMR δ (Hz)	Multiplet
1	126.98	7.86-7.79	m
2	125.56	-	-
3	121.75	8.09	m
4	131.88	7.73	dd
5	152.53	-	-
6	141.56	-	-
7	56.73	-	-
8	144.11	-	-
9	153.53	-	-
10	122.12	8.19-8.27	m
11	128.08	8.42	m
12	136.31	-	-
13	122.61	8.58	d
14	149.98	-	-
15	121.78	9.35	s
16	159.62	-	-
17	158.80	-	-
18	125.27	8.93	dt

Position	^{13}C-NMR δ (Hz)	^{1}H-NMR δ (Hz)	Multiplet
19	129.13	7.58	ddd
20	139.63	8.19-8.27	m
21	154.28	8.01-8.07	m
22	152.26	7.86-7.79	m
23	127.87	7.29	ddd
24	138.54	8.00	td
25	123.67	8.72	dt
26	158.84	-	-
27	157.02	-	-
28	124.63	8.97	dt
29	138.83	8.50	td
30	128.80	8.12	ddd
31	153.62	9.96	ddd
32	126.67	-	-
33	3.96	2.38	s
34	40.89	2.36-2.29	m
35	32.42, 23.27	1.23-1.08	m
36	14.28	0.87	m
37	91.77	-	-

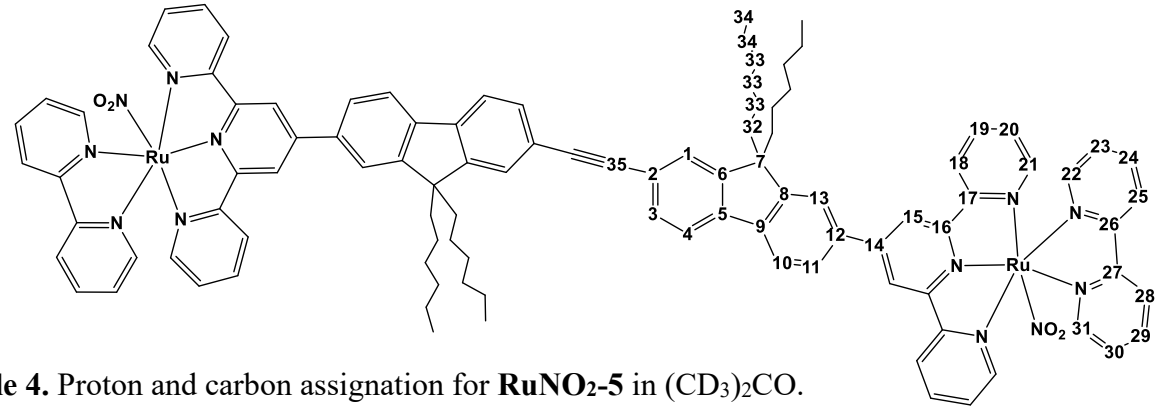

Table 4. Proton and carbon assignation for **RuNO$_2$-5** in $(CD_3)_2CO$.

Position	^{13}C-NMR δ (Hz)	^{1}H-NMR δ (Hz)	Multiplet
1	127.23	7.83-7.78	m
2	138.13	-	-
3	131.91	7.70	dd
4	121.16	8.05	dd
5	152.49	-	-
6	143.61	-	-
7	56.67	-	-
8	141.69	-	-
9	153.58	-	-
10	121.98	8.20	dd
11	128.00	8.35	dd
12	136.16	-	-
13	121.64	8.54	d
14	152.30	-	-
15	121.13	9.17	s
16	159.91	-	-
17	159.32	-	-
18	138.54	8.15-8.08	m
19	126.98	8.78	dt
20	128.44	7.47	ddd

Position	^{13}C-NMR δ (Hz)	^{1}H-NMR δ (Hz)	Multiplet
21	153.43	7.98-7.92	m
22	148.62	7.83-7.78	m
23	127.92	7.25	ddd
24	136.98	7.98-7.92	m
25	122.83	8.70-8.66	m
26	157.99	-	-
27	156.87	-	-
28	124.65	8.90	dd
29	137.93	8.46-8.39	m
30	127.95	8.15-8.08	m
31	154.15	10.06	s
32	40.93	2.36-2.29	m
33	32.40, 24.78	1.34 – 1.22	m
34	14.29	0.87	m
35	92.49	-	-

Appendix 3:

Crystallographic data

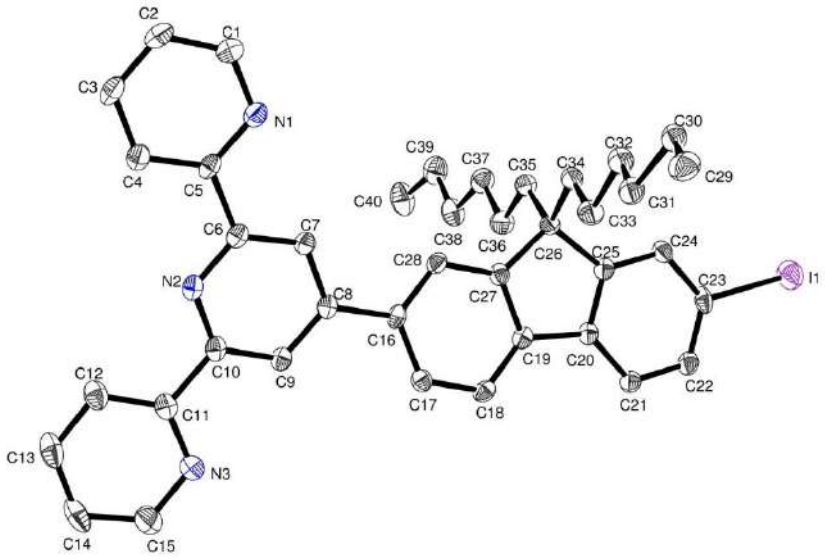

Empirical formula	$C_{40}H_{42}IN_3$, C_3H_6O
Formula weight	1441.41
Temperature	101(2) K
Wavelength	0.71073 A
Crystal system, space group	Triclinic, P -1
Unit cell dimensions	a = 11.5993(9) A alpha = 84.417(3) deg. b = 16.2306(12) A beta = 89.766(4) deg. c = 20.2615(16) A gamma = 71.183(3) deg.
Volume	3592.0(5) A^3
Z, Calculated density	2, 1.333 Mg/m^3
Absorption coefficient	0.925 mm^-1
F(000)	1488
Crystal size	0.200 x 0.200 x 0.100 mm
Theta range for data collection	1.010 to 25.026 deg.
Limiting indices	-13<=h<=13, -19<=k<=19, -24<=l<=24

Reflections collected / unique	129229 / 12689 [R(int) = 0.0463]
Completeness to theta = 25.026	100.0 %
Refinement method	Full-matrix least-squares on F^2
Data / restraints / parameters	12689 / 309 / 925
Goodness-of-fit on F^2	1.136
Final R indices [I>2sigma(I)]	R1 = 0.0573, wR2 = 0.1545
R indices (all data)	R1 = 0.0610, wR2 = 0.1569
Largest diff. peak and hole	1.689 and -2.436 e.A^-3

Atomic coordinates

U(eq) is defined as one third of the trace of the orthogonalized Uij tensor.

	x	y	z	U(eq)
C(1)	4479(5)	8180(4)	387(3)	29(1)
C(2)	4603(5)	8807(4)	-99(3)	29(1)
C(3)	3641(5)	9571(4)	-223(3)	27(1)
C(4)	2601(5)	9681(3)	142(3)	24(1)
C(5)	2564(5)	9022(3)	626(2)	19(1)
C(6)	1445(5)	9127(3)	1028(2)	18(1)
C(7)	1331(5)	8431(3)	1453(2)	19(1)
C(8)	260(4)	8541(3)	1805(2)	18(1)
C(9)	-635(5)	9356(3)	1708(2)	20(1)
C(10)	-427(5)	10023(3)	1289(2)	19(1)
C(11)	-1372(5)	10907(3)	1201(2)	21(1)
C(12)	-1296(5)	11528(4)	695(3)	28(1)
C(13)	-2215(6)	12319(4)	622(3)	36(1)
C(14)	-3175(6)	12493(4)	1052(3)	37(1)
C(15)	-3164(6)	11824(4)	1541(3)	36(1)
C(16)	81(4)	7817(3)	2266(2)	18(1)
C(17)	-840(5)	8001(3)	2725(2)	20(1)
C(18)	-1019(4)	7355(3)	3174(2)	20(1)
C(19)	-249(4)	6504(3)	3163(2)	18(1)
C(20)	-192(4)	5689(3)	3571(2)	18(1)
C(21)	-935(4)	5530(3)	4079(3)	22(1)
C(22)	-661(5)	4683(3)	4385(3)	24(1)
C(23)	320(5)	4015(3)	4186(3)	24(1)
C(24)	1055(4)	4164(3)	3674(3)	21(1)
C(25)	787(4)	5013(3)	3369(2)	20(1)

C(26)	1435(4)	5339(3)	2797(2)	20(1)
C(27)	685(4)	6305(3)	2707(2)	19(1)
C(28)	847(4)	6953(3)	2256(2)	19(1)
C(29)	6187(5)	6338(4)	4933(3)	31(1)
C(30)	5899(5)	5734(4)	4490(3)	26(1)
C(31)	4582(5)	6066(4)	4223(3)	26(1)
C(32)	4318(5)	5467(4)	3751(3)	27(1)
C(33)	2971(5)	5714(4)	3546(3)	26(1)
C(34)	2782(5)	5200(3)	2993(3)	24(1)
C(35)	1388(5)	4879(3)	2173(3)	24(1)
C(36)	114(5)	4992(4)	1907(3)	28(1)
C(37)	166(5)	4502(4)	1293(3)	30(1)
C(38)	-1046(6)	4681(4)	943(3)	34(1)
C(39)	-938(6)	4184(4)	330(3)	37(1)
C(40)	-2114(7)	4422(4)	-66(4)	46(2)
C(41)	8189(8)	1964(6)	5604(4)	62(2)
C(42)	8439(7)	1757(6)	6271(4)	56(2)
C(43)	7719(7)	1385(5)	6639(3)	45(2)
C(44)	6779(6)	1212(4)	6322(3)	36(1)
C(45)	6599(5)	1434(4)	5643(3)	29(1)
C(46)	5568(5)	1311(3)	5286(2)	23(1)
C(47)	5385(5)	1563(3)	4603(2)	20(1)
C(48)	4375(5)	1479(3)	4290(2)	19(1)
C(49)	3617(5)	1128(3)	4668(2)	21(1)
C(50)	3850(5)	901(3)	5343(2)	21(1)
C(51)	3025(5)	535(3)	5751(3)	25(1)
C(52)	3357(6)	160(4)	6400(3)	30(1)
C(53)	2570(6)	-207(4)	6748(3)	38(2)
C(54)	1502(8)	-159(5)	6449(4)	54(2)
C(55)	1237(8)	239(6)	5811(4)	58(2)
C(56)	4099(4)	1761(3)	3569(2)	17(1)
C(57)	4411(4)	2459(3)	3252(2)	18(1)
C(58)	4141(4)	2731(3)	2580(2)	17(1)
C(59)	3544(4)	2289(3)	2226(2)	16(1)
C(60)	3132(4)	2417(3)	1526(2)	17(1)
C(61)	3196(4)	3024(3)	1004(2)	18(1)
C(62)	2686(5)	3001(3)	388(2)	21(1)
C(63)	2115(5)	2377(3)	304(2)	21(1)
C(64)	2054(5)	1764(3)	822(2)	22(1)
C(65)	2573(5)	1790(3)	1429(2)	20(1)
C(67)	3233(5)	1595(3)	2537(2)	20(1)
C(68)	3511(5)	1324(3)	3203(2)	20(1)
C(66)	2618(5)	1196(3)	2061(2)	24(1)
C(74)	1292(8)	1311(7)	2298(8)	26(2)
C(73)	421(11)	2246(7)	2348(9)	27(2)
C(72)	-776(10)	2325(9)	2695(6)	31(2)
C(71)	-1645(10)	3225(8)	2699(6)	39(2)
C(70)	-2826(10)	3310(9)	3079(6)	41(2)
C(69)	-2670(14)	3135(11)	3813(6)	41(3)
C(74')	1399(9)	1122(7)	2279(8)	27(2)

C(73')	510(11)	2046(8)	2368(9)	27(2)
C(72')	-512(10)	1957(9)	2808(6)	28(2)
C(71')	-1338(10)	2795(8)	2999(6)	35(2)
C(70')	-2293(11)	2681(8)	3499(6)	38(2)
C(69')	-3048(14)	3494(10)	3766(8)	43(3)
C(75)	3426(6)	228(4)	1975(3)	30(1)
C(76)	4771(6)	86(4)	1877(3)	30(1)
C(77)	5512(6)	-843(4)	1735(3)	35(1)
C(78)	5460(6)	-1557(4)	2271(3)	35(1)
C(79)	6281(6)	-2464(4)	2161(3)	34(1)
C(80)	6218(7)	-3138(5)	2729(4)	49(2)
O(1')	4480(20)	4570(17)	1259(17)	87(6)
C(82')	4700(30)	5957(16)	1190(20)	107(6)
C(81')	5040(40)	5004(16)	1370(20)	89(5)
C(83')	5830(20)	4679(19)	1969(16)	83(5)
O(1)	4807(13)	4539(9)	1042(10)	88(4)
C(82)	5082(14)	5860(9)	641(12)	95(5)
C(81)	5030(20)	5155(12)	1143(11)	88(4)
C(83)	5532(19)	5170(16)	1796(12)	108(5)
I(1)	748(1)	2751(1)	4673(1)	38(1)
I(2)	1343(1)	2350(1)	-627(1)	30(1)
N(1)	3487(4)	8274(3)	754(2)	24(1)
N(2)	591(4)	9912(3)	945(2)	19(1)
N(3)	-2292(4)	11045(3)	1618(2)	28(1)
N(4)	7285(6)	1802(5)	5283(3)	49(2)
N(5)	4816(4)	991(3)	5655(2)	22(1)
N(6)	1976(5)	584(4)	5463(3)	42(1)

Bond lengths

C(1)-N(1)	1.343(7)	C(9)-C(10)	1.394(7)
C(1)-C(2)	1.386(8)	C(9)-H(9)	0.9500
C(1)-H(1)	0.9500	C(10)-N(2)	1.339(7)
C(2)-C(3)	1.376(8)	C(10)-C(11)	1.492(7)
C(2)-H(2)	0.9500	C(11)-N(3)	1.334(7)
C(3)-C(4)	1.384(8)	C(11)-C(12)	1.390(7)
C(3)-H(3)	0.9500	C(12)-C(13)	1.374(8)
C(4)-C(5)	1.389(7)	C(12)-H(12)	0.9500
C(4)-H(4)	0.9500	C(13)-C(14)	1.384(9)
C(5)-N(1)	1.338(7)	C(13)-H(13)	0.9500
C(5)-C(6)	1.502(7)	C(14)-C(15)	1.395(9)
C(6)-N(2)	1.333(7)	C(14)-H(14)	0.9500
C(6)-C(7)	1.393(7)	C(15)-N(3)	1.335(7)
C(7)-C(8)	1.399(7)	C(15)-H(15)	0.9500
C(7)-H(7)	0.9500	C(16)-C(17)	1.391(7)
C(8)-C(9)	1.390(7)	C(16)-C(28)	1.399(7)
C(8)-C(16)	1.497(7)	C(17)-C(18)	1.387(7)

C(17)-H(17)	0.9500	C(38)-H(38B)	0.9900
C(18)-C(19)	1.385(7)	C(39)-C(40)	1.504(9)
C(18)-H(18)	0.9500	C(39)-H(39A)	0.9900
C(19)-C(27)	1.398(7)	C(39)-H(39B)	0.9900
C(19)-C(20)	1.472(7)	C(40)-H(40A)	0.9800
C(20)-C(25)	1.394(7)	C(40)-H(40B)	0.9800
C(20)-C(21)	1.398(7)	C(40)-H(40C)	0.9800
C(21)-C(22)	1.389(7)	C(41)-N(4)	1.346(9)
C(21)-H(21)	0.9500	C(41)-C(42)	1.369(11)
C(22)-C(23)	1.385(8)	C(41)-H(41)	0.9500
C(22)-H(22)	0.9500	C(42)-C(43)	1.361(11)
C(23)-C(24)	1.392(7)	C(42)-H(42)	0.9500
C(23)-I(1)	2.093(5)	C(43)-C(44)	1.385(9)
C(24)-C(25)	1.392(7)	C(43)-H(43)	0.9500
C(24)-H(24)	0.9500	C(44)-C(45)	1.386(8)
C(25)-C(26)	1.521(7)	C(44)-H(44)	0.9500
C(26)-C(27)	1.521(7)	C(45)-N(4)	1.318(8)
C(26)-C(35)	1.540(7)	C(45)-C(46)	1.478(7)
C(26)-C(34)	1.552(7)	C(46)-N(5)	1.341(7)
C(27)-C(28)	1.385(7)	C(46)-C(47)	1.401(7)
C(28)-H(28)	0.9500	C(47)-C(48)	1.386(7)
C(29)-C(30)	1.504(8)	C(47)-H(47)	0.9500
C(29)-H(29A)	0.9800	C(48)-C(49)	1.384(7)
C(29)-H(29B)	0.9800	C(48)-C(56)	1.491(6)
C(29)-H(29C)	0.9800	C(49)-C(50)	1.386(7)
C(30)-C(31)	1.528(7)	C(49)-H(49)	0.9500
C(30)-H(30A)	0.9900	C(50)-N(5)	1.344(7)
C(30)-H(30B)	0.9900	C(50)-C(51)	1.488(7)
C(31)-C(32)	1.525(8)	C(51)-N(6)	1.327(8)
C(31)-H(31A)	0.9900	C(51)-C(52)	1.395(8)
C(31)-H(31B)	0.9900	C(52)-C(53)	1.397(8)
C(32)-C(33)	1.530(7)	C(52)-H(52)	0.9500
C(32)-H(32A)	0.9900	C(53)-C(54)	1.357(11)
C(32)-H(32B)	0.9900	C(53)-H(53)	0.9500
C(33)-C(34)	1.518(8)	C(54)-C(55)	1.377(11)
C(33)-H(33A)	0.9900	C(54)-H(54)	0.9500
C(33)-H(33B)	0.9900	C(55)-N(6)	1.331(9)
C(34)-H(34A)	0.9900	C(55)-H(55)	0.9500
C(34)-H(34B)	0.9900	C(56)-C(68)	1.392(7)
C(35)-C(36)	1.522(8)	C(56)-C(57)	1.396(7)
C(35)-H(35A)	0.9900	C(57)-C(58)	1.395(7)
C(35)-H(35B)	0.9900	C(57)-H(57)	0.9500
C(36)-C(37)	1.530(8)	C(58)-C(59)	1.390(7)
C(36)-H(36A)	0.9900	C(58)-H(58)	0.9500
C(36)-H(36B)	0.9900	C(59)-C(67)	1.386(7)
C(37)-C(38)	1.506(8)	C(59)-C(60)	1.472(6)
C(37)-H(37A)	0.9900	C(60)-C(61)	1.393(7)
C(37)-H(37B)	0.9900	C(60)-C(65)	1.400(7)
C(38)-C(39)	1.528(9)	C(61)-C(62)	1.392(7)
C(38)-H(38A)	0.9900	C(61)-H(61)	0.9500

C(62)-C(63)	1.400(7)	C(70')-C(69')	1.480(13)
C(62)-H(62)	0.9500	C(70')-H(70C)	0.9900
C(63)-C(64)	1.391(7)	C(70')-H(70D)	0.9900
C(63)-I(2)	2.103(5)	C(69')-H(69D)	0.9800
C(64)-C(65)	1.383(7)	C(69')-H(69E)	0.9800
C(64)-H(64)	0.9500	C(69')-H(69F)	0.9800
C(65)-C(66)	1.517(6)	C(75)-C(76)	1.518(9)
C(67)-C(68)	1.383(7)	C(75)-H(75A)	0.9900
C(67)-C(66)	1.512(6)	C(75)-H(75B)	0.9900
C(68)-H(68)	0.9500	C(76)-C(77)	1.530(8)
C(66)-C(74')	1.516(9)	C(76)-H(76A)	0.9900
C(66)-C(74)	1.567(9)	C(76)-H(76B)	0.9900
C(66)-C(75)	1.574(8)	C(77)-C(78)	1.525(7)
C(74)-C(73)	1.540(11)	C(77)-H(77A)	0.9900
C(74)-H(74A)	0.9900	C(77)-H(77B)	0.9900
C(74)-H(74B)	0.9900	C(78)-C(79)	1.511(9)
C(73)-C(72)	1.528(10)	C(78)-H(78A)	0.9900
C(73)-H(73A)	0.9900	C(78)-H(78B)	0.9900
C(73)-H(73B)	0.9900	C(79)-C(80)	1.527(8)
C(72)-C(71)	1.484(15)	C(79)-H(79A)	0.9900
C(72)-H(72A)	0.9900	C(79)-H(79B)	0.9900
C(72)-H(72B)	0.9900	C(80)-H(80A)	0.9800
C(71)-C(70)	1.542(12)	C(80)-H(80B)	0.9800
C(71)-H(71A)	0.9900	C(80)-H(80C)	0.9800
C(71)-H(71B)	0.9900	O(1')-C(81')	1.139(18)
C(70)-C(69)	1.486(13)	C(82')-C(81')	1.476(18)
C(70)-H(70A)	0.9900	C(82')-H(82A)	0.9800
C(70)-H(70B)	0.9900	C(82')-H(82B)	0.9800
C(69)-H(69A)	0.9800	C(82')-H(82C)	0.9800
C(69)-H(69B)	0.9800	C(81')-C(83')	1.469(18)
C(69)-H(69C)	0.9800	C(83')-H(83A)	0.9800
C(74')-C(73')	1.549(11)	C(83')-H(83B)	0.9800
C(74')-H(74C)	0.9900	C(83')-H(83C)	0.9800
C(74')-H(74D)	0.9900	O(1)-C(81)	1.147(14)
C(73')-C(72')	1.516(10)	C(82)-C(81)	1.471(16)
C(73')-H(73C)	0.9900	C(82)-H(82D)	0.9800
C(73')-H(73D)	0.9900	C(82)-H(82E)	0.9800
C(72')-C(71')	1.475(15)	C(82)-H(82F)	0.9800
C(72')-H(72C)	0.9900	C(81)-C(83)	1.453(16)
C(72')-H(72D)	0.9900	C(83)-H(83D)	0.9800
C(71')-C(70')	1.541(12)	C(83)-H(83E)	0.9800
C(71')-H(71C)	0.9900	C(83)-H(83F)	0.9800
C(71')-H(71D)	0.9900		

Angles

N(1)-C(1)-C(2)	124.3(5)	C(18)-C(17)-H(17)	119.0
N(1)-C(1)-H(1)	117.8	C(16)-C(17)-H(17)	119.0
C(2)-C(1)-H(1)	117.8	C(19)-C(18)-C(17)	118.5(5)
C(3)-C(2)-C(1)	118.2(5)	C(19)-C(18)-H(18)	120.8
C(3)-C(2)-H(2)	120.9	C(17)-C(18)-H(18)	120.8
C(1)-C(2)-H(2)	120.9	C(18)-C(19)-C(27)	120.4(5)
C(2)-C(3)-C(4)	118.7(5)	C(18)-C(19)-C(20)	131.5(5)
C(2)-C(3)-H(3)	120.6	C(27)-C(19)-C(20)	108.1(4)
C(4)-C(3)-H(3)	120.6	C(25)-C(20)-C(21)	120.9(5)
C(3)-C(4)-C(5)	119.1(5)	C(25)-C(20)-C(19)	108.4(4)
C(3)-C(4)-H(4)	120.4	C(21)-C(20)-C(19)	130.7(5)
C(5)-C(4)-H(4)	120.4	C(22)-C(21)-C(20)	118.3(5)
N(1)-C(5)-C(4)	123.2(5)	C(22)-C(21)-H(21)	120.9
N(1)-C(5)-C(6)	116.8(4)	C(20)-C(21)-H(21)	120.9
C(4)-C(5)-C(6)	120.0(5)	C(23)-C(22)-C(21)	120.6(5)
N(2)-C(6)-C(7)	123.4(5)	C(23)-C(22)-H(22)	119.7
N(2)-C(6)-C(5)	115.9(4)	C(21)-C(22)-H(22)	119.7
C(7)-C(6)-C(5)	120.7(5)	C(22)-C(23)-C(24)	121.6(5)
C(6)-C(7)-C(8)	119.3(5)	C(22)-C(23)-I(1)	119.9(4)
C(6)-C(7)-H(7)	120.3	C(24)-C(23)-I(1)	118.5(4)
C(8)-C(7)-H(7)	120.3	C(23)-C(24)-C(25)	118.1(5)
C(9)-C(8)-C(7)	117.0(4)	C(23)-C(24)-H(24)	121.0
C(9)-C(8)-C(16)	121.2(4)	C(25)-C(24)-H(24)	121.0
C(7)-C(8)-C(16)	121.8(4)	C(24)-C(25)-C(20)	120.6(5)
C(8)-C(9)-C(10)	119.8(5)	C(24)-C(25)-C(26)	128.1(5)
C(8)-C(9)-H(9)	120.1	C(20)-C(25)-C(26)	111.3(4)
C(10)-C(9)-H(9)	120.1	C(27)-C(26)-C(25)	100.9(4)
N(2)-C(10)-C(9)	123.0(5)	C(27)-C(26)-C(35)	112.2(4)
N(2)-C(10)-C(11)	117.1(4)	C(25)-C(26)-C(35)	111.4(4)
C(9)-C(10)-C(11)	119.9(5)	C(27)-C(26)-C(34)	111.6(4)
N(3)-C(11)-C(12)	123.0(5)	C(25)-C(26)-C(34)	111.0(4)
N(3)-C(11)-C(10)	116.2(4)	C(35)-C(26)-C(34)	109.6(4)
C(12)-C(11)-C(10)	120.8(5)	C(28)-C(27)-C(19)	120.6(5)
C(13)-C(12)-C(11)	118.3(6)	C(28)-C(27)-C(26)	128.1(5)
C(13)-C(12)-H(12)	120.9	C(19)-C(27)-C(26)	111.3(4)
C(11)-C(12)-H(12)	120.9	C(27)-C(28)-C(16)	119.5(5)
C(12)-C(13)-C(14)	120.5(6)	C(27)-C(28)-H(28)	120.3
C(12)-C(13)-H(13)	119.8	C(16)-C(28)-H(28)	120.3
C(14)-C(13)-H(13)	119.8	C(30)-C(29)-H(29A)	109.5
C(13)-C(14)-C(15)	116.6(5)	C(30)-C(29)-H(29B)	109.5
C(13)-C(14)-H(14)	121.7	H(29A)-C(29)-H(29B)	109.5
C(15)-C(14)-H(14)	121.7	C(30)-C(29)-H(29C)	109.5
N(3)-C(15)-C(14)	124.1(6)	H(29A)-C(29)-H(29C)	109.5
N(3)-C(15)-H(15)	117.9	H(29B)-C(29)-H(29C)	109.5
C(14)-C(15)-H(15)	117.9	C(29)-C(30)-C(31)	113.1(5)
C(17)-C(16)-C(28)	119.0(4)	C(29)-C(30)-H(30A)	109.0
C(17)-C(16)-C(8)	120.0(4)	C(31)-C(30)-H(30A)	109.0
C(28)-C(16)-C(8)	121.0(4)	C(29)-C(30)-H(30B)	109.0
C(18)-C(17)-C(16)	122.0(5)	C(31)-C(30)-H(30B)	109.0

H(30A)-C(30)-H(30B)	107.8	C(40)-C(39)-H(39A)	108.9
C(32)-C(31)-C(30)	112.6(5)	C(38)-C(39)-H(39A)	108.9
C(32)-C(31)-H(31A)	109.1	C(40)-C(39)-H(39B)	108.9
C(30)-C(31)-H(31A)	109.1	C(38)-C(39)-H(39B)	108.9
C(32)-C(31)-H(31B)	109.1	H(39A)-C(39)-H(39B)	107.7
C(30)-C(31)-H(31B)	109.1	C(39)-C(40)-H(40A)	109.5
H(31A)-C(31)-H(31B)	107.8	C(39)-C(40)-H(40B)	109.5
C(31)-C(32)-C(33)	113.9(5)	H(40A)-C(40)-H(40B)	109.5
C(31)-C(32)-H(32A)	108.8	C(39)-C(40)-H(40C)	109.5
C(33)-C(32)-H(32A)	108.8	H(40A)-C(40)-H(40C)	109.5
C(31)-C(32)-H(32B)	108.8	H(40B)-C(40)-H(40C)	109.5
C(33)-C(32)-H(32B)	108.8	N(4)-C(41)-C(42)	123.9(7)
H(32A)-C(32)-H(32B)	107.7	N(4)-C(41)-H(41)	118.1
C(34)-C(33)-C(32)	111.8(5)	C(42)-C(41)-H(41)	118.1
C(34)-C(33)-H(33A)	109.3	C(43)-C(42)-C(41)	118.7(6)
C(32)-C(33)-H(33A)	109.3	C(43)-C(42)-H(42)	120.6
C(34)-C(33)-H(33B)	109.3	C(41)-C(42)-H(42)	120.6
C(32)-C(33)-H(33B)	109.3	C(42)-C(43)-C(44)	118.7(6)
H(33A)-C(33)-H(33B)	107.9	C(42)-C(43)-H(43)	120.7
C(33)-C(34)-C(26)	115.6(4)	C(44)-C(43)-H(43)	120.7
C(33)-C(34)-H(34A)	108.4	C(43)-C(44)-C(45)	118.8(6)
C(26)-C(34)-H(34A)	108.4	C(43)-C(44)-H(44)	120.6
C(33)-C(34)-H(34B)	108.4	C(45)-C(44)-H(44)	120.6
C(26)-C(34)-H(34B)	108.4	N(4)-C(45)-C(44)	123.1(5)
H(34A)-C(34)-H(34B)	107.4	N(4)-C(45)-C(46)	115.9(5)
C(36)-C(35)-C(26)	115.3(4)	C(44)-C(45)-C(46)	121.0(5)
C(36)-C(35)-H(35A)	108.5	N(5)-C(46)-C(47)	123.5(5)
C(26)-C(35)-H(35A)	108.5	N(5)-C(46)-C(45)	116.5(5)
C(36)-C(35)-H(35B)	108.5	C(47)-C(46)-C(45)	119.9(5)
C(26)-C(35)-H(35B)	108.5	C(48)-C(47)-C(46)	118.4(5)
H(35A)-C(35)-H(35B)	107.5	C(48)-C(47)-H(47)	120.8
C(35)-C(36)-C(37)	111.3(5)	C(46)-C(47)-H(47)	120.8
C(35)-C(36)-H(36A)	109.4	C(49)-C(48)-C(47)	118.0(4)
C(37)-C(36)-H(36A)	109.4	C(49)-C(48)-C(56)	120.5(4)
C(35)-C(36)-H(36B)	109.4	C(47)-C(48)-C(56)	121.5(5)
C(37)-C(36)-H(36B)	109.4	C(48)-C(49)-C(50)	120.3(5)
H(36A)-C(36)-H(36B)	108.0	C(48)-C(49)-H(49)	119.9
C(38)-C(37)-C(36)	114.6(5)	C(50)-C(49)-H(49)	119.9
C(38)-C(37)-H(37A)	108.6	N(5)-C(50)-C(49)	122.3(5)
C(36)-C(37)-H(37A)	108.6	N(5)-C(50)-C(51)	117.4(4)
C(38)-C(37)-H(37B)	108.6	C(49)-C(50)-C(51)	120.3(5)
C(36)-C(37)-H(37B)	108.6	N(6)-C(51)-C(52)	122.6(5)
H(37A)-C(37)-H(37B)	107.6	N(6)-C(51)-C(50)	116.5(5)
C(37)-C(38)-C(39)	112.4(5)	C(52)-C(51)-C(50)	120.9(5)
C(37)-C(38)-H(38A)	109.1	C(51)-C(52)-C(53)	118.3(6)
C(39)-C(38)-H(38A)	109.1	C(51)-C(52)-H(52)	120.9
C(37)-C(38)-H(38B)	109.1	C(53)-C(52)-H(52)	120.9
C(39)-C(38)-H(38B)	109.1	C(54)-C(53)-C(52)	118.7(6)
H(38A)-C(38)-H(38B)	107.9	C(54)-C(53)-H(53)	120.7
C(40)-C(39)-C(38)	113.3(6)	C(52)-C(53)-H(53)	120.7

C(53)-C(54)-C(55)	119.1(6)	C(74)-C(66)-C(75)	115.4(6)
C(53)-C(54)-H(54)	120.4	C(73)-C(74)-C(66)	118.3(8)
C(55)-C(54)-H(54)	120.4	C(73)-C(74)-H(74A)	107.7
N(6)-C(55)-C(54)	123.5(7)	C(66)-C(74)-H(74A)	107.7
N(6)-C(55)-H(55)	118.2	C(73)-C(74)-H(74B)	107.7
C(54)-C(55)-H(55)	118.2	C(66)-C(74)-H(74B)	107.7
C(68)-C(56)-C(57)	119.0(4)	H(74A)-C(74)-H(74B)	107.1
C(68)-C(56)-C(48)	119.5(4)	C(72)-C(73)-C(74)	116.5(9)
C(57)-C(56)-C(48)	121.5(4)	C(72)-C(73)-H(73A)	108.2
C(58)-C(57)-C(56)	121.6(4)	C(74)-C(73)-H(73A)	108.2
C(58)-C(57)-H(57)	119.2	C(72)-C(73)-H(73B)	108.2
C(56)-C(57)-H(57)	119.2	C(74)-C(73)-H(73B)	108.2
C(59)-C(58)-C(57)	118.3(4)	H(73A)-C(73)-H(73B)	107.3
C(59)-C(58)-H(58)	120.8	C(71)-C(72)-C(73)	116.1(9)
C(57)-C(58)-H(58)	120.8	C(71)-C(72)-H(72A)	108.3
C(67)-C(59)-C(58)	120.4(4)	C(73)-C(72)-H(72A)	108.3
C(67)-C(59)-C(60)	108.2(4)	C(71)-C(72)-H(72B)	108.3
C(58)-C(59)-C(60)	131.4(4)	C(73)-C(72)-H(72B)	108.3
C(61)-C(60)-C(65)	120.3(4)	H(72A)-C(72)-H(72B)	107.4
C(61)-C(60)-C(59)	131.8(4)	C(72)-C(71)-C(70)	116.1(9)
C(65)-C(60)-C(59)	107.9(4)	C(72)-C(71)-H(71A)	108.3
C(62)-C(61)-C(60)	118.9(5)	C(70)-C(71)-H(71A)	108.3
C(62)-C(61)-H(61)	120.5	C(72)-C(71)-H(71B)	108.3
C(60)-C(61)-H(61)	120.5	C(70)-C(71)-H(71B)	108.3
C(61)-C(62)-C(63)	119.9(4)	H(71A)-C(71)-H(71B)	107.4
C(61)-C(62)-H(62)	120.1	C(69)-C(70)-C(71)	115.4(10)
C(63)-C(62)-H(62)	120.1	C(69)-C(70)-H(70A)	108.4
C(64)-C(63)-C(62)	121.7(4)	C(71)-C(70)-H(70A)	108.4
C(64)-C(63)-I(2)	118.8(4)	C(69)-C(70)-H(70B)	108.4
C(62)-C(63)-I(2)	119.6(4)	C(71)-C(70)-H(70B)	108.4
C(65)-C(64)-C(63)	117.8(5)	H(70A)-C(70)-H(70B)	107.5
C(65)-C(64)-H(64)	121.1	C(70)-C(69)-H(69A)	109.5
C(63)-C(64)-H(64)	121.1	C(70)-C(69)-H(69B)	109.5
C(64)-C(65)-C(60)	121.4(4)	H(69A)-C(69)-H(69B)	109.5
C(64)-C(65)-C(66)	127.3(4)	C(70)-C(69)-H(69C)	109.5
C(60)-C(65)-C(66)	111.3(4)	H(69A)-C(69)-H(69C)	109.5
C(68)-C(67)-C(59)	121.0(4)	H(69B)-C(69)-H(69C)	109.5
C(68)-C(67)-C(66)	127.2(4)	C(66)-C(74')-C(73')	109.3(7)
C(59)-C(67)-C(66)	111.8(4)	C(66)-C(74')-H(74C)	109.8
C(67)-C(68)-C(56)	119.7(4)	C(73')-C(74')-H(74C)	109.8
C(67)-C(68)-H(68)	120.2	C(66)-C(74')-H(74D)	109.8
C(56)-C(68)-H(68)	120.2	C(73')-C(74')-H(74D)	109.8
C(67)-C(66)-C(74')	115.0(7)	H(74C)-C(74')-H(74D)	108.3
C(67)-C(66)-C(65)	100.8(4)	C(72')-C(73')-C(74')	109.0(8)
C(74')-C(66)-C(65)	115.3(7)	C(72')-C(73')-H(73C)	109.9
C(67)-C(66)-C(74)	108.4(7)	C(74')-C(73')-H(73C)	109.9
C(65)-C(66)-C(74)	109.9(7)	C(72')-C(73')-H(73D)	109.9
C(67)-C(66)-C(75)	110.6(4)	C(74')-C(73')-H(73D)	109.9
C(74')-C(66)-C(75)	104.5(6)	H(73C)-C(73')-H(73D)	108.3
C(65)-C(66)-C(75)	110.8(4)	C(71')-C(72')-C(73')	114.2(9)

C(71')-C(72')-H(72C)	108.7	C(79)-C(78)-H(78B)	108.7
C(73')-C(72')-H(72C)	108.7	C(77)-C(78)-H(78B)	108.7
C(71')-C(72')-H(72D)	108.7	H(78A)-C(78)-H(78B)	107.6
C(73')-C(72')-H(72D)	108.7	C(78)-C(79)-C(80)	111.5(5)
H(72C)-C(72')-H(72D)	107.6	C(78)-C(79)-H(79A)	109.3
C(72')-C(71')-C(70')	113.1(9)	C(80)-C(79)-H(79A)	109.3
C(72')-C(71')-H(71C)	109.0	C(78)-C(79)-H(79B)	109.3
C(70')-C(71')-H(71C)	109.0	C(80)-C(79)-H(79B)	109.3
C(72')-C(71')-H(71D)	109.0	H(79A)-C(79)-H(79B)	108.0
C(70')-C(71')-H(71D)	109.0	C(79)-C(80)-H(80A)	109.5
H(71C)-C(71')-H(71D)	107.8	C(79)-C(80)-H(80B)	109.5
C(69')-C(70')-C(71')	115.1(10)	H(80A)-C(80)-H(80B)	109.5
C(69')-C(70')-H(70C)	108.5	C(79)-C(80)-H(80C)	109.5
C(71')-C(70')-H(70C)	108.5	H(80A)-C(80)-H(80C)	109.5
C(69')-C(70')-H(70D)	108.5	H(80B)-C(80)-H(80C)	109.5
C(71')-C(70')-H(70D)	108.5	C(81')-C(82')-H(82A)	109.5
H(70C)-C(70')-H(70D)	107.5	C(81')-C(82')-H(82B)	109.5
C(70')-C(69')-H(69D)	109.5	H(82A)-C(82')-H(82B)	109.5
C(70')-C(69')-H(69E)	109.5	C(81')-C(82')-H(82C)	109.5
H(69D)-C(69')-H(69E)	109.5	H(82A)-C(82')-H(82C)	109.5
C(70')-C(69')-H(69F)	109.5	H(82B)-C(82')-H(82C)	109.5
H(69D)-C(69')-H(69F)	109.5	O(1')-C(81')-C(83')	114(2)
H(69E)-C(69')-H(69F)	109.5	O(1')-C(81')-C(82')	126(3)
C(76)-C(75)-C(66)	115.6(4)	C(83')-C(81')-C(82')	114(2)
C(76)-C(75)-H(75A)	108.4	C(81')-C(83')-H(83A)	109.5
C(66)-C(75)-H(75A)	108.4	C(81')-C(83')-H(83B)	109.5
C(76)-C(75)-H(75B)	108.4	H(83A)-C(83')-H(83B)	109.5
C(66)-C(75)-H(75B)	108.4	C(81')-C(83')-H(83C)	109.5
H(75A)-C(75)-H(75B)	107.4	H(83A)-C(83')-H(83C)	109.5
C(75)-C(76)-C(77)	114.3(5)	H(83B)-C(83')-H(83C)	109.5
C(75)-C(76)-H(76A)	108.7	C(81)-C(82)-H(82D)	109.5
C(77)-C(76)-H(76A)	108.7	C(81)-C(82)-H(82E)	109.5
C(75)-C(76)-H(76B)	108.7	H(82D)-C(82)-H(82E)	109.5
C(77)-C(76)-H(76B)	108.7	C(81)-C(82)-H(82F)	109.5
H(76A)-C(76)-H(76B)	107.6	H(82D)-C(82)-H(82F)	109.5
C(78)-C(77)-C(76)	114.6(5)	H(82E)-C(82)-H(82F)	109.5
C(78)-C(77)-H(77A)	108.6	O(1)-C(81)-C(83)	117.4(16)
C(76)-C(77)-H(77A)	108.6	O(1)-C(81)-C(82)	126.0(16)
C(78)-C(77)-H(77B)	108.6	C(83)-C(81)-C(82)	115.6(15)
C(76)-C(77)-H(77B)	108.6	C(81)-C(83)-H(83D)	109.5
H(77A)-C(77)-H(77B)	107.6	C(81)-C(83)-H(83E)	109.5
C(79)-C(78)-C(77)	114.4(5)	H(83D)-C(83)-H(83E)	109.5
C(79)-C(78)-H(78A)	108.7	C(81)-C(83)-H(83F)	109.5
C(77)-C(78)-H(78A)	108.7	H(83D)-C(83)-H(83F)	109.5
H(83E)-C(83)-H(83F)	109.5	C(45)-N(4)-C(41)	116.9(6)
C(5)-N(1)-C(1)	116.4(5)	C(46)-N(5)-C(50)	117.4(4)
C(6)-N(2)-C(10)	117.4(4)	C(51)-N(6)-C(55)	117.7(6)
C(11)-N(3)-C(15)	117.5(5)		

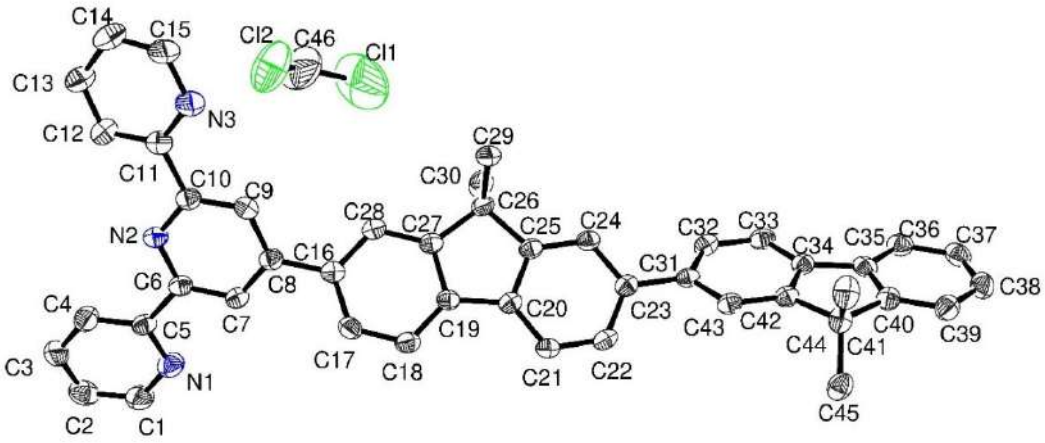

Empirical formula	$C_{45}H_{35}N_3$, 0.5(CH_2Cl_2)
Formula weight	660.22
Temperature	133(2) K
Wavelength	0.71073 A
Crystal system, space group	Triclinic, P $\bar{1}$
Unit cell dimensions	a = 9.9896(15) A alpha = 107.935(5) deg. b = 12.578(2) A beta = 97.369(5) deg. c = 14.548(2) A gamma = 92.078(5) deg.
Volume	1719.2(5) A^3
Z, Calculated density	2, 1.275 Mg/m^3
Absorption coefficient	0.149 mm^-1
F(000)	694
Crystal size	0.160 x 0.040 x 0.040 mm
Theta range for data collection	1.878 to 24.839 deg.
Limiting indices	-11<=h<=11, -14<=k<=14, -17<=l<=17
Reflections collected / unique	51627 / 5874 [R(int) = 0.1325]
Completeness to theta = 24.839	98.8 %
Refinement method	Full-matrix least-squares on F^2

Data / restraints / parameters	5874 / 16 / 465
Goodness-of-fit on F^2	1.017
Final R indices [I>2sigma(I)]	R1 = 0.0604, wR2 = 0.1220
R indices (all data)	R1 = 0.1398, wR2 = 0.1534
Largest diff. peak and hole	0.273 and -0.482 e.A^-3

Atomic coordinates

U(eq) is defined as one third of the trace of the orthogonalized Uij tensor.

	x	y	z	U(eq)
C(1)	-1042(4)	-2065(3)	7584(3)	48(1)
C(2)	-2299(4)	-2623(3)	7254(3)	48(1)
C(3)	-3194(4)	-2264(3)	6639(3)	45(1)
C(4)	-2803(3)	-1368(3)	6367(2)	38(1)
C(5)	-1506(3)	-855(3)	6706(2)	31(1)
C(6)	-998(3)	90(3)	6399(2)	30(1)
C(7)	189(3)	738(3)	6870(2)	30(1)
C(8)	646(3)	1587(3)	6544(2)	29(1)
C(9)	-113(3)	1750(3)	5735(2)	29(1)
C(10)	-1282(3)	1059(3)	5290(2)	30(1)
C(11)	-2104(3)	1153(3)	4386(2)	33(1)
C(12)	-3170(3)	372(3)	3887(2)	38(1)
C(13)	-3840(4)	450(3)	3043(3)	44(1)
C(14)	-3472(4)	1303(4)	2700(3)	54(1)
C(15)	-2444(4)	2062(4)	3253(3)	56(1)
C(16)	1927(3)	2276(3)	7047(2)	28(1)
C(17)	2258(3)	2545(3)	8054(2)	32(1)
C(18)	3465(3)	3143(3)	8546(2)	31(1)
C(19)	4369(3)	3463(3)	8017(2)	26(1)
C(20)	5704(3)	4068(2)	8337(2)	26(1)
C(21)	6446(3)	4535(2)	9259(2)	27(1)
C(22)	7723(3)	5029(3)	9352(2)	30(1)
C(23)	8304(3)	5070(2)	8535(2)	27(1)
C(24)	7541(3)	4596(3)	7608(2)	28(1)
C(25)	6249(3)	4111(3)	7512(2)	26(1)
C(26)	5252(3)	3566(3)	6587(2)	29(1)
C(27)	4067(3)	3189(3)	7001(2)	26(1)
C(28)	2843(3)	2607(3)	6515(2)	29(1)
C(29)	4869(3)	4402(3)	6042(2)	38(1)
C(30)	5842(3)	2563(3)	5908(2)	42(1)

C(31)	9687(3)	5594(3)	8653(2)	26(1)
C(32)	10600(3)	5112(3)	8020(2)	30(1)
C(33)	11910(3)	5579(3)	8143(2)	31(1)
C(34)	12326(3)	6555(3)	8899(2)	27(1)
C(35)	13638(3)	7219(3)	9228(2)	29(1)
C(36)	14875(3)	7050(3)	8885(2)	35(1)
C(37)	15970(3)	7816(3)	9359(3)	38(1)
C(38)	15845(3)	8735(3)	10149(3)	39(1)
C(39)	14600(3)	8905(3)	10485(2)	36(1)
C(40)	13507(3)	8146(3)	10029(2)	30(1)
C(41)	12076(3)	8152(3)	10281(2)	32(1)
C(42)	11416(3)	7068(3)	9529(2)	27(1)
C(43)	10125(3)	6588(3)	9414(2)	28(1)
C(44)	11369(3)	9163(3)	10125(3)	43(1)
C(45)	12050(3)	8149(3)	11332(2)	39(1)
Cl(1)	1297(7)	4672(8)	4828(5)	151(3)
C(46)	-184(8)	4518(10)	4513(8)	99(3)
Cl(2)	-1370(6)	5345(5)	4765(4)	93(2)
N(1)	-635(3)	-1177(2)	7332(2)	43(1)
N(2)	-1745(3)	247(2)	5618(2)	30(1)
N(3)	-1734(3)	2011(3)	4085(2)	45(1)

Bond lengths

C(1)-N(1)	1.343(4)	C(12)-H(12)	0.9500
C(1)-C(2)	1.369(5)	C(13)-C(14)	1.372(5)
C(1)-H(1)	0.9500	C(13)-H(13)	0.9500
C(2)-C(3)	1.370(5)	C(14)-C(15)	1.363(5)
C(2)-H(2)	0.9500	C(14)-H(14)	0.9500
C(3)-C(4)	1.364(5)	C(15)-N(3)	1.343(4)
C(3)-H(3)	0.9500	C(15)-H(15)	0.9500
C(4)-C(5)	1.385(4)	C(16)-C(17)	1.389(4)
C(4)-H(4)	0.9500	C(16)-C(28)	1.402(4)
C(5)-N(1)	1.341(4)	C(17)-C(18)	1.384(4)
C(5)-C(6)	1.487(5)	C(17)-H(17)	0.9500
C(6)-N(2)	1.349(4)	C(18)-C(19)	1.382(4)
C(6)-C(7)	1.385(4)	C(18)-H(18)	0.9500
C(7)-C(8)	1.379(4)	C(19)-C(27)	1.400(4)
C(7)-H(7)	0.9500	C(19)-C(20)	1.457(4)
C(8)-C(9)	1.391(4)	C(20)-C(21)	1.386(4)
C(8)-C(16)	1.487(4)	C(20)-C(25)	1.395(4)
C(9)-C(10)	1.387(4)	C(21)-C(22)	1.370(4)
C(9)-H(9)	0.9500	C(21)-H(21)	0.9500
C(10)-N(2)	1.345(4)	C(22)-C(23)	1.402(4)
C(10)-C(11)	1.497(4)	C(22)-H(22)	0.9500
C(11)-N(3)	1.341(4)	C(23)-C(24)	1.401(4)
C(11)-C(12)	1.382(5)	C(23)-C(31)	1.475(4)
C(12)-C(13)	1.354(5)	C(24)-C(25)	1.380(4)

C(24)-H(24)	0.9500	C(36)-H(36)	0.9500
C(25)-C(26)	1.520(4)	C(37)-C(38)	1.380(5)
C(26)-C(27)	1.519(4)	C(37)-H(37)	0.9500
C(26)-C(29)	1.531(4)	C(38)-C(39)	1.393(5)
C(26)-C(30)	1.533(4)	C(38)-H(38)	0.9500
C(27)-C(28)	1.387(4)	C(39)-C(40)	1.376(4)
C(28)-H(28)	0.9500	C(39)-H(39)	0.9500
C(29)-H(29A)	0.9800	C(40)-C(41)	1.520(4)
C(29)-H(29B)	0.9800	C(41)-C(42)	1.523(4)
C(29)-H(29C)	0.9800	C(41)-C(45)	1.534(5)
C(30)-H(30A)	0.9800	C(41)-C(44)	1.539(4)
C(30)-H(30B)	0.9800	C(42)-C(43)	1.372(4)
C(30)-H(30C)	0.9800	C(43)-H(43)	0.9500
C(31)-C(32)	1.400(4)	C(44)-H(44A)	0.9800
C(31)-C(43)	1.402(4)	C(44)-H(44B)	0.9800
C(32)-C(33)	1.381(4)	C(44)-H(44C)	0.9800
C(32)-H(32)	0.9500	C(45)-H(45A)	0.9800
C(33)-C(34)	1.380(4)	C(45)-H(45B)	0.9800
C(33)-H(33)	0.9500	C(45)-H(45C)	0.9800
C(34)-C(42)	1.406(4)	Cl(1)-C(46)	1.479(9)
C(34)-C(35)	1.469(4)	C(46)-Cl(2)	1.609(9)
C(35)-C(36)	1.391(4)	C(46)-H(46A)	0.9900
C(35)-C(40)	1.396(4)	C(46)-H(46B)	0.9900
C(36)-C(37)	1.386(5)		

Angles

N(1)-C(1)-C(2)	123.1(3)	C(7)-C(8)-C(9)	117.8(3)
N(1)-C(1)-H(1)	118.4	C(7)-C(8)-C(16)	119.8(3)
C(2)-C(1)-H(1)	118.4	C(9)-C(8)-C(16)	122.4(3)
C(1)-C(2)-C(3)	118.9(4)	C(10)-C(9)-C(8)	119.2(3)
C(1)-C(2)-H(2)	120.5	C(10)-C(9)-H(9)	120.4
C(3)-C(2)-H(2)	120.5	C(8)-C(9)-H(9)	120.4
C(4)-C(3)-C(2)	119.1(3)	N(2)-C(10)-C(9)	123.1(3)
C(4)-C(3)-H(3)	120.4	N(2)-C(10)-C(11)	115.1(3)
C(2)-C(3)-H(3)	120.4	C(9)-C(10)-C(11)	121.8(3)
C(3)-C(4)-C(5)	119.3(3)	N(3)-C(11)-C(12)	122.5(3)
C(3)-C(4)-H(4)	120.3	N(3)-C(11)-C(10)	116.6(3)
C(5)-C(4)-H(4)	120.3	C(12)-C(11)-C(10)	120.9(3)
N(1)-C(5)-C(4)	122.1(3)	C(13)-C(12)-C(11)	119.1(4)
N(1)-C(5)-C(6)	116.1(3)	C(13)-C(12)-H(12)	120.5
C(4)-C(5)-C(6)	121.8(3)	C(11)-C(12)-H(12)	120.5
N(2)-C(6)-C(7)	122.6(3)	C(12)-C(13)-C(14)	120.1(4)
N(2)-C(6)-C(5)	115.6(3)	C(12)-C(13)-H(13)	119.9
C(7)-C(6)-C(5)	121.7(3)	C(14)-C(13)-H(13)	119.9
C(8)-C(7)-C(6)	120.0(3)	C(15)-C(14)-C(13)	117.2(4)
C(8)-C(7)-H(7)	120.0	C(15)-C(14)-H(14)	121.4
C(6)-C(7)-H(7)	120.0	C(13)-C(14)-H(14)	121.4

N(3)-C(15)-C(14)	124.9(4)	H(29B)-C(29)-H(29C)	109.5
N(3)-C(15)-H(15)	117.5	C(26)-C(30)-H(30A)	109.5
C(14)-C(15)-H(15)	117.5	C(26)-C(30)-H(30B)	109.5
C(17)-C(16)-C(28)	119.3(3)	H(30A)-C(30)-H(30B)	109.5
C(17)-C(16)-C(8)	119.7(3)	C(26)-C(30)-H(30C)	109.5
C(28)-C(16)-C(8)	120.9(3)	H(30A)-C(30)-H(30C)	109.5
C(18)-C(17)-C(16)	121.6(3)	H(30B)-C(30)-H(30C)	109.5
C(18)-C(17)-H(17)	119.2	C(32)-C(31)-C(43)	118.2(3)
C(16)-C(17)-H(17)	119.2	C(32)-C(31)-C(23)	121.3(3)
C(19)-C(18)-C(17)	118.9(3)	C(43)-C(31)-C(23)	120.5(3)
C(19)-C(18)-H(18)	120.6	C(33)-C(32)-C(31)	121.7(3)
C(17)-C(18)-H(18)	120.6	C(33)-C(32)-H(32)	119.1
C(18)-C(19)-C(27)	120.6(3)	C(31)-C(32)-H(32)	119.1
C(18)-C(19)-C(20)	130.5(3)	C(34)-C(33)-C(32)	119.3(3)
C(27)-C(19)-C(20)	108.9(3)	C(34)-C(33)-H(33)	120.3
C(21)-C(20)-C(25)	120.2(3)	C(32)-C(33)-H(33)	120.3
C(21)-C(20)-C(19)	131.5(3)	C(33)-C(34)-C(42)	119.9(3)
C(25)-C(20)-C(19)	108.2(3)	C(33)-C(34)-C(35)	131.8(3)
C(22)-C(21)-C(20)	119.5(3)	C(42)-C(34)-C(35)	108.2(3)
C(22)-C(21)-H(21)	120.3	C(36)-C(35)-C(40)	120.4(3)
C(20)-C(21)-H(21)	120.3	C(36)-C(35)-C(34)	131.1(3)
C(21)-C(22)-C(23)	121.5(3)	C(40)-C(35)-C(34)	108.4(3)
C(21)-C(22)-H(22)	119.2	C(37)-C(36)-C(35)	118.6(3)
C(23)-C(22)-H(22)	119.2	C(37)-C(36)-H(36)	120.7
C(24)-C(23)-C(22)	118.3(3)	C(35)-C(36)-H(36)	120.7
C(24)-C(23)-C(31)	121.1(3)	C(38)-C(37)-C(36)	121.3(3)
C(22)-C(23)-C(31)	120.6(3)	C(38)-C(37)-H(37)	119.4
C(25)-C(24)-C(23)	120.3(3)	C(36)-C(37)-H(37)	119.4
C(25)-C(24)-H(24)	119.9	C(37)-C(38)-C(39)	119.9(3)
C(23)-C(24)-H(24)	119.9	C(37)-C(38)-H(38)	120.0
C(24)-C(25)-C(20)	120.1(3)	C(39)-C(38)-H(38)	120.0
C(24)-C(25)-C(26)	128.8(3)	C(40)-C(39)-C(38)	119.6(3)
C(20)-C(25)-C(26)	111.1(3)	C(40)-C(39)-H(39)	120.2
C(27)-C(26)-C(25)	101.2(2)	C(38)-C(39)-H(39)	120.2
C(27)-C(26)-C(29)	112.4(3)	C(39)-C(40)-C(35)	120.3(3)
C(25)-C(26)-C(29)	111.6(3)	C(39)-C(40)-C(41)	128.5(3)
C(27)-C(26)-C(30)	111.2(3)	C(35)-C(40)-C(41)	111.3(3)
C(25)-C(26)-C(30)	110.6(3)	C(40)-C(41)-C(42)	101.1(3)
C(29)-C(26)-C(30)	109.6(3)	C(40)-C(41)-C(45)	112.1(3)
C(28)-C(27)-C(19)	120.2(3)	C(42)-C(41)-C(45)	112.3(3)
C(28)-C(27)-C(26)	129.3(3)	C(40)-C(41)-C(44)	111.3(3)
C(19)-C(27)-C(26)	110.5(3)	C(42)-C(41)-C(44)	110.2(3)
C(27)-C(28)-C(16)	119.4(3)	C(45)-C(41)-C(44)	109.6(3)
C(27)-C(28)-H(28)	120.3	C(43)-C(42)-C(34)	120.4(3)
C(16)-C(28)-H(28)	120.3	C(43)-C(42)-C(41)	128.8(3)
C(26)-C(29)-H(29A)	109.5	C(34)-C(42)-C(41)	110.8(3)
C(26)-C(29)-H(29B)	109.5	C(42)-C(43)-C(31)	120.4(3)
H(29A)-C(29)-H(29B)	109.5	C(42)-C(43)-H(43)	119.8
C(26)-C(29)-H(29C)	109.5	C(31)-C(43)-H(43)	119.8
H(29A)-C(29)-H(29C)	109.5	C(41)-C(44)-H(44A)	109.5

C(41)-C(44)-H(44B)	109.5	H(45B)-C(45)-H(45C)	109.5
H(44A)-C(44)-H(44B)	109.5	Cl(1)-C(46)-Cl(2)	132.2(9)
C(41)-C(44)-H(44C)	109.5	Cl(1)-C(46)-H(46A)	104.2
H(44A)-C(44)-H(44C)	109.5	Cl(2)-C(46)-H(46A)	104.2
H(44B)-C(44)-H(44C)	109.5	Cl(1)-C(46)-H(46B)	104.2
C(41)-C(45)-H(45A)	109.5	Cl(2)-C(46)-H(46B)	104.2
C(41)-C(45)-H(45B)	109.5	H(46A)-C(46)-H(46B)	105.5
H(45A)-C(45)-H(45B)	109.5	C(5)-N(1)-C(1)	117.4(3)
C(41)-C(45)-H(45C)	109.5	C(10)-N(2)-C(6)	117.3(3)
H(45A)-C(45)-H(45C)	109.5	C(11)-N(3)-C(15)	116.1(3)

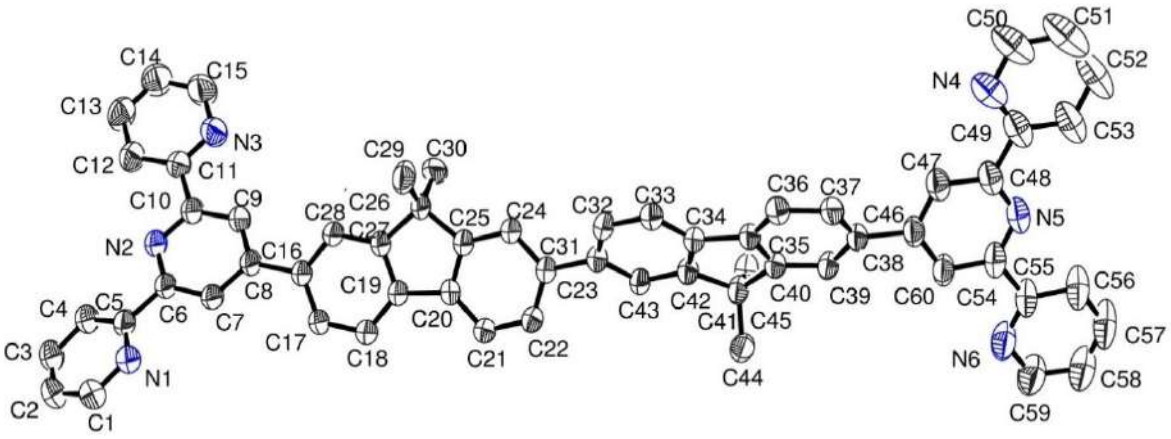

Empirical formula	$C_{60}H_{44}N_6$
Formula weight	849.01
Temperature	180(2) K
Wavelength	1.54184 A
Crystal system, space group	Triclinic, P -1
Unit cell dimensions	a = 9.6440(6) A alpha = 107.209(5) deg. b = 14.7061(9) A beta = 100.924(5) deg. c = 19.0602(11) A gamma = 100.765(5) deg.
Volume	2449.0(3) A^3
Z, Calculated density	2, 1.151 Mg/m^3
Absorption coefficient	0.528 mm^-1
F(000)	892
Crystal size	0.26 x 0.24 x 0.04 mm
Theta range for data collection	3.257 to 71.715 deg.
Limiting indices	-8<=h<=11, -16<=k<=17, -23<=l<=21
Reflections collected / unique	25924 / 9339 [R(int) = 0.0519]
Completeness to theta = 67.684	99.7 %
Refinement method	Full-matrix least-squares on F^2
Data / restraints / parameters	9339 / 0 / 599
Goodness-of-fit on F^2	0.970

Final R indices [I>2sigma(I)]	R1 = 0.0618, wR2 = 0.1515
R indices (all data)	R1 = 0.1132, wR2 = 0.1891
Largest diff. peak and hole	0.281 and -0.190 e.A^-3

Atomic coordinates

U(eq) is defined as one third of the trace of the orthogonalized Uij tensor.

	x	y	z	U(eq)
C(1)	14188(4)	3362(3)	452(2)	69(1)
C(2)	15501(5)	3453(3)	254(2)	78(1)
C(3)	16468(4)	4358(3)	513(2)	78(1)
C(4)	16085(4)	5159(3)	947(2)	66(1)
C(5)	14751(3)	5000(2)	1122(2)	55(1)
C(6)	14363(3)	5835(2)	1641(2)	51(1)
C(7)	13332(3)	5661(2)	2043(2)	51(1)
C(8)	13087(3)	6467(2)	2571(2)	51(1)
C(9)	13844(3)	7400(2)	2640(2)	55(1)
C(10)	14806(3)	7510(2)	2197(2)	54(1)
C(11)	15597(3)	8500(2)	2232(2)	60(1)
C(12)	16563(4)	8596(3)	1785(2)	69(1)
C(13)	17256(5)	9531(3)	1835(2)	87(1)
C(14)	16949(5)	10327(3)	2300(3)	95(1)
C(15)	15991(5)	10172(3)	2733(3)	98(2)
C(16)	12030(3)	6324(2)	3031(2)	50(1)
C(17)	11725(3)	5460(2)	3207(2)	54(1)
C(18)	10742(3)	5318(2)	3629(2)	53(1)
C(19)	10033(3)	6041(2)	3876(2)	46(1)
C(20)	8953(3)	6102(2)	4328(1)	46(1)
C(21)	8382(3)	5470(2)	4675(2)	49(1)
C(22)	7309(3)	5684(2)	5042(2)	50(1)
C(23)	6813(3)	6527(2)	5069(2)	48(1)
C(24)	7435(3)	7178(2)	4735(2)	50(1)
C(25)	8513(3)	6964(2)	4373(2)	48(1)
C(26)	9335(3)	7568(2)	3980(2)	52(1)
C(27)	10289(3)	6901(2)	3683(2)	48(1)
C(28)	11282(3)	7043(2)	3270(2)	51(1)
C(29)	8273(4)	7678(3)	3323(2)	77(1)
C(30)	10244(4)	8577(2)	4538(2)	72(1)
C(31)	5604(3)	6712(2)	5427(2)	49(1)
C(32)	4457(3)	6995(2)	5067(2)	52(1)
C(33)	3290(3)	7137(2)	5373(2)	51(1)
C(34)	3291(3)	7008(2)	6068(2)	46(1)
C(35)	2229(3)	7106(2)	6529(2)	46(1)
C(36)	883(3)	7337(2)	6408(2)	51(1)

C(37)	178(3)	7469(2)	6989(2)	53(1)
C(38)	772(3)	7364(2)	7675(2)	50(1)
C(39)	2087(3)	7076(2)	7774(2)	49(1)
C(40)	2797(3)	6947(2)	7202(2)	47(1)
C(41)	4262(3)	6695(2)	7213(2)	49(1)
C(42)	4453(3)	6750(2)	6448(2)	48(1)
C(43)	5603(3)	6589(2)	6131(2)	47(1)
C(44)	4180(3)	5660(2)	7247(2)	59(1)
C(45)	5484(3)	7462(3)	7865(2)	64(1)
C(46)	119(3)	7646(2)	8329(2)	54(1)
C(47)	-543(3)	8421(2)	8429(2)	59(1)
C(48)	-1081(3)	8724(2)	9063(2)	62(1)
C(49)	-1817(4)	9532(3)	9177(2)	74(1)
C(50)	-2560(6)	10689(4)	8729(3)	116(2)
C(51)	-3184(6)	11008(4)	9322(4)	124(2)
C(52)	-3105(5)	10561(4)	9858(3)	116(2)
C(53)	-2408(4)	9813(3)	9789(3)	92(1)
C(54)	-301(3)	7565(3)	9517(2)	64(1)
C(55)	-136(3)	7160(3)	10142(2)	70(1)
C(56)	-688(4)	7518(4)	10766(2)	91(1)
C(57)	-537(5)	7105(4)	11326(2)	105(2)
C(58)	137(4)	6363(4)	11260(2)	95(1)
C(59)	713(5)	6074(4)	10645(2)	94(1)
C(60)	234(3)	7207(3)	8887(2)	60(1)
N(1)	13805(3)	4122(2)	883(2)	60(1)
N(2)	15082(3)	6742(2)	1710(1)	53(1)
N(3)	15315(4)	9270(2)	2704(2)	81(1)
N(4)	-1892(4)	9959(3)	8651(2)	88(1)
N(5)	-957(3)	8306(2)	9601(2)	66(1)
N(6)	572(4)	6458(3)	10087(2)	83(1)

Bond lengths

C(1)-N(1)	1.337(4)	C(8)-C(16)	1.490(3)
C(1)-C(2)	1.383(5)	C(9)-C(10)	1.387(4)
C(1)-H(1)	0.9500	C(9)-H(9)	0.9500
C(2)-C(3)	1.364(6)	C(10)-N(2)	1.340(4)
C(2)-H(2)	0.9500	C(10)-C(11)	1.488(4)
C(3)-C(4)	1.382(5)	C(11)-N(3)	1.331(4)
C(3)-H(3)	0.9500	C(11)-C(12)	1.392(4)
C(4)-C(5)	1.385(4)	C(12)-C(13)	1.379(5)
C(4)-H(4)	0.9500	C(12)-H(12)	0.9500
C(5)-N(1)	1.327(4)	C(13)-C(14)	1.363(6)
C(5)-C(6)	1.489(4)	C(13)-H(13)	0.9500
C(6)-N(2)	1.339(4)	C(14)-C(15)	1.382(5)
C(6)-C(7)	1.397(3)	C(14)-H(14)	0.9500
C(7)-C(8)	1.401(4)	C(15)-N(3)	1.344(5)
C(7)-H(7)	0.9500	C(15)-H(15)	0.9500
C(8)-C(9)	1.384(4)	C(16)-C(17)	1.401(4)

C(16)-C(28)	1.405(4)	C(39)-C(40)	1.379(3)
C(17)-C(18)	1.380(3)	C(39)-H(39)	0.9500
C(17)-H(17)	0.9500	C(40)-C(41)	1.524(3)
C(18)-C(19)	1.385(4)	C(41)-C(45)	1.524(4)
C(18)-H(18)	0.9500	C(41)-C(42)	1.527(3)
C(19)-C(27)	1.410(4)	C(41)-C(44)	1.532(4)
C(19)-C(20)	1.472(3)	C(42)-C(43)	1.384(3)
C(20)-C(21)	1.384(4)	C(43)-H(43)	0.9500
C(20)-C(25)	1.394(4)	C(44)-H(44A)	0.9800
C(21)-C(22)	1.387(4)	C(44)-H(44B)	0.9800
C(21)-H(21)	0.9500	C(44)-H(44C)	0.9800
C(22)-C(23)	1.401(4)	C(45)-H(45A)	0.9800
C(22)-H(22)	0.9500	C(45)-H(45B)	0.9800
C(23)-C(24)	1.405(3)	C(45)-H(45C)	0.9800
C(23)-C(31)	1.486(3)	C(46)-C(47)	1.391(4)
C(24)-C(25)	1.385(3)	C(46)-C(60)	1.397(4)
C(24)-H(24)	0.9500	C(47)-C(48)	1.390(4)
C(25)-C(26)	1.528(3)	C(47)-H(47)	0.9500
C(26)-C(30)	1.525(5)	C(48)-N(5)	1.341(4)
C(26)-C(27)	1.528(3)	C(48)-C(49)	1.478(5)
C(26)-C(29)	1.530(4)	C(49)-N(4)	1.329(5)
C(27)-C(28)	1.374(3)	C(49)-C(53)	1.383(5)
C(28)-H(28)	0.9500	C(50)-N(4)	1.338(5)
C(29)-H(29A)	0.9800	C(50)-C(51)	1.382(7)
C(29)-H(29B)	0.9800	C(50)-H(50)	0.9500
C(29)-H(29C)	0.9800	C(51)-C(52)	1.367(8)
C(30)-H(30A)	0.9800	C(51)-H(51)	0.9500
C(30)-H(30B)	0.9800	C(52)-C(53)	1.380(6)
C(30)-H(30C)	0.9800	C(52)-H(52)	0.9500
C(31)-C(32)	1.386(4)	C(53)-H(53)	0.9500
C(31)-C(43)	1.407(3)	C(54)-N(5)	1.343(4)
C(32)-C(33)	1.383(4)	C(54)-C(60)	1.395(4)
C(32)-H(32)	0.9500	C(54)-C(55)	1.477(5)
C(33)-C(34)	1.392(4)	C(55)-N(6)	1.330(5)
C(33)-H(33)	0.9500	C(55)-C(56)	1.396(4)
C(34)-C(42)	1.392(4)	C(56)-C(57)	1.375(6)
C(34)-C(35)	1.472(3)	C(56)-H(56)	0.9500
C(35)-C(36)	1.396(4)	C(57)-C(58)	1.357(7)
C(35)-C(40)	1.398(4)	C(57)-H(57)	0.9500
C(36)-C(37)	1.391(4)	C(58)-C(59)	1.381(5)
C(36)-H(36)	0.9500	C(58)-H(58)	0.9500
C(37)-C(38)	1.390(4)	C(59)-N(6)	1.341(5)
C(37)-H(37)	0.9500	C(59)-H(59)	0.9500
C(38)-C(39)	1.407(4)	C(60)-H(60)	0.9500
C(38)-C(46)	1.485(3)		

Angles

N(1)-C(1)-C(2)	123.3(3)	C(3)-C(2)-H(2)	120.5
N(1)-C(1)-H(1)	118.3	C(1)-C(2)-H(2)	120.5
C(2)-C(1)-H(1)	118.3	C(2)-C(3)-C(4)	118.8(3)
C(3)-C(2)-C(1)	119.0(3)	C(2)-C(3)-H(3)	120.6

C(4)-C(3)-H(3)	120.6	C(21)-C(20)-C(19)	130.7(2)
C(3)-C(4)-C(5)	118.4(3)	C(25)-C(20)-C(19)	108.3(2)
C(3)-C(4)-H(4)	120.8	C(20)-C(21)-C(22)	118.8(3)
C(5)-C(4)-H(4)	120.8	C(20)-C(21)-H(21)	120.6
N(1)-C(5)-C(4)	123.6(3)	C(22)-C(21)-H(21)	120.6
N(1)-C(5)-C(6)	116.9(2)	C(21)-C(22)-C(23)	121.1(2)
C(4)-C(5)-C(6)	119.4(3)	C(21)-C(22)-H(22)	119.5
N(2)-C(6)-C(7)	123.0(3)	C(23)-C(22)-H(22)	119.5
N(2)-C(6)-C(5)	116.3(2)	C(22)-C(23)-C(24)	119.4(2)
C(7)-C(6)-C(5)	120.7(3)	C(22)-C(23)-C(31)	120.1(2)
C(6)-C(7)-C(8)	118.8(3)	C(24)-C(23)-C(31)	120.4(2)
C(6)-C(7)-H(7)	120.6	C(25)-C(24)-C(23)	119.3(2)
C(8)-C(7)-H(7)	120.6	C(25)-C(24)-H(24)	120.4
C(9)-C(8)-C(7)	117.6(2)	C(23)-C(24)-H(24)	120.4
C(9)-C(8)-C(16)	121.3(3)	C(24)-C(25)-C(20)	120.3(2)
C(7)-C(8)-C(16)	121.1(3)	C(24)-C(25)-C(26)	127.8(2)
C(8)-C(9)-C(10)	119.9(3)	C(20)-C(25)-C(26)	111.9(2)
C(8)-C(9)-H(9)	120.0	C(30)-C(26)-C(27)	112.2(2)
C(10)-C(9)-H(9)	120.0	C(30)-C(26)-C(25)	111.7(2)
N(2)-C(10)-C(9)	122.7(3)	C(27)-C(26)-C(25)	100.4(2)
N(2)-C(10)-C(11)	115.7(2)	C(30)-C(26)-C(29)	110.6(3)
C(9)-C(10)-C(11)	121.6(3)	C(27)-C(26)-C(29)	110.9(2)
N(3)-C(11)-C(12)	122.9(3)	C(25)-C(26)-C(29)	110.6(3)
N(3)-C(11)-C(10)	116.3(3)	C(28)-C(27)-C(19)	120.2(2)
C(12)-C(11)-C(10)	120.8(3)	C(28)-C(27)-C(26)	128.5(2)
C(13)-C(12)-C(11)	118.3(3)	C(19)-C(27)-C(26)	111.3(2)
C(13)-C(12)-H(12)	120.8	C(27)-C(28)-C(16)	119.9(2)
C(11)-C(12)-H(12)	120.8	C(27)-C(28)-H(28)	120.0
C(14)-C(13)-C(12)	119.5(3)	C(16)-C(28)-H(28)	120.0
C(14)-C(13)-H(13)	120.2	C(26)-C(29)-H(29A)	109.5
C(12)-C(13)-H(13)	120.2	C(26)-C(29)-H(29B)	109.5
C(13)-C(14)-C(15)	118.6(4)	H(29A)-C(29)-H(29B)	109.5
C(13)-C(14)-H(14)	120.7	C(26)-C(29)-H(29C)	109.5
C(15)-C(14)-H(14)	120.7	H(29A)-C(29)-H(29C)	109.5
N(3)-C(15)-C(14)	123.2(4)	H(29B)-C(29)-H(29C)	109.5
N(3)-C(15)-H(15)	118.4	C(26)-C(30)-H(30A)	109.5
C(14)-C(15)-H(15)	118.4	C(26)-C(30)-H(30B)	109.5
C(17)-C(16)-C(28)	119.0(2)	H(30A)-C(30)-H(30B)	109.5
C(17)-C(16)-C(8)	120.9(2)	C(26)-C(30)-H(30C)	109.5
C(28)-C(16)-C(8)	120.1(2)	H(30A)-C(30)-H(30C)	109.5
C(18)-C(17)-C(16)	121.4(2)	H(30B)-C(30)-H(30C)	109.5
C(18)-C(17)-H(17)	119.3	C(32)-C(31)-C(43)	119.2(2)
C(16)-C(17)-H(17)	119.3	C(32)-C(31)-C(23)	120.5(2)
C(17)-C(18)-C(19)	119.2(2)	C(43)-C(31)-C(23)	120.3(2)
C(17)-C(18)-H(18)	120.4	C(33)-C(32)-C(31)	121.8(2)
C(19)-C(18)-H(18)	120.4	C(33)-C(32)-H(32)	119.1
C(18)-C(19)-C(27)	120.3(2)	C(31)-C(32)-H(32)	119.1
C(18)-C(19)-C(20)	131.6(2)	C(32)-C(33)-C(34)	118.7(3)
C(27)-C(19)-C(20)	108.1(2)	C(32)-C(33)-H(33)	120.7
C(21)-C(20)-C(25)	121.0(2)	C(34)-C(33)-H(33)	120.7

C(33)-C(34)-C(42)	120.4(2)	C(48)-C(47)-C(46)	120.0(3)
C(33)-C(34)-C(35)	131.2(3)	C(48)-C(47)-H(47)	120.0
C(42)-C(34)-C(35)	108.4(2)	C(46)-C(47)-H(47)	120.0
C(36)-C(35)-C(40)	120.3(2)	N(5)-C(48)-C(47)	122.2(3)
C(36)-C(35)-C(34)	131.7(2)	N(5)-C(48)-C(49)	116.6(3)
C(40)-C(35)-C(34)	108.0(2)	C(47)-C(48)-C(49)	121.2(3)
C(37)-C(36)-C(35)	118.5(3)	N(4)-C(49)-C(53)	122.3(4)
C(37)-C(36)-H(36)	120.8	N(4)-C(49)-C(48)	115.9(3)
C(35)-C(36)-H(36)	120.8	C(53)-C(49)-C(48)	121.8(4)
C(38)-C(37)-C(36)	121.6(3)	N(4)-C(50)-C(51)	123.1(6)
C(38)-C(37)-H(37)	119.2	N(4)-C(50)-H(50)	118.4
C(36)-C(37)-H(37)	119.2	C(51)-C(50)-H(50)	118.4
C(37)-C(38)-C(39)	119.2(2)	C(52)-C(51)-C(50)	118.4(5)
C(37)-C(38)-C(46)	120.9(3)	C(52)-C(51)-H(51)	120.8
C(39)-C(38)-C(46)	119.6(3)	C(50)-C(51)-H(51)	120.8
C(40)-C(39)-C(38)	119.5(3)	C(51)-C(52)-C(53)	119.1(5)
C(40)-C(39)-H(39)	120.3	C(51)-C(52)-H(52)	120.5
C(38)-C(39)-H(39)	120.3	C(53)-C(52)-H(52)	120.5
C(39)-C(40)-C(35)	120.7(2)	C(52)-C(53)-C(49)	119.1(5)
C(39)-C(40)-C(41)	127.6(3)	C(52)-C(53)-H(53)	120.5
C(35)-C(40)-C(41)	111.6(2)	C(49)-C(53)-H(53)	120.5
C(40)-C(41)-C(45)	111.5(2)	N(5)-C(54)-C(60)	122.5(3)
C(40)-C(41)-C(42)	100.4(2)	N(5)-C(54)-C(55)	116.3(3)
C(45)-C(41)-C(42)	110.7(2)	C(60)-C(54)-C(55)	121.2(3)
C(40)-C(41)-C(44)	111.3(2)	N(6)-C(55)-C(56)	122.1(4)
C(45)-C(41)-C(44)	111.0(3)	N(6)-C(55)-C(54)	117.3(3)
C(42)-C(41)-C(44)	111.6(2)	C(56)-C(55)-C(54)	120.6(4)
C(43)-C(42)-C(34)	120.7(2)	C(57)-C(56)-C(55)	118.7(4)
C(43)-C(42)-C(41)	127.8(2)	C(57)-C(56)-H(56)	120.7
C(34)-C(42)-C(41)	111.5(2)	C(55)-C(56)-H(56)	120.7
C(42)-C(43)-C(31)	119.2(2)	C(58)-C(57)-C(56)	119.6(4)
C(42)-C(43)-H(43)	120.4	C(58)-C(57)-H(57)	120.2
C(31)-C(43)-H(43)	120.4	C(56)-C(57)-H(57)	120.2
C(41)-C(44)-H(44A)	109.5	C(57)-C(58)-C(59)	118.7(4)
C(41)-C(44)-H(44B)	109.5	C(57)-C(58)-H(58)	120.6
H(44A)-C(44)-H(44B)	109.5	C(59)-C(58)-H(58)	120.6
C(41)-C(44)-H(44C)	109.5	N(6)-C(59)-C(58)	122.9(5)
H(44A)-C(44)-H(44C)	109.5	N(6)-C(59)-H(59)	118.5
H(44B)-C(44)-H(44C)	109.5	C(58)-C(59)-H(59)	118.5
C(41)-C(45)-H(45A)	109.5	C(54)-C(60)-C(46)	119.2(3)
C(41)-C(45)-H(45B)	109.5	C(54)-C(60)-H(60)	120.4
H(45A)-C(45)-H(45B)	109.5	C(46)-C(60)-H(60)	120.4
C(41)-C(45)-H(45C)	109.5	C(5)-N(1)-C(1)	117.0(3)
H(45A)-C(45)-H(45C)	109.5	C(6)-N(2)-C(10)	117.8(2)
H(45B)-C(45)-H(45C)	109.5	C(11)-N(3)-C(15)	117.4(3)
C(47)-C(46)-C(60)	117.6(3)	C(49)-N(4)-C(50)	118.0(4)
C(47)-C(46)-C(38)	119.8(3)	C(48)-N(5)-C(54)	118.5(3)
C(60)-C(46)-C(38)	122.4(3)	C(55)-N(6)-C(59)	117.9(3)

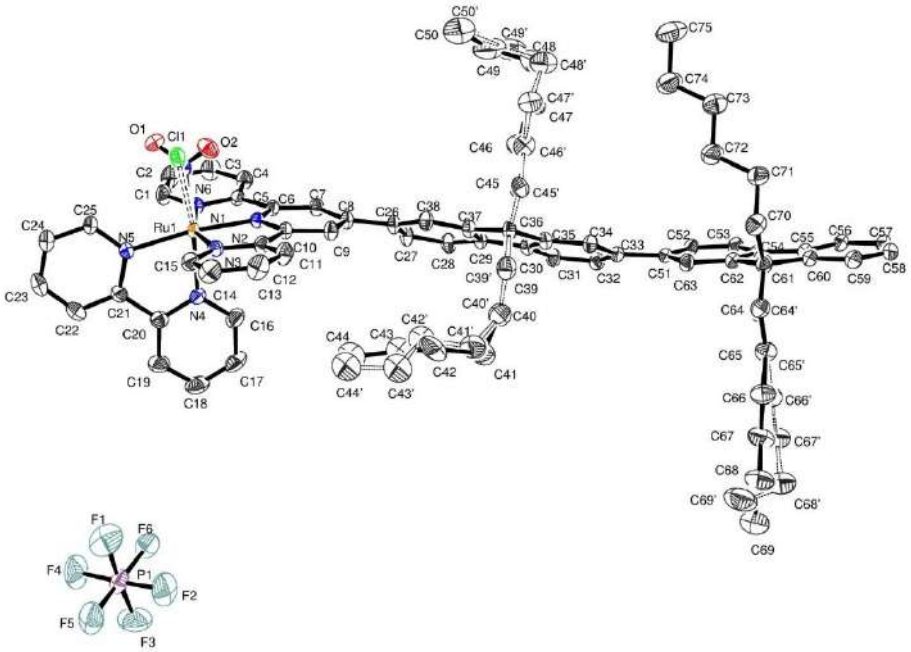

Empirical formula	$C_{75}H_{83}Cl_{0.16}N_{5.84}O_{1.68}RuF_6P$
Formula weight	1344.85
Temperature	193(2) K
Wavelength	0.71073 A
Crystal system, space group	Triclinic, P -1
Unit cell dimensions	a = 10.6127(8) A alpha = 95.125(2) deg. b = 13.2976(10) A beta = 98.326(2) deg. c = 24.8420(19) A gamma = 91.055(3) deg.
Volume	3453.2(5) A^3
Z, Calculated density	2, 1.293 Mg/m^3
Absorption coefficient	0.321 mm^-1
F(000)	1406
Crystal size	0.180 x 0.160 x 0.040 mm
Theta range for data collection	1.664 to 28.547 deg.
Limiting indices	-14<=h<=14, -17<=k<=17, -33<=l<=33
Reflections collected / unique	90987 / 17263 [R(int) = 0.0768]

Completeness to theta = 25.242	99.5 %
Refinement method	Full-matrix least-squares on F^2
Data / restraints / parameters	17263 / 494 / 979
Goodness-of-fit on F^2	1.026
Final R indices [I>2sigma(I)]	R1 = 0.0461, wR2 = 0.0916
R indices (all data)	R1 = 0.0782, wR2 = 0.1042
Largest diff. peak and hole	0.610 and -0.766 e.A^-3

Atomic coordinates

U(eq) is defined as one third of the trace of the orthogonalized Uij tensor.

	x	y	z	U(eq)
C(1)	9153(3)	10095(2)	6374(1)	34(1)
C(2)	9316(3)	11128(2)	6385(1)	42(1)
C(3)	9063(3)	11575(2)	5907(1)	39(1)
C(4)	8664(2)	10981(2)	5426(1)	31(1)
C(5)	8522(2)	9945(2)	5435(1)	23(1)
C(6)	8175(2)	9242(2)	4939(1)	22(1)
C(7)	7761(2)	9485(2)	4415(1)	25(1)
C(8)	7421(2)	8715(2)	3993(1)	25(1)
C(9)	7583(2)	7713(2)	4115(1)	26(1)
C(10)	8017(2)	7502(2)	4643(1)	23(1)
C(11)	8154(2)	6494(2)	4844(1)	25(1)
C(12)	8058(3)	5607(2)	4505(1)	34(1)
C(13)	8205(3)	4694(2)	4730(1)	41(1)
C(14)	8445(3)	4694(2)	5288(1)	41(1)
C(15)	8537(2)	5597(2)	5611(1)	30(1)
C(16)	5683(2)	7962(2)	5476(1)	37(1)
C(17)	4424(3)	7826(2)	5542(1)	44(1)
C(18)	4135(3)	7578(2)	6034(1)	45(1)
C(19)	5117(3)	7469(2)	6446(1)	41(1)
C(20)	6369(2)	7610(2)	6365(1)	28(1)
C(21)	7473(2)	7495(2)	6784(1)	28(1)
C(22)	7376(3)	7289(2)	7313(1)	46(1)
C(23)	8467(3)	7175(3)	7677(1)	49(1)
C(24)	9630(3)	7283(2)	7505(1)	39(1)
C(25)	9676(2)	7487(2)	6976(1)	30(1)
C(26)	6836(2)	8929(2)	3438(1)	26(1)
C(27)	6092(3)	9779(2)	3364(1)	30(1)

C(28)	5453(2)	9952(2)	2857(1)	28(1)
C(29)	5559(2)	9264(2)	2409(1)	24(1)
C(30)	4997(2)	9227(2)	1832(1)	23(1)
C(31)	4203(2)	9878(2)	1547(1)	26(1)
C(32)	3823(2)	9650(2)	992(1)	26(1)
C(33)	4235(2)	8793(2)	705(1)	23(1)
C(34)	5026(2)	8141(2)	1002(1)	25(1)
C(35)	5387(2)	8350(2)	1559(1)	24(1)
C(37)	6305(2)	8412(2)	2480(1)	25(1)
C(38)	6946(2)	8252(2)	2986(1)	27(1)
C(36)	6215(2)	7729(2)	1950(1)	25(1)
C(39)	5519(12)	6724(4)	2026(7)	31(1)
C(40)	4191(7)	6827(7)	2177(4)	41(1)
C(41)	3623(7)	5861(6)	2357(2)	58(1)
C(42)	4249(7)	5596(5)	2917(2)	76(2)
C(43)	4076(7)	6374(6)	3379(3)	115(2)
C(44)	4465(6)	6010(7)	3939(2)	115(2)
C(39')	5550(40)	6696(13)	1990(30)	39(3)
C(40')	4220(20)	6750(30)	2144(13)	49(3)
C(41')	3880(30)	5860(20)	2457(7)	61(2)
C(42')	4420(30)	6023(15)	3070(7)	79(3)
C(43')	4190(20)	5060(15)	3326(6)	115(2)
C(44')	4590(20)	5130(20)	3931(6)	115(2)
C(45)	7539(14)	7546(17)	1793(12)	29(3)
C(46)	8359(19)	8490(17)	1767(10)	38(3)
C(47)	9543(17)	8253(13)	1501(9)	54(4)
C(48)	10373(17)	9200(14)	1475(6)	75(4)
C(49)	10973(13)	9702(10)	2027(8)	80(4)
C(50)	11910(13)	8991(15)	2330(5)	101(5)
C(45')	7480(20)	7460(20)	1747(17)	29(5)
C(46')	8320(30)	8380(20)	1682(15)	39(4)
C(47')	9620(20)	8099(17)	1535(13)	46(4)
C(48')	10370(20)	8970(17)	1358(8)	59(4)
C(49')	10730(20)	9870(13)	1777(10)	77(5)
C(50')	11630(20)	9550(20)	2265(7)	95(8)
C(51)	3899(2)	8605(2)	103(1)	23(1)
C(52)	3596(2)	9407(2)	-217(1)	25(1)
C(53)	3350(2)	9263(2)	-780(1)	27(1)
C(54)	3408(2)	8300(2)	-1037(1)	24(1)
C(55)	3238(2)	7930(2)	-1619(1)	26(1)
C(56)	2963(2)	8440(2)	-2085(1)	32(1)
C(57)	2863(2)	7889(2)	-2592(1)	37(1)
C(58)	3024(3)	6856(2)	-2632(1)	39(1)
C(59)	3314(3)	6346(2)	-2170(1)	35(1)
C(60)	3438(2)	6889(2)	-1658(1)	28(1)
C(62)	3707(2)	7482(2)	-728(1)	25(1)
C(63)	3935(2)	7630(2)	-163(1)	25(1)
C(61)	3786(2)	6513(2)	-1098(1)	28(1)
C(64)	2943(14)	5610(13)	-1001(15)	32(2)
C(65)	1535(13)	5817(12)	-1026(12)	35(2)

C(66)	791(10)	4862(12)	-943(7)	44(2)
C(67)	-554(9)	5006(7)	-875(4)	52(2)
C(68)	-1243(7)	4017(6)	-810(4)	56(2)
C(69)	-2571(6)	4161(5)	-709(3)	62(2)
C(64')	2824(18)	5695(17)	-989(19)	35(3)
C(65')	1422(16)	5942(16)	-1047(14)	40(2)
C(66')	618(12)	4967(14)	-1026(8)	45(2)
C(67')	-761(11)	5138(9)	-1062(5)	52(2)
C(68')	-1632(9)	4225(7)	-1068(4)	58(2)
C(69')	-1486(9)	3680(8)	-567(4)	80(3)
C(70)	5160(3)	6114(2)	-1037(1)	37(1)
C(71)	6239(3)	6844(2)	-1118(1)	41(1)
C(72)	7013(3)	7327(3)	-597(1)	48(1)
C(73)	8232(3)	7865(2)	-680(1)	43(1)
C(74)	9037(3)	8288(3)	-155(2)	60(1)
C(75)	10333(3)	8703(3)	-236(2)	68(1)
N(1)	8749(2)	9499(2)	5911(1)	24(1)
N(2)	8277(2)	8261(1)	5045(1)	21(1)
N(3)	8395(2)	6494(2)	5401(1)	24(1)
N(4)	6659(2)	7858(2)	5878(1)	25(1)
N(5)	8626(2)	7599(2)	6613(1)	24(1)
N(6)	10517(12)	7955(13)	5786(6)	30(3)
O(1)	11236(2)	8455(2)	6160(1)	38(1)
O(2)	10949(2)	7495(2)	5411(1)	35(1)
Cl(1)	10810(20)	7890(20)	5840(10)	31(3)
F(1)	1875(2)	4077(2)	6967(1)	83(1)
F(2)	135(2)	3794(2)	6344(1)	83(1)
F(3)	-1020(2)	4659(2)	6894(1)	98(1)
F(4)	733(2)	4912(2)	7532(1)	85(1)
F(5)	92(2)	3332(2)	7193(1)	84(1)
F(6)	739(2)	5360(1)	6684(1)	53(1)
P(1)	401(1)	4356(1)	6948(1)	41(1)
Ru(1)	8582(1)	7932(1)	5806(1)	20(1)

Bond lengths

C(1)-N(1)	1.348(3)	C(7)-C(8)	1.401(3)
C(1)-C(2)	1.378(4)	C(7)-H(7)	0.9500
C(1)-H(1)	0.9500	C(8)-C(9)	1.401(3)
C(2)-C(3)	1.368(4)	C(8)-C(26)	1.482(3)
C(2)-H(2)	0.9500	C(9)-C(10)	1.382(3)
C(3)-C(4)	1.379(4)	C(9)-H(9)	0.9500
C(3)-H(3)	0.9500	C(10)-N(2)	1.349(3)
C(4)-C(5)	1.385(3)	C(10)-C(11)	1.474(3)
C(4)-H(4)	0.9500	C(11)-N(3)	1.370(3)
C(5)-N(1)	1.363(3)	C(11)-C(12)	1.379(3)
C(5)-C(6)	1.475(3)	C(12)-C(13)	1.383(4)
C(6)-N(2)	1.357(3)	C(12)-H(12)	0.9500
C(6)-C(7)	1.381(3)	C(13)-C(14)	1.373(4)

C(13)-H(13)	0.9500	C(36)-C(39')	1.549(9)
C(14)-C(15)	1.377(4)	C(36)-C(39)	1.553(4)
C(14)-H(14)	0.9500	C(39)-C(40)	1.515(5)
C(15)-N(3)	1.346(3)	C(39)-H(39A)	0.9900
C(15)-H(15)	0.9500	C(39)-H(39B)	0.9900
C(16)-N(4)	1.348(3)	C(40)-C(41)	1.539(5)
C(16)-C(17)	1.380(4)	C(40)-H(40A)	0.9900
C(16)-H(16)	0.9500	C(40)-H(40B)	0.9900
C(17)-C(18)	1.368(4)	C(41)-C(42)	1.525(6)
C(17)-H(17)	0.9500	C(41)-H(41A)	0.9900
C(18)-C(19)	1.372(4)	C(41)-H(41B)	0.9900
C(18)-H(18)	0.9500	C(42)-C(43)	1.510(9)
C(19)-C(20)	1.384(4)	C(42)-H(42A)	0.9900
C(19)-H(19)	0.9500	C(42)-H(42B)	0.9900
C(20)-N(4)	1.358(3)	C(43)-C(44)	1.517(8)
C(20)-C(21)	1.470(3)	C(43)-H(43A)	0.9900
C(21)-N(5)	1.360(3)	C(43)-H(43B)	0.9900
C(21)-C(22)	1.385(4)	C(44)-H(44A)	0.9800
C(22)-C(23)	1.381(4)	C(44)-H(44B)	0.9800
C(22)-H(22)	0.9500	C(44)-H(44C)	0.9800
C(23)-C(24)	1.374(4)	C(39')-C(40')	1.519(9)
C(23)-H(23)	0.9500	C(39')-H(39C)	0.9900
C(24)-C(25)	1.371(3)	C(39')-H(39D)	0.9900
C(24)-H(24)	0.9500	C(40')-C(41')	1.542(9)
C(25)-N(5)	1.348(3)	C(40')-H(40C)	0.9900
C(25)-H(25)	0.9500	C(40')-H(40D)	0.9900
C(26)-C(38)	1.395(3)	C(41')-C(42')	1.542(11)
C(26)-C(27)	1.401(3)	C(41')-H(41C)	0.9900
C(27)-C(28)	1.384(3)	C(41')-H(41D)	0.9900
C(27)-H(27)	0.9500	C(42')-C(43')	1.512(12)
C(28)-C(29)	1.395(3)	C(42')-H(42C)	0.9900
C(28)-H(28)	0.9500	C(42')-H(42D)	0.9900
C(29)-C(37)	1.404(3)	C(43')-C(44')	1.495(11)
C(29)-C(30)	1.466(3)	C(43')-H(43C)	0.9900
C(30)-C(31)	1.387(3)	C(43')-H(43D)	0.9900
C(30)-C(35)	1.396(3)	C(44')-H(44D)	0.9800
C(31)-C(32)	1.385(3)	C(44')-H(44E)	0.9800
C(31)-H(31)	0.9500	C(44')-H(44F)	0.9800
C(32)-C(33)	1.401(3)	C(45)-C(46)	1.525(10)
C(32)-H(32)	0.9500	C(45)-H(45A)	0.9900
C(33)-C(34)	1.400(3)	C(45)-H(45B)	0.9900
C(33)-C(51)	1.483(3)	C(46)-C(47)	1.527(10)
C(34)-C(35)	1.384(3)	C(46)-H(46A)	0.9900
C(34)-H(34)	0.9500	C(46)-H(46B)	0.9900
C(35)-C(36)	1.524(3)	C(47)-C(48)	1.535(10)
C(37)-C(38)	1.377(3)	C(47)-H(47A)	0.9900
C(37)-C(36)	1.520(3)	C(47)-H(47B)	0.9900
C(38)-H(38)	0.9500	C(48)-C(49)	1.517(12)
C(36)-C(45)	1.531(9)	C(48)-H(48A)	0.9900
C(36)-C(45')	1.542(12)	C(48)-H(48B)	0.9900

C(49)-C(50)	1.548(12)	C(64)-H(64A)	0.9900
C(49)-H(49A)	0.9900	C(64)-H(64B)	0.9900
C(49)-H(49B)	0.9900	C(65)-C(66)	1.528(9)
C(50)-H(50A)	0.9800	C(65)-H(65A)	0.9900
C(50)-H(50B)	0.9800	C(65)-H(65B)	0.9900
C(50)-H(50C)	0.9800	C(66)-C(67)	1.475(9)
C(45')-C(46')	1.529(12)	C(66)-H(66A)	0.9900
C(45')-H(45C)	0.9900	C(66)-H(66B)	0.9900
C(45')-H(45D)	0.9900	C(67)-C(68)	1.526(8)
C(46')-C(47')	1.522(13)	C(67)-H(67A)	0.9900
C(46')-H(46C)	0.9900	C(67)-H(67B)	0.9900
C(46')-H(46D)	0.9900	C(68)-C(69)	1.480(9)
C(47')-C(48')	1.526(14)	C(68)-H(68A)	0.9900
C(47')-H(47C)	0.9900	C(68)-H(68B)	0.9900
C(47')-H(47D)	0.9900	C(69)-H(69A)	0.9800
C(48')-C(49')	1.519(14)	C(69)-H(69B)	0.9800
C(48')-H(48C)	0.9900	C(69)-H(69C)	0.9800
C(48')-H(48D)	0.9900	C(64')-C(65')	1.518(12)
C(49')-C(50')	1.526(15)	C(64')-H(64C)	0.9900
C(49')-H(49C)	0.9900	C(64')-H(64D)	0.9900
C(49')-H(49D)	0.9900	C(65')-C(66')	1.548(11)
C(50')-H(50D)	0.9800	C(65')-H(65C)	0.9900
C(50')-H(50E)	0.9800	C(65')-H(65D)	0.9900
C(50')-H(50F)	0.9800	C(66')-C(67')	1.477(11)
C(51)-C(52)	1.402(3)	C(66')-H(66C)	0.9900
C(51)-C(63)	1.406(3)	C(66')-H(66D)	0.9900
C(52)-C(53)	1.379(3)	C(67')-C(68')	1.510(10)
C(52)-H(52)	0.9500	C(67')-H(67C)	0.9900
C(53)-C(54)	1.386(3)	C(67')-H(67D)	0.9900
C(53)-H(53)	0.9500	C(68')-C(69')	1.485(11)
C(54)-C(62)	1.401(3)	C(68')-H(68C)	0.9900
C(54)-C(55)	1.471(3)	C(68')-H(68D)	0.9900
C(55)-C(56)	1.390(3)	C(69')-H(69D)	0.9800
C(55)-C(60)	1.401(4)	C(69')-H(69E)	0.9800
C(56)-C(57)	1.388(4)	C(69')-H(69F)	0.9800
C(56)-H(56)	0.9500	C(70)-C(71)	1.534(4)
C(57)-C(58)	1.383(4)	C(70)-H(70A)	0.9900
C(57)-H(57)	0.9500	C(70)-H(70B)	0.9900
C(58)-C(59)	1.385(4)	C(71)-C(72)	1.512(4)
C(58)-H(58)	0.9500	C(71)-H(71A)	0.9900
C(59)-C(60)	1.391(3)	C(71)-H(71B)	0.9900
C(59)-H(59)	0.9500	C(72)-C(73)	1.516(4)
C(60)-C(61)	1.519(3)	C(72)-H(72A)	0.9900
C(62)-C(63)	1.385(3)	C(72)-H(72B)	0.9900
C(62)-C(61)	1.525(3)	C(73)-C(74)	1.508(4)
C(63)-H(63)	0.9500	C(73)-H(73A)	0.9900
C(61)-C(64)	1.542(10)	C(73)-H(73B)	0.9900
C(61)-C(64')	1.547(11)	C(74)-C(75)	1.520(4)
C(61)-C(70)	1.552(4)	C(74)-H(74A)	0.9900
C(64)-C(65)	1.518(9)	C(74)-H(74B)	0.9900

C(75)-H(75A)	0.9800	N(6)-Ru(1)	2.060(13)
C(75)-H(75B)	0.9800	Cl(1)-Ru(1)	2.35(2)
C(75)-H(75C)	0.9800	F(1)-P(1)	1.609(2)
N(1)-Ru(1)	2.079(2)	F(2)-P(1)	1.598(2)
N(2)-Ru(1)	1.9610(18)	F(3)-P(1)	1.558(2)
N(3)-Ru(1)	2.071(2)	F(4)-P(1)	1.558(2)
N(4)-Ru(1)	2.076(2)	F(5)-P(1)	1.588(2)
N(5)-Ru(1)	2.0876(19)	F(6)-P(1)	1.5960(18)
N(6)-O(2)	1.219(16)		
N(6)-O(1)	1.246(15)		

Angles

N(1)-C(1)-C(2)	122.8(3)	C(13)-C(12)-H(12)	120.2
N(1)-C(1)-H(1)	118.6	C(14)-C(13)-C(12)	118.9(3)
C(2)-C(1)-H(1)	118.6	C(14)-C(13)-H(13)	120.6
C(3)-C(2)-C(1)	119.2(3)	C(12)-C(13)-H(13)	120.6
C(3)-C(2)-H(2)	120.4	C(13)-C(14)-C(15)	119.6(2)
C(1)-C(2)-H(2)	120.4	C(13)-C(14)-H(14)	120.2
C(2)-C(3)-C(4)	119.2(3)	C(15)-C(14)-H(14)	120.2
C(2)-C(3)-H(3)	120.4	N(3)-C(15)-C(14)	122.5(2)
C(4)-C(3)-H(3)	120.4	N(3)-C(15)-H(15)	118.8
C(3)-C(4)-C(5)	119.6(2)	C(14)-C(15)-H(15)	118.8
C(3)-C(4)-H(4)	120.2	N(4)-C(16)-C(17)	122.8(3)
C(5)-C(4)-H(4)	120.2	N(4)-C(16)-H(16)	118.6
N(1)-C(5)-C(4)	121.3(2)	C(17)-C(16)-H(16)	118.6
N(1)-C(5)-C(6)	115.1(2)	C(18)-C(17)-C(16)	119.4(3)
C(4)-C(5)-C(6)	123.6(2)	C(18)-C(17)-H(17)	120.3
N(2)-C(6)-C(7)	120.3(2)	C(16)-C(17)-H(17)	120.3
N(2)-C(6)-C(5)	112.35(19)	C(17)-C(18)-C(19)	118.4(3)
C(7)-C(6)-C(5)	127.4(2)	C(17)-C(18)-H(18)	120.8
C(6)-C(7)-C(8)	119.8(2)	C(19)-C(18)-H(18)	120.8
C(6)-C(7)-H(7)	120.1	C(18)-C(19)-C(20)	120.5(3)
C(8)-C(7)-H(7)	120.1	C(18)-C(19)-H(19)	119.8
C(9)-C(8)-C(7)	118.1(2)	C(20)-C(19)-H(19)	119.8
C(9)-C(8)-C(26)	119.7(2)	N(4)-C(20)-C(19)	121.3(2)
C(7)-C(8)-C(26)	122.1(2)	N(4)-C(20)-C(21)	115.0(2)
C(10)-C(9)-C(8)	120.2(2)	C(19)-C(20)-C(21)	123.7(2)
C(10)-C(9)-H(9)	119.9	N(5)-C(21)-C(22)	121.3(2)
C(8)-C(9)-H(9)	119.9	N(5)-C(21)-C(20)	114.9(2)
N(2)-C(10)-C(9)	120.1(2)	C(22)-C(21)-C(20)	123.8(2)
N(2)-C(10)-C(11)	113.0(2)	C(23)-C(22)-C(21)	119.8(3)
C(9)-C(10)-C(11)	126.7(2)	C(23)-C(22)-H(22)	120.1
N(3)-C(11)-C(12)	121.5(2)	C(21)-C(22)-H(22)	120.1
N(3)-C(11)-C(10)	114.9(2)	C(24)-C(23)-C(22)	118.8(3)
C(12)-C(11)-C(10)	123.6(2)	C(24)-C(23)-H(23)	120.6
C(11)-C(12)-C(13)	119.6(3)	C(22)-C(23)-H(23)	120.6
C(11)-C(12)-H(12)	120.2	C(25)-C(24)-C(23)	119.2(3)

C(25)-C(24)-H(24)	120.4	C(35)-C(36)-C(39)	111.2(7)
C(23)-C(24)-H(24)	120.4	C(45)-C(36)-C(39)	111.7(9)
N(5)-C(25)-C(24)	123.1(2)	C(40)-C(39)-C(36)	115.6(4)
N(5)-C(25)-H(25)	118.5	C(40)-C(39)-H(39A)	108.4
C(24)-C(25)-H(25)	118.5	C(36)-C(39)-H(39A)	108.4
C(38)-C(26)-C(27)	119.0(2)	C(40)-C(39)-H(39B)	108.4
C(38)-C(26)-C(8)	120.4(2)	C(36)-C(39)-H(39B)	108.4
C(27)-C(26)-C(8)	120.4(2)	H(39A)-C(39)-H(39B)	107.4
C(28)-C(27)-C(26)	121.5(2)	C(39)-C(40)-C(41)	114.6(5)
C(28)-C(27)-H(27)	119.3	C(39)-C(40)-H(40A)	108.6
C(26)-C(27)-H(27)	119.3	C(41)-C(40)-H(40A)	108.6
C(27)-C(28)-C(29)	119.0(2)	C(39)-C(40)-H(40B)	108.6
C(27)-C(28)-H(28)	120.5	C(41)-C(40)-H(40B)	108.6
C(29)-C(28)-H(28)	120.5	H(40A)-C(40)-H(40B)	107.6
C(28)-C(29)-C(37)	119.7(2)	C(42)-C(41)-C(40)	113.6(4)
C(28)-C(29)-C(30)	132.0(2)	C(42)-C(41)-H(41A)	108.8
C(37)-C(29)-C(30)	108.3(2)	C(40)-C(41)-H(41A)	108.8
C(31)-C(30)-C(35)	119.9(2)	C(42)-C(41)-H(41B)	108.8
C(31)-C(30)-C(29)	131.7(2)	C(40)-C(41)-H(41B)	108.8
C(35)-C(30)-C(29)	108.4(2)	H(41A)-C(41)-H(41B)	107.7
C(32)-C(31)-C(30)	119.0(2)	C(43)-C(42)-C(41)	113.8(6)
C(32)-C(31)-H(31)	120.5	C(43)-C(42)-H(42A)	108.8
C(30)-C(31)-H(31)	120.5	C(41)-C(42)-H(42A)	108.8
C(31)-C(32)-C(33)	122.2(2)	C(43)-C(42)-H(42B)	108.8
C(31)-C(32)-H(32)	118.9	C(41)-C(42)-H(42B)	108.8
C(33)-C(32)-H(32)	118.9	H(42A)-C(42)-H(42B)	107.7
C(34)-C(33)-C(32)	117.7(2)	C(42)-C(43)-C(44)	113.1(6)
C(34)-C(33)-C(51)	120.9(2)	C(42)-C(43)-H(43A)	109.0
C(32)-C(33)-C(51)	121.3(2)	C(44)-C(43)-H(43A)	109.0
C(35)-C(34)-C(33)	120.5(2)	C(42)-C(43)-H(43B)	109.0
C(35)-C(34)-H(34)	119.8	C(44)-C(43)-H(43B)	109.0
C(33)-C(34)-H(34)	119.8	H(43A)-C(43)-H(43B)	107.8
C(34)-C(35)-C(30)	120.6(2)	C(43)-C(44)-H(44A)	109.5
C(34)-C(35)-C(36)	128.1(2)	C(43)-C(44)-H(44B)	109.5
C(30)-C(35)-C(36)	111.3(2)	H(44A)-C(44)-H(44B)	109.5
C(38)-C(37)-C(29)	120.8(2)	C(43)-C(44)-H(44C)	109.5
C(38)-C(37)-C(36)	128.0(2)	H(44A)-C(44)-H(44C)	109.5
C(29)-C(37)-C(36)	111.1(2)	H(44B)-C(44)-H(44C)	109.5
C(37)-C(38)-C(26)	119.9(2)	C(40')-C(39')-C(36)	115.1(13)
C(37)-C(38)-H(38)	120.0	C(40')-C(39')-H(39C)	108.5
C(26)-C(38)-H(38)	120.0	C(36)-C(39')-H(39C)	108.5
C(37)-C(36)-C(35)	100.81(19)	C(40')-C(39')-H(39D)	108.5
C(37)-C(36)-C(45)	110.8(11)	C(36)-C(39')-H(39D)	108.5
C(35)-C(36)-C(45)	113.3(10)	H(39C)-C(39')-H(39D)	107.5
C(37)-C(36)-C(45')	116.6(16)	C(39')-C(40')-C(41')	112.6(13)
C(35)-C(36)-C(45')	112.1(15)	C(39')-C(40')-H(40C)	109.1
C(37)-C(36)-C(39')	112(2)	C(41')-C(40')-H(40C)	109.1
C(35)-C(36)-C(39')	111(3)	C(39')-C(40')-H(40D)	109.1
C(45')-C(36)-C(39')	104.7(16)	C(41')-C(40')-H(40D)	109.1
C(37)-C(36)-C(39)	108.3(6)	H(40C)-C(40')-H(40D)	107.8

C(42')-C(41')-C(40')	112.0(13)	C(50)-C(49)-H(49A)	109.4
C(42')-C(41')-H(41C)	109.2	C(48)-C(49)-H(49B)	109.4
C(40')-C(41')-H(41C)	109.2	C(50)-C(49)-H(49B)	109.4
C(42')-C(41')-H(41D)	109.2	H(49A)-C(49)-H(49B)	108.0
C(40')-C(41')-H(41D)	109.2	C(49)-C(50)-H(50A)	109.5
H(41C)-C(41')-H(41D)	107.9	C(49)-C(50)-H(50B)	109.5
C(43')-C(42')-C(41')	108.3(12)	H(50A)-C(50)-H(50B)	109.5
C(43')-C(42')-H(42C)	110.0	C(49)-C(50)-H(50C)	109.5
C(41')-C(42')-H(42C)	110.0	H(50A)-C(50)-H(50C)	109.5
C(43')-C(42')-H(42D)	110.0	H(50B)-C(50)-H(50C)	109.5
C(41')-C(42')-H(42D)	110.0	C(46')-C(45')-C(36)	114.1(19)
H(42C)-C(42')-H(42D)	108.4	C(46')-C(45')-H(45C)	108.7
C(44')-C(43')-C(42')	114.3(13)	C(36)-C(45')-H(45C)	108.7
C(44')-C(43')-H(43C)	108.7	C(46')-C(45')-H(45D)	108.7
C(42')-C(43')-H(43C)	108.7	C(36)-C(45')-H(45D)	108.7
C(44')-C(43')-H(43D)	108.7	H(45C)-C(45')-H(45D)	107.6
C(42')-C(43')-H(43D)	108.7	C(47')-C(46')-C(45')	113.4(15)
H(43C)-C(43')-H(43D)	107.6	C(47')-C(46')-H(46C)	108.9
C(43')-C(44')-H(44D)	109.5	C(45')-C(46')-H(46C)	108.9
C(43')-C(44')-H(44E)	109.5	C(47')-C(46')-H(46D)	108.9
H(44D)-C(44')-H(44E)	109.5	C(45')-C(46')-H(46D)	108.9
C(43')-C(44')-H(44F)	109.5	H(46C)-C(46')-H(46D)	107.7
H(44D)-C(44')-H(44F)	109.5	C(46')-C(47')-C(48')	114.4(17)
H(44E)-C(44')-H(44F)	109.5	C(46')-C(47')-H(47C)	108.7
C(46)-C(45)-C(36)	115.9(13)	C(48')-C(47')-H(47C)	108.7
C(46)-C(45)-H(45A)	108.3	C(46')-C(47')-H(47D)	108.7
C(36)-C(45)-H(45A)	108.3	C(48')-C(47')-H(47D)	108.7
C(46)-C(45)-H(45B)	108.3	H(47C)-C(47')-H(47D)	107.6
C(36)-C(45)-H(45B)	108.3	C(49')-C(48')-C(47')	117.0(15)
H(45A)-C(45)-H(45B)	107.4	C(49')-C(48')-H(48C)	108.0
C(45)-C(46)-C(47)	112.3(11)	C(47')-C(48')-H(48C)	108.0
C(45)-C(46)-H(46A)	109.1	C(49')-C(48')-H(48D)	108.0
C(47)-C(46)-H(46A)	109.1	C(47')-C(48')-H(48D)	108.0
C(45)-C(46)-H(46B)	109.1	H(48C)-C(48')-H(48D)	107.3
C(47)-C(46)-H(46B)	109.1	C(48')-C(49')-C(50')	110.0(14)
H(46A)-C(46)-H(46B)	107.9	C(48')-C(49')-H(49C)	109.7
C(46)-C(47)-C(48)	112.5(11)	C(50')-C(49')-H(49C)	109.7
C(46)-C(47)-H(47A)	109.1	C(48')-C(49')-H(49D)	109.7
C(48)-C(47)-H(47A)	109.1	C(50')-C(49')-H(49D)	109.7
C(46)-C(47)-H(47B)	109.1	H(49C)-C(49')-H(49D)	108.2
C(48)-C(47)-H(47B)	109.1	C(49')-C(50')-H(50D)	109.5
H(47A)-C(47)-H(47B)	107.8	C(49')-C(50')-H(50E)	109.5
C(49)-C(48)-C(47)	114.5(11)	H(50D)-C(50')-H(50E)	109.5
C(49)-C(48)-H(48A)	108.6	C(49')-C(50')-H(50F)	109.5
C(47)-C(48)-H(48A)	108.6	H(50D)-C(50')-H(50F)	109.5
C(49)-C(48)-H(48B)	108.6	H(50E)-C(50')-H(50F)	109.5
C(47)-C(48)-H(48B)	108.6	C(52)-C(51)-C(63)	118.2(2)
H(48A)-C(48)-H(48B)	107.6	C(52)-C(51)-C(33)	120.6(2)
C(48)-C(49)-C(50)	110.9(10)	C(63)-C(51)-C(33)	121.1(2)
C(48)-C(49)-H(49A)	109.4	C(53)-C(52)-C(51)	121.9(2)

C(53)-C(52)-H(52)	119.1	C(64)-C(65)-H(65B)	109.6
C(51)-C(52)-H(52)	119.1	C(66)-C(65)-H(65B)	109.6
C(52)-C(53)-C(54)	119.2(2)	H(65A)-C(65)-H(65B)	108.1
C(52)-C(53)-H(53)	120.4	C(67)-C(66)-C(65)	115.3(9)
C(54)-C(53)-H(53)	120.4	C(67)-C(66)-H(66A)	108.4
C(53)-C(54)-C(62)	120.3(2)	C(65)-C(66)-H(66A)	108.4
C(53)-C(54)-C(55)	131.2(2)	C(67)-C(66)-H(66B)	108.4
C(62)-C(54)-C(55)	108.5(2)	C(65)-C(66)-H(66B)	108.4
C(56)-C(55)-C(60)	121.0(2)	H(66A)-C(66)-H(66B)	107.5
C(56)-C(55)-C(54)	130.9(2)	C(66)-C(67)-C(68)	112.3(7)
C(60)-C(55)-C(54)	108.1(2)	C(66)-C(67)-H(67A)	109.1
C(57)-C(56)-C(55)	118.4(3)	C(68)-C(67)-H(67A)	109.1
C(57)-C(56)-H(56)	120.8	C(66)-C(67)-H(67B)	109.1
C(55)-C(56)-H(56)	120.8	C(68)-C(67)-H(67B)	109.1
C(58)-C(57)-C(56)	120.7(3)	H(67A)-C(67)-H(67B)	107.9
C(58)-C(57)-H(57)	119.6	C(69)-C(68)-C(67)	112.8(6)
C(56)-C(57)-H(57)	119.6	C(69)-C(68)-H(68A)	109.0
C(57)-C(58)-C(59)	121.1(3)	C(67)-C(68)-H(68A)	109.0
C(57)-C(58)-H(58)	119.4	C(69)-C(68)-H(68B)	109.0
C(59)-C(58)-H(58)	119.4	C(67)-C(68)-H(68B)	109.0
C(58)-C(59)-C(60)	118.9(3)	H(68A)-C(68)-H(68B)	107.8
C(58)-C(59)-H(59)	120.6	C(68)-C(69)-H(69A)	109.5
C(60)-C(59)-H(59)	120.6	C(68)-C(69)-H(69B)	109.5
C(59)-C(60)-C(55)	119.8(2)	H(69A)-C(69)-H(69B)	109.5
C(59)-C(60)-C(61)	128.8(3)	C(68)-C(69)-H(69C)	109.5
C(55)-C(60)-C(61)	111.4(2)	H(69A)-C(69)-H(69C)	109.5
C(63)-C(62)-C(54)	120.1(2)	H(69B)-C(69)-H(69C)	109.5
C(63)-C(62)-C(61)	128.9(2)	C(65')-C(64')-C(61)	118.3(13)
C(54)-C(62)-C(61)	110.9(2)	C(65')-C(64')-H(64C)	107.7
C(62)-C(63)-C(51)	120.2(2)	C(61)-C(64')-H(64C)	107.7
C(62)-C(63)-H(63)	119.9	C(65')-C(64')-H(64D)	107.7
C(51)-C(63)-H(63)	119.9	C(61)-C(64')-H(64D)	107.7
C(60)-C(61)-C(62)	101.0(2)	H(64C)-C(64')-H(64D)	107.1
C(60)-C(61)-C(64)	113.5(13)	C(64')-C(65')-C(66')	109.4(11)
C(62)-C(61)-C(64)	116.2(12)	C(64')-C(65')-H(65C)	109.8
C(60)-C(61)-C(64')	112.1(16)	C(66')-C(65')-H(65C)	109.8
C(62)-C(61)-C(64')	111.0(15)	C(64')-C(65')-H(65D)	109.8
C(60)-C(61)-C(70)	109.9(2)	C(66')-C(65')-H(65D)	109.8
C(62)-C(61)-C(70)	111.5(2)	H(65C)-C(65')-H(65D)	108.2
C(64)-C(61)-C(70)	104.8(7)	C(67')-C(66')-C(65')	113.4(11)
C(64')-C(61)-C(70)	110.9(9)	C(67')-C(66')-H(66C)	108.9
C(65)-C(64)-C(61)	115.1(11)	C(65')-C(66')-H(66C)	108.9
C(65)-C(64)-H(64A)	108.5	C(67')-C(66')-H(66D)	108.9
C(61)-C(64)-H(64A)	108.5	C(65')-C(66')-H(66D)	108.9
C(65)-C(64)-H(64B)	108.5	H(66C)-C(66')-H(66D)	107.7
C(61)-C(64)-H(64B)	108.5	C(66')-C(67')-C(68')	117.4(9)
H(64A)-C(64)-H(64B)	107.5	C(66')-C(67')-H(67C)	108.0
C(64)-C(65)-C(66)	110.5(8)	C(68')-C(67')-H(67C)	108.0
C(64)-C(65)-H(65A)	109.6	C(66')-C(67')-H(67D)	108.0
C(66)-C(65)-H(65A)	109.6	C(68')-C(67')-H(67D)	108.0

H(67C)-C(67')-H(67D)	107.2	C(1)-N(1)-Ru(1)	128.17(17)
C(69')-C(68')-C(67')	116.7(8)	C(5)-N(1)-Ru(1)	113.64(15)
C(69')-C(68')-H(68C)	108.1	C(10)-N(2)-C(6)	121.40(19)
C(67')-C(68')-H(68C)	108.1	C(10)-N(2)-Ru(1)	118.85(15)
C(69')-C(68')-H(68D)	108.1	C(6)-N(2)-Ru(1)	119.24(15)
C(67')-C(68')-H(68D)	108.1	C(15)-N(3)-C(11)	117.9(2)
H(68C)-C(68')-H(68D)	107.3	C(15)-N(3)-Ru(1)	128.75(17)
C(68')-C(69')-H(69D)	109.5	C(11)-N(3)-Ru(1)	113.27(15)
C(68')-C(69')-H(69E)	109.5	C(16)-N(4)-C(20)	117.6(2)
H(69D)-C(69')-H(69E)	109.5	C(16)-N(4)-Ru(1)	126.02(18)
C(68')-C(69')-H(69F)	109.5	C(20)-N(4)-Ru(1)	116.25(16)
H(69D)-C(69')-H(69F)	109.5	C(25)-N(5)-C(21)	117.8(2)
H(69E)-C(69')-H(69F)	109.5	C(25)-N(5)-Ru(1)	126.36(16)
C(71)-C(70)-C(61)	117.6(2)	C(21)-N(5)-Ru(1)	115.86(16)
C(71)-C(70)-H(70A)	107.9	O(2)-N(6)-O(1)	120.6(11)
C(61)-C(70)-H(70A)	107.9	O(2)-N(6)-Ru(1)	120.4(10)
C(71)-C(70)-H(70B)	107.9	O(1)-N(6)-Ru(1)	119.0(11)
C(61)-C(70)-H(70B)	107.9	F(4)-P(1)-F(3)	93.04(15)
H(70A)-C(70)-H(70B)	107.2	F(4)-P(1)-F(5)	91.20(12)
C(72)-C(71)-C(70)	115.1(3)	F(3)-P(1)-F(5)	91.89(14)
C(72)-C(71)-H(71A)	108.5	F(4)-P(1)-F(6)	90.50(11)
C(70)-C(71)-H(71A)	108.5	F(3)-P(1)-F(6)	89.52(12)
C(72)-C(71)-H(71B)	108.5	F(5)-P(1)-F(6)	177.73(13)
C(70)-C(71)-H(71B)	108.5	F(4)-P(1)-F(2)	177.04(15)
H(71A)-C(71)-H(71B)	107.5	F(3)-P(1)-F(2)	89.60(15)
C(71)-C(72)-C(73)	114.1(3)	F(5)-P(1)-F(2)	90.04(12)
C(71)-C(72)-H(72A)	108.7	F(6)-P(1)-F(2)	88.19(11)
C(73)-C(72)-H(72A)	108.7	F(4)-P(1)-F(1)	89.06(14)
C(71)-C(72)-H(72B)	108.7	F(3)-P(1)-F(1)	176.30(14)
C(73)-C(72)-H(72B)	108.7	F(5)-P(1)-F(1)	91.11(13)
H(72A)-C(72)-H(72B)	107.6	F(6)-P(1)-F(1)	87.41(11)
C(74)-C(73)-C(72)	113.8(3)	F(2)-P(1)-F(1)	88.23(14)
C(74)-C(73)-H(73A)	108.8	N(2)-Ru(1)-N(6)	90.2(4)
C(72)-C(73)-H(73A)	108.8	N(2)-Ru(1)-N(3)	79.58(8)
C(74)-C(73)-H(73B)	108.8	N(6)-Ru(1)-N(3)	90.7(5)
C(72)-C(73)-H(73B)	108.8	N(2)-Ru(1)-N(4)	93.92(8)
H(73A)-C(73)-H(73B)	107.7	N(6)-Ru(1)-N(4)	175.8(4)
C(73)-C(74)-C(75)	113.5(3)	N(3)-Ru(1)-N(4)	89.07(8)
C(73)-C(74)-H(74A)	108.9	N(2)-Ru(1)-N(1)	79.06(8)
C(75)-C(74)-H(74A)	108.9	N(6)-Ru(1)-N(1)	86.4(5)
C(73)-C(74)-H(74B)	108.9	N(3)-Ru(1)-N(1)	158.44(7)
C(75)-C(74)-H(74B)	108.9	N(4)-Ru(1)-N(1)	95.31(8)
H(74A)-C(74)-H(74B)	107.7	N(2)-Ru(1)-N(5)	171.77(8)
C(74)-C(75)-H(75A)	109.5	N(6)-Ru(1)-N(5)	98.0(4)
C(74)-C(75)-H(75B)	109.5	N(3)-Ru(1)-N(5)	100.86(8)
H(75A)-C(75)-H(75B)	109.5	N(4)-Ru(1)-N(5)	77.89(8)
C(74)-C(75)-H(75C)	109.5	N(1)-Ru(1)-N(5)	100.71(8)
H(75A)-C(75)-H(75C)	109.5	N(2)-Ru(1)-Cl(1)	94.1(6)
H(75B)-C(75)-H(75C)	109.5	N(3)-Ru(1)-Cl(1)	90.1(7)
C(1)-N(1)-C(5)	117.9(2)	N(4)-Ru(1)-Cl(1)	171.6(6)

N(1)-Ru(1)-Cl(1)	88.5(8)
N(5)-Ru(1)-Cl(1)	94.1(6)

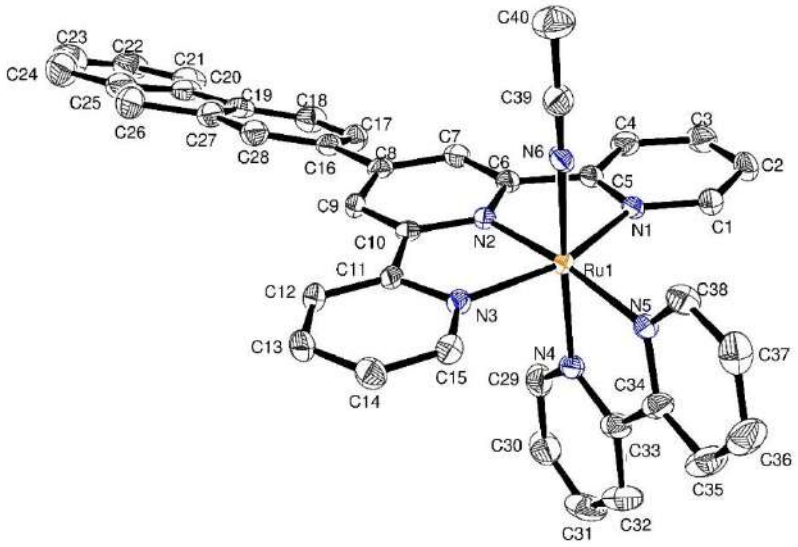

Empirical formula	$C_{40}H_{30}N_6Ru$, 2(F_6P),2(C_3H_6O)
Formula weight	1101.87
Temperature	133(2) K
Wavelength	0.71073 A
Crystal system, space group	Monoclinic, P 21/c
Unit cell dimensions	a = 8.9330(13) A alpha = 90 deg. b = 19.725(3) A beta = 90.883(4) deg. c = 26.047(4) A gamma = 90 deg.
Volume	4589.0(12) A^3
Z, Calculated density	4, 1.595 Mg/m^3
Absorption coefficient	0.507 mm^-1
F(000)	2232
Crystal size	0.200 x 0.180 x 0.080 mm
Theta range for data collection	1.564 to 26.372 deg.
Limiting indices -32<=l<=32	-11<=h<=11, -24<=k<=24,
Reflections collected / unique	89810 / 9387 [R(int) = 0.0655]
Completeness to theta = 25.242	100.0 %

Refinement method	Full-matrix least-squares on F^2
Data / restraints / parameters	9387 / 279 / 692
Goodness-of-fit on F^2	1.154
Final R indices [I>2sigma(I)]	R1 = 0.0463, wR2 = 0.0994
R indices (all data)	R1 = 0.0531, wR2 = 0.1023
Largest diff. peak and hole	0.682 and -0.945 e.A^-3

Atomic coordinates

U(eq) is defined as one third of the trace of the orthogonalized Uij tensor.

	x	y	z	U(eq)
C(1)	8359(4)	9371(2)	6099(1)	25(1)
C(2)	9579(4)	9122(2)	5828(1)	29(1)
C(3)	9536(4)	8467(2)	5644(1)	31(1)
C(4)	8259(4)	8082(2)	5719(1)	26(1)
C(5)	7059(3)	8358(2)	5979(1)	21(1)
C(6)	5641(3)	7989(2)	6062(1)	20(1)
C(7)	5301(4)	7338(2)	5901(1)	22(1)
C(8)	3920(4)	7047(2)	6031(1)	21(1)
C(9)	2912(3)	7439(2)	6311(1)	20(1)
C(10)	3289(3)	8095(2)	6458(1)	18(1)
C(11)	2389(3)	8567(2)	6768(1)	19(1)
C(12)	960(3)	8421(2)	6934(1)	22(1)
C(13)	213(4)	8894(2)	7231(1)	27(1)
C(14)	904(4)	9500(2)	7354(1)	27(1)
C(15)	2330(4)	9622(2)	7175(1)	23(1)
C(16)	3574(4)	6334(2)	5884(1)	24(1)
C(17)	4753(4)	5879(2)	5798(1)	27(1)
C(18)	4479(4)	5202(2)	5668(1)	31(1)
C(19)	3003(4)	4983(2)	5634(1)	28(1)
C(20)	2409(4)	4304(2)	5518(1)	29(1)
C(21)	3129(5)	3692(2)	5406(1)	38(1)
C(22)	2260(5)	3117(2)	5323(1)	42(1)
C(23)	722(6)	3158(2)	5337(2)	47(1)
C(24)	-28(5)	3764(2)	5449(2)	44(1)
C(25)	839(5)	4336(2)	5548(1)	37(1)
C(26)	348(4)	5052(2)	5691(2)	35(1)
C(27)	1819(4)	5428(2)	5726(1)	30(1)
C(28)	2092(4)	6102(2)	5849(1)	27(1)
C(29)	6388(4)	8279(2)	7387(1)	32(1)

C(30)	6996(4)	8074(2)	7853(2)	37(1)
C(31)	7344(4)	8566(2)	8213(1)	42(1)
C(32)	7115(4)	9242(2)	8091(1)	38(1)
C(33)	6515(4)	9418(2)	7610(1)	27(1)
C(34)	6266(4)	10126(2)	7434(1)	27(1)
C(35)	6526(4)	10690(2)	7740(2)	39(1)
C(36)	6253(5)	11319(2)	7542(2)	42(1)
C(37)	5723(4)	11388(2)	7044(2)	36(1)
C(38)	5472(4)	10804(2)	6753(1)	28(1)
C(39)	3709(4)	9933(2)	5591(1)	28(1)
C(40)	2985(5)	10245(2)	5145(1)	40(1)
C(41)	2717(5)	8300(2)	8220(2)	48(1)
C(42)	1206(6)	8011(3)	8343(2)	62(1)
C(43)	3284(6)	8848(3)	8568(2)	77(2)
C(44)	721(5)	1053(2)	6323(2)	41(1)
C(45)	-562(5)	1159(2)	6665(2)	45(1)
C(46)	1711(5)	1641(2)	6212(2)	58(1)
P(1)	8329(5)	6344(2)	6869(2)	30(1)
F(1)	7456(7)	5649(2)	6750(2)	66(1)
F(2)	9844(7)	5922(3)	6904(3)	67(2)
F(3)	9118(9)	7029(3)	6995(3)	101(2)
F(4)	6724(7)	6702(5)	6834(4)	65(2)
F(5)	8085(13)	6219(5)	7472(2)	54(2)
F(6)	8527(6)	6463(3)	6265(2)	57(2)
P(1')	8456(16)	6455(7)	6910(5)	45(2)
F(1')	7919(18)	5837(8)	6571(6)	69(3)
F(2')	10097(16)	6181(10)	6938(8)	68(3)
F(3')	9079(18)	7066(6)	7255(6)	63(3)
F(4')	6920(20)	6839(12)	6867(12)	64(4)
F(5')	7950(30)	6086(11)	7424(6)	40(3)
F(6')	9018(15)	6825(8)	6398(4)	60(3)
F(7)	3984(4)	7906(2)	4066(1)	80(1)
F(8)	3434(4)	7386(2)	4807(1)	84(1)
F(9)	3027(3)	8404(2)	5180(1)	59(1)
F(10)	3602(3)	8920(1)	4429(1)	62(1)
F(11)	5213(3)	8184(2)	4809(1)	71(1)
F(12)	1780(4)	8132(2)	4446(1)	88(1)
N(1)	7116(3)	9001(1)	6179(1)	19(1)
N(2)	4645(3)	8354(1)	6332(1)	17(1)
N(3)	3071(3)	9172(1)	6888(1)	18(1)
N(4)	6137(3)	8922(1)	7260(1)	22(1)
N(5)	5731(3)	10180(1)	6943(1)	20(1)
N(6)	4262(3)	9700(1)	5941(1)	21(1)
O(1)	3408(4)	8089(2)	7853(1)	69(1)
O(2)	978(5)	507(2)	6138(2)	84(1)
P(2)	3509(1)	8149(1)	4622(1)	41(1)
Ru(1)	5196(1)	9263(1)	6586(1)	

Bond lengths

C(1)-N(1)	1.349(4)	C(24)-H(24)	0.9500
C(1)-C(2)	1.396(5)	C(25)-C(26)	1.526(5)
C(1)-H(1)	0.9500	C(26)-C(27)	1.510(5)
C(2)-C(3)	1.378(5)	C(26)-H(26A)	0.9900
C(2)-H(2)	0.9500	C(26)-H(26B)	0.9900
C(3)-C(4)	1.387(5)	C(27)-C(28)	1.389(5)
C(3)-H(3)	0.9500	C(28)-H(28)	0.9500
C(4)-C(5)	1.389(4)	C(29)-N(4)	1.329(5)
C(4)-H(4)	0.9500	C(29)-C(30)	1.384(5)
C(5)-N(1)	1.370(4)	C(29)-H(29)	0.9500
C(5)-C(6)	1.480(4)	C(30)-C(31)	1.380(6)
C(6)-N(2)	1.351(4)	C(30)-H(30)	0.9500
C(6)-C(7)	1.382(4)	C(31)-C(32)	1.386(6)
C(7)-C(8)	1.408(4)	C(31)-H(31)	0.9500
C(7)-H(7)	0.9500	C(32)-C(33)	1.398(5)
C(8)-C(9)	1.401(5)	C(32)-H(32)	0.9500
C(8)-C(16)	1.488(4)	C(33)-N(4)	1.378(4)
C(9)-C(10)	1.390(4)	C(33)-C(34)	1.485(5)
C(9)-H(9)	0.9500	C(34)-N(5)	1.362(4)
C(10)-N(2)	1.359(4)	C(34)-C(35)	1.386(5)
C(10)-C(11)	1.478(4)	C(35)-C(36)	1.365(6)
C(11)-N(3)	1.373(4)	C(35)-H(35)	0.9500
C(11)-C(12)	1.385(4)	C(36)-C(37)	1.381(6)
C(12)-C(13)	1.389(5)	C(36)-H(36)	0.9500
C(12)-H(12)	0.9500	C(37)-C(38)	1.394(5)
C(13)-C(14)	1.380(5)	C(37)-H(37)	0.9500
C(13)-H(13)	0.9500	C(38)-N(5)	1.346(4)
C(14)-C(15)	1.384(5)	C(38)-H(38)	0.9500
C(14)-H(14)	0.9500	C(39)-N(6)	1.128(4)
C(15)-N(3)	1.342(4)	C(39)-C(40)	1.459(5)
C(15)-H(15)	0.9500	C(40)-H(40A)	0.9800
C(16)-C(28)	1.402(5)	C(40)-H(40B)	0.9800
C(16)-C(17)	1.405(5)	C(40)-H(40C)	0.9800
C(17)-C(18)	1.399(5)	C(41)-O(1)	1.217(5)
C(17)-H(17)	0.9500	C(41)-C(43)	1.494(7)
C(18)-C(19)	1.389(5)	C(41)-C(42)	1.505(6)
C(18)-H(18)	0.9500	C(42)-H(42A)	0.9800
C(19)-C(27)	1.399(5)	C(42)-H(42B)	0.9800
C(19)-C(20)	1.469(5)	C(42)-H(42C)	0.9800
C(20)-C(21)	1.400(5)	C(43)-H(43A)	0.9800
C(20)-C(25)	1.408(5)	C(43)-H(43B)	0.9800
C(21)-C(22)	1.390(5)	C(43)-H(43C)	0.9800
C(21)-H(21)	0.9500	C(44)-O(2)	1.204(5)
C(22)-C(23)	1.378(6)	C(44)-C(45)	1.477(6)
C(22)-H(22)	0.9500	C(44)-C(46)	1.490(6)
C(23)-C(24)	1.403(6)	C(45)-H(45A)	0.9800
C(23)-H(23)	0.9500	C(45)-H(45B)	0.9800
C(24)-C(25)	1.390(5)	C(45)-H(45C)	0.9800

C(46)-H(46A)	0.9800	P(1')-F(6')	1.607(12)
C(46)-H(46B)	0.9800	F(7)-P(2)	1.589(3)
C(46)-H(46C)	0.9800	F(8)-P(2)	1.584(3)
P(1)-F(3)	1.558(5)	F(9)-P(2)	1.603(3)
P(1)-F(2)	1.589(5)	F(10)-P(2)	1.603(3)
P(1)-F(4)	1.599(5)	F(11)-P(2)	1.593(3)
P(1)-F(6)	1.602(5)	F(12)-P(2)	1.605(3)
P(1)-F(1)	1.605(5)	N(1)-Ru(1)	2.096(3)
P(1)-F(5)	1.609(6)	N(2)-Ru(1)	1.972(2)
P(1')-F(2')	1.564(13)	N(3)-Ru(1)	2.074(2)
P(1')-F(4')	1.569(13)	N(4)-Ru(1)	2.047(3)
P(1')-F(1')	1.576(12)	N(5)-Ru(1)	2.085(3)
P(1')-F(5')	1.596(13)	N(6)-Ru(1)	2.053(3)
P(1')-F(3')	1.598(12)		

Angles

N(1)-C(1)-C(2)	122.5(3)	N(3)-C(11)-C(10)	115.4(3)
N(1)-C(1)-H(1)	118.7	C(12)-C(11)-C(10)	123.4(3)
C(2)-C(1)-H(1)	118.7	C(11)-C(12)-C(13)	119.1(3)
C(3)-C(2)-C(1)	119.3(3)	C(11)-C(12)-H(12)	120.4
C(3)-C(2)-H(2)	120.4	C(13)-C(12)-H(12)	120.4
C(1)-C(2)-H(2)	120.4	C(14)-C(13)-C(12)	119.6(3)
C(2)-C(3)-C(4)	118.8(3)	C(14)-C(13)-H(13)	120.2
C(2)-C(3)-H(3)	120.6	C(12)-C(13)-H(13)	120.2
C(4)-C(3)-H(3)	120.6	C(13)-C(14)-C(15)	118.8(3)
C(3)-C(4)-C(5)	119.8(3)	C(13)-C(14)-H(14)	120.6
C(3)-C(4)-H(4)	120.1	C(15)-C(14)-H(14)	120.6
C(5)-C(4)-H(4)	120.1	N(3)-C(15)-C(14)	122.5(3)
N(1)-C(5)-C(4)	121.6(3)	N(3)-C(15)-H(15)	118.7
N(1)-C(5)-C(6)	115.3(3)	C(14)-C(15)-H(15)	118.7
C(4)-C(5)-C(6)	123.1(3)	C(28)-C(16)-C(17)	119.4(3)
N(2)-C(6)-C(7)	120.7(3)	C(28)-C(16)-C(8)	121.1(3)
N(2)-C(6)-C(5)	112.7(3)	C(17)-C(16)-C(8)	119.4(3)
C(7)-C(6)-C(5)	126.7(3)	C(18)-C(17)-C(16)	121.3(3)
C(6)-C(7)-C(8)	119.7(3)	C(18)-C(17)-H(17)	119.4
C(6)-C(7)-H(7)	120.1	C(16)-C(17)-H(17)	119.4
C(8)-C(7)-H(7)	120.1	C(19)-C(18)-C(17)	118.4(3)
C(9)-C(8)-C(7)	118.2(3)	C(19)-C(18)-H(18)	120.8
C(9)-C(8)-C(16)	121.5(3)	C(17)-C(18)-H(18)	120.8
C(7)-C(8)-C(16)	120.3(3)	C(18)-C(19)-C(27)	120.9(3)
C(10)-C(9)-C(8)	120.2(3)	C(18)-C(19)-C(20)	129.5(3)
C(10)-C(9)-H(9)	119.9	C(27)-C(19)-C(20)	109.6(3)
C(8)-C(9)-H(9)	119.9	C(21)-C(20)-C(25)	120.7(3)
N(2)-C(10)-C(9)	119.7(3)	C(21)-C(20)-C(19)	131.5(4)
N(2)-C(10)-C(11)	112.9(3)	C(25)-C(20)-C(19)	107.8(3)
C(9)-C(10)-C(11)	127.3(3)	C(22)-C(21)-C(20)	118.6(4)
N(3)-C(11)-C(12)	121.2(3)	C(22)-C(21)-H(21)	120.7

C(20)-C(21)-H(21)	120.7	C(36)-C(37)-H(37)	120.7
C(23)-C(22)-C(21)	120.2(4)	C(38)-C(37)-H(37)	120.7
C(23)-C(22)-H(22)	119.9	N(5)-C(38)-C(37)	122.1(3)
C(21)-C(22)-H(22)	119.9	N(5)-C(38)-H(38)	119.0
C(22)-C(23)-C(24)	122.4(4)	C(37)-C(38)-H(38)	119.0
C(22)-C(23)-H(23)	118.8	N(6)-C(39)-C(40)	178.9(4)
C(24)-C(23)-H(23)	118.8	C(39)-C(40)-H(40A)	109.5
C(25)-C(24)-C(23)	117.6(4)	C(39)-C(40)-H(40B)	109.5
C(25)-C(24)-H(24)	121.2	H(40A)-C(40)-H(40B)	109.5
C(23)-C(24)-H(24)	121.2	C(39)-C(40)-H(40C)	109.5
C(24)-C(25)-C(20)	120.5(4)	H(40A)-C(40)-H(40C)	109.5
C(24)-C(25)-C(26)	129.4(4)	H(40B)-C(40)-H(40C)	109.5
C(20)-C(25)-C(26)	110.2(3)	O(1)-C(41)-C(43)	123.4(5)
C(27)-C(26)-C(25)	102.5(3)	O(1)-C(41)-C(42)	120.4(5)
C(27)-C(26)-H(26A)	111.3	C(43)-C(41)-C(42)	116.2(4)
C(25)-C(26)-H(26A)	111.3	C(41)-C(42)-H(42A)	109.5
C(27)-C(26)-H(26B)	111.3	C(41)-C(42)-H(42B)	109.5
C(25)-C(26)-H(26B)	111.3	H(42A)-C(42)-H(42B)	109.5
H(26A)-C(26)-H(26B)	109.2	C(41)-C(42)-H(42C)	109.5
C(28)-C(27)-C(19)	120.7(3)	H(42A)-C(42)-H(42C)	109.5
C(28)-C(27)-C(26)	129.4(3)	H(42B)-C(42)-H(42C)	109.5
C(19)-C(27)-C(26)	109.9(3)	C(41)-C(43)-H(43A)	109.5
C(27)-C(28)-C(16)	119.3(3)	C(41)-C(43)-H(43B)	109.5
C(27)-C(28)-H(28)	120.3	H(43A)-C(43)-H(43B)	109.5
C(16)-C(28)-H(28)	120.3	C(41)-C(43)-H(43C)	109.5
N(4)-C(29)-C(30)	124.0(4)	H(43A)-C(43)-H(43C)	109.5
N(4)-C(29)-H(29)	118.0	H(43B)-C(43)-H(43C)	109.5
C(30)-C(29)-H(29)	118.0	O(2)-C(44)-C(45)	121.5(4)
C(31)-C(30)-C(29)	118.2(4)	O(2)-C(44)-C(46)	120.1(4)
C(31)-C(30)-H(30)	120.9	C(45)-C(44)-C(46)	118.4(4)
C(29)-C(30)-H(30)	120.9	C(44)-C(45)-H(45A)	109.5
C(30)-C(31)-C(32)	119.3(3)	C(44)-C(45)-H(45B)	109.5
C(30)-C(31)-H(31)	120.3	H(45A)-C(45)-H(45B)	109.5
C(32)-C(31)-H(31)	120.3	C(44)-C(45)-H(45C)	109.5
C(31)-C(32)-C(33)	119.8(4)	H(45A)-C(45)-H(45C)	109.5
C(31)-C(32)-H(32)	120.1	H(45B)-C(45)-H(45C)	109.5
C(33)-C(32)-H(32)	120.1	C(44)-C(46)-H(46A)	109.5
N(4)-C(33)-C(32)	120.3(3)	C(44)-C(46)-H(46B)	109.5
N(4)-C(33)-C(34)	115.3(3)	H(46A)-C(46)-H(46B)	109.5
C(32)-C(33)-C(34)	124.3(3)	C(44)-C(46)-H(46C)	109.5
N(5)-C(34)-C(35)	122.0(3)	H(46A)-C(46)-H(46C)	109.5
N(5)-C(34)-C(33)	114.4(3)	H(46B)-C(46)-H(46C)	109.5
C(35)-C(34)-C(33)	123.6(3)	F(3)-P(1)-F(2)	93.4(4)
C(36)-C(35)-C(34)	119.1(4)	F(3)-P(1)-F(4)	91.8(4)
C(36)-C(35)-H(35)	120.4	F(2)-P(1)-F(4)	174.6(5)
C(34)-C(35)-H(35)	120.4	F(3)-P(1)-F(6)	91.4(3)
C(35)-C(36)-C(37)	120.0(3)	F(2)-P(1)-F(6)	91.6(3)
C(35)-C(36)-H(36)	120.0	F(4)-P(1)-F(6)	89.6(4)
C(37)-C(36)-H(36)	120.0	F(3)-P(1)-F(1)	177.6(4)
C(36)-C(37)-C(38)	118.7(4)	F(2)-P(1)-F(1)	88.6(3)

F(4)-P(1)-F(1)	86.1(4)	C(38)-N(5)-C(34)	118.2(3)
F(6)-P(1)-F(1)	89.8(3)	C(38)-N(5)-Ru(1)	126.3(2)
F(3)-P(1)-F(5)	89.6(4)	C(34)-N(5)-Ru(1)	115.2(2)
F(2)-P(1)-F(5)	89.5(5)	C(39)-N(6)-Ru(1)	178.0(3)
F(4)-P(1)-F(5)	89.3(5)	F(8)-P(2)-F(7)	90.23(17)
F(6)-P(1)-F(5)	178.5(5)	F(8)-P(2)-F(11)	89.6(2)
F(1)-P(1)-F(5)	89.1(4)	F(7)-P(2)-F(11)	91.44(19)
F(2')-P(1')-F(4')	171.3(13)	F(8)-P(2)-F(9)	90.47(17)
F(2')-P(1')-F(1')	92.0(10)	F(7)-P(2)-F(9)	179.29(18)
F(4')-P(1')-F(1')	94.3(11)	F(11)-P(2)-F(9)	88.67(15)
F(2')-P(1')-F(5')	94.5(12)	F(8)-P(2)-F(10)	179.3(2)
F(4')-P(1')-F(5')	91.3(13)	F(7)-P(2)-F(10)	89.14(15)
F(1')-P(1')-F(5')	91.6(11)	F(11)-P(2)-F(10)	90.04(18)
F(2')-P(1')-F(3')	85.2(10)	F(9)-P(2)-F(10)	90.16(15)
F(4')-P(1')-F(3')	88.5(11)	F(8)-P(2)-F(12)	91.3(2)
F(1')-P(1')-F(3')	177.2(12)	F(7)-P(2)-F(12)	90.2(2)
F(5')-P(1')-F(3')	88.4(10)	F(11)-P(2)-F(12)	178.1(2)
F(2')-P(1')-F(6')	83.8(10)	F(9)-P(2)-F(12)	89.65(18)
F(4')-P(1')-F(6')	90.4(12)	F(10)-P(2)-F(12)	89.15(19)
F(1')-P(1')-F(6')	89.0(9)	N(2)-Ru(1)-N(4)	94.92(11)
F(5')-P(1')-F(6')	178.2(13)	N(2)-Ru(1)-N(6)	90.59(10)
F(3')-P(1')-F(6')	90.9(8)	N(4)-Ru(1)-N(6)	174.36(11)
C(1)-N(1)-C(5)	118.0(3)	N(2)-Ru(1)-N(3)	79.80(10)
C(1)-N(1)-Ru(1)	128.8(2)	N(4)-Ru(1)-N(3)	90.70(10)
C(5)-N(1)-Ru(1)	113.24(19)	N(6)-Ru(1)-N(3)	89.08(10)
C(6)-N(2)-C(10)	121.5(3)	N(2)-Ru(1)-N(5)	173.09(10)
C(6)-N(2)-Ru(1)	119.8(2)	N(4)-Ru(1)-N(5)	79.31(11)
C(10)-N(2)-Ru(1)	118.6(2)	N(6)-Ru(1)-N(5)	95.12(10)
C(15)-N(3)-C(11)	118.7(3)	N(3)-Ru(1)-N(5)	96.36(10)
C(15)-N(3)-Ru(1)	128.1(2)	N(2)-Ru(1)-N(1)	78.89(10)
C(11)-N(3)-Ru(1)	113.2(2)	N(4)-Ru(1)-N(1)	91.40(10)
C(29)-N(4)-C(33)	118.3(3)	N(6)-Ru(1)-N(1)	90.85(10)
C(29)-N(4)-Ru(1)	126.3(2)	N(3)-Ru(1)-N(1)	158.69(10)
C(33)-N(4)-Ru(1)	115.4(2)	N(5)-Ru(1)-N(1)	104.87(10)

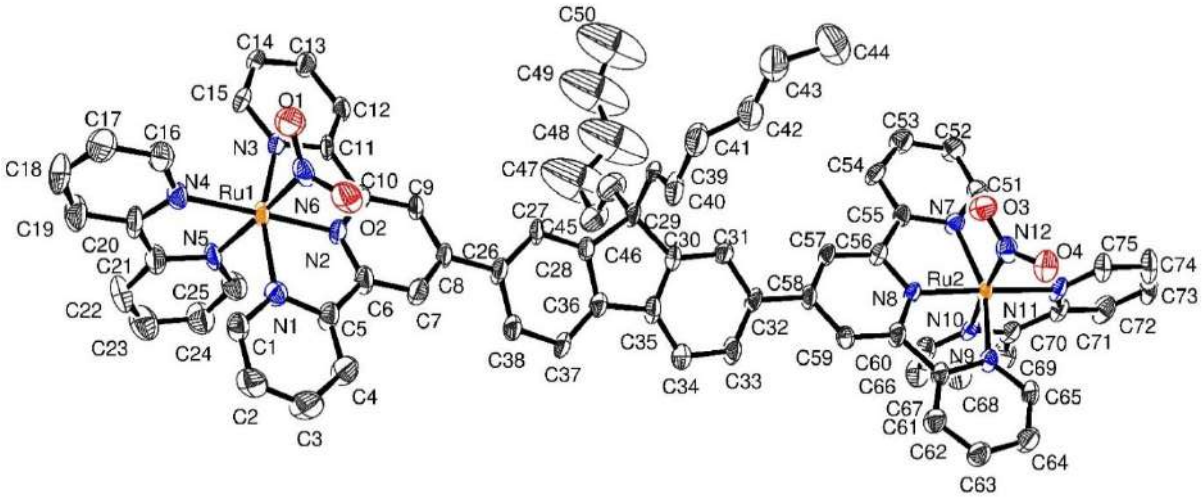

Empirical formula	$C_{75}H_{68}N_{12}O_4Ru_2$, $2(F_6P)$
Formula weight	1693.50
Temperature	135(2) K
Wavelength	0.71073 A
Crystal system, space group	Monoclinic, P 21/c
Unit cell dimensions	a = 13.837(3) A alpha = 90 deg. b = 21.178(3) A beta = 90.387(6) deg. c = 29.037(5) A gamma = 90 deg.
Volume	8509(3) A^3
Z, Calculated density	4, 1.322 Mg/m^3
Absorption coefficient	0.470 mm^-1
F(000)	3440
Crystal size	0.120 x 0.100 x 0.080 mm
Theta range for data collection	1.190 to 26.136 deg.
Limiting indices	-17<=h<=17, -26<=k<=25, -35<=l<=35
Reflections collected / unique	90705 / 16790 [R(int) = 0.1054]
Completeness to theta = 25.242	100.0 %

Refinement method	Full-matrix least-squares on F^2
Data / restraints / parameters	16790 / 390 / 1091
Goodness-of-fit on F^2	1.050
Final R indices [I>2sigma(I)]	R1 = 0.0809, wR2 = 0.1918
R indices (all data)	R1 = 0.1359, wR2 = 0.2222
Largest diff. peak and hole	1.938 and -1.135 e.A^-3

Atomic coordinates

U(eq) is defined as one third of the trace of the orthogonalized Uij tens

	x	y	z	U(eq)
C(1)	10590(5)	7044(4)	7750(2)	38(2)
C(2)	11417(5)	6931(4)	7506(3)	47(2)
C(3)	11373(6)	6822(5)	7040(3)	57(2)
C(4)	10464(5)	6814(4)	6830(3)	47(2)
C(5)	9659(5)	6932(4)	7085(2)	36(2)
C(6)	8674(5)	6896(4)	6893(2)	36(2)
C(7)	8418(5)	6806(4)	6437(2)	38(2)
C(8)	7441(5)	6739(3)	6307(2)	31(2)
C(9)	6741(5)	6799(3)	6649(2)	29(2)
C(10)	7035(5)	6907(3)	7105(2)	27(2)
C(11)	6398(5)	6987(3)	7507(2)	28(2)
C(12)	5414(5)	6913(3)	7488(2)	30(2)
C(13)	4861(5)	7001(3)	7886(2)	35(2)
C(14)	5351(5)	7154(3)	8294(2)	29(2)
C(15)	6334(5)	7217(3)	8296(2)	32(2)
C(16)	8761(6)	7855(5)	8766(3)	54(2)
C(17)	9016(7)	7904(5)	9227(3)	71(3)
C(18)	9257(8)	7367(6)	9462(3)	78(3)
C(19)	9274(7)	6792(5)	9244(3)	59(3)
C(20)	9018(6)	6767(4)	8782(2)	43(2)
C(21)	8968(5)	6178(4)	8519(2)	43(2)
C(22)	9280(6)	5598(4)	8682(3)	57(2)
C(23)	9145(7)	5060(4)	8424(3)	61(3)
C(24)	8705(6)	5110(4)	7995(3)	55(2)
C(25)	8442(6)	5709(4)	7834(3)	44(2)
C(26)	7186(5)	6598(4)	5819(2)	35(2)
C(27)	6311(5)	6780(3)	5616(2)	32(2)
C(28)	6128(5)	6644(3)	5157(2)	30(2)
C(30)	5534(5)	6535(3)	4396(2)	31(2)
C(31)	5044(5)	6545(3)	3975(2)	30(2)

C(32)	5479(5)	6265(4)	3586(2)	32(2)
C(33)	6380(5)	5975(4)	3630(2)	39(2)
C(34)	6869(6)	5957(4)	4047(2)	41(2)
C(35)	6444(5)	6249(4)	4426(2)	36(2)
C(36)	6819(5)	6313(4)	4899(2)	38(2)
C(37)	7696(5)	6118(4)	5091(2)	40(2)
C(29)	5242(5)	6806(4)	4861(2)	34(2)
C(39)	5030(18)	7519(6)	4869(15)	33(5)
C(40)	5799(19)	7983(8)	4728(13)	51(3)
C(41)	5452(17)	8664(8)	4737(9)	57(3)
C(42)	4700(20)	8838(10)	4373(8)	63(3)
C(43)	4345(17)	9514(10)	4377(8)	74(3)
C(44)	3653(17)	9656(12)	3954(9)	97(6)
C(39')	5060(30)	7520(7)	4830(20)	50(4)
C(40')	5900(20)	7928(9)	4685(15)	51(3)
C(41')	5720(20)	8627(9)	4749(11)	57(3)
C(42')	4880(20)	8899(11)	4478(9)	63(3)
C(43')	4626(19)	9579(10)	4592(8)	69(3)
C(44')	3786(19)	9835(13)	4271(10)	90(5)
C(38)	7867(5)	6264(4)	5551(2)	38(2)
C(45)	4374(13)	6430(12)	5048(10)	60(5)
C(46)	4376(14)	5762(10)	5049(9)	59(4)
C(47)	3412(17)	5497(13)	5251(16)	210(9)
C(48)	2473(17)	5698(14)	5043(14)	210(9)
C(49)	1419(17)	5621(13)	5309(14)	210(9)
C(50)	620(18)	5945(14)	5302(14)	210(9)
C(45')	4268(15)	6543(17)	5046(13)	14(5)
C(46')	4170(30)	5879(19)	5100(20)	60(6)
C(47')	3210(30)	5680(20)	5340(30)	210(9)
C(48')	2270(30)	5970(30)	5200(20)	210(9)
C(49')	1380(30)	6250(30)	5520(20)	210(9)
C(50')	620(30)	6590(30)	5490(20)	210(9)
C(51)	1579(5)	6557(3)	1829(2)	33(2)
C(52)	787(5)	6521(4)	2113(2)	39(2)
C(53)	946(5)	6442(4)	2584(3)	42(2)
C(54)	1867(5)	6407(4)	2757(2)	36(2)
C(55)	2649(5)	6450(3)	2457(2)	29(2)
C(56)	3662(5)	6416(3)	2595(2)	29(2)
C(57)	4035(5)	6357(3)	3044(2)	30(2)
C(58)	5032(5)	6313(3)	3118(2)	32(2)
C(59)	5626(5)	6329(3)	2733(2)	31(2)
C(60)	5230(5)	6383(3)	2295(2)	32(2)
C(61)	5782(5)	6426(3)	1860(2)	31(2)
C(62)	6765(5)	6388(3)	1830(2)	36(2)
C(63)	7208(5)	6463(4)	1411(2)	41(2)
C(64)	6654(5)	6565(4)	1025(3)	41(2)
C(65)	5670(5)	6592(3)	1067(2)	33(2)
C(66)	3852(5)	5117(4)	1742(2)	41(2)
C(67)	3702(6)	4491(4)	1640(3)	49(2)
C(68)	3246(6)	4348(4)	1221(3)	50(2)

C(69)	2980(6)	4840(4)	929(3)	48(2)
C(70)	3158(5)	5457(4)	1055(2)	33(2)
C(71)	2910(5)	6010(4)	765(2)	32(2)
C(72)	2464(6)	5960(4)	336(2)	45(2)
C(73)	2266(6)	6496(4)	86(2)	50(2)
C(74)	2505(6)	7075(4)	270(3)	49(2)
C(75)	2946(5)	7095(4)	700(2)	38(2)
N(1)	9712(4)	7046(3)	7545(2)	33(1)
N(2)	7970(4)	6949(3)	7214(2)	30(1)
N(3)	6874(4)	7135(3)	7916(2)	27(1)
N(4)	8777(4)	7292(3)	8537(2)	38(2)
N(5)	8566(4)	6228(3)	8088(2)	33(1)
N(6)	8311(4)	8079(3)	7673(2)	38(2)
N(7)	2484(4)	6531(3)	1985(2)	30(1)
N(8)	4267(4)	6438(3)	2237(2)	27(1)
N(9)	5223(4)	6526(3)	1471(2)	26(1)
N(10)	3590(4)	5596(3)	1467(2)	29(1)
N(11)	3152(4)	6574(3)	946(2)	32(1)
N(12)	3854(4)	7501(3)	1693(2)	37(2)
Ru(1)	8373(1)	7144(1)	7852(1)	31(1)
Ru(2)	3749(1)	6550(1)	1610(1)	29(1)
P(1)	2080(2)	7602(2)	8903(1)	68(1)
F(1)	2533(4)	8307(3)	8905(2)	76(2)
F(2)	2576(4)	7484(3)	8416(2)	71(2)
F(3)	1633(5)	6910(3)	8894(2)	109(3)
F(4)	1592(4)	7745(4)	9392(2)	99(2)
F(5)	3022(4)	7355(4)	9159(2)	101(2)
F(6)	1142(4)	7874(3)	8647(2)	73(2)
O(1)	7895(4)	8479(3)	7912(2)	51(1)
O(2)	8690(4)	8250(3)	7299(2)	52(2)
O(3)	3488(4)	7777(3)	2030(2)	44(1)
O(4)	4317(4)	7832(2)	1406(2)	43(1)
P(2)	9105(5)	9428(3)	5388(2)	91(2)
F(7)	8828(13)	9498(8)	5905(4)	136(4)
F(11)	9091(12)	10157(6)	5452(5)	123(4)
F(8)	10140(10)	9463(9)	5589(6)	143(4)
F(9)	8863(12)	9549(6)	4876(4)	125(4)
F(12)	8931(12)	8682(6)	5376(5)	120(3)
F(10)	7922(10)	9465(9)	5373(6)	163(4)
P(2')	9736(4)	8306(3)	5747(2)	64(2)
F(7')	9500(8)	8124(6)	6249(3)	79(3)
F(11')	10455(11)	7802(7)	5843(5)	128(4)
F(8')	8987(12)	7805(8)	5602(5)	139(4)
F(9')	9166(11)	8966(7)	5806(5)	119(3)
F(12')	9954(9)	8554(7)	5237(3)	94(3)
F(10')	10498(11)	8811(7)	5908(5)	119(3)

Bond lengths

C(1)-N(1)	1.349(8)	C(23)-H(23)	0.9500
C(1)-C(2)	1.371(11)	C(24)-C(25)	1.400(11)
C(1)-H(1)	0.9500	C(24)-H(24)	0.9500
C(2)-C(3)	1.374(11)	C(25)-N(5)	1.333(9)
C(2)-H(2)	0.9500	C(25)-H(25)	0.9500
C(3)-C(4)	1.395(10)	C(26)-C(27)	1.397(9)
C(3)-H(3)	0.9500	C(26)-C(38)	1.416(10)
C(4)-C(5)	1.363(10)	C(27)-C(28)	1.386(8)
C(4)-H(4)	0.9500	C(27)-H(27)	0.9500
C(5)-N(1)	1.361(8)	C(28)-C(36)	1.405(10)
C(5)-C(6)	1.471(9)	C(28)-C(29)	1.531(9)
C(6)-N(2)	1.359(9)	C(30)-C(31)	1.393(8)
C(6)-C(7)	1.381(9)	C(30)-C(35)	1.401(10)
C(7)-C(8)	1.408(9)	C(30)-C(29)	1.525(9)
C(7)-H(7)	0.9500	C(31)-C(32)	1.415(9)
C(8)-C(9)	1.397(9)	C(31)-H(31)	0.9500
C(8)-C(26)	1.488(8)	C(32)-C(33)	1.395(10)
C(9)-C(10)	1.400(8)	C(32)-C(58)	1.493(8)
C(9)-H(9)	0.9500	C(33)-C(34)	1.383(9)
C(10)-N(2)	1.333(8)	C(33)-H(33)	0.9500
C(10)-C(11)	1.479(9)	C(34)-C(35)	1.395(10)
C(11)-C(12)	1.370(9)	C(34)-H(34)	0.9500
C(11)-N(3)	1.388(8)	C(35)-C(36)	1.471(9)
C(12)-C(13)	1.404(9)	C(36)-C(37)	1.394(10)
C(12)-H(12)	0.9500	C(37)-C(38)	1.391(9)
C(13)-C(14)	1.399(9)	C(37)-H(37)	0.9500
C(13)-H(13)	0.9500	C(29)-C(39')	1.538(16)
C(14)-C(15)	1.367(9)	C(29)-C(39)	1.539(14)
C(14)-H(14)	0.9500	C(29)-C(45)	1.542(14)
C(15)-N(3)	1.348(8)	C(29)-C(45')	1.557(16)
C(15)-H(15)	0.9500	C(39)-C(40)	1.507(15)
C(16)-N(4)	1.366(10)	C(39)-H(39A)	0.9900
C(16)-C(17)	1.386(11)	C(39)-H(39B)	0.9900
C(16)-H(16)	0.9500	C(40)-C(41)	1.521(16)
C(17)-C(18)	1.365(14)	C(40)-H(40A)	0.9900
C(17)-H(17)	0.9500	C(40)-H(40B)	0.9900
C(18)-C(19)	1.372(14)	C(41)-C(42)	1.524(17)
C(18)-H(18)	0.9500	C(41)-H(41A)	0.9900
C(19)-C(20)	1.384(10)	C(41)-H(41B)	0.9900
C(19)-H(19)	0.9500	C(42)-C(43)	1.513(18)
C(20)-N(4)	1.361(10)	C(42)-H(42A)	0.9900
C(20)-C(21)	1.463(11)	C(42)-H(42B)	0.9900
C(21)-N(5)	1.370(8)	C(43)-C(44)	1.58(2)
C(21)-C(22)	1.385(11)	C(43)-H(43A)	0.9900
C(22)-C(23)	1.375(12)	C(43)-H(43B)	0.9900
C(22)-H(22)	0.9500	C(44)-H(44A)	0.9800
C(23)-C(24)	1.389(12)	C(44)-H(44B)	0.9800

C(44)-H(44C)	0.9800	C(49')-C(50')	1.28(3)
C(39')-C(40')	1.506(17)	C(49')-H(49C)	0.9900
C(39')-H(39C)	0.9900	C(49')-H(49D)	0.9900
C(39')-H(39D)	0.9900	C(50')-H(50D)	0.9800
C(40')-C(41')	1.512(17)	C(50')-H(50E)	0.9800
C(40')-H(40C)	0.9900	C(50')-H(50F)	0.9800
C(40')-H(40D)	0.9900	C(51)-N(7)	1.330(8)
C(41')-C(42')	1.515(18)	C(51)-C(52)	1.378(10)
C(41')-H(41C)	0.9900	C(51)-H(51)	0.9500
C(41')-H(41D)	0.9900	C(52)-C(53)	1.394(10)
C(42')-C(43')	1.520(18)	C(52)-H(52)	0.9500
C(42')-H(42C)	0.9900	C(53)-C(54)	1.369(10)
C(42')-H(42D)	0.9900	C(53)-H(53)	0.9500
C(43')-C(44')	1.58(2)	C(54)-C(55)	1.396(9)
C(43')-H(43C)	0.9900	C(54)-H(54)	0.9500
C(43')-H(43D)	0.9900	C(55)-N(7)	1.397(8)
C(44')-H(44D)	0.9800	C(55)-C(56)	1.457(9)
C(44')-H(44E)	0.9800	C(56)-N(8)	1.340(8)
C(44')-H(44F)	0.9800	C(56)-C(57)	1.404(8)
C(38)-H(38)	0.9500	C(57)-C(58)	1.399(10)
C(45)-C(46)	1.416(16)	C(57)-H(57)	0.9500
C(45)-H(45A)	0.9900	C(58)-C(59)	1.391(9)
C(45)-H(45B)	0.9900	C(59)-C(60)	1.386(8)
C(46)-C(47)	1.56(2)	C(59)-H(59)	0.9500
C(46)-H(46A)	0.9900	C(60)-N(8)	1.346(8)
C(46)-H(46B)	0.9900	C(60)-C(61)	1.485(9)
C(47)-C(48)	1.49(3)	C(61)-C(62)	1.367(10)
C(47)-H(47A)	0.9900	C(61)-N(9)	1.381(8)
C(47)-H(47B)	0.9900	C(62)-C(63)	1.376(10)
C(48)-C(49)	1.66(3)	C(62)-H(62)	0.9500
C(48)-H(48A)	0.9900	C(63)-C(64)	1.372(10)
C(48)-H(48B)	0.9900	C(63)-H(63)	0.9500
C(49)-C(50)	1.30(3)	C(64)-C(65)	1.369(10)
C(49)-H(49A)	0.9900	C(64)-H(64)	0.9500
C(49)-H(49B)	0.9900	C(65)-N(9)	1.336(8)
C(50)-H(50A)	0.9800	C(65)-H(65)	0.9500
C(50)-H(50B)	0.9800	C(66)-N(10)	1.339(9)
C(50)-H(50C)	0.9800	C(66)-C(67)	1.374(11)
C(45')-C(46')	1.42(2)	C(66)-H(66)	0.9500
C(45')-H(45C)	0.9900	C(67)-C(68)	1.402(11)
C(45')-H(45D)	0.9900	C(67)-H(67)	0.9500
C(46')-C(47')	1.57(3)	C(68)-C(69)	1.392(11)
C(46')-H(46C)	0.9900	C(68)-H(68)	0.9500
C(46')-H(46D)	0.9900	C(69)-C(70)	1.378(11)
C(47')-C(48')	1.49(3)	C(69)-H(69)	0.9500
C(47')-H(47C)	0.9900	C(70)-N(10)	1.366(8)
C(47')-H(47D)	0.9900	C(70)-C(71)	1.483(10)
C(48')-C(49')	1.65(4)	C(71)-N(11)	1.346(9)
C(48')-H(48C)	0.9900	C(71)-C(72)	1.389(9)
C(48')-H(48D)	0.9900	C(72)-C(73)	1.374(11)

C(72)-H(72)	0.9500	N(12)-O(4)	1.266(7)
C(73)-C(74)	1.377(11)	N(12)-Ru(2)	2.035(6)
C(73)-H(73)	0.9500	P(1)-F(5)	1.584(6)
C(74)-C(75)	1.387(9)	P(1)-F(3)	1.590(7)
C(74)-H(74)	0.9500	P(1)-F(2)	1.595(6)
C(75)-N(11)	1.344(9)	P(1)-F(6)	1.597(6)
C(75)-H(75)	0.9500	P(1)-F(4)	1.607(6)
N(1)-Ru(1)	2.071(6)	P(1)-F(1)	1.618(6)
N(2)-Ru(1)	1.973(5)	P(2)-F(9)	1.542(12)
N(3)-Ru(1)	2.084(6)	P(2)-F(8)	1.546(14)
N(4)-Ru(1)	2.087(5)	P(2)-F(11)	1.556(14)
N(5)-Ru(1)	2.076(6)	P(2)-F(7)	1.559(13)
N(6)-O(1)	1.238(8)	P(2)-F(12)	1.597(13)
N(6)-O(2)	1.264(8)	P(2)-F(10)	1.639(15)
N(6)-Ru(1)	2.048(7)	P(2')-F(11')	1.485(13)
N(7)-Ru(2)	2.068(5)	P(2')-F(8')	1.542(12)
N(8)-Ru(2)	1.968(5)	P(2')-F(7')	1.545(10)
N(9)-Ru(2)	2.082(5)	P(2')-F(10')	1.570(15)
N(10)-Ru(2)	2.074(6)	P(2')-F(12')	1.600(10)
N(11)-Ru(2)	2.092(5)	P(2')-F(9')	1.614(14)
N(12)-O(3)	1.249(8)		

Angles

N(1)-C(1)-C(2)	121.7(7)	C(8)-C(9)-C(10)	119.2(6)
N(1)-C(1)-H(1)	119.2	C(8)-C(9)-H(9)	120.4
C(2)-C(1)-H(1)	119.2	C(10)-C(9)-H(9)	120.4
C(1)-C(2)-C(3)	120.5(7)	N(2)-C(10)-C(9)	120.8(6)
C(1)-C(2)-H(2)	119.8	N(2)-C(10)-C(11)	112.7(5)
C(3)-C(2)-H(2)	119.8	C(9)-C(10)-C(11)	126.5(6)
C(2)-C(3)-C(4)	117.8(8)	C(12)-C(11)-N(3)	121.8(6)
C(2)-C(3)-H(3)	121.1	C(12)-C(11)-C(10)	123.5(6)
C(4)-C(3)-H(3)	121.1	N(3)-C(11)-C(10)	114.7(6)
C(5)-C(4)-C(3)	119.9(7)	C(11)-C(12)-C(13)	119.9(6)
C(5)-C(4)-H(4)	120.0	C(11)-C(12)-H(12)	120.1
C(3)-C(4)-H(4)	120.0	C(13)-C(12)-H(12)	120.1
N(1)-C(5)-C(4)	121.8(6)	C(14)-C(13)-C(12)	117.7(6)
N(1)-C(5)-C(6)	115.2(6)	C(14)-C(13)-H(13)	121.2
C(4)-C(5)-C(6)	122.9(6)	C(12)-C(13)-H(13)	121.2
N(2)-C(6)-C(7)	119.3(6)	C(15)-C(14)-C(13)	120.2(6)
N(2)-C(6)-C(5)	113.7(6)	C(15)-C(14)-H(14)	119.9
C(7)-C(6)-C(5)	127.0(7)	C(13)-C(14)-H(14)	119.9
C(6)-C(7)-C(8)	120.6(7)	N(3)-C(15)-C(14)	122.8(6)
C(6)-C(7)-H(7)	119.7	N(3)-C(15)-H(15)	118.6
C(8)-C(7)-H(7)	119.7	C(14)-C(15)-H(15)	118.6
C(9)-C(8)-C(7)	118.0(6)	N(4)-C(16)-C(17)	122.0(9)
C(9)-C(8)-C(26)	122.3(6)	N(4)-C(16)-H(16)	119.0
C(7)-C(8)-C(26)	119.7(6)	C(17)-C(16)-H(16)	119.0

C(18)-C(17)-C(16)	118.7(9)	C(35)-C(34)-H(34)	120.9
C(18)-C(17)-H(17)	120.7	C(34)-C(35)-C(30)	121.7(6)
C(16)-C(17)-H(17)	120.7	C(34)-C(35)-C(36)	129.1(7)
C(17)-C(18)-C(19)	120.9(8)	C(30)-C(35)-C(36)	109.2(6)
C(17)-C(18)-H(18)	119.6	C(37)-C(36)-C(28)	121.9(6)
C(19)-C(18)-H(18)	119.6	C(37)-C(36)-C(35)	130.2(7)
C(18)-C(19)-C(20)	118.4(9)	C(28)-C(36)-C(35)	107.9(6)
C(18)-C(19)-H(19)	120.8	C(38)-C(37)-C(36)	117.4(7)
C(20)-C(19)-H(19)	120.8	C(38)-C(37)-H(37)	121.3
N(4)-C(20)-C(19)	122.3(8)	C(36)-C(37)-H(37)	121.3
N(4)-C(20)-C(21)	114.3(6)	C(30)-C(29)-C(28)	101.4(5)
C(19)-C(20)-C(21)	123.4(8)	C(30)-C(29)-C(39')	111(2)
N(5)-C(21)-C(22)	120.3(8)	C(28)-C(29)-C(39')	113(2)
N(5)-C(21)-C(20)	115.4(7)	C(30)-C(29)-C(39)	115.7(16)
C(22)-C(21)-C(20)	124.3(7)	C(28)-C(29)-C(39)	111.3(15)
C(23)-C(22)-C(21)	120.5(8)	C(30)-C(29)-C(45)	109.2(12)
C(23)-C(22)-H(22)	119.8	C(28)-C(29)-C(45)	108.1(12)
C(21)-C(22)-H(22)	119.8	C(39)-C(29)-C(45)	110.6(14)
C(22)-C(23)-C(24)	118.9(8)	C(30)-C(29)-C(45')	113.9(16)
C(22)-C(23)-H(23)	120.5	C(28)-C(29)-C(45')	114.8(13)
C(24)-C(23)-H(23)	120.5	C(39')-C(29)-C(45')	103.3(19)
C(23)-C(24)-C(25)	118.7(8)	C(40)-C(39)-C(29)	120.1(14)
C(23)-C(24)-H(24)	120.7	C(40)-C(39)-H(39A)	107.3
C(25)-C(24)-H(24)	120.7	C(29)-C(39)-H(39A)	107.3
N(5)-C(25)-C(24)	122.0(7)	C(40)-C(39)-H(39B)	107.3
N(5)-C(25)-H(25)	119.0	C(29)-C(39)-H(39B)	107.3
C(24)-C(25)-H(25)	119.0	H(39A)-C(39)-H(39B)	106.9
C(27)-C(26)-C(38)	119.0(6)	C(39)-C(40)-C(41)	113.0(14)
C(27)-C(26)-C(8)	123.0(6)	C(39)-C(40)-H(40A)	109.0
C(38)-C(26)-C(8)	118.0(6)	C(41)-C(40)-H(40A)	109.0
C(28)-C(27)-C(26)	120.0(7)	C(39)-C(40)-H(40B)	109.0
C(28)-C(27)-H(27)	120.0	C(41)-C(40)-H(40B)	109.0
C(26)-C(27)-H(27)	120.0	H(40A)-C(40)-H(40B)	107.8
C(27)-C(28)-C(36)	119.7(6)	C(40)-C(41)-C(42)	115.6(15)
C(27)-C(28)-C(29)	129.3(6)	C(40)-C(41)-H(41A)	108.4
C(36)-C(28)-C(29)	111.0(6)	C(42)-C(41)-H(41A)	108.4
C(31)-C(30)-C(35)	119.6(6)	C(40)-C(41)-H(41B)	108.4
C(31)-C(30)-C(29)	129.9(6)	C(42)-C(41)-H(41B)	108.4
C(35)-C(30)-C(29)	110.5(5)	H(41A)-C(41)-H(41B)	107.4
C(30)-C(31)-C(32)	119.2(6)	C(43)-C(42)-C(41)	116.3(15)
C(30)-C(31)-H(31)	120.4	C(43)-C(42)-H(42A)	108.2
C(32)-C(31)-H(31)	120.4	C(41)-C(42)-H(42A)	108.2
C(33)-C(32)-C(31)	119.7(6)	C(43)-C(42)-H(42B)	108.2
C(33)-C(32)-C(58)	118.6(6)	C(41)-C(42)-H(42B)	108.2
C(31)-C(32)-C(58)	121.6(6)	H(42A)-C(42)-H(42B)	107.4
C(34)-C(33)-C(32)	121.7(7)	C(42)-C(43)-C(44)	111.5(16)
C(34)-C(33)-H(33)	119.2	C(42)-C(43)-H(43A)	109.3
C(32)-C(33)-H(33)	119.2	C(44)-C(43)-H(43A)	109.3
C(33)-C(34)-C(35)	118.1(7)	C(42)-C(43)-H(43B)	109.3
C(33)-C(34)-H(34)	120.9	C(44)-C(43)-H(43B)	109.3

H(43A)-C(43)-H(43B)	108.0	C(29)-C(45)-H(45B)	107.1
C(43)-C(44)-H(44A)	109.5	H(45A)-C(45)-H(45B)	106.8
C(43)-C(44)-H(44B)	109.5	C(45)-C(46)-C(47)	111.0(14)
H(44A)-C(44)-H(44B)	109.5	C(45)-C(46)-H(46A)	109.4
C(43)-C(44)-H(44C)	109.5	C(47)-C(46)-H(46A)	109.4
H(44A)-C(44)-H(44C)	109.5	C(45)-C(46)-H(46B)	109.4
H(44B)-C(44)-H(44C)	109.5	C(47)-C(46)-H(46B)	109.4
C(40')-C(39')-C(29)	117(2)	H(46A)-C(46)-H(46B)	108.0
C(40')-C(39')-H(39C)	108.1	C(48)-C(47)-C(46)	119(2)
C(29)-C(39')-H(39C)	108.1	C(48)-C(47)-H(47A)	107.5
C(40')-C(39')-H(39D)	108.1	C(46)-C(47)-H(47A)	107.5
C(29)-C(39')-H(39D)	108.1	C(48)-C(47)-H(47B)	107.5
H(39C)-C(39')-H(39D)	107.3	C(46)-C(47)-H(47B)	107.5
C(39')-C(40')-C(41')	113.9(17)	H(47A)-C(47)-H(47B)	107.0
C(39')-C(40')-H(40C)	108.8	C(47)-C(48)-C(49)	123(3)
C(41')-C(40')-H(40C)	108.8	C(47)-C(48)-H(48A)	106.5
C(39')-C(40')-H(40D)	108.8	C(49)-C(48)-H(48A)	106.5
C(41')-C(40')-H(40D)	108.8	C(47)-C(48)-H(48B)	106.5
H(40C)-C(40')-H(40D)	107.7	C(49)-C(48)-H(48B)	106.5
C(40')-C(41')-C(42')	115.6(17)	H(48A)-C(48)-H(48B)	106.5
C(40')-C(41')-H(41C)	108.4	C(50)-C(49)-C(48)	134(3)
C(42')-C(41')-H(41C)	108.4	C(50)-C(49)-H(49A)	103.8
C(40')-C(41')-H(41D)	108.4	C(48)-C(49)-H(49A)	103.8
C(42')-C(41')-H(41D)	108.4	C(50)-C(49)-H(49B)	103.8
H(41C)-C(41')-H(41D)	107.4	C(48)-C(49)-H(49B)	103.8
C(41')-C(42')-C(43')	115.3(16)	H(49A)-C(49)-H(49B)	105.4
C(41')-C(42')-H(42C)	108.5	C(49)-C(50)-H(50A)	109.5
C(43')-C(42')-H(42C)	108.5	C(49)-C(50)-H(50B)	109.5
C(41')-C(42')-H(42D)	108.5	H(50A)-C(50)-H(50B)	109.5
C(43')-C(42')-H(42D)	108.5	C(49)-C(50)-H(50C)	109.5
H(42C)-C(42')-H(42D)	107.5	H(50A)-C(50)-H(50C)	109.5
C(42')-C(43')-C(44')	111.6(18)	H(50B)-C(50)-H(50C)	109.5
C(42')-C(43')-H(43C)	109.3	C(46')-C(45')-C(29)	118(2)
C(44')-C(43')-H(43C)	109.3	C(46')-C(45')-H(45C)	107.7
C(42')-C(43')-H(43D)	109.3	C(29)-C(45')-H(45C)	107.7
C(44')-C(43')-H(43D)	109.3	C(46')-C(45')-H(45D)	107.7
H(43C)-C(43')-H(43D)	108.0	C(29)-C(45')-H(45D)	107.7
C(43')-C(44')-H(44D)	109.5	H(45C)-C(45')-H(45D)	107.1
C(43')-C(44')-H(44E)	109.5	C(45')-C(46')-C(47')	113(2)
H(44D)-C(44')-H(44E)	109.5	C(45')-C(46')-H(46C)	108.9
C(43')-C(44')-H(44F)	109.5	C(47')-C(46')-H(46C)	108.9
H(44D)-C(44')-H(44F)	109.5	C(45')-C(46')-H(46D)	108.9
H(44E)-C(44')-H(44F)	109.5	C(47')-C(46')-H(46D)	108.9
C(37)-C(38)-C(26)	122.0(6)	H(46C)-C(46')-H(46D)	107.7
C(37)-C(38)-H(38)	119.0	C(48')-C(47')-C(46')	121(3)
C(26)-C(38)-H(38)	119.0	C(48')-C(47')-H(47C)	107.1
C(46)-C(45)-C(29)	121.0(17)	C(46')-C(47')-H(47C)	107.1
C(46)-C(45)-H(45A)	107.1	C(48')-C(47')-H(47D)	107.1
C(29)-C(45)-H(45A)	107.1	C(46')-C(47')-H(47D)	107.1
C(46)-C(45)-H(45B)	107.1	H(47C)-C(47')-H(47D)	106.8

C(47')-C(48')-C(49')	130(4)	N(9)-C(61)-C(60)	114.7(6)
C(47')-C(48')-H(48C)	104.7	C(61)-C(62)-C(63)	119.9(7)
C(49')-C(48')-H(48C)	104.7	C(61)-C(62)-H(62)	120.0
C(47')-C(48')-H(48D)	104.7	C(63)-C(62)-H(62)	120.0
C(49')-C(48')-H(48D)	104.7	C(64)-C(63)-C(62)	119.4(7)
H(48C)-C(48')-H(48D)	105.7	C(64)-C(63)-H(63)	120.3
C(50')-C(49')-C(48')	142(5)	C(62)-C(63)-H(63)	120.3
C(50')-C(49')-H(49C)	101.6	C(65)-C(64)-C(63)	118.9(7)
C(48')-C(49')-H(49C)	101.6	C(65)-C(64)-H(64)	120.5
C(50')-C(49')-H(49D)	101.6	C(63)-C(64)-H(64)	120.5
C(48')-C(49')-H(49D)	101.6	N(9)-C(65)-C(64)	122.8(6)
H(49C)-C(49')-H(49D)	104.6	N(9)-C(65)-H(65)	118.6
C(49')-C(50')-H(50D)	109.5	C(64)-C(65)-H(65)	118.6
C(49')-C(50')-H(50E)	109.5	N(10)-C(66)-C(67)	124.3(7)
H(50D)-C(50')-H(50E)	109.5	N(10)-C(66)-H(66)	117.9
C(49')-C(50')-H(50F)	109.5	C(67)-C(66)-H(66)	117.9
H(50D)-C(50')-H(50F)	109.5	C(66)-C(67)-C(68)	117.5(8)
H(50E)-C(50')-H(50F)	109.5	C(66)-C(67)-H(67)	121.2
N(7)-C(51)-C(52)	123.0(6)	C(68)-C(67)-H(67)	121.2
N(7)-C(51)-H(51)	118.5	C(69)-C(68)-C(67)	118.9(8)
C(52)-C(51)-H(51)	118.5	C(69)-C(68)-H(68)	120.6
C(51)-C(52)-C(53)	118.2(7)	C(67)-C(68)-H(68)	120.6
C(51)-C(52)-H(52)	120.9	C(70)-C(69)-C(68)	120.1(7)
C(53)-C(52)-H(52)	120.9	C(70)-C(69)-H(69)	119.9
C(54)-C(53)-C(52)	120.4(7)	C(68)-C(69)-H(69)	119.9
C(54)-C(53)-H(53)	119.8	N(10)-C(70)-C(69)	120.9(7)
C(52)-C(53)-H(53)	119.8	N(10)-C(70)-C(71)	115.2(6)
C(53)-C(54)-C(55)	119.5(6)	C(69)-C(70)-C(71)	123.9(6)
C(53)-C(54)-H(54)	120.3	N(11)-C(71)-C(72)	121.7(7)
C(55)-C(54)-H(54)	120.3	N(11)-C(71)-C(70)	115.0(6)
C(54)-C(55)-N(7)	119.8(6)	C(72)-C(71)-C(70)	123.3(7)
C(54)-C(55)-C(56)	124.9(6)	C(73)-C(72)-C(71)	119.7(7)
N(7)-C(55)-C(56)	115.3(6)	C(73)-C(72)-H(72)	120.1
N(8)-C(56)-C(57)	119.8(6)	C(71)-C(72)-H(72)	120.1
N(8)-C(56)-C(55)	112.9(5)	C(72)-C(73)-C(74)	118.9(6)
C(57)-C(56)-C(55)	127.3(6)	C(72)-C(73)-H(73)	120.6
C(58)-C(57)-C(56)	120.2(6)	C(74)-C(73)-H(73)	120.6
C(58)-C(57)-H(57)	119.9	C(73)-C(74)-C(75)	118.8(7)
C(56)-C(57)-H(57)	119.9	C(73)-C(74)-H(74)	120.6
C(59)-C(58)-C(57)	117.7(6)	C(75)-C(74)-H(74)	120.6
C(59)-C(58)-C(32)	119.3(6)	N(11)-C(75)-C(74)	122.9(7)
C(57)-C(58)-C(32)	123.0(6)	N(11)-C(75)-H(75)	118.6
C(60)-C(59)-C(58)	120.4(6)	C(74)-C(75)-H(75)	118.6
C(60)-C(59)-H(59)	119.8	C(1)-N(1)-C(5)	118.4(6)
C(58)-C(59)-H(59)	119.8	C(1)-N(1)-Ru(1)	128.1(5)
N(8)-C(60)-C(59)	120.5(6)	C(5)-N(1)-Ru(1)	113.4(4)
N(8)-C(60)-C(61)	113.7(5)	C(10)-N(2)-C(6)	121.9(5)
C(59)-C(60)-C(61)	125.7(6)	C(10)-N(2)-Ru(1)	120.4(4)
C(62)-C(61)-N(9)	120.7(6)	C(6)-N(2)-Ru(1)	117.6(4)
C(62)-C(61)-C(60)	124.6(6)	C(15)-N(3)-C(11)	117.8(6)

C(15)-N(3)-Ru(1)	129.0(4)	N(8)-Ru(2)-N(9)	79.9(2)
C(11)-N(3)-Ru(1)	113.1(4)	N(12)-Ru(2)-N(9)	88.7(2)
C(20)-N(4)-C(16)	117.6(6)	N(7)-Ru(2)-N(9)	159.2(2)
C(20)-N(4)-Ru(1)	116.1(5)	N(10)-Ru(2)-N(9)	92.3(2)
C(16)-N(4)-Ru(1)	126.1(5)	N(8)-Ru(2)-N(11)	174.2(2)
C(25)-N(5)-C(21)	119.5(7)	N(12)-Ru(2)-N(11)	96.5(2)
C(25)-N(5)-Ru(1)	124.8(5)	N(7)-Ru(2)-N(11)	99.0(2)
C(21)-N(5)-Ru(1)	115.1(5)	N(10)-Ru(2)-N(11)	78.4(2)
O(1)-N(6)-O(2)	118.9(7)	N(9)-Ru(2)-N(11)	101.7(2)
O(1)-N(6)-Ru(1)	122.6(5)	F(5)-P(1)-F(3)	91.3(4)
O(2)-N(6)-Ru(1)	118.5(5)	F(5)-P(1)-F(2)	90.4(4)
C(51)-N(7)-C(55)	119.1(6)	F(3)-P(1)-F(2)	90.7(4)
C(51)-N(7)-Ru(2)	128.1(5)	F(5)-P(1)-F(6)	178.1(4)
C(55)-N(7)-Ru(2)	112.7(4)	F(3)-P(1)-F(6)	90.6(3)
C(56)-N(8)-C(60)	121.5(5)	F(2)-P(1)-F(6)	89.9(3)
C(56)-N(8)-Ru(2)	119.8(4)	F(5)-P(1)-F(4)	89.8(3)
C(60)-N(8)-Ru(2)	118.7(4)	F(3)-P(1)-F(4)	91.2(4)
C(65)-N(9)-C(61)	118.2(6)	F(2)-P(1)-F(4)	178.1(4)
C(65)-N(9)-Ru(2)	128.9(4)	F(6)-P(1)-F(4)	89.9(3)
C(61)-N(9)-Ru(2)	112.9(4)	F(5)-P(1)-F(1)	89.1(3)
C(66)-N(10)-C(70)	118.3(6)	F(3)-P(1)-F(1)	179.3(3)
C(66)-N(10)-Ru(2)	126.2(5)	F(2)-P(1)-F(1)	88.8(3)
C(70)-N(10)-Ru(2)	115.5(5)	F(6)-P(1)-F(1)	89.0(3)
C(75)-N(11)-C(71)	118.0(6)	F(4)-P(1)-F(1)	89.3(4)
C(75)-N(11)-Ru(2)	126.2(5)	F(9)-P(2)-F(8)	123.5(10)
C(71)-N(11)-Ru(2)	115.7(4)	F(9)-P(2)-F(11)	87.0(8)
O(3)-N(12)-O(4)	117.8(6)	F(8)-P(2)-F(11)	85.3(9)
O(3)-N(12)-Ru(2)	121.9(5)	F(9)-P(2)-F(7)	149.1(10)
O(4)-N(12)-Ru(2)	120.4(5)	F(8)-P(2)-F(7)	82.2(9)
N(2)-Ru(1)-N(6)	87.4(2)	F(11)-P(2)-F(7)	77.6(8)
N(2)-Ru(1)-N(1)	79.9(2)	F(9)-P(2)-F(12)	96.4(8)
N(6)-Ru(1)-N(1)	91.4(2)	F(8)-P(2)-F(12)	101.3(9)
N(2)-Ru(1)-N(5)	98.6(2)	F(11)-P(2)-F(12)	168.9(10)
N(6)-Ru(1)-N(5)	173.1(2)	F(7)-P(2)-F(12)	94.4(9)
N(1)-Ru(1)-N(5)	86.3(2)	F(9)-P(2)-F(10)	75.9(7)
N(2)-Ru(1)-N(3)	78.8(2)	F(8)-P(2)-F(10)	158.4(10)
N(6)-Ru(1)-N(3)	89.5(2)	F(11)-P(2)-F(10)	86.6(9)
N(1)-Ru(1)-N(3)	158.6(2)	F(7)-P(2)-F(10)	76.5(9)
N(5)-Ru(1)-N(3)	95.0(2)	F(12)-P(2)-F(10)	84.0(9)
N(2)-Ru(1)-N(4)	176.3(2)	F(11')-P(2')-F(8')	90.2(10)
N(6)-Ru(1)-N(4)	96.2(2)	F(11')-P(2')-F(7')	77.8(7)
N(1)-Ru(1)-N(4)	101.0(2)	F(8')-P(2')-F(7')	86.5(7)
N(5)-Ru(1)-N(4)	77.9(2)	F(11')-P(2')-F(10')	89.2(9)
N(3)-Ru(1)-N(4)	100.2(2)	F(8')-P(2')-F(10')	178.5(8)
N(8)-Ru(2)-N(12)	89.1(2)	F(7')-P(2')-F(10')	91.9(7)
N(8)-Ru(2)-N(7)	79.3(2)	F(11')-P(2')-F(12')	106.2(8)
N(12)-Ru(2)-N(7)	90.9(2)	F(8')-P(2')-F(12')	96.0(7)
N(8)-Ru(2)-N(10)	96.0(2)	F(7')-P(2')-F(12')	175.2(8)
N(12)-Ru(2)-N(10)	174.9(2)	F(10')-P(2')-F(12')	85.6(7)
N(7)-Ru(2)-N(10)	89.9(2)	F(11')-P(2')-F(9')	158.4(10)

F(8')-P(2')-F(9')	107.3(10)	F(10')-P(2')-F(9')	72.9(8)
F(7')-P(2')-F(9')	90.5(7)	F(12')-P(2')-F(9')	84.8(8)

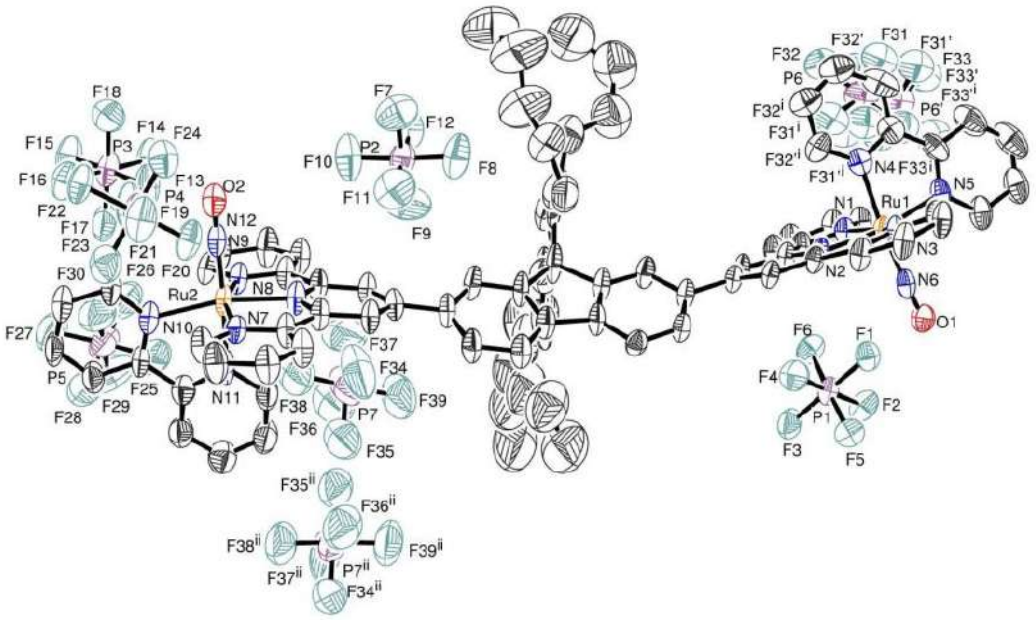

Empirical formula	$C_{75}H_{68}N_{12}O_2Ru_2$, 6($F_6P$)
Formula weight	2241.38
Temperature	100(2) K
Wavelength	0.71073 A
Crystal system, space group	Orthorhombic, P b c n
Unit cell dimensions	a = 16.992(3) A alpha = 90 deg.
	b = 51.812(11) A beta = 90 deg.
	c = 25.472(5) A gamma = 90 deg.
Volume	22425(8) A^3
Z, Calculated density	8, 1.328 Mg/m^3
Absorption coefficient	0.457 mm^-1
F(000)	8960
Crystal size	0.20 x 0.18 x 0.08 mm
Theta range for data collection	1.121 to 26.150 deg.

Limiting indices	-20<=h<=20, -61<=k<=63,
	-31<=l<=31
Reflections collected / unique	240214 / 22099 [R(int) = 0.0856]
Completeness to theta = 25.242	99.9 %
Refinement method	Full-matrix least-squares on F^2
Data / restraints / parameters	22099 / 485 / 1367
Goodness-of-fit on F^2	1.108
Final R indices [I>2sigma(I)]	R1 = 0.1024, wR2 = 0.2603
R indices (all data)	R1 = 0.1284, wR2 = 0.2812
Largest diff. peak and hole	3.952 and -0.603 e.A^-3

Atomic coordinates

U(eq) is defined as one third of the trace of the orthogonalized Uij tensor

	x	y	z	U(eq)
C(15)	9141(4)	5161(1)	6111(3)	48(2)
C(14)	9930(4)	5098(1)	6053(4)	59(2)
C(13)	10133(4)	4876(1	5775(4)	57(2)
C(12)	9545(4)	4716(1)	5580(3)	50(2)
C(11)	8765(4)	4790(1)	5641(3)	39(2)
C(10)	8095(4)	4629(1)	5470(3)	39(2)
C(9)	8119(4)	4386(1)	5252(3)	42(2)
C(8)	7421(4)	4251(1)	5152(3)	43(2)
C(7)	6701(4)	4366(1)	5280(3)	45(2)
C(6)	6697(4)	4615(1)	5483(3)	42(2)
C(5)	6001(4)	4771(1)	5631(3)	45(2)
C(4)	5232(4)	4695(2)	5539(4)	58(2)
C(3)	4616(4)	4855(2)	5688(4)	65(2)
C(2)	4783(4)	5085(2)	5935(4)	57(2)
C(1)	5559(4)	5158(1)	6014(3)	47(2)
C(25)	7342(5)	5654(2)	6248(4)	64(2)
C(24)	7275(6)	5854(2)	6613(5)	78(3)
C(23)	7186(8)	5802(2)	7119(6)	102(4)
C(22)	7177(7)	5546(2)	7286(4)	89(3)
C(21)	7256(5)	5348(2)	6920(3)	60(2)

C(20)	7282(5)	5071(2)	7054(4)	58(2)
C(19)	7254(6)	4979(3)	7557(4)	87(3)
C(18)	7293(7)	4710(2)	7647(5)	88(3)
C(17)	7341(6)	4550(2)	7226(4)	76(3)
C(16)	7365(5)	4652(2)	6741(4)	61(2)
C(26)	7450(4)	3987(1)	4919(3)	47(2)
C(27)	8018(4)	3933(1)	4550(3)	49(2)
C(28)	8092(4)	3685(1)	4324(3)	47(2)
C(29)	7598(4)	3492(1)	4525(4)	52(2)
C(30)	7585(5)	3212(1)	4421(4)	57(2)
C(31)	8044(5)	3063(2)	4090(4)	62(2)
C(32)	7937(5)	2798(2)	4085(4)	64(2)
C(33)	7397(5)	2678(1)	4424(4)	57(2)
C(34)	6927(5)	2831(1)	4753(4)	62(2)
C(35)	7027(5)	3096(1)	4750(4)	59(2)
C(37)	7028(4)	3546(1)	4908(4)	55(2)
C(38)	6934(4)	3792(1)	5104(4)	55(2)
C(39)	6725(14)	3250(5)	5667(6)	77(5)
C(40)	7581(14)	3231(6)	5851(8)	98(6)
C(41)	7715(16)	3084(5)	6380(9)	148(7)
C(42)	7059(19)	2990(8)	6763(11)	226(11)
C(43)	7060(30)	2920(9)	7359(12)	272(15)
C(44)	6390(30)	2792(9)	7601(12)	290(20)
C(39')	6530(40)	3227(1)	5654(11)	96(11)
C(40')	7370(40)	3203(1)	5893(15)	111(9)
C(41')	7300(30)	3233(8)	6507(16)	133(9)
C(42')	7000(40)	3483(8)	6789(17)	152(14)
C(43')	6710(40)	3492(1)	7376(18)	167(16)
C(44')	6600(50)	3235(1)	7620(20)	210(20)
C(36)	6592(5)	3297(1)	5077(5)	70(3)
C(45)	5743(6)	3312(6)	4920(5)	90(5)
C(46)	5588(8)	3347(3)	4360(6)	102(6)
C(47)	4716(8)	3335(5)	4151(6)	129(7)
C(48)	4572(9)	3383(7)	3569(7)	194(10)
C(49)	3710(13)	3364(7)	3346(9)	219(11)
C(50)	3299(19)	3451(7)	2871(11)	310(20)
C(45')	5714(6)	3305(7)	5024(6)	70(3)
C(46')	5409(9)	3371(6)	4504(8)	90(8)
C(47')	4548(11)	3289(9)	4348(7)	124(9)
C(48')	4315(17)	3302(6)	3772(7)	176(10)
C(49')	4720(20)	3507(6)	3404(10)	210(13)
C(50')	4490(30)	3660(7)	2944(12)	250(30)
C(51)	8608(5)	1344(2)	3787(4)	63(2)
C(52)	9363(5)	1394(2)	3645(4)	74(3)
C(53)	9654(5)	1645(2)	3698(4)	68(2)
C(54)	9167(5)	1835(2)	3892(4)	65(2)
C(55)	8406(5)	1778(1)	4036(4)	58(2)
C(56)	7835(5)	1971(1)	4232(4)	53(2)
C(57)	7932(5)	2235(1)	4272(4)	57(2)
C(58)	7303(5)	2392(1)	4422(4)	54(2)

C(59)	6588(4)	2275(1)	4546(3)	54(2)
C(60)	6510(4)	2009(1)	4519(4)	55(2)
C(61)	5780(4)	1858(1)	4610(4)	55(2)
C(62)	5101(5)	1958(2)	4795(4)	71(3)
C(63)	4452(6)	1798(2)	4858(5)	83(3)
C(64)	4501(5)	1539(2)	4722(5)	75(3)
C(65)	5213(5)	1445(1)	4544(4)	57(2)
C(66)	6846(5)	892(1)	230(4)	60(2)
C(67)	6710(5)	652(2)	000(4)	66(2)
C(68)	6445(6)	644(2)	499(4)	77(3)
C(69)	6320(6)	871(2)	233(4)	69(2)
C(70)	6478(5)	1106(1)	3470(4)	54(2)
C(71)	6354(5)	1357(2)	3202(4)	56(2)
C(72)	6057(6)	1383(2)	2720(4)	70(2)
C(73)	5977(6)	1626(2)	2493(4)	78(3)
C(74)	6220(6)	1837(2)	2778(4)	78(3)
C(75)	6508(6)	1803(2)	3270(4)	75(3)
F(1)	8126(2)	4997(1)	4480(2)	58(1)
F(2)	7195(3)	5121(1)	3897(2)	66(1)
F(3)	7114(3)	4710(1)	3598(2)	74(1)
F(4)	8082(4)	4595(1)	4169(2)	76(2)
F(5)	8291(2)	4927(1)	3611(2)	59(1)
F(6)	6961(2)	4794(1)	4462(2)	64(1)
F(7)	5775(4)	2366(2)	6545(3)	119(2)
F(8)	5606(4)	2743(1)	6152(3)	115(2)
F(9)	4829(5)	2544(2)	5558(3)	143(3)
F(10)	4982(5)	2169(1)	5991(4)	134(3)
F(11)	6023(5)	2391(2)	5691(3)	127(3)
F(12)	4559(3)	2524(1)	6408(3)	91(2)
F(13)	6221(3)	1034(1)	5370(3)	97(2)
F(14)	4976(3)	1065(1)	5685(3)	90(2)
F(15)	4845(3)	628(1)	607(3)	85(2)
F(16)	6113(3)	598(1)	322(2)	81(2)
F(17)	5242(4)	854(1)	914(3)	92(2)
F(18)	5825(3)	793(1)	091(2)	85(2)
F(19)	10000(3)	919(1)	5017(3)	82(2)
F(20)	8989(3)	1198(1)	4864(2)	75(2)
F(21)	8137(2)	893(1)	146(3)	75(2)
F(22)	9143(3)	619(1)	297(2)	70(1)
F(23)	8993(4)	797(1)	514(2)	86(2)
F(24)	9138(3)	1017(1)	5660(2)	81(2)
F(25)	4438(5)	1241(1)	3460(3)	122(3)
F(26)	3650(5)	1060(2)	4042(3)	132(3)
F(27)	3782(5)	670(1)	597(3)	127(3)
F(28)	4549(5)	875(1)	022(3)	116(2)
F(29)	3359(5)	1026(2)	3157(4)	167(4)
F(30)	4813(5)	887(2)	880(3)	121(3)
N(3)	8571(3)	5009(1)	5903(2)	41(1)
N(2)	7390(3)	4737(1)	5571(2)	41(1)
N(1)	6152(3)	5003(1)	5863(2)	43(1)

N(5)	7321(3)	5404(1)	6410(3)	50(2)
N(4)	7330(3)	4906(1)	6644(3)	49(1)
N(6)	7361(3)	5261(1)	5336(3)	45(1)
N(7)	8109(4)	1530(1)	3976(3)	55(2)
N(8)	7134(4)	1868(1)	4363(3)	55(2)
N(9)	5839(4)	1599(1)	4486(3)	54(2)
N(10)	6739(4)	1115(1)	3955(3)	53(2)
N(11)	6604(4)	1566(1)	3507(3)	58(2)
N(12)	7269(4)	1404(1)	4885(3)	53(2)
O(1)	7333(3)	5390(1)	4969(2)	53(1)
O(2)	7457(3)	1357(1)	5305(3)	62(2)
P(1)	7627(1)	4853(1)	4031(1)	45(1)
P(2)	5304(2)	2457(1)	6051(1)	74(1)
P(3)	5542(1)	832(1)	505(1)	63(1)
P(4)	9078(1)	909(1)	083(1)	57(1)
P(5)	4051(2)	963(1)	538(1)	94(1)
P(7)	4669(7)	2332(2)	3382(4)	144(3)
F(34)	5537(16)	2341(3)	3591(9)	204(7)
F(35)	5052(12)	2326(3)	2785(6)	146(5)
F(36)	3746(13)	2319(4)	3132(8)	166(6)
F(37)	4110(20)	2315(4)	3943(7)	221(9)
F(38)	4693(12)	2039(3)	3453(7)	150(5)
F(39)	4644(15)	2641(3)	3327(8)	183(7)
Ru(1)	7363(1)	5082(1)	5912(1)	40(1)
Ru(2)	6969(1)	1490(1)	4247(1)	50(1)
P(6)	5000	5136(2)	7500	90(2)
F(31)	5692(5)	5138(2)	7923(4)	100(2)
F(32)	4541(5)	4919(2)	7836(4)	95(2)
F(33)	4556(5)	5353(3)	7824(4)	101(2)
P(6')	5000	5357(4)	7500	99(2)
F(31')	5709(10)	5363(5)	7902(8)	100(3)
F(32')	4566(13)	5126(5)	7829(9)	100(3)
F(33')	4560(13)	557(5)	7882(9)	110(4)

Bond lengths

C(15)-N(3)	1.354(9)	C(9)-C(8)	1.401(9)
C(15)-C(14)	1.388(10)	C(9)-H(9)	0.9500
C(15)-H(15)	0.9500	C(8)-C(7)	1.399(9)
C(14)-C(13)	1.395(11)	C(8)-C(26)	1.490(9)
C(14)-H(14)	0.9500	C(7)-C(6)	1.391(9)
C(13)-C(12)	1.390(10)	C(7)-H(7)	0.9500
C(13)-H(13)	0.9500	C(6)-N(2)	1.354(8)
C(12)-C(11)	1.388(9)	C(6)-C(5)	1.480(9)
C(12)-H(12)	0.9500	C(5)-N(1)	1.365(9)
C(11)-N(3)	1.359(8)	C(5)-C(4)	1.384(10)
C(11)-C(10)	1.478(9)	C(4)-C(3)	1.391(11)
C(10)-N(2)	1.346(8)	C(4)-H(4)	0.9500
C(10)-C(9)	1.376(9)	C(3)-C(2)	1.374(11)

C(3)-H(3)	0.9500	C(39)-H(39A)	0.9900
C(2)-C(1)	1.386(10)	C(39)-H(39B)	0.9900
C(2)-H(2)	0.9500	C(40)-C(41)	1.57(3)
C(1)-N(1)	1.347(9)	C(40)-H(40A)	0.9900
C(1)-H(1)	0.9500	C(40)-H(40B)	0.9900
C(25)-N(5)	1.363(10)	C(41)-C(42)	1.558(18)
C(25)-C(24)	1.395(12)	C(41)-H(41A)	0.9900
C(25)-H(25)	0.9500	C(41)-H(41B)	0.9900
C(24)-C(23)	1.327(17)	C(42)-C(43)	1.562(18)
C(24)-H(24)	0.9500	C(42)-H(42A)	0.9900
C(23)-C(22)	1.392(17)	C(42)-H(42B)	0.9900
C(23)-H(23)	0.9500	C(43)-C(44)	1.45(4)
C(22)-C(21)	1.392(12)	C(43)-H(43A)	0.9900
C(22)-H(22)	0.9500	C(43)-H(43B)	0.9900
C(21)-N(5)	1.338(11)	C(44)-H(44A)	0.9800
C(21)-C(20)	1.474(12)	C(44)-H(44B)	0.9800
C(20)-N(4)	1.350(10)	C(44)-H(44C)	0.9800
C(20)-C(19)	1.368(14)	C(39')-C(36)	1.52(2)
C(19)-C(18)	1.415(16)	C(39')-C(40')	1.558(19)
C(19)-H(19)	0.9500	C(39')-H(39C)	0.9900
C(18)-C(17)	1.358(15)	C(39')-H(39D)	0.9900
C(18)-H(18)	0.9500	C(40')-C(41')	1.58(3)
C(17)-C(16)	1.346(13)	C(40')-H(40C)	0.9900
C(17)-H(17)	0.9500	C(40')-H(40D)	0.9900
C(16)-N(4)	1.344(10)	C(41')-C(42')	1.568(19)
C(16)-H(16)	0.9500	C(41')-H(41C)	0.9900
C(26)-C(27)	1.375(10)	C(41')-H(41D)	0.9900
C(26)-C(38)	1.418(9)	C(42')-C(43')	1.571(19)
C(27)-C(28)	1.414(10)	C(42')-H(42C)	0.9900
C(27)-H(27)	0.9500	C(42')-H(42D)	0.9900
C(28)-C(29)	1.400(10)	C(43')-C(44')	1.49(4)
C(28)-H(28)	0.9500	C(43')-H(43C)	0.9900
C(29)-C(37)	1.403(11)	C(43')-H(43D)	0.9900
C(29)-C(30)	1.478(9)	C(44')-H(44D)	0.9800
C(30)-C(31)	1.384(11)	C(44')-H(44E)	0.9800
C(30)-C(35)	1.401(11)	C(44')-H(44F)	0.9800
C(31)-C(32)	1.382(11)	C(36)-C(45)	1.499(13)
C(31)-H(31)	0.9500	C(36)-C(45')	1.499(13)
C(32)-C(33)	1.406(12)	C(45)-C(46)	1.462(15)
C(32)-H(32)	0.9500	C(45)-H(45A)	0.9900
C(33)-C(34)	1.403(11)	C(45)-H(45B)	0.9900
C(33)-C(58)	1.490(9)	C(46)-C(47)	1.575(14)
C(34)-C(35)	1.385(9)	C(46)-H(46A)	0.9900
C(34)-H(34)	0.9500	C(46)-H(46B)	0.9900
C(35)-C(36)	1.526(11)	C(47)-C(48)	1.523(7)
C(37)-C(38)	1.379(10)	C(47)-H(47A)	0.9900
C(37)-C(36)	1.548(10)	C(47)-H(47B)	0.9900
C(38)-H(38)	0.9500	C(48)-C(49)	1.575(16)
C(39)-C(40)	1.530(9)	C(48)-H(48A)	0.9900
C(39)-C(36)	1.540(17)	C(48)-H(48B)	0.9900

C(49)-C(50)	1.47(2)	C(64)-C(65)	1.381(12)
C(49)-H(49A)	0.9900	C(64)-H(64)	0.9500
C(49)-H(49B)	0.9900	C(65)-N(9)	1.336(9)
C(50)-H(50A)	0.9800	C(65)-H(65)	0.9500
C(50)-H(50B)	0.9800	C(66)-N(10)	1.362(10)
C(50)-H(50C)	0.9800	C(66)-C(67)	1.393(11)
C(45')-C(46')	1.462(15)	C(66)-H(66)	0.9500
C(45')-H(45C)	0.9900	C(67)-C(68)	1.354(13)
C(45')-H(45D)	0.9900	C(67)-H(67)	0.9500
C(46')-C(47')	1.575(14)	C(68)-C(69)	1.374(12)
C(46')-H(46C)	0.9900	C(68)-H(68)	0.9500
C(46')-H(46D)	0.9900	C(69)-C(70)	1.388(11)
C(47')-C(48')	1.523(7)	C(69)-H(69)	0.9500
C(47')-H(47C)	0.9900	C(70)-N(10)	1.315(11)
C(47')-H(47D)	0.9900	C(70)-C(71)	1.483(11)
C(48')-C(49')	1.575(16)	C(71)-C(72)	1.333(12)
C(48')-H(48C)	0.9900	C(71)-N(11)	1.396(10)
C(48')-H(48D)	0.9900	C(72)-C(73)	1.394(13)
C(49')-C(50')	1.47(2)	C(72)-H(72)	0.9500
C(49')-H(49C)	0.9900	C(73)-C(74)	1.374(13)
C(49')-H(49D)	0.9900	C(73)-H(73)	0.9500
C(50')-H(50D)	0.9800	C(74)-C(75)	1.356(13)
C(50')-H(50E)	0.9800	C(74)-H(74)	0.9500
C(50')-H(50F)	0.9800	C(75)-N(11)	1.379(11)
C(51)-C(52)	1.357(12)	C(75)-H(75)	0.9500
C(51)-N(7)	1.371(10)	F(1)-P(1)	1.607(5)
C(51)-H(51)	0.9500	F(2)-P(1)	1.608(5)
C(52)-C(53)	1.400(12)	F(3)-P(1)	1.588(5)
C(52)-H(52)	0.9500	F(4)-P(1)	1.584(5)
C(53)-C(54)	1.375(11)	F(5)-P(1)	1.601(5)
C(53)-H(53)	0.9500	F(6)-P(1)	1.603(5)
C(54)-C(55)	1.377(12)	F(7)-P(2)	1.563(7)
C(54)-H(54)	0.9500	F(8)-P(2)	1.592(7)
C(55)-N(7)	1.390(9)	F(9)-P(2)	1.560(7)
C(55)-C(56)	1.479(11)	F(10)-P(2)	1.594(7)
C(56)-N(8)	1.346(10)	F(11)-P(2)	1.564(7)
C(56)-C(57)	1.385(10)	F(12)-P(2)	1.598(7)
C(57)-C(58)	1.395(11)	F(13)-P(3)	1.596(5)
C(57)-H(57)	0.9500	F(14)-P(3)	1.609(6)
C(58)-C(59)	1.394(11)	F(15)-P(3)	1.611(5)
C(59)-C(60)	1.387(9)	F(16)-P(3)	1.620(5)
C(59)-H(59)	0.9500	F(17)-P(3)	1.593(7)
C(60)-N(8)	1.347(10)	F(18)-P(3)	1.582(6)
C(60)-C(61)	1.484(10)	F(19)-P(4)	1.577(5)
C(61)-C(62)	1.350(11)	F(20)-P(4)	1.604(5)
C(61)-N(9)	1.386(9)	F(21)-P(4)	1.610(5)
C(62)-C(63)	1.388(12)	F(22)-P(4)	1.603(5)
C(62)-H(62)	0.9500	F(23)-P(4)	1.570(7)
C(63)-C(64)	1.388(12)	F(24)-P(4)	1.575(6)
C(63)-H(63)	0.9500	F(25)-P(5)	1.596(7)

F(26)-P(5)	1.538(9)	P(7)-F(38)	1.526(18)
F(27)-P(5)	1.592(7)	P(7)-F(34)	1.57(2)
F(28)-P(5)	1.628(9)	P(7)-F(39)	1.609(18)
F(29)-P(5)	1.557(9)	P(7)-F(35)	1.65(2)
F(30)-P(5)	1.612(8)	P(7)-F(36)	1.69(2)
N(3)-Ru(1)	2.087(5)	P(7)-F(37)	1.72(3)
N(2)-Ru(1)	1.988(5)	P(6)-F(33)	1.587(12)
N(1)-Ru(1)	2.102(5)	P(6)-F(33)#1	1.587(13)
N(5)-Ru(1)	2.095(6)	P(6)-F(31)	1.595(9)
N(4)-Ru(1)	2.074(7)	P(6)-F(31)#1	1.595(9)
N(6)-O(1)	1.147(8)	P(6)-F(32)#1	1.613(11)
N(6)-Ru(1)	1.739(7)	P(6)-F(32)	1.613(11)
N(7)-Ru(2)	2.067(7)	P(6')-F(31')#1	1.581(15)
N(8)-Ru(2)	2.002(6)	P(6')-F(31')	1.581(15)
N(9)-Ru(2)	2.091(6)	P(6')-F(33')#1	1.60(2)
N(10)-Ru(2)	2.116(6)	P(6')-F(33')	1.60(2)
N(11)-Ru(2)	2.023(8)	P(6')-F(32')	1.64(2)
N(12)-O(2)	1.141(9)	P(6')-F(32')#1	1.64(2)
N(12)-Ru(2)	1.761(8)		

Angles

N(3)-C(15)-C(14)	120.8(7)	C(8)-C(7)-H(7)	120.5
N(3)-C(15)-H(15)	119.6	N(2)-C(6)-C(7)	119.3(6)
C(14)-C(15)-H(15)	119.6	N(2)-C(6)-C(5)	113.6(5)
C(15)-C(14)-C(13)	119.2(7)	C(7)-C(6)-C(5)	127.1(6)
C(15)-C(14)-H(14)	120.4	N(1)-C(5)-C(4)	120.1(6)
C(13)-C(14)-H(14)	120.4	N(1)-C(5)-C(6)	116.1(6)
C(12)-C(13)-C(14)	119.6(7)	C(4)-C(5)-C(6)	123.8(6)
C(12)-C(13)-H(13)	120.2	C(5)-C(4)-C(3)	119.6(7)
C(14)-C(13)-H(13)	120.2	C(5)-C(4)-H(4)	120.2
C(11)-C(12)-C(13)	118.9(7)	C(3)-C(4)-H(4)	120.2
C(11)-C(12)-H(12)	120.5	C(2)-C(3)-C(4)	119.1(7)
C(13)-C(12)-H(12)	120.5	C(2)-C(3)-H(3)	120.4
N(3)-C(11)-C(12)	121.1(6)	C(4)-C(3)-H(3)	120.4
N(3)-C(11)-C(10)	115.5(5)	C(3)-C(2)-C(1)	120.1(7)
C(12)-C(11)-C(10)	123.2(6)	C(3)-C(2)-H(2)	119.9
N(2)-C(10)-C(9)	119.0(6)	C(1)-C(2)-H(2)	119.9
N(2)-C(10)-C(11)	113.2(6)	N(1)-C(1)-C(2)	120.3(7)
C(9)-C(10)-C(11)	127.7(6)	N(1)-C(1)-H(1)	119.8
C(10)-C(9)-C(8)	120.3(6)	C(2)-C(1)-H(1)	119.8
C(10)-C(9)-H(9)	119.9	N(5)-C(25)-C(24)	120.2(10)
C(8)-C(9)-H(9)	119.9	N(5)-C(25)-H(25)	119.9
C(7)-C(8)-C(9)	119.0(6)	C(24)-C(25)-H(25)	119.9
C(7)-C(8)-C(26)	120.8(6)	C(23)-C(24)-C(25)	120.3(10)
C(9)-C(8)-C(26)	120.1(6)	C(23)-C(24)-H(24)	119.8
C(6)-C(7)-C(8)	119.1(6)	C(25)-C(24)-H(24)	119.8
C(6)-C(7)-H(7)	120.5	C(24)-C(23)-C(22)	119.5(10)

C(24)-C(23)-H(23)	120.3	C(34)-C(35)-C(30)	120.8(7)
C(22)-C(23)-H(23)	120.3	C(34)-C(35)-C(36)	128.1(7)
C(23)-C(22)-C(21)	119.9(11)	C(30)-C(35)-C(36)	111.2(6)
C(23)-C(22)-H(22)	120.1	C(38)-C(37)-C(29)	121.0(7)
C(21)-C(22)-H(22)	120.1	C(38)-C(37)-C(36)	127.9(7)
N(5)-C(21)-C(22)	119.9(9)	C(29)-C(37)-C(36)	111.0(6)
N(5)-C(21)-C(20)	115.6(7)	C(37)-C(38)-C(26)	117.9(7)
C(22)-C(21)-C(20)	124.5(9)	C(37)-C(38)-H(38)	121.0
N(4)-C(20)-C(19)	120.5(9)	C(26)-C(38)-H(38)	121.1
N(4)-C(20)-C(21)	116.0(8)	C(40)-C(39)-C(36)	116.6(15)
C(19)-C(20)-C(21)	123.5(9)	C(40)-C(39)-H(39A)	108.1
C(20)-C(19)-C(18)	119.5(10)	C(36)-C(39)-H(39A)	108.1
C(20)-C(19)-H(19)	120.3	C(40)-C(39)-H(39B)	108.1
C(18)-C(19)-H(19)	120.3	C(36)-C(39)-H(39B)	108.1
C(17)-C(18)-C(19)	118.5(10)	H(39A)-C(39)-H(39B)	107.3
C(17)-C(18)-H(18)	120.7	C(39)-C(40)-C(41)	115.6(17)
C(19)-C(18)-H(18)	120.7	C(39)-C(40)-H(40A)	108.4
C(16)-C(17)-C(18)	119.2(10)	C(41)-C(40)-H(40A)	108.4
C(16)-C(17)-H(17)	120.4	C(39)-C(40)-H(40B)	108.4
C(18)-C(17)-H(17)	120.4	C(41)-C(40)-H(40B)	108.4
N(4)-C(16)-C(17)	123.6(9)	H(40A)-C(40)-H(40B)	107.4
N(4)-C(16)-H(16)	118.2	C(42)-C(41)-C(40)	126(2)
C(17)-C(16)-H(16)	118.2	C(42)-C(41)-H(41A)	105.8
C(27)-C(26)-C(38)	120.9(6)	C(40)-C(41)-H(41A)	105.8
C(27)-C(26)-C(8)	119.0(6)	C(42)-C(41)-H(41B)	105.8
C(38)-C(26)-C(8)	120.0(7)	C(40)-C(41)-H(41B)	105.8
C(26)-C(27)-C(28)	121.8(6)	H(41A)-C(41)-H(41B)	106.2
C(26)-C(27)-H(27)	119.1	C(41)-C(42)-C(43)	133(3)
C(28)-C(27)-H(27)	119.1	C(41)-C(42)-H(42A)	104.0
C(29)-C(28)-C(27)	116.5(6)	C(43)-C(42)-H(42A)	104.0
C(29)-C(28)-H(28)	121.8	C(41)-C(42)-H(42B)	104.0
C(27)-C(28)-H(28)	121.8	C(43)-C(42)-H(42B)	104.0
C(28)-C(29)-C(37)	121.7(6)	H(42A)-C(42)-H(42B)	105.5
C(28)-C(29)-C(30)	130.2(7)	C(44)-C(43)-C(42)	121(3)
C(37)-C(29)-C(30)	108.1(6)	C(44)-C(43)-H(43A)	107.1
C(31)-C(30)-C(35)	120.4(7)	C(42)-C(43)-H(43A)	107.1
C(31)-C(30)-C(29)	130.5(8)	C(44)-C(43)-H(43B)	107.1
C(35)-C(30)-C(29)	108.9(7)	C(42)-C(43)-H(43B)	107.1
C(32)-C(31)-C(30)	119.1(8)	H(43A)-C(43)-H(43B)	106.8
C(32)-C(31)-H(31)	120.5	C(43)-C(44)-H(44A)	109.5
C(30)-C(31)-H(31)	120.5	C(43)-C(44)-H(44B)	109.5
C(31)-C(32)-C(33)	121.3(8)	H(44A)-C(44)-H(44B)	109.5
C(31)-C(32)-H(32)	119.4	C(43)-C(44)-H(44C)	109.5
C(33)-C(32)-H(32)	119.4	H(44A)-C(44)-H(44C)	109.5
C(34)-C(33)-C(32)	119.3(7)	H(44B)-C(44)-H(44C)	109.5
C(34)-C(33)-C(58)	120.1(7)	C(36)-C(39')-C(40')	110(4)
C(32)-C(33)-C(58)	120.6(7)	C(36)-C(39')-H(39C)	109.8
C(35)-C(34)-C(33)	119.1(8)	C(40')-C(39')-H(39C)	109.8
C(35)-C(34)-H(34)	120.4	C(36)-C(39')-H(39D)	109.7
C(33)-C(34)-H(34)	120.4	C(40')-C(39')-H(39D)	109.7

H(39C)-C(39')-H(39D)	108.2	C(47)-C(46)-H(46A)	107.4
C(39')-C(40')-C(41')	108(2)	C(45)-C(46)-H(46B)	107.4
C(39')-C(40')-H(40C)	110.1	C(47)-C(46)-H(46B)	107.4
C(41')-C(40')-H(40C)	110.1	H(46A)-C(46)-H(46B)	106.9
C(39')-C(40')-H(40D)	110.1	C(48)-C(47)-C(46)	118.3(10)
C(41')-C(40')-H(40D)	110.1	C(48)-C(47)-H(47A)	107.7
H(40C)-C(40')-H(40D)	108.4	C(46)-C(47)-H(47A)	107.7
C(42')-C(41')-C(40')	124(3)	C(48)-C(47)-H(47B)	107.7
C(42')-C(41')-H(41C)	106.3	C(46)-C(47)-H(47B)	107.7
C(40')-C(41')-H(41C)	106.3	H(47A)-C(47)-H(47B)	107.1
C(42')-C(41')-H(41D)	106.3	C(47)-C(48)-C(49)	119.3(11)
C(40')-C(41')-H(41D)	106.3	C(47)-C(48)-H(48A)	107.5
H(41C)-C(41')-H(41D)	106.4	C(49)-C(48)-H(48A)	107.5
C(41')-C(42')-C(43')	124(3)	C(47)-C(48)-H(48B)	107.5
C(41')-C(42')-H(42C)	106.3	C(49)-C(48)-H(48B)	107.5
C(43')-C(42')-H(42C)	106.3	H(48A)-C(48)-H(48B)	107.0
C(41')-C(42')-H(42D)	106.3	C(50)-C(49)-C(48)	136(2)
C(43')-C(42')-H(42D)	106.3	C(50)-C(49)-H(49A)	103.1
H(42C)-C(42')-H(42D)	106.4	C(48)-C(49)-H(49A)	103.2
C(44')-C(43')-C(42')	114(3)	C(50)-C(49)-H(49B)	103.2
C(44')-C(43')-H(43C)	108.7	C(48)-C(49)-H(49B)	103.1
C(42')-C(43')-H(43C)	108.7	H(49A)-C(49)-H(49B)	105.1
C(44')-C(43')-H(43D)	108.7	C(49)-C(50)-H(50A)	109.5
C(42')-C(43')-H(43D)	108.7	C(49)-C(50)-H(50B)	109.5
H(43C)-C(43')-H(43D)	107.6	H(50A)-C(50)-H(50B)	109.5
C(43')-C(44')-H(44D)	109.5	C(49)-C(50)-H(50C)	109.5
C(43')-C(44')-H(44E)	109.5	H(50A)-C(50)-H(50C)	109.5
H(44D)-C(44')-H(44E)	109.5	H(50B)-C(50)-H(50C)	109.5
C(43')-C(44')-H(44F)	109.5	C(46')-C(45')-C(36)	116.1(10)
H(44D)-C(44')-H(44F)	109.5	C(46')-C(45')-H(45C)	108.3
H(44E)-C(44')-H(44F)	109.5	C(36)-C(45')-H(45C)	108.3
C(45')-C(36)-C(39')	91(3)	C(46')-C(45')-H(45D)	108.3
C(45)-C(36)-C(35)	110.8(12)	C(36)-C(45')-H(45D)	108.3
C(45')-C(36)-C(35)	116.8(14)	H(45C)-C(45')-H(45D)	107.4
C(39')-C(36)-C(35)	113(3)	C(45')-C(46')-C(47')	119.7(11)
C(45)-C(36)-C(39)	114.2(11)	C(45')-C(46')-H(46C)	107.4
C(35)-C(36)-C(39)	110.6(13)	C(47')-C(46')-H(46C)	107.4
C(45)-C(36)-C(37)	110.2(13)	C(45')-C(46')-H(46D)	107.4
C(45')-C(36)-C(37)	115.5(15)	C(47')-C(46')-H(46D)	107.4
C(39')-C(36)-C(37)	120(3)	H(46C)-C(46')-H(46D)	106.9
C(35)-C(36)-C(37)	100.7(6)	C(48')-C(47')-C(46')	118.2(10)
C(39)-C(36)-C(37)	109.5(10)	C(48')-C(47')-H(47C)	107.7
C(46)-C(45)-C(36)	116.1(10)	C(46')-C(47')-H(47C)	107.8
C(46)-C(45)-H(45A)	108.3	C(48')-C(47')-H(47D)	107.8
C(36)-C(45)-H(45A)	108.3	C(46')-C(47')-H(47D)	107.7
C(46)-C(45)-H(45B)	108.3	H(47C)-C(47')-H(47D)	107.1
C(36)-C(45)-H(45B)	108.3	C(47')-C(48')-C(49')	119.3(12)
H(45A)-C(45)-H(45B)	107.4	C(47')-C(48')-H(48C)	107.5
C(45)-C(46)-C(47)	119.6(11)	C(49')-C(48')-H(48C)	107.5
C(45)-C(46)-H(46A)	107.4	C(47')-C(48')-H(48D)	107.5

C(49')-C(48')-H(48D)	107.5	C(64)-C(63)-C(62)	120.0(9)
H(48C)-C(48')-H(48D)	107.0	C(64)-C(63)-H(63)	120.0
C(50')-C(49')-C(48')	136(2)	C(62)-C(63)-H(63)	120.0
C(50')-C(49')-H(49C)	103.1	C(65)-C(64)-C(63)	118.5(8)
C(48')-C(49')-H(49C)	103.2	C(65)-C(64)-H(64)	120.8
C(50')-C(49')-H(49D)	103.2	C(63)-C(64)-H(64)	120.8
C(48')-C(49')-H(49D)	103.2	N(9)-C(65)-C(64)	121.5(7)
H(49C)-C(49')-H(49D)	105.1	N(9)-C(65)-H(65)	119.2
C(49')-C(50')-H(50D)	109.5	C(64)-C(65)-H(65)	119.2
C(49')-C(50')-H(50E)	109.5	N(10)-C(66)-C(67)	121.2(9)
H(50D)-C(50')-H(50E)	109.5	N(10)-C(66)-H(66)	119.4
C(49')-C(50')-H(50F)	109.5	C(67)-C(66)-H(66)	119.4
H(50D)-C(50')-H(50F)	109.5	C(68)-C(67)-C(66)	118.8(8)
H(50E)-C(50')-H(50F)	109.5	C(68)-C(67)-H(67)	120.6
C(52)-C(51)-N(7)	123.0(7)	C(66)-C(67)-H(67)	120.6
C(52)-C(51)-H(51)	118.5	C(67)-C(68)-C(69)	119.1(8)
N(7)-C(51)-H(51)	118.5	C(67)-C(68)-H(68)	120.4
C(51)-C(52)-C(53)	119.1(8)	C(69)-C(68)-H(68)	120.4
C(51)-C(52)-H(52)	120.4	C(68)-C(69)-C(70)	120.6(9)
C(53)-C(52)-H(52)	120.4	C(68)-C(69)-H(69)	119.7
C(54)-C(53)-C(52)	119.0(8)	C(70)-C(69)-H(69)	119.7
C(54)-C(53)-H(53)	120.5	N(10)-C(70)-C(69)	120.3(7)
C(52)-C(53)-H(53)	120.5	N(10)-C(70)-C(71)	116.8(7)
C(53)-C(54)-C(55)	120.6(7)	C(69)-C(70)-C(71)	122.9(8)
C(53)-C(54)-H(54)	119.7	C(72)-C(71)-N(11)	123.3(8)
C(55)-C(54)-H(54)	119.7	C(72)-C(71)-C(70)	124.4(8)
C(54)-C(55)-N(7)	120.6(7)	N(11)-C(71)-C(70)	112.3(7)
C(54)-C(55)-C(56)	124.2(7)	C(71)-C(72)-C(73)	120.7(9)
N(7)-C(55)-C(56)	115.1(7)	C(71)-C(72)-H(72)	119.6
N(8)-C(56)-C(57)	118.6(7)	C(73)-C(72)-H(72)	119.6
N(8)-C(56)-C(55)	113.4(6)	C(74)-C(73)-C(72)	117.8(10)
C(57)-C(56)-C(55)	127.9(7)	C(74)-C(73)-H(73)	121.1
C(56)-C(57)-C(58)	120.2(7)	C(72)-C(73)-H(73)	121.1
C(56)-C(57)-H(57)	119.9	C(75)-C(74)-C(73)	119.7(9)
C(58)-C(57)-H(57)	119.9	C(75)-C(74)-H(74)	120.1
C(59)-C(58)-C(57)	118.6(6)	C(73)-C(74)-H(74)	120.1
C(59)-C(58)-C(33)	121.6(7)	C(74)-C(75)-N(11)	124.1(8)
C(57)-C(58)-C(33)	119.7(7)	C(74)-C(75)-H(75)	117.9
C(60)-C(59)-C(58)	120.1(7)	N(11)-C(75)-H(75)	117.9
C(60)-C(59)-H(59)	119.9	C(15)-N(3)-C(11)	120.3(6)
C(58)-C(59)-H(59)	119.9	C(15)-N(3)-Ru(1)	126.4(4)
N(8)-C(60)-C(59)	118.7(7)	C(11)-N(3)-Ru(1)	113.2(4)
N(8)-C(60)-C(61)	114.7(6)	C(10)-N(2)-C(6)	123.2(5)
C(59)-C(60)-C(61)	126.5(7)	C(10)-N(2)-Ru(1)	118.5(4)
C(62)-C(61)-N(9)	120.8(7)	C(6)-N(2)-Ru(1)	118.1(4)
C(62)-C(61)-C(60)	124.6(7)	C(1)-N(1)-C(5)	120.7(6)
N(9)-C(61)-C(60)	114.6(6)	C(1)-N(1)-Ru(1)	126.8(5)
C(61)-C(62)-C(63)	119.4(8)	C(5)-N(1)-Ru(1)	112.4(4)
C(61)-C(62)-H(62)	120.3	C(21)-N(5)-C(25)	120.2(7)
C(63)-C(62)-H(62)	120.3	C(21)-N(5)-Ru(1)	114.7(5)

C(25)-N(5)-Ru(1)	125.1(6)	F(10)-P(2)-F(12)	89.3(4)
C(16)-N(4)-C(20)	118.7(8)	F(18)-P(3)-F(17)	176.5(3)
C(16)-N(4)-Ru(1)	126.5(6)	F(18)-P(3)-F(13)	94.0(4)
C(20)-N(4)-Ru(1)	114.8(5)	F(17)-P(3)-F(13)	89.0(4)
O(1)-N(6)-Ru(1)	176.1(5)	F(18)-P(3)-F(14)	90.5(3)
C(51)-N(7)-C(55)	117.6(7)	F(17)-P(3)-F(14)	91.4(4)
C(51)-N(7)-Ru(2)	128.9(5)	F(13)-P(3)-F(14)	90.1(3)
C(55)-N(7)-Ru(2)	113.3(5)	F(18)-P(3)-F(15)	89.1(4)
C(56)-N(8)-C(60)	123.7(6)	F(17)-P(3)-F(15)	87.9(3)
C(56)-N(8)-Ru(2)	118.3(5)	F(13)-P(3)-F(15)	176.8(4)
C(60)-N(8)-Ru(2)	117.7(5)	F(14)-P(3)-F(15)	90.3(3)
C(65)-N(9)-C(61)	119.7(7)	F(18)-P(3)-F(16)	89.6(3)
C(65)-N(9)-Ru(2)	127.0(5)	F(17)-P(3)-F(16)	88.5(3)
C(61)-N(9)-Ru(2)	113.2(5)	F(13)-P(3)-F(16)	89.8(3)
C(70)-N(10)-C(66)	119.9(7)	F(14)-P(3)-F(16)	179.9(4)
C(70)-N(10)-Ru(2)	115.1(5)	F(15)-P(3)-F(16)	89.7(3)
C(66)-N(10)-Ru(2)	125.0(6)	F(23)-P(4)-F(24)	178.0(4)
C(75)-N(11)-C(71)	114.2(8)	F(23)-P(4)-F(19)	90.3(3)
C(75)-N(11)-Ru(2)	128.0(6)	F(24)-P(4)-F(19)	91.4(3)
C(71)-N(11)-Ru(2)	117.5(5)	F(23)-P(4)-F(22)	88.4(3)
O(2)-N(12)-Ru(2)	177.5(6)	F(24)-P(4)-F(22)	90.6(3)
F(4)-P(1)-F(3)	91.6(3)	F(19)-P(4)-F(22)	89.9(3)
F(4)-P(1)-F(5)	90.3(3)	F(23)-P(4)-F(20)	91.0(3)
F(3)-P(1)-F(5)	91.9(3)	F(24)-P(4)-F(20)	90.0(3)
F(4)-P(1)-F(6)	91.9(3)	F(19)-P(4)-F(20)	91.5(3)
F(3)-P(1)-F(6)	90.0(3)	F(22)-P(4)-F(20)	178.4(3)
F(5)-P(1)-F(6)	177.1(3)	F(23)-P(4)-F(21)	88.9(3)
F(4)-P(1)-F(1)	88.7(3)	F(24)-P(4)-F(21)	89.4(3)
F(3)-P(1)-F(1)	178.5(3)	F(19)-P(4)-F(21)	178.8(3)
F(5)-P(1)-F(1)	89.6(3)	F(22)-P(4)-F(21)	89.2(3)
F(6)-P(1)-F(1)	88.5(3)	F(20)-P(4)-F(21)	89.4(3)
F(4)-P(1)-F(2)	177.8(3)	F(26)-P(5)-F(29)	96.8(6)
F(3)-P(1)-F(2)	90.2(3)	F(26)-P(5)-F(27)	95.9(5)
F(5)-P(1)-F(2)	88.5(3)	F(29)-P(5)-F(27)	92.4(5)
F(6)-P(1)-F(2)	89.3(3)	F(26)-P(5)-F(25)	89.6(5)
F(1)-P(1)-F(2)	89.5(3)	F(29)-P(5)-F(25)	92.6(5)
F(9)-P(2)-F(7)	179.3(6)	F(27)-P(5)-F(25)	172.1(6)
F(9)-P(2)-F(11)	89.7(5)	F(26)-P(5)-F(30)	89.0(5)
F(7)-P(2)-F(11)	90.4(4)	F(29)-P(5)-F(30)	174.2(6)
F(9)-P(2)-F(8)	91.5(5)	F(27)-P(5)-F(30)	86.8(4)
F(7)-P(2)-F(8)	89.2(5)	F(25)-P(5)-F(30)	87.5(4)
F(11)-P(2)-F(8)	92.6(4)	F(26)-P(5)-F(28)	174.7(5)
F(9)-P(2)-F(10)	90.9(5)	F(29)-P(5)-F(28)	87.1(5)
F(7)-P(2)-F(10)	88.3(5)	F(27)-P(5)-F(28)	87.6(5)
F(11)-P(2)-F(10)	90.6(5)	F(25)-P(5)-F(28)	86.6(4)
F(8)-P(2)-F(10)	176.0(5)	F(30)-P(5)-F(28)	87.1(5)
F(9)-P(2)-F(12)	89.1(4)	F(38)-P(7)-F(34)	88.0(11)
F(7)-P(2)-F(12)	90.8(4)	F(38)-P(7)-F(39)	178.1(12)
F(11)-P(2)-F(12)	178.8(5)	F(34)-P(7)-F(39)	91.3(12)
F(8)-P(2)-F(12)	87.6(4)	F(38)-P(7)-F(35)	94.6(10)

F(34)-P(7)-F(35)	86.6(14)	F(31)#1-P(6)-F(32)#1	90.2(5)
F(39)-P(7)-F(35)	87.1(12)	F(33)-P(6)-F(32)	89.4(5)
F(38)-P(7)-F(36)	91.8(12)	F(33)#1-P(6)-F(32)	179.0(7)
F(34)-P(7)-F(36)	177.7(14)	F(31)-P(6)-F(32)	90.2(5)
F(39)-P(7)-F(36)	89.0(11)	F(31)#1-P(6)-F(32)	90.4(5)
F(35)-P(7)-F(36)	91.1(10)	F(32)#1-P(6)-F(32)	91.7(9)
F(38)-P(7)-F(37)	82.3(12)	F(31')#1-P(6')-F(31')	178(2)
F(34)-P(7)-F(37)	103.9(15)	F(31')#1-P(6')-F(33')#1	87.2(12)
F(39)-P(7)-F(37)	96.1(12)	F(31')-P(6')-F(33')#1	91.5(13)
F(35)-P(7)-F(37)	168.8(14)	F(31')#1-P(6')-F(33')	91.5(13)
F(36)-P(7)-F(37)	78.3(14)	F(31')-P(6')-F(33')	87.2(12)
N(6)-Ru(1)-N(2)	96.4(3)	F(33')#1-P(6')-F(33')	100(2)
N(6)-Ru(1)-N(4)	173.4(2)	F(31')#1-P(6')-F(32')	90.1(13)
N(2)-Ru(1)-N(4)	90.0(2)	F(31')-P(6')-F(32')	91.4(12)
N(6)-Ru(1)-N(3)	95.2(2)	F(33')#1-P(6')-F(32')	172.6(18)
N(2)-Ru(1)-N(3)	79.1(2)	F(33')-P(6')-F(32')	87.2(12)
N(4)-Ru(1)-N(3)	87.6(2)		
N(6)-Ru(1)-N(5)	94.9(3)		
N(2)-Ru(1)-N(5)	168.7(3)		
N(4)-Ru(1)-N(5)	78.7(3)		
N(3)-Ru(1)-N(5)	100.6(2)		
N(6)-Ru(1)-N(1)	92.9(2)		
N(2)-Ru(1)-N(1)	79.7(2)		
N(4)-Ru(1)-N(1)	86.6(2)		
N(3)-Ru(1)-N(1)	158.0(2)		
N(5)-Ru(1)-N(1)	99.1(2)		
N(12)-Ru(2)-N(8)	94.0(3)		
N(12)-Ru(2)-N(11)	176.5(2)		
N(8)-Ru(2)-N(11)	89.5(3)		
N(12)-Ru(2)-N(7)	93.6(3)		
N(8)-Ru(2)-N(7)	79.7(2)		
N(11)-Ru(2)-N(7)	87.5(3)		
N(12)-Ru(2)-N(9)	93.8(3)		
N(8)-Ru(2)-N(9)	79.7(2)		
N(11)-Ru(2)-N(9)	86.4(3)		
N(7)-Ru(2)-N(9)	158.5(2)		
N(12)-Ru(2)-N(10)	98.4(3)		
N(8)-Ru(2)-N(10)	167.6(3)		
N(11)-Ru(2)-N(10)	78.1(2)		
N(7)-Ru(2)-N(10)	98.5(2)		
N(9)-Ru(2)-N(10)	100.4(2)		
F(33)-P(6)-F(33)#1	89.6(9)		
F(33)-P(6)-F(31)	89.7(6)		
F(33)#1-P(6)-F(31)	89.7(6)		
F(33)-P(6)-F(31)#1	89.7(6)		
F(33)#1-P(6)-F(31)#1	89.7(6)		
F(31)-P(6)-F(31)#1	179.1(10)		
F(33)-P(6)-F(32)#1	179.0(8)		
F(33)#1-P(6)-F(32)#1	89.4(5)		
F(31)-P(6)-F(32)#1	90.4(5)		

Appendix 4:

Electron paramagnetic resonance (EPR)

As nitric oxide ·NO is a free radical with a relatively short lifetime in solution, the use of a spin trap by a metal-chelator complex consisting in N-mhetyl-D-glucamine dithiocarbamate (MGD) and reduced iron (Fe^{2+}) to form a stable water-soluble complex [$(MGD)_2$-Fe^{2+}-NO] was utilized (scheme 4).[1] This complex gives a characteristic three lines spectrum that is detected in EPR.

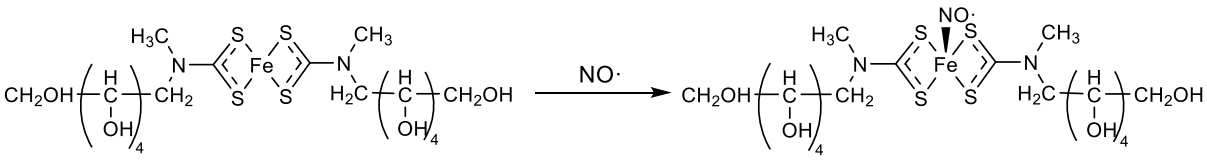

Scheme. 4. Formation reaction of [$(MGD)_2$-Fe^{2+}-NO] by the spin trap and NO radical.

N-methyl-D-glucamine dithiocarbamate previously synthesized[2] reacted with Mohr salts to get [Fe(MGD)2]. 90 µL of 1 mM of Ru(NO) complexes in acetonitrile were mixed with 10 µL of an aqueous solution of 20 mM [$Fe(MGD)_2$] and injected into quartz capillaries. Samples were irradiated directly in the EPR cavity.

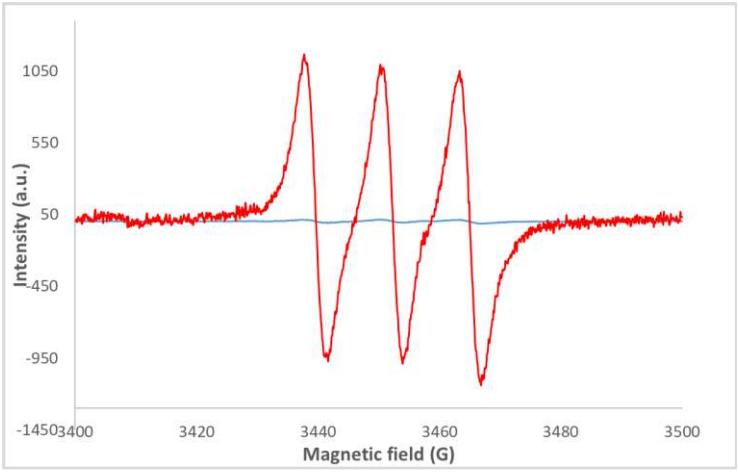

Figure 4.1. Triplet EPR signals from NO**.** trapped by [Fe(MGD)2] for [**RuNO-2**]$(PF6)_3$ under one photon excitation at room temperature and at λ>400 nm (Hg lamp).

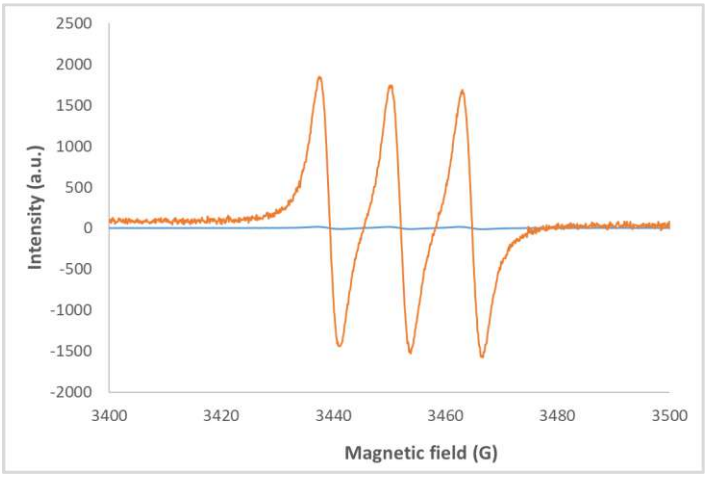

Figure 4.2. Triplet EPR signals from NO**.** trapped by [Fe(MGD)2] for [**RuNO-3**](PF6)$_6$ under one photon excitation at room temperature and at λ>400 nm (Hg lamp).

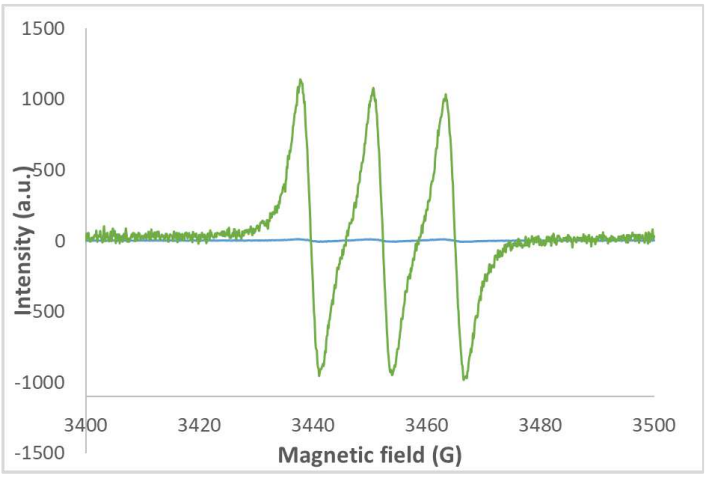

Figure 4.3. Triplet EPR signals from NO**.** trapped by [Fe(MGD)2] for [**RuNO-4**](PF6)$_6$ under one photon excitation at room temperature and at λ>400 nm (Hg lamp).

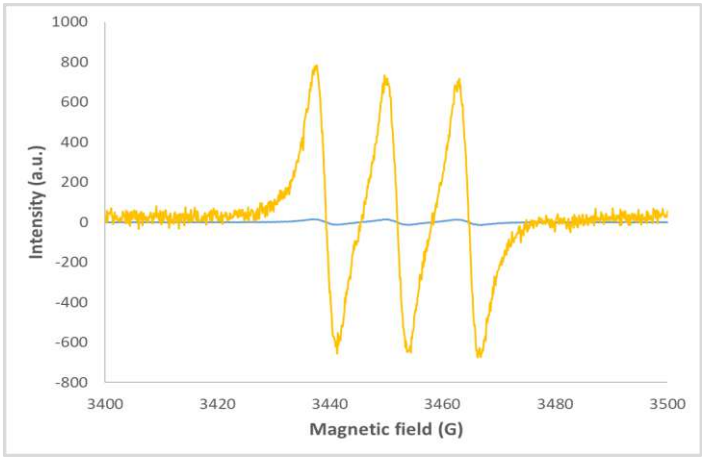

Figure 4.4. Triplet EPR signals from NO**.** trapped by [Fe(MGD)2] for [**RuNO-5**](PF6)$_6$ under one photon excitation at room temperature and at λ>400 nm (Hg lamp).

Appendix 5 :

Photochemistry and measurement of quantum yield of ·NO liberation.

-Experimental data

Table 5.1. Experimental data for the determination of Φ_{NOirr} for the **RuNO-1** in CH_3CN under different irradiation wavelength (λ_{irr}) equal to 490, 455, 400 and 365 nm. The wavelengths of observation (λ_{obs}) are equal to 380, 380, 300 and 381 nm respectively.

RuNO-1 / (λ_{irr})	**490 nm** $\lambda_{Obs} = 380\ nm$	**455 nm** $\lambda_{Obs} = 380\ nm$	**400 nm** $\lambda_{Obs} = 300\ nm$	**365 nm** $\lambda_{Obs} = 381\ nm$
Φ_{NO}^{irr}	0.0024	0.0024	0.0062	0.0084
I_0 (mol.L^{-1}.s^{-1}.)	9.67x10^{-6}	6.85x10^{-6}	6,02x10^{-6}	6,59x10^{-6}
[A]initial (mol.L^{-1})	3.61x10^{-5}	4.78x10^{-5}	4,38x10^{-5}	3,60x10^{-5}
[B]initial (mol.L^{-1})	3.40x10^{-5}	4.78x10^{-5}	4,38x10^{-5}	3,60x10^{-5}
ε_A^{irr} (mol.L^{-1}.cm^{-1}.)	11414	16704	15297	18630
ε_A^{obs} (mol.L^{-1}.cm^{-1}.)	17001	17016	45367	17966
ε_B^{irr} (mol.L^{-1}.cm^{-1}.)	11514	18902	10316	22561
ε_B^{obs} (mol.L^{-1}.cm^{-1}.)	7905	10418	56589	10759

Table 5.2. Experimental data for the determination of Φ_{NOirr} for the RuNO-2 in CH_3CN under different irradiation wavelength (λ_{irr}) equal to 455, 400 and 365 nm. The wavelengths of observation (λ_{obs}) are equal to 500 and 516 nm respectively.

RuNO-2 / (λ_{irr})	**490 nm** $\lambda_{Obs} = 450\ nm$	**455 nm** $\lambda_{Obs} = 500\ nm$	**400 nm** $\lambda_{Obs} = 500\ nm$	**365 nm** $\lambda_{Obs} = 516\ nm$
Φ_{NO}^{irr}	0.0024	0.0068	0.0085	0.012
I_0 (mol.L^{-1}.s^{-1}.)	9,67x10^{-6}	6,85x10^{-6}	6,02x10^{-6}	6,35x10^{-6}
[A]$_{initial}$ (mol.L^{-1})	2,51x10^{-5}	3,64x10^{-5}	4,85x10^{-5}	3,98x10^{-5}
[B]$_{initial}$ (mol.L^{-1})	2,40x10^{-5}	3,64x10^{-5}	4,85x10^{-5}	3,98x10^{-5}
ε_A^{irr} (mol.L^{-1}.cm^{-1}.)	24804	10560	12702	16676
ε_A^{obs} (mol.L^{-1}.cm^{-1}.)	20645	12125	12151	11212
ε_B^{irr} (mol.L^{-1}.cm^{-1}.)	17459	15812	15228	26176
ε_B^{obs} (mol.L^{-1}.cm^{-1}.)	32553	5336	5587	2382

Table 5.4 Experimental data for the determination of Φ_{NOirr} for the RuNO-4 and RuNO-5 in CH_3CN under irradiation wavelength (λ_{irr}) equal to 490 nm. The wavelengths of observation (λ_{obs}) are equal to 450 nm.

Compound	**RuNO-4** $\lambda_{Obs} = 450\ nm$	**RuNO-5** $\lambda_{Obs} = 450\ nm$
Φ_{NO}^{irr}	0.0030	0.0038
I_0 (mol.L^{-1}.s^{-1}.)	9,67x10^{-6}	9,340^{-6}
$[A]_{initial}$ (mol.L^{-1})	1,94x10^{-5}	1,92x10^{-5}
$[B]_{initial}$ (mol.L^{-1})	1,93x10^{-5}	1,92x10^{-5}
ε_A^{irr} (mol.L^{-1}.cm^{-1}.)	35345	45114
ε_A^{obs} (mol.L^{-1}.cm^{-1}.)	28428	38061
ε_B^{irr} (mol.L^{-1}.cm^{-1}.)	30231	37498
ε_B^{obs} (mol.L^{-1}.cm^{-1}.)	41636	46585

Table 5.5. Experimental data for the determination of Φ_{NOirr} for the Ru(NO)MeCH$_3$-5 in CH$_3$CN under different irradiation wavelength (λ_{irr}) equal to 490, 455, 400 and 365 nm. The wavelengths of observation (λ_{obs}) are equal to 300, 500 and 520 nm respectively.

Ru(NO)MeCH$_3$-5 / (λ_{irr})	**490 nm** $\lambda_{Obs} = 300\ nm$	**455 nm** $\lambda_{Obs} = 500\ nm$	**400 nm** $\lambda_{Obs} = 500\ nm$	**365 nm** $\lambda_{Obs} = 520\ nm$
Φ_{NO}^{irr}	0.05	0.05	0.08	0.09
I_0 (mol.L^{-1}.s^{-1}.)	2.08x10^{-5}	1.95x10^{-5}	1.79x10^{-5}	6.96x10^{-6}
[A]$_{initial}$ (mol.L^{-1})	2.32x10^{-5}	2.29x10^{-5}	2.29x10^{-5}	2.27x10^{-5}
[B]$_{initial}$ (mol.L^{-1})	2.32x10^{-5}	2.29x10^{-5}	2.29x10^{-5}	2.27x10^{-5}
ε_B^{irr} (mol.L^{-1}.cm^{-1}.)	40389	43084	51540	67588
ε_B^{obs} (mol.L^{-1}.cm^{-1}.)	81403	32442	32498	21349
ε_C^{irr} (mol.L^{-1}.cm^{-1}.)	32003	50095	64424	72140
ε_C^{obs} (mol.L^{-1}.cm^{-1}.)	87099	16813	16478	4829

Appendix 6 :

Z-Scan.

The Z-scan technique[4] was used to measure the nonlinear absorption coefficient of the samples in the wavelength range 700 – 1000 nm using short laser pulses of 80 fs at 1 KHz of repetition rate. The characterization at 800 nm was performed by the train of pulses delivered by an by a Ti:Sa amplifier (Libra HE from Coherent). For other wavelengths, the Z-scan method was implemented with an optical parametric amplifier (TOPAs, from Light Conversion). Molecules under study were dissolved in acetonitrile at the concentration of 5×10^{-3} mol.L^{-1}. The nonlinear absorption of all samples was measured at different excitation energies. All samples were measured at least three times for each energy. To verify the measurements, the Z-scan apparatus was calibrated in closed aperture mode to measure the nonlinear refractive index n_2 of the CS_2, obtaining values in the interval $1 – 2\times10^{-15}$ cm^2/W, which is in very good agreement with the literature values; also, the dye rhodamine B (RB) (dissolved in methanol at a concentration of 1×10^{-2} M) was also measured in open aperture mode to be able to compare the value of σ_{TPA} with the samples[5]. The TPA cross-section (σ_{TPA}) is obtained from the following expression equation:

$$\sigma_{TPA} = \frac{\hbar\omega}{N}\,\beta \qquad (1)$$

Were N is the molecular density and ω is the optical frequency, and β is the nonlinear absorption coefficient. The nonlinear coefficient β was calculated from the equation:[6a, 6b]

$$T(z) = 1 - \frac{1}{2\sqrt{2}}\,\beta\,\frac{I_0 L_{eff}}{1+(Z/Z_0)^2} \qquad (2)$$

where I_0 is the peak intensity, L_{eff} is the effective length of the sample with $\mathbf{L_{eff}} = [1 - \mathbf{exp}(-\boldsymbol{\alpha_0 L})]/\boldsymbol{\alpha_0}$, where L is the sample thickness and $\boldsymbol{\alpha_0}$ the absorption coefficient, Z the sample position and $\mathbf{Z_0} = (\boldsymbol{\pi\omega_0^2} / \boldsymbol{\lambda})$.

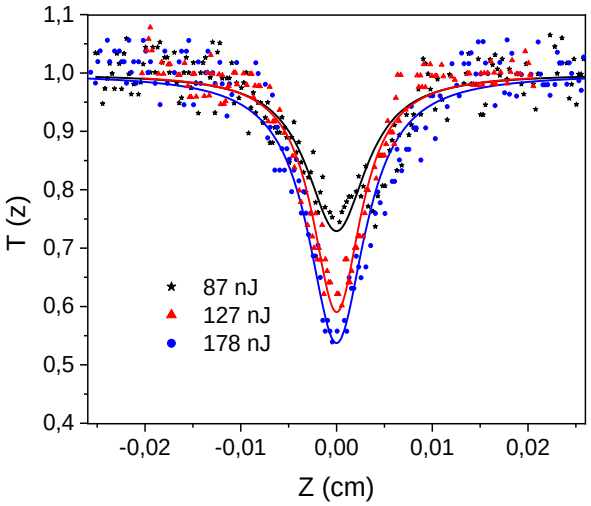

Figure 6.1. Normalized transmission T(Z) in Z-scan experiment at various laser pulse energies for **RuNO-2** at λ = 700 nm. [C] = 1 x 10^{-3} mol L^{-1} in CH_3CN.

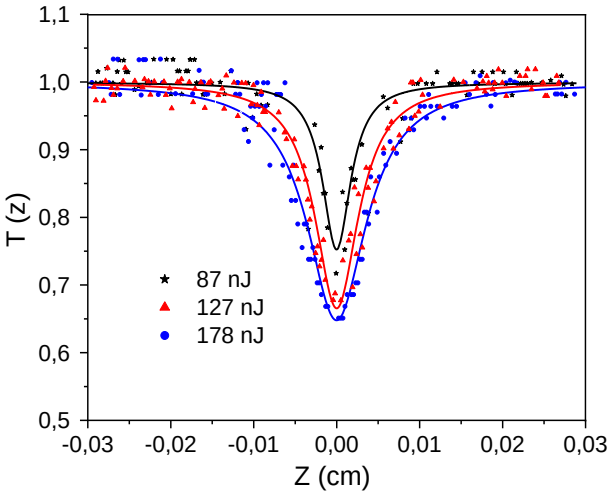

Figure 6.2. Normalized transmission T(Z) in Z-scan experiment at various laser pulse energies for **RuNO-3** at λ = 700 nm. [C] = 2 x 10^{-3} mol L^{-1} in CH_3CN.

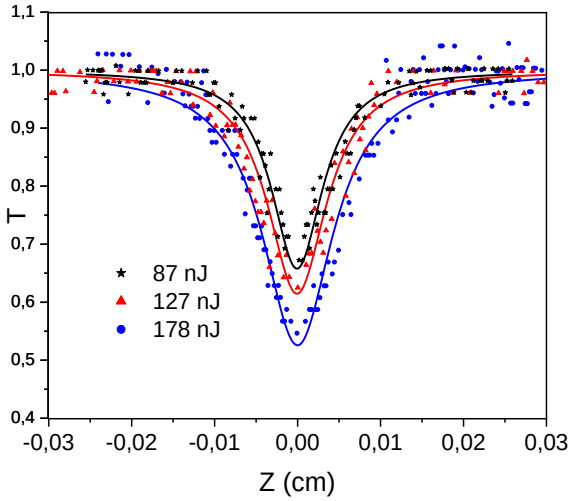

Figure 6.3. Normalized transmission T(Z) in Z-scan experiment at various laser pulse energies for **RuNO-4** at λ = 700 nm. [C] = 2 x 10^{-3} mol L^{-1} in CH_3CN.

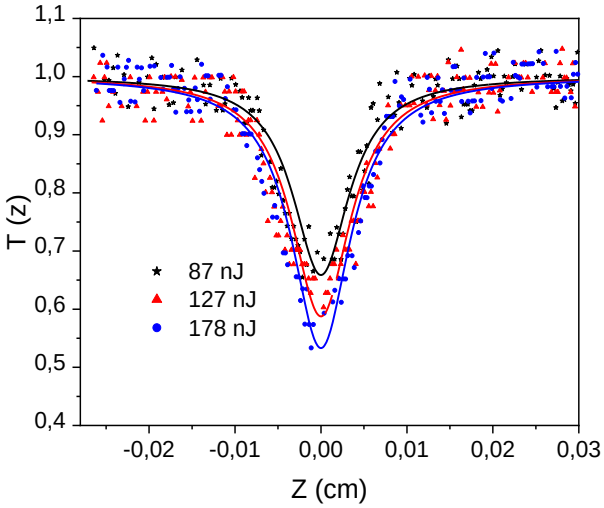

Figure 6.4. Normalized transmission T(Z) in Z-scan experiment at various laser pulse energies for **RuNO-5** at λ = 700 nm. [C] = 4 x 10^{-3} mol L^{-1} in CH_3CN.

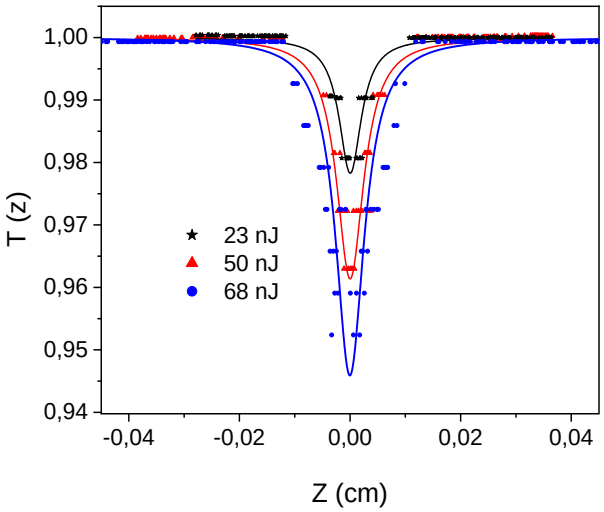

Figure 6.5. Normalized transmission T(Z) in Z-scan experiment at various laser pulse energies for **RuNO-1** at λ = 800 nm. [C] = 4 x 10^{-3} mol L^{-1} in CH_3CN.

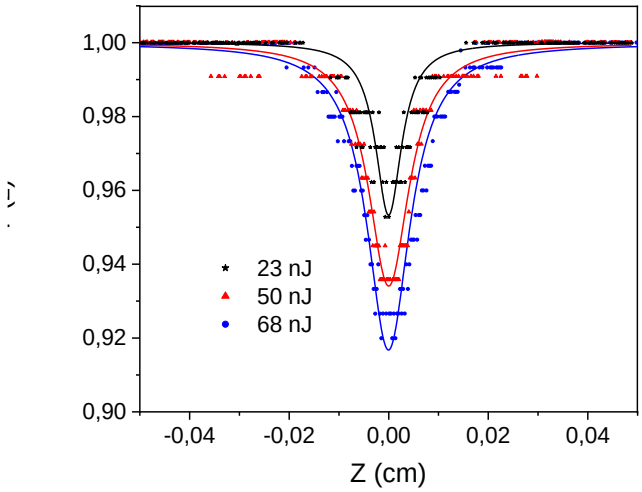

Figure 6.6. Normalized transmission T(Z) in Z-scan experiment at various laser pulse energies for **RuNO-2** at λ = 800 nm. [C] = 4.7 x 10^{-3} mol L^{-1} in CH_3CN.

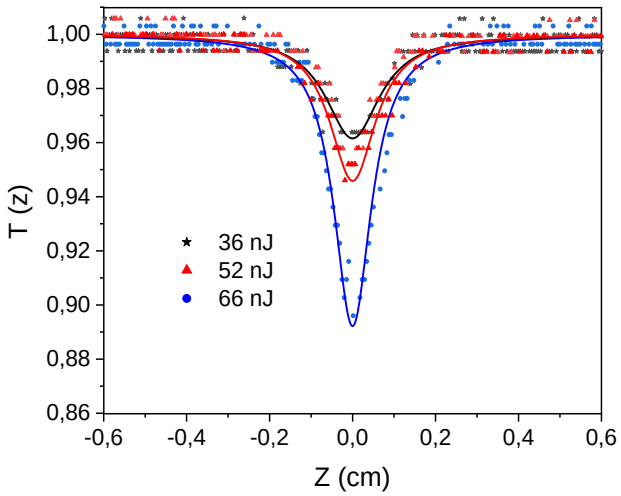

Figure 6.7. Normalized transmission T(Z) in Z-scan experiment at various laser pulse energies for **RuNO-3** at λ = 800 nm. [C] = 5 x 10^{-3} mol L^{-1} in CH_3CN.

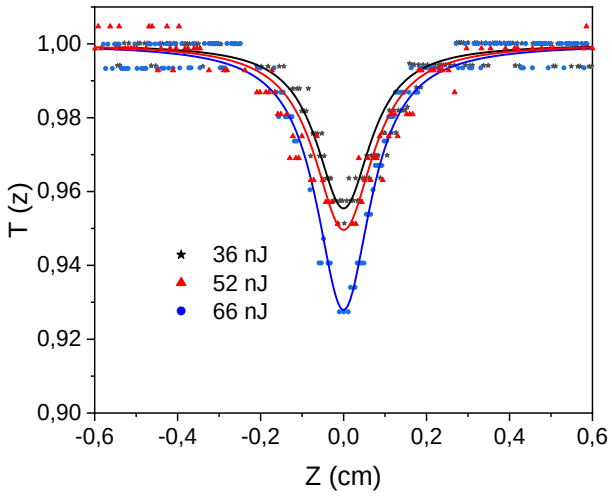

Figure 6.8. Normalized transmission T(Z) in Z-scan experiment at various laser pulse energies for **RuNO-4** at λ = 800 nm. [C] = 5 x 10^{-3} mol L^{-1} in CH_3CN.

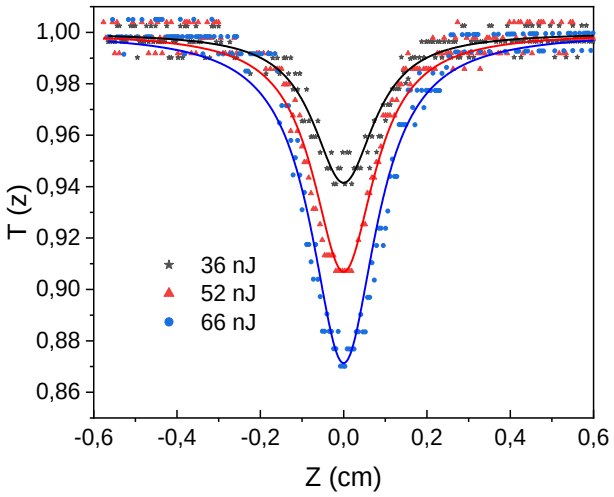

Figure 6.9. Normalized transmission T(Z) in Z-scan experiment at various laser pulse energies for **RuNO-5** at λ = 800 nm. [C] = 5 x 10^{-3} mol L^{-1} in CH_3CN.

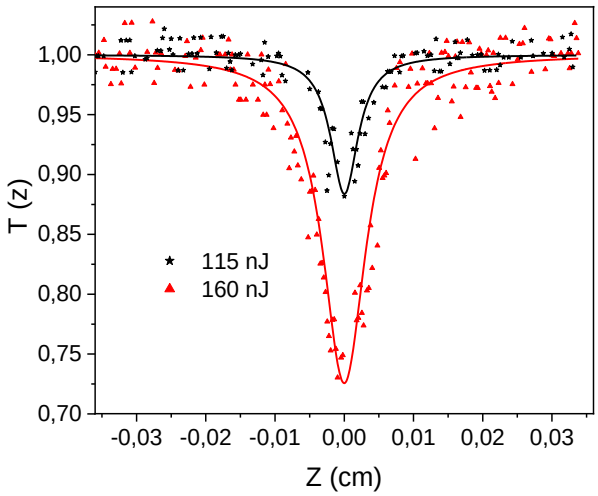

Figure 6.10. Normalized transmission T(Z) in Z-scan experiment at various laser pulse energies for **RuNO-1** at λ = 850 nm. [C] = 4 x 10^{-3} mol L^{-1} in CH_3CN.

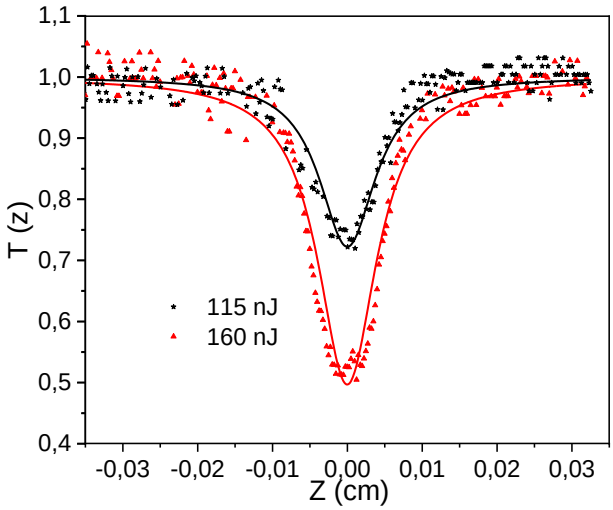

Figure 6.11. Normalized transmission T(Z) in Z-scan experiment at various laser pulse energies for **RuNO-2** at λ = 850 nm. [C] = 5 x 10^{-3} mol L^{-1} in CH_3CN.

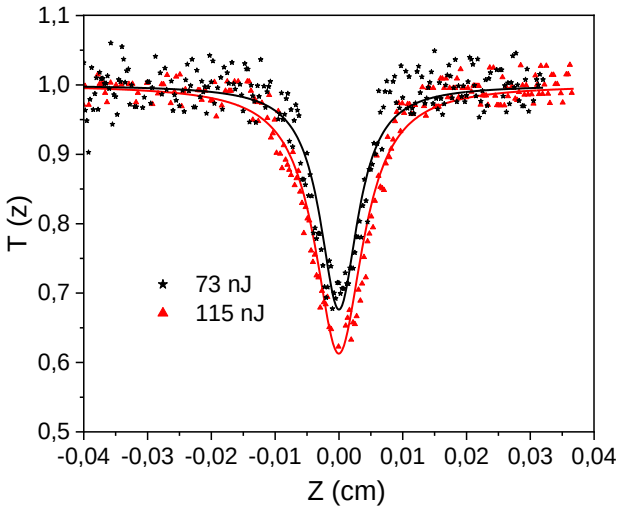

Figure 6.12. Normalized transmission T(Z) in Z-scan experiment at various laser pulse energies for **RuNO-3** at λ = 850 nm. [C] = 5 x 10^{-3} mol L^{-1} in CH_3CN.

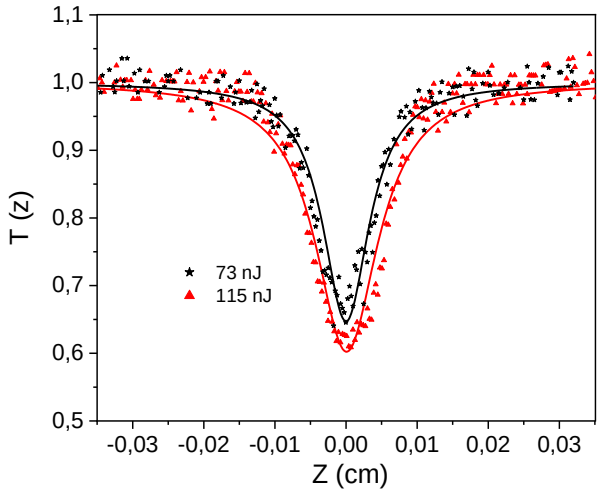

Figure 6.13. Normalized transmission T(Z) in Z-scan experiment at various laser pulse energies for **RuNO-4** at λ = 850 nm. [C] = 5 x 10^{-3} mol L^{-1} in CH_3CN.

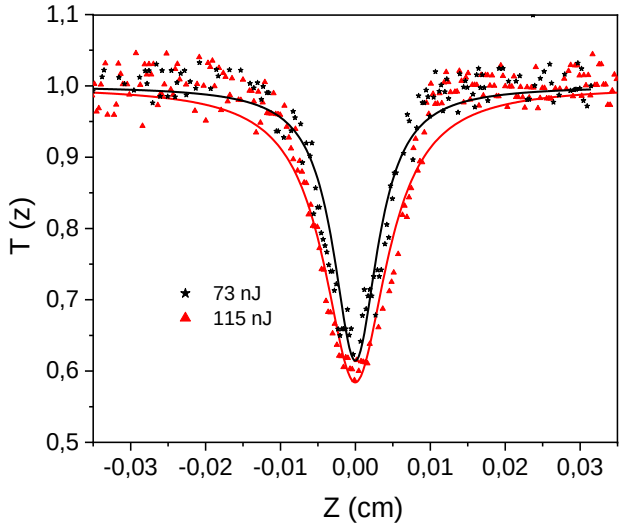

Figure 6.14. Normalized transmission T(Z) in Z-scan experiment at various laser pulse energies for **RuNO-5** at λ = 850 nm. [C] = 4 x 10^{-3} mol L^{-1} in CH_3CN.

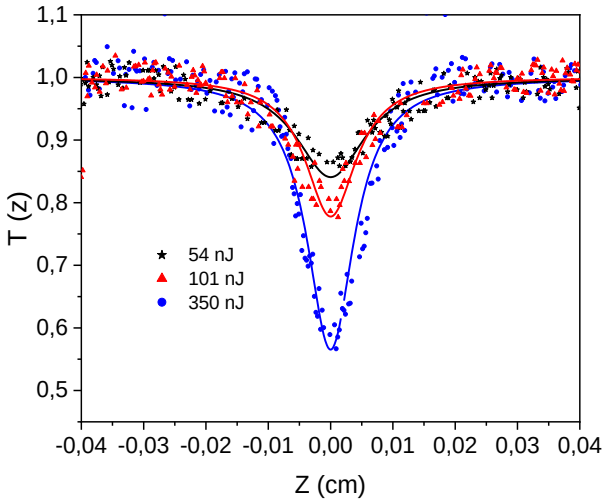

Figure 6.15. Normalized transmission T(Z) in Z-scan experiment at various laser pulse energies for **RuNO-1** at λ = 900 nm. [C] = 4 x 10^{-3} mol L^{-1} in CH_3CN.

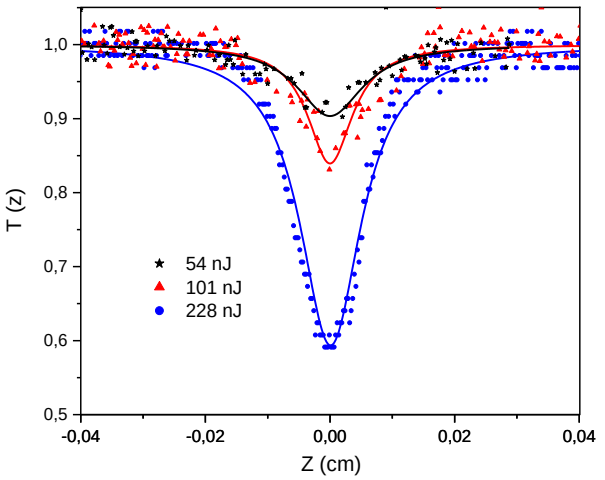

Figure 6.16. Normalized transmission T(Z) in Z-scan experiment at various laser pulse energies for **RuNO-2** at λ = 900 nm. [C] = 5 x 10^{-3} mol L^{-1} in CH_3CN.

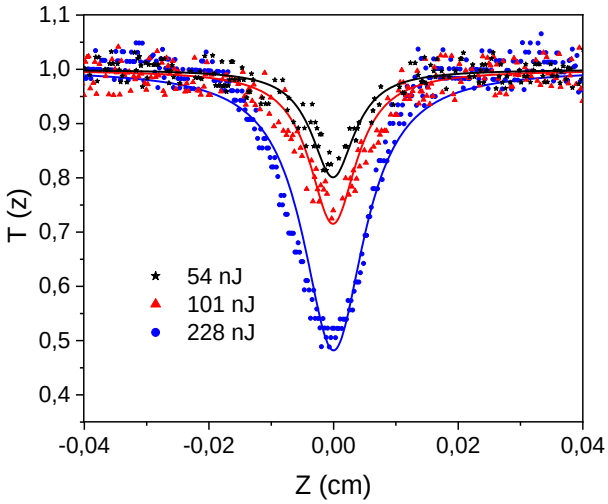

Figure 6.17. Normalized transmission T(Z) in Z-scan experiment at various laser pulse energies for **RuNO-3** at λ = 900 nm. [C] = 5 x 10^{-3} mol L^{-1} in CH_3CN.

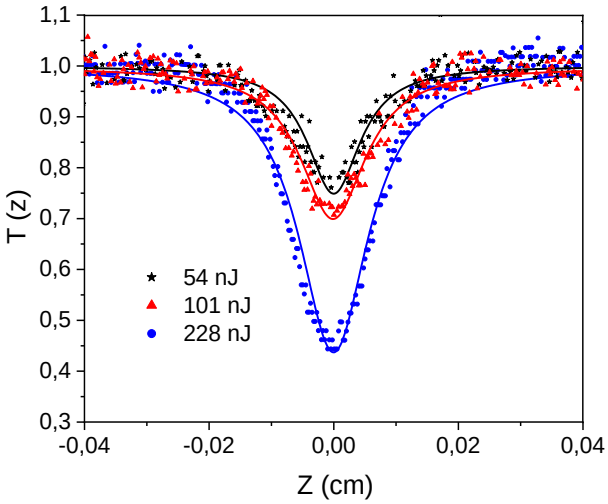

Figure 6.18. Normalized transmission T(Z) in Z-scan experiment at various laser pulse energies for **RuNO-4** at λ = 900 nm. [C] = 5 x 10^{-3} mol L^{-1} in CH_3CN.

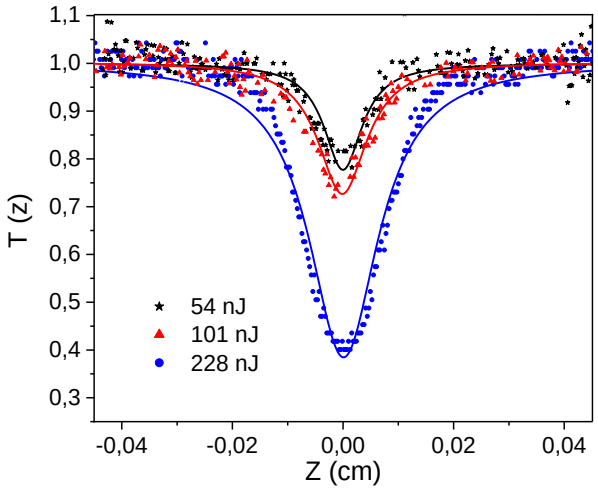

Figure 6.19. Normalized transmission T(Z) in Z-scan experiment at various laser pulse energies for **RuNO-5** at λ = 900 nm. [C] = 4 x 10^{-3} mol L^{-1} in CH_3CN.

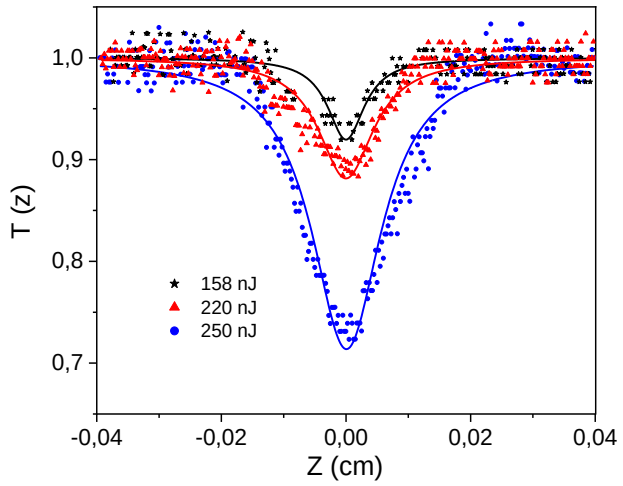

Figure 6.20. Normalized transmission T(Z) in Z-scan experiment at various laser pulse energies for **RuNO-1** at λ = 950 nm. [C] = 4 x 10^{-3} mol L^{-1} in CH_3CN.

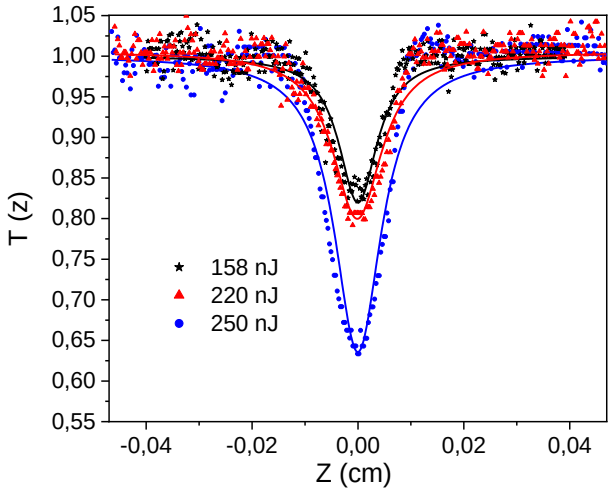

Figure 6.21. Normalized transmission T(Z) in Z-scan experiment at various laser pulse energies for **RuNO-2** at λ = 950 nm. [C] = 5 x 10^{-3} mol L^{-1} in CH_3CN.

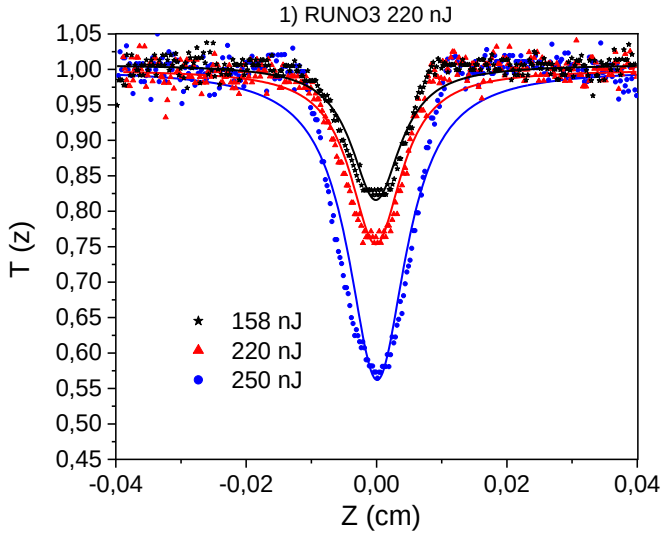

Figure 6.22. Normalized transmission T(Z) in Z-scan experiment at various laser pulse energies for **RuNO-3** at λ = 950 nm. [C] = 5 x 10^{-3} mol L^{-1} in CH_3CN.

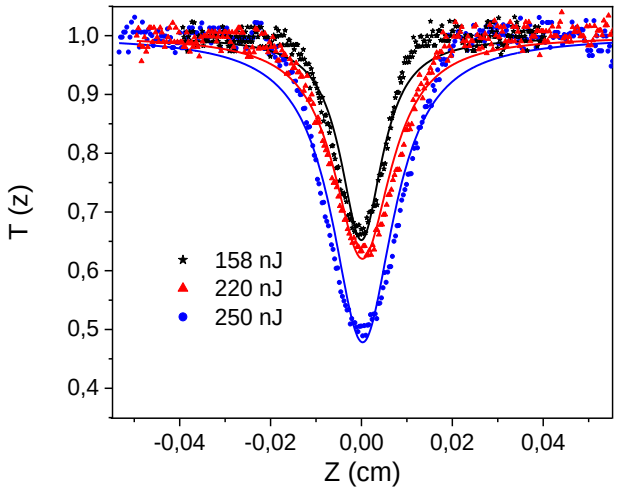

Figure 6.23. Normalized transmission T(Z) in Z-scan experiment at various laser pulse energies for **RuNO-4** at λ = 950 nm. [C] = 5 x 10^{-3} mol L^{-1} in CH_3CN.

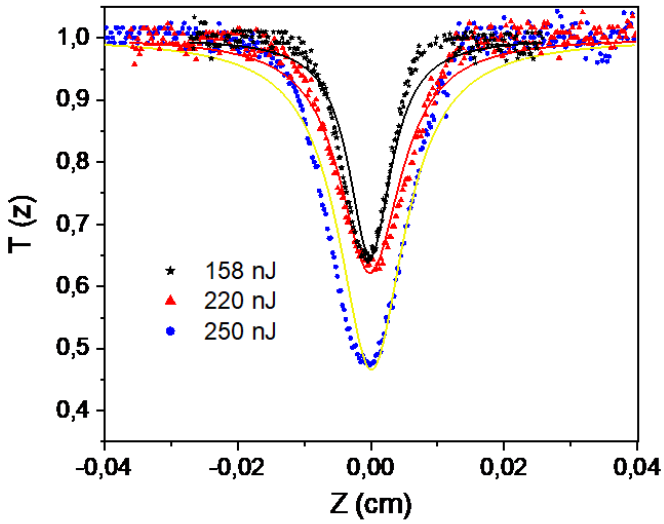

Figure 6.24. Normalized transmission T(Z) in Z-scan experiment at various laser pulse energies for **RuNO-5** at λ = 950 nm. [C] = 4 x 10^{-3} mol L^{-1} in CH_3CN.

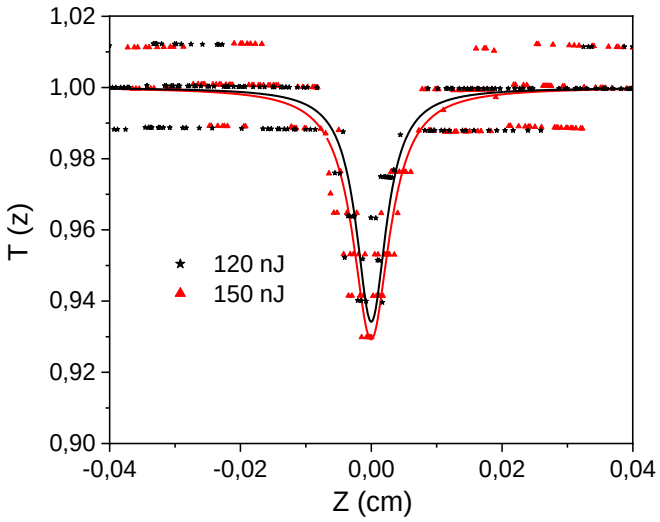

Figure 6.25. Normalized transmission T(Z) in Z-scan experiment at various laser pulse energies for **RuNO-1** at λ = 1000 nm. [C] = 4 x 10^{-3} mol L^{-1} in CH_3CN.

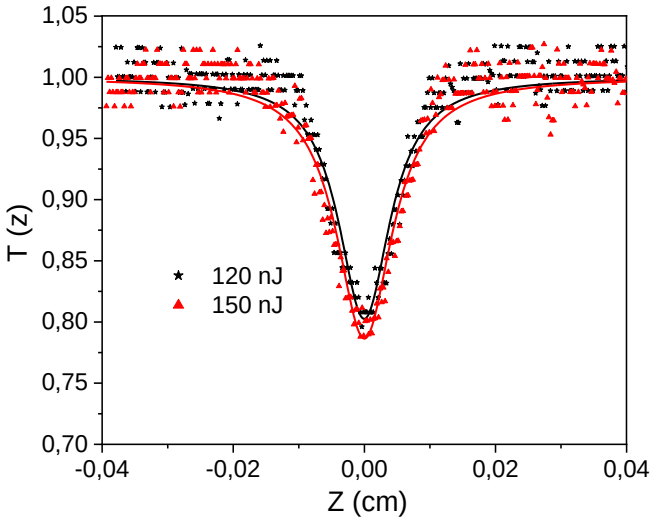

Figure 6.26. Normalized transmission T(Z) in Z-scan experiment at various laser pulse energies for **RuNO-2** at λ = 1000 nm. [C] = 5 x 10^{-3} mol L^{-1} in CH_3CN.

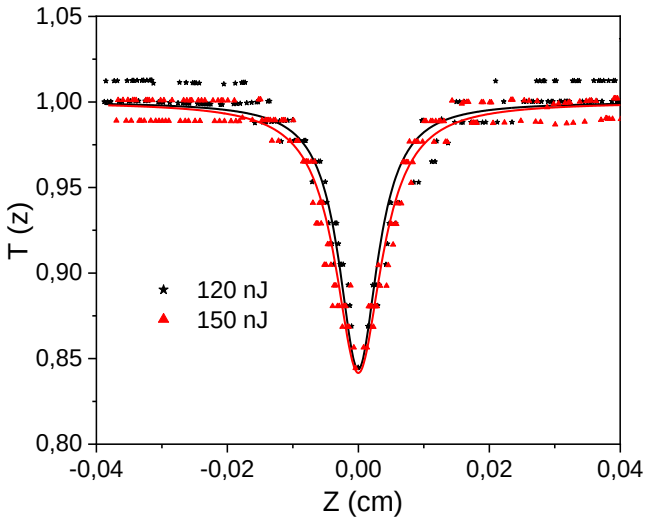

Figure 6.27. Normalized transmission T(Z) in Z-scan experiment at various laser pulse energies for **RuNO-3** at λ = 1000 nm. [C] = 5 x 10^{-3} mol L^{-1} in CH_3CN.

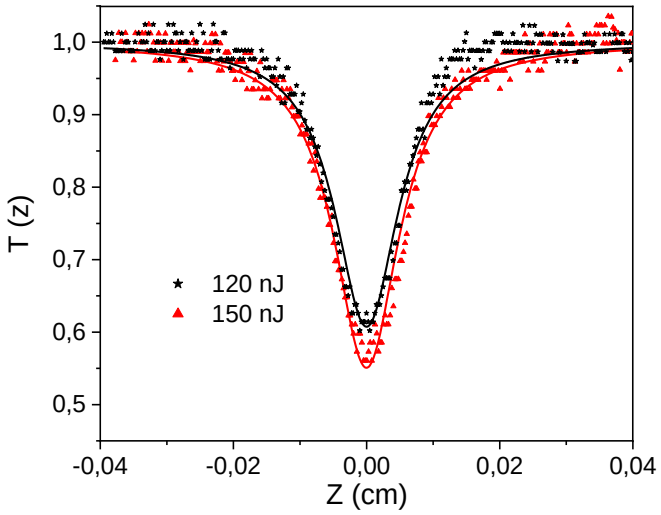

Figure 6.28. Normalized transmission T(Z) in Z-scan experiment at various laser pulse energies for **RuNO-4** at λ= 1000 nm. [C] = 5 x 10^{-3} mol L^{-1} in CH_3CN.

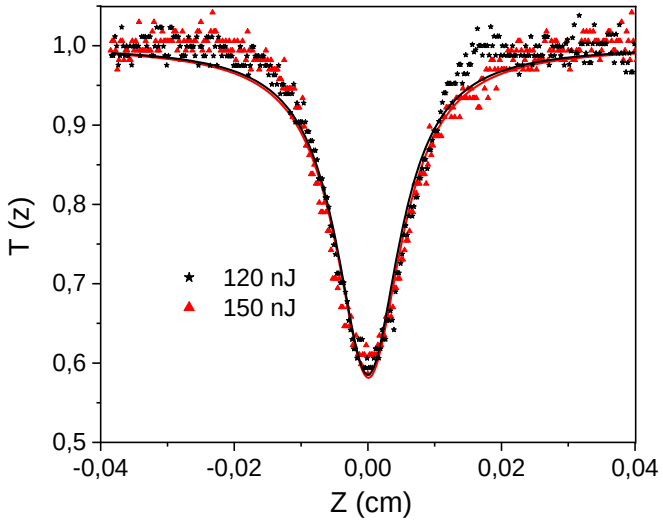

Figure 6.29. Normalized transmission T(Z) in Z-scan experiment at various laser pulse energies for **RuNO-5** at λ = 1000 nm. [C] = 4 x 10^{-3} mol L^{-1} in CH_3CN.

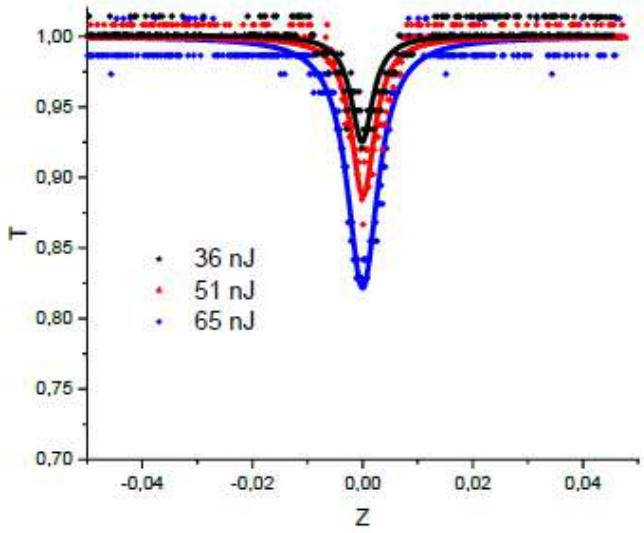

Figure 6.30. Normalized transmission T(Z) in Z-scan experiment at various laser pulse energies for **trans, trans-$RuNOCl_2$-3** at λ = 800 nm in H_2O.

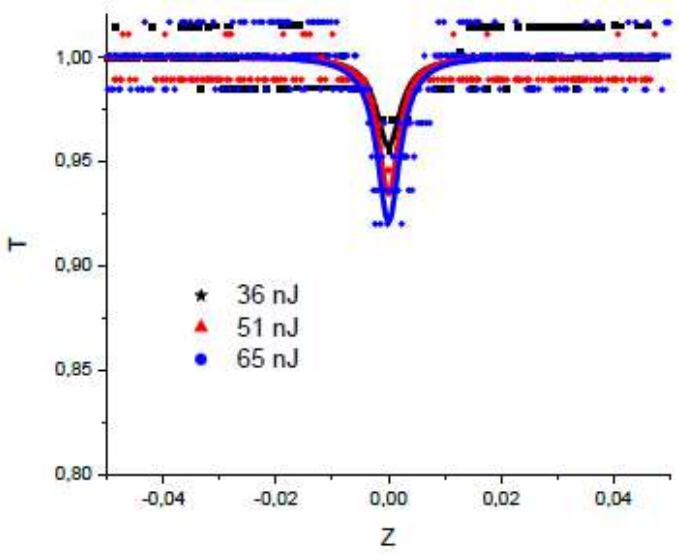

Figure 6.31. Normalized transmission T(Z) in Z-scan experiment at various laser pulse energies for **trans-Ru(NO)OH-3** at λ = 800 nm in H_2O.

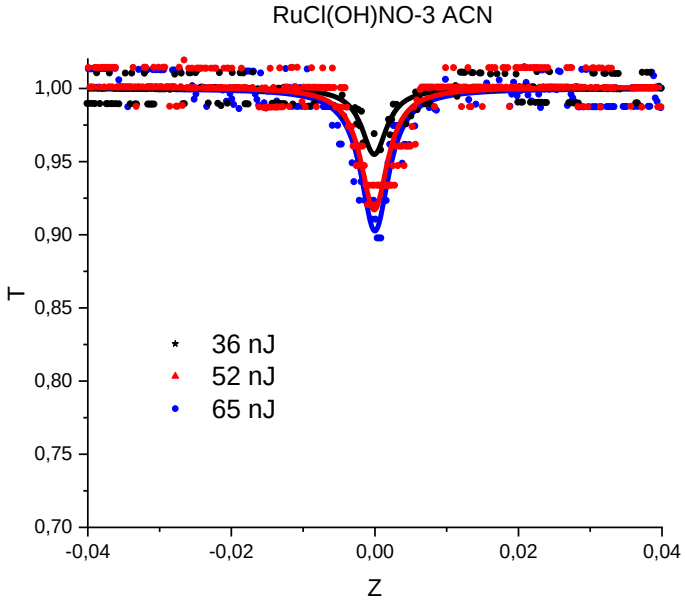

Figure 6.32. Normalized transmission T(Z) in Z-scan experiment at various laser pulse energies for **trans-Ru(NO)OH-3** at λ = 800 nm in CH_3CN.

Appendix 7:

UV-vis spectra.

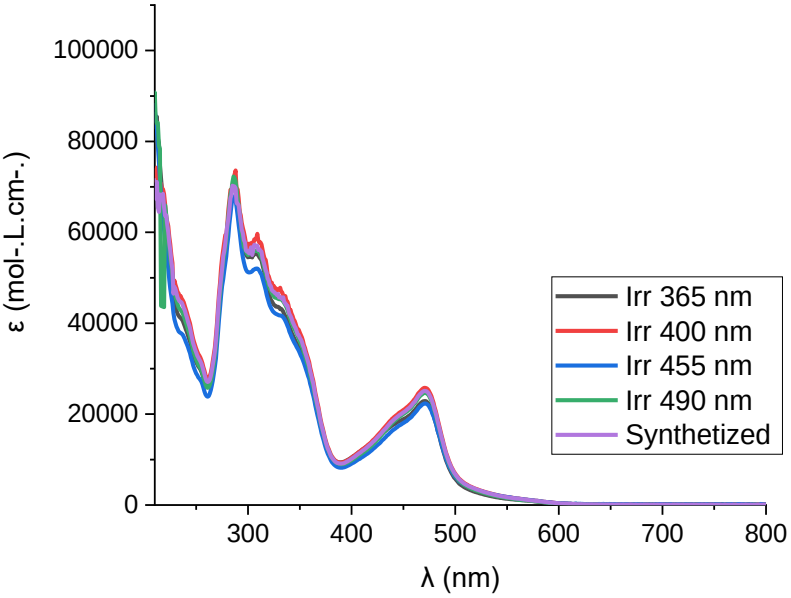

Figure 7.1. UV-visible absorption spectra for **RuMeCH$_3$-1** in acetonitrile obtained by irradiation of **RuNO-1** at the end of the experiment for different wavelengths (365, 400, 455 and 490 nm) and synthetized one.

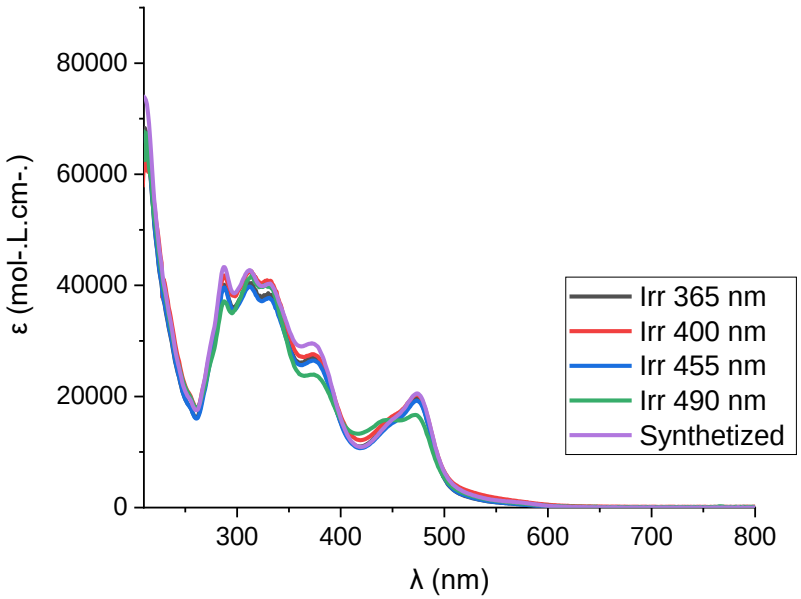

Figure 7.2. UV-visible absorption spectra for **RuMeCH$_3$-2** in acetonitrile obtained by irradiation of **RuNO-2** at the end of the experiment for different wavelengths (365, 400, 455 and 490 nm) and synthetized one.

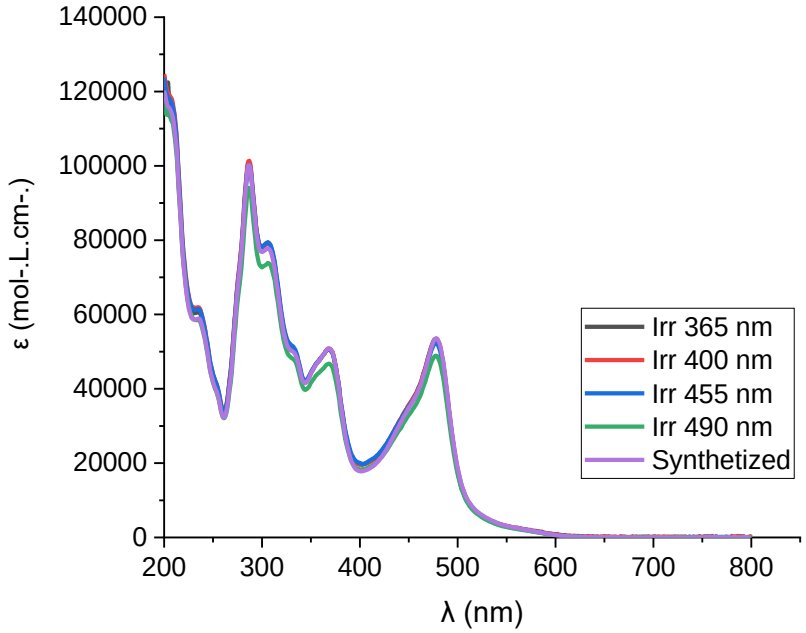

Figure 7.3. UV-visible absorption spectra for **RuMeCH$_3$-3** in acetonitrile obtained by irradiation of **RuNO-3** at the end of the experiment for different wavelengths (365, 400, 455 and 490 nm) and synthetized one.

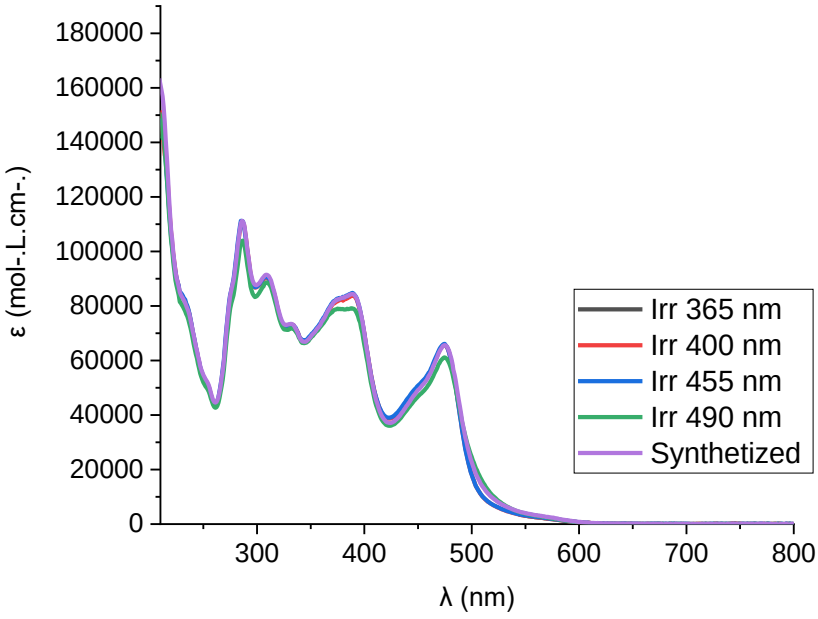

Figure 7.4. UV-visible absorption spectra for **RuMeCH$_3$-5** in acetonitrile obtained by irradiation of **RuNO-4** at the end of the experiment for different wavelengths (365, 400, 455 and 490 nm) and synthetized one.

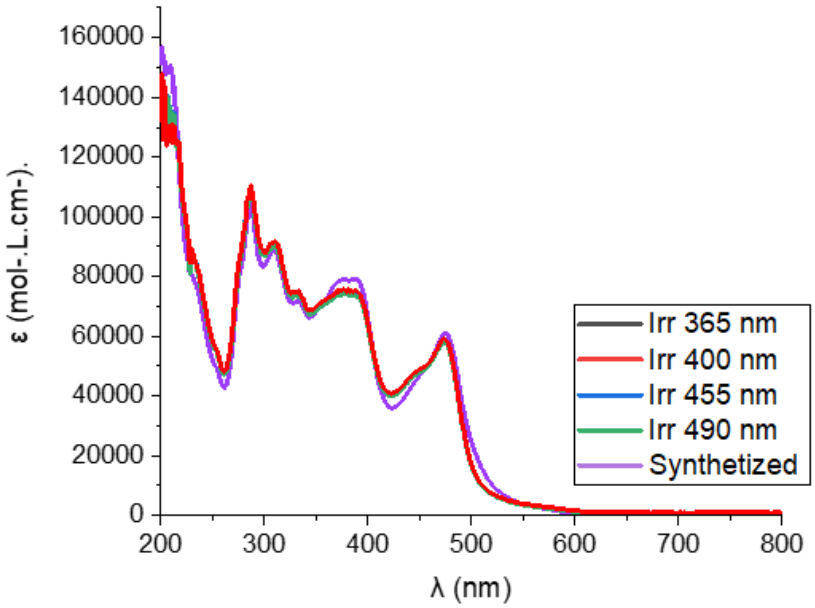

Figure 7.5. UV-visible absorption spectra for **RuMeCH$_3$-5** in acetonitrile obtained by irradiation of **Ru(NO)MeCH$_3$-5** at the end of the experiment for different wavelengths (365, 400, 455 and 490 nm) and synthetized one.

References

[1] W. Smith. D. A History of Nitrous Oxide and Oxygen Anaesthesia. I. Joseph Priestley to Humphry Davy. Br. *J. Anaesth*. **1965**. 37 (10). 790–798. https://doi.org/10.1093/bja/37.10.790

[2] S. Katsuki, W. Arnold, C. Mittal, F. Murad. Stimulation of Guanylate Cyclase by Sodium Nitroprusside, Nitroglycerin and Nitric Oxide in Various Tissue Preparations and Comparison to the Effects of Sodium Azide and Hydroxylamine. *J. Cycl. Nucl. Prot. Phosphoryl. Res.* **1977**. 3. 23–25.

[3] R. Furchgott, J. V. Zawadzki. The Obligatory Role of Endothelial Cells in the Relaxation of Arterial Smooth Muscle by Acetylcholine. *Nature.* **1980**. 288. 373–376. https://doi.org/10.1038/288373a0

[4] P. D. Cherry, R. F. Furchgott, J. V. Zawadzki, D. Jothianandan. Role of Endothelial Cells in Relaxation of Isolated Arteries by Bradykinin. *Proc. Natl. Acad. Sci*. **1982**. 72. 2106–2110. https://doi.org/10.1073/pnas.79.6.2106

[5] C. A. Gruetter, B. K. Barry, D. B. McNamara, D. Y. Gruetter, P. J. Kadowitz, L. Ignarro. Relaxation of Bovine Coronary Artery and Activation of Coronary Arterial Guanylate Cyclase by Nitric Oxide, Nitroprusside and a Carcinogenic Nitrosoamine. *J. Cyclic Nucleotide Res*. **1979**. 5 (3). 211–224. https://pubmed.ncbi.nlm.nih.gov/39089/

[6] L. J. Ignarro. Biological Actions and Properties of Endothelium-Derived Nitric Oxide Formed and Released from Artery and Vein. *Circ. Res.* **1989**. 65, 1–21. https://doi.org/10.1161/01.res.65.1.1

[7] L. J. Ignarro, B. A. Freeman. Chapter 1 - A Concise History of the Discovery of Mammalian Nitric Oxide (Nitrogen Monoxide) Biogenesis. In Nitric Oxide, 3rd ed.; *Academic Press*. **2017**. 1-7. https://doi.org/10.1016/B978-0-12-804273-1.00001-6

[8] D. S. Bredt, P. M. Hwang, S. H. Snyder. Localization of Nitric Oxide Synthase Indicating a Neural Role for Nitric Oxide. *Nature*. **1990**. 347 (6295). 768-770. https://doi.org/10.1038/347768a0

[9] J. B. Hibbs, R. R. Taintor, Z. Vavrin, E. M. Rachlin. Nitric oxide: a cytotoxic activated macrophage effector molecule*. Biochem. Biophys. Res. Commun.* **1988**. 157. 87–94. https://doi.org/10.1016/s0006-291x(88)80015-9

[10] M. A. Marletta, P. S. Yoon, R. Iyengar, C. D. Leaf, J. S. Wishnok. Macrophage oxidation of L-arginine to nitrite and nitrate: nitric oxide is an intermediate. *Biochemistry*. **1988**. 27. 8706–8711. https://doi.org/10.1021/bi00424a003

[11] D. Alonso, M. W. Radomski. The Nitric Oxide-Endothelin-1. *Connection Heart Failure Rev*., **2003**. 8. 47–54. https://doi.org/10.1023/A:1022155206928

[12] R. A. Cohen, R. M. Weisbrod, M. Gericke, M. Yaghoubi, C. Bierl, V. M. Bolotina. Mechanism of nitric oxide-induced vasodilatation: refilling of intracellular stores by sarcoplasmic reticulum Ca2+ ATPase and inhibition of store-operated Ca2+ influx. *Circ. Res*. **1999.** 84. 210–221. https://doi.org/10.1161/01.res.84.2.210

[13] B. W. Allen, J. S. Stamler, C. A. Piantadosi. Hemoglobin, nitric oxide and molecular mechanisms of hypoxic vasodilation. *Trends Mol. Med*. **2009**. 10. 452–460. https://doi.org/10.1016/j.molmed.2009.08.002

[14] L. Morbidelli, L. S. Donnini, M. Zich. Role of nitric oxide in the modulation of angiogenesis. *Curr. Pharm. Des*. **2003**. 9. 521–530. https://doi.org/10.2174/1381612033391405

[15] G. Zacharia, W. M. Deen. Diffusivity and Solubility of Nitric Oxide in Water and Saline*. Ann. Biomed. Eng*. **2005.** 33 (2). 214–222. https://doi.org/10.1007/s10439-005-8980-9

[16] T. A. Heinrich, R. S. da Silva, K. M. Miranda, C. H. Switzer, D. A. Wink, J. M. Fukuto. Biological Nitric Oxide Signalling: Chemistry and Terminology. *Br. J. Pharmacol*. **2013**. 169 (7). 1417–1429. https://doi.org/10.1111%2Fbph.12217

[17] R. P. Orenha, S. E. Galembeck. Molecular Orbitals of NO, NO^+, and NO^- : A Computational Quantum Chemistry Experiment. *J. Chem. Educ*. **2014**. 91 (7). 1064–1069. https://doi.org/10.1021/ed400618j

[18] D. D. Thomas, L. A. Ridnour, J. S. Isenberg, W. Flores-Santana, C. H. Switzer, S. Donzelli, P. Hussain, C. Vecoli, N. Paolocci, S. Ambs, C. A. Colton, C. C. Harris, D. D. Roberts, D. A. Wink. The Chemical Biology of Nitric Oxide: Implications in Cellular Signaling. *Free Radical Biol. Med*. **2008**. 45 (1). 18-31. https://doi.org/10.1016/j.freeradbiomed.2008.03.020

[19] S. Habib, A. Ali. Biochemistry of Nitric Oxide. *Indian J. Clin. Biochem*. **2011**. 26 (1). 3-17. https://doi.org/10.1007/s12291-011-0108-4

[20] B. Galliker, R. Kissner, T. Nauser, W. Koppenol. H. Intermediates in the Autoxidation of Nitrogen Monoxide. *Chem. Eur. J*. **2009**. 15 (25). 6161–6168. https://doi.org/10.1002/chem.200801819

[21] A. Ali, J. A. Coulter, C. H. Ogle, M. M. Migaud, D. G. Hirst, T. Robson, H. O. McCarthy. The Contribution of N_2O_3 to the Cytotoxicity of the Nitric Oxide Donor DETA/NO: An Emerging Role for S-Nitrosylation. *Biosci. Rep.* **2013**, 33 (2), e00031. https://doi.org/10.1042%2FBSR20120120

[22] M. N. Möller, N. Rios, M. Trujillo, R. Radi, A. Denicola, B. Alvarez. Detection and Quantification of Nitric Oxide–Derived Oxidants in Biological Systems. *J. Biol. Chem.* **2019**. 294 (40). 14776-14802. https://doi.org/10.1074/jbc.REV119.006136

[23] P. C. Ford, I. M. Lorkovic. Mechanistic Aspects of the Reactions of Nitric Oxide with Transition-Metal Complexes. *Chem. Rev*. **2002**. 102 (4). 993–1018. https://doi.org/10.1021/cr0000271

[24] G. K. Lahiri, W. Kaim. Electronic Structure Alternatives in Nitrosylruthenium Complexes. *Dalton Trans*. **2010**. 39. 4471-4478. https://doi.org/10.1039/C002173C

[25] M. Pavlovich, T. Ono, C. Galleher, B. Curtis, D. Clark, Z. Machala, D. Graves. Air spark-like plasma source for antimicrobial NOx generation. *Journal of Physics D. Applied Physics*. **2014**. 47 (50). 505202. http://dx.doi.org/10.1088/0022-3727/47/50/505202

[26] S. Klein, C. Harreiß, C. Menter, J. Hümmer, L. V. R. Distel, K. Meyer, R. Hock, C. Kryschi. $NOBF_4$-Functionalized Au–Fe_3O_4 Nanoheterodimers for Radiation Therapy: Synergy Effect Due to Simultaneous Reactive Oxygen and Nitrogen Species Formation. *ACS Appl. Mater. Interfaces.* **2018**. 10 (20). 17071-17080. https://doi.org/10.1021/acsami.8b03660

[27] P. C. Ford, J. C. M. Pereira, K. M. Miranda. Mechanisms of Nitric Oxide Reactions Mediated by Biologically Relevant Metal Centers. In Nitrosyl Complexes in Inorganic Chemistry, Biochemistry and Medicine II; Mingos, D., Ed.; Structure and Bonding; *Springer*: Berlin, Heidelberg. **2013**. Vol. 154. https://doi.org/10.1007/430_2013_117

[28] D. Schaniel, T. Woike. Necessary Conditions for the Photogeneration of Nitrosyl Linkage Isomers. *Phys. Chem. Chem. Phys.* **2009**. 11 (21). 4391–4395. https://doi.org/10.1039/b900546c

[29] R. R. Allison, K. Moghissi. Photodynamic Therapy (PDT): PDT Mechanisms. Clin. *Endosc.* **2013**. 46 (1). 24–29. https://doi.org/10.5946/ce.2013.46.1.24

[30] S. Tsukagoshi. [Porfimer sodium (Photofrin-II)]. *Gan To Kagaku Ryoho*. **1995**. 22 (9). 1271–1278. https://pubmed.ncbi.nlm.nih.gov/7661580/

[31] M. Wachowska, A. Muchowicz, M. Firczuk, M. Gabrysiak, M. Winiarska, M. Wańczyk, K. Bojarczuk, J. Golab. Aminolevulinic Acid (ALA) as a Prodrug in Photodynamic Therapy of Cancer. *Molecules*. **2011**. 16 (5). 4140–4164. https://doi.org/10.3390/molecules16054140

[32] W. Jiang, M. Liang, Q. Lei, G. Li, S. Wu. The Current Status of Photodynamic Therapy in Cancer Treatment. Cancers. **2023**. 15 (3). 585. https://doi.org/10.3390/cancers15030585

[33] M. T. Wan, J. Y. Lin. Current Evidence and Applications of Photodynamic Therapy in Dermatology. *Clin., Cosmet. Investig. Dermatol*. **2014**. 7. 145–163. https://doi.org/10.2147/ccid.s35334

[34] E. H. C. van Dijk, T. J. van Rijssen, Y. Subhi, C. J. F. Boon. Photodynamic Therapy for Chorioretinal Diseases: A Practical Approach. *Ophthalmol. Ther.* **2020**. 9 (2). 329–342. https://doi.org/10.1007/s40123-020-00250-0

[35] P. C. Gøtzsche. Niels Finsen's Treatment for Lupus Vulgaris. J. R. Soc. Med. **2011**, 104 (1), 41–42. https://doi.org/10.1258%2Fjrsm.2010.10k066

[36] J. H. Correia, J. A. Rodrigues, S. Pimenta, T. Dong, Z. Yang. Photodynamic Therapy Review: Principles, Photosensitizers, Applications, and Future Directions. *Pharmaceutics*. **2021**. 13 (9). 1332. https://doi.org/10.3390%2Fpharmaceutics13091332

[37] T. J. Dougherty, J. E. Kaufman, A. Goldfarb, K. R. Weishaupt, D. Boyle, A. Mittleman. Photoradiation Therapy for the Treatment of Malignant Tumors. *Cancer Res.* **1978**. 38 (8). 2628-2635. PMID: 667856

[38] D. Kessel. Photodynamic Therapy: A Brief History. *J. Clin. Med.* **2019**. 8 (10). 1581. https://doi.org/10.3390/jcm8101581

[39] A. G. Niculescu, A. M. Grumezescu. Photodynamic Therapy—An Up-to-Date. *Review. Appl. Sci.* **2021**. 11. 3626. https://doi.org/10.3390/app11083626

[40] D. Sharma, K. S. Singh, P. Kumar, G. K. Jain, G. Aggarwal, W. H. Almalki, P. Kesharwani. Mechanisms of Photodynamic Therapy in Nanomaterials for Photodynamic Therapy, *Woodhead Publishing*. **2023**. 41-54. https://doi.org/10.1016/B978-0-323-85595-2.00017-7

[41] G. Gunaydin, M. E. Gedik, S. Ayan. Photodynamic Therapy-Current Limitations and Novel Approaches. *Front. Chem.* **2021**. 9. 691697. https://doi.org/10.3389/fchem.2021.691697

[42] N. J. Farrer, L. Salassa, P. J. Sadler. Photoactivated Chemotherapy (PACT): The Potential of Excited-State D-Block Metals in Medicine. *Dalton Trans*. **2009**. (48). 10690–10701. https://doi.org/10.1039/B917753A

[43] A. W. Carpenter, M. H. Schoenfisch. Nitric Oxide Release: Part II. Therapeutic Applications. *Chem. Soc. Rev.* **2012**. 41. 3742-3752. https://doi.org/10.1039/C2CS15273H

[44] M. M. Pereira, C. J. P. Monteiro, N. M. M. Moura, R. F. Mendes, A. C. Fernandes, A. J. L. Pombeiro. Light-Assisted and Remote Delivery of Carbon Monoxide to Malignant Cells and Tissues: Photochemotherapy in the Spotlight. *J. Photochem. Photobiol.* **2020**. 42. 100341. https://doi.org/10.1016/j.jphotochemrev.2020.100341

[45] B. Muz, P. de la Puente, F. Azab, A. K. Azab. The Role of Hypoxia in Cancer Progression, Angiogenesis, Metastasis, and Resistance to Therapy. *Hypoxia* **2015**. 3. 83–92. https://doi.org/10.2147/HP.S93413

[46] C. Matera, A. M. J. Gomila, N. Camarero, M. Libergoli, C. Soler, P. Gorostiza. Photoswitchable Antimetabolite for Targeted Photoactivated Chemotherapy. *J. Am. Chem. Soc.* **2018**. 140 (46). 15764–15773. https://doi.org/10.1021/jacs.8b08249

[47] L. Gourdon, K. Cariou, G. Gasser, G. Phototherapeutic Anticancer Strategies with First-Row Transition Metal Complexes: A Critical Review. *Chem. Soc. Rev.* **2022**. 51. 1167-1195. https://doi.org/10.1039/d1cs00609f

[48] A. Kumar, A. Dixit, S. Sahoo, S. Banerjee, A. Bhattacharyya, A. Garai, A. A. Karande, A. R. Chakravarty. Crystal Structure, DNA Crosslinking and Photo-Induced Cytotoxicity of Oxovanadium(IV) Conjugates of Boron-Dipyrromethene. *J. Inorg. Biochem*. **2020**. 202. 110817. https://doi.org/10.1016/j.jinorgbio.2019.110817

[49] C. Imberti, P. Zhang, H. Huang, P. J. Sadler. New Designs for Phototherapeutic Transition Metal Complexes. *Angew. Chem*. **2020**, 132 (1), 61-73. https://doi.org/10.1002/ange.201905171

[50] Y. Chen, L. Bai, P. Zhang, H. Zhao, Q. Zhou, Q. The Development of Ru(II)-Based Photoactivated Chemotherapy Agents. *Molecules*. **2021**. 26 (18). 5679. https://doi.org/10.3390/molecules26185679

[51] M. A. Munegowda, A. Manalac, M. Weersink, S. A. McFarland, L. Lilge. Ru(II) Containing Photosensitizers for Photodynamic Therapy: A Critique on Reporting and an Attempt to Compare Efficacy. *Coord. Chem. Rev.* **2022**. 470. 214712. https://doi.org/10.1016/j.ccr.2022.214712

[52] G. Han, G. Li, J. Huang. C. Han, C. Turro. Two-Photon-Absorbing Ruthenium Complexes Enable Near Infrared Light-Driven Photocatalysis. *Nat. Commun*. **2022**. 13. 2288. https://doi.org/10.1038/s41467-022-29981-3

[53] B. Bonavida, Nitric Oxide and Cancer: Prognosis, Prevention and Therapy, Springer, New-York, **2010.** 513. https://link.springer.com/book/10.1007/978-1-4419-1432-3?page=2#toc

[54] S. Huerta. Nitric Oxide for Cancer Therapy. *Future Sci. OA*. **2015.** 1 (1). FSO44. https://doi.org/10.4155/fso.15.44

[55] D. D. Thomas, M. G. Espey, L. A. Ridnour, L. J. Hofseth, D. Mancardi, C. C. Harris, D. A. Wink. Hypoxic Inducible Factor 1α, Extracellular Signal-Regulated Kinase, and P53 Are Regulated by Distinct Threshold Concentrations of Nitric Oxide. *Proc. Natl. Acad. Sci*. **2004**. 101 (24). 8894–8899. https://doi.org/10.1073%2Fpnas.0400453101

[56] S. N. Kaore, H. S. Amane, N. M. Kaore. Citrulline: pharmacological perspectives and its role as an emerging biomarker in future. *Fundam. Clin. Pharmacol.* **2013**. 27(1). 35-50. https://doi.org/10.1111/j.1472-8206.2012.01059.x

[57] J. C. Marini. Interrelationships between glutamine and citrulline metabolism. *Curr. Opin. Clin. Nutr. Metab. Care.* **2016**. 19 (1). 62-6. doi: https://doi.org/10.1097/mco.0000000000000233

[58] J. M. Phang. Proline Metabolism in Cell Regulation and Cancer Biology: Recent Advances and Hypotheses. *Antioxid. Redox. Signal.* **2019**. 30 (4). 635-649. https://doi.org/10.1089%2Fars.2017.7350

[59] M. E. Brosnan, J. T. Brosnan. Renal arginine metabolism. *J Nutr.* **2004.** 134 (10). 2791S-2795S. https://doi.org/10.1093/jn/134.10.2791s

[60] N. W. Rajapakse, D. L. Mattson. Role of L-arginine in nitric oxide production in health and hypertension. *Clin. Exp. Pharmacol. Physiol*. **2009**. 36 (3). 249-55. https://doi.org/10.1111/j.1440-1681.2008.05123.x

[61] U. Förstermann, W. C. Sessa. Nitric oxide synthases: regulation and function. *Eur. Heart. J.* **2012**. 33 (7). 829-37. https://doi.org/10.1093%2Feurheartj%2Fehr304

[62] I. D. Weiner, W. E. Mitch, J. M. Sands. Urea and Ammonia Metabolism and the Control of Renal Nitrogen Excretion. *Clin. J Am. Soc. Nephrol*. **2015**. 10 (8). 1444-58. https://doi.org/10.2215/cjn.10311013

[63] R. Govinda, S. Singh, G. Kaushik. NO donors as the wonder molecules with therapeutic potential: Recent trends and future perspectives. *Coord. Chem. Rev.* **2023**. 481. 215052. https://doi.org/10.1016/j.ccr.2023.215052

[64] J. Abrams. Glyceryl trinitrate (nitroglycerin) and the organic nitratorganicg the method of administration. *Drugs*. **1987.** 34 (3). 391-403. https://doi.org/10.2165/00003495-198734030-00005

[65] Y. Yang, Z. Huang, L. L. Li. Advanced nitric oxide donors: chemical structure of NO drugs, NO nanomedicines and biomedical applications. *Nanoscale*. **2021.** 13 (2). 444-459. https://doi.org/10.1039/d0nr07484e

[66] I. L. Megson, D. J. Webb. Nitric oxide donor drugs: current status and future trends. *Expert Opin. Investig. Drugs.* **2002**. 11 (5), 587-601. https://doi.org/10.1517/13543784.11.5.587

[67] M. G. Mason, R. S. Holladay, P. Nicholls, M. Shepherd, C. E. Cooper. Chapter 8 - A Quantitative Approach to Nitric Oxide Inhibition of Terminal Oxidases of the Respiratory Chain. R. K. Poole, Methods in Enzymology, *Academic Press*, **2008**. 437. 135-159. doi: https://doi.org/10.1016/S0076-6879(07)37008-0

[68] M. A. Cinelli, H. T. Do, G. P. Miley, R. B. Silverman. Inducible nitric oxide synthase: Regulation, structure, and inhibition. *Med. Res. Rev.* **2020**. 40 (1). 158-189. https://doi.org/10.1002/med.21599

[69] S. Toyokuni. Iron and Thiols as Two Major Players in Carcinogenesis: Friends or Foes? *Front. Pharmacol.* **2014**. 5. 200. https://doi.org/10.3389/fphar.2014.00200

[70] N. Lehnert, N, E. Kim, H. T. Dong, J. B. Harland, A. P. Hunt, E. C. Manickas, K. M. Oakley, J. Pham, G. C. Reed, V. S. Alfaro. The Biologically Relevant Coordination Chemistry of Iron and Nitric Oxide: Electronic Structure

and Reactivity. *Chem. Rev*. **2021**. 121 (24). 14682-14905. https://doi.org/10.1021/acs.chemrev.1c00253

[71] H. Lewandowska, M. Kalinowska, K. Brzóska, K. Wójciuk, G. Wójciuk, M. Kruszewski. Nitrosyl Iron Complexes—Synthesis, Structure and Biology. *Dalton Trans*. **2011**. 40. 8273-8289. https://doi.org/10.1039/C0DT01244K

[72] J. Chen, W. R. Browne. Photochemistry of Iron Complexes. *Coord. Chem. Rev.* **2018**. 374. 15-35. https://doi.org/10.1016/j.ccr.2018.06.008

[73] A. B. Seabra. Editor. Nitric Oxide Donors: Novel Biomedical Applications and Perspectives; Chapter 4 - Nitric Oxide Donors and Therapeutic Applications in Cancer, K. Kashfi, P. L. Duvalsaint; *Academic Press*. **2017**. 75-119. https://doi.org/10.1016/B978-0-12-809275-0.00004-1

[74] J. E. Maddison, S. W. Page, D. B. Church. Chapter 17 - Drugs used in the management of heart disease and cardiac arrhythmias. In Small Animal Clinical Pharmacology, 2nd ed.; W.B. Saunders; Edinburgh. **2008**. 380-457. https://doi.org/10.1016/B978-070202858-8.50019-1

[75] J. Bourassa, W. DeGraff, S. Kudo, D. A. Wink, J. B. Mitchell, P. C. Ford. Photochemistry of Roussin's Red Salt, $Na_2[Fe_2S_2(NO)_4]$, and of Roussin's Black Salt, $NH_4[Fe_4S_3(NO)_7]$. In Situ Nitric Oxide Generation to Sensitize γ-Radiation Induced Cell Death. *J. Am. Chem. Soc.* **1997**. 119 (12). 2853–2860. https://doi.org/10.1021/ja963914n

[76] E. Meade, C. Fowley, M. Savage, M. Slattery. Antibacterial Activity of Roussin's Black Salt Against Multidrug Resistant Zoonotic Pathogens Isolated from Companion Animals. *Acta Sci. Vet. Sci*. **2020**. 2. 01-09. https://doi.org/10.31080/ASVS.2020.02.0046

[77] D. R. Truzzi, N. M. Medeiros, O. Augusto, P. C. Ford. Dinitrosyl Iron Complexes (DNICs). From Spontaneous Assembly to Biological Roles. *Inorg.*

Chem. **2021**. 60 (21). 15835–15845. https://doi.org/10.1021/acs.inorgchem.1c00823

[78] S.-C. Wu, C.-Y. Lu, Y.-L. Chen F.-C. Lo, T.-Y. Wang, Y.-J. Chen, S.-S. Yuan, W.-F. Liaw, Y.-M. Wang. Water-Soluble Dinitrosyl Iron Complex (DNIC): a Nitric Oxide Vehicle Triggering Cancer Cell Death via Apoptosis. *Inorg. Chem.* **2016**. 55 (18). 9383–9392. https://doi.org/10.1021/acs.inorgchem.6b01562

[79] N. A. Sanina, S. M. Aldoshin. Influence of Nitrosyl Iron Complex with Thiosulfate Ligands on Therapeutically Important Targets Related to Type 2 Diabetes Mellitus. *Russ. Chem. Bull*. **2011**. 60 (7). 1223–1251. https://doi.org/10.3390/membranes13070615

[80] A. K. Patra, R. K. Afshar, J. M. Rowland, M. M. Olmstead, P. K. Mascharak, Iron Nitrosyls of a Pentadentate Ligand Containing a Single Carboxamide Group: Syntheses, Structures, Electronic Properties, and Photolability of NO. *Angew. Chem. Int. Ed.* **2003**. 42(37). 4517–4521. https://doi.org/10.1021/ic0301627

[81] D. C. de Santana, K. Dias, J. G. Souza, A. T. Ogunjimi, M. C. Souza, R. S. Silva, R. F. Lopez. NO Exchange for a Water Molecule Favorably Changes Iontophoretic Release of Ruthenium Complexes to the Skin. *Molecules*. **2017**. 22 (1). 104. https://doi.org/10.3390/molecules22010104

[82] M. J. Rose, P. K. Mascharak. Photoactive Ruthenium Nitrosyls: Effects of Light and Potential Application as NO Donors. *Coord. Chem. Rev*. **2008**. 252. 2093-2114. https://doi.org/10.1016/j.ccr.2007.11.011

[83] A. B. Cox, R. M. Wallace. Photolysis of Nitrosylruthenium Chloro Complexes. *Inorg. Nucl. Chem. Lett*. **1971**. 7 (12). 1191-1194. https://doi.org/10.1016/0020-1650(71)80064-8

[84] P. Komozin, V. Kazakova, I. Miroshnichenko, N. Sinitsyn. Etude du processus de photolyse des nitroso composés de ruthénium par la méthode de RPE. *Zh Neorganich Khim*. **1983**. 28(12). 3186-3187.

[85] N. L. Fry, P. K. Mascharak. Photoactive ruthenium nitrosyls as NO donors: how to sensitize them toward visible light. *Acc. Chem. Res.* **2011.** 44. 289–298. https://doi.org/10.1021/ar100155t

[86] I. Stepanenko, M. Zalibera, D. Schaniel, J. Telser, V. B. Arion. Ruthenium-nitrosyl complexes as NO-releasing molecules, potential anticancer drugs, and photoswitches based on linkage isomerism. *Dalton Trans.* **2022**. 51. 5367-5393. https://doi.org/10.1039/D2DT00290F

[87] B. Pauwels, C. Boydens, L. Vanden-Daele, J. Van-Voorde. Ruthenium-based Nitric Oxide donating, and Carbon Monoxide donating Molecules. J. *Pharm. Pharmacol*. **2016**. 68 (3). 293-304. https://doi.org/10.1111/jphp.12511

[88] J. Akl, I. Sasaki, P. G. Lacroix, I. Malfant, S. Mallet-Ladeira, P. Vicendo, N. Farfán, R. Santillan. Comparative photo-release of nitric oxide from isomers of substituted terpyridinenitrosylruthenium(II) complexes: experimental and computational investigations *Dalton Trans*. **2014**. 43 (33). 12721–12733. https://doi.org/10.1039/c4dt00974f

[89] J. Akl, I. Sasaki, P. G. Lacroix, V. Hugues, P. Vicendo, M. Bocé, S. Mallet-Ladeira, M. Blanchard-Desce, I. Malfant. trans- and cis-(Cl,Cl)-$[Ru^{II}(FT)Cl_2(NO)](PF_6)$: promising candidates for NO release in the NIR region. *Photochem. Photobiol. Sci*. **2016**. 15 (12). 1484–1491. https://doi.org/10.1039/C6PP00181E

[90] A. Castellarin, S. Zorzet, A. Bergamo, G. Sava. Pharmacological Activities of Ruthenium Complexes Related to Their NO Scavenging Properties. *Int. J. Mol. Sci*. **2016**. 17 (8). 1254. https://doi.org/10.3390/ijms17081254

[91] M. Małecka, A. Skoczyńska, D. M. Goodman, C. G. Hartinger, E. Budzisz. Biological Properties of Ruthenium(II)/(III) Complexes with Flavonoids as Ligands. *Coord. Chem. Rev.* **2021**. 436. 213849. https://doi.org/10.1016/j.ccr.2021.213849

[92] K. Lin, Z. Z. Zhao, H. B. Bo, X. J. Hao, J. Q. Wang. Applications of Ruthenium Complex in Tumor Diagnosis and Therapy. Front. Pharmacol. **2018**. 9. 1323. https://doi.org/10.3389/fphar.2018.01323

[93] F. Mark, W. F. Chen, C. T. Pan, M. C. Lin, Z. H. Wen, C. F. Liao, Y. L. Shiue. Competitive Real-Time Near Infrared (NIR) Vein Finder Imaging Device to Improve Peripheral Subcutaneous Vein Selection in Venipuncture for Clinical Laboratory Testing. *Micromachines*. **2021**. 12 (4). 373. http://dx.doi.org/10.3390/mi12040373

[94] M. Champeau, S. Vignoud, L. Mortier, S. Mordo. Photodynamic therapy for skin cancer: How to enhance drug penetration? *J. Photochem. Photobiol. B, Biol*. **2019**. 197. 111544. https://doi.org/10.1016/j.jphotobiol.2019.111544

[95] C. De Angelis. Nonlinear Optics, *Front. Photon.* **2021,** Volume 1. 628215. https://doi.org/10.3389/fphot.2020.628215

[96] H.S. Nalwa, S. Miyata. Nonlinear Optics of Organic Molecules and Polymers. first ed. *CRC Press*. **2019**. 896.

[97] P. A. Shaw, E. Forsyth, F. Haseeb, S. Yang, M. Bradley, M. Klausen. Two-Photon Absorption: An Open Door to the NIR-II Biological Window? *Front. Chem*. **2022**. 10:921354. https://doi.org/10.3389/fchem.2022.921354

[98] F. Steinlechner, N. Hermosa, V. Pruneri. Frequency Conversion of Structured *Light. Sci Rep*. **2016**. 6. 21390. https://doi.org/10.1038/srep21390

[99] A. D. Li, W. C. Liu. Optical Properties of Ferroelectric Nanocrystal/Polymer Composites. *Woodhead Publishing*. **2010.** 108-158. https://doi.org/10.1533/9780857090249.1.108

[100] R. A. Serway, J. W. Jewett. Physics for Scientists and Engineers. 10th ed.; *Cengage Learning*. **2014**. Vol. 2, 756–757. https://n9.cl/e3vnz7

[101] P. W. Atkins, L. Jones. Chemical Principles: The Quest for Insight, 5th ed.; *Macmillan Learning*. **2010**. 1170. https://archive.org/details/AtkinsChemicalPrinciples5thEdition

[102] C. Bastos, B. Leite. Analysis and Validation of Dipole Moment Calculations in Chemistry Teaching. *Orbital: The Electronic Journal of Chemistry*. **2017**. 9. 360-368. http://dx.doi.org/10.17807/orbital.v9i5.1020

[103] Chang, Raymond. Chapter 13: Intermolecular Forces/ Ion-Induced Dipole and Dipole-Induced Dipole Interactions/ Dispersion, or London, Interactions. *Physical Chemistry for the Biosciences. Sansalito*, CA: University Science, **2005**. 495-98.

[104] G. D. Stucky, S. R. Marder, J. E. Sohn. Linear and Nonlinear Polarizability. **1991**. *Am. Chem. So*. 1-30. https://doi.org/10.1002/actp.1993.010440216

[105] C. Paorici. In Organic Crystals for Nonlinear Optics. K. H. J. Buschow, R. W. Cahn, M. C. Flemings, B. Ilschner, E. J. Kramer, S. Mahajan, P. Veyssière. Encyclopedia of Materials: Science and Technology; *Elsevier*: 2001. 6526-6534. http://dx.doi.org/10.1201/9780429126086-8

[106] N. Bloembergen. Nonlinear Optics: Past, Present and Future. In Guided Wave Nonlinear Optics. D. B. Ostrowsky, R. Reinisch, Eds. NATO ASI Series, *Springe*r. **1992**. Vol. 214 1-9. https://link.springer.com/chapter/10.1007/978-94-011-2536-9_1

[107] M. Bass. OSA Handbook of Optics, Vol. IV; *Op. So. of Am*. **2000**. Chapter 17. 832. https://www.academia.edu/28111062/Handbook_of_Optics_5_Volumes

[108] A. Lahiri. In Basic Optics. *Elsevier*: **2016**. 901-968. https://www.sciencedirect.com/book/9780128053577/basic-optics

[109] Y. Li. Plasmonic Optics: Theory and Applications; *SPIE*. **2017**. 250. https://spie.org/Publications/Book/2263756?SSO=1

[110] M. Thalhammer, A. Penzkofer. Measurement of Third-Order Nonlinear Susceptibilities by Non-Phase Matched Third-Harmonic Generation. *Appl. Phys. B*. **1983**. 32. 137-143. https://link.springer.com/article/10.1007/BF00688819

[111] M. Bass. Ed. Handbook of Optics. Volume IV Fiber Optics and Nonlinear Optics, 2nd ed.; School of Optics/The Center for Research and Education in Optics and Lasers (CREOL), *University of Central Florida*. **2001**. 1248. https://dl.acm.org/doi/book/10.5555/1594759

[112] M. Rumi, J. Perry. Two-photon absorption: An overview of measurements and principles. *Ad. Opt. Photonics*. **2010**. 2. 451-458. https://doi.org/10.1364/AOP.2.000451

[113] J.-C. Gâcon. Two-photon Spectroscopy; Buschow. K. H. J., Cahn, R. W., Flemings, M. C., Ilschner, B., Kramer, E. J., Mahajan, S., Veyssière, P., Eds.; Encyclopedia of Materials: Science and Technology; *Elsevier*. **2001**. 9425-9429.https://www.sciencedirect.com/referencework/9780080431529/encyclopedia-of-materials-science-and-technology

[114] Q. Cui, Y. Li, J. Chang, H. Zhao, C. Xu. Temporally Resolving Synchronous Degenerate and Nondegenerate Two-Photon Absorption in 2D Semiconducting Monolayers. *Laser & Photonics Rev*. **2018**. 13. https://doi.org/10.1002/lpor.201800225

[115] N. V. Kachenko. Optical Spectroscopy: Methods and Instrumentations. *Elsevier*: **2006**. 293. https://www.sciencedirect.com/book/9780444521262/optical-spectroscopy

[116] G. S. He, L. Tan, Q. Zheng, P. N. Multiphoton absorbing materials: molecular designs, characterizations, and applications. Prasad. *Chem. Rev*. **2008**. 108 (4). 1245–1330. https://doi.org/10.1021/cr050054x

[117] E. Zojer, D. Beljonne, T. Kogej, H. Vogel, S. R. Marder, J. W. Perry, J. L. Brédas. Tuning the Two-Photon Absorption Response of Quadrupolar Organic Molecules. J. *Chem. Phys*. **2002**. 116 (9). 3646–3658. https://doi.org/10.1063/1.1445118

[118] M. Oheim, J. D. Michael, M. Geisbauer, D. Madsen, R. H. Chow. Principles of two-photon excitation fluorescence microscopy and other nonlinear imaging approaches. *Adv. Drug Deliv.* **2006**. 58 (7). 788-808. https://doi.org/10.1016/j.addr.2006.07.005

[119] C. Xu, W. W. Webb. Determination of absolute two-photon excitation cross sections by in situ second-order autocorrelation. *J. Opt. Soc. Am.* **1996**. 13(3). 481. https://doi.org/10.1364/OL.20.002372

[120] M. Dudek, N. Tarnowicz-Staniak, M. Deiana, Z. Pokładek, M. Samoć, K. Matczyszyn. Two-photon Absorption and Two-photon-induced Isomerization of Azobenzene Compounds. *RSC Adv.* **2020**. 10 (66). 40489-40507. https://doi.org/10.1039/d0ra07693g

[121] a) H. A. Majeed, A. B. Sharba. Environment-Induced Effects on The Nonlinear Refractive Index of Methyl Orange at Different Spectral Regions. J. *Phys.: Conf. Ser.* **2021**. 1818. 012131. http://dx.doi.org/10.1088/1742-6596/1818/1/012131

b) S. Jeyaram. Study of Third-order Nonlinear Optical Properties of Basic Violet 3 Dye in Polar Protic and Aprotic Solvents. *Journal of Fluorescence*. **2021** 31 (6). 02796. https://link.springer.com/article/10.1007/s10895-021-02796-z

[122] M. Chen, J. Shao, Y. Zhao, G. Hu, M. Zhu, Y. Chai, K. Zhang, H. Ma. High-Sensitivity Measurements of the Nonlinear Absorption Coefficient of Wide Bandgap Oxide Thin Films with the Z-Scan Method. *Op. Mater. Express*. **2022**. 12 (2). 533-544. https://ui.adsabs.harvard.edu/link_gateway/2022OMExp..12..533C/doi:10.1364/OME.447678

[123] L. Lamaignère, G. Toci, B. Patrizi, M. Vannini, A. Pirri, S. Fanetti, R. Bini, G. Mennerat, A. Melninkaitis, L. Lukas, J. Hein. Determination of Non-Linear Refractive Index of Laser Crystals and Ceramics via Different Optical Techniques. *Opt. Mater*. **2020**. 8. 100065. https://doi.org/10.1016/j.omx.2020.100065

[124] Y. Xu, Y. Lu, Y. Zuo, F. Xu, D. Zuo. Z-Scan Measurements of Nonlinear Refraction and Absorption for Aluminum-Doped Zinc Oxide Thin Film. *Appl. Opt.* **2019**. 58. 6112. https://doi.org/10.1364/ao.58.006112

[125] S. D. G. Mariano, N. A. M. Saraiva, J. C. S. Costa, C. A. Sousa, J. B. N. Silva, H. A. Garcia, F. E. P. Santos. Nonresonant Nonlinear Optical Switching Behavior of Ag Monometallic and Ag@Au Bimetallic Investigated by Femtosecond Z-Scan Measurements. *Opt. Laser Technol.* **2021**. 142. 107247. https://doi.org/10.1016/j.optlastec.2021.107247

[126] V. S. G. Krishna, M. G. Mahesha. "ZnS, an Excellent Material in Photonics" - A Review Based on Z-Scan Study. *Physica B. Condensed Matter*. **2022.** 628. 413628. https://doi.org/10.1016/j.physb.2021.413628

[127] A. E. Siegman. Lasers. *University Science Book: Palo Alto, CA-USA*. **1986**. 1283. https://uscibooks.aip.org/books/lasers/

[128] P. L. Kelley. Self-Focusing of Optical Beams. Phys. Rev. Lett. **1965**. 15 (26). 1005. https://doi.org/10.1103/PhysRevLett.15.1005

[129] a) S. L. Gomez, F. L. S. Cuppo, A. M. Figueiredo Neto. Nonlinear Optical Properties of Liquid Crystals Probed by Z-Scan Technique. *Braz. J. Phys.* **2003**. 33 (4). 813-820. https://dx.doi.org/10.1590/s0103-97332003000400035

b) A. Ortega, J. Dávila, E. Lara (2011). Modification to the z-scan technique by widths measurements. Journal of Physics: Conference Series. *Journal of Physics: Conference Series*. **2011**. 274 (1). 012139. http://dx.doi.org/10.1088/1742-6596/274/1/012139

[130] R. M. Barba-Barba. Nonlinear Absorption in Organic Semiconductor Molecules and Their Study Through Transient Absorption. *Centro de Investigaciones en Óptica, A.C.*: León, Guanajuato. **2016**.

[131] P. B. Chapple, J. Staromlynska, A. J. Hermann, T. J. McKay, R. McDuff. Single-Beam Z-Scan: Measurement Techniques and Analysis. Journal of Nonlinear *Opt. Phys. Mat*. **1997**. 06 (3). 251-293. https://ui.adsabs.harvard.edu/link_gateway/1997JNOPM...6..251C/doi:10.1142/S0218863597000204

[132] IUPAC. Compendium of Chemical Terminology, 2nd ed. (the "Gold Book"). *Blackwell Scientific Publications, Oxford*. **1997**. https://goldbook.iupac.org/

[133] S. Shaik. The Lewis legacy: The chemical bond—A territory and heartland of chemistry*. I. J. of Quantum Chem*. **2007**. 28 (1). 51-61. https://doi.org/10.1002/jcc.20517

[134] R. Emanuelsson. Conjugation in Organic Group 14 Element Compounds: Design, Synthesis and Experimental Evaluation. Digital Comprehensive Summaries of Uppsala Dissertations from the Faculty of Science and

Technology 1140, *Uppsala University*. **2014**. 1-70. https://www.diva-portal.org/smash/get/diva2:709833/FULLTEXT01.pdf

[135] B. Milián-Medina, J. Gierschner. π-Conjugation. *Wires Comput. Mol. Sci*. **2012**. 2 (04). 513-524. https://doi.org/10.1002/wcms.95

[136] R. W. Boyd, G. L. Fischer. Nonlinear Optical Materials. K.H. Jürgen-Buschow, W. R. Cahn, C. Merton-Flemings, B. Ilschner, E. J. Kramer, S. Mahajan, P. Veyssière. Eds. Encyclopedia of Materials: Science and Technology. *Elsevier*. **2001**. 434. https://www.sciencedirect.com/referencework/9780080431529/encyclopedia-of-materials-science-and-technology

[137] P. Simon, J. Andrés-Castán, P. Josse, M. Blais, A. Habibi, I. Ramirez, K. Walzer, P. Blanchard, C. Cabanetos. Effect of 4-biphenyl groups on the charge transport and photovoltaic properties of arylamine-based push-pull systems. *New J. Chem*. **2020**. 44. 11441-11447. https://doi.org/10.1039/D0NJ02019B

[138] P. G. Lacroix, I. Malfant, P. Labra-Vázquez, N. Fárfan, G. Ramos-Ortiz. Two-photon absorption-based delivery of nitric oxide from ruthenium nitrosyl complexes. *Dalton Trans*. **2022**. 51(39). 14833-14841. http://dx.doi.org/10.1039/d2dt02553a

[139] E. Zojer, D. Beljonne, P. Pacher, J. L. Brédas. Two-Photon Absorption in Quadrupolar π-Conjugated Molecules: Influence of the Nature of the Conjugated Bridge and the Donor-Acceptor Separation. *Chem. (Weinheim an der Bergstrasse)*. **2004**. 10 (11). 2668–2680. https://doi.org/10.1002/chem.200305650

[140] W. H. Lee, H. Lee, J. A. Kim, J. H. Choi, M. Cho, S. J. Jeon, B. R. Cho. Two-Photon Absorption and Nonlinear Optical Properties of Octupolar Molecules. *J. Am. Chem. Soc*. **2001**. 123 (43). 10658–10667. https://doi.org/10.1021/ja004226d

[141] C. C. Jiménez, A. Enríquez-Cabrera, O. González-Antonio, J. Ordóñez-Hernández, P. G. Lacroix, P. Labra-Vázquez, N. Farfán, R. Santillan. State of the Art of Boron and Tin Complexes in Second- and Third-Order Nonlinear *Optics. Inorganics*. **2018**. 6. 131. http://dx.doi.org/10.3390/inorganics6040131

[142] C. Su-Lim, B. R. Cho. Two-photon probes for biomedical imaging. *Tetrahedron*. **2015**. 43 (71). 8219-8249. https://doi.org/10.1016/j.tet.2015.06.083

[143] S. Maruo, O. Nakamura, S. Kawata. Three-dimensional microfabrication with two-photon-absorbed photopolymerization. *Opt Lett.* **1997**. 22(2). 132-4. https://doi.org/10.1364/ol.22.000132

[144] A. Srinivasa-Rao. Optical limiting in the presence of simultaneous one and two photon absorption. *Optik.* **2018**. 157. 900-905. https://doi.org/10.1016/j.ijleo.2017.11.163

[145] I. F. A. Mariz, S. N. Pinto, A. M. Santiago. J. M. G. Marthino, J. Recio, J. J. Vaquero, A. M. Cuadro, E. Macoas. Two-Photon Activated Precision Molecular Photosensitizer Targeting Mitochondria. *Commun. Chem.* **2021**. 4. 142. https://doi.org/10.1038/s42004-021-00581-4

[146] A. Enriquez-Cabrera, P. G. Lacroix, I. Sasaki, S. Mallet-Ladeira, N. Farfán, R. M. Barba-Barba, G. Ramos-Ortiz, I. Malfant. Comparison of Carbazole and Fluorene Donating Effects on the Two-Photon Absorption and Nitric Oxide Photorelease Capabilities of a Ruthenium–Nitrosyl Complex. *Eur. J. Inorg.* **2017**. 3 (4). 531-543. https://doi.org/10.1002/ejic.201700895

[147] V. Bukhanko, A. F. León-Rojas, P. G. Lacroix, M. Tassé, G. Ramos-Ortiz, R. M. Barba-Barba, N. Farfán, R. Santillan, I. Malfant. Two-Photon Absorption Properties in “Push-Pull” Ruthenium Nitrosyl Complexes with various Fluorenylterpyridine-Based Ligands. *Eur. J. Inorg.* **2021**. 17. 1679-1684. https://doi.org/10.1002/ejic.202100109

[148] R. Chinchilla, C. Nájera. The Sonogashira Reaction: A Booming Methodology in Synthetic Organic Chemistry. *Chem. Rev*. **2007**. 107. 874. https://doi.org/10.1021/cr050992x

[149] I. Yu, I. V. Ananyev, E. A. Pidko. Revisiting van der Waals Radii: From Comprehensive Structural Analysis to Knowledge-Based Classification of Interatomic Contacts. *Chem. Phys. Chem.* **2020**. 21 (5). 370-376. https://doi.org/10.1002/cphc.201901083

[150] B. P. Cherniawski, S. A. Lopez, E. K. Burnett, I. Yavuz, L. Zhang, S. R. Parkin, K. N. Houk, A. L. Briseno. The Effect of Hexyl Side Chains on Molecular Conformations, Crystal Packing, and Charge Transport of Oligothiophenes. *J. Mater. Chem.* **2017**. 5 (3). 582–588. https://doi.org/10.1039/C6TC04612F

[151] A. A. Thomas, A. F. Zahrt, C. P. Delaney, S. E. Denmark. Elucidating the Role of the Boronic Esters in the Suzuki-Miyaura Reaction: Structural, Kinetic, and Computational Investigations. *J. Am. Chem. Soc*. **2018**. 140 (12). 4401–4416. https://doi.org/10.1021/jacs.8b00400

[152] H. C. Beachell, D. W. Beistel. Nuclear Magnetic Resonance Spectra of Phenylboronic Acids. *Inorg. Chem*. **1964**. 3 (7). 1028–1032. https://doi.org/10.1021/ic50017a025

[153] Z. Ji, S. Li, Y. Li, W. Sun. Back-to-back dinuclear platinum terpyridyl complexes: synthesis and photophysical studies. *Inorg. Chem*. **2010**. 49. 1337–1346. http://dx.doi.org/10.1021/ic9009674

[154] H. Elsbernd, H.; Beattie, J. K. The NMR Spectra of Terpyridine and the Bis-Terpyridine Complexes of Cobalt(III) and Iron(II). *J. Inorg. Nucl. Chem*. **1972**. 34 (2). 771–774. https://doi.org/10.1016/0022-1902(72)80463-9

[155] X. Chen, L. Ma, Y. Cheng, Z. Xie, L. Wang. Luminescent Supramolecular Polymers: Cd2+-Directed Polymerization and Properties. *Polym. Int.* **2007**. 56 (5). 648–654. https://acortar.link/jZSxya

[156] R. S. Rowland, R. Taylor. Intermolecular nonbonded contact distances in organic crystal structures: comparison with distances expected from van der Waals radii. J. Phys. Chem. **1996**. 100 (18). 7384–7391. https://doi.org/10.1021%2Fjp953141%2B

[157] D. Neuhaus, M. P. Williamson. The Nuclear Overhauser Effect in Structural and Conformational Analysis. *John Wiley & Sons, Inc*. **2000**. 611. https://catalogimages.wiley.com/images/db/pdf/0471246751.pdf

[158] D. Frath, P. Didier, Y. Mély, J. Massue, G. Ulrich. Vectorization and Intracellular Distribution of a Two-Photon-Absorbing, Near-Infrared-Emitting π-Extended Boranil *Dye. Chem Photo. Chem.* 2017. 1. 109. https://doi.org/10.1002/cptc.201700052

[159] R. Ganeev, A. Ryasnyansky, M. Baba, M. Suzuki, N. Ishizawa, M. Turu, S. Sakakibara, H. KurodaNonlinear. Refraction in CS2. *Appl. Phys.* **2004**. 78. 433–438. https://doi.org/10.1007/S00340-003-1389-Y

[160] F. Terenziani, C. Katan, E. Badaeva, S. Tretiak, M. Blanchard-Desce. Enhanced Two-Photon Absorption of Organic Chromophores: Theoretical and Experimental Assessments *Adv. Mater.* **2008**. 20. 4641–4678. https://doi.org/10.1002/ADMA.200800402

[161] P. V. Simpson, L. A. Watson, A. Barlow, G. Wang, M. P. Cifuentes, M. G. Humphrey. Record Multiphoton-Absorption Cross-Sections by Dendrimer Organometallation. *Angew. Chem*. Int. Ed. **2016**. 55. 2387–2391. http://dx.doi.org/10.1002/anie.201509223

[162] Y. Juarez-Martinez, P. Labra-Vázquez, A. Enríquez-Cabrera, A. F. Leon-Rojas, D. Martínez Bourget, P. G. Lacroix, M. Tassé, S. Mallet-Ladeira, N. Farfán, R. Santillan, G. Ramos-Ortiz, J.-P. Malval, I. Malfant, Bimetallic Ruthenium Nitrosyl Complexes with Enhanced Two-Photon Absorption

Properties for Nitric Oxide Delivery. *Chem. Eur. J*. **2022**. 28. e202201692 (1-14). https://doi.org/10.1002/chem.202201692

[163] A. E. Cabrera, I. Sasaki, V. Bukhanko, M. Tassé, S. Mallet-Ladeira, P. G. Lacroix, R. M. Barba-Barba, G. Ramos-Ortiz, N. Farfán, Z. Voitenko, I. Malfant. Replacing Two Chlorido Ligands by a Bipyridine Ligand in Ruthenium Nitrosyl Complexes with NO-Release Capabilities: A Comparative Study. *Chem. Eur. J*. **2017**, 23, 11, 1446-1456. https://doi.org/10.1002/ejic.201601387

[164] D. Tsikas. Analysis of nitrite and nitrate in biological fluids by assays based on the Griess reaction: appraisal of the Griess reaction in the L-arginine/nitric oxide area of research. *J. Chromatogr. B.* **2007**, 851, 51-70. https://doi.org/10.1016/j.jchromb.2006.07.054

[165] A. J. Liu, Q. Duan, J. Wang, Z. Song, X. Qiao, H. Wang. Targeting the mitochondrial VDAC in hepatocellular carcinoma using a polyclonal antibody-conjugated to a nitrosyl ruthenium complex. *J. Biomed. Opt*. **2015**. 20. 015004–1- 015004–7. https://doi.org/10.1007%2Fs00775-018-1589-x

[166] J. Shen, P. T. Griffiths, S. J. Campbell, B, Utinger, M. Kalberer, S. E. Paulso. Ascorbate Oxidation by Iron, Copper, and Reactive Oxygen Species: Review, Model Development, and Derivation of Key Rate Constants. *Sci. Rep*. **2021**, 11, 7417. https://doi.org/10.1038/s41598-021-86477-8

[167] L. M. Loftus, K. F. Al-Afyouni, T. N. Rohrabaugh Jr., J. C. Gallucci, C. E. Moore, J. J. Rack, C. Turro. "Unexpected role of Ru(II) orbital and spin contribution on photoinduced ligand exchange: new mechanism to access the photodynamic therapy window." *J. Phys. Chem. C*. **2019**, 123 (16), 10291-10299. https://doi.org/10.1021/acs.jpcc.9b01576

[168] M. Schilz, H. Plenio. "A Guide to Sonogashira Cross-Coupling Reactions: The Influence of Substituents in Aryl Bromides, Acetylenes, and Phosphines." *J. Org. Chem*. **2012**, 77 (6), 2798-2807. https://doi.org/10.1021/jo202644g

[169] S. Gujral, S. Khatri, P. Riyal. Suzuki Cross Coupling Reaction - A Review. Indo Global J. Pharm. Sci. **2012**, 2, 351-367. http://dx.doi.org/10.35652/IGJPS.2012.41

[170] P. H. Dixneuf. Activation of alkynes with ruthenium complexes. *Pure & App. Chem.* **1989**, *61,* 1763-1770. https://doi.org/10.1351/pac198961101763

[171] J. Akl, I. Sasaki, P. G. Lacroix, I. Malfant, S. Mallet-Ladeira, P. Vicendo, N.Farfán, R. Santillan, Comparative photo-release of nitric oxide from isomers of substituted terpyridinenitrosylruthenium(ii) complexes: experimental and computational investigations. *Dalton Trans.* **2014**, 43, 12721–12733. https://doi.org/10.1039/C4DT00974F

[172] S. Li P. A. Crooks, X. Wei, J. de Leon, J. Toxicity of dipyridyl compounds and related compounds. *Crit. Rev. Toxicol*. **2004**. 34(5). 447–460. https://doi.org/10.1080/10408440490503143

[173] K. Karidi, A. Garoufis, N. Hadjiliadis, M. Lutz, A. L. Spek, J. Reedijk. Synthesis, Characterization, and DNA-Binding Studies o Nitro(oligopyridine)ruthenium(II) Complexes. *Inorg. Chem*. **2006.** 45.10282-10292. https://doi.org/10.1021/ic0608039

References (Anex)

[1] A. Komarov, D. Mattson, M.M. Jones, P.K. Singh, C.S. Lai, “In Vivo Spin Trapping of Nitric Oxide in Mice”, *Biochem. Biophys. Res. Commun*. **1993**. 195. 1191-1198.

[2] L. A. Shinobu, S. G. Jones, M. M. Jones. Effects of sodium N-methyl-N-dithiocarboxyglucamine on cadmium distribution and excretion. *Acta Pharmacol. Et Toxicol*. **1984.** 54. 189–194.

[3] Program Sa3.3 written by D. Lavabre and V. Pimienta (http://cinet.chim.pagesperso-orange.fr/tele_sa/install_Sa.html).

[4] A. Enriquez-Cabrera, I. Sasaki, V. Bukhanko, M. Tassé, S. Mallet-Ladeira, P. G. Lacroix, R. Barba-Barba, G. Ramos-Ortiz, N. Farfán, Z. Voitenko, I. Malfant, Eur. J. Inorg. Chem. 2017. 2017. 1446–1456.

[5] N. S. Makarov, M. Drobizhev, A. Rebane, Opt. Express 2008, 16, 4029– 4047.

[6] a) Sheik-Bahae M, Said AA, Wei TH, Hagan DJ, Van Stryland EW. Sensitive measurement of optical nonlinearities using a single beam. IEEE J Quant Electron 1990; 26(4):760–9.

b) Stryland EWV, Sheik-Bahae M. Z-scan measurements of optical nonlinearities. 1998.

RÉSUMÉ

1. Introduction

Le monoxyde d'azote (NO•) est une molécule largement étudiée au cours des 30 dernières années en raison de son implication dans diverses fonctions biologiques (à la fois physiologiques) et de ses applications en tant qu'antioxydant et antibactérien.

Cela a suscité un intérêt pour l'utilisation de NO• en tant qu'agent thérapeutique. Cependant, les médicaments actuellement utilisés libèrent NO• de manière spontanée et non contrôlée. Étant donné que de nombreux processus biologiques impliquant NO• sont régulés par sa concentration locale, l'objectif est de développer de nouvelles molécules capables de libérer NO• de manière contrôlée par un stimulus externe. La lumière offre un moyen élégant et finement ajustable d'introduire des agents thérapeutiques *in vivo* de manière non invasive. Cependant, l'un des principaux inconvénients est la longueur d'onde de la lumière utilisée, car beaucoup de ces composés absorbent dans la région ultraviolette (UV) ou visible, ce qui peut endommager les tissus.

Ce travail se concentre sur la conception, le développement et l'évaluation de composés capables de libérer NO• en utilisant la technique de l'absorption à deux photons (TPA) dans la fenêtre thérapeutique (λ = 600-1300 nm). A cette fin, des complexes nitrosyles ruthénium ont été synthétisés avec des ligands tels que la 2,2'-bipyridine et la 2,2';6',2''-terpyridine substituée par un groupement fluorène.

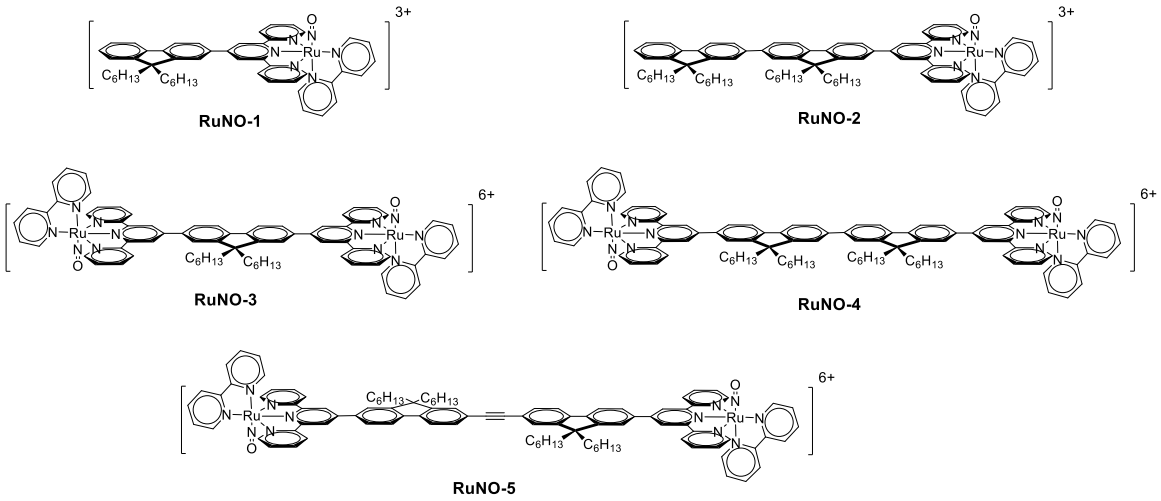

Schéma 1. Série de complexes **RuNO** synthétisés pour ce projet.

2. Synthèse des Ligands 1-5 et Ligands 2’ et 4’.

Pour la synthèse des complexes ciblés, nous avons débuté par la synthèse du composé principal, le 4'-(9,9-dihexyl-7-iodo-fluoren-2-yl)-2,2':6',2''-terpyridine (**3**), illustrée au **Schéma 2**. Tous les ligands des complexes contiennent deux chaînes hexyles alkylées en position C-9 du motif fluorène pour éviter toute réaction ultérieure des protons acides dans cette position. Cette modification a pour but d'améliorer la solubilité des complexes finaux.

La synthèse a commencé par une réaction de condensation aldolique entre le 9,9-dihexyl-7-iodo-fluorène-2-carbaldehyde (**1**) et la 2-acétylpyridine, produisant exclusivement la (E)-3-(9,9-dihexyl-7-iodo-fluorène-2-yl)-1-(pyridin-2-yl)prop-2-en-1-one (**2**). Par la suite, le composé (**2**) a subi une réaction d'addition de Michael avec l'énoate du sel de Krönhke. Cela a résulté en un intermédiaire 1,5-dicarbonyl non isolé qui s’est cyclisé *in situ* en présence d'ammoniac, aboutissant finalement à la 4'-(9,9-dihexyl-7-iodo-fluorène-2-yl)-2,2':6',2''-terpyridine souhaitée (**3**).

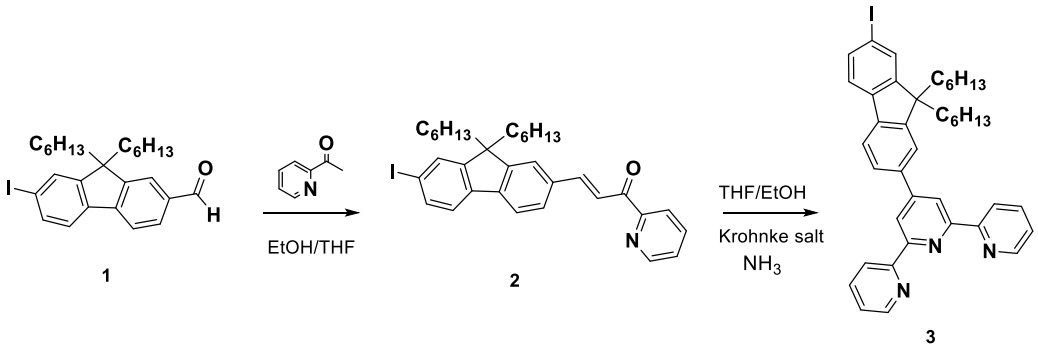

Schéma 2. Synthèse du composé **3** servant à la formation ultérieure des ligands **L1** à **L5**.

La synthèse du **Ligand 1** (**L1**) a été réalisée par la réduction de la 4'-(9,9-Dihexyl-7-iodo-fluoren-2-yl)-2,2':6',2''-terpyridine (**3**) en formant un complexe organométallique avec un cation lithium, suivi d'une protonation en milieu acide pour obtenir le produit final, 4'-(9,9-Dihexylfluoren-2-yl)-2,2':6',2''-terpyridine (**L1**) (**Schéma 3**).

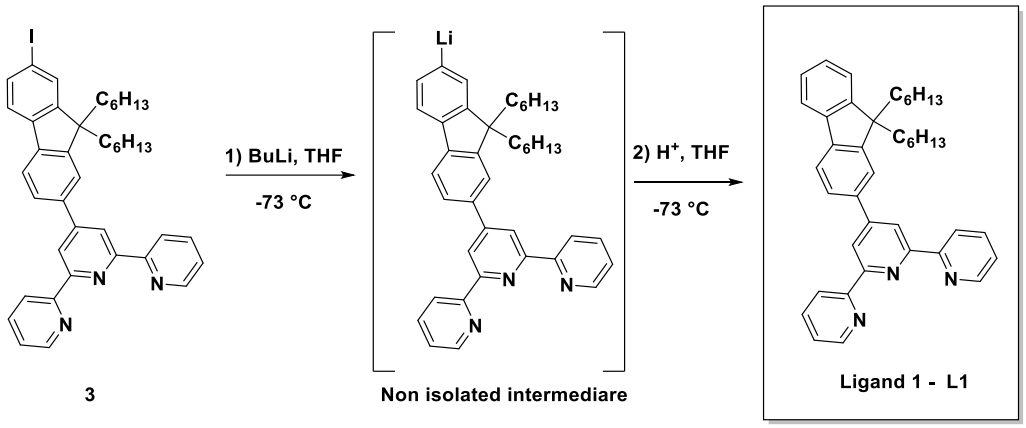

Schéma 3. Synthèse du **L1** par réaction de lithiation suivie d'un traitement acide (l'intermédiaire instable non isolé généré *in-situ* est montré au milieu du schéma).

Le **Ligand 2** (**L2**) a été synthétisé par une réaction de couplage Suzuki-Miyaura avec l'acide 9,9-dihexylfluorène -2-boronique (**4**) (**Schéma 4**).

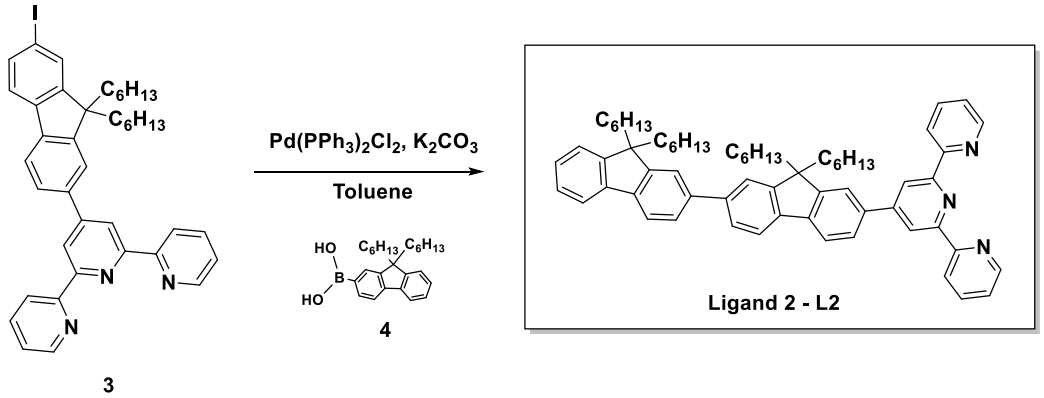

Schéma 4. Synthèse du **L2** par réaction de Suzuki-Miyaura utilisant l'acide boronique (**4**) en milieu basique.

Pour le **Ligand 3** (**L3**), une nouvelle voie synthétique a été adoptée. Au lieu de la 4'-bromo-2,2':6',2''-terpyridine utilisée précédemment, la condensation aldolique entre le composé **3** et la 2-acetylpyridine a été utilisée (**Schéma 5**).

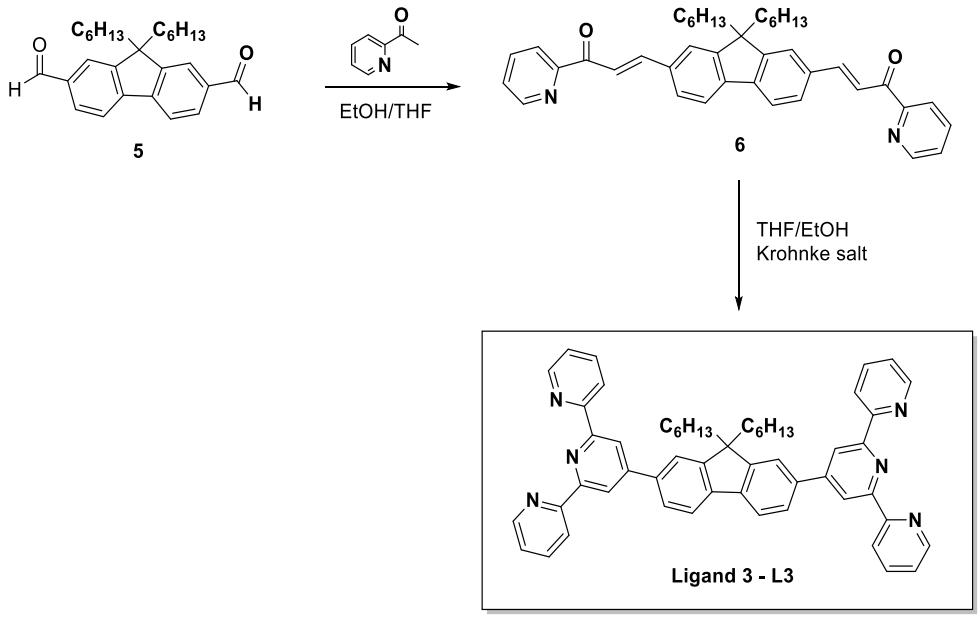

Schéma 5. Obtention du **L3** par la synthèse de terpyridine de Kröhnke.

Concernant le **Ligand 4** (**L4**), un défi a été rencontré avec la faible solubilité de l'intermédiaire double énone (**6**). Cela a conduit à une modification de l'approche synthétique, où la méthode convergente a été privilégiée. Cette stratégie, basée sur la réaction de Suzuki-Miyaura, a montré une efficacité remarquable, évitant les défis associés à l'utilisation d'acides boroniques.

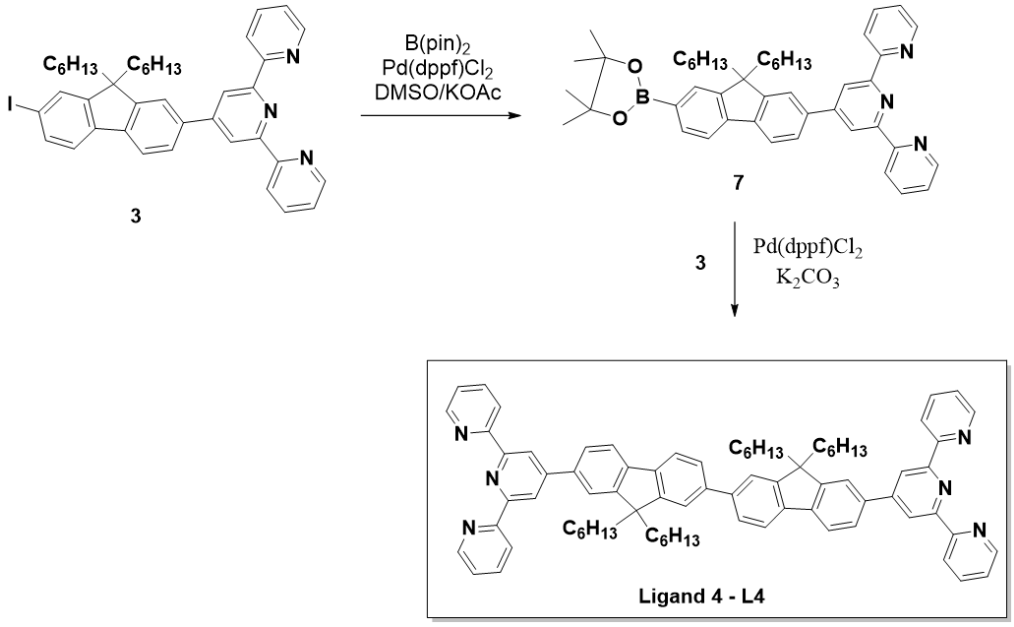

Schéma 7. Synthèse de **L4** via la réaction de Suzuki-Miyaura.

Le **Ligand 5** (**L5**) a été synthétisé en utilisant une voie convergente via la réaction de Sonogashira. L'utilisation d'un iodure sur le fluorène est un choix délibéré en raison de sa réactivité connue avec le palladium. Durant la purification, la forte affinité de la terpyridine pour la silice a nécessité l'utilisation d'une colonne courte afin d'optimiser le rendement.

La séquence de synthèse a commencé avec la (E)-3-(7-éthynyl-9,9-dihexyl-fluorén-2-yl)-1-(pyridin-2-yl)prop-2-en-1-one (**8)**, qui a subi une addition de Michael pour former l'intermédiaire énone (**9**). Ensuite, le composé (**9**) a été converti en terpyridine de Kröhnke, similaire aux ligands précédents, conduisant à la formation du composé (**10**). Enfin, **L5** a été obtenu par la réaction de Sonogashira. Les analyses ^{1}H-NMR, ^{13}C-NMR, NOESY, COSY, HMBC et HMQC ont confirmé la structure des ligands **L1**-**L5**.

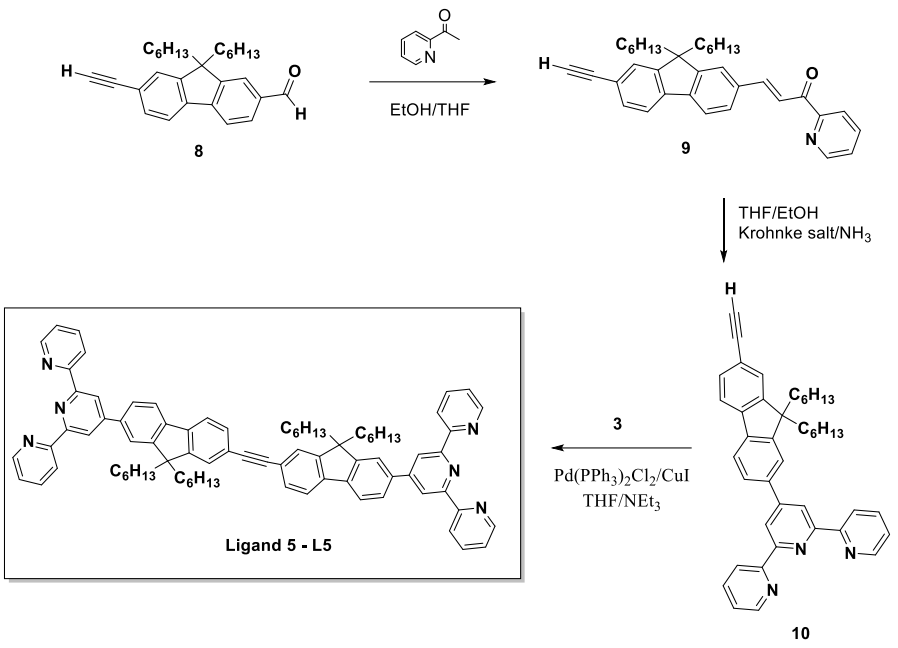

Schéma 8. Synthèse de **L5** via la réaction de Sonogashira.

Afin d'obtenir des structures cristallines, des homologues des ligands **L2** et **L4** ont été synthétisés (**Fig. 1**). Ces homologues, intégrant des chaînes méthyles plutôt qu'hexyles, sont plus propices à la cristallisation. En particulier, le **Ligand 2'** (**L2'**) a été synthétisé à partir du 7-bromo-9,9-dimethyl-9H-fluorene. Sa synthèse

implique une réaction de Suzuki-Miyaura. Le **Ligand 4'** (**L4')** a été synthétisé en utilisant une condensation aldolique suivie de la synthèse Kröhnke. L'ajout de dichlorométhane a été nécessaire en raison de la faible solubilité du composé. Cependant, le rendement pour **L4'** a été inférieur à celui de **L4**.

L'analyse par diffraction des rayons X des cristaux de L2' et L4' a montré que les deux ligands cristallisent dans le groupe d'espace triclinique P-1. Dans ce groupe, deux unités moléculaires sont reliées par un centre d'inversion.

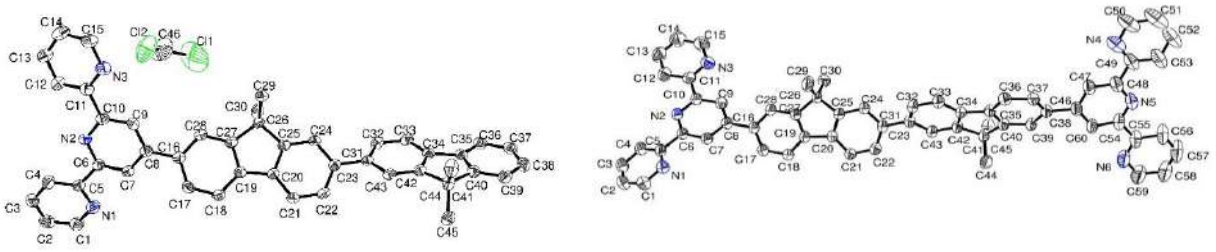

Figure 1. Structure de **L2'** (à gauche) et **L4'** (à droite), les atomes d'hydrogène sont omis pour plus de clarté.

3. Synthèses de complexes RuNO-1 à RuNO-5

Les ligands **L1**-**L5** synthétisés ont permis l'obtention des complexes **RuNO** ciblés en 4 étapes. Cette route comprend la métallation avec $RuCl_3 \cdot xH_2O$, le remplacement de deux ligands chlorido par un ligand 2,2'-bipyridine, l'échange d'un ligand chlorido par $NaNO_2$, et enfin le traitement avec de l'acide chlorhydrique concentré, aboutissant aux complexes **RuNO-1** à **RuNO-5**.

L'identité des complexes Ru^{II} a été confirmée par des analyses ^{1}H-NMR et ^{13}C-NMR. Des changements caractéristiques ont été observés dans les déplacements chimiques, liés à la proximité spatiale de ces atomes d'hydrogène avec des ligands monodentés variés. De plus, ces complexes ont été également confirmés par des analyses HRMS.

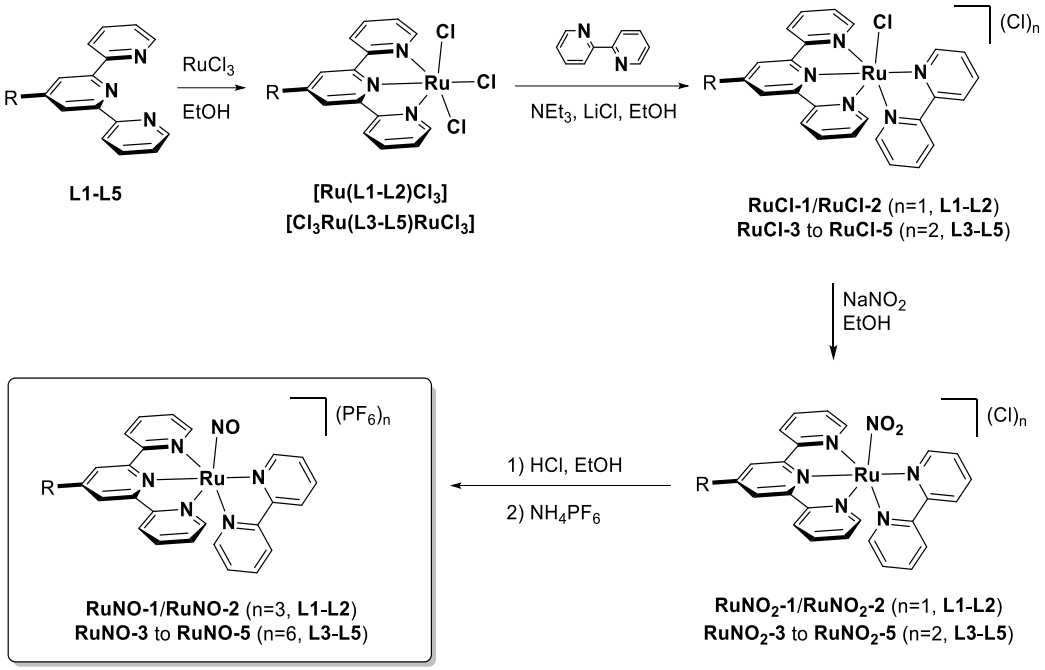

Schéma 9. Synthèse des complexes **RuNO-1** à **RuNO-5**.

4. Études sur les chaînes hexyles dans $RuNO_2$-2 par analyses de rayons X

La structure de **$RuNO_2$-2** est illustrée **Figure 2**, contenant une impureté de **RuCl-2**, dans un rapport NO_2^- / Cl^- de 84/16. Sa structure cristalline est triclinique (groupe d'espace P-1). Cette étude sur les cristaux de complexe ruthénium nitrite (**$RuNO_2$**) est motivée par les difficultés de croissance cristalline des échantillons à chaînes hexyles.

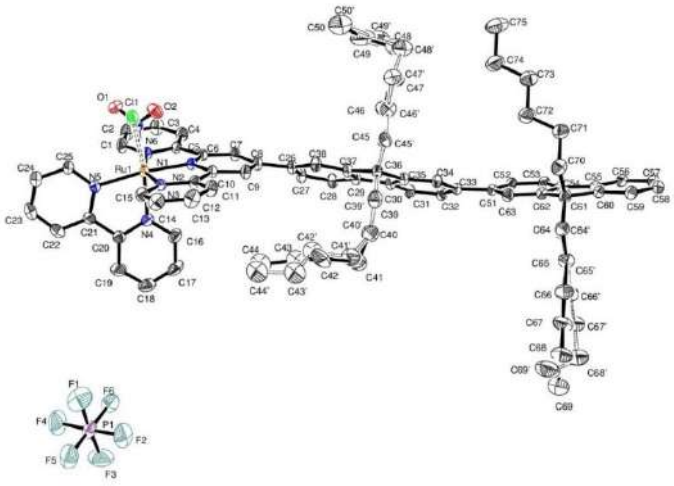

Figure 2. Structure de **$RuNO_2$-2.**

Les chaînes hexyles adoptent une conformation cisoid, contrairement aux structures **L2'** et **L4'** (**Fig. 1**) qui ont des chaînes méthyles en conformation transoid. Cette orientation pourrait s'expliquer par l'interaction entre les deux chaînes hexyles, stabilisant la structure. Malgré le potentiel encombrement stérique, l'interaction entre ces chaînes pourraient contribuer à la stabilité cristalline.

Des calculs, réalisées par le Dr. P. Lacroix, sur des molécules bis- fluorène avec des chaînes alkylées ont été menées (**Fig. 3**). Les résultats indiquent une préférence pour la conformation cisoid en solution, d'autant plus marquée que les chaînes sont plus longues. Des analyses ^{1}H-RMN et NOESY-RMN ont mis en évidence des interactions entre les chaînes hexyles, confirmant une interaction significative des protons dans certaines positions.

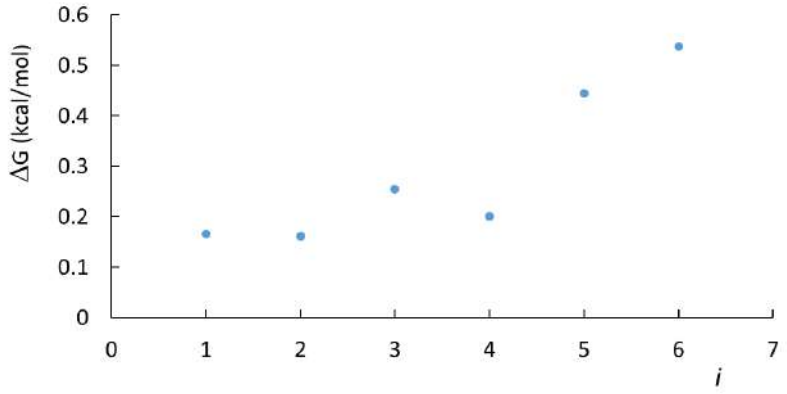

Figure 3. Stabilisation de la forme cisoid ($\Delta G = G_{transoid} - G_{cisoid}$) dans les bis-fluorènes tétrasubstitués par des chaînes alkyles de différentes longueurs (*i* = nombre d'atomes de carbone dans les chaînes).

5. Spectres UV-vis et infrarouge pour les séries RuCl, $RuNO_2$ et RuNO 1-5

Les spectres UV-vis pour les complexes **RuCl** et **$RuNO_2$** ont été enregistrés qualitativement dans l'acétonitrile. Pour la série **RuNO** (**Fig. 4**) trois groupes de transitions ont également été identifiés. Une tendance vers des bandes plus intenses à haute énergie a été observée. Pour la bande (**a**), les complexes avec deux unités fluorényle, possèdent des maxima d'absorption décalés vers des valeurs plus basses

en énergie, et les complexes bimétalliques montrent des intensités significativement plus grandes.

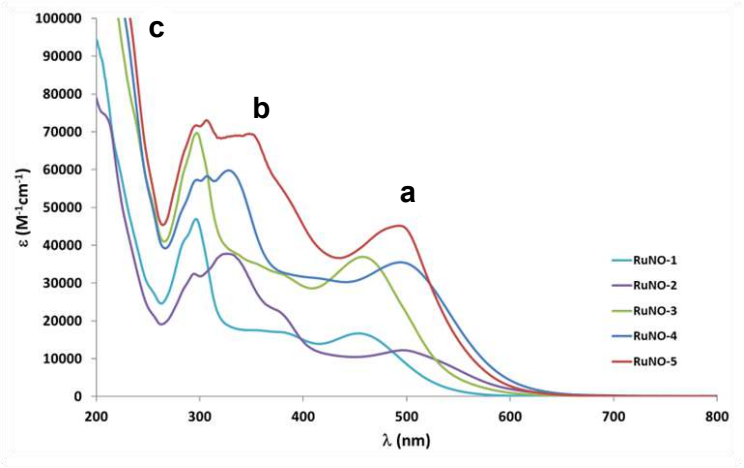

Compound	λ Max (nm)	Ɛ ($M^{-1}cm^{-1}$)
RuNO-1	453	16700
RuNO-2	497	12200
RuNO-3	457	37000
RuNO-4	494	35500
RuNO-5	493	45100

Figure 4. Spectres d'absorption UV-visible pour **RuNO-1** à **RuNO-5**, dans l'acétonitrile avec longueurs d'onde d'absorption maximales et coefficients d'extinction molaires.

Les spectres infrarouges (IR) ont également été mesurés pour la série **RuNO**. Les valeurs des bandes IR ν(NO) sont de 1942 cm^{-1} pour **RuNO-1**, 1938 cm^{-1} pour **RuNO-2**, 1940 cm^{-1} pour **RuNO-3**, 1937 cm^{-1} pour **RuNO-4** et 1934 cm^{-1} pour **RuNO-5**. Ce résultat montre que **L5** agit comme le meilleur ligand donneur d'électrons, comme on s'y attendait.

6. Molécules dipolaires et quadrupolaires pour TPA

Pour obtenir une réponse TPA accrue, les complexes **RuNO-1** et **RuNO-2** ont été synthétisés avec une architecture dipolaire (**Accepteur**-**Donateur**) (**Schéma 10**), tandis que les complexes **RuNO-3** à **RuNO-5** ont été conçus avec une architecture quadrupolaire (**Accepteur**-**Donateur**-**Accepteur**) (**Schéma 11**).

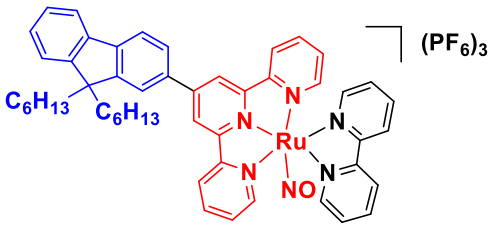

RuNO-1

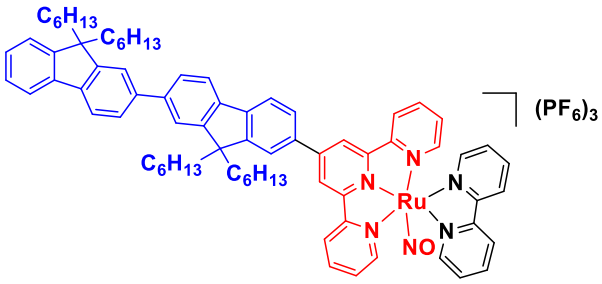

RuNO-2

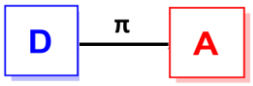

Schéma 10. Structure des complexes dipolaires (**Donateur**-**Accepteur**, **D**-**A**) pour **RuNO-1** et **RuNO-2.**

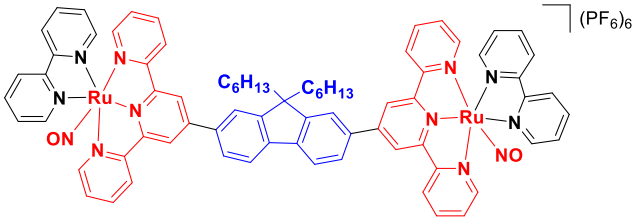

RuNO-3

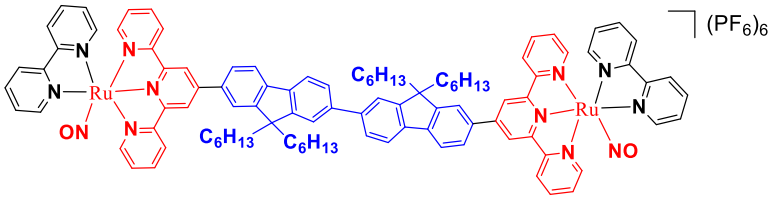

RuNO-4

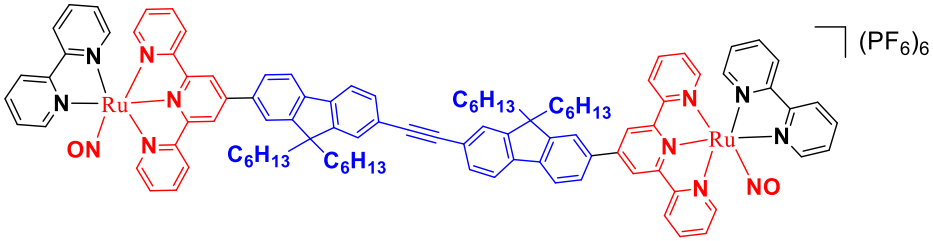

RuNO-5

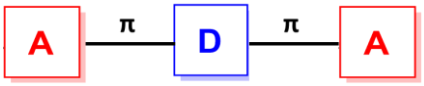

Schéma 11. Structure des complexes quadrupolaires (**Accepteur**-**Donateur**-**Accepteur**, **A**-**D**-**A**) pour **RuNO-3**, **RuNO-4** et **RuNO-5**.

La technique Z-Scan a été utilisée pour évaluer les propriétés TPA des molécules, car les complexes **RuNO** montrent une faible photoluminescence (PL) dans le domaine infrarouge. Le signal PL pour ces complexes est faible, rendant difficile l'obtention d'une valeur fiable de réponse TPA. Pour la méthode plus courante (TPEF) qui est basée sur l'étude de la photoluminescence.

7. Valeurs de la section efficace (σ_{TPA}) pour la série RuNO

Plusieurs facteurs influencent le processus TPA. Pour éliminer ces incertitudes, une substance de référence, la rhodamine B, a été utilisée. Les valeurs σ_{TPA} obtenues des expériences Z-Scan varient selon le complexe et la longueur d'onde incidente (**Tableau 1**). La symétrie des molécules affecte leurs propriétés optiques. **RuNO-1** et **RuNO-2** n'ont pas de symétrie, tandis que **RuNO-3** et **RuNO-4** possèdent la symétrie C2. **RuNO-5** est centrosymétrique, ce qui affecte ses transitions optiques. Les spectres TPA des complexes **RuNO** ne peuvent pas être prédits uniquement par leurs spectres d'absorption à un photon (OPA), d'où la nécessité d'explorations approfondies. Les résultats des expériences Z-Scan pour chaque longueur d'onde montrent une bonne stabilité pendant les expériences.

Tableau 1. Sections efficaces d'absorption à deux photons (σ_{TPA} en GM) pour les différents complexes de ruthénium nitrosyle.

	700 nm	**800 nm**	**850 nm**	**900 nm**	**950 nm**	**1000 nm**
RuNO-1	279 ± 39	115 ± 20	233 ± 50	62 ± 14	18 ± 4	34 ± 0.2
RuNO-2	662 ± 140	152 ± 13	421 ± 14	68 ± 19	34 ± 12	109 ± 18
RuNO-3	1182 ± 180	401 ± 40	452 ± 63	82 ± 24	37 ± 11	80 ± 14
RuNO-4	838 ± 250	185 ± 19	435 ± 70	87 ± 19	49 ± 18	200 ± 43
RuNO-5	1523 ± 98	309 ± 35	510 ± 63	103 ± 19	63 ± 25	229 ± 46

Des observations intéressantes ont été faites lors de l'analyse des spectres TPA des complexes **RuNO** à λ = 1000 nm. L'amplification des spectres peut être attribuée à la coïncidence entre l'énergie de deux photons infrarouges et la bande (**a**) détectée dans les spectres d'absorption OPA (**Fig. 4**). Les complexes ayant deux motifs

fluorènes montrent des valeurs de σ_{TPA} plus élevées comparativement à ceux ayant un seul motif.

Entre 950-800 nm, les complexes ayant une structure quadrupolaire montrent de plus hautes valeurs de σ_{TPA}, en particulier **RuNO-5** qui se démarque. À 850 nm, une autre amplification est observée, avec les complexes quadrupolaires ayant des valeurs σ_{TPA} maximales, suggérant que l'introduction d'un motif fluorène supplémentaire augmente les non-linéarités.

L'augmentation la plus significative des spectres σ_{TPA} est observée à 700 nm. Les spectres TPA sont regroupés **Figure 5**.

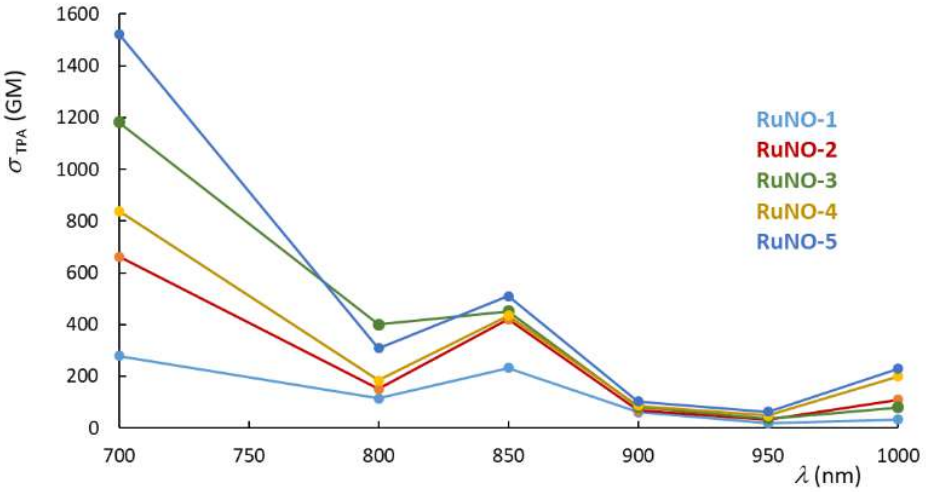

Figure 5. Spectres TPA pour les cinq complexes **RuNO** enregistrés dans l'acétonitrile à différentes longueurs d'onde incidentes.

L'étude des complexes de ruthénium a clarifié le processus TPA et son lien avec les règles de sélection de transition. Il est suggéré que les chromophores quadrupolaires présentent une meilleure efficacité TPA que les espèces dipolaires. L'intérêt se porte aussi sur la propriété moléculaire exprimée par unité de masse (σ_{TPA}/MW). Notamment, [**RuNO-5**]$^{6+}$ atteint une valeur de 0,88 GM.mol.g^{-1}, se rapprochant des records précédemment établis.

L'extension des spectres TPA à 600 nm a été entravée par la saturation d'absorption due aux processus OPA. Toutefois, entre 700-1000 nm, une telle compétition n'est pas observée.

8. Capacités de libération de NO• mesurées par Résonance Paramagnétique Électronique (RPE) et par le test de Griess

La formation de NO• pendant la photolyse a été confirmée par la résonance paramagnétique électronique (RPE). Les cinq complexes **RuNO** ont été étudiés dans l'acétonitrile. L'utilisation d'un piège à radical a conduit à la formation d'un complexe stable identifiable par RPE. Lors de la photolyse de la solution contenant le complexe **RuNO-3**, la formation de NO• a été observée uniquement sous irradiation. (**Fig. 6**).

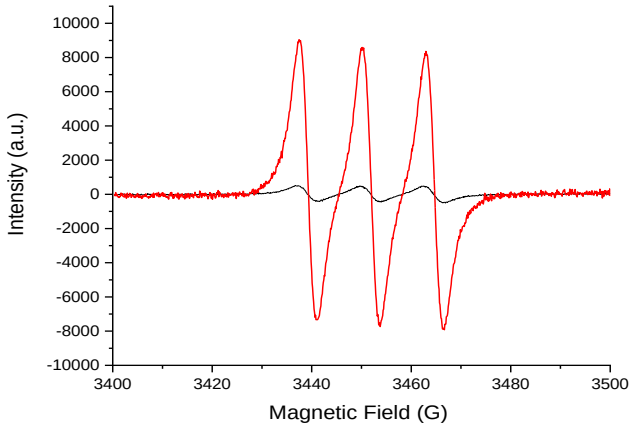

Figure 6. Signaux EPR triplet du NO• piégé par $[Fe(MGD)_2]$ pour **RuNO-3**.

Le test de Griess, qui se base sur la production d'un colorant azoïque, a attesté la formation de NO_2^- dans la solution, issu de la production puis de l'oxydation de NO•. Cette méthode a été utilisée pour tous les complexes **RuNO**. L'objectif est de confirmer la photodissociation des complexes Ru-NO à 490 nm, une longueur d'onde choisie pour son absorption importante. Les tests ont montré des différences marquées dans les spectres d'absorption avant et après irradiation.

9. Irradiation sous une longueur d'onde de 490 nm et synthèse des photoproduits finaux "C" et intermédiaire "B"

Après la confirmation de libération de NO•, l'expérience vise à confirmer la photodissociation des complexes **RuNO** à 490 nm. Cette longueur d'onde a été choisie car la bande la plus prometteuse, largement dominée par un fort transfert de charge fluorène $\rightarrow$ Ru(NO), se situe autour de 400–550 nm. Dans le cas des complexes bimétalliques, deux scénarios peuvent être envisagés : libération du NO· en une seule

étape ou en deux étapes. Les études pour calculer l'efficacité de la photolibération (Φ_{NO}) commencent avec les espèces monométalliques **RuNO-1** et **RuNO-2**. Dans ce cas, le model photocinétique **A** $\xrightarrow{\Phi_A}$ **C** est satisfaisant. Les complexes bimétalliques ont révélé des comportements plus complexes, comme la perte du point isosbestique, impliquant une photodissociation en deux étapes.

La synthèse des photoproduits **C** a été cruciale pour mieux comprendre cet effet et pouvoir faire la comparaison des produits finaux après l'irradiation. La première tentative de synthèse a utilisé de l'acide ascorbique comme agent réducteur, mais le protocole a dû être modifié pour obtenir les produits souhaités. Tous les photoproduits finaux ont été synthétisés avec succès en suivant le protocole montré dans le **Schéma 12**.

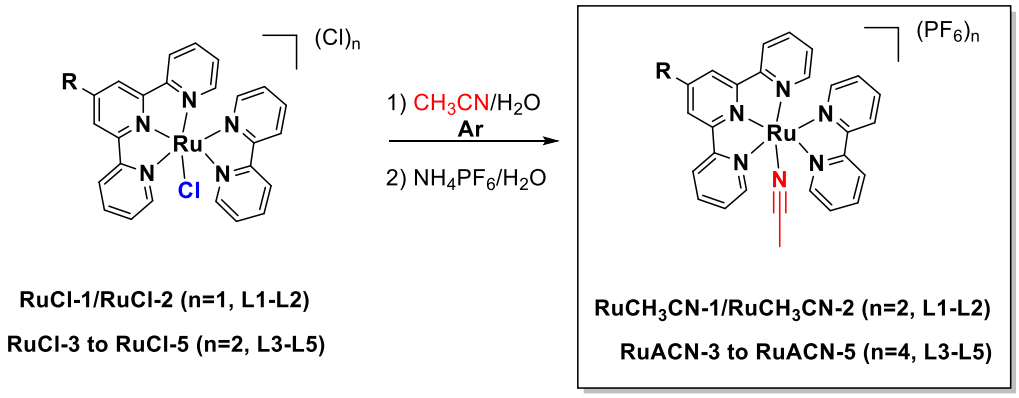

RuCl-1/RuCl-2 (n=1, L1-L2)
RuCl-3 to RuCl-5 (n=2, L3-L5)

RuCH$_3$CN-1/RuCH$_3$CN-2 (n=2, L1-L2)
RuACN-3 to RuACN-5 (n=4, L3-L5)

Schéma 12. Synthèse des photoproduits R**uCH$_3$CN-1** à **5** à partir de **RuCl-1** à **5**.

Le complexe **Ru(NO)CH$_3$CN-5** a été synthétisé en utilisant une séquence de réaction multi-étapes, comme indiqué dans les **Schéma 2**. Cette stratégie a été préférée au recours à l'intermédiaire **Ru(NO)CH$_3$CN-4**, en raison de la nécessité d'une réaction Suzuki-Miyaura, qui nécessite des températures plus élevées, pouvant affecter la stabilité du produit. Cette approche n'a pas été possible pour **RuNO-3**. Des analyses ^{1}H-NMR ont été effectuées pour prouver le succès de la synthèse des complexes

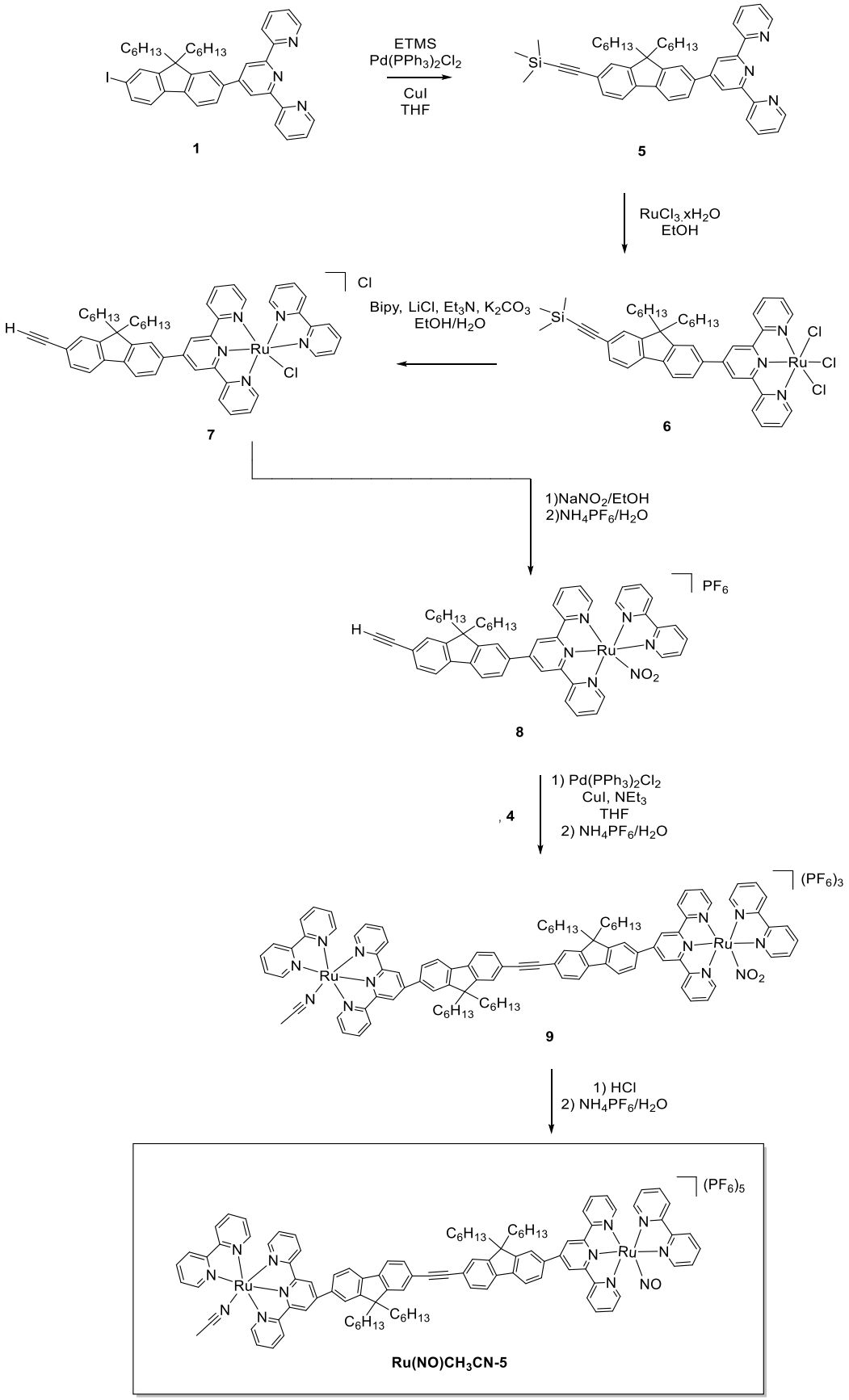

Schéma 2. Synthèse de l'intermédiaire souhaité **Ru(NO)CH$_3$CN-5.**

10. Spectres UV-vis des photoproduits C

Les spectres UV-Vis ont montré que les complexes monométalliques ont des coefficients d'extinction plus faibles que les bimétalliques. **RuNO-1** présente la valeur la plus basse, 20300 $M^{-1}.cm^{-1}$, tandis que les complexes bimétalliques possèdent des valeurs environ deux fois plus élevées. Parmi ceux-ci, **RuNO-3** a la valeur la plus basse, 53300 $M^{-1}.cm^{-1}$, et **RuNO-5** la plus élevée, 65100 $M^{-1}.cm^{-1}$.

Tableau 1. Coefficients d'extinction molaires (Ɛ) et maximum d'absorption (λ_{max}) pour la série de photoproduits **C** allant de **RuCH$_3$CN-1** à **RuCH$_3$CN-5** mesurées dans CH_3CN.

	Complexes	λ_{Max} in nm	Ɛ in $M^{-1}.cm^{-1}$
Monometallique	**RuCH$_3$CN-1**	471	20300
	RuCH$_3$CN-2	474	25100
Bimetallique	**RuCH$_3$CN-3**	478	53300
	RuCH$_3$CN-4	475	58700
	RuCH$_3$CN-5	475	65700

11. Calcul du rendement quantique de l'oxyde nitrique (Φ_{NO}) pour RuNO-1 et RuNO-2 à différentes longueurs d'onde

Les échantillons ont été étudiés dans l'acétonitrile pur et soumis à des irradiations de différentes longueurs d'onde. Une méthode informatique, Sa3.3, a permis d'analyser l'évolution de l'absorbance pour déterminer le rendement quantique de la réaction. L'expérience a été menée sur les cinq complexes différents. Les résultats montrent des variations distinctes des spectres d'absorption avant et après irradiation. Il est possible de déduire l'efficacité de libération du NO• à partir de deux modèles photocinétiques : en une seule étape, **A** $\overset{\Phi_A}{\longrightarrow}$ **C** pour les complexes monométalliques, et en deux étapes **A** $\overset{\Phi_A}{\longrightarrow}$ **B** $\overset{\Phi_B}{\longrightarrow}$ **C** pour les bimétalliques.

Les graphiques photocinétiques sont généralement similaires, mais les taux de réaction sont différents selon la longueur d'onde d'irradiation. La **Figure 7** montre comment le spectre d'absorption évolue pour **RuNO-1**. Des points isosbestiques sont observés, suggérant une conversion directe. Les résultats expérimentaux confirment l'exactitude du modèle photocinétique. Le complexe **RuNO-2** suit la même tendance que **RuNO-1**.

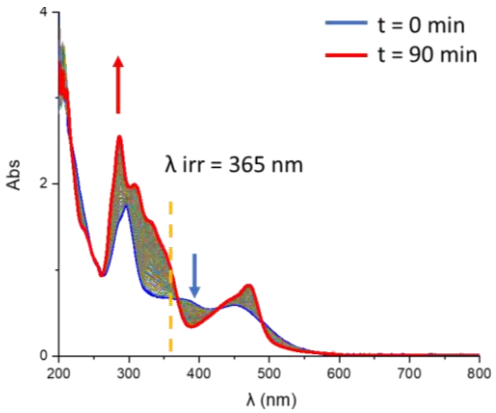

Figure 7. Évolution des spectres d'absorption pour **RuNO-1** à λ_{irr} = 365 nm.

12. Détermination du rendement quantique d'oxyde nitrique (Φ_{NO}) pour RuNO-3 et RuNO-5 à différentes longueurs d'onde

L'étude cinétique pour **RuNO-3** est basée sur des évolutions spectrales lors de quatre expériences à différentes longueurs d'onde. Les évolutions montrent des tendances qualitativement similaires. Le spectre final dans les expériences d'irradiation correspond au spectre obtenu par synthèse.

Bien que le composé intermédiaire **Ru(NO)CH_3CN-3** n'ait pas pu être synthétisé, sa présence durant le processus d'irradiation est manifestement observable dans les données spectrales.

Pour décrire pleinement le processus de photoréaction, il est nécessaire d'obtenir deux rendements quantiques ϕ_A^{λ} et ϕ_B^{λ} aux quatre longueurs d'onde d'irradiation. L'utilisation du programme conçu par la Pr. Véronique Pimienta nous a permis d'extraire ces données. Les courbes modèles correspondent parfaitement aux données expérimentales, comme illustré dans la **Figure 8**.

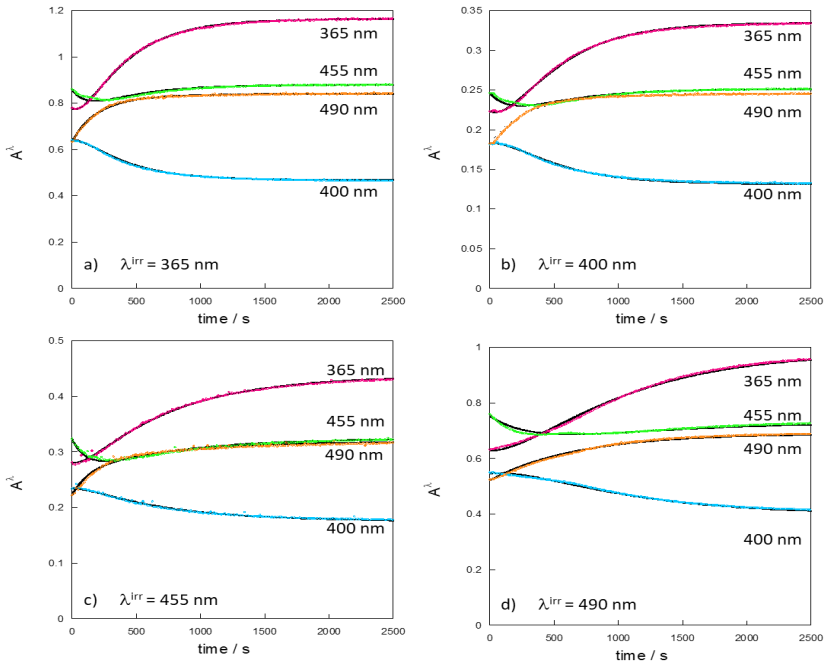

Figure 8. Évolution cinétique sous irradiation continue à a) λ_{irr} = 365 nm ; b) λ_{irr} = 400 nm ; c) λ_{irr} = 455 nm ; d) λ_{irr} = 490 nm de **RuNO-3**. Les symboles colorés représentent les points expérimentaux aux quatre longueurs d'onde, tandis que la ligne continue provient du modèle.

Les évolutions spectrales pour **RuNO-5**, ont été obtenues sous irradiation continue lors des quatre expériences distinctes. L'application de la même méthodologie pour les complexes **RuNO-5** et **RuNO-3** a été possible grâce la détermination du Φ_{NO} pour **Ru(NO)CH$_3$CN-5** à différentes longueurs d'onde.

13. Résultats globaux

Dans le **Tableau 2**, les valeurs de Φ_{NO} obtenues jusqu'à présent sont présentées. Dans le cas des complexes monométalliques, un seul modèle peut être appliqué. Pour les complexes bimétalliques, des valeurs en utilisant le modèle **A→C** ont également été obtenues à λ_{irr} = 490 nm, car la concentration de **B** est la plus faible parmi les différentes longueurs d'onde d'irradiation. La valeur la plus élevée obtenue est pour **RuNO-5** avec $\Phi_{B\ 365}$ = 0.090 et pour le même complexe $\Phi_{A\ 455}$ ayant la même valeur. Dans le premier cas, comme $\Phi_{B\ 365} > \Phi_{A\ 365}$, le complexe **B** est consommé rapidement pour générer **C**, tandis que dans le second cas, il y a une accumulation de **B** car $\Phi_{A\ 455} > \Phi_{B\ 455}$.

Tableau 2. Φ_{NO} en GM à différentes longueurs d'onde d'irradiation dans l'acétonitrile pour les complexes **RuNO-1-5**.

Complexe	Modele	365 nm		400 nm		455 nm		490 nm	
RuNO-1	A→C	0.0084		0.0062		0.0024		0.0024	
RuNO-2	A→C	0.0120		0.0085		0.0068		0.0024	
RuNO-3	A→C	-		-		-		0.0039	
	A→B→C	0.029	0.018	0.019	0.070	0.019	0.040	0.006	0.005
RuNO-4	A→C	-		-		-		0.0030	
	A→B→C	0.015	0.020	0.080	0.020	0.060	0.10	-	-
RuNO-5	A→C	-		-		-		0.0038	
	A→B→C	0.028	0.090	0.022	0.080	0.090	0.050	0.080	0.050

14. Conclusion

L'étude a mis l'accent sur la recherche de **RuNO** pour la libération de NO• sous irradiation. La découverte de complexes bimétalliques avec des valeurs de σ_{TPA} dépassant 1500 GM est prometteuse pour la thérapie photodynamique.

La détermination du rendement quantique pour les différents complexes a révélé des comportements distincts en fonction des complexes et des longueurs d'onde d'irradiation. Alors que les complexes monométalliques montrent une conversion directe, les complexes bimétalliques nécessitent une approche en deux étapes pour la photodissociation.

RuNO-5 est particulièrement remarquable, car il présente des rendements quantiques élevés et une adaptabilité selon la longueur d'onde d'irradiation. De plus, l'évaluation de l'efficacité réelle de la photoréaction a révélé que **RuNO-5** est le candidat le plus prometteur pour des applications potentielles.

14. Perspective

Les résultats observés avec les complexes **RuNO-3** et **RuNO-5** soulignent le besoin de modifications dans le ligand bipyridine, pour pouvoir faire des tests *in vitro*. Malgré l'attrait des voies de transfert de charge de la 2,2'-bipyridine, ces complexes nitrosyl de ruthénium peuvent convertir le ligand nitrosyle en nitrite en milieu aqueux et peuvent être toxiques pour les cellules. Par conséquent, la synthèse des séries trans, trans-Ru(NO)Cl(OH)-n apparaît comme une alternative prometteuse.

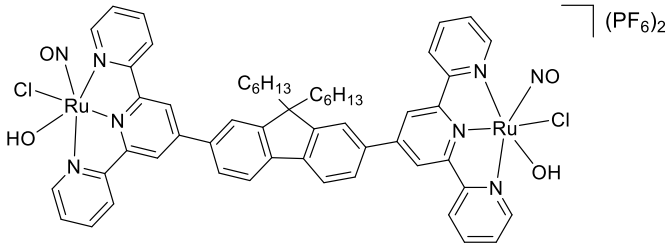

Figure 9. Structure du **trans-Ru(NO)Cl(OH)-3.**

Abstract

Dipolar and quadripolar ruthenium nitrosyl complexes with enhanced two-photon absorption for nitric oxide delivery: syntheses and mechanism

Nitric oxide (NO•) is important for its biological functions. In this context, photoreactive ruthenium nitrosyl complexes are of special interest because they can release nitric oxide under controlled excitation. In our group, Two Photon Absorption (TPA) materials are considered because it circumvents the main shortcomings that the nitric oxide is released out of the therapeutic window (700 – 1100 nm). The analyses presented in this thesis represent our current understanding and progress in TPA and photokinetic on **RuNO** compounds. ***Chapter I*** delves into how NO• has therapeutic potential, emphasis is placed on Photodynamic Therapy (PDT) and Photoactivated Chemotherapy (PACT) as innovative solutions against cancer and microbial infections. Additionally, the work explores nonlinear optics, focusing on conjugation, dipolar structures, and quadrupolar structures, elucidating their importance in TPA processes. In ***Chapter II***, two types of molecular design containing [**Fluorene-Terpyridine-Ru(bipyridine)(NO)**] (**RuNO-1**) as the benchmark reference are synthetized and characterized: dipolar structures (**RuNO-1 and 2**) where the "push-pull" effect determines the ability to get a good TPA response and quadrupolar structures (**RuNO-3** to **5**). The Z-scan analysis at different wavelengths of the comparative dipolar and multipolar chromophores is presented. ***Chapter III*** explores the release capacities of NO• from **RuNO** complexes upon irradiation. Also, it is examining the photoresponse of these complexes at a different wavelength of irradiation. Through various analyses, it is observed that monometallic complexes show direct conversion following **A**→**C** mechanism, while bimetallic complexes have a two-step photodissociation **A**→**B**→**C**. With synthesis of one intermediate **B** and final photoproduct **C** it was possible to extract the nitric oxide quantum yield (Φ_{NO}). In ***Chapter IV*** we discussed on how **RuNO-3** complex is one of the most appealing compounds for PACT, but modifications are required for *in vitro* testing due to the instability in aqueous environments. As a solution, the synthesis of **trans, trans-Ru(NO)Cl(OH)-3** is suggested.

Résumé

Photolibération de NO et absorption à deux photons remarquable dans des complexes dipolaires et quadripolaires de ruthénium à ligand nitrosyle : synthèses et mécanismes

Le monoxyde d'azote (NO•) est important pour ses fonctions biologiques. Dans ce contexte, les complexes de ruthénium à ligand nitrosyle (**RuNO**) photoréactifs suscitent un intérêt particulier car ils peuvent libérer du monoxyde d'azote sous une excitation contrôlée. Dans notre groupe, les matériaux à Absorption Biphotonique (TPA) sont considérés car ils contournent les principaux inconvénients liés à la libération du NO• en dehors de la fenêtre thérapeutique (700 – 1100 nm). Les analyses présentées dans cette thèse font état de notre compréhension actuelle et de notre progression dans le domaine de l'absorption à deux photons et de la photocinétique des complexes **RuNO**. Le ***Chapitre I*** explore le potentiel thérapeutique du NO• sur la Thérapie Photodynamique (PDT) et la Chimiothérapie Photoactivée (PACT) comme solutions innovantes contre le cancer et les infections microbiennes. De plus, le travail explore l'optique non linéaire, la conjugaison, les structures dipolaires et quadrupolaires, élucidant leur importance dans les processus TPA. Dans le ***Chapitre II***, deux complexes moléculaires contenant le fragment **[Fluorène-Terpyridine-Ru(bipyridine)(NO)]** (**RuNO-1**) sont synthétisés et caractérisés : Les structures dipolaires (**RuNO-1** et **2**) où l'effet "push-pull" détermine la capacité à obtenir une bonne réponse TPA et les structures quadrupolaires (**RuNO-3** à **5**). L'analyse par Z-scan à différentes longueurs d'onde est présentée. Le ***Chapitre III*** explore les capacités de libération du NO• à partir des complexes **RuNO** lors de l'irradiation. Il examine également la photo-réponse de ces complexes à différentes longueurs d'onde d'irradiation. À travers diverses analyses, on observe que les complexes monométalliques montrent une conversion directe suivant le mécanisme **A**→**C**, tandis que les complexes bimétalliques ont une photodissociation en deux étapes **A**→**B**→**C**. Avec la synthèse d'un intermédiaire **B** et les photoproduits finaux **C**, il a été possible d'extraire le rendement quantique du monoxyde d'azote (Φ_{NO}). Dans le ***Chapitre IV***, nous nous focalisons sur le complexe **RuNO-3** qui est l'un des composés les plus prometteurs en PACT mais des modifications sont nécessaires pour les tests *in vitro* en raison de l'instabilité dans les environnements aqueux. Le complexe **trans, trans-Ru(NO)Cl(OH)-3** est obtenu et ses propriétés étudiées.